# The Josephson effect in superconductors and quantum gases

Nicolas Didier

## To cite this version:

Nicolas Didier. The Josephson effect in superconductors and quantum gases. Condensed Matter [cond-mat]. Université Joseph-Fourier - Grenoble I, 2009. English. NNT : . tel-00459413

HAL Id: tel-00459413
https://theses.hal.science/tel-00459413

Submitted on 23 Feb 2010

**Thèse**

*présentée par*

**Nicolas DIDIER**

*pour obtenir le grade de*

**Docteur de l'Université Joseph Fourier – Grenoble I**

Spécialité : **Physique**

# THE JOSEPHSON EFFECT
# IN SUPERCONDUCTORS AND QUANTUM GASES

*Thèse préparée au*

**Laboratoire de Physique et de Modélisation des Milieux Condensés**

*sous la direction de*

Frank W. J. HEKKING et Anna MINGUZZI

*Soutenue publiquement le*

**Mardi 24 novembre 2009**

*Composition du jury :*

| | | | |
|---|---|---|---|
| Mr | Alain JOYE | Institut Fourier, Grenoble | Président du jury |
| Mr | Christoph BRUDER | Université de Bâle, Suisse | Rapporteur |
| Mr | Benoit DOUÇOT | LPTHE, Paris | Rapporteur |
| Mr | Leonid I. GLAZMAN | Université de Yale, États-Unis | Examinateur |
| Mr | Yaroslav M. BLANTER | Université de Delft, Pays-Bas | Examinateur |
| Mr | Frank W. J. HEKKING | LPMMC, Grenoble | Directeur de thèse |
| Mme | Anna MINGUZZI | LPMMC, Grenoble | Co-directrice de thèse |

*À mes Grands-Parents*

*“Rien ne se fait sans un peu d’enthousiasme.”*
VOLTAIRE

# Remerciements

Le LPMMC m'a ouvert ses portes il y a maintenant quatre ans, lorsque j'étais à la recherche d'un stage mettant en œuvre la Mécanique Quantique. Les sujets de recherche proposés par Frank Hekking sur les nanocircuits supraconducteurs m'ont immédiatement séduit. Je le remercie sincèrement de m'avoir fait confiance, j'ai pris beaucoup de plaisir à travailler à ses côtés. Ses qualités pédagogiques, reconnues par les étudiants grenoblois, alliées à sa compréhension de la physique en font un encadrant exceptionnel. J'ai apprécié tout particulièrement la liberté dans le choix des projets. C'est ainsi que j'ai pu également travailler avec Anna Minguzzi sur les gaz quantiques. Cela a été une expérience passionnante, je tiens à la remercier pour son optimisme et son efficacité. Lors de cette thèse, j'ai pu profiter de leur entourage pour collaborer avec des chercheurs théoriciens et expérimentateurs d'exception. Je tiens à remercier tout d'abord Alex Zazunov, auprès de qui j'ai énormément appris, mais également Fabio Taddei, Yaroslav Blanter, Roberta Citro et Leonid Glazman. L'intérêt de cette thèse a aussi été de confronter nos résultats aux expériences. Je remercie le groupe de Cohérence Quantique de l'Institut Néel, notamment Wiebke Guichard et Olivier Buisson ainsi que Emile Hoskinson, Aurélien Fay et Florent Lecocq pour toutes leurs suggestions. Je remercie également le groupe Quantronique, en particulier Patrice Bertet, Daniel Estève et Denis Vion, de m'avoir accueilli, ce fut un séjour très enrichissant. J'espère prolonger cette interaction dans les années à venir. Enfin, je tiens à remercier Rosario Fazio pour son invitation à visiter le groupe de Transport et Information Quantique à la Scuola Normale Superiore de Pise. Je suis très honoré d'y commencer un postdoc.

Je remercie Alain Joye d'avoir présidé le jury de thèse, Christoph Bruder et Benoit Douçot d'avoir examiné mon manuscrit, Leonid Glazman et Yaroslav Blanter d'avoir participé au jury. Leurs commentaires m'ont été précieux.

Tout au long de la thèse, j'ai pris beaucoup de plaisir à enseigner à l'Université de Grenoble. Je remercie Monique Giroud, Claudine Chaffy, Éric Fontenas et Sylvie Rozier de m'avoir épaulé.

Je remercie Frédéric Peyret mon tout premier professeur de Physique, avec qui j'ai pris goût pour la science, d'être venu à ma soutenance. Je remercie aussi Pierre Panine de m'avoir fait découvrir la recherche scientifique, je garde ses conseils en mémoire.

Je remercie l'ensemble du LPMMC pour l'ambiance agréable qui y règne, à l'image de Bart Van Tiggelen son directeur. Un grand merci à Françoise Berthoud et Jean-Daniel Dubois pour leur soutien informatique, Michèle Peretto, Emmanuelle Gennai, Julie Farrugia, Laurence Magnino et Sandrine Ferrari du secrétariat.

C'est avec Sébastien Labarthe, Timothée Kouriba et Sébastien Kawka que nous avons inauguré la salle de lecture 1 de la Maison des Magistères. Nous ont ensuite rejoint Nicolas PAUGET et Nicolas CHERRORET puis Giulia FERRINI. Je remercie en particulier Seb pour ses bonnes idées de pause, Nico pour ses talents gastronomiques et Giulia pour toutes ces discussions toujours trop courtes mais ô combien intéressantes. L'atmosphère y a été chaleureuse et il m'a été difficile de la quitter. Je suis toutefois rassuré par la relève, assurée par Arthur GOETSCHY, Vladimir FEDOROV et Christoph SCHENKE. Je leur souhaite à tous la réussite dans leurs recherches.

Je remercie aussi mes amis "grenoblois" pour toutes ces soirées mémorables. Sébastien, Jérémy et Anne ne manquaient jamais à l'appel. Cela a été un grand plaisir de rencontrer les Génois expatriés, merci à Giulia, Alessandro et Carlotta pour leur hospitalité. Un joyeux merci à Guillaume pour les virées sur la route de la bière à vélo. C'était toujours agréable de retrouver les anciens de Champo comme Sébastien, Hugo et Jérémy ainsi que Matthieu et Christophe du côté de Paris. Les week-ends aussi étaient bien remplis sur Chambéry. Je remercie tout particulièrement Guillaume et Julien, mes amis d'enfance, mais aussi Manu, Micka, Martin et Julie.

Mes remerciements vont enfin à toute ma famille, venue en nombre à la soutenance. Je remercie tout d'abord mes grands-parents, qui sont depuis toujours un modèle et auprès de qui je peux me ressourcer. Un grand merci à mes parents, dont l'aide a été sans faille, spécialement pour le pot Savoyard-sized. Un clin d'œil aux cousin(e)s, c'est toujours un plaisir de se retrouver. Je remercie Floriane pour son soutien, elle est ma plus grande fierté.

*Pise, Novembre 2009.*

# Introduction

The behavior of physical systems at the atomic scale is governed by *Quantum Mechanics*, giving rise to surprising phenomena. At very low temperature, notably, the energy of the system is reduced and only a few number of quantum states are involved in the dynamics. As physicists understood the magic of electrons and photons in the beginning of last century, they wondered if their exciting characteristics could appear at a macroscopic scale. With the progress of both theoretical and experimental research, physicists realized that quantum physics can be seen with the naked eye in superconductors, superfluids, or Bose-Einstein condensates, where the quantum states stretch on large distances. About sixteen Nobel prizes rewarded these breakthroughs, among the dozens of awarded physicists we can cite John Bardeen, Leon Neil Cooper, and John Robert Schrieffer in 1972, Ivar Giaever and Brian David Josephson in 1973 for the understanding of superconductivity and the Josephson effect; Steven Chu, Claude Cohen-Tannoudji, and William D. Phillips in 1997, Eric A. Cornell, Wolfgang Ketterle, and Carl E. Wieman in 2001 for the manipulation of cold atoms and the realization of Bose-Einstein condensates. Richard P. Feynman was the first to foresee the development of nanotechnology and the practical application of systems which involve strictly the Schrödinger equation. With the technical advances of nanofabrication and laser cooling of the last decade, superconducting circuits as well as Bose Einstein condensates are now commonly created, manipulated and measured in research laboratories.

The possibility to build a quantum computer has attracted a lot of attention since the discovery of macroscopically coherent systems. Among the most promising building blocks of such computers, the equivalent to transistors in classical computers, is the Josephson junction-based quantum bit (*qubit*). They are composed of two or more Josephson junctions with a dynamics reduced to two states, the ground state and the first excited state, which serve as a bit to treat the information. Coupling many qubits and using quantum entanglement would exponentially speed up data processing. Charge qubits, flux qubits and phase qubits have been realized and coupled but the finalization of a quantum computer remains highly challenging. The limitation comes mainly from the decoherence and dissipation of the superconducting nanocircuits due to their unavoidable coupling with the environment, which decreases the lifetime of the quantum states. The attempts to fight against noise remain intense and the coherence time of superconducting qubit is continuously increasing. The experimental progress in the fabrication of nanocircuits happened basically at the time of advances in laser cooling and trapping of alkali atoms. Since cold atoms are highly tunable and quasi-isolated from the environment, they constitute excellent quantum simulators of solid states systems.

The possibility to integrate Bose Einstein condensates and couple them to superconducting systems, for instance with the on-chip technique, is an active field of research. The exchange of ideas between these two communities is very profitable and rich physics is expected to follow from this collaboration.

The aim of this Ph.D. thesis is to study theoretically a few mesoscopic systems which exhibit interesting quantum phenomena with potentially new applications. In close collaboration with experimentalists we explore the quantum, playing with electrons and atoms to observe appealing features. We focus on one of the most outstanding exclusive peculiarities of the quantum world, namely the tunneling effect. When the tunneling occurs between two macroscopically coherent systems, it is often called the *Josephson effect*. The manuscript comprises one general chapter on the Josephson effect followed by four chapters, each one being dedicated to a specific system and completed by an appendix which details the calculations.

The first chapter presents the Josephson effect between two general coherent systems. The specificities of superconductors and cold atoms are then described.

In the second chapter we study a single *underdamped* Josephson junction that was realized experimentally by Wiebke Guichard in the group of David Haviland at the KTH royal institute of technology in Stockholm. Within the Keldysh formalism, we obtain the current-voltage characteristics in the classical and zero temperature regime as well as the quantum Smoluchowski equation that describes the first quantum corrections to the quasicharge dynamics.

In the third chapter we use the instanton formalism to calculate the escape rate from a metastable state of a quartic potential, which we call the *camel back potential*. This barrier shape was realized experimentally with a dc SQUID by Emile Hoskinson in the group of Olivier Buisson at the Néel institute in Grenoble. Beforehand, simulations were analyzed to find an optimal line where the SQUID is weakly sensitive to current noise. Our results fit well the experimental data concerning the escape probability histograms and the critical diagram. The optimization of the SQUID parameters as well as the working points enabled us to manipulate the circuit as a phase qubit. This work was part of the "European Superconducting Quantum Information Processor" (EuroSQIP) European integrated project (for a review, see Ref. [1]).

In the fourth chapter we study the *lasing effect* for a qubit coupled to cavities. We use the Lindblad master equations to describe quantum mechanically the system and derive the output spectrum. We concentrate first on the pioneer experiment of the group of Jaw-Shen Tsai at Riken laboratory in Tokyo. We then analyze the configuration where a transmon is coupled to two cavities, one cavity were the lasing effect occurs and another one which controls the relaxation rate of the upper transition according to the Purcell effect. This experiment of cavity QED will be realized in the Quantronics group of Daniel Estève at CEA Saclay. This work is part of the "Quantum Physics with Josephson Circuits" (QUANTJO) French National Research Agency project.

The fifth chapter is devoted to the Josephson effect in cold atoms. We consider a one dimensional ring comprising a localized barrier potential that creates a *Bose Josephson junction*. We use the Luttinger liquid formalism to characterize the long range order through the one-body density matrix and various spatial correlation functions. The subleading corrections to the one-body density matrix in the thermodynamic limit for arbitrary interaction strength are also found. Compared to the exact result in the Tonks Girardeau gas, our treatment turns out to generate the complete series of the leading corrections. The realization of such one-dimensional systems with cold atoms, known in the condensed matter community, is currently investigated in several groups in Europe and America. This work is part of the “Macroscopic Interference Devices for Atomic and Solid-State Systems: Quantum Control of Supercurrents” (MIDAS) European project.

All along the manuscript, we study the Josephson effect in more and more sophisticated systems. We start with a single Josephson junction in a an unusual domain of parameters. We then combine two Josephson junctions to create a dc SQUID phase qubit in the “camel back” regime. Next, a qubit is coupled to one or two cavities to give rise to the lasing phenomenon. Finally a Bose Josephson junction, created with a quantum gas confined to a ring shape potential with a localized barrier, is investigated. The chapters are independent and have their own notations, as a consequence the meaning of a given symbol may change from chapter to chapter.

The manuscript ends with a general conclusion together with a presentation of the projects that stem from this thesis. This work fits into our present exciting times where physicists profit more and more from the beauty of quantum mechanics.

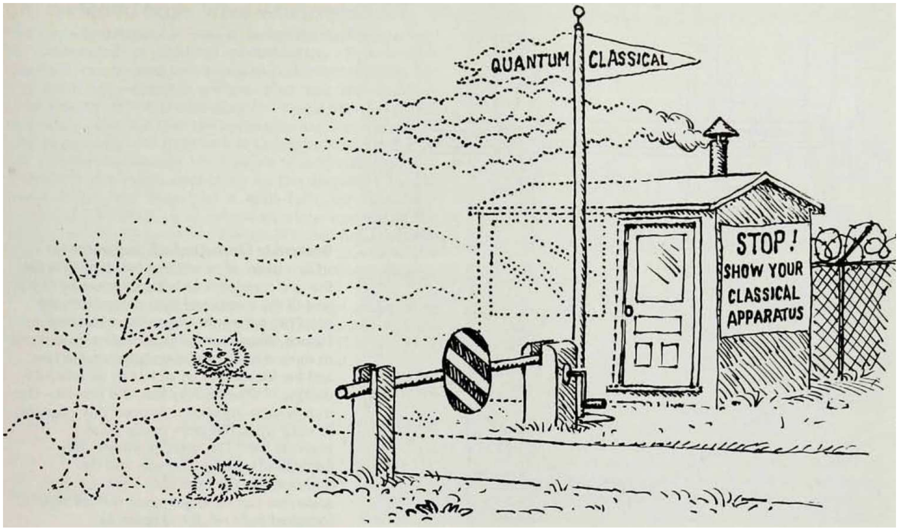

Figure 1: Scheme of the border between the classical and quantum worlds, from [2].

# Contents

Chapter 1

# The Josephson effects

## Contents

## Introduction

In this first chapter we introduce the Josephson effect and present the physical consequences of this phenomenon. We start from a phenomenological approach to describe the general case of two coupled macroscopically phase-coherent systems and then illustrate how the Josephson effects manifest themselves in two different physical systems: BCS superconductors and atomic quantum gases. The study is completed with a quantum treatment of the Josephson effect using a model tunnel Hamiltonian. Finally, we highlight the differences and similarities among these two systems by comparing their characteristic physical scales.

## 1.1 Semiclassical Josephson effect

Let us consider two quantum coherent systems, labelled by $S_{j=1,2}$, characterized each by a macroscopic wavefunction $\Psi_{j=1,2}(\vec{r},t)$. We focus on the case where the two systems are weakly connected, namely when $\Psi_1(\vec{r},t)$ can leak into $S_2$ and vice versa. To study the dynamics of the coupling between the two systems, the spatial degrees of freedom of the wavefunctions can be integrated out. Then the time-dependent Schrödinger equation for the resulting wavefunctions $\psi_j(t)$ corresponds to (see [3, 4] and Sec. 1.3)

$$i\hbar\frac{\partial\psi_1}{\partial t} = \mathcal{E}_1\psi_1 - \mathcal{T}\psi_2, \tag{1.1a}$$

$$i\hbar\frac{\partial\psi_2}{\partial t} = \mathcal{E}_2\psi_2 - \mathcal{T}\psi_1, \tag{1.1b}$$

where $\mathcal{E}_{1,2}$ is the energy of each isolated system and where the parameter $\mathcal{T}$ characterizes the leakage. One may think of two systems separated by a barrier. In this specific case, $\mathcal{T}$ corresponds to the tunneling strength and depends on the shape of the barrier potential. Writing the wave function in terms of the number of particles $n_j = |\psi_j|^2$ and the phase $\varphi_j$, we have $\psi_j = \sqrt{n_j}\,\mathrm{e}^{i\varphi_j}$. The Schrödinger equations (1.1) give

$$\frac{\partial n_2}{\partial t} = -\frac{\partial n_1}{\partial t} = \frac{2\mathcal{T}}{\hbar}\sqrt{n_1 n_2}\,\sin(\varphi_2 - \varphi_1), \tag{1.2a}$$

$$\frac{\partial\,(\varphi_2 - \varphi_1)}{\partial t} = \frac{\mathcal{E}_2 - \mathcal{E}_1}{\hbar} + \frac{\mathcal{T}}{\hbar}\frac{n_1 - n_2}{\sqrt{n_1 n_2}}\cos(\varphi_2 - \varphi_1). \tag{1.2b}$$

In the case of small particle number imbalance, $|n_1 - n_2|/(n_1 + n_2) \ll 1$, the dynamical equations for the particle current $J = (\dot{n}_1 - \dot{n}_2)/2$ and for the phase difference $\varphi = \varphi_2 - \varphi_1$ are

$$J = J_0 \sin\varphi, \tag{1.3a}$$

$$\dot{\varphi} = \mathcal{V}, \tag{1.3b}$$

where $J_0 = 2\mathcal{T}\sqrt{n_1 n_2}/\hbar$ and $\mathcal{V} = (\mathcal{E}_2 - \mathcal{E}_1)/\hbar$. These are the constitutive equations for the Josephson effect, predicted in 1962 by Brian David Josephson in the case of two coupled superconductors (see [5, 6] and Sec. 1.2). Eqs. (1.3) show that a particle current flows through the Josephson junction with a maximal value $J_0$ proportional to the tunneling strength. The Josephson current being proportional to $\sin\varphi$, it is essential that the phase difference $\varphi$ be well established.

The Josephson junction displays surprising effects when the energy imbalance $\mathcal{V}$ can be controlled and eventually modulated in time. From Eqs. (1.3), the Josephson current has the general expression

$$J(t) = J_0 \sin\left(\varphi_0 + \int^t \mathrm{d}\tau\,\mathcal{V}(\tau)\right). \tag{1.4}$$

When the energies are the same on the two electrodes, $\mathcal{V} = 0$, due to the phase coherence a constant current $J = J_0 \sin\varphi_0$ flows through the junction. This phenomenon is known as the dc Josephson effect.

When a constant energy difference $\mathcal{V}_0$ is imposed, the phase grows linearly and the current oscillates with the frequency $\mathcal{V}_0$ and the amplitude $J_0$: $J(t) = J_0 \sin(\varphi_0 + \mathcal{V}_0 t)$. This phenomenon is known as the ac Josephson effect. The time-averaged current $\langle J(t)\rangle$ vanishes except for $\mathcal{V}_0 = 0$ and the resulting graph $\langle J\rangle(\mathcal{V}_0)$ has a finite central peak of height $J_0$. This defines the particle supercurrent branch.

When the applied energy imbalance oscillates with a frequency $\omega$, *i.e.* $\mathcal{V}(t) = \mathcal{V}_0 + v\cos\omega t$, then the current reads

$$J = J_0 \sum_{k\in\mathbb{Z}} \mathrm{J}_k(v/\omega)\,\sin(\varphi_0 + \mathcal{V}_0 t + k\omega t), \tag{1.5}$$

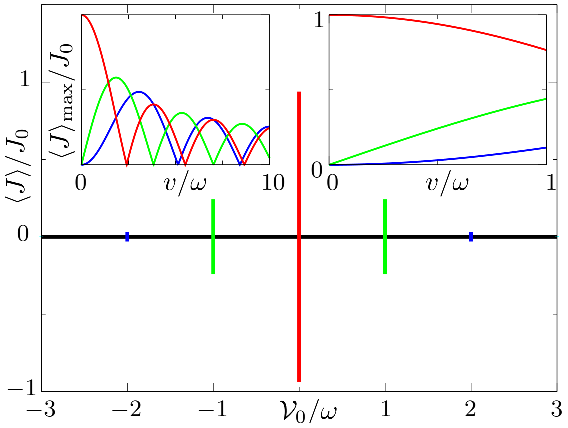

Figure 1.1: Time-averaged particle current through the junction as a function of the energy imbalance (in units of the frequency) for $v = \omega/2$. *Insets:* Maximum current for $\mathcal{V}_0 = 0$ (red), $\mathcal{V}_0 = \omega$ (green) and $\mathcal{V}_0 = 2\omega$ (blue) as a function of the amplitude of the oscillations (in units of the frequency). The right inset is a zoom of the left one for small values of the oscillation amplitude. When the energy imbalance is constant ($v = 0$), there is only the supercurrent peak.

where $\mathrm{J}_k$ is a Bessel function and the relation $\mathrm{e}^{\frac{z}{2}\left(t-\frac{1}{t}\right)} = \sum_{k\in\mathbb{Z}} \mathrm{J}_k(z)t^k$ has been used. The time-averaged current vanishes except for values of $\mathcal{V}_0$ which are multiples of the frequency: $\mathcal{V}_0 = k_0\omega$. At this value, the current is $J = J_0 \sin\varphi_0\, \mathrm{J}_{-k_0}(v/\omega)$. As a consequence, for the special values $\mathcal{V}_0 = k_0\omega$ the inequality

$$|J/J_0| \le |\mathrm{J}_{k_0}(v/\omega)| \tag{1.6}$$

holds, and the time- and configuration-averaged current shows steps of width $2|\mathrm{J}_{k_0}(v/\omega)|$ (see Fig. 1.1). They are called Shapiro steps after their discovery in superconductors by Sidney Shapiro [7]. The use of the Josephson effects gives rise to a rich variety of applications.

## 1.2 The superconducting Josephson junction

Until now we have treated the general case of two coupled macroscopically phase-coherent systems. In the following we will look at the Josephson effects in specific physical systems, starting with the BCS superconductors in which these phenomena were first discovered.

In such metals, in addition to the repulsive Coulomb force, electrons are coupled to phonons originating from lattice vibrations [8, 9]. Below a critical temperature $T_c$, the electron-electron interaction via phonons is attractive and a two-electron bound state becomes energetically favorable. The attractive interaction renders the Fermi sea unstable and electrons group themselves in pairs to form Cooper pairs [10]. The Cooper pairs behave in many senses like bosons and condense at temperature lower than $T_c$, giving rise to a macroscopically occupied coherent state. This is the so-called BCS state, named after the microscopic theory of superconductivity by John Bardeen, Leon Neil Cooper and John Robert Schrieffer in 1957 [11, 12]. The condensation energy is found to be equal to $-g(E_F)\Delta^2/2$ where $g(E)$ is the electronic density of states, $E_F$ is the Fermi energy and $\Delta$ is the BCS order parameter, which vanishes at the critical temperature as

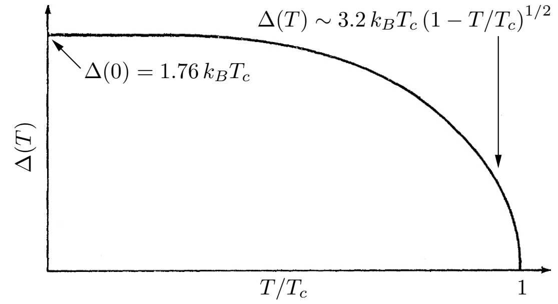

Figure 1.2: Temperature dependence of the order parameter $\Delta$ in BCS superconductors.

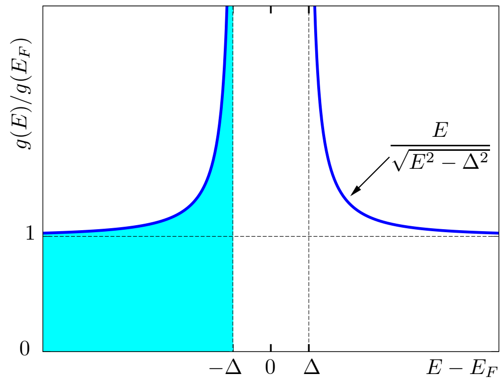

Figure 1.3: Density of states of quasiparticles of a superconductor. Cooper pairs condense at the energy $E_F - \Delta$.

depicted in Fig. 1.2 (in metals $\Delta \ll E_F$ and $E_F - g(E_F)\Delta^2/2 \simeq E_F$). The first excited states correspond to breaking a pair, which at least needs an energy of $2\Delta$. These excitations are called (Bogoliubov) quasiparticles [13]. At the level of the density of states, the paring opens a gap of width $2\Delta$ around the Fermi energy, as depicted in Fig. 1.3.

In 1962, Brian David Josephson predicted that if two superconducting samples are put into contact, a supercurrent

$$I_S = I_c \sin\varphi, \tag{1.7}$$

can flow across them, even in the absence of a voltage difference (dc Josephson effect, as presented in the previous section) [5]. Here $I_c$ is the critical current of the junction. Moreover, he predicted that if a voltage difference $V$ is applied between the two samples, this will result in an alternating current (ac Josephson effect) [6] according to the phase dynamics

$$\dot{\varphi} = \frac{2e}{\hbar}V. \tag{1.8}$$

Josephson obtained Eqs. (1.7) and (1.8) from the BCS theory. His microscopic derivation (which I do not detail here) gives the same results Eqs. (1.3) as the phenomenological description of Sec. 1.1. The system composed of two superconducting samples in weak electrical contact constitutes the superconducting Josephson junction (SJJ) (see Fig. 1.4). The two Josephson effects have been experimentally observed for the first time

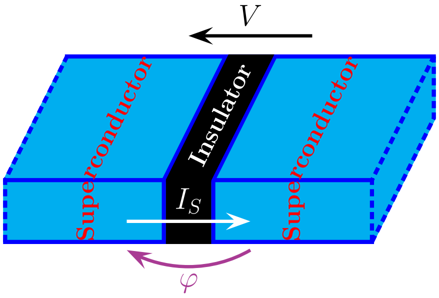

Figure 1.4: A schematic representation of a superconducting Josephson junction. Two superconducting electrodes are connected to each other via an insulating layer.

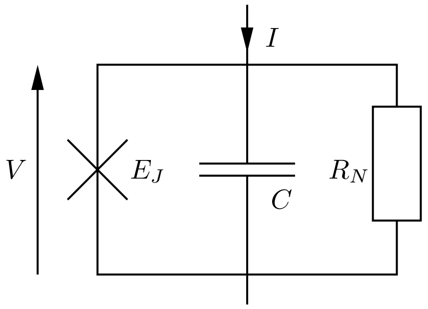

Figure 1.5: RCSJ model of a Josephson junction.

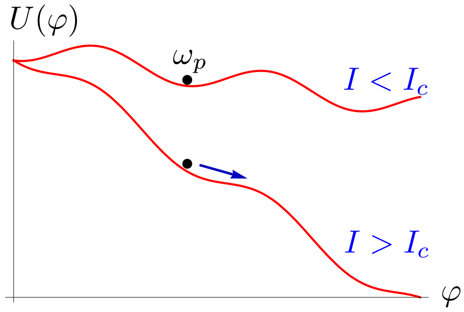

Figure 1.6: The washboard potential in the two limits $I \lessgtr I_c$.

in 1961 [14, 15]. Since then, SJJs have been extensively studied, both theoretically and experimentally [16]. The Josephson equations lead to the Josephson Hamiltonian

$$\mathcal{H}_J = -E_J \cos \varphi, \tag{1.9}$$

where the Josephson energy $E_J$ is proportional to the critical current $I_c$: $E_J = \hbar I_c / 2e$.

The two superconducting electrodes are separated by an insulating layer which constitutes a capacitance $C$. With the progress of nanofabrication in the last decade, it is possible to build ultra-small junctions. For such SJJs, the charging energy of one electron on the capacitance

$$E_c = \frac{e^2}{2C}, \tag{1.10}$$

has a non-negligible effect. Indeed, for a typical capacitance of one femtofarad, the charging energy is equal to one Kelvin. Consequently, the total Hamiltonian is

$$\mathcal{H} = \frac{Q^2}{2C} - E_J \cos \varphi, \tag{1.11}$$

where $Q = 2en = CV$ is the charge on the junction.

Cooper pairs are charged particles (twice the electron charge) and compensate the background of positive ions that make up the lattice of the metal. As a result, the electrostatic forces across the barrier and the tendency towards charge neutrality in the metal lead to a small Cooper pair imbalance compared to the total number of charges. Actually, in experiments electrodes are connected to a current or voltage source that keep the charge imbalance small even when a current flows through the junction. This observation explains why in superconductors we obtain directly Eqs. (1.3) instead of Eqs. (1.2).

Moreover, to describe a real SJJ that is used in experiments, it is necessary to take into account the dissipation of the junction due to the presence of quasiparticles and to the unavoidable coupling with the environment. There are two sources of damping. Quasiparticles are present near the critical temperature or when a voltage above $2\Delta/e$ is applied on the junction. The quasiparticle current is ohmic, with a resistance corresponding to the resistance $R_N$ in the normal state. The complete model of a real junction is thus an ideal junction in parallel with a capacitance and a resistance, called the Resistively and Capacitively Shunted Junction (RCSJ) model [17] (see Fig. 1.5). From the

Kirchhoff law $I = I_c \sin\varphi + C\dot{V} + V/R_N$, we derive the dynamic equation for the phase

$$C\left(\frac{\hbar}{2e}\right)^2 \ddot{\varphi} = \frac{\hbar}{2e} I - E_J \sin\varphi - \frac{1}{R_N}\left(\frac{\hbar}{2e}\right)^2 \dot{\varphi}, \tag{1.12}$$

which is the equation of motion of a fictitious particle of mass $(\hbar/2e)^2\, C$ moving in the washboard potential

$$U(\varphi) = -\frac{\hbar}{2e} I\varphi - E_J \cos\varphi, \tag{1.13}$$

with the friction force $-R_N^{-1}\,(\hbar/2e)^2\,\dot{\varphi}$. The presence of quasiparticles results in the damping of the phase dynamics. For small bias currents $I < I_c$, the phase oscillates around a minimum $\varphi_0$ of the potential $U(\varphi)$ with the plasma frequency $\omega_p = \sqrt{8E_cE_J}$. Because $\langle\varphi\rangle = \varphi_0$ and $\langle\dot{\varphi}\rangle = 0$, a finite current at zero voltage appears, it is the supercurrent branch. For high bias currents $I > I_c$, the potential does not have any minimum and the particle runs down the washboard potential (see Fig. 1.6). The quasiparticles are excited and the current voltage characteristic is an ohmic law at voltages higher than the gap, *i.e.* $V > 2\Delta/e$ (see Fig. 1.7, left curve).

Another source of dissipation comes from the the environment, namely the resistive external circuit and the thermal fluctuations. The general impedance is complicated but it can be modeled by a resistance as a first approximation. Let us consider for instance the case of voltage biased junction, that is to say a real junction in series with a voltage source $V_B$ and a resistance $R$. The total current $I$ in the first term of the right-hand side of Eq. (1.12) is equal to

$$I = \frac{V_B}{R} - \frac{\hbar\dot{\varphi}}{2eR}. \tag{1.14}$$

The effect of the temperature and the resistive environment can be accounted for with a fluctuating part in the bias voltage with a white noise. The treatment can be performed with a Fokker-Planck equation for the phase and the resulting current is [18]

$$I(V_B) = I_c\, \mathrm{Im}\left[\frac{\mathrm{I}_{1-2i\beta eV_B/\hbar R}(\beta E_J)}{\mathrm{I}_{-2i\beta eV_B/\hbar R}(\beta E_J)}\right], \tag{1.15}$$

where $\mathrm{I}_\nu(z)$ is the modified Bessel function and $\beta = 1/k_BT$ is the inverse temperature. The corresponding experimental current-voltage characteristics are presented on the right graph of Fig. 1.7. The effect of the environment is to smear the supercurrent branch. This is the phenomenon of phase diffusion due to thermal fluctuations. The Josephson effects are thus affected by the environment. The quantum treatment of dissipation will be presented in Chap. 2.

Finally, it is important to mention that the Shapiro steps in SJJs are commonly used in quantum metrology to connect the definition of the voltage to the one of the frequency in the quantum metrological triangle [20].

## 1.3 Quantum Josephson effect

In this section we give a quantum derivation of the phenomenological equations presented in Sec. 1.1. We will focus on the specific case of two bosonic superfluids, having in mind that it applies as well to paired Fermi systems [21–23]. Indeed, the size of the pair does not enter in the Josephson equations of motion, but it affects the value of the critical current.

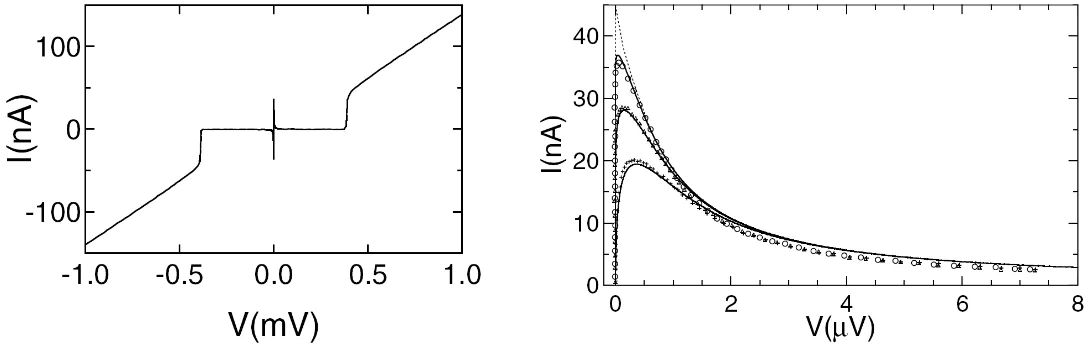

Figure 1.7: Current-Voltage characteristics of an overdamped Josephson junction, from experiment [19] where the gap is equal to $\Delta/e = 200\,\mu$V and the critical current to $I_c = 45\,$nA. *Left*: Transition between the supercurrent branch and the ohmic branch at a voltage equal to $2\Delta/e$. *Right*: Smearing of the supercurrent branch due to the resistive external circuit and the temperature. From top to bottom: $T = 0,\ 34,\ 157,$ and $400\,$mK.

For the sake of simplicity, we will restrict to the simplest quantum model which takes into account the physics of the Josephson effect. This is the so-called two-mode approximation, which describes the bosons in system 1 and 2 by a single operator $\hat{a}_{j=1,2}$ for each system. The corresponding tunneling Hamiltonian reads

$$\mathcal{H}_J = -\mathcal{T}\left(\hat{a}_1^\dagger \hat{a}_2 + \hat{a}_1 \hat{a}_2^\dagger\right), \tag{1.16}$$

where $\mathcal{T}$ is the tunneling strength of the barrier. The operators $\hat{a}_j$ and $\hat{a}_j^\dagger$ respectively annihilate and create a boson in the system $j$, satisfying the commutation rule

$$\left[\hat{a}_i, \hat{a}_j^\dagger\right] = \delta_{i,j}. \tag{1.17}$$

At a truly quantum level, we express the operators $\hat{a}_j$ and $\hat{a}_j^\dagger$ in the density-phase representation [24]

$$\hat{a}_j = \sqrt{\hat{n}_j + 1}\,\mathrm{e}^{i\hat{\varphi}_j}, \qquad \hat{a}_j^\dagger = \mathrm{e}^{-i\hat{\varphi}_j}\sqrt{\hat{n}_j + 1}, \tag{1.18}$$

where $\hat{n}_j$ and $\hat{\varphi}_j$ are respectively the number operator and the phase operator of the corresponding system. The variables $\hat{n}_j$ and $\hat{\varphi}_j$ are conjugate variables which satisfy the commutation rule

$$\left[\hat{n}_j, \mathrm{e}^{\pm i\hat{\varphi}_j}\right] = \mp \mathrm{e}^{\pm i\hat{\varphi}_j}. \tag{1.19}$$

The bosonic particle number is related to the number imbalance operator $\hat{n} = \frac{1}{2}\left(\hat{n}_1 - \hat{n}_2\right)$, and the corresponding conjugate phase difference operator[1] $\hat{\varphi} = \hat{\varphi}_2 - \hat{\varphi}_1$. The total number of bosons is denoted by $N$. In terms of these operators the tunneling Hamiltonian reads

$$\begin{aligned}\mathcal{H}_J = -\,\mathcal{T}\Big[\; &\left(\sqrt{N/2+\hat{n}}\sqrt{N/2-\hat{n}+1} + \sqrt{N/2+\hat{n}+1}\sqrt{N/2-\hat{n}}\right)\;\cos\hat{\varphi} \\ &+ \left(\sqrt{N/2+\hat{n}}\sqrt{N/2-\hat{n}+1} - \sqrt{N/2+\hat{n}+1}\sqrt{N/2-\hat{n}}\right) i\sin\hat{\varphi}\Big],\end{aligned} \tag{1.20}$$

---

[1] The rigorous definition of $\hat{\varphi}$ should be taken with care since the operator $\mathrm{e}^{i\hat{\varphi}}$ is not unitary at the boundary of the Fock basis.

where the relation $\mathrm{e}^{\pm i\hat{\varphi}}\sqrt{N/2 \pm \hat{n} + 1} = \sqrt{N/2 \pm \hat{n}}\,\mathrm{e}^{\pm i\hat{\varphi}}$ has been used.

The Josephson Hamiltonian $\mathcal{H}_J$ plays the role of a potential in the phase representation. In addition, let us add an on-site Hamiltonian quadratic in the number imbalance $\hat{n}$ which will act as a kinetic Hamiltonian

$$\mathcal{H} = \mathcal{U}\,(\hat{n} - n_0)^2 - \mathcal{T}\left(\hat{a}_1^\dagger \hat{a}_2 + \hat{a}_1 \hat{a}_2^\dagger\right), \tag{1.21}$$

where $\mathcal{U}$ is the characteristic on-site energy. The physical origin of this term comes from the interaction between bosons [see Secs. 1.2 and 1.4 for a microscopic derivation in the case of a Bose Josephson junction (BJJ)]. The quantum dynamics of the number and the phase, in the Heisenberg picture with respect to the total Hamiltonian (1.21), can then be derived

$$\dot{\hat{n}} = \frac{1}{i\hbar}\,[\hat{n}, \mathcal{H}] = i\frac{\mathcal{T}}{\hbar}\left[\sqrt{N/2 + \hat{n}}\sqrt{N/2 - \hat{n} + 1}\,\mathrm{e}^{i\hat{\varphi}} - \sqrt{N/2 + \hat{n} + 1}\sqrt{N/2 - \hat{n}}\,\mathrm{e}^{-i\hat{\varphi}}\right], \tag{1.22}$$

$$\begin{aligned}\dot{\hat{\varphi}} = \frac{1}{i\hbar}\,[\hat{\varphi}, \mathcal{H}] = {} & \frac{2\mathcal{U}}{\hbar}(\hat{n} - n_0) \\ & + \frac{\mathcal{T}}{2\hbar}\left[\frac{2\hat{n} - 1}{\sqrt{N/2 + \hat{n}}\sqrt{N/2 - \hat{n} + 1}}\,\mathrm{e}^{i\hat{\varphi}} + \frac{2\hat{n} + 1}{\sqrt{N/2 + \hat{n} + 1}\sqrt{N/2 - \hat{n}}}\,\mathrm{e}^{-i\hat{\varphi}}\right],\end{aligned} \tag{1.23}$$

where the commutator $\left[\hat{\varphi}, \sqrt{N/2 + \hat{n}}\right] = i/(2\sqrt{N/2 + \hat{n}})$ has been used. This generalizes the usual Josephson equations (1.3).

When the particle imbalance is small compared to the total number $\langle \hat{n} \rangle \ll N$, the Josephson Hamiltonian (1.20) reduces to

$$\mathcal{H}_J \simeq -E_J\sqrt{1 - \left(\frac{2\hat{n}}{N}\right)^2}\cos\hat{\varphi}, \tag{1.24}$$

where $E_J = N\mathcal{T}$ is the so-called Josephson energy. The particle current operator reads

$$\dot{\hat{n}} \simeq -\frac{E_J}{\hbar}\sqrt{1 - \left(\frac{2\hat{n}}{N}\right)^2}\sin\hat{\varphi}, \tag{1.25}$$

where $E_J/\hbar$ corresponds the maximal particle current that can flow through the junction. The phase dynamics is mainly governed by $\mathcal{U}$

$$\dot{\hat{\varphi}} \simeq \frac{2\mathcal{U}}{\hbar}(\hat{n} - n_0) + 4\frac{E_J}{\hbar N^2}\frac{\hat{n}}{\sqrt{1 - (\frac{2\hat{n}}{N})^2}}\cos\hat{\varphi}. \tag{1.26}$$

This derivation shows that in the mean-field limit $\langle \hat{a}_j \rangle = \psi_j$ the Hamiltonian (1.16) yields Eqs. (1.1) discussed in Sec. 1.1.

We will now briefly recall the various dynamical behaviors expected for the BJJ. In the mean-field regime, where $n = \langle \hat{n} \rangle$ and $\mathrm{e}^{\pm i\varphi} = \left\langle \mathrm{e}^{\pm i\hat{\varphi}} \right\rangle$, the classical equations corresponding to Eqs. (1.25) and (1.26) can be solved in terms of Weierstrass elliptic functions [25, 26]. To find the stationary points in the weak link limit, we linearize these two equations of motion in $n$. The calculation of $\ddot{\varphi}$ shows that the system is equivalent to a fictitious particle of mass $M = \hbar^2/2\mathcal{U}$ moving in the potential

$$U(\varphi) = -E_J\left[\cos\varphi + \frac{1}{4\Upsilon}\cos 2\varphi\right], \tag{1.27}$$

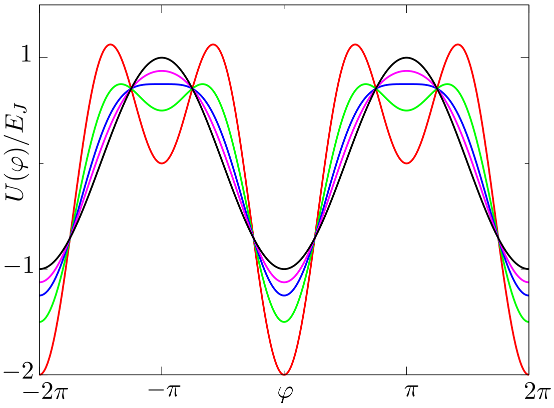

Figure 1.8: Effective potential (1.27) for a BJJ in the classical limit for $\Upsilon/\Upsilon_c = 0.25$ in *red*, 0.5 in *green*, 1 in *blue*, 2 in *magenta* and $\Upsilon \gg \Upsilon_c$ in *black*, showing the possibility of stable $\pi$-oscillations for $\Upsilon < 1$.

where $\Upsilon = N^2\mathcal{U}/2E_J$. The quantity $E_J/N^2\mathcal{U}$ represents the ratio between the Josephson energy and the total on-site energy. In bulk superconductors $N \gg 1$ and the last term of Eq. (1.27) does not exist. There are two types of local minima, namely at $\varphi \equiv 0$ and $\varphi \equiv \pi$ (see Fig. 1.8).

The dynamics around the position $\varphi = 0$ is governed by the differential equations

$$\ddot{n} + \omega_p^2 n = 0, \tag{1.28a}$$

$$\ddot{\varphi} + \omega_p^2 \varphi = 0. \tag{1.28b}$$

The particle oscillates around the position $\varphi = 0$ with the plasma frequency $\omega_p$ of the junction

$$\omega_p = \sqrt{2E_J\mathcal{U}}\sqrt{1+\Upsilon^{-1}}/\hbar. \tag{1.29}$$

When $\Upsilon < 1$, the other local minimum $\varphi = \pi$ appears in the potential, and $\pi$-oscillations occur with the frequency $\omega_\pi = 2E_J\sqrt{1-\Upsilon}/N\hbar$.

Finally, there can be oscillations with a macroscopically self-trapping. Indeed, if the interaction between bosons is larger than the tunneling strength, tunnel events are strongly suppressed and a non-zero boson number imbalance remains across the junction (see Fig. 1.13, right panel).

Eqs. (1.25)–(1.26) are equivalent to the equations of motion of a non-rigid pendulum located with the angle $\varphi$ and the length $\sqrt{1-z^2}$, with angular momentum $z$ and with moment of inertia $\Upsilon^{-1}$. These different regime are illustrated in the various phase-space trajectories $z(\varphi)$ of Fig. 1.9, where $z = (n_1 - n_2)/(n_1 + n_2) = 2n/N$. The different trajectories correspond to different values of $\Upsilon$ expressed in units of the critical value $\Upsilon_c = 2\left[1 + \sqrt{1 - z(0)^2}\cos\varphi(0)\right]/z(0)^2$ above which macroscopic quantum self trapping is possible [26].

## 1.4 The Bose Josephson junction

In 1925, Satyendra Nath Bose [27] and Albert Einstein [28] predicted that a gas of ideal bosons would undergo a phase transition below a critical temperature to a state corresponding to a macroscopic occupation of the lowest energy level (actually Einstein

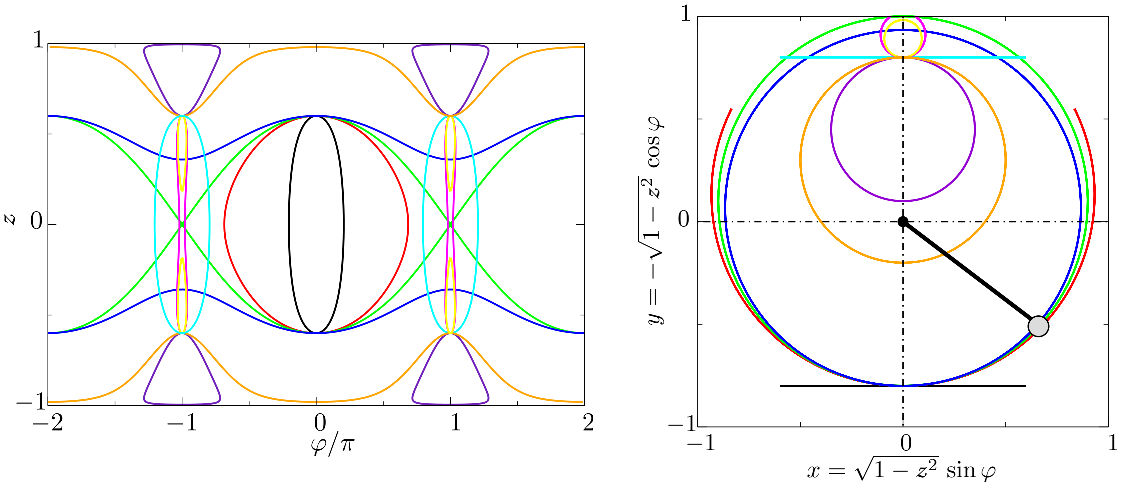

Figure 1.9: *Left panel*: phase-space trajectories $z(\varphi)$ of Eqs. (1.25)–(1.26). *Right panel*: the corresponding motions of the non-rigid pendulum. The different trajectories corresponds to $\Upsilon/\Upsilon_c = 0$ in *black* and *cyan*, 0.8 in *red*, 0.99 in *magenta*, 1 in *green*, 1.01 in *yellow*, 1.5 in *blue*, 2 in *orange* and 2.7 in *violet*. Initial values are $z(0) = \pm 0.6$ and $\varphi(0) = 0$ except for orbits around $\pi$ for which $\varphi(0) = \pi$. The macroscopic quantum self-trapped states are the trajectories with nonzero $\langle z \rangle$ (curves with $\Upsilon > \Upsilon_c$). For a rigid pendulum (which simulates SJJs), only phase-space trajectories in *black*, *red*, *green*, and *blue* are possible (the last one is however not observed in SJJs). Non-rigidity is also necessary to reach the orbits around $\pi$.

generalized the result of Bose from photons to massive bosons). Bose Einstein condensation was first observed seventy years later in 1995, in ultracold vapors of alkali atoms such as Rubidium [29], Sodium [30] or Lithium [31] (see Fig. 1.10). The whole gas forming a giant matter wave [33], Bose Einstein condensates constitute a novel class of physical systems that display macroscopic phase coherence. In experiments, atoms are cooled using laser or evaporative cooling and trapped in magnetic or optical traps (see Sec. 5.1 and Ref. [34] for more details). Atoms are cooled down to $T \sim 10$–$100\,\mathrm{nK}$; at such ultralow temperatures the thermodynamically stable state of alkali atoms is the solid phase and the gas phase is metastable. Experimental conditions (ultra high vacuum. . . ) allow this metastable state to have a sufficiently long lifetime (several minutes) to perform various manipulation and measurements. The phase coherence is experimentally demonstrated on Fig. 1.11 where the interference pattern between two Bose Einstein condensates clearly shows interference fringes [32]. Another way to highlight the phase coherence of a Bose Einstein condensate is to perform a double-slit experiment, as was first done in Ref. [35].

The initial prediction for Bose Einstein condensation was done for noninteracting bosons but this phenomenon is also possible in the presence of interaction. A criterion to observe Bose Einstein condensation in interacting bosons was given by Oliver Penrose and Lars Onsager in the case of liquid Helium [36]. In the specific case of quantum gases, interactions are due to two-body collisions. Although the resulting interaction potential has a complex form, in the case of dilute gases it can be replaced by an effective potential giving rise to the same scattering length. The simplest pseudo-potential is the hard-core

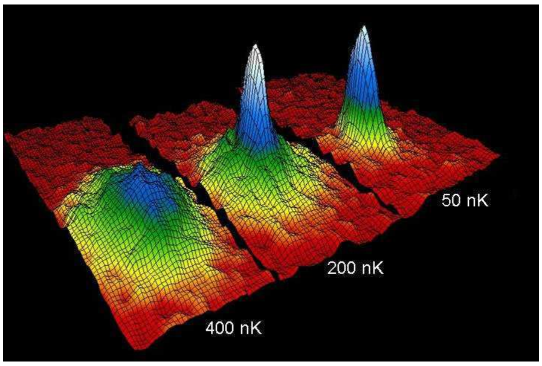

Figure 1.10: Bose Einstein condensation of $^{87}$Rb atoms, as observed by absorption of laser light [29]. At $T \simeq 200\,\mathrm{nK}$ a macroscopic fraction of atoms condenses, corresponding to the central peak.

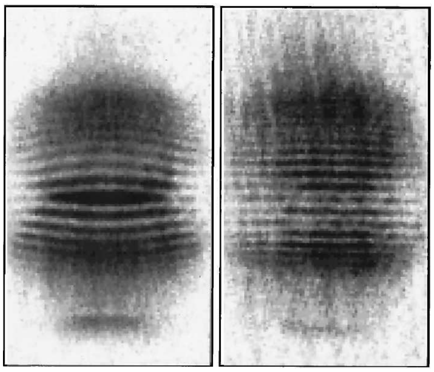

Figure 1.11: Interference patterns resulting from the expansion and overlapping of two Bose Einstein condensates, from Ref. [32].

repulsive potential

$$V_{\text{int}}(\vec{r}) = g\delta(\vec{r}), \tag{1.30}$$

where the interaction strength $g$ is related to the scattering length $a_S$ through $g = 4\pi\hbar^2 a_S/m$ [37]. In the following, we consider a dilute ultracold gas of interacting bosons trapped in an external potential. Using the experimental parameters for typical densities and scattering lengths, in the zero-temperature limit we can safely suppose that the number of non-condensed atoms is negligible as compared to the total number and thus treat the gas as full condensate.

In the following we give a microscopic derivation of the Hamiltonian (1.21) and of the microscopic parameters $\mathcal{T}$ and $\mathcal{U}$ entering it, for the case of Bose-Einstein condensates realized with ultracold atomic gases.

The general Hamiltonian of a system of interacting bosons in an external potential $V_{\text{trap}}$ reads

$$\begin{aligned} \hat{\mathcal{H}} = & \int \mathrm{d}^3 r \hat{\Psi}^\dagger(\vec{r}) \left( -\frac{\hbar^2}{2m}\Delta + V_{\text{trap}}(\vec{r},t) \right) \hat{\Psi}(\vec{r}) \\ & + \frac{1}{2} \int \mathrm{d}^3 r \int \mathrm{d}^3 r' \hat{\Psi}^\dagger(\vec{r}) \hat{\Psi}^\dagger(\vec{r}\,') V_{\text{int}}(|\vec{r}-\vec{r}\,'|) \hat{\Psi}(\vec{r}) \hat{\Psi}(\vec{r}\,'), \end{aligned} \tag{1.31}$$

where $\hat{\Psi}(\vec{r})$ ($\hat{\Psi}^\dagger(\vec{r})$) is the bosonic field operator annihilating (creating) a particle at position $\vec{r}$ satisfying the commutation relations

$$[\Psi(\vec{r}), \Psi^\dagger(\vec{r}\,')] = \delta(\vec{r}-\vec{r}\,'), \qquad [\Psi(\vec{r}), \Psi(\vec{r}\,')] = 0. \tag{1.32}$$

With the hard core pseudopotential (1.30), the Hamiltonian becomes

$$\hat{\mathcal{H}} = \int \mathrm{d}^3 r \hat{\Psi}^\dagger(\vec{r}) \left( -\frac{\hbar^2}{2m}\Delta + V_{\text{ext}}(\vec{r},t) + \frac{g}{2}\hat{\Psi}^\dagger(\vec{r})\hat{\Psi}(\vec{r}) \right) \hat{\Psi}(\vec{r}). \tag{1.33}$$

The Heisenberg equation for the time evolution of $\Psi$ related to this Hamiltonian gives rise to the equation

$$i\hbar\frac{\partial}{\partial t}\hat{\Psi}(\vec{r},t) = \left( -\frac{\hbar^2}{2m}\Delta + V_{\text{ext}}(\vec{r},t) + g\hat{\Psi}^\dagger(\vec{r},t)\hat{\Psi}(\vec{r},t) \right) \hat{\Psi}(\vec{r},t). \tag{1.34}$$

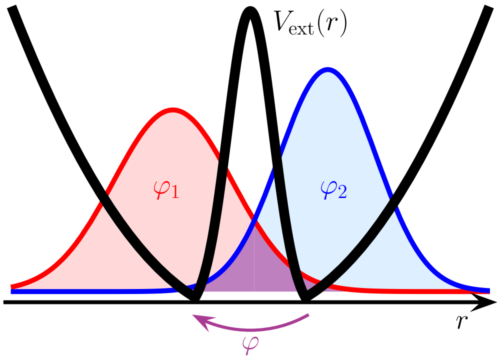

Figure 1.12: Typical double well potential considered for the Bose Josephson junction.

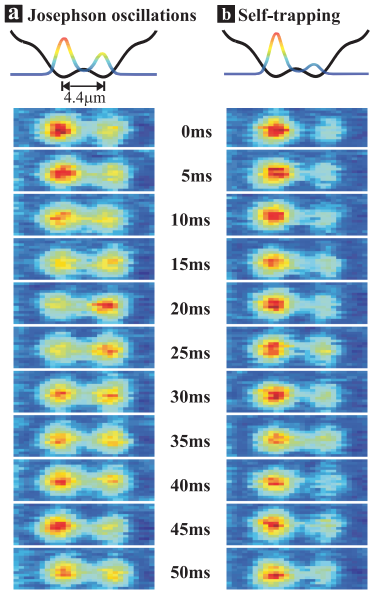

Figure 1.13: Direct observation of tunneling in a single Bose Josephson junction [40]. *Left:* time-resolved Josephson oscillations. *Right:* macroscopic quantum self-trapping.

In the mean field approximation, Eq. (1.34) yields the so-called time-dependent Gross-Pitaevskii equation [38, 39], leading to the time evolution of the condensate wavefunction.

Now we focus on a double well potential with a barrier higher than the zero-point energies in each well as depicted in Fig. 1.12. This potential is obtained experimentally by superposing a periodic potential on the harmonic confinement. The initial condensate is split into two parts by the barrier of this effective double-well potential, realizing a single weak link (see Fig. 1.13). In this case the field operator can be, in a variational approach, split into two parts

$$\hat{\Psi}(\vec{r},t) = \phi_1(\vec{r})\hat{a}_1(t) + \phi_2(\vec{r})\hat{a}_2(t), \tag{1.35}$$

where $\hat{a}_j$ ($\hat{a}_j^\dagger$) annihilates (creates) a boson in the well $j$ and satisfies the commutation rule $\left[\hat{a}_i^\dagger, \hat{a}_j\right] = \delta_{i,j}$. This yields the two-mode approximation where $\phi_j(\vec{r})$ is the wave function of the condensate in each well. Substituting the ansatz (1.35) into the Hamiltonian (1.33), we obtain the Hamiltonian

$$\mathcal{H} = E_1\hat{a}_1^\dagger\hat{a}_1 + E_2\hat{a}_2^\dagger\hat{a}_2 + \frac{1}{2}U_1\hat{a}_1^\dagger\hat{a}_1^\dagger\hat{a}_1\hat{a}_1 + \frac{1}{2}U_2\hat{a}_2^\dagger\hat{a}_2^\dagger\hat{a}_2\hat{a}_2 - \mathcal{T}\left(\hat{a}_1^\dagger\hat{a}_2 + \hat{a}_1\hat{a}_2^\dagger\right), \tag{1.36}$$

with [26]

$$E_j = \int \mathrm{d}^3r \left[\frac{\hbar^2}{2m}|\vec{\nabla}\phi_j(\vec{r})|^2 + V_{\text{ext}}(\vec{r})|\phi_j(\vec{r})|^2\right], \tag{1.37}$$

$$U_j = g\int \mathrm{d}^3r|\phi_j(\vec{r})|^4, \tag{1.38}$$

$$\mathcal{T} = \int \mathrm{d}^3r \left[\frac{\hbar^2}{2m}\vec{\nabla}\phi_1^*(\vec{r})\vec{\nabla}\phi_2(\vec{r}) + V_{\text{ext}}(\vec{r})\phi_1^*(\vec{r})\phi_2(\vec{r})\right]. \tag{1.39}$$

In Eq. (1.39) we clearly see the correspondence between the tunneling strength of the tunnel Hamiltonian $\mathcal{T}$ and the external potential which produces the barrier. In terms of the imbalance number operator $\hat{n} = \hat{a}_1^\dagger \hat{a}_1 - \hat{a}_2^\dagger \hat{a}_2$, we recover the Hamiltonian (1.21) with

$$\mathcal{U} = \frac{U_1 + U_2}{2}, \tag{1.40}$$

$$n_0 = \frac{E_2 - E_1}{U_1 + U_2} + \frac{N-1}{2} \frac{U_2 - U_1}{U_1 + U_2}. \tag{1.41}$$

This microscopic derivation of the Josephson Hamiltonian enabled us to express the parameters of the general Hamiltonian (1.21) in terms of the interaction strength $g$ between atoms, the trapping potential $V_{\text{ext}}$ and the wavefunctions of the condensate in each trap.

In the mean-field limit $\langle \hat{a}_j \rangle = \psi_j$, Eqs. (1.1) are recovered with $\mathcal{E}_j = E_j + n_j U_j$. In BJJs there is no restriction on the particle number imbalance (except of course $-N/2 < n < N/2$). Consequently, contrary to SJJs, we need to keep the terms $\sqrt{1-(2n/N)^2}$ in Eqs. (1.25) and (1.26). As we have seen in the previous section, the possibility to reach large particle number imbalance gives rise to new configurations like the macroscopic quantum self trapping or the $\pi$-oscillations.

A complete description of BJJs must take into account the presence of non-condensed atoms. Indeed, for an ideal Bose gas, the fraction of non-condensed atoms goes like $f_{nc} = (T/T_c)^\gamma$ where $\gamma$ depends on the confinement ($\gamma = 3/2$ for a homogeneous gas and $\gamma = 3$ in the case of a harmonic trapping potential). At finite temperatures a substantial fraction of atoms is out of the condensate [*e.g.* $f_{nc}(T_c/2) = 13$–$35\,\%$]. The non-condensed atoms act as a thermal reservoir and the incoherent exchange of these thermal atoms induce damping which is for instance responsible for the decay of the macroscopic quantum self trapping state [41]. A simple way to model damping is to add an ohmic contribution to the particle flow [42]

$$J_R = -G\,\Delta\mu, \tag{1.42}$$

where $\Delta\mu$ is the chemical potential defined as

$$\Delta\mu = -\hbar\dot{\varphi}. \tag{1.43}$$

This contribution is transposed in the dynamical equation of $n$ as follows

$$\dot{n} = -\frac{E_J}{\hbar}\sqrt{1-\left(\frac{2n}{N}\right)^2}\sin\varphi - \eta\dot{\varphi}, \tag{1.44}$$

where $\eta = \hbar G$ is the dimensionless damping constant. This ohmic contribution is equivalent to the quasiparticle current of SJJs in the RCSJ model.

The Josephson effect has been observed in several groups, both on single junctions [40, 43] and on arrays [44, 45]. The population imbalance as a function of time is measured by a sequence of in situ images (see Fig. 1.13 for small oscillations and self trapping) and both the dc and ac aspects have been explored (see Fig. 1.14). The ground state and dynamical evolution for a Bose Josephson junction realized by an ultracold Bose gas in a double-well trap has been studied in Ref. [46].

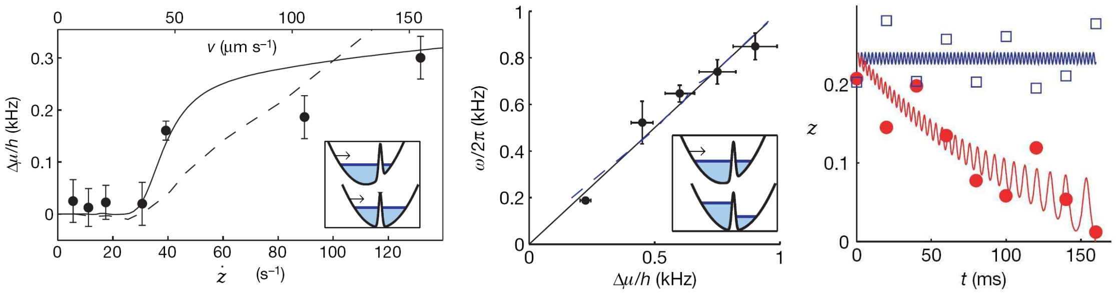

Figure 1.14: Josephson effects in a Bose Josephson junction [43]. *Left*: dc Josephson effect. The chemical potential is measured as a function of $\dot{z}$ proportional to the particle current. The population imbalance is achieved by an adiabatic shift of the harmonic trap with respect to the barrier. While tilting the potential, a supercurrent branch and then an ohmic branch are observed. *Center*: ac Josephson effect. The frequency of the current oscillations $\omega$ is plotted as a function of the chemical potential. A current bias is achieved by a non-adiabatic shift. The measured frequency $\omega$ is proportional to the chemical potential. *Right*: decay of the macroscopic quantum self trapping state for two different fractions of non-condensed atoms: $f_{nc} \simeq 5\,\%$ in blue and $f_{nc} \simeq 20\,\%$ in red. The decay of the MQST shows that the thermal cloud significantly modifies the behaviour of the two condensates.

## 1.5 The Josephson effect at two different physical scales

The Josephson effect has been predicted and observed in two very different physical systems, superconducting nanocircuits and quantum gases. We discuss here (some of) the most striking differences and their physical origin.

- The physical origin of the one-site energy is the interaction between particles but, due to the fact that Cooper pairs are charged particle and alkali atoms are neutral, the forces coming into play are not the same. It comes from the electrostatic force of the capacitance of the barrier on the Cooper pairs in superconductors and from the two-body interaction between atoms in cold gases.

- The particle number imbalance remains small in SJJs due to electrostatic forces and tendency towards neutrality. In BJJs large population imbalances are reachable and the macroscopic quantum self-trapping regime is accessible.

- From the comparison between experimental results on Figs. 1.7 and 1.13, we notice that dissipation plays an important role in SJJs. Damping is due to non-condensed atoms in BJJs and to the electromagnetic environment in SJJs (at low currents).

- The observation of time-resolved Josephson oscillations in Bosonic junctions highlights the difference on the temporal scales. Indeed, typical frequencies for superconductors are above the gigahertz whereas it takes 50 ms for a Bose Josephson junction to perform one oscillation. This is directly linked to the coherence time of this systems. While the "lifetime" of a SJJ reaches hundreds of nanoseconds, the lifetime of a atomic cloud is counted in seconds.

- A low temperature is needed in both systems but, due to different critical temperature scales, it goes down to tenths of millikelvins for superconductors and tenths of nanokelvins for cold atoms.

The comparison is presented in Tab. 1.1.

| Josephson junction | Superconducting | Bosonic |
|---|---|---|
| Boson | Cooper pair (charged) | alkali atom (neutral) |
| Interaction force | Coulomb | short-range, repulsive |
| On-site energy $\mathcal{U}$ | capacitance $C$ | interaction $g$ |
| Josephson energy $E_J$ | $\hbar I_c/2e$ | $N\mathcal{T}$ |
| Plasma frequency $\omega_p$ | 1–$10^3$ GHz | $\sim$ 10 Hz |
| Temperature | 10 mK–1 K | 10–100 nK |
| Damping | external circuit | non-condensed atoms |

Table 1.1: Comparison of the physical scales between a superconducting Josephson junction and a Bose Josephson junction.

## Conclusion and perspectives

This chapter presented the Josephson effect from a phenomenological starting point, completed by a rigorous derivation of the quantum Josephson Hamiltonian. The implementation to superconductors and Bose Einstein condensates enables us to show the characteristics of each system.

The Josephson effect will be exploited in various applications in the following chapters.

Chapter 2

# The underdamped Josephson junction

**Contents**

## Introduction

A small-capacitance Josephson junction is a quantum system with rich dynamics. The two conjugate variables are the superconducting phase difference $\varphi$ across the junction and the charge $Q$ on its electrodes. Correspondingly, at low temperatures the behavior of the junction is determined by the competition between the Josephson energy $E_J$ and the charging energy $E_C = e^2/2C$, where $C$ is the junction capacitance [16]. If $E_J \gg E_C$, $\varphi$ is well-defined and a phase-coherent Cooper-pair current can flow through the junction in the absence of an external voltage $V$. In the opposite limit $E_J \ll E_C$ an insulating state with a well-defined charge $Q$ on the electrodes is possible. At the same time, the dynamics of $\varphi$ and $Q$ is crucially influenced by dissipation caused by the electromagnetic environment surrounding the junction. Because of the mutual interplay of quantum mechanics, nonlinearity and dissipation, the consistent theoretical description of Josephson junctions still remains far from being complete.

The dc current-voltage ($I$-$V$) characteristics of a Josephson junction embedded in a circuit of resistance $R$ have been well studied in the so-called overdamped [16] case corresponding to small values of $R/R_Q$ ($R_Q = h/4e^2$ is the resistance quantum) and the ratio $E_J/E_C$ [18, 47–52]. For small $R < R_Q$, the supercurrent peak at zero voltage acquires a finite width. With increasing $R$, quantum fluctuations of the phase become more important and the supercurrent peak gradually moves to higher voltages. This corresponds to the transition (driven by the environment) from superconducting behavior found for small $R$ to a complete Coulomb blockade when $R > R_Q$. Meanwhile, the opposite underdamped regime, which has been extremely difficult to achieve experimentally, has attracted less attention. However, recently experiments were performed [53–55] on junctions with $E_J/E_C > 1$, embedded in a tunable, highly resistive environment, $R \gg R_Q$, enabling the study of the same junction in different environments. In particular, a voltage peak near zero current followed by a back-bending to lower voltages at higher currents was observed (see Fig. 2.1). This is the so-called Bloch nose [56, 57] which, in accordance with a duality property [47, 58–60], resembles the $I$-$V$ characteristic of an overdamped junction but with the role of voltage and current interchanged (see Sec. 2.8 and Fig. 2.9 therein). A quantitative comparison between theory and experiment has been made in the classical limit where thermal fluctuations dominate [55, 61].

In this chapter we study for the first time the influence of quantum fluctuations on the $I$-$V$ characteristics of an underdamped Josephson junction. Our treatment, based on the Keldysh formalism, enables us to obtain the quantum Smoluchowski equation which describes the first quantum corrections to the quasicharge dynamics, as well as the $I$-$V$ characteristics in the zero temperature limit [62].

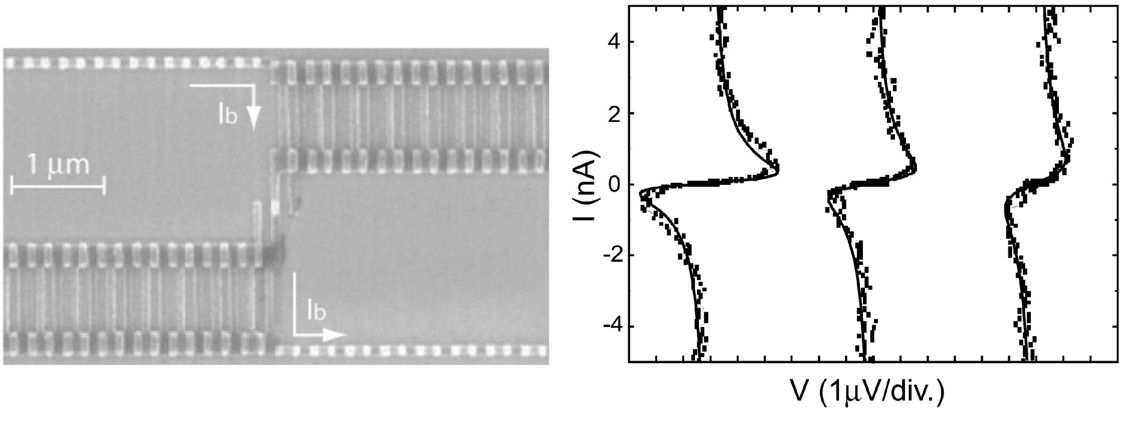

Figure 2.1: *Left*: SEM picture of the experimental circuit of Ref. [55]. The Josephson junction (central white square) is surrounded by two Josephson junction arrays that create the resistive environment.*Right*: Experimental current-voltage characteristics for different temperatures. From left to right the temperatures are $T = 50\,\text{mK}$, $250\,\text{mK}$, $300\,\text{mK}$. The critical voltage and the resistance are fitted to be, respectively, $V_c = 30\,\mu\text{V}$ and $R = 150\,\text{k}\Omega$ with a ratio between the Josephson and the charging energy being equal to $E_J/E_C = 3$. The solid lines correspond to the classical $I$-$V$ characteristics of Ref. [61].

## 2.1 Model

### 2.1.1 Current-biased Josephson junction

We start our analysis by considering a current-biased Josephson junction (see Fig. 2.2). The junction is shunted by a resistance $R$ and biased by an external dc current $I_b$. The resistor $R$ in series with the inductance $L$ constitutes the admittance $Y$ of the circuit, which models the dissipation of the system (see next section). The current flowing through the resistor is noted $I_x$, and the current through the junction is then $I = I_b - I_x$. The Lagrangian of the circuit reads

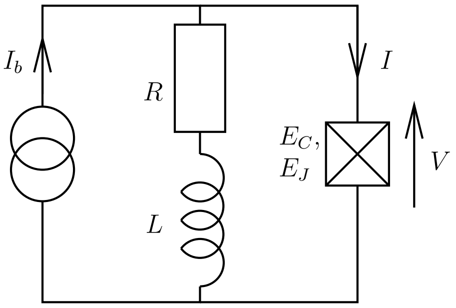

Figure 2.2: Scheme of the circuit. The Josephson junction is characterized by its critical voltage $I_c$ and its capacitance $C$. The environment is modeled by the $R$-$L$ circuit, defining the cutoff frequency $\omega_c = R/L$.

$$\mathcal{L} = \frac{C}{2}\phi_0^2\dot{\varphi}^2 + E_J\cos\varphi + \frac{\hbar}{2e}(I_b - I_x)\varphi, \tag{2.1}$$

where $\phi_0 = \hbar/2e$ is the reduced flux quantum ($\Phi_0 = h/2e$ is the flux quantum). The equation of motion of this Lagrangian leads to the Kirchhoff law $I_b - I_x = I_c \sin\varphi + C\phi_0\ddot{\varphi}$.

### 2.1.2 Environment

The environment is treated in the framework of the Caldeira-Leggett model, where the system is coupled to a bath of harmonic oscillators [63]. The number of oscillators is sufficiently large to render the energy exchange irreversible during the experiment. In the case of superconducting nanocircuits, the oscillators can be seen as a set of $L$-$C$ circuits in parallel characterized by a capacitance $C_\alpha$ and an inductance $L_\alpha$ with the eigenfrequency $\omega_\alpha = 1/\sqrt{L_\alpha C_\alpha}$. The voltage is written in the form of $V_\alpha = \phi_0\dot{\varphi}_\alpha$ and the current through the circuit is $I_\alpha = \dot{Q}_\alpha$ with the charge $Q_\alpha = C_\alpha\omega_\alpha\phi_0\varphi_\alpha$. The current through the resistor is then $I_x = \dot{Q}_x$ with the fluctuating charge $Q_x = \sum_\alpha Q_\alpha$. The Lagrangian of the bath is then $\mathcal{L}_{\text{bath}} = \sum\limits_\alpha \frac{C_\alpha}{2}\phi_0^2\dot{\varphi}_\alpha^2 - \frac{1}{2L_\alpha}\phi_0^2\varphi_\alpha^2$.

The total Lagrangian is equal to the Lagrangian (2.1) plus the Lagrangian of the bath $\mathcal{L}_{\text{bath}}$. It gives rise to the Hamiltonian

$$\mathcal{H} = \frac{Q^2}{2C} - E_J\cos\varphi - \phi_0\varphi I_b + \sum_\alpha\left(\frac{1}{2C_\alpha}\left(q_\alpha + \omega_\alpha C_\alpha\phi_0\varphi\right)^2 + \frac{1}{2L_\alpha}\phi_0^2\varphi_\alpha^2\right), \tag{2.2}$$

where the conjugate momenta are the quasicharges

$$q = C\phi_0\dot{\varphi}, \tag{2.3}$$
$$q_\alpha = C_\alpha\phi_0\dot{\varphi}_\alpha - \omega_\alpha C_\alpha\phi_0\varphi, \tag{2.4}$$

and satisfy $[\varphi, Q] = i2e$, $[\varphi_\alpha, q_\alpha] = i2e$. The canonical transformation

$$\begin{cases} q_\alpha \to -C_\alpha\omega_\alpha\phi_0\varphi_\alpha, \\ \phi_0\varphi_\alpha \to \dfrac{1}{C_\alpha\omega_\alpha}q_\alpha, \end{cases} \tag{2.5}$$

leads to the form

$$\mathcal{H} = \frac{Q^2}{2C} - E_J\cos\varphi - \phi_0\varphi I_b + \sum_\alpha\left(\frac{q_\alpha^2}{2C_\alpha} + \frac{1}{2L_\alpha}\phi_0^2(\varphi-\varphi_\alpha)^2\right). \tag{2.6}$$

We will now turn to the Bloch band description of the underdamped Josephson junction.

### 2.1.3 Bloch band description

In the case of interest here, $E_J \gg E_C$, it is advantageous to switch to the Bloch-band description of the Josephson junction [56, 57] (see Fig. 2.3). Assuming that the junction dynamics is confined to the lowest energy band, we can replace the Josephson potential by $U_0\cos(\pi q/e)$ where

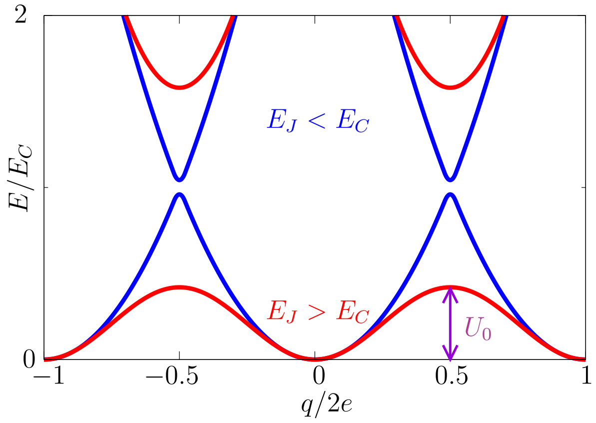

Figure 2.3: Energy spectra as a function of the quasicharge in the case $E_J \ll E_C$ where the bands are close to hyperbola and the opposite one $E_J \ll E_C$ where the bands are sinusoidal.

$$U_0 = \frac{8}{\sqrt{\pi}}E_C\left(\frac{2E_J}{E_C}\right)^{3/4}\exp\left(-2\sqrt{\frac{2E_J}{E_C}}\right), \tag{2.7}$$

is the Bloch bandwidth. The expression of the bandwidth $U_0$ can be obtained directly from the instanton formalism described in appendix B.

In terms of the reduced bath variables $x_\alpha = \left(\frac{L_\alpha}{\hbar^2 C_\alpha}\right)^{1/4} q_\alpha$ and $p_\alpha = -\left(\frac{C_\alpha}{\hbar^2 L_\alpha}\right)^{1/4} \phi_0\varphi_\alpha$, the reduced fluctuating charge $\xi = \pi Q_x/e$ obeys

$$\xi = 2\pi\sum_\alpha \varsigma_\alpha x_\alpha, \tag{2.8}$$

where $\varsigma_\alpha = (\hbar^2 C_\alpha / L_\alpha)^{1/4}$. After performing the canonical transformation $\mathrm{e}^{\frac{i}{2\pi}\xi\varphi}\,\mathcal{H}\,\mathrm{e}^{-\frac{i}{2\pi}\xi\varphi}$, we arrive at the tight-binding (TB) model of our system with the Hamiltonian:

$$\mathcal{H}_{\mathrm{TB}} = -U_0 \cos(\pi q/e - \xi) - (\hbar/2e) I_b \varphi + \sum_\alpha \frac{\omega_\alpha}{2}\left(p_\alpha^2 + x_\alpha^2\right). \tag{2.9}$$

The influence of the bath on the junction dynamics is entirely determined by the weighted spectral function, calculated in appendix A.2, $K(\omega) = (\pi/2)\sum_\alpha \varsigma_\alpha^2 \delta(|\omega| - \omega_\alpha)$. As follows from the equations of motion generated by $\mathcal{H}_{\mathrm{TB}}$, the choice $K(\omega) = R_Q \mathrm{Re}Y(\omega)/2\pi\omega$ with $Y(0) = 1/R$ reproduces the linear response (Ohm's law) of current $I_x$ to the voltage drop $V = (\hbar/2e)\dot{\varphi}$ on the resistor, $I_x(\omega) = Y(\omega)V(\omega)$ (for Fourier transforms).

The reduced fluctuating charge gives rise to the bath correlation function $J(\tau) = \langle (\xi(\tau) - \xi(0))\,\xi(0)\rangle$, which explicitly reads (see appendix A.3)

$$J(\tau) = 2R_Q \int_{-\infty}^{+\infty} \mathrm{d}\omega\, \frac{\mathrm{Re}Y(\omega)}{\omega}\, \frac{\mathrm{e}^{-i\omega\tau} - 1}{1 - \mathrm{e}^{-\beta\hbar\omega}}, \tag{2.10}$$

where $\beta = 1/k_B T$ is the inverse temperature.

### 2.1.4 Cutoff

We now turn to the effect of fluctuations and introduce a cutoff of the bath spectrum at frequency $\omega_c$, chosen to be smaller than the gap $\omega_p = \sqrt{8E_J E_C}/\hbar$ between the lowest Bloch bands but larger than the Bloch bandwidth. Furthermore, the competition between the cutoff energy and the temperature determines the nature, rather classical or quantum, of the environment. Indeed, starting from a classical thermal bath when $k_B T \sim \hbar\omega_c$, quantum fluctuations appear in the quasiclassical region $k_B T \lesssim \hbar\omega_c$ and become dominant at low temperatures $k_B T \ll \hbar\omega_c$. Assuming that the effective impedance seen by the junction is given by a resistance $R$ in series with an inductance $L$, we can set $Y(\omega) = 1/(R - i\omega L)$, leading to $\omega_c = R/L$. Then, from evaluating the integral (2.10) one obtains (see appendix A.3):

$$J(\tau) = -i\,\mathrm{sgn}(\tau)\, A(\tau) - M(\tau), \tag{2.11}$$

with

$$A(\tau) = \pi g \left(1 - \mathrm{e}^{-\omega_c|\tau|}\right), \tag{2.12}$$

$$M(\tau) = 2g\left[\frac{\pi|\tau|}{\beta\hbar} - \frac{\pi}{2}\cot\!\left(\frac{\beta\hbar\omega_c}{2}\right)\left\{1 - \mathrm{e}^{-\omega_c|\tau|}\right\} \sum_{k=1}^{+\infty} \frac{1 - \mathrm{e}^{-\omega_k|\tau|}}{k\left(1 - \omega_k^2/\omega_c^2\right)}\right], \tag{2.13}$$

where $g = R_Q/R$ is the dimensionless conductance, and $\omega_k = 2\pi k/\hbar\beta$ is a Matsubara frequency.

Before proceeding, we want to comment on the magnitude of the effective inductance $L$ which has been associated with the cutoff $\omega_c$. The restriction $\omega_c < \omega_p$ imposes a lower bound on the values of $L$ to be consistent with our assumption of single–band charge dynamics:

$$L > \frac{2\pi g^{-1}}{\sqrt{2E_C/E_J}}\, L_J, \tag{2.14}$$

where $L_J = \phi_0^2/E_J$ is the Josephson inductance. For relatively large $g > 1$, the condition (2.14) can be satisfied even for an autonomous Josephson junction, where $L \sim L_J$ corresponds to the Bloch inductance [64]. In the opposite limit of small $g \ll 1$, an experimental realization of this model would be the use of an environment composed of Josephson junction SQUID arrays, whose effective inductance can be tuned to relatively large values by magnetic flux [65]. Another option includes the use of a quantum phase–slip junction where there is no limitation on $\omega_c$, as discussed at the end of the chapter.

## 2.2 Current-voltage characteristics

### 2.2.1 Voltage operator

The voltage operator $V = \phi_0\dot{\varphi}$ is the group velocity associated with the quasicharge $V = \partial_q \mathcal{H}$

$$V = V_c \sin\Theta(t), \qquad \Theta = \pi q/e - \xi, \tag{2.15}$$

where $V_c = \pi U_0/e$ is the maximal (critical) voltage the junction can sustain. To determine the *I-V* characteristics, we calculate the average of the operator for the voltage across the junction $\langle V(t)\rangle$.

### 2.2.2 Evolution operator

We construct a perturbation theory to all orders in the Bloch bandwidth $U_0$. The Hamiltonian is divided into two parts, $\mathcal{H}_0$ and $\mathcal{H}_1$, as follows

$$\mathcal{H} = \mathcal{H}_0 + \mathcal{H}_1, \qquad \mathcal{H}_0 = -\phi_0 I_b \phi + \mathcal{H}_{\text{bath}}, \qquad \mathcal{H}_1 = -U_0 \cos\Theta(t). \tag{2.16}$$

In the interaction picture, the charge operator becomes

$$q(t) = q + \frac{i}{\hbar} t \underbrace{[\mathcal{H}_0, q]}_{=-i\hbar I_b} = q + I_b t. \tag{2.17}$$

The average value of the voltage operator is calculated via the density matrix $\rho$ and the evolution operator $\mathcal{U}$

$$\langle V(t)\rangle = \mathrm{Tr}\{\rho(t)V\} = \mathrm{Tr}\Big\{\rho(t_0)\mathcal{U}^\dagger(t,t_0)V\mathcal{U}(t,t_0)\Big\}. \tag{2.18}$$

The evolution operator satisfies the differential equation

$$i\hbar\frac{\partial \mathcal{U}(t,t_0)}{\partial t} = \mathcal{H}_1(t)\mathcal{U}(t,t_0). \tag{2.19}$$

The time integration, detailed for instance in Refs. [66, 67], leads to

$$\mathcal{U}(t,t_0) = \sum_{n=0}^{\infty}\left(\frac{-i}{\hbar}\right)^n \frac{1}{n!}\int_{t_0}^{t}\mathrm{d}t_1 \ldots \int_{t_0}^{t}\mathrm{d}t_n \mathcal{T}\mathcal{H}_1(t_1)\ldots\mathcal{H}_1(t_n), \tag{2.20}$$

or formally

$$\mathcal{U}(t,t_0) = \mathcal{T}\mathrm{e}^{\frac{-i}{\hbar}\int_{t_0}^{t}\mathrm{d}t'\mathcal{H}_1(t')}, \tag{2.21}$$

where $\mathcal{T}$ is the time-ordering operator which orders the Hamiltonians $\mathcal{H}_1(t_k)$ in decreasing time from left to right. Equivalently, we have

$$\mathcal{U}^\dagger(t, t_0) = \widetilde{\mathcal{T}} \mathrm{e}^{\frac{+i}{\hbar}\int_{t_0}^{t} \mathrm{d}t' \mathcal{H}_1(t')}, \tag{2.22}$$

where $\widetilde{\mathcal{T}}$ is the anti-time ordering operator. We choose $t_0 = 0$, and write $\sin x$ in the form $\sum_{\eta=\pm} \eta \mathrm{e}^{i\eta x}/2i$. We obtain

$$\mathcal{U}(t, 0) = \sum_{n=0}^{\infty} \left(\frac{iU_0}{2\hbar}\right)^n \int_0^t \mathrm{d}t_1 \ldots \int_0^{t_{n-1}} \mathrm{d}t_n \mathcal{T} \sum_{\{\eta\}} \mathrm{e}^{i\frac{\pi}{e}\sum_k \eta_k (q + I_b t_k)} \mathrm{e}^{-i\sum_k \eta_k \xi(t_k)}. \tag{2.23}$$

This expression as well as its adjoint have to be substituted into Eq. (2.18) to calculate the average voltage. This formulation is however cumbersome. A way to simplify the calculations is to use the Keldysh formalism.

### 2.2.3 Keldysh formalism

To calculate integrals involving time-ordering operators, we use the Keldysh formalism [68, 69]. The Keldysh technique is based on the Keldysh contour, depicted in Fig. 2.4. It is composed of two branches, $[0, t]$ and $[t, 0]$, differentiated with the Keldysh indices $s = +/-$, respectively. We introduce two operators, the global evolution operator $\mathcal{U}_\mathcal{C}(t, 0) = \mathcal{U}^\dagger(t, 0)\mathcal{U}(t, 0)$ and the global time-ordering operator $\mathcal{T}_\mathcal{C}$. The interest remains in the global character of these operators: in opposition with the time (anti) ordering operator which acts on the two branches separately, they act on the entire contour.

In terms of these operators, Eq. (2.18) becomes

$$\langle V(t)\rangle = \langle \mathcal{T}_\mathcal{C} \left(\mathcal{U}_\mathcal{C}(t, 0)V(t)\right)\rangle, \tag{2.24}$$

with

$$\mathcal{U}_\mathcal{C} = \mathcal{T}_\mathcal{C} \exp\left(\frac{iU_0}{\hbar} \int_0^\infty \mathrm{d}\tau \sum_{s=\pm} s \cos \Theta^s(\tau)\right). \tag{2.25}$$

We then calculate $\mathcal{T}_\mathcal{C} \left(\mathcal{U}_\mathcal{C}(t, 0)V(t)\right)$, which leads to

$$\begin{aligned} \langle V(t)\rangle = \frac{\pi U_0}{i2e} \sum_{n=0}^{\infty} \left(\frac{iU_0}{2\hbar}\right)^n \int_0^t \mathrm{d}t_1 \ldots \int_0^{t_{n-1}} \mathrm{d}t_n \\ \times \sum_{s_1 \ldots s_n = \pm} \sum_{\eta_0 \ldots \eta_n = \pm} \eta_0 \prod_{k=1}^{n} s_k \exp\left(i\frac{\pi}{e} \sum_{k=0}^{n} \eta_k (q + I_b t_k)\right) \langle \mathcal{T}_\mathcal{C}\, \mathrm{e}^{-iX}\rangle, \end{aligned} \tag{2.26}$$

where we note

$$X = \sum_{k=0}^{n} \eta_k \xi^{s_k}(t_k). \tag{2.27}$$

We thus understand the advantage of the Keldysh formalism, which reduces the average of Eq. (2.18) over the bath degrees of freedom with the evolution operator (2.23) to the average of an exponential. The latter is performed using Wick's theorem with Keldysh operators, derived in appendix A.1. The result is

$$\langle \mathcal{T}_\mathcal{C}\, \mathrm{e}^{-iX}\rangle = \mathrm{e}^{-\frac{1}{2}\overline{XX}}, \tag{2.28}$$

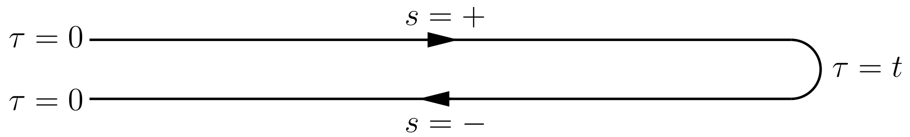

Figure 2.4: Keldysh contour and its two branches denoted by the Keldysh index $s$.

with

$$\overline{XX} = \langle \mathcal{T}_{\mathcal{C}}\, X^2\rangle. \tag{2.29}$$

The sum yields

$$\overline{XX} = 2\sum_{k=1}^{n}\sum_{k'=0}^{k-1}\eta_k\eta_{k'}\left(\overline{\xi_k\xi_{k'}} - \overline{\xi(0)\xi(0)}\right) + \overline{\xi(0)\xi(0)}\sum_{k=0}^{n}\eta_k\sum_{k'=0}^{n}\eta_{k'}, \tag{2.30}$$

where we note $\overline{\xi_k\xi_{k'}} = \langle \mathcal{T}_{\mathcal{C}}\, \xi^{s_k}(t_k)\xi^{s_{k'}}(t_{k'})\rangle$. Double sums are of the type $\sum_{k=1}^{n}\sum_{k'=0}^{k-1}$, implying $k'<k$. The order of multiple integrals gives then $t_{k'}>t_k$. From this we obtain

$$\overline{\xi_k\xi_{k'}} = \begin{cases} \langle\xi(t_{k'}-t_k)\xi(0)\rangle \text{ if } s_k=+ \text{ and } s_{k'}=+,\\ \langle\xi(t_{k'}-t_k)\xi(0)\rangle \text{ if } s_k=+ \text{ and } s_{k'}=-,\\ \langle\xi(t_k-t_{k'})\xi(0)\rangle \text{ if } s_k=- \text{ and } s_{k'}=+,\\ \langle\xi(t_k-t_{k'})\xi(0)\rangle \text{ if } s_k=- \text{ and } s_{k'}=-, \end{cases} \tag{2.31}$$

which is equivalent to

$$\langle \mathcal{T}_{\mathcal{C}}\, \xi^{s_k}(t_k)\xi^{s_{k'}}(t_{k'})\rangle = \langle\xi(s_k(t_{k'}-t_k))\xi(0)\rangle. \tag{2.32}$$

Therefore, the evolution operation is replaced by the Keldysh index, much easier to manipulate.

The average $\overline{\xi_k\xi_{k'}}$ can be expressed in terms of the bath autocorrelation function

$$\overline{\xi_k\xi_{k'}} - \overline{\xi(0)\xi(0)} = J(s_k(t_{k'}-t_k)). \tag{2.33}$$

The term $\overline{\xi(0)\xi(0)}\sum_{k=0}^{n}\eta_k\sum_{k'=0}^{n}\eta_{k'}$ leads to a divergence. It imposes the constraint $\sum_{k=0}^{n}\eta_k=0$, *i.e.* $n$ odd since $\eta_k=\pm1$. This condition is used for instance in plasma physics, where it imposes the neutrality condition for a gas of charges ±1 [58]. Replacing $n$ by $2n+1$, we have

$$\langle V(t)\rangle = \frac{\pi U_0}{i2e}\sum_{n=0}^{\infty}\left(\frac{iU_0}{2\hbar}\right)^{2n+1}\int_0^t \mathrm{d}t_1\ldots\int_0^{t_{2n}}\mathrm{d}t_{2n+1}\sum_{\{s\}}\sum_{\{\eta\}}\eta_0\prod_{k=1}^{2n+1}s_k\,\mathrm{e}^{\Gamma_n}, \tag{2.34}$$

$$\Gamma_n = i\frac{\pi}{e}I_b\sum_{k=0}^{2n+1}\eta_k t_k - \sum_{k=1}^{2n+1}\sum_{k'=0}^{k-1}\eta_k\eta_{k'}J(s_k(t_{k'}-t_k)). \tag{2.35}$$

The last task is to perform the sum over Keldysh indices. Noting $g_k = \sum_{k'=0}^{k-1}\eta_{k'}A(\tau_{k'}-\tau_k)$, we find

$$\sum_{\{s\}}s_1\ldots s_n\mathrm{e}^{i\sum_{k=1}^{2n+1}s_k\eta_k g_k} = \prod_{k=1}^{2n+1}\sum_{s_k=\pm}s_k\mathrm{e}^{is_k\eta_k g_k} = -i2^{2n+1}\eta_0\prod_{k=1}^{2n+1}\sin(g_k), \tag{2.36}$$

because $\prod_{k=1}^{2n+1}\eta_k = \eta_0 \prod_{k=0}^{2n+1}\eta_k = \eta_0(-1)^{n+1}$. This yields

$$V(t) = \frac{V_c}{2i}\sum_{n=0}^{+\infty}(-1)^n\left(\frac{U_0}{\hbar}\right)^{2n+1}\int_0^t \mathrm{d}\tau_1 \ldots \int_0^{\tau_{2n}} \mathrm{d}\tau_{2n+1} \sum_{\{f_k\}}\left(\prod_{k=1}^{2n+1}\sin g_k\right)\mathrm{e}^{\Gamma_n}\,. \tag{2.37}$$

For a given integer $n$ the discrete variables $f_k$ satisfy

$$|f_{k+1} - f_k| = 1, \tag{2.38}$$

with the constraint $f_0 = f_{2n+2} = 0$ [49, 70]. A set of such integers represents a graph which links the two extremal points $(0,0)$ and $(2n+2,0)$ by steps of unit length (see Fig. 2.5). The elements $g_k$ and $\Gamma_n$ are defined as follows

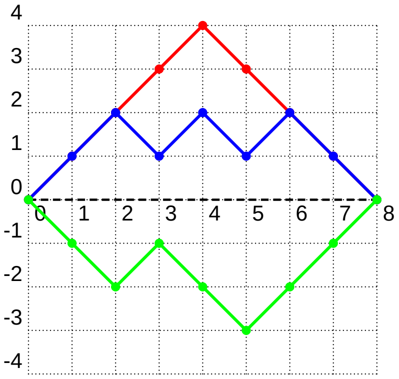

Figure 2.5: Example of graphs $f_k$ for $n = 3$.

$$g_k = A_{k,k-1}f_k + \sum_{k'=1}^{k-1}\delta A_{kk'}f_{k-k'}\,, \tag{2.39}$$

$$\Gamma_n = -i(\pi/e)I_b\sum_{k=1}^{2n+1}(\tau_k - \tau_{k-1})\,f_k - \sum_{k=1}^{2n+1}M_{k,k-1}f_k^2 + \sum_{k=2}^{2n+1}\sum_{k'=1}^{k-1}\delta M_{kk'}f_k f_{k'}\,. \tag{2.40}$$

Here $\delta M_{kk'} = M_{kk'} + M_{k-1,k'-1} - M_{k-1,k'} - M_{k,k'-1}$, $\delta A_{kk'} = A_{k,k-k'-1} - A_{k,k-k'}$, with the shorthand notation $A_{kk'} = A(\tau_k - \tau_{k'})$, and similar for $M_{kk'}$. The above equations are in a form suitable to apply the "nearest-neighbor approximation" (NNA), where one assumes that $\delta M_{kk'} \approx 0$ and $\delta A_{kk'} \approx 0$ [49] on the relevant time scale $\tau > 1/\omega_c$. Then, in the limit $t \to \infty$, the expression (2.37) can be evaluated exactly, and one obtains for the dc voltage $V$ across the junction:

$$V = V_c\,\mathrm{Im}(W_1/W_0)\;, \tag{2.41}$$

where $W_n$ obey the following recurrence relation $(n \geq 1)$

$$ia_n\,(W_{n-1} - W_{n+1}) = W_n\,, \tag{2.42}$$

with

$$a_n = \frac{U_0}{i\hbar}\int_0^{+\infty}\mathrm{d}\tau\,\sin\left(nA(\tau)\right)\,\mathrm{e}^{i(\pi/e)I_b n\tau - n^2 M(\tau)}\,. \tag{2.43}$$

The quantities $W_n$ should be identified with the Fourier transform of the quasicharge distribution function $W(q)$ in the steady state,

$$W(q) = \sum_{n=-\infty}^{+\infty} \mathrm{e}^{-in\pi q/e}\, W_n \,, \tag{2.44}$$

with the property $W_{-n} = W_n^*$. This becomes obvious by noticing that Eq. (2.41) can be viewed as a result of averaging the voltage operator with the quasicharge distribution $W(q)$,

$$V/V_c = W_0^{-1} \int_{-e}^{+e} \mathrm{d}q\, W(q) \sin\left(\pi q/e\right) \,. \tag{2.45}$$

From the recurrence relation of the coefficients $a_n$, the steady state voltage $V$ can be expressed in the form of a continued fraction (see appendix A.4)

$$V = V_c \,\mathrm{Re}\, \frac{a_1}{1 - \frac{a_1 a_2}{1 - \frac{a_2 a_3}{1 - \ldots}}} \,. \tag{2.46}$$

This formulation has analytical and numerical advantages.

## 2.3 Classical limit

Classically, the problem is equivalent to the equation of motion [56, 57],

$$\dot{q} = I_b - (V_c/R)\sin(\pi q/e)\,, \tag{2.47}$$

describing overdamped quasicharge diffusion with damping rate $\pi V_c/eR$. A stationary solution $\dot{q} = 0$ exists if $I_b < V_c/R$: all the current flows through the resistor, while the junction stays in a zero-current Coulomb blockade state with a voltage drop $V = RI_b$. If $I_b > V_c/R$, $\dot{q} \neq 0$ and a dynamical state exists at finite current with Bloch oscillations of the voltage. From Eq. (2.47) one finds the frequency of the oscillations to be $f_B = I/2e$, which was observed in the experiment of Ref. [71]. By direct integration of Eq. (2.47) over one period one obtains the dc voltage [56, 57]

$$V = RI_b - \sqrt{\left(RI_b\right)^2 - V_c^2}\,. \tag{2.48}$$

The resulting $I$-$V$ characteristic corresponds to the aforementioned Bloch nose and is depicted in Fig. 2.6.

The classical behavior is found in the limit where the temperature equals the cutoff frequency. Indeed, in this limit the environment loses its quantum properties and is characterized only by the temperature. When $g \ll 1$, the coefficients $a_n$ are reduced to

$$a_n = \frac{1}{2}\frac{z}{in + \eta}, \tag{2.49}$$

where $z = \beta U_0$ and $\eta = (e/\pi)\beta RI_b$. The recurrences (2.42) can then be solved analytically in terms of modified Bessel functions, $W_n = \mathrm{I}_{n-i\eta}(z)$ (see appendix A.5), resulting in the $I$-$V$ characteristics obtained in Ref. [61] from a Fokker-Planck approach

$$V = RI_b - \frac{\sinh\left(\pi\eta\right)}{e\beta\,|\mathrm{I}_{i\eta}(z)|^2}\,. \tag{2.50}$$

Generally speaking, all the results of Ref. [61], obtained in the classical regime, can be derived from our treatment. The classical *I*-*V* characteristic are in good agreement with the experimental results of Ref. [55], as can be seen in Fig. 2.1. This *I*-*V* characteristic is also the dual expression of Ref. [18], obtained in the overdamped regime.

## 2.4 Quasiclassical limit

To shed light on the range of applicability of the NNA for our system, we first study the quasiclassical limit where the typical time scale of the quasicharge dynamics, determined by the damping rate $gU_0/\hbar$ and the frequency of Bloch oscillations $f_B$ [see Eq. (2.47)], is slow. Indeed, if

$$gU_0/\hbar,\ f_B \ll 1/\hbar\beta,\ \omega_c\,, \tag{2.51}$$

one can neglect the terms $O(\mathrm{e}^{-\omega_k\tau},\, \mathrm{e}^{-\omega_c\tau})$ in Eqs. (2.12) and (2.13). We thus approximate [$\Xi(\tau)$ is the unit step function]

$$A(\tau) = \pi g\, \Xi(|\tau| - 1/\omega_c)\,, \tag{2.52}$$

and

$$M(\tau) = (g\omega_1|\tau| + \lambda)\, \Xi(|\tau| - 1/\omega_c)\,, \tag{2.53}$$

with

$$\lambda = 2g\left[\gamma + \frac{\pi}{\beta\hbar\omega_c} + \Psi\left(\frac{\beta\hbar\omega_c}{2\pi}\right)\right]\,, \tag{2.54}$$

where $\gamma = 0.577\ldots$ is the Euler constant and $\Psi(x)$ is the digamma function. Introducing the short–time cutoff for the approximated $A(\tau)$ and $M(\tau)$ is the simplest way to provide that they vanish at $\tau = 0$ [see the exact expressions (2.12) and (2.13)], which is necessary for the consistency of the applied NNA. Assuming also $g \ll 1$, one obtains for $a_n$ entering the recurrence relation (2.42),

$$a_n = \frac{z}{2i}\frac{\mathrm{e}^{-\Lambda n^2}}{n - i\eta}\,, \tag{2.55}$$

where [72, 73]

$$\Lambda = 2g\left[\gamma + \frac{2\pi}{\beta\hbar\omega_c} + \Psi\left(\frac{\beta\hbar\omega_c}{2\pi}\right)\right]\,. \tag{2.56}$$

Inspection of the terms dropped in the NNA reveals that in the range (2.51), where $A(\tau)$ and $M(\tau)$ can be simplified by their asymptotic expressions, the NNA becomes exact in the quasiclassical region where $\lambda$ is small. Note that for small $g$, the NNA can be applicable even at low temperature.

## 2.5 Quantum Smoluchowski equation

The crossover between the classical and quantum limit is controlled by the parameter $\lambda$ which is related to quantum corrections to the position dispersion of a fictitious Brownian particle in the harmonic potential [74].

- The classical limit corresponds to $\hbar\omega_c \sim k_BT$ and $g \ll 1$, or equivalently $\lambda,\, \Lambda \to 0$ ($\beta\hbar\omega_c \simeq 4.2$).

- The quantum regime corresponds to a large cutoff compared to the temperature, $\hbar\omega_c \gg k_B T$, so that the environment becomes fully quantum.
- The "quasi-isolated" regime corresponds to the limit $\hbar\omega_c \ll k_B T$. Indeed, in this regime, the exchanges with the environment are reduced and in the limit $\beta\hbar\omega_c \to 0$ the junction is isolated.

Expanding $a_n$ in Eq. (2.55) to the first order in $\Lambda$ to include quantum corrections, one can go to the continuum limit, using the properties of the Fourier coefficients $\mathrm{FC}_n$

$$\mathrm{FC}_n\left\{\frac{\partial^m W(q)}{\partial q^m}\right\} = \left(-i\frac{\pi}{e}\right)^m n^m\, W_n \tag{2.57}$$

$$\mathrm{FC}_n\left\{\cos(\pi q/e)\frac{\partial^{2m} W(q)}{\partial q^{2m}}\right\} = \frac{(-1)^m}{2}\left(\frac{\pi}{e}\right)^{2m}\left((n+1)^{2m}\, W_{n+1} + (n-1)^{2m}\, W_{n-1}\right) \tag{2.58}$$

$$\mathrm{FC}_n\left\{\sin(\pi q/e)\frac{\partial^{2m+1} W(q)}{\partial q^{2m+1}}\right\} = \frac{(-1)^{m+1}}{2}\left(\frac{\pi}{e}\right)^{2m+1} \times \left((n+1)^{2m+1}\, W_{n+1} - (n-1)^{2m+1}\, W_{n-1}\right) \tag{2.59}$$

One can then derive from Eq. (2.42) a differential equation for the quasicharge distribution $W(q)$,

$$\partial_q\left[\hat{\mathscr{S}}(q,\partial_q) - \Lambda\,(e/\pi)^4\, U'''(q)\,\partial_q^2\right] W(q) = 0\,, \tag{2.60}$$

where $U(q) = -U_0\cos(\pi q/e) - RI_b q$ is a washboard potential in the charge variable, $U'(q) \equiv \partial_q U$. The corresponding Smoluchowski differential operator,

$$\hat{\mathscr{S}}(q,\partial_q) = U'_{\mathrm{eff}}(q) + \beta^{-1} D(q)\,\partial_q\,, \tag{2.61}$$

is renormalized by quantum fluctuations through both the effective potential

$$U_{\mathrm{eff}}(q) = U(q) + \Lambda(e/\pi)^2\, U''(q) \tag{2.62}$$

and the $q$-dependent diffusion coefficient

$$D(q) = 1 + 2\beta\Lambda(e/\pi)^2\, U''(q)\,. \tag{2.63}$$

Eq. (2.60) is the so-called Quantum Smoluchowski Equation (QSE) which describes the leading quantum corrections to the charge dynamics which originate from the quantum nature of the bath. It was named after Marian Smoluchowski, who described the Brownian motion in 1906 independently of Albert Einstein with an equation which became an important basis of the theory of stochastic processes [75]. According to Eq. (2.56), the influence of quantum fluctuations becomes more substantial with increasing parameter $\beta\hbar\omega_c$. The *I-V* characteristics, parametrically dependent on the bias $I_b$ and calculated for different $\beta\hbar\omega_c$, are shown in Fig. 2.7. For $\beta\hbar\omega_c \gg 1$, quantum fluctuations reduce the blockade voltage and facilitate a crossover to the Bloch oscillations. Interestingly, for small $\beta\hbar\omega_c < 1$, the influence of thermal fluctuations becomes suppressed by the inertia effect of the "heavy" Brownian particle with an effective mass scaled as $\omega_c^{-1}$. For a wide range of $I_b$, the junction is locked in the insulating state because of the lack of energy exchange with the environment, which results in a sharp crossover to the Bloch oscillations. In other words, reducing the cutoff energy below the temperature is equivalent to

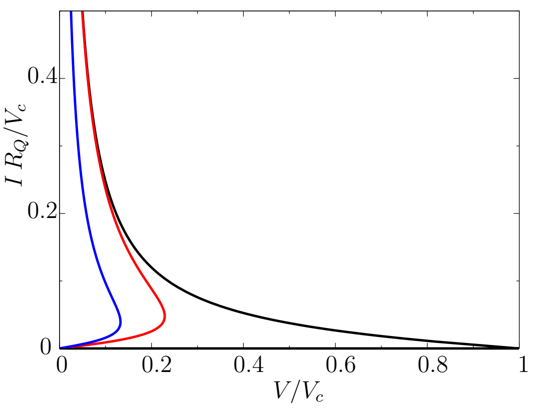

Figure 2.6: (from right to left) the classical limit without fluctuations (2.48), the result (2.50), and the solution from (2.41) for $g$=0.1, $\beta U_0$=0.5, and $\beta\hbar\omega_c$=50.

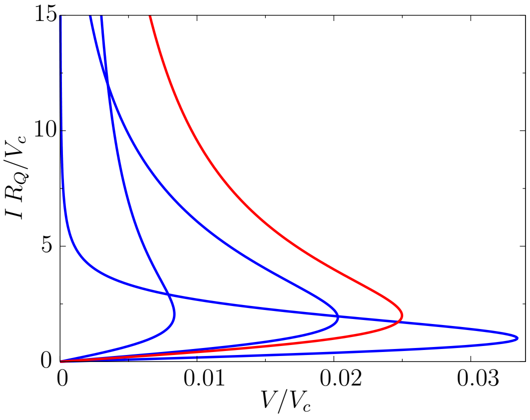

Figure 2.7: $I$-$V$ characteristics for $g$=0.1 and $\beta U_0$=0.1. The red line corresponds to the classical expression (2.50). Blue lines depict the result from (2.41) with, from right to left, $\beta\hbar\omega_c$=0.5, 5, and 50.

decoupling the junction from the environment (see Fig. 2.7).

We note in passing that the structure of the QSE obtained here from the series expansion (2.41) is different from the one derived in Ref. [74] for a Brownian particle in a slightly anharmonic potential and later applied to an overdamped junction [72, 73]. Therefore we cannot exploit the duality property (see below) to treat the Smoluchowski range for underdamped junctions using the results of Ref. [72, 73]. Another approximation consists of evaluating expression (2.37) using the asymptotes for long times (2.52) and (2.53) [60]. Such an approach leads to coefficients $a_n = \beta U_0\, \mathrm{e}^{-\lambda/2} \exp(-2\pi g n^2/\beta\hbar\omega_c)/2i(n - i\eta)$, which tend towards the result (2.55) in the quasiclassical region. As a consequence, a QSE equivalent to the solution (2.60) is also recovered.

## 2.6 Low temperatures

We proceed by studying Eqs. (2.41)–(2.43) in the low temperature limit, beyond the quasiclassical region (2.51). At very low temperature, $\beta\hbar\omega_c \gg 1$, the $I$-$V$ characteristics are entirely determined by the first coefficient $a_1$, Eq. (2.43), consistent with the fact that the NNA is exact to the lowest order in $U_0^2$. Closed-form analytical expressions can be obtained in several cases. For instance, at finite temperatures and for small values of $g$, the $I$-$V$ characteristic can be written as

$$V/V_c = u\,\frac{|\Gamma(g + i\hbar\beta I_b/2e)|^2}{\Gamma(2g)}\,\sinh\left(\pi\hbar\beta I_b/2e\right)\,, \tag{2.64}$$

where $u = (\beta U_0/4\pi)\,(\beta\hbar\omega_c\,\mathrm{e}^{\gamma}/2\pi)^{-2g}$ and $\Gamma(x)$ is the Gamma function (see appendix A.6). The resulting linear resistance $R$ varies as a power law with temperature, $R \propto T^{2(g-1)}$, in agreement with the asymptotic analysis of Ref. [47]. At zero-temperature one recovers

$$V/V_c = (\pi U_0/2)\,P(hI_b/2e)\,, \tag{2.65}$$

where $P(E) = 1/h \int \mathrm{d}t \exp\left[J(t) + iEt/\hbar\right]$, dual to the well-known result for the $I$-$V$ characteristic for incoherent Cooper pair tunneling in an overdamped junction [48]. In

Fig. 2.8, we plot $I$-$V$ characteristics for different $g$, both at zero and at finite temperatures. As $g$ increases, the voltage peak shifts to finite values of the supercurrent. This behavior can be interpreted in terms of incoherent tunneling of the phase [76]. Indeed, for small values of $g$, few environmental modes are available. Consequently, only elastic tunneling is allowed and a flat Bloch nose is recovered. When $g$ is large, the equivalent circuit consists of a loop containing the junction closed by the inductance $L$. A phase-slip event occurs when the energy to be released $\Phi_0 I_b$ corresponds to the energy $\Phi_0^2/2L$ to add one flux quantum $\Phi_0$ in the loop, *i.e.*, when $I_b = \Phi_0/2L$. At this finite current, phase tunneling disrupts the Bloch oscillations and gives rise to a voltage peak.

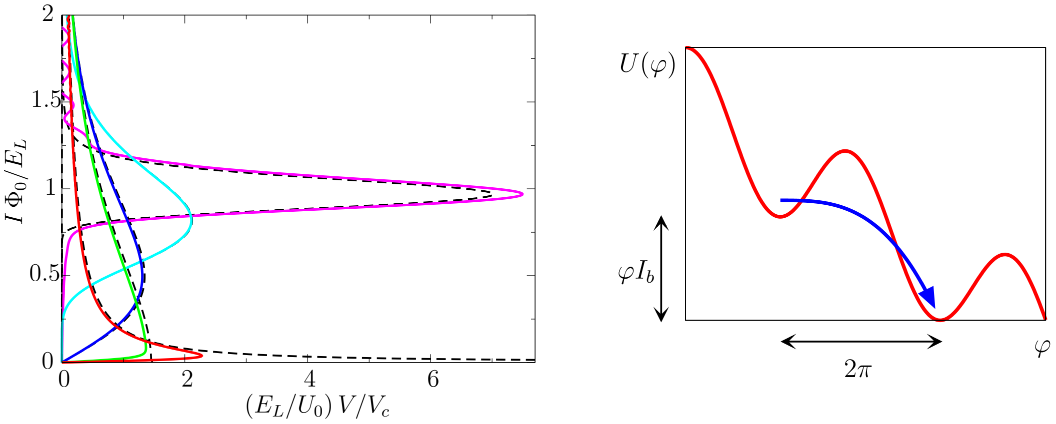

Figure 2.8: *Left panel*: $I$-$V$ characteristics at $T=0$ for $\hbar\omega_c = 100\,U_0$. From top to bottom, solid lines represent (2.41) for $\beta U_0$=0.5 and with $g$=100, 5, 1, 0.5 and 0.1. Dashed lines are the corresponding curves for the solution from (2.65). While decreasing $R$ the Bloch nose is shifted to the finite current $I = \Phi_0/2L$, where the tunneling of a flux quantum in the washboard potential $U(\varphi)$ requires an energy exchange with the bath, sketched on the *right panel*.

## 2.7 Quasi-isolated limit

When the cutoff frequency of the bath is small ($\beta\hbar\omega_c \ll 1$), the coupling with the environment is weak and the junction is quasi-isolated from the thermal bath. In this limit

$$a_n = \frac{z}{2in}, \qquad z = 2\beta U_0 \int_0^\infty \mathrm{d}x\, \sin(\pi g \beta\hbar\omega_c x)\, \mathrm{e}^{i\frac{\pi}{e}\beta\hbar I_b x - \pi g\beta\hbar\omega_c x^2}, \tag{2.66}$$

and the voltage reads

$$\frac{V}{V_c} = \mathrm{Im}\left\{\frac{\mathrm{I}_1(z)}{\mathrm{I}_0(z)}\right\}. \tag{2.67}$$

The $I$-$V$ characteristic tends to the supercurrent peak of an isolated junction, as represented in Fig. 2.7.

## 2.8 Overdamped Josephson junctions

A similar analysis within the Keldysh formalism can be achieved in the case of a voltage-biased overdamped Josephson junction in series with a resistance $R$. This circuit is conventionally described by the Hamiltonian $\mathcal{H} = (Q + Q_x)^2/2C - E_J \cos\varphi - V_b Q_x + \mathcal{H}_{\rm bath}$, where $Q_x$ is a fluctuating charge on the junction capacitor and $V_b$ is the bias voltage. Using an analysis of the equations of motion similar to the one preceding Eq. (2.9) and performing canonical transformations, one can show that the model description of the junction is equivalently given by the weak-binding (WB) Hamiltonian

$$\mathcal{H}_{\rm WB} = -E_J \cos(\varphi - \xi/2\pi) + V_b Q + \mathcal{H}_{\rm bath}\,, \tag{2.68}$$

with $\xi$ the bath variable defined as before, Eq. (2.8). In this representation, the junction capacitance $C$ is encoded in terms of the bath parameters, $C^{-1} = (R_Q/2\pi)\sum_\alpha \varsigma_\alpha^2 \omega_\alpha$, while the weighted spectral function of the bath is given by $K_{\rm WB}(\omega) = 2\pi {\rm Re} Z(\omega)/R_Q\,\omega$, with $Z^{-1}(\omega) = 1/R - i\omega C$. The operator for the current flowing through the junction is given by $I = I_c \sin(\varphi - \xi/2\pi)$, where $I_c = 2eE_J/\hbar$ is the critical current. The Hamiltonians $\mathcal{H}_{\rm TB}$ and $\mathcal{H}_{\rm WB}$ are related by the following transformation:

$$\begin{gathered}(\,\pi q/e,\ \varphi\,) \leftrightarrow (\,\varphi,\ -\pi Q/e\,)\,,\\ U_0 \leftrightarrow E_J\,,\quad I_b \leftrightarrow V_b/R_Q\,,\quad \xi \leftrightarrow \xi/2\pi\,.\end{gathered} \tag{2.69}$$

Consequently, the series expansions for $V/V_c$ in the TB model and for $I/I_c$ in the WB model are dual: we can transpose our results obtained for the quasicharge dynamics in an underdamped junction onto the dual case of the phase dynamics in an overdamped junction. A unified approach is thus provided, as well as new results such as the series expansion for $I/I_c$ [1]) and the quantum Smoluchowski equation.

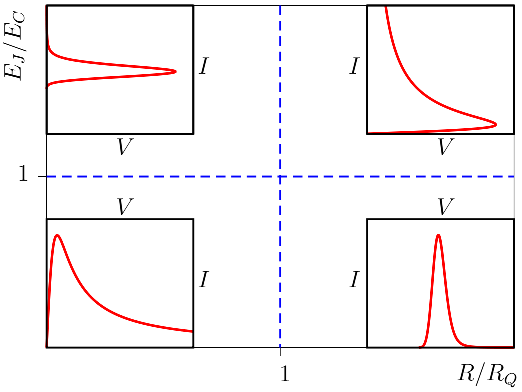

Figure 2.9: The overdamped regime $E_C \gg E_J$, $R \ll R_Q$ and the underdamped regime $E_J \gg E_C$, $R \gg R_Q$ are dual.

## 2.9 Superconducting nanowires

We conclude by considering quantum phase-slip (QPS) dynamics in superconducting nanowires. Based on a duality argument, Ref. [77] suggests the following model Hamiltonian to describe QPS events:

$$\mathcal{H}_{\rm QPS}(\varphi, Q) = E_L\,(\varphi/2\pi)^2 - E_S \cos(\pi Q/e)\,, \tag{2.70}$$

---

[1] The WB expansion for $I/I_c$, which is dual to (2.37), is similar but not identical to the one obtained in Ref. [51] using a different kind of approximation (not the NNA).

where $E_S$ is an energy associated with the phase-slip process which changes the phase difference $\varphi$ over the nanowire by $2\pi$, and $E_L = \Phi_0^2/2L$ is an inductive energy of the wire with a kinetic inductance $L$. Correspondingly, the Hamiltonian of a current-biased QPS junction (see Fig. 2.10) can be written as

$$\mathcal{H} = \mathcal{H}_{\mathrm{QPS}}(\varphi + \varphi_x, Q) + (\hbar/2e)\, I_b\, \varphi_x + \mathcal{H}_{\mathrm{bath}}\,, \tag{2.71}$$

where a fluctuating phase across the junction $\varphi_x$ is related to the voltage drop $V_R = R(\dot{Q} - I_b)$ on the resistor, $\dot{\varphi}_x = (2e/\hbar)V_R$. It is straightforward to see that the Hamiltonian (2.71) is exactly dual to the Hamiltonian of a voltage–biased Josephson junction, and can correspondingly be mapped onto the Hamiltonian (2.9) with $U_0$ replaced by $E_S$, while the inductance $L$ of nanowire is encoded in terms of the bath parameters, $L^{-1} = (2\pi/R_Q)\sum_\alpha \varsigma_\alpha^2 \omega_\alpha$. With this device, the frequency $\omega_c = R/L$ results from the physical resistance and inductance of the wire, providing a natural cutoff of the bath. Our previous analysis for an underdamped Josephson junction, and thus the $I$-$V$ characteristics, can be directly applied to a superconducting nanowire (not being restricted by the TB limit). A typical case of nanowire inductance $L \sim 1\,\mathrm{nH}$ corresponds to $\omega_c/2\pi \sim g^{-1} \times 1\,\mathrm{THz}$. Assuming $E_S/h \gtrsim 10\,\mathrm{GHz}$ [77] and $T \sim 1\,\mathrm{K}$, as follows from Eq. (2.51), we estimate that the QSE range for nanowires is relevant for $g \lesssim 0.1$. Note from the parameters used in Fig. 2.7 that the quantum fluctuations in QPS junctions should be substantial.

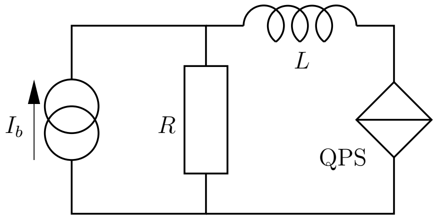

Figure 2.10: Equivalent circuit of Fig. 2.2 with a quantum phase slip junction represented by the diamond symbol.

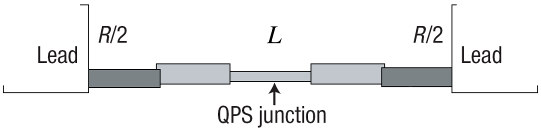

Figure 2.11: Quantum phase slip junction realized with a nanowire [77].

## 2.10 Towards a Josephson current standard

When the bias current has a time-oscillating term, for instance induced by a microwave, it is possible to create phase-locking [78]. If we note $\Omega$ the frequency of the sinusoidal part of the bias current, Shapiro current steps are obtained at currents that are multiple of $e\Omega/\pi$ (if the junction is voltage biased, we obtain Shapiro voltage steps). The proportionality between a current and a frequency can be used to define a Josephson-based current standard. This is the dual to the Josephson voltage standard [79].

Let us note

$$I_b(t) = I_b^0 + I_b^1 \sin \Omega t, \tag{2.72}$$

the time-dependent bias current and $\dot{q} = i_0 - i_1 \cos(\Omega t + \theta)$ the resulting current. Once put into Eq. (2.47), and following the method presented in Sec. 1.1, we obtain current Shapiro steps at $i_0 = en\Omega/\pi$ (see Fig. 2.12).

The width of the steps is given, approximately, by

$$\left|i_0 - I_b^0\right| \leq \frac{V_c}{R}\left|\mathrm{J}_n\left(\pi I_b^1/e\Omega\right)\right| , \tag{2.73}$$

where $\mathrm{J}_n$ is the modified Bessel function.

In quantum metrology, units are defined from the Hertz, the Volt and the Ampere. These three units form the so-called metrological triangle and are connected with each other. The link between Volt and Ampere is performed with the quantum Hall effect and the connection between Hertz and Volt with the Josephson effect. With the relation $I \propto \Omega$ on the Shapiro steps it is possible to close the quantum metrological triangle [20]. This would permit to redefine the international system of units with the Josephson effects and the quantum Hall effect.

## Conclusion and perspectives

To summarize, we have studied the influence of quantum fluctuations on the $I$-$V$ characteristics of an underdamped Josephson junction. We have applied a unifying approach based on the Keldysh formalism that enables us to obtain quantitative results for a wide range of parameters. Using the NNA approximation, we show the significant role of quantum fluctuations revealed both in the quasiclassical Smoluchowski regime and in the low-temperature quantum regime. In the Smoluchowski regime, compared to the case of thermal fluctuations, quantum fluctuations mainly lead to a renormalization of the parameters describing the quasicharge dynamics of the junction [60]. The NNA becomes exact in the case of incoherent phase-slip events at low temperatures. In this limit, phase tunneling disrupts the Bloch oscillations, leading to a voltage peak at finite current. The quantum effects are sensitive to both the dissipation strength and cutoff frequency, and could be observed in experiments as in Refs. [53–55] with a tunable environment. Besides Josephson junctions, our results are also relevant for superconducting nanowires modeled as quantum phase-slip junctions at low temperature.

The treatment presented in this chapter can be extended to access interesting properties and applications of Josephson junction based nanocircuits. The formalism can be generalized to calculate two-point correlation functions such as the voltage noise. The

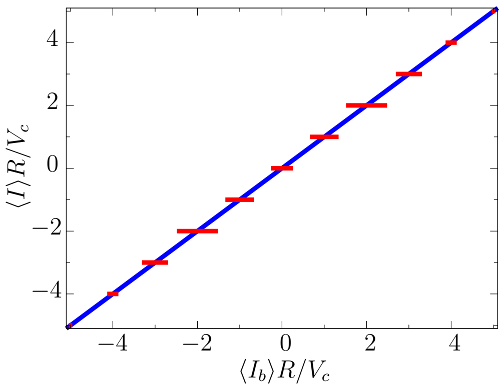

Figure 2.12: Current-voltage characteristics of an underdamped Josephson junction biased with an oscillating current. Current Shapiro steps appear at $\langle I\rangle = n\, e\Omega/\pi$. Parameters are $R = R_Q/5$, $I_b^1 = 3V_c/R$, and $\Omega = 5V_c/\phi_0$.

full counting statistics [80] can also be calculated, at least in the classical regime or with an extended NNA. The nonlinear behavior of the Josephson junction can be exploited to amplify the moments (many-points correlation functions) of a mesoscopic device [81–83]. Finally, the possibility to realize a Josephson current standard is currently investigated experimentally in the group of Wiebke Guichard at the Néel institute in Grenoble [78].

# La jonction Josephson sous-amortie

## Résumé du chapitre

Nous étudions la dynamique quantique d'une jonction Josephson polarisée en courant dans le régime sous-amorti. Ce régime, où l'énergie Josephson domine l'énergie de charge et où l'environnement est hautement résistif, a été peu étudié mais récemment atteint expérimentalement à l'Institut Royal de Technologie de Stockholm. Notre traitement s'appuie sur le formalisme de Keldysh et permet d'obtenir les caractéristiques courant-tension du régime classique à la limite de température nulle. Les fluctuations quantiques induisent une transition entre une branche de blocage de Coulomb et une branche supraconductrice. La forme du nez de Bloch dépend de la température mais aussi de la résistance de l'environnement. Dans le régime semi-classique, nous obtenons l'équation de Smoluchowski quantique qui décrit les corrections dues aux fluctuations quantiques à la dynamique de la quasi-charge. L'effet majeur des fluctuations quantiques est de renormaliser la largeur de la bande de Bloch. Nos résultats peuvent être directement appliqués au régime sur-amorti en utilisant la dualité entre ces deux limites. Notre étude peut également être étendue aux nano-fils supraconducteurs, jouant le rôle de jonction à saut de phase.

Chapter 3

# Superconducting phase qubit in a camel-back potential

**Contents**

## Introduction

We study the tunneling effect from a metastable state of a quartic potential $\frac{1}{2}M\omega_0^2z^2(1-u_3z-u_4z^2)$, with a double escape path. The escape rate is calculated in the framework of the instanton formalism. This novel potential shape is realized with a superconducting circuit comprised of a loop interrupted by two Josephson junctions (dc SQUID), with near-zero current bias and flux bias near half a flux quantum [84]. The dynamics is restricted to the ground state and the first excited state of the well, giving rise to a phase qubit. A new experimental technique has been developed to measure the state of the qubit as well as the critical lines. A good agreement is found between our result and the experimental data. We also demonstrate that this system exhibits an “optimal line” in current and flux bias space along which the oscillator is insensitive to decoherence due to low-frequency current fluctuations.

## 3.1 Quantum dynamics of the dc-SQUID phase qubit

### 3.1.1 Circuit and Hamiltonian

The SQUID (Superconducting Quantum Interference Device) is a superconducting loop interrupted by two Josephson junctions [16]. The Josephson junctions are characterized by their critical currents $I_{c_{1,2}}$, their capacitances $C_{1,2}$, and the phase differences $\varphi_{1,2}$ across them. Each arm of the loop has a self-inductance $L_{1,2}$ and carries a partial current $I_{1,2}$. The SQUID is biased by the current bias $I_b = I_1 + I_2$ and the flux bias $\Phi_b$. The electric circuit of the SQUID is represented in Fig. 3.1. Applying Faraday's law for magnetic flux conservation and Kirchhoff's law for current conservation, we get

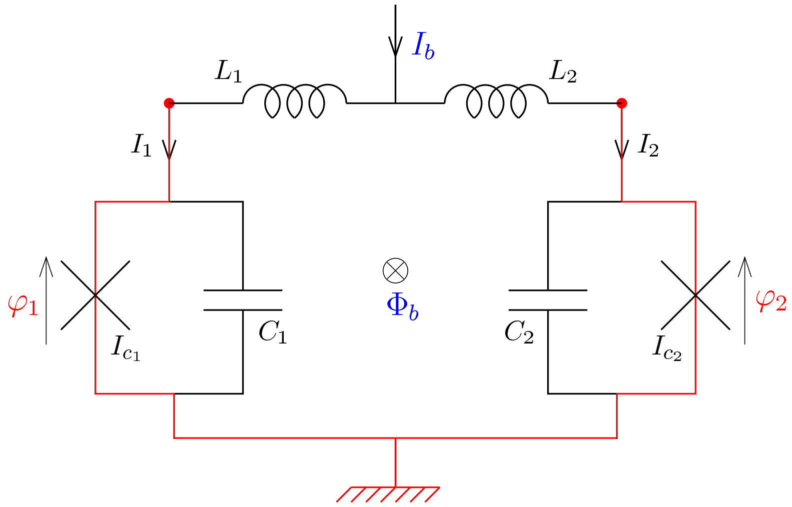

Figure 3.1: Electric circuit of the dc-SQUID.

$$\begin{cases} I_1 = I_{c_1} \sin\varphi_1 + \phi_0 C_1 \ddot{\varphi}_1, \\ I_2 = I_{c_2} \sin\varphi_2 + \phi_0 C_2 \ddot{\varphi}_2, \end{cases} \tag{3.1}$$

and

$$\Phi_b = \phi_0(\varphi_1 - \varphi_2) + L_1 I_1 - L_2 I_2, \tag{3.2}$$

where $\phi_0 = \hbar/2e$ is the reduced flux quantum. Eqs. (3.1) correspond to the equations of motion $\dfrac{\partial\mathcal{L}}{\partial\varphi_i} = \dfrac{\mathrm{d}}{\mathrm{d}t}\dfrac{\partial\mathcal{L}}{\partial\dot{\varphi}_i}$ of the Lagrangian

$$\begin{aligned} \mathcal{L} = \frac{\phi_0^2}{2}\left(C_1\dot{\varphi}_1^2 + C_2\dot{\varphi}_2^2\right) + E_{J_1}\cos\varphi_1 + E_{J_2}\cos\varphi_2 \\ + \frac{\phi_0 I_b}{L_1+L_2}\left(L_2\varphi_1 + L_1\varphi_2\right) - \frac{\phi_0^2}{2(L_1+L_2)}\left(\varphi_1 - \varphi_2 - \Phi_b/\phi_0\right)^2. \end{aligned} \tag{3.3}$$

The momentum conjugate to $\phi_0\varphi_i$ is the charge $Q_i = C_i\phi_0\varphi_i$. The corresponding Hamiltonian reads

$$\begin{aligned} \mathcal{H} =& \frac{Q_1^2}{2C_1} + \frac{Q_2^2}{2C_2} - E_{J_1}\cos\varphi_1 - E_{J_2}\cos\varphi_2 \\ &- \frac{\phi_0 I_b}{L_1+L_2}\left(L_2\varphi_1 + L_1\varphi_2\right) + \frac{\phi_0^2}{2(L_1+L_2)}\left(\varphi_1 - \varphi_2 - \Phi_b/\phi_0\right)^2. \end{aligned} \tag{3.4}$$

The potential energy $\mathcal{U}(\varphi_1, \varphi_2)$ of the SQUID is defined in the plane $(\varphi_1, \varphi_2)$. In the following, we consider a SQUID with almost the same capacitances in each arm, *i.e.* $C_1 \simeq C_2$. In this limit we introduce the reduced variables

$$x = \frac{\varphi_1 + \varphi_2}{2}, \qquad y = \frac{\varphi_1 - \varphi_2}{2}, \tag{3.5}$$

with the corresponding charges $Q_x$ and $Q_y$, the reduced biases

$$s = I_b/I_c, \qquad y_b = \frac{\Phi_b}{2\phi_0}, \tag{3.6}$$

and the following dimensionless parameters

- the critical current asymmetry $\alpha = (I_{c_2} - I_{c_1})/I_c$, with $I_c = I_{c_2} + I_{c_1}$,
- the loop inductance asymmetry $\eta = (L_2 - L_1)/L$, with $L = L_2 + L_1$,
- the junction to loop inductance ratio $b = 2\phi_0/LI_c$.

The Hamiltonian in the $(x, y)$ space reads

$$\mathcal{H} = \frac{Q_x^2 + Q_y^2}{2C} + E_J u(x, y), \tag{3.7}$$

where $C^{-1} = C_1^{-1} + C_2^{-1}$ and $E_J = E_{J_1} + E_{J_2}$. In the limit $C_1 \simeq C_2$, the coupling terms between $Q_x$ and $Q_y$ are neglected. The reduced potential energy $u(x, y)$ is

$$u(x, y) = -\cos x \cos y - \alpha \sin x \sin y - sx - s\eta y + b(y - y_B)^2. \tag{3.8}$$

The dynamics is then equivalent to a free fictitious particle of mass $M = \phi_0^2 C$ and coordinates $(x, y)$ moving in the potential $u(x, y)$.

The characteristic energy scale of the SQUID is given by its plasma frequency $\omega_p$. We define $\omega_p$ as the frequency of the phase fluctuations in a local minimum of a symmetric SQUID at zero bias current and bias flux

$$\hbar\omega_p = \sqrt{8E_J E_C}, \tag{3.9}$$

where $E_C = \dfrac{e^2}{2C} = E_{C_1} + E_{C_2}$ is the charging energy of the SQUID. The effective frequency of the phase oscillations depends on the working points and is lower than $\omega_p$. The plasma frequency is about one half of the mean plasma frequency of the junctions.

## 3.1.2 The SQUID potential

### 3.1.2.a Topography of the potential

The presence of the cosine and sine terms in the potential $u(x, y)$ of Eq. (3.8) gives rise to local minima connected by saddle points, as plotted on Fig. 3.2. The extremum points are determined with the spatial derivatives of the potential $\partial_x u(x, y)$, $\partial_y u(x, y)$, $\partial_{xx}^2 u(x, y)$, $\partial_{xy}^2 u(x, y)$, $\partial_{yy}^2 u(x, y)$. In the following, we notice the derivatives $u_x(x, y) = \partial_x u(x, y)$ and so on for the others. The location of the extremum points of the potential are obtained by solving the set of equations $u_x(x, y) = u_y(x, y) = 0$, *i.e.*

$$\begin{cases} \sin x \cos y - \alpha \cos x \sin y = s, \\ \cos x \sin y - \alpha \sin x \cos y + 2b(y - y_B) = \eta s. \end{cases} \tag{3.10}$$

This is performed numerically. The position of the extremum points is $2\pi$-periodic in the $x$ direction and, due to the quadratic confinement in the $y$ direction, the coordinate $y$ is constrained to the region

$$y_B + \frac{\eta s + |s + \alpha| - 1}{2b} < y < y_B + \frac{\eta s - |s - \alpha| + 1}{2b}. \tag{3.11}$$

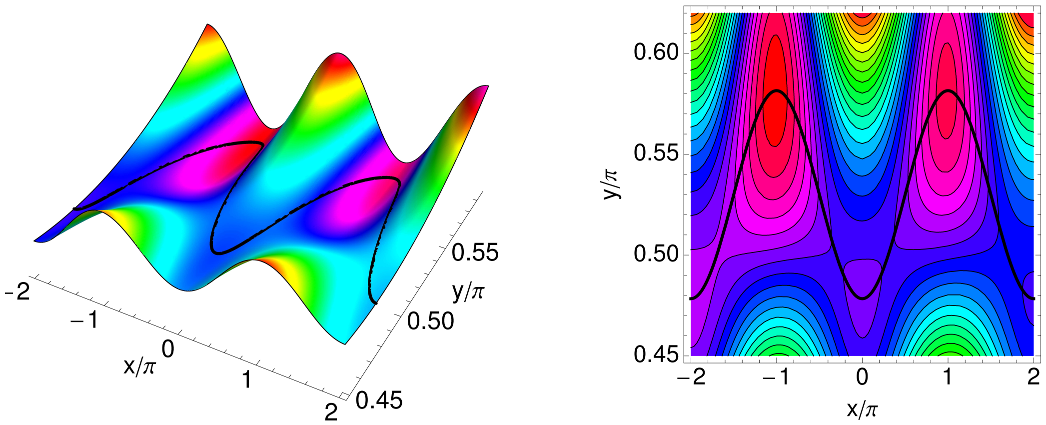

Figure 3.2: Potential $u(x, y)$ of the SQUID at the bias fields $I_b = -70\,\mathrm{nA}$ and $\Phi_b = 0.531\,\phi_0$.

The classification of extremum points is obtained with the Hessian matrix

$$F(x, y) = \begin{pmatrix} u_{xx}(x, y) & u_{xy}(x, y) \\ u_{yx}(x, y) & u_{yy}(x, y) \end{pmatrix}, \tag{3.12}$$

- minimum: $\det F > 0$ and $\operatorname{Tr} F > 0$,
- maximum: $\det F > 0$ and $\operatorname{Tr} F < 0$,
- saddle point: $\det F < 0$.

In practice, $|\alpha| \ll 1$ and $b > 1$, as a consequence $\operatorname{Tr} F > 0$ and there are only minima and saddle points.

### 3.1.2.b Fluxoid states

If the fictitious particle is trapped in a minimum, the phases $\varphi_1$ and $\varphi_2$ oscillate with a constant mean value depending in particular on the bias current. According to the dc Josephson equation there is no voltage across the junction, the SQUID is therefore in a superconducting state. The characteristics of the superconducting state depend on the local minima. The extremum points being $2\pi$-periodic in the $x$ direction, the minimum at a given value of the coordinate $y$ are locally equivalent. They constitute a fluxoid state family, characterized by the number $f$ of flux quanta trapped in the loop.

Starting from the state $[f]$, the path that minimizes the potential energy passes through a saddle point and then reaches the minimum corresponding to the state $[f \pm 1]$. This is the path that would take a thermally excited classical particle to go from the minimum $[f]$ to the minimum $[f \pm 1]$. As we are dealing with very low temperatures, thermal excitations are suppressed and the fictitious particle has quantum properties. In particular, the particle can tunnel through the potential barrier that separates it from the other minima. As we will see in the following, the tunneling rate decreases exponentially with the barrier height. This ensures that the tunneling events occur along the path that minimizes the potential energy. The quantum dynamics between the states $[f]$ and $[f \pm 1]$ can thus be treated using the one-dimensional potential that corresponds to the two-dimensional potential along the path of minimum potential energy. The reduction of dimension is treated in Sec. 3.1.3.

### 3.1.2.c Critical diagram

The presence of extremum points is governed by the bias fields. Indeed, if $s$ is larger than unity for example, there are no minima. For a given value of the flux, we define the critical current as the value $s_c$ at which the critical extremum points satisfy $\det F = 0$. At this value of the bias current, the minima merge with the saddle points and there are no minima nor saddle points for bias current $s$ above $s_c$. The diagram $s_c(y_B)$ is called the critical diagram (see Fig. 3.12).

The critical diagram is obtained from the numerical solutions of $u_x = u_y = \det F = 0$ for a given value of the flux bias. This set of equations reads

$$\begin{cases} \sin x_c \cos y_c - \alpha \cos x_c \sin y_c = s_c, \\ \cos x_c \sin y_c - \alpha \sin x_c \cos y_c + 2b(y_c - y_B) = \eta s_c, \\ (\cos x_c \cos y_c + \alpha \sin x_c \sin y_c)(\cos x_c \cos y_c + \alpha \sin x_c \sin y_c + 2b) \\ \qquad\qquad\qquad\qquad = (\sin x_c \sin y_c + \alpha \cos x_c \cos y_c)^2. \end{cases} \tag{3.13}$$

The whole diagram can be obtained from the solution in the range $s > 0$ and $-\pi/2 < y_B \leq \pi/2$ using the symmetries

$$\begin{cases} y_B \to y_B + \pi f, \\ s_c \to s_c, \\ x_c \to x_c + \pi f, \\ y_c \to y_c + \pi f, \end{cases} \tag{3.14}$$

$$\begin{cases} y_B \to 2\pi f - y_B, \\ s_c \to -s_c, \\ x_c \to 2\pi f - x_c, \\ y_c \to 2\pi f - y_c. \end{cases} \tag{3.15}$$

For the particular flux bias $y_B = \pi/2 - (1 + \eta\alpha)/2b$ the solution is $x_c = \pi$, $y_c = \pi/2$, and $s_c = \alpha$. The critical diagram is used to determine the region of existence of the states $[f]$ in the plane $(y_B, s)$.

## 3.1.3 Reduction to one dimension

### 3.1.3.a Average over the transverse motion

The typical shape of the potential $u(x, y)$ is composed of local minima and saddle points connected by narrow valleys. To study the phase dynamics from minima to minima in this potential, we will suppose that the fictitious particle follows the path of minimal curvature. We can then describe the dynamics with one variable, since the path in the plane $(x, y)$ is determined by $x$ and $y = \zeta(x)$. We call $z(x)$ the curvilinear abscissa along the path of minimum potential, defined by

$$z(x) = z_0 + \int_{x_0}^{x} \mathrm{d}x' \sqrt{1 + \zeta'^2(x')}. \tag{3.16}$$

Now let us consider a point $(x_0, y_0)$ at abscissa $z_0$ on this path and call $\theta$ the angle between the $x$ axis and the direction of minimal curvature ($\theta \in [-\pi, \pi]$)

$$\theta(x_0) = \frac{1}{2} \arctan\left( \frac{2\partial^2_{xy} u(x_0, y_0)}{\partial^2_{xx} u(x_0, y_0) - \partial^2_{yy} u(x_0, y_0)} \right). \tag{3.17}$$

The direction of minimal curvature is denoted by $X_{//}$ and the perpendicular direction, given by the angle $\theta + \pi/2$, is denoted by $X_\perp$. The correspondence between $(x, y)$ and

$(X_{//}, X_\perp)$ is given by the rotation matrix

$$\begin{pmatrix} X_{//} \\ X_\perp \end{pmatrix} = \begin{pmatrix} \cos\theta_0 & \sin\theta_0 \\ -\sin\theta_0 & \cos\theta_0 \end{pmatrix} \cdot \begin{pmatrix} x - x_0 \\ y - y_0 \end{pmatrix} . \tag{3.18}$$

We can then express the Hamiltonian in terms of $X_{//}$, $X_\perp$, $P_{//} = M\dot{X}_{//}$, and $P_\perp = M\dot{X}_\perp$.

In the transverse direction, the transverse frequency is much larger than the plasma frequency $\omega_p = \sqrt{8E_C E_J}$. The transverse potential is thus safely approximated by a harmonic potential of bottom well frequency $\omega_\perp$. The fictitious particle can then be treated as a harmonic oscillator in the ground state in the transverse direction. To show that the transverse dynamics is frozen in the ground state, we can evaluate the overlap of the transverse wavefunctions $\psi_z(x_\perp)$ at two points $z_1$ and $z_2$ along the path of minimal curvature. The overlap $\mathcal{R}(z_1, z_2)$ of the ground state wavefunctions

$$\Psi_{1,2}(x) = \left[\frac{m\omega_\perp(z_{1,2})}{\pi\hbar}\right]^{1/4} \exp\left\{-\frac{m\omega_\perp(z_{1,2})}{2\hbar}x^2\right\}, \tag{3.19}$$

reads

$$\mathcal{R}(z_1, z_2) = \int_{-\infty}^{+\infty} \mathrm{d}x\, \Psi_1(x)\Psi_2(x) = \frac{\sqrt{2}\,[\omega_\perp(z_1)\omega_\perp(z_2)]^{1/4}}{[\omega_\perp(z_1) + \omega_\perp(z_2)]^{1/2}}. \tag{3.20}$$

If we choose $z_2 = z + \delta z$ close to $z_1 \equiv z$, we have

$$\mathcal{R}(z, z+\delta z) \simeq 1 - \left(\frac{\omega_\perp'(z)\,\delta z}{4\omega_\perp(z)}\right)^2 . \tag{3.21}$$

In order to obtain an adiabatic evolution in the ground state, the condition is thus $\dfrac{\omega_\perp(z)}{\omega_\perp'(z)} \gg \delta z$, where the characteristical distance $\delta z$ is of the order of unity ($\delta z < 2\pi$). The numerical evaluation of these quantities shows that the adiabaticity condition is satisfied ($\omega_\perp(z)/\omega_\perp'(z) \gg 1$ and $\mathcal{R}(z_1, z_2) \lesssim 1$, see Fig. 3.3)

The transverse oscillations being much faster than the plasma frequency, the transverse motion can be averaged out. The dynamics in the longitudinal direction is then governed by the effective Hamiltonian $\mathcal{H}_{//} = \langle\mathcal{H}\rangle_\perp$ obtained after averaging $\mathcal{H}$ over the transverse degree of freedom. The kinetic part of the Hamiltonian is obtained using $P_x^2 + P_y^2 = P_{//}^2 + P_\perp^2$. At second order in the transverse motion, the dynamics is governed by the Hamiltonian

$$\mathcal{H}_\perp = \frac{P_\perp^2}{2M} + \frac{M\omega_\perp^2}{2}(X_\perp - X_0)^2 - \frac{M\omega_\perp^2}{2}X_0^2, \tag{3.22}$$

where the parameter $X_0$ comes from the slope of the potential in the transverse direction. Defining $\partial_\perp$ as the derivative in the transverse direction $\frac{\partial}{\partial X_\perp}$, the transverse frequency and $X_0$ read

$$\omega_\perp = \sqrt{\partial_\perp^2 u(x, y)}\,\omega_p, \tag{3.23}$$

$$X_0 = \frac{\partial_\perp u(x, y)}{\partial_{\perp\perp}^2 u(x, y)}, \tag{3.24}$$

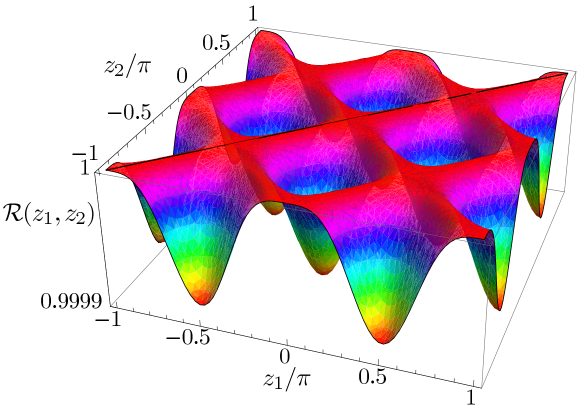

Figure 3.3: Overlap $\mathcal{R}(z_1,z_2)$ of the wavefunctions $\Psi_1(x)$ and $\Psi_2(x)$ of the harmonic oscillator ground state at two points $z_1$ and $z_2$ with different curvatures along the path of minimal curvature.

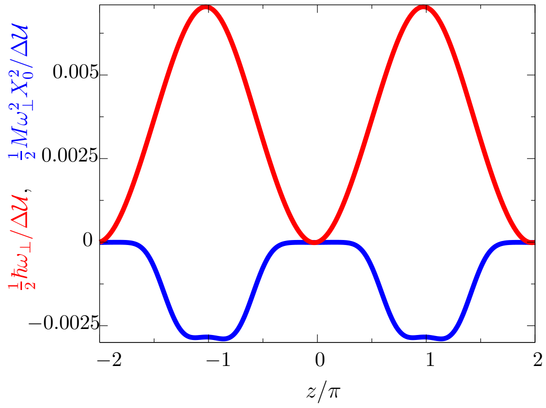

Figure 3.4: Corrections $\langle\mathcal{H}_\perp\rangle_\perp$ to the potential due to the transverse motion, in units of the barrier height $\Delta\mathcal{U}$. The potential is shifted to satisfy $\langle\mathcal{H}_\perp\rangle_\perp(z=0)=0$.

where the derivatives satisfy

$$\partial_\perp u(x,y) = -\sin\theta u_x(x,y) + \cos\theta u_y(x,y), \tag{3.25}$$

$$\partial^2_{\perp\perp} u(x,y) = u_{xx}(x,y) - \sin 2\theta\, u_{xy}(x,y) + 2b\cos^2\theta. \tag{3.26}$$

As a consequence, averaging on the transverse direction gives rise to two contributions to the potential of $\mathcal{H}_{//}$

$$\langle\mathcal{H}_\perp\rangle_\perp = \tfrac{1}{2}\hbar\omega_\perp - \tfrac{1}{2}M\omega_\perp^2 X_0^2. \tag{3.27}$$

We notice in passing that the value $\langle X_\perp^2\rangle = \dfrac{\omega_p}{\omega_\perp}\sqrt{\dfrac{2E_C}{E_J}} \ll 1$ corroborates the validity of the hamonic approximation.

The effective Hamiltonian reads

$$\mathcal{H}_{//} = \frac{P_{//}^2}{2M} + \mathcal{U}(x), \tag{3.28}$$

where $\mathcal{U}(x) = E_J\left[u(x,\zeta(x)) + \mu(x)\right]$, with $\mu(x) = \langle\mathcal{H}_\perp\rangle_\perp/E_J$. In practice, however, the additional potential $\mu$ is a small correction to $u$ (see Fig. 3.4).

### 3.1.3.b One-dimensional potential

We choose the origin of the curvilinear abscissa at a particular minimum $\text{Min}_C$ with coordinates $(x_m, y_m)$ and fluxoid state $[f]$. Along the path of minimum potential $(x,\zeta(x))$, this minimum is connected to two saddle points $\text{Saddle}_{R,L}$, which are both connected to another minimum $\text{Min}_{R,L}$ according to the one-dimensional potential $\mathcal{U}(z) = E_J[u(z) + \mu(z)]$. The convention is to call $\text{Min}_R$ the peripheral minimum with the lowest potential energy and to orient $z$ towards $\text{Min}_R$.

If we focus on the dynamics around the minimum, this potential is well approximated by its Taylor expansion up to fourth order, *i.e.* $\mathcal{U}(z) = \mathcal{U}(0) + U(z) + O(z^5)$ with

$$U(z) \simeq \frac{1}{2}M\omega_0^2 z^2\left(1 - u_3 z - u_4 z^2\right), \tag{3.29}$$

where the bottom well frequency $\omega_0$ and the coefficients $u_3 \geq 0$, $u_4 \geq 0$ are obtained numerically or with approximate expressions in specific cases (see Fig. 3.14). The abscissa $q_{R,L} = z(\text{Saddle}_{R,L})$ of the saddle points are

$$q_{R,L} = \frac{-3u_3 \pm \sqrt{9u_3^4 + 32u_4}}{8u_4}. \tag{3.30}$$

We also define the escape points at abscissa $\sigma_{R,L}$ where $U(\sigma_{R,L}) = 0$

$$\sigma_{R,L} = \frac{-u_3 \pm \sqrt{u_3^4 + 4u_4}}{2u_4}. \tag{3.31}$$

The point at $\sigma_R$ is always defined whereas $\sigma_L$ has a physical meaning only when $\mathcal{U}(\text{Min}_L) \leq \mathcal{U}(\text{Min}_C)$.

When the coefficient $u_4$ is larger than $u_3$, the potential is composed of two barriers. Because of these two "humps", we decide to call this potential the "camel-back" potential.

### 3.1.4 Anharmonic quantum oscillator

The dynamics in a given minimum is governed by the Hamiltonian

$$\mathcal{H}_{\text{aho}} = \hbar\omega_0 \left(P_z^2 + Z^2\right) - a\hbar\omega_0 Z^3 - b\hbar\omega_0 Z^4, \tag{3.32}$$

where $Z = \sqrt{M\omega_0/\hbar}z$ is the reduced position operator, $P_z$ is the corresponding momentum operator, $a = u_3\sqrt{\hbar/M\omega_0}/2$, and $b = u_4\hbar/2M\omega_0$. At sufficiently low temperatures below the plasma frequency, the energy spectrum of the particle is quantized in the minimum. A second order perturbation theory [85] in $a$ and $b$ leads to a transition frequency between the levels $n$ and $n-1$

$$h\nu_{n,n-1} = \hbar\omega_0 \left(1 - n\lambda_n\right), \tag{3.33}$$

where $\lambda_n$ is the anharmonicity of the oscillator

$$\lambda_n = 3b + \frac{15}{4}a^2 + \frac{3}{4}b^2\left(\frac{7}{n} + 17n\right). \tag{3.34}$$

The anharmonicity depends on the working point $(I_b, \Phi_b)$. A sufficiently large anharmonicity is necessary to reach the two-level limit. Indeed, the manipulation of the states is performed with a microwave in resonance with the energy difference between the ground state and the first excited state. For a harmonic oscillator, where the anharmonicity is zero by definition, this microwave would excite all the levels. The two states $|0\rangle$ and $|1\rangle$ constitute a qubit. The confining potential depending on the phases, this two level system is called a phase qubit [86–89].

## 3.2 Macroscopic quantum tunneling in a general quartic potential

The quantum dynamics of the dc-SQUID phase qubit is governed by the tunneling through the quartic potential (3.29). The expression of the corresponding escape rate, with a double escape path, is not explicitly given in the literature of macroscopic quantum tunneling (see *e.g.* Refs. [90–92]) and has to be calculated. We use the instanton

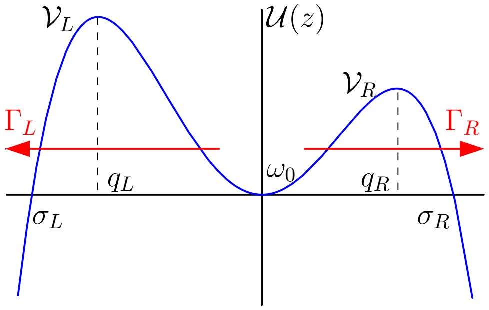

Figure 3.5: Scheme of the general quartic potential with a metastable state and two escape paths.

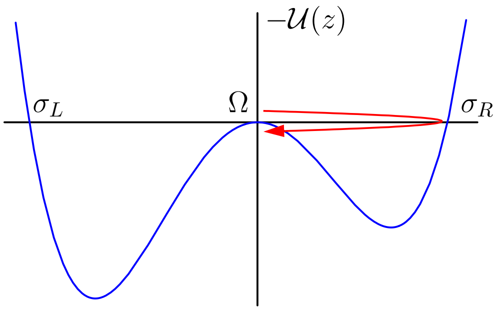

Figure 3.6: Inverted potential corresponding to Fig. 3.5.

technique [93, 94], detailed with further explanations in appendix B, to derive the escape rate from the metastable state of the potential sketched on Fig. 3.5.

The escape rate $\Gamma$ is obtained from the imaginary part of the energy $E$ of the fictitious particle in the local minimum. Indeed, in the well, the norm of the particle wave-function $\Psi(z,t)$ satisfies the temporal evolution

$$\int \mathrm{d}z\, |\Psi(z,t)|^2 = \mathrm{e}^{-2\mathrm{Im}\, Et/\hbar}, \tag{3.35}$$

which decays exponentially with the decay rate

$$\Gamma = -\frac{2}{\hbar}\, \mathrm{Im}\, E. \tag{3.36}$$

The lifetime of the state is equal to $\Gamma^{-1}$.

To find the energy $E$, we start from the general Hamiltonian

$$\mathcal{H} = \frac{P^2}{2M} + \mathcal{U}(z), \tag{3.37}$$

where $P = M\frac{\mathrm{d}z}{\mathrm{d}t}$ is the momentum of the particle. The classical version of this system possesses a stable equilibrium state in which the particle is at rest at $z = 0$. However, quantum corrections render this state unstable: it is a false ground state. The probability amplitude for the particle to go from a point $z_i$ at time $t_i$ to the point $z_f$ at time $t_f$ is then given by the propagator

$$K(z_i, t_i; z_f, t_f) = \langle z_f | \mathrm{e}^{-i\mathcal{H}(t_f - t_i)/\hbar} | z_i \rangle, \tag{3.38}$$

where $|z_{i,f}\rangle$ are position eigenstates. To calculate this probability amplitude we sum the contributions of all possible trajectories satisfying the boundary conditions. For a given path, the phase of the contribution is the corresponding action $S$ in units of the quantum action $\hbar$ [95]. To calculate this integration, let us perform first a Wick rotation: time $t$ is replace by the imaginary time $\tau = it$. Then the action $S$ becomes the Euclidean action $\mathcal{S}$

$$\mathcal{S} = \int_{-\frac{T}{2}}^{\frac{T}{2}} \mathrm{d}\tau \left[ \frac{M}{2}\dot{z}^2 + \mathcal{U}(z) \right], \tag{3.39}$$

where the dot means time derivative with respect to $\tau$ and $it_i = -T/2$, $it_f = T/2$. In terms of path integrals the propagator reads

$$\langle z_f|\mathrm{e}^{-\mathcal{H}T/\hbar}|z_i\rangle = \mathcal{N}\int_{z_i}^{z_f} \mathcal{D}z\,\mathrm{e}^{-\mathcal{S}/\hbar}. \tag{3.40}$$

The parameter $\mathcal{N}$ is a normalization factor and $\mathcal{D}z$ denotes the integration over all functions $z(t)$ obeying the boundary conditions $z(t_i) = z_i$ and $z(t_f) = z_f$. The effect of the Wick rotation on the action is thus to invert the potential. In other words, in the part of space between $z = 0$ and $z = \sigma_{L,R}$, the momentum of the particle is imaginary: $P^2 = -2M\mathcal{U} < 0$. But if we choose the time variable $t$ as an imaginary variable $\tau = it$, then the motion is possible in the sense of classical dynamics in the inverted potential $-\mathcal{U}(q)$ (see fig. 3.6). The propagator (3.40) can be evaluated in the semiclassical limit, where the functional integral is dominated by the stationary point $\bar{z}$ of $\mathcal{S}$. The stationary point satisfies

$$\left.\frac{\delta\mathcal{S}}{\delta z}\right|_{\bar{z}} = 0, \qquad \text{with} \qquad \frac{\delta\mathcal{S}}{\delta z} = -\frac{\mathrm{d}}{\mathrm{d}\tau}\left(\frac{\partial\mathcal{L}}{\partial\dot{z}}\right) + \frac{\partial\mathcal{L}}{\partial z} = -M\ddot{z} + \mathcal{U}'(z). \tag{3.41}$$

The corresponding action is

$$\mathcal{S}_0 = \int_{-T/2}^{T/2} \mathrm{d}\tau \left[\frac{M}{2}\dot{\bar{z}}^2 + \mathcal{U}(\bar{z})\right]. \tag{3.42}$$

To determine the prefactor $\mathcal{N}$, we express $\mathcal{N}$ in terms of the functional determinant of a solvable equivalent system. The expression of the propagator of a particle in a smooth potential (B.46) can be applied to the case of a harmonic oscillator. If we focus on the case $z_i = z_f = 0$ and define the bottom well frequency $\omega_0$ by $M\omega_0^2 = \mathcal{U}''(0)$, the propagator becomes

$$\langle 0|\mathrm{e}^{-\mathcal{H}T/\hbar}|0\rangle = \sqrt{\frac{M\omega_0}{\pi\hbar}}\,\mathrm{e}^{-\omega_0 T/2-\mathcal{S}_0/\hbar}\left(\frac{\det\left[-M\partial_t^2 + \mathcal{U}''(\bar{z})\right]}{\det\left[-M\partial_t^2 + M\omega_0^2\right]}\right)^{-\frac{1}{2}}. \tag{3.43}$$

Now we consider the case $\sigma_{L,R}$ finite (see Figs. 3.5 and 3.6). There are nontrivial solutions of Eq. (3.41): the particle can start at the top of the hill, bounces off the potential on the right at $z = \sigma_R$ or on the left at $z = \sigma_L$ and returns on the top of the hill. For $T \to \infty$, we call this trajectory the right, and respectively the left, "bounce". The bounce has an energy $E_0 = 0$, thus $\frac{\mathrm{d}\bar{z}}{\mathrm{d}\tau} = \sqrt{\frac{2}{M}\mathcal{U}(\bar{z})}$. The bounce actions read

$$\mathcal{S}_0^R = 2\int_0^{\sigma_R} \mathrm{d}z\sqrt{2M\mathcal{U}(z)} \qquad \text{and} \qquad \mathcal{S}_0^L = 2\int_0^{\sigma_L} \mathrm{d}z\sqrt{2M\mathcal{U}(z)}. \tag{3.44}$$

We define "the center of the bounce" the time when $\dot{z} = 0$ or equivalently $\bar{z} = \sigma_{L,R}$. For large $T$, a bounce centered anywhere in the interval of integration is an approximated stationary point of the functional integrand. The multibounce configurations consist of $n_R$ right bounces and $n_L$ left bounces with centers at $t_1, \ldots, t_{n_R+n_L}$ where $T/2 > t_1 > \cdots > t_{n_R+n_L} > -T/2$. From now on, we apply the so-called dilute instanton gas approximation. Within this approximation we consider that the bounces are independent, which is valid when the time between two successive attempts is smaller than the tunneling time. The resulting propagator reads

$$\langle 0|\mathrm{e}^{-\frac{1}{\hbar}\mathcal{H}T}|0\rangle = \sqrt{\frac{M\omega_0}{\pi\hbar}}\,\exp\Big(-\omega_0 T/2 + \mathcal{K}_R\,\mathrm{e}^{-\mathcal{S}_0^R/\hbar}T + \mathcal{K}_L\,\mathrm{e}^{-\mathcal{S}_0^L/\hbar}T\Big). \tag{3.45}$$

This leads to the total decay rate

$$\Gamma = \Gamma_R + \Gamma_L, \qquad \Gamma_{R,L} = 2\,\mathrm{e}^{-\mathcal{S}_0^{R,L}/\hbar}\mathrm{Im}\,\mathcal{K}_{R,L}. \tag{3.46}$$

As a conclusion, in the limit of a dilute gas of instantons, the total escape rate is simply the sum of the tunneling rates in each barrier.

Using a steepest-descent method to perform the integrations over the paths in the semiclassical limit, it is possible to determine the coefficients $\mathcal{K}_{R,L}$. After some algebra we get

$$\mathrm{Im}\mathcal{K}_{L,R} = \frac{1}{2}\sqrt{\frac{\mathcal{S}_0^{L,R}}{2M\pi\hbar}}\left|\frac{\det'\big[-M\partial_\tau^2 + \mathcal{U}''(\bar{z})\big]}{\det\big[-M\partial_\tau^2 + M\omega_0^2)\big]}\right|^{-\frac{1}{2}}. \tag{3.47}$$

This ratio of functional determinants can be calculated with the Gelfand-Yaglom formula (see Sec. B.1.4) using the bounce orbit $\bar{z}(\tau)$.

As a result, the tunneling rate of a particle of mass $M$ from an unstable state through the barrier potential $\mathcal{U}(z)$ with a double escape path reads

$$\Gamma = \Gamma_L + \Gamma_R, \tag{3.48}$$

$$\Gamma_{L,R} = \mathcal{A}_{L,R}\,\mathrm{e}^{-\mathcal{B}_{L,R}/\hbar}, \tag{3.49}$$

$$\mathcal{A}_{L,R} = \omega_0\sqrt{\frac{M\omega_0}{\pi\hbar}}\,\sigma_{L,R}\,\mathrm{e}^{\mathcal{I}_{L,R}}, \tag{3.50}$$

$$\mathcal{B}_{L,R} = 2\int_0^{\sigma_{L,R}} \mathrm{d}z\sqrt{2M\mathcal{U}(z)}, \tag{3.51}$$

$$\mathcal{I}_{L,R} = \int_0^{\sigma_{L,R}} \mathrm{d}z\left[\sqrt{\frac{M\omega_0^2}{2\mathcal{U}(z)}} - \frac{1}{z}\right]. \tag{3.52}$$

Applied to the potential of Eq. (3.29), this general result gives rise to the total tunneling rate $\Gamma = \Gamma_L + \Gamma_R$

$$\Gamma_{L,R} = 4\omega_0\sqrt{\frac{M\omega_0}{\pi\hbar}}\frac{\mp\sigma_{L,R}}{2 - u_3\sigma_{L,R}} \times \exp\left(-\frac{2m\omega_0}{u_4\hbar}\left[\frac{1}{3} + \frac{u_3^2}{8u_4} \pm u_3\frac{u_3^2 + 4u_4}{16u_4^{3/2}}\arccos\left(\mp\frac{u_3}{\sqrt{u_3^2 + 4u_4}}\right)\right]\right). \tag{3.53}$$

Applied to a cubic potential ($u_4 = 0$), the standard MQT tunneling rate is recovered [90]

$$\Gamma_{\text{cubic}} = 12\frac{\omega_0}{2\pi}\sqrt{\frac{6\pi\mathcal{V}}{\hbar\omega_0}}\,\exp\left[-\frac{36}{5}\frac{\mathcal{V}}{\hbar\omega_0}\right]. \tag{3.54}$$

In the case of the symmetric camel-back potential ($u_3 = 0$), we get the new tunneling rate

$$\Gamma_{\substack{\text{camel}\\ \text{sym.}}} = 16\frac{\omega_0}{2\pi}\sqrt{\frac{2\pi\mathcal{V}}{\hbar\omega_0}}\,\exp\left[-\frac{16}{3}\frac{\mathcal{V}}{\hbar\omega_0}\right]. \tag{3.55}$$

In this case, the bounce orbit is equal to $\bar{z}(\tau) = \dfrac{\sigma_{L,R}}{\cosh(\omega_0\tau)}$ (see Fig. 3.7). The tunneling time is of the order of $\omega_0^{-1}$.

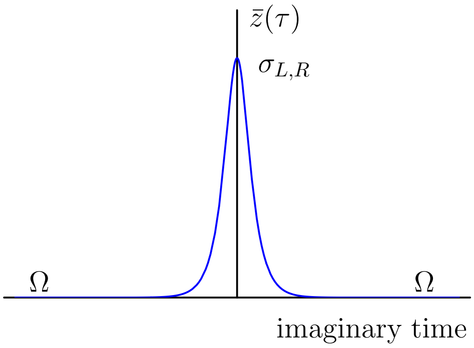

Figure 3.7: Bounce orbit. Points $\Omega$ and $\sigma_{L,R}$ are the same as in Fig. 3.6.

## 3.3 Manipulation of the qubit

### 3.3.1 Properties of the sample

A schematic of the experimental setup is shown on Fig. 3.8. The SQUID was fabricated at the Physikalisch-Technische Bundesanstalt in Braunschweig using a Nb/AlO$_x$/Nb trilayer process with SiO$_2$ dielectric. The two $5\,\mu\mathrm{m}^2$ junctions are embedded in a $10 \times 10\,\mu\mathrm{m}^2$ square loop. The circuit is cooled down to 30 mK.

The experimental parameters are

$$C_1 = C_2 = 250.3\,\mathrm{fF}, \qquad \begin{cases} I_{c_1} = 5.65\,\mu\mathrm{A}, \\ I_{c_2} = 5.57\,\mu\mathrm{A}, \end{cases} \qquad \begin{cases} L_1 = 2.69\,\mathrm{pH}, \\ L_2 = 16.5\,\mathrm{pH}. \end{cases} \tag{3.56}$$

The corresponding values of the reduced parameters are

$$\alpha = 0.0072, \qquad \eta = 0.72, \qquad b = 3.05. \tag{3.57}$$

The plasma frequency of the sample is

$$\omega_p = 2\pi \times 83\,\mathrm{GHz}, \tag{3.58}$$

with also

$$\frac{E_J}{E_C} = 36 \times 10^3, \qquad \frac{M\omega_p}{2\hbar} = 33.5. \tag{3.59}$$

The typical bottom well frequency of a minimum is $\omega_0 = 2\pi \times 15\,\mathrm{GHz}$ with a high transverse frequency $\omega_\perp = 2\pi \times 100\,\mathrm{GHz}$. The property of coherence of the qubit is determined with

- The relaxation time of the excited state $|1\rangle$: $T_1 \simeq 100\,\mathrm{ns}$. A $\pi$-pulse (*i.e.* a microwave excitation of duration calibrated to swap the states) is applied and the state is measured after a delay varying between 0 and 300 ns (see Fig. 3.9).
- The decay rate of the coherent oscillations between the states $|0\rangle$ and $|1\rangle$ under a microwave excitation, *i.e.* Rabi oscillations: $T_2^{\mathrm{Rabi}} \simeq 67\,\mathrm{ns}$. The state is measured after a varying time of excitation, from 0 to 200 ns (see Fig. 3.10).
- The decoherence time between two $\pi/2$-pulses, *i.e.* Ramsey oscillations: $T_2^{\mathrm{Ramsey}} \simeq 20\,\mathrm{ns}$. The state is measured after two $\pi/2$-pulses with a varying delay between the pulses, from 0 to 40 ns (see Fig. 3.11).

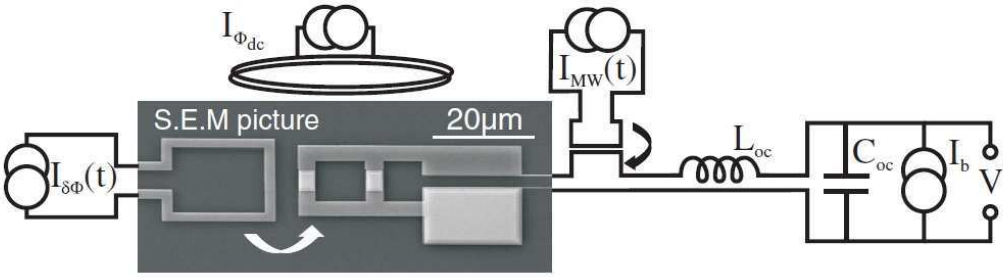

Figure 3.8: Circuit layout. The two small white squares in the central loop are the SQUID Josephson junctions. Connected on the right are current bias and voltage leads. These are heavily filtered at various stages of the cryostat, including the on-chip low-pass filter formed by $L_{\mathrm{oc}} = 10\,\mathrm{nH}$ and $C_{\mathrm{oc}} = 200\,\mathrm{pF}$. Fast flux pulses $\delta\Phi$ inductively couple via the on-chip loop to the left of the SQUID. Microwave excitation is applied via an on-chip loop which couples inductively to the current bias leads. An off-chip coil provides a dc flux bias $\Phi_{\mathrm{dc}}$. The total externally applied flux is $\Phi_{\mathrm{ext}} = \Phi_{\mathrm{dc}} + \delta\Phi$. The SQUID chip is enclosed in a copper box thermally anchored to the mixing chamber of a dilution refrigerator with a 30 mK base temperature. The cryostat is surrounded by superconducting Pb, $\mu$-metal, and soft iron shielding.

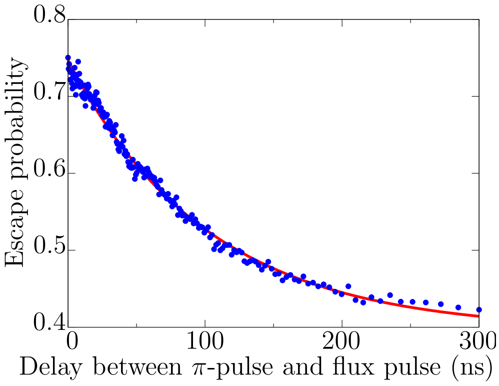

Figure 3.9: Energy relaxation of the first excited state.

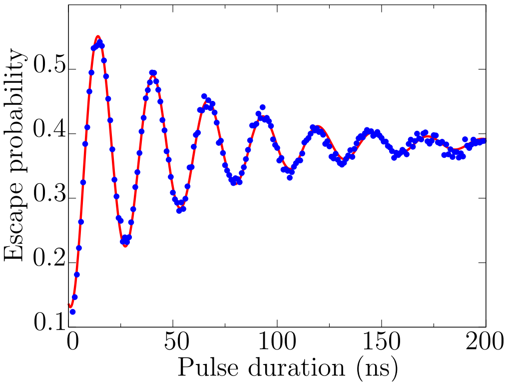

Figure 3.10: Rabi oscillations.

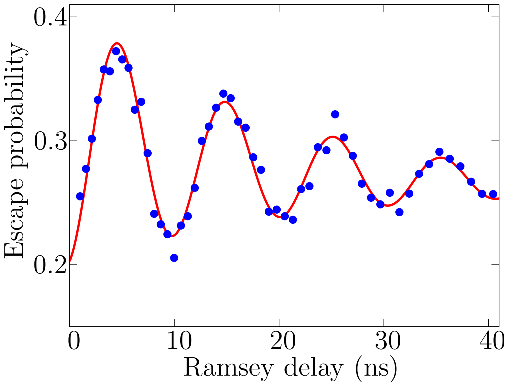

Figure 3.11: Ramsey oscillations.

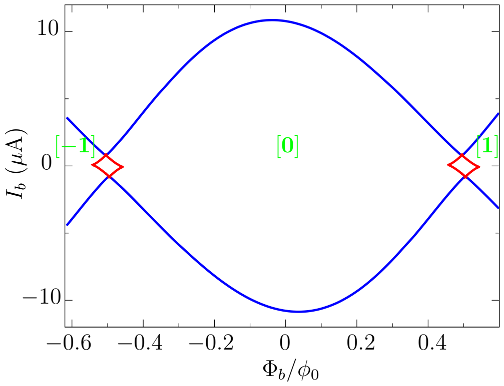

Figure 3.12: Experimental measurement of the critical diagram of the dc SQUID ($s_{50\%}(y_B)$). The theory fits very well with the experimental points.

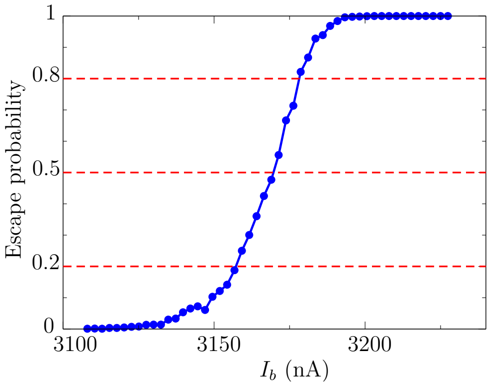

Figure 3.13: Experimental measurement of the escape probability as a function of the bias current. This histogram is used to determine the current $s_{50\%}$ that ensures the escape with a probability of 50 %.

### 3.3.2 Determination of the critical lines

The current and flux biases set the shape of the two-dimensional potential and hence the one-dimensional confining potential and the energy spectrum of the fluxoid state. The manipulation at low temperature as well as the external filters and shieldings ensure that the qubit is in the ground state $|0\rangle$. However, the ground state has a finite lifetime due to the possibility of tunneling through the barrier to a neighboring minimum. The tunneling rate decreasing exponentially with the barrier height, phase tunneling of the ground state occurs only close to the critical lines. According to the dc Josephson effect, a phase tunneling event is accompanied with a voltage peak.

To measure the critical diagram, the SQUID is initialized in a fluxoid state at a fixed flux bias and small current bias. Then the current bias is increased many times to $s_c$. For each run the voltage is measured to detect a phase tunneling event. This leads to the escape probability as a function of the bias current, which has a sharp transition from 0 to 1 at the value $s_{50\%}$, corresponding to a probability of tunneling of 50 %. The graph $s_{50\%}(y_B)$ is the critical diagram at 50 % (see Fig. 3.12). The typical escape probability as a function of the applied bias current is presented in Fig. 3.13.

By comparison with the numerical solutions, the critical diagram is used to find the parameters $\alpha$, $\eta$ and $b$ of the SQUID.

### 3.3.3 Readout of the state

The experimental setup decreases the external noises and excitations so that the SQUID remains in the ground state $|0\rangle$. To excite the state $|1\rangle$ a microwave radiation in resonance with the transition $\nu_{10}$ is applied on the SQUID. The properties of the microwave signal can be determined using optimal control theory to reach a desired final state [96]. To measure the state of the qubit, we exploit the energy dependence of the tunneling rate of the anharmonic oscillator through the barrier. It is then possible to find another working point closer to the critical line where the excited state tunnels with high probability and the ground state stays in the minimum. Once the microwave manipulation is finished, a flux pulse is applied to approach the critical line and a voltage peak appears if the qubit was in the state $|1\rangle$. The measurement of the quantum state is performed within a few nanoseconds using adiabatic dc flux pulses [97].

### 3.3.4 One-dimensional motion close to the critical lines

For non-zero bias current, or for flux bias far from half a flux quantum, we look at the shape of the potential around the critical points (in the half plane $s_c > 0$). In this region, the one-dimensional potential has a washboard shape and the barrier between a local minimum and the following is close to a cubic potential. We do not take into account the correction $\mu(x)$ here for the sake of simplicity. We Taylor expand the potential in $x$, $y$ and $s$ at third order around $x_c$, $y_c$, and $s_c$ in the direction of vanishing curvature, given by the angle

$$\tan\theta_c = -\frac{u_{xx}(x_c, y_c)}{u_{xy}(x_c, y_c)} = -\frac{u_{xy}(x_c, y_c)}{u_{yy}(x_c, y_c)}, \qquad \text{with } s = s_c. \tag{3.60}$$

In terms of the curvilinear abscissa $z$ starting from the minimum, the one-dimensional potential then reads

$$\begin{aligned} u(z) &= c_0 + \frac{1}{2}c_2 z^2 - \frac{1}{6}c_3 z^3 && (3.61)\\ c_0 &= u(x_m, y_m), && (3.62)\\ c_2 &= \sqrt{2c_1 c_3}, && (3.63)\\ c_3 &= \cos\theta_c(1 + 2\sin^2\theta_c)(\sin x_c \cos y_c - \alpha\cos x_c \sin y_c) \\ &\quad + \sin\theta_c(1 + 2\cos^2\theta_c)(\cos x_c \sin y_c - \alpha \sin x_c \cos y_c), && (3.64) \end{aligned}$$

where $c_1 = (s_c - s)(\cos\theta_c + \eta\sin\theta_c)$ is the slope at the critical point $z_c = \sqrt{2c_1/c_3}$. The potential $\mu(x)$ slightly changes the coefficient $c_3$[1]. The coordinates of the minimum $(x_m, y_m)$ at $z_m = 0$ and the saddle point $(x_s, y_s)$ at $z_s = 2z_c$ are

$$\begin{cases} x_m = x_c - z_c\cos\theta_c, \\ y_m = y_c - z_c\sin\theta_c, \end{cases} \quad (3.66) \qquad \begin{cases} x_s = x_c + z_c\cos\theta_c, \\ y_s = y_c + z_c\sin\theta_c, \end{cases} \quad (3.67)$$

The expansion of the potential gives also access to the bottom well frequency $\omega_0$ at the minimum and the reduced barrier height $\Delta u$

$$\omega_0 = \sqrt{c_2}\,\omega_p, \qquad \text{and} \qquad \Delta u = \frac{2}{3}\left(\frac{c_2}{c_3}\right)^2. \tag{3.68}$$

---

[1] The potential $\mu(x) \simeq \sqrt{bE_C/E_J}\,u_{xy}/4b^2$ induces the coefficient

$$\begin{aligned} c_3^{\perp} = \frac{3}{b^{3/2}}\sqrt{\frac{E_C}{E_J}}\,&[u_{xxx}\sin\theta_c(3\sin 2\theta_c u_{xx} + (5 + \cos 2\theta_c)u_{xy}) \\ &+ u_{xxy}\cos\theta_c(3\sin 2\theta_c u_{xx} + (5 - \sin 2\theta_c)u_{xy})]\,. \end{aligned} \tag{3.65}$$

in addition to $c_3$.

The potential can be expressed in terms of the barrier height $\Delta\mathcal{U}$ and the bottom well frequency $\omega_0$ as follows

$$\begin{aligned} \mathcal{U}(z) =& \mathcal{U}(x_m, y_m) + \frac{1}{2}M\omega_0^2 z^2 - \frac{1}{6}\left(M\omega_0^2\right)^{3/2}\sqrt{\frac{2}{3\Delta U}}z^3, && (3.69)\\ \Delta\mathcal{U} =& \frac{4}{3}\left(\frac{2s_c}{c_3}\right)^{1/2}(\cos\theta_c + \eta\sin\theta_c)^{3/2}\left(1 - \frac{I_b}{I_c}\right)^{3/2} E_J, && (3.70)\\ \omega_0 =& \left(\frac{c_3}{2s_c}\right)^{1/4}(\cos\theta_c + \eta\sin\theta_c)^{1/4}\left(1 - \frac{I_b}{I_c}\right)^{1/4}\omega_p. && (3.71) \end{aligned}$$

These results generalize the known results for a symmetric SQUID [98]. These two parameters are sufficient to calculate the tunneling rate through the barrier. The main problem of this kind of working point is its dependence on bias current. The average slope of the potential being nonzero, the barrier height is sensitive to current fluctuations.

## 3.4 The camel-back potential

### 3.4.1 Potential around the working point ($\mathbf{I_b = 0, \Phi_b = \frac{1}{2}\phi_0}$)

We focus on the domain of bias fields around the working point $\left(I_b = 0, \Phi_b = (2k+1)\dfrac{\phi_0}{2}\right)$. In this region, two fluxoid states $[k]$ and $[k+1]$ coexist. The extremal critical points are

$$\begin{cases} y_{B_c} = (2k+1)\dfrac{\pi}{2} + \dfrac{1+\eta\alpha}{2b}(-1)^{f-k}, \\ s_c = -(-1)^{f-k}\alpha, \end{cases} \qquad \begin{cases} x_c = (2n+f)\pi, \\ y_c = (2k+1)\dfrac{\pi}{2}. \end{cases} \tag{3.72}$$

Every minimum is connected to two equivalent minima by two saddle points. For a given couple of bias fields, let us denote $[f_0]$ the fluxoid state which has the highest spot height, or equivalently the smallest barrier height, and $[f_1]$ the other one. For $k = 0$ for instance, $[f_0] = [0]$ and $[f_1] = [1]$ when $y_B > \pi/2$. In the following, we study the tunneling effect from a minimum of the fluxoid state $[f_0]$ to the two neighboring minima of the fluxoid state $[f_1]$. The position of the minima and the saddle points are, at second order in $s$,

$$\begin{cases} x_m = (2n+f)\pi + \dfrac{p}{\tilde{y}} - \dfrac{\alpha p^2}{2\tilde{y}^3}, \\ y_m = y_B - \dfrac{(-1)^{f-k}}{2b}, \end{cases} \tag{3.73}$$

and

$$\begin{cases} x_s = (2n+f)\pi \pm \arccos\Big[2b(-1)^{f-k}(y_B - k\pi - \pi/2)\Big], \\ y_s = (2k+1)\dfrac{\pi}{2}, \end{cases} \tag{3.74}$$

where we note $p = \alpha + (-1)^{f-k}s$ and $\tilde{y} = \pi/2 + k\pi - y_m$. Starting from a minimum $(x_{m_0}, y_{m_0})$ of the state $[f_0]$, the path of minimum potential of curvilinear abscissa $z$ follows the trajectory

$$\left(x(z) = x_{m_0} + z,\ y(z) = y_B - \frac{(-1)^k}{2b}\cos(x_{m_0} + z)\right). \tag{3.75}$$

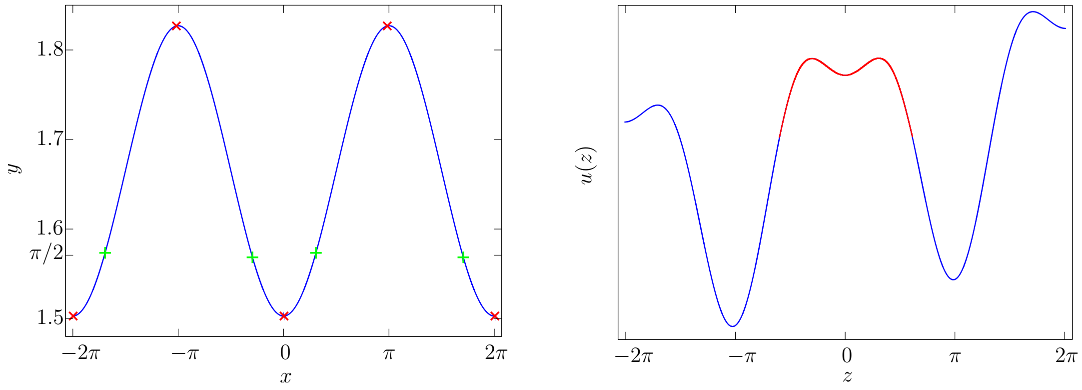

Figure 3.14: Path $y = \zeta(x)$ (*left panel*) and the corresponding one-dimensional potential $u(x, \zeta(x))$ (*right panel*) at the bias fields $I_b = -70\,\mathrm{nA}$ and $\Phi_b = 0.531\,\phi_0$. The minima are on the red crosses of the path and the saddle points on the green ones. The quartic approximation of the potential is the red part of the curve.

The Tailor expansion of the one-dimensional potential up to fourth order in $z$ reads

$$\begin{aligned} u(z) =& u(0) + \frac{(-1)^{f-k}}{2}\left[\tilde{y} + \frac{p(2\alpha - p)}{2\tilde{y}} - \frac{3(-1)^{f-k}}{4}\frac{p^2}{b\tilde{y}^2} - \frac{\alpha^2 p^2}{2\tilde{y}^3}\right] z^2 \\ &+ \frac{1}{6}\left[(-1)^{f-k}(\alpha - p) - \frac{3}{2}\frac{p}{b\tilde{y}} + \frac{3}{4}\frac{\alpha p^2}{b\tilde{y}^3}\right] z^3 \\ &+ \frac{(-1)^{f-k}}{24}\left[-\tilde{y} - \frac{3(-1)^{f-k}}{2b} + \frac{p(p-2\alpha)}{2\tilde{y}} + \frac{15(-1)^{f-k}}{4}\frac{p^2}{b\tilde{y}^2} + \frac{\alpha^2 p^2}{2\tilde{y}^3}\right] z^4. \end{aligned} \tag{3.76}$$

The potential $\mu$ due to the transverse motion can also be calculated along the path

$$\mu(z) = \frac{1}{2b}\sqrt{\frac{E_C}{bE_J}}\left[\frac{p}{\tilde{y}}z + \frac{z^2}{2} - \frac{2p}{3\tilde{y}}z^3 - \frac{z^4}{6}\right]. \tag{3.77}$$

The total one-dimensional potential $\mathcal{U}(z)$ leads to the bottom well frequency of the minimum

$$\omega_0 = \omega_p\left[(-1)^{f-k}\tilde{y} + \frac{p(-1)^{f-k}(2\alpha - p)}{2\tilde{y}} - \frac{3}{4}\frac{p^2}{b\tilde{y}^2} - \frac{(-1)^{f-k}\alpha^2 p^2}{2\tilde{y}^3} + \frac{1}{2b}\sqrt{\frac{E_C}{bE_J}}\right]^{1/2}. \tag{3.78}$$

The dependence on the bias current of the bottom well frequency, and hence the energy difference between the two levels of the qubit, permits to define the optimal line.

### 3.4.2 Optimal line

The manipulation of the qubit is done with a microwave in resonance with the transition frequency $\nu_{10}$ between the two levels of the qubit. However, current fluctuations "shake" the potential inducing fluctuations of $\nu_{10}$. The detuning between the microwave frequency and the transition frequency decreases the coherence times of the qubit. To improve the lifetime of the qubit it is necessary to find optimal lines in the critical diagram where the bottom well frequency does not depend on the bias current at first order, *i.e.* $\partial_s \omega_0(s_{\mathrm{opt}}) = 0$ from Eq. (3.78). The optimal lines are then found to be

$$s_{\mathrm{opt}} = -(-1)^{f-k}\alpha + \frac{2\alpha b\tilde{y}^2}{2b\tilde{y}^2 + 2b\alpha^2 + 3(-1)^{f-k}\tilde{y}}, \tag{3.79}$$

which is quasi-constant, equal to $s_{\text{opt}} \simeq -(-1)^{f-k}\alpha$. The optimal lines correspond to a very weak bias current, equal to $I_b \approx \pm 80\,\text{nA}$. Although the optimal lines are designed to minimize the current noise, the sensibility to flux noise is of the order of $\partial_{y_B}\omega_0/\omega_0 = -(-1)^{f-k}\left(\omega_p/\omega_0\right)^2$, which is also low.

Figure 3.16 shows the experimental measurement of the sensitivity to current noise. The measurement proves that on the optimal line the current noise is strongly reduced. The manipulation is limited by flux noise.

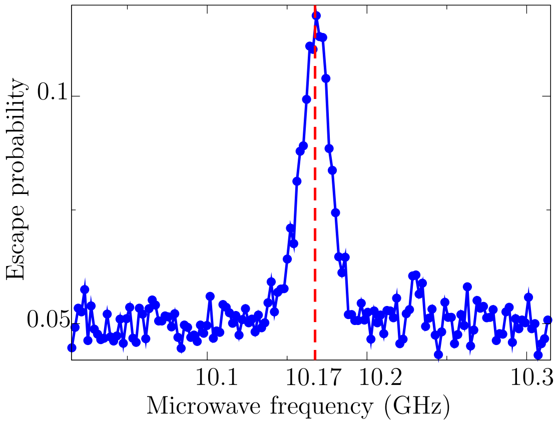

Figure 3.15: Spectroscopic measurement of the energy difference $\hbar\nu_{01}$ between the two states for $I_b = -73\,\text{nA}$ and $\Phi_b = -0.472\,\phi_0$. The energy difference is found to be $\nu_{01} = 10.17\,\text{GHz}$ an the linewidth, due to low frequency noises, to be equal to 18 MHz.

### 3.4.3 Measurement of the critical diagram

To measure the four arcs of the critical diagram (see Fig. 3.18) around the optimal line, where two fluxoid states coexist, a novel experimental technique has been developed. The technique is reported here around the working point $I_b = 0$ and $\Phi_b = -\phi_0/2$ where the two fluxoid states [0] and [−1] coexist. The measurement procedure is composed of three parts, represented on Fig. 3.17

1. Initialization in the fluxoid state [0], at $\Phi_b \simeq -\phi_0/2$.

2. Fast flux pulse (100 ns) in the direction $\Phi_b < -\phi_0/2$.

3. After the flux pulse, at $\Phi_b \simeq -\phi_0/2$, the state depends on the amplitude of the pulse compared to the critical flux. If the pulse amplitude is smaller than the critical flux, the state stays in the fluxoid state [0] and tunnels to the state [−1] otherwise.

4. The resulting state is measured with a current pulse ($60\,\mu$s). The amplitude is designed so that the fluxoid state [0] is stable and the fluxoid state [−1] has no minimum. With this technique, a voltage peak is measured if the final state is [−1].

After many measurements, the typical escape probability as a function of the flux bias is represented on Fig. 3.19. The value $\Phi_{b_{50\%}}$ is then reported on the critical diagram.

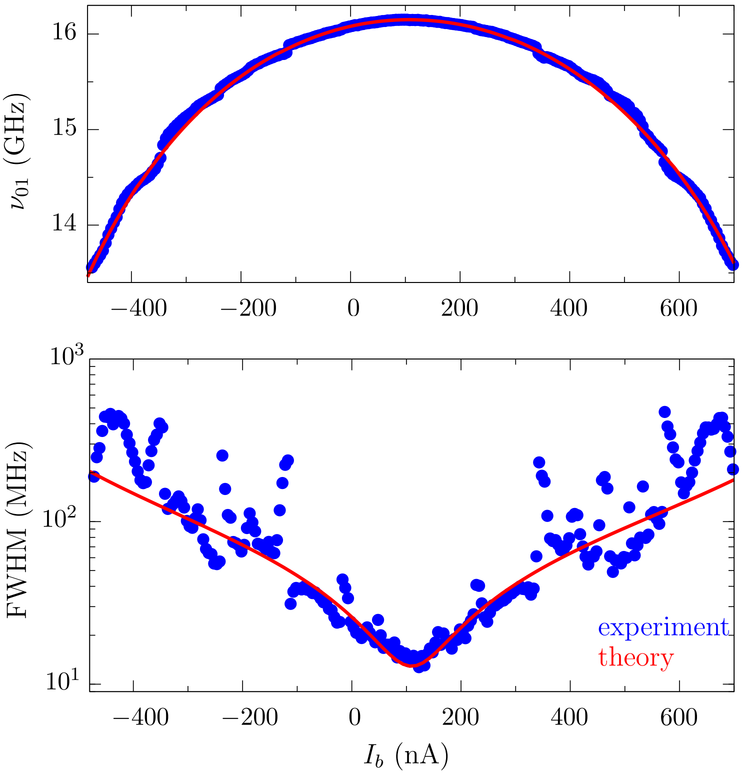

Figure 3.16: Energy difference $\hbar\nu_{01}$ between the two levels of the qubit as a function of the bias current (*top panel*). The experimental points are in blue and the fit from our model in red. The current noise contribution is in dashed line and the flux noise contribution in dotted line. Width of the spectroscopy $\nu_{01}(\omega)$ (see Fig. 3.15) as a function of the bias current, in logarithmic scale (*bottom panel*). On the optimal line, where $I_b \simeq 80\,\text{nA}$, the energy difference is maximum and, as predicted, the current noise in minimal. The width is limited by the flux noise ($40\,\mu\phi_0$ RMS).

### 3.4.4 Experimental versus theoretical results for the double-escape camel-back potential.

Along the optimal line, the one-dimensional potential around a minimum of the fluxoid state $[f_0]$ is quartic with a double escape path to the neighboring minima of the state $[f_1]$. To understand the quantum dynamics in this potential, it is necessary to study the tunneling effect in a general quartic potential. The theory developed in Sec. 3.2 using the instanton formalism can be compared to the known MQT results in the case of a cubic potential, valid far from the optimal lines.
Figure 3.20 represents the experimental critical diagram on the optimal line, the MQT result Eq. (3.53) for the general quartic potential and for the cubic one. The rounding of the cusp is possible only if the symmetric quartic potential is taken into account.

The new treatment is also needed to explain the strong reduction of the linewidth on the optimal line observed on Fig. 3.21. This is directly due to the presence of a symmetric double escape path on the critical line.

The manipulation of the qubit in the camel-back region permits to multiply by a factor two the coherence time $T_2$, the main limitation for qubit operations.

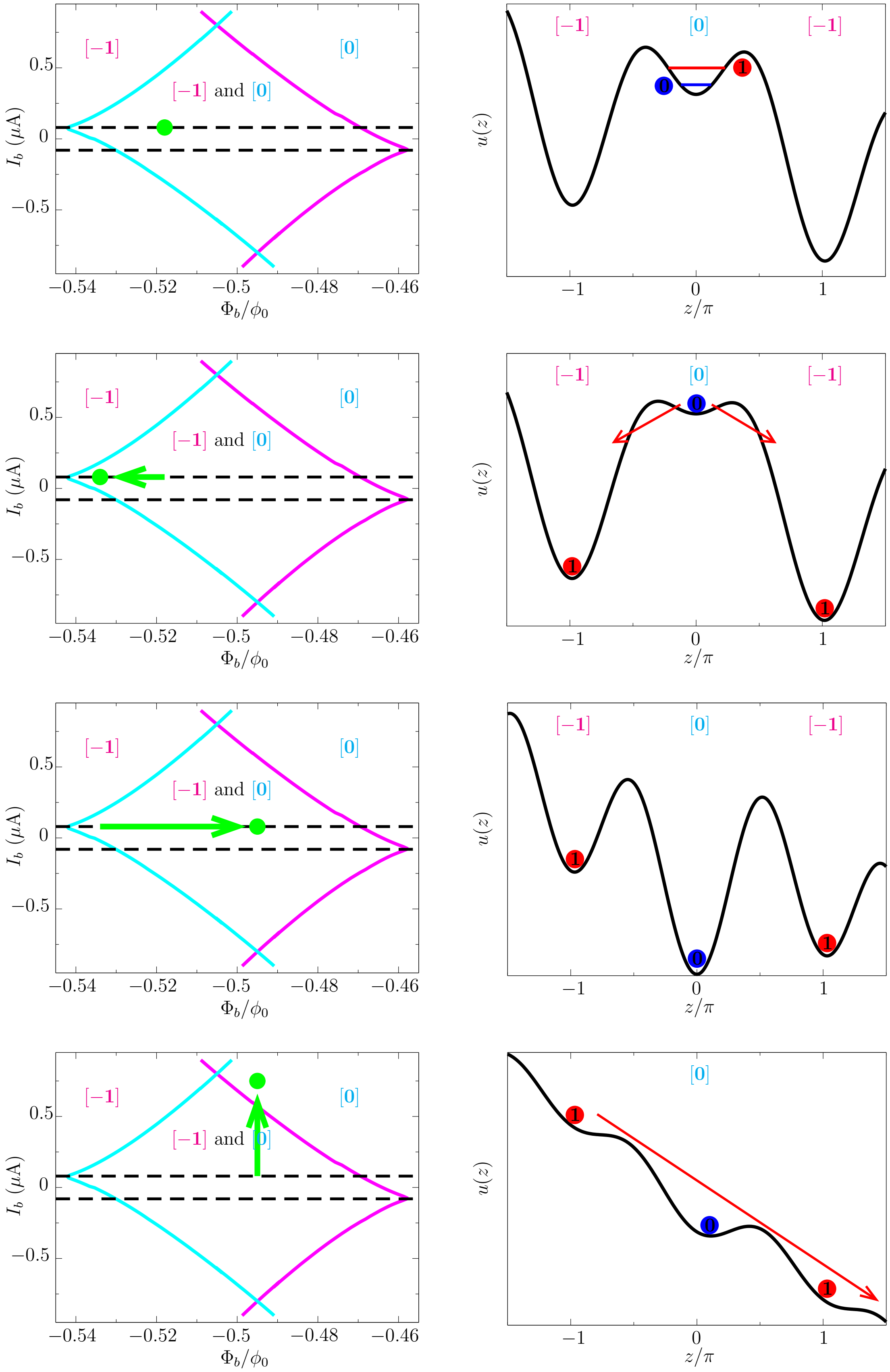

Figure 3.17: Different steps of the new method of measurement. A voltage appears if the qubit was initially in the state $|1\rangle$.

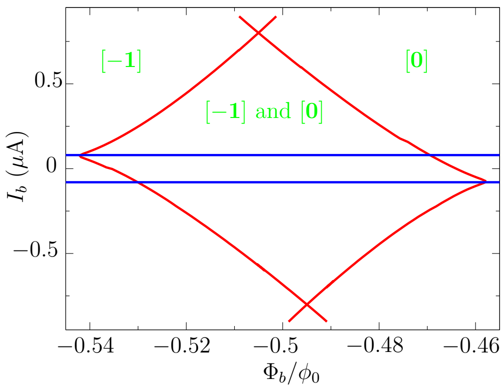

Figure 3.18: Critical diagram, in red, around the optimal lines, in blue.

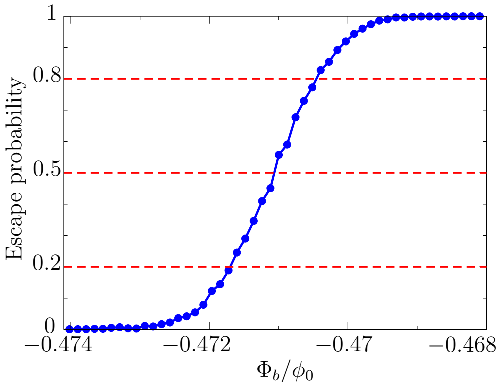

Figure 3.19: Escape probability as a function of the flux bias.

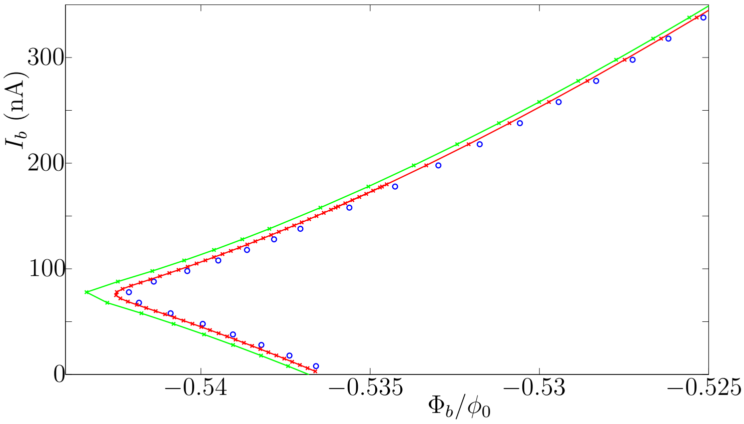

Figure 3.20: Comparison of the critical diagram close to the optimal lines between the experimental measurement (blue points) and the theoretical results for a general quartic potential (red line) and a cubic one (green line).

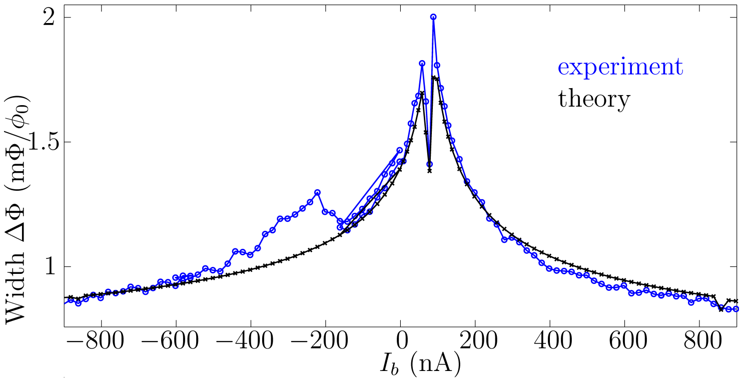

Figure 3.21: Linewidth as a function of the current bias. The experimental points are in blue and the black line corresponds to the general quartic model with a low frequency current noise. The symmetry of the double escape path strongly reduces the linewidth on the optimal line.

## Conclusion and perspectives

In conclusion, we have studied theoretically the quantum dynamics of a novel quartic camel back potential. Our new results are obtained from a generalized double-path MQT escape theory based on the instanton formalism. Ground state escape exhibits critical line cusps and a dip in the escape width versus bias current. Because of symmetry, quantum dynamics are insensitive in first order to current fluctuations along an optimal line $s_{\mathrm{opt}}$. Along this line, the dc SQUID can be used as a phase qubit whose main decoherence source is residual flux noise.

Future optimization and exploitation of the unique properties of this system will aid in the understanding of decoherence mechanisms in quantum circuits and has the potential to yield a competitive phase qubit. The investigation of the transverse motion with different confining strengths would be an interesting way to study the transition from two to one dimension.

# Qubit de phase dans un potentiel quartique

## Résumé du chapitre

Deux jonctions Josephson insérées dans une boucle supraconductrice forment un SQUID, un objet quantique qui peut être contrôlé par un courant et un champ magnétique. Il se comporte comme une particule quantique dans un relief montagneux, constitué de cuvettes reliées par des cols. À basse température, la quantification des niveaux d'énergie dans un minimum permet d'utiliser un SQUID dc comme un qubit de phase lorsque seuls l'état fondamental et le premier état excité sont impliqués. Nos simulations ont abouti à un point de fonctionnement, optimal vis-à-vis des bruits de courant et de flux, où le courant de polarisation est faible et le flux proche d'un demi quantum. Sur cette ligne optimale le potentiel présente deux familles de minima, associées à deux états de flux dans la boucle. Le qubit de phase est réalisé dans un type de minima et l'autre état de flux sert à la lecture du qubit. La nouvelle méthode expérimentale de mesure de l'état du qubit est basée sur le transfert par effet tunnel d'un minimum à l'autre. Cette dynamique peut être raisonnablement supposée unidimensionnelle, car la fréquence transverse le long du chemin de courbure minimale est très grande par rapport à la fréquence longitudinale et à la température. Le potentiel unidimensionnel effectif résultant a une forme de dos de chameau, et la particule peut tunneller à travers deux barrières quartiques. Nous avons calculé le taux d'échappement tunnel dans ce nouveau potentiel quartique à double échappement avec la technique des instantons. Nos résultats décrivent bien les mesures expérimentales réalisées à l'Institut Néel et permettent notamment de prouver le caractère optimal du point de fonctionnement.

Chapter 4

# Josephson atom lasing

## Contents

## Introduction

Motivated by a recent experiment where a single artificial atom has been realized [99], we analyze in this chapter the coupling between a three-level quantum system, based on a superconducting qubit, and cavities. The qubit acts as an artificial atom and with the appropriate parameters, a lasing effect can occur. Photons are created in the cavity at the plasma frequency of the qubit, in the microwave domain (10 GHz–1 cm). The level quantization of the qubit being due to the Josephson effect, this phenomenon is called Josephson atom lasing. This coherent coupling between the qubit and the cavity gives rise to the field of circuit quantum electrodynamics, equivalent in many senses to cavity QED in atomic physics and quantum optics. Circuit QED can also be exploited for quantum information processing and quantum communication.

The chapter is composed of three parts. In the first part we present the derivation of the Lindblad master equation that governs the dynamics of the density matrix and the method to calculate the output spectrum of the system, which enables us to characterize the laser field. This formalism is then applied to two different experiments. In the first one, a charge qubit is coupled to a superconducting resonator. This experiment constitutes the first observation of the Josephson lasing effect. Our quantum-mechanical treatment gives access to the time evolution of the photon number in the cavity and allows us to compare the output spectrum with the semiclassical approximation. The second experiment exploits the interesting properties of the transmon, a Cooper pair box with a large Josephson energy which is weakly sensitive to charge fluctuations. The transmon is coupled to two cavities, one of high quality factor where the lasing effect takes place and another one with a low quality factor which uses the Purcell effect to control the relaxation rate of non-lasing transition.

## 4.1 The Lindblad master equation

This section is devoted to the derivation of the Lindblad master equation that governs the dynamics of the density matrix of the system. For the sake of simplicity, we consider the case of a three-level quantum system $\{|0\rangle, |1\rangle, |2\rangle\}$ where the transition $|1\rangle \rightarrow |0\rangle$ is coupled to a cavity of high quality factor. The quality factor $Q$ is the ratio between the mode frequency $\omega_0/2\pi$ of the cavity and its loss $\kappa$: $Q = \frac{\omega_0}{\kappa}$. The three-level system is pumped incoherently from the level $|0\rangle$ the level $|2\rangle$ at a rate $\Gamma$ and the third level can relax spontaneously to the second one at a rate $\gamma_{21}$. The general case where a coherent pumping is taken into account as well as the presence of a second cavity is derived with further details in appendix C.

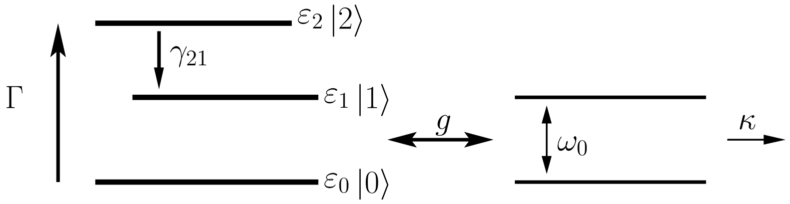

Figure 4.1: Scheme of the artificial atom coupled to the cavity.

### 4.1.1 Tracing out the external baths

The incoherent processes are modeled by a coupling of the system to external baths composed of a large number of harmonic oscillators [100, 101]. The bath coupled to the cavity mimics the losses of photons, the bath coupled to the transition $|2\rangle \rightarrow |1\rangle$ enables the spontaneous emission of a photon necessary for the relaxation of the level $|2\rangle$, and the bath coupled to the transition $|0\rangle \rightarrow |2\rangle$ is responsible for the incoherent pumping of the qubit. The dynamics of the density matrix $\rho_{\text{tot}}$ of the total system $\{\text{qubit} \oplus \text{cavity} \oplus \text{baths}\}$ depends only on the total Hamiltonian $\mathcal{H}_{\text{tot}}$ as follows

$$i\hbar \frac{\mathrm{d}\rho_{\text{tot}}}{\mathrm{d}t} = [\mathcal{H}_{\text{tot}}, \rho_{\text{tot}}], \tag{4.1}$$

in the Schrödinger picture. The total Hamiltonian is composed of the Hamiltonian $\mathcal{H}_S$ of the system $S = \{\text{qubit} \oplus \text{cavity}\}$, the Hamiltonian $\mathcal{H}_B$ of the baths and the coupling Hamiltonian $\mathcal{H}_{S-B}$ between the system $S$ and the baths

$$\mathcal{H}_{\text{tot}} = \mathcal{H}_S + \mathcal{H}_B + \mathcal{H}_{S-B}. \tag{4.2}$$

We note $\sigma_{ij} = |i\rangle\langle j|$ the operators of the qubit ($\sigma_i \equiv \sigma_{ii}$), $\varepsilon_i$ the energy of the level $i$, $a$ and $a^\dagger$ the annihilation and creation operators of the cavity. Then

$$\mathcal{H}_{QB} = \sum_{i=0}^{2} \varepsilon_i \sigma_i, \tag{4.3}$$

$$\mathcal{H}_C = \hbar\omega_0 a^\dagger a. \tag{4.4}$$

We note $\hbar g$ the coupling energy between the transition $|1\rangle - |0\rangle$ and the cavity

$$\mathcal{H}_{QB-C} = i\hbar g(\sigma_{10} + \sigma_{01})(a^\dagger - a). \tag{4.5}$$

The evolution equation for the density matrix $\rho(t)$ of the system $S$ can be derived from the evolution of $\rho_{\text{tot}}(t)$ by tracing out the degrees of freedom of the environment $\rho(t) = \text{Tr}_B\{\rho_{\text{tot}}(t)\}$. The trace on the commutator of Eq. (4.1) is not trivial for terms that contain operators of the bath, *i.e.* $\mathcal{H}_B$ and $\mathcal{H}_{S-B}$. To trace out the bath in Eq. (4.1), we can use the general result of the coupling between a free field and the baths derived in appendix C.1.

The resulting time evolution of the reduced density matrix $\rho$ has two contributions, the coherent evolution is governed by the commutator $[\mathcal{H}, \rho]$ and the incoherent processes are described by the Lindbladian L

$$\frac{\mathrm{d}\rho}{\mathrm{d}t} = \frac{1}{i\hbar}[\mathcal{H}, \rho] + \mathrm{L}\rho, \tag{4.6}$$

where the Lindblad operator has three contributions $\mathrm{L} = \mathrm{L}_{\text{QB}} + \mathrm{L}_C + \mathrm{L}_\Gamma$

- The relaxation of the qubit from the level $|i\rangle$ to the level $|j\rangle$ due to spontaneous emission is characterized by the rates $\gamma_{ij}$

$$\mathrm{L}_{\text{QB}} = \sum_{i>j} \frac{\gamma_{ij}}{2}(2\sigma_{ji}\rho\sigma_{ij} - \sigma_i\rho - \rho\sigma_i). \tag{4.7}$$

- The loss in the cavity is characterized by the damping rate $\kappa$ and the thermal temperature of the photons $n^{\text{th}}$

$$\mathrm{L}_C = \sum_{\alpha=1}^{2} \frac{\kappa}{2}(1 + n^{\text{th}})(2a\rho a^\dagger - a^\dagger a\rho - \rho a^\dagger a) + \frac{\kappa}{2} n^{\text{th}}(2a^\dagger\rho a - aa^\dagger\rho - \rho aa^\dagger), \tag{4.8}$$

  where $n^{\text{th}}$ satisfies the Bose Einstein statistics $n^{\text{th}} = \dfrac{1}{\exp(\hbar\omega/k_BT) - 1}$ at temperatures $T$, which vanishes at zero temperature.

- The incoherent pumping in resonance with the transition $|0\rangle - |2\rangle$ at the rate $\Gamma$

$$\mathrm{L}_\Gamma = \frac{\Gamma}{2}(2\sigma_{20}\rho\sigma_{02} - \sigma_0\rho - \rho\sigma_0). \tag{4.9}$$

The coherent evolution can be simplified with the rotating wave approximation, as explained in the following section.

### 4.1.2 The rotating wave approximation

The Hamiltonian of the system can be separated in two parts, first the Hamiltonian of the isolated qubit and the isolated cavity and second the coupling Hamiltonian

$$\mathcal{H} = \mathcal{H}_0 + \mathcal{H}_1, \qquad \begin{cases} \mathcal{H}_0 = \displaystyle\sum_{j=0}^{2} \varepsilon_j \sigma_{jj} + \hbar\omega a^\dagger a, \\ \mathcal{H}_1 = i\hbar g(\sigma_{10} + \sigma_{01})(a^\dagger - a). \end{cases} \tag{4.10}$$

We turn to the interaction picture with respect to the Hamiltonian $\mathcal{H}_0$: for a general operator $\mathcal{O}$ in the Schrödinger picture, the expression in the interaction picture is $\widetilde{\mathcal{O}}(t) =$

$\exp(i\mathcal{H}_0 t/\hbar)\mathcal{O}\exp(-i\mathcal{H}_0 t/\hbar)$. In this representation, the different operators have the expression

$$\tilde{\sigma}_{kl}(t) = \sigma_{kl}\,\mathrm{e}^{i(\varepsilon_k-\varepsilon_l)t/\hbar}, \qquad \tilde{\sigma}_i(t) = \sigma_i, \tag{4.11}$$

$$\tilde{a}(t) = a\,\mathrm{e}^{-i\omega_0 t}, \qquad \tilde{a}^\dagger(t) = a^\dagger\,\mathrm{e}^{i\omega_0 t}. \tag{4.12}$$

From now on we will consider that the effect of the Hamiltonian $\mathcal{H}_1$ is a small perturbation compared to the Hamiltonian $\mathcal{H}_0$, that is to say that the coupling energy is small compared to the energy difference between the levels of the qubit and to the energy of the cavity modes. In this limit, the dynamics of the operators $\sigma_{ij}$ and $a$ is mainly governed by the free Hamiltonian $\mathcal{H}_0$ and their expectation values oscillate at the frequencies $|\varepsilon_i - \varepsilon_j|/h$ or $\omega_0/2\pi$, which is of the order of 10 GHz for superconducting systems. This dynamics cannot be time-resolved experimentally, and the corresponding expectation values are averaged to zero. Consequently, we will keep only the slowly varying terms compared to $\omega_0$ in the coupling Hamiltonian. The selection of the leading terms is performed using the expression of $\tilde{\mathcal{H}}_1$

$$\tilde{\mathcal{H}}_1(t) = i\hbar g\left(\sigma_{01}a^\dagger\,\mathrm{e}^{-i(\omega_{10}-\omega_0)t} - \sigma_{10}a^\dagger\,\mathrm{e}^{-i(\omega_{10}+\omega_0)t}\right) + H.c., \tag{4.13}$$

where $\omega_{ij} = |\varepsilon_i - \varepsilon_j|/\hbar$ are the transition frequencies. The transition $|1\rangle - |0\rangle$ is in (close to) resonance with the cavity. As a result, we will keep only oscillating terms at $\omega_{10} - \omega_0$ and remove those at $\omega_{10}+\omega_0$. This constitutes the Rotating Wave Approximation (RWA). The evolution equation of the density matrix in the interaction picture is then given by

$$\dot{\tilde{\rho}}(t) = \frac{1}{i\hbar}\left[\tilde{\mathcal{H}}_1, \tilde{\rho}(t)\right] + \mathrm{L}\tilde{\rho}(t), \tag{4.14}$$

with

$$\tilde{\mathcal{H}}_1 = i\hbar g\left(\sigma_{01}a^\dagger\,\mathrm{e}^{-i\delta t} - \sigma_{10}a\,\mathrm{e}^{i\delta t}\right), \tag{4.15}$$

where we define the detuning between the qubit transition and the cavity mode $\delta = \omega_{10} - \omega_0$.

The general Lindblad master equation Eq. (4.14) can be used to calculate the temporal evolution of the density matrix, and hence the temporal evolution of all the observables of the system such as the level populations, the photon number or the correlations between the qubit and the cavities. This calculation cannot be done analytically and needs a numerical treatment. To obtain approximate expressions for the observables, one can use a semiclassical approach that neglects the correlations between the qubit and the cavity.

### 4.1.3 Dynamics of the qubit levels and resonator populations

#### 4.1.3.a From the density matrix

The expectation value $\langle\mathcal{O}\rangle$ of an observable $\mathcal{O}$ (*e.g.* $\sigma_{ij}$ or $a^{(\dagger)}$) is obtained from the density matrix

$$\langle\mathcal{O}\rangle = \mathrm{Tr}\{\rho\mathcal{O}\} = \sum_{i=0}^{2}\sum_{n=0}^{\infty}\langle i,n|\rho\mathcal{O}|i,n\rangle, \tag{4.16}$$

where $\{|i,n\rangle\}$ is the basis where $|i\rangle$ is the level of the qubit and $|n\rangle$ is the state with $n$ photons in the cavity. The dynamical equation for the expectation value is

$$\frac{\mathrm{d}\langle\mathcal{O}\rangle}{\mathrm{d}t} = \frac{1}{i\hbar}\langle[\mathcal{O},\mathcal{H}]\rangle + \mathrm{Tr}\{\mathcal{O}\mathrm{L}\rho\}\,. \tag{4.17}$$

The dynamics is simpler in the rotating frame of the expectation value, *i.e.* when we consider only the oscillations around the main frequency given by $\mathcal{H}_0$. We define

$$\left\langle\bar{\mathcal{O}}\right\rangle = \left\langle \mathrm{e}^{-i\mathcal{H}_0 t/\hbar}\mathcal{O}\,\mathrm{e}^{i\mathcal{H}_0 t/\hbar}\right\rangle = \mathrm{Tr}\{\tilde{\rho}\mathcal{O}\}\,, \tag{4.18}$$

and then

$$\frac{\mathrm{d}\left\langle\bar{\mathcal{O}}\right\rangle}{\mathrm{d}t} = \mathrm{Tr}\{\dot{\tilde{\rho}}\mathcal{O}\}\,, \tag{4.19}$$

therefore it is sufficient to know the time evolution of the density matrix in the interaction picture to find the time evolution of the observables in the rotating frame.

The time evolution of the qubit levels $\langle\sigma_i\rangle(t)$ and the resonator populations $\mathcal{P}_n(t) = \sum_{i=0}^{2}\langle i,n|\rho(t)|i,n\rangle$ is determined by the matrix elements $\langle i,n|\rho(t)|i,n\rangle$ of the density matrix. The Hilbert space of the qubit is reduced to the levels $\{|0\rangle,|1\rangle,|2\rangle\}$ while the one of the cavity is infinite. We need to truncate the latter at a state $M$ sufficiently large so that $P_M(t)$ remains small compared to unity (in practice $M$ is fixed according to the desired precision). The time-derivatives of these elements satisfy

$$\begin{aligned}\langle i,n|\dot{\rho}(t)|i,n\rangle &= \kappa\left[(n+1)\langle i,n+1|\rho(t)|i,n+1\rangle - n\langle i,n|\rho(t)|i,n\rangle\right]\\ &\quad + \Gamma\langle 0,n|\rho(t)|0,n\rangle(\delta_{i,2}-\delta_{i,0}) + \gamma_{21}\langle 2,n|\rho(t)|2,n\rangle(\delta_{i,1}-\delta_{i,2})\\ &\quad + 2g\left[\sqrt{n}\langle 0,n|\rho(t)|1,n-1\rangle\delta_{i,0} - \sqrt{n+1}\langle 0,n+1|\rho(t)|1,n\rangle\delta_{i,1}\right]\,,\end{aligned} \tag{4.20}$$

where we used the property $\langle 1,n|\rho|0,n+1\rangle = \langle 0,n+1|\rho|1,n\rangle$ when the qubit is in resonance with the cavity. To obtain a closed set of equations for $\{\langle i,n|\rho(t)|i,n\rangle\}_{i\in\{0,1,2\},n\in\{0,\ldots,M\}}$, we need the additional matrix elements $\{\langle 0,n|\rho(t)|1,n-1\rangle\}_{n\in\{1,\ldots,M\}}$. Their time-derivative reads

$$\begin{aligned}\langle 0,n|\dot{\rho}(t)|1,n-1\rangle &= \kappa\left[\sqrt{n(n+1)}\langle 0,n+1|\rho(t)|1,n\rangle - (n-1/2)\langle 0,n|\rho(t)|1,n-1\rangle\right]\\ &\quad - \frac{\Gamma}{2}\langle 0,n|\rho(t)|1,n-1\rangle + g\sqrt{n}\left[\langle 1,n-1|\rho(t)|1,n-1\rangle - \langle 0,n|\rho(t)|0,n\rangle\right]\,.\end{aligned} \tag{4.21}$$

This set of equations leads to the time-evolution of the different populations but also to their steady state values. This is achieved by setting the time derivatives to zero and using the relation $\mathrm{Tr}\rho = 1$, *i.e.* $\sum_{i=0}^{2}\sum_{n=0}^{M}\langle i,n|\rho(t)|i,n\rangle = 1$. The method to solve a more general case is presented in appendix C.2.1.

### 4.1.3.b Semiclassical treatment

The average number of photons $N(t) = \langle a^\dagger a\rangle(t)$ in the cavity in the steady state can be found in the semiclassical approximation, valid for a large number of photons. To find the stationary solution of the photon number, we start with the differential equation satisfied by $N(t)$ for an incoherent pumping,

$$\dot{N}(t) = -\kappa N(t) + g\mathcal{C}_{1r}(t), \tag{4.22}$$

where $\mathcal{C}_{1r}(t) = \langle \bar{a}^\dagger(t)\bar{\sigma}_{01}(t) + \bar{a}(t)\bar{\sigma}_{10}(t)\rangle$. The temporal evolutions for the additional fields read

$$\dot{\mathcal{C}}_{1r}(t) = -(\Gamma+\kappa)\mathcal{C}_{1r}(t)/2 - \delta\mathcal{C}_{1i}(t) + 2g\langle\sigma_1\rangle(t) + 2g\langle\sigma_z\rangle(t)N(t), \tag{4.23}$$

$$\dot{\mathcal{C}}_{1i}(t) = -(\Gamma+\kappa)\mathcal{C}_{1i}(t)/2 + \delta\mathcal{C}_{1r}(t), \tag{4.24}$$

$$\langle\dot{\sigma}_1(t)\rangle = \gamma_{21}(1 - 2\langle\sigma_1\rangle(t) + \langle\sigma_z\rangle(t)) - g\mathcal{C}_{1r}(t), \tag{4.25}$$

$$\langle\dot{\sigma}_z(t)\rangle = \gamma_{21}(1 - 2\langle\sigma_1\rangle(t) + \langle\sigma_z\rangle(t)) + \Gamma(\langle\sigma_1\rangle(t) - \langle\sigma_z\rangle(t)) - 2g\mathcal{C}_{1r}(t). \tag{4.26}$$

where $\mathcal{C}_{1i}(t) = i\langle \bar{a}^\dagger(t)\bar{\sigma}_{01}(t) - \bar{a}(t)\bar{\sigma}_{10}(t)\rangle$ and $\langle\sigma_z\rangle(t) = \langle\sigma_1(t) - \sigma_0(t)\rangle$. In the semiclassical limit, *i.e.* for a large photon number, we can factorize $\langle\langle\sigma_z\rangle(t)N(t)\rangle = \langle\langle\sigma_z\rangle(t)\rangle\langle N(t)\rangle$. The stationary solution is then

$$\begin{aligned} N = {} & \frac{1 - \kappa\left(\frac{1}{\Gamma} + \frac{1}{\gamma_{21}}\right) - \frac{\kappa}{4g^2}(\Gamma+\kappa)\left(1 + \frac{4\delta^2}{(\Gamma+\kappa)^2}\right)}{2\kappa\left(\frac{2}{\Gamma} + \frac{1}{\gamma_{21}}\right)} \\ & + \frac{\sqrt{\left[1 - \kappa\left(\frac{1}{\Gamma} + \frac{1}{\gamma_{21}}\right) - \frac{\kappa}{4g^2}(\Gamma+\kappa)\left(1 + \frac{4\delta^2}{(\Gamma+\kappa)^2}\right)\right]^2 + 4\kappa\left(\frac{2}{\Gamma} + \frac{1}{\gamma_{21}}\right)}}{2\kappa\left(\frac{2}{\Gamma} + \frac{1}{\gamma_{21}}\right)} \qquad (4.27) \\ \simeq {} & \frac{\gamma_{21}}{2\kappa g^2}\frac{2g^2(\Gamma+\kappa) - \kappa(\Gamma^2/2 + 2\delta^2)}{\Gamma + 2\gamma_{21}}, \qquad (4.28) \end{aligned}$$

for $\kappa \ll \Gamma$ and

$$\langle\sigma_0\rangle = \frac{\kappa}{\Gamma}N, \tag{4.29}$$

$$\langle\sigma_1\rangle = 1 - \kappa\left(\frac{1}{\Gamma} + \frac{1}{\gamma_{21}}\right)N, \tag{4.30}$$

$$\mathcal{C}_{1r} = \frac{\kappa}{g}N, \tag{4.31}$$

$$\mathcal{C}_{1i} = \frac{2\kappa\delta}{g(\Gamma+\kappa)}N. \tag{4.32}$$

These expressions can be used to find a good estimation of the photon number, the qubit populations and the correlation $\sigma_{10}a^\dagger$. The comparison with the results from the density matrix will be presented in Sec. 4.2.

### 4.1.4 Output spectrum

#### 4.1.4.a Relation to the steady state density matrix

The output spectrum $\hat{\mathcal{S}}(\omega)$ is defined as the Fourier transform of the correlator $\mathcal{S}(\tau) = \langle a^\dagger(\tau)a(0)\rangle$. We calculate the output spectrum once the steady state is reached. If we call $t_{SS}$ the time beyond which the physical observables are time-independent (according to a given precision), the time $\tau$ is equal to $\tau = t - t_{SS}$. This average being independent of the representation, we choose the Heisenberg one [102]:

$$\begin{aligned} \mathcal{S}(\omega) &= \int_{-\infty}^{+\infty} \mathrm{d}\tau\, \mathrm{e}^{-i\omega\tau}\langle a_H^\dagger(\tau)a_H(0)\rangle \\ &= 2\,\mathrm{Re}\int_0^{\infty} \mathrm{d}\tau\, \mathrm{e}^{i\omega\tau}\langle a_H^\dagger(0)a_H(\tau)\rangle. \end{aligned} \tag{4.33}$$

The density matrix $\rho_I(\tau = 0)$ is obtained after a sufficiently long time to reach the steady state. The different pictures used in this section (Schrödinger picture, subscript

$S$; Heisenberg, $H$; interaction, $I$) are defined with respect to the time $\tau$. In the following, we will use the convention $\mathrm{TL}\{f(\tau)\}(\omega) = \int_0^\infty \mathrm{d}\tau\, \mathrm{e}^{i\omega\tau} f(\tau)$ and the notation $\mathcal{S}(\tau) = \langle a_H^\dagger(0) a_H(\tau)\rangle$. The integral over all frequencies of the spectrum is equal to

$$\int_{-\infty}^{+\infty} \mathrm{d}\omega \mathcal{S}(\omega) = 2\pi N \tag{4.34}$$

To go back to the interaction representation we use the superoperator, *i.e.* an operator which acts on operators, $\mathcal{U}(\tau)$

$$\mathcal{U}(\tau)[\mathcal{O}] = \mathrm{e}^{i\mathcal{H}_0\tau/\hbar}\, \mathrm{e}^{-i\mathcal{H}\tau/\hbar} \mathcal{O} U^\dagger(\tau) \mathrm{e}^{i\mathcal{H}\tau/\hbar}\, \mathrm{e}^{-i\mathcal{H}_0\tau/\hbar}, \tag{4.35}$$

$$\mathcal{O}_I(\tau) = \mathcal{U}(\tau)[\mathcal{O}_H(\tau)]\,. \tag{4.36}$$

In particular, for the density matrix we have

$$\rho_I(\tau) = \mathcal{U}(\tau)[\rho_I(0)]\,, \tag{4.37}$$

where $\rho_I(0) = \rho_H$ is the steady state density matrix. Then, it is possible to express the temporal spectral function

$$\mathcal{S}(\tau) = \mathrm{Tr}\Big\{a_H^\dagger(0) a_H(\tau) \rho_H\Big\} \tag{4.38}$$

$$= \mathrm{Tr}\{a_I(\tau) A_I(\tau)\}\,, \tag{4.39}$$

where $A_I(\tau) = \mathcal{U}(\tau)\left[\rho_I(0) a_I^\dagger(0)\right]$. The temporal dependence of $a_I(\tau)$ reads

$$a_I(\tau) = \mathrm{e}^{i\mathcal{H}_0\tau/\hbar}\, a_S\, \mathrm{e}^{-i\mathcal{H}_0\tau/\hbar} = \mathrm{e}^{-i\omega_0\tau}\, a_S, \tag{4.40}$$

and then

$$\langle n, i| a_I(\tau) = \mathrm{e}^{-i\omega_0\tau} \sqrt{n+1}\, \langle n+1, i|. \tag{4.41}$$

The resulting trace is

$$\mathrm{Tr}\{a_I(\tau) A_I(\tau)\} = \mathrm{e}^{-i\omega_0\tau} \sum_{i=0}^{2} \sum_{n=0}^{\infty} \sqrt{n+1} \langle n+1, i| A_I(\tau) |n, i\rangle. \tag{4.42}$$

Fourier transforming yields

$$\hat{\mathcal{S}}(\omega) = 2\mathrm{Re} \sum_{i=0}^{2} \sum_{n=0}^{\infty} \sqrt{n+1} \langle n+1, i| \widehat{A}(\Delta\omega) |n, i\rangle, \tag{4.43}$$

where $\widehat{A}(\Delta\omega) = \mathrm{TL}\{A_I(\tau)\}(\omega_0 + \Delta\omega)$ and $\Delta\omega = \omega - \omega_0$. In the preceding relation we used $\mathrm{TL}\big\{\mathrm{e}^{-i\omega_0\tau} f(\tau)\big\}(\omega) = \mathrm{TL}\{f(\tau)\}(\omega - \omega_0)$.

Concerning the density matrix, we know that the formal solution of the master equation is the equation (4.37) with suitable initial conditions. The temporal evolution of the density matrix $\rho_I(\tau) = \mathcal{U}(\tau)[\rho_I(0)]$ is governed by the superoperator $\mathscr{L}(\tau)$

$$\mathscr{L}(\tau)[\mathcal{O}] = \frac{1}{i\hbar} [\mathcal{H}_{1I}(\tau), \mathcal{O}] + L\mathcal{O}, \tag{4.44}$$

according to the relation

$$\dot{\rho}_I(\tau) = \mathscr{L}(\tau)[\rho_I(\tau)]\,. \tag{4.45}$$

The definition of the operator $A_I(\tau) = \mathcal{U}(\tau)\Big[\rho_I(0)a_I^\dagger(0)\Big]$ reveals that $A_I(\tau)$ has a dynamics equivalent to the time evolution of the density matrix but with a different initial value. This property of the operator $A$ leads to its time derivative

$$\dot{A}_I(\tau) = \mathscr{L}(\tau)[A_I(\tau)]\,, \tag{4.46}$$

$$A_I(0) = \rho_I(0)a_I^\dagger(0). \tag{4.47}$$

These relations can be directly derived using the quantum regression theorem, also called the Lax-Onsager regression theorem due to the work of Lars Onsager [103] and Melvin Lax [104].

### 4.1.4.b Use of the quantum regression theorem

Let us suppose that the expectation value of an operator $\mathcal{O}$ at a time $t_0 + \tau$ can be expressed in terms of a set of operators $\{\mathcal{O}_i\}$ at time $t_0$, namely

$$\langle \mathcal{O}(t_0 + \tau)\rangle = \sum_i f_i(\tau)\langle \mathcal{O}_i(t_0)\rangle. \tag{4.48}$$

Then, if we want to calculate the correlation between $\mathcal{O}$ at time $t_0+\tau$ and $\mathcal{O}^l$ or $\mathcal{O}^r$ at time $t_0$, *i.e.* the quantity $\langle \mathcal{O}^l(t_0)\mathcal{O}(t_0+\tau)\mathcal{O}^r(t_0)\rangle$, the quantum regression theorem [105, 106] states that $\mathcal{O}(t_0 + \tau)$ can be replaced by the set $\{\mathcal{O}_i(t_0)\}$. The resulting correlator contains all operators at the initial time $t_0$:

$$\langle \mathcal{O}^l(t_0)\mathcal{O}(t_0 + \tau)\mathcal{O}^r(t_0)\rangle = \sum_i f_i(\tau)\langle \mathcal{O}^l(t_0)\mathcal{O}_i(t_0)\mathcal{O}^r(t_0)\rangle. \tag{4.49}$$

The quantum regression theorem is valid in the Born-Markov approximation that we used to derive the Lindbladian. Applied to the spectral function, this theorem leads directly to Eq. (4.46) for $A_I(\tau)$.

To calculate the spectral function, we need the $3(M-1)$ elements $\langle i, n+1|A_I(\tau)|i, n\rangle$ for $n \in \{0, \ldots, M-1\}$:

$$\begin{aligned}
&\langle i, n+1|\dot{A}_I(\tau)|i, n\rangle \\
&= \kappa\left[\sqrt{(n+1)(n+2)}\langle i, n+2|A_I(\tau)|i, n+1\rangle - (n+1/2)\langle i, n+1|A_I(\tau)|i, n\rangle\right] \\
&+ \Gamma\langle 0, n+1|A_I(\tau)|0, n\rangle(\delta_{i,2} - \delta_{i,0}) + \gamma_{21}\langle 2, n+1|A_I(\tau)|2, n\rangle(\delta_{i,1} - \delta_{i,2}) \\
&+ g\left[\sqrt{n+1}\langle 1, n|A_I(\tau)|0, n\rangle + \sqrt{n}\langle 0, n+1|A_I(\tau)|1, n-1\rangle\right]\delta_{i,0} \\
&- g\left[\sqrt{n+1}\langle 1, n+1|A_I(\tau)|0, n+1\rangle + \sqrt{n+2}\langle 0, n+2|A_I(\tau)|1, n\rangle\right]\delta_{i,1}.
\end{aligned} \tag{4.50}$$

This set of equations induces two additional matrix elements, namely $\langle 0, n+2|A_I(\tau)|1, n\rangle$ and $\langle 1, n|A_I(\tau)|0, n\rangle$. This leads us to define the column matrix $B(\tau) = \big(b_0(\tau), \ldots, b_{M-1}(\tau)\big)^{\mathrm{t}}$ of dimension $5M-1$ as follows

$$b_{n<M-1}(\tau) = \begin{pmatrix} \langle n+1, 0|A_I(\tau)|n, 0\rangle \\ \langle n+1, 1|A_I(\tau)|n, 1\rangle \\ \langle n+1, 2|A_I(\tau)|n, 2\rangle \\ \langle n+2, 0|A_I(\tau)|n, 1\rangle \\ \langle n, 1|A_I(\tau)|n, 0\rangle \end{pmatrix}, \quad b_{M-1}(\tau) = \begin{pmatrix} \langle M, 0|A_I(\tau)|M-1, 0\rangle \\ \langle M, 1|A_I(\tau)|M-1, 1\rangle \\ \langle M, 2|A_I(\tau)|M-1, 2\rangle \\ \langle M-1, 1|A_I(\tau)|M-1, 0\rangle \end{pmatrix}. \tag{4.51}$$

The temporal derivative of $A_I(\tau)$ is equivalent to a matrix equation involving $B(\tau)$ and $\dot{B}(\tau)$ connected with the matrix $\mathcal{W}$ by $\dot{B}(\tau) = \mathcal{W} \cdot B(\tau)$. The expression for the matrix $\mathcal{W}$ is given in the appendix C.2.2. The temporal spectral function then reads

$$\mathcal{S}(\tau) = \mathrm{e}^{-i\omega_0\tau} \sum_{n=0}^{M-1} \sum_{j=0}^{2} \sqrt{n+1}\, B_{5n+j}(\tau). \tag{4.52}$$

Next, noting the Fourier transform $\widehat{B}(\omega) = \mathrm{TL}\{B(\tau)\}(\omega)$, and using the property $\mathrm{TL}\{f'(\tau)\}(\omega) = -i\omega\mathrm{TL}\{f(\tau)\}(\omega) - f(0)$, we get

$$i\omega\widehat{A}(\omega) + \mathscr{L}\Big[\widehat{A}(\omega)\Big] = -A_I(0), \tag{4.53}$$

or equivalently

$$\widehat{B}(\omega) = -\left(\mathcal{W} + i\omega\mathbb{I}\right)^{-1} \cdot B(0), \tag{4.54}$$

where

$$b_n(0) = \sqrt{n+1}\begin{pmatrix} \langle n+1,0|\rho_H|n+1,0\rangle \\ \langle n+1,1|\rho_H|n+1,1\rangle \\ \langle n+1,2|\rho_H|n+1,2\rangle \\ \langle n+2,0|\rho_H|n+1,1\rangle \\ \langle n,1|\rho_H|n+1,0\rangle \end{pmatrix}, \quad b_{M-1}(0) = \sqrt{M}\begin{pmatrix} \langle M,0|\rho_H|M,0\rangle \\ \langle M,1|\rho_H|M,1\rangle \\ \langle M,2|\rho_H|M,2\rangle \\ \langle M-1,1|\rho_H|M,0\rangle \end{pmatrix}. \tag{4.55}$$

The density matrix in the steady state can be found using the method of Sec. 4.1.3.a. The use of the quantum regression theorem reduces the time integration of the Fourier transform to a matrix inversion, and is a powerful tool for numerical calculations.

#### 4.1.4.c Semiclassical derivation

The temporal derivative of $\mathcal{S}(\tau)$ depends on the function $F(\tau) = \langle\sigma_{10I}(\tau)a_I(0)\rangle$. The derivative of $F(\tau)$ generates the correlator $\langle[\sigma_1(\tau) - \sigma_0(\tau)]\, a_I^\dagger(\tau)a_I(0)\rangle$ which is factorized according to $\langle\sigma_z(0)\rangle\mathcal{S}(\tau)$ in the semiclassical approximation. The dynamics is then reduced to the matrix equation

$$\partial_\tau \begin{pmatrix} \mathcal{S}(\tau) \\ F(\tau) \end{pmatrix} = \begin{pmatrix} i\omega_0 - \frac{\kappa}{2} & g \\ g\langle\sigma_z\rangle & i(\omega_0+\delta) - \frac{\Gamma}{2} \end{pmatrix} \cdot \begin{pmatrix} \mathcal{S}(\tau) \\ F(\tau) \end{pmatrix}. \tag{4.56}$$

Fourier transforming yields

$$\begin{pmatrix} \hat{\mathcal{S}}(\omega) \\ \hat{F}(\omega) \end{pmatrix} = \begin{pmatrix} i\Delta\omega + \kappa/2 & -g \\ -g\langle\sigma_z\rangle & i(\Delta\omega - \delta) + \Gamma/2 \end{pmatrix}^{-1} \cdot \begin{pmatrix} \mathcal{S}(0) \\ F(0) \end{pmatrix}, \tag{4.57}$$

where $\mathcal{S}(0) = N$ and $F(0) = (\mathcal{C}_1 + i\mathcal{C}_2)/2$ found in Sec. 4.1.3.b. This leads to

$$\hat{\mathcal{S}}(\omega_0 + \Delta\omega) = 2N\,\mathrm{Re}\left[\frac{\frac{\Gamma}{2} + \frac{\kappa}{2} + i\left(\Delta\omega - \frac{\Gamma}{\Gamma+\kappa}\delta\right)}{\left(\Gamma/2 + i(\Delta\omega - \delta)\right)\left(\kappa/2 + i\Delta\omega\right) - g^2\langle\sigma_z\rangle}\right]. \tag{4.58}$$

The spectral function $\hat{\mathcal{S}}(\omega)$ can be approximated by a Lorentzian

$$\hat{\mathcal{S}}(\omega_0 + \Delta\omega) \simeq \frac{2Nk_d}{(\Delta\omega - \delta\omega_0)^2 + k_d^2} \tag{4.59}$$

with the width and the dephasing given by

$$k_d = \frac{\kappa}{2} - 2g^2 \frac{\Gamma}{\Gamma^2 + 4\delta^2} \langle \sigma_z \rangle, \qquad \delta\omega_0 = 4g^2 \frac{\delta}{\Gamma^2 + 4\delta^2} \langle \sigma_z \rangle. \tag{4.60}$$

The coupling to the cavity reduces the width of the output spectrum with respect to the case of an isolated cavity where $k_d = \kappa/2$.

It is worth mentioning that the semiclassical approximation constitutes a perturbative treatment in the coupling between the qubit and the cavity. This approach needs to be handled with care close to the resonance where the coupling is maximum. We will see in Sec. 4.2.3.b a method to improve the factorization.

## 4.2 Lasing effect in the JQP cycle of a charge qubit

In this section we apply the general formalism of the previous one to the first experiment where the lasing effect of a superconducting qubit coupled to a cavity has been observed [99]. We use the parameters of their three-level artificial atom to compare our treatment to the experimental results and to obtain the temporal dynamics, not measured experimentally. We also analyse the validity of the semiclassical approximation. The truncation of the correlations is inspired from Ref. [107], where the lasing effect of a two-level artificial atom is studied.

### 4.2.1 The JQP cycle

In the experiment of Ref. [99], a charge qubit is coupled to a superconducting waveguide resonator. To achieve the population inversion necessary to induce lasing, the Josephson quasiparticle (JQP) cycle [108, 109] has been used. The two states $|0\rangle$ and $|1\rangle$ of the qubit correspond to 1 and 0 Cooper pair, respectively, and the third state $|2\rangle$, with an energy higher than both qubit states, describes an unpaired electron. To extract one electron by breaking a Cooper pair, an energy equal to twice the superconducting gap $\Delta$ is needed in addition to the charging energy $E_C = e^2/2C$ of the junction. The JQP cycle provides incoherent pumping between the states $|0\rangle$ and $|2\rangle$ with the rate $\widetilde{\Gamma} = (eV_b + E_C)/e^2 R_b$ and a relaxation rate $\widetilde{\gamma}_{21} = (eV_b - E_C)/e^2 R_b$ from $|2\rangle$ to $|1\rangle$, obtained using the Fermi golden rule. As a result, the state $|0\rangle$ decays to $|1\rangle$ with two sequential single-electron tunneling events. In the experiment, a voltage equal to $V_b = 0.65\,\mathrm{mV}$ larger than $(2\Delta + E_C)/e = 0.54\,\mathrm{mV}$ (the superconducting gap energy of aluminum is $\Delta/h = 55\,\mathrm{GHz}$) is applied. The resulting rates are $\widetilde{\Gamma} = 4.6\,\mathrm{GHz}$ and $\widetilde{\gamma}_{21} = 3.5\,\mathrm{GHz}$. The cavity is described with the bosonic annihilation and creation operators $a$ and $a^\dagger$, satisfying $\left[a, a^\dagger\right] = 1$. The resonator has a bare resonance frequency $\omega_0/2\pi = 9.899\,\mathrm{GHz}$ and a quality factor equal to 7600, corresponding to a damping rate $\kappa = 8.2\,\mathrm{MHz}$. The Hamiltonian of the charge qubit coupled to the cavity reads [99]

$$\mathcal{H} = \frac{\epsilon}{2}\left(|1\rangle\langle 1| - |0\rangle\langle 0|\right) - \frac{E_J}{2}\left(|1\rangle\langle 0| + |0\rangle\langle 1|\right) + \hbar\omega_0\left(a^\dagger a + \frac{1}{2}\right) + \hbar g_0 (a^\dagger + a)\left(|0\rangle\langle 0| - |1\rangle\langle 1|\right), \tag{4.61}$$

where the electrostatic energy difference $\epsilon = 4E_C(n_g - 1)$ between the two states is controlled by the normalized gate charge $n_g = C_g V_g/e$ where $C_g$ is the gate capacitance and $V_g$ the gate voltage (see Fig. 4.2). The qubit is characterized by the charging energy

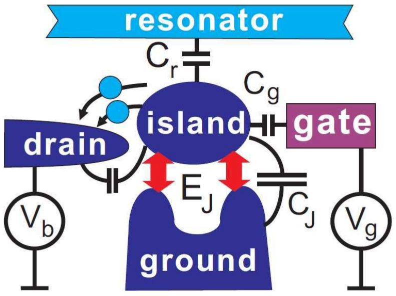

Figure 4.2: Schematic representation of the experimental circuit of Ref. [99] studied in this section.

$E_C/h = 20\,\mathrm{GHz}$ and the Josephson energy $E_J/h = 5.4\,\mathrm{GHz}$ ($E_J < E_C$). The bare coupling energy is equal to $g_0/2\pi = 80\,\mathrm{MHz}$. The eigenvalues $\pm\hbar\omega_{10}/2$ of the Hamiltonian of the qubit $\mathcal{H}_{\mathrm{QB}} = \frac{1}{2}\begin{pmatrix} -\epsilon & -E_J \\ -E_J & \epsilon \end{pmatrix}$ are given by

$$\hbar\omega_{10} = \sqrt{E_J^2 + \epsilon^2}. \tag{4.62}$$

The corresponding eigenvectors $\{|\psi_0\rangle, |\psi_1\rangle\}$ are obtained after a rotation of the basis $\{|0\rangle, |1\rangle\}$ around the state $|\psi_2\rangle \equiv |2\rangle$ of the angle $\theta$ satisfying

$$\tan 2\theta = E_J/\varepsilon. \tag{4.63}$$

We note $\sigma_{ij} = |\psi_i\rangle\langle\psi_j|$ the operators of the qubit in the eigenbasis, in which the Hamiltonian is reduced to the usual form

$$\mathcal{H} = \frac{\hbar\omega_{10}}{2}(\sigma_1 - \sigma_0) + \hbar\omega_0\left(a^\dagger a + \frac{1}{2}\right) + i\hbar g(\sigma_{01}a^\dagger - \sigma_{10}a). \tag{4.64}$$

This Hamiltonian is obtained after applying the RWA and the unitary transformation $a \rightarrow ia$. The effective coupling energy depends on the gate voltage according to

$$g = \sin 2\theta\, g_0. \tag{4.65}$$

The resonance is achieved at $\epsilon/h = 8.3\,\mathrm{GHz}$ where $g/2\pi = 44\,\mathrm{MHz}$.

### 4.2.2 Lindblad operator

The pumping and relaxation rates $\widetilde{\Gamma}$ and $\widetilde{\gamma}_{21}$ concern the charge states $\{|0\rangle, |1\rangle, |2\rangle\}$ of the qubit. In the eigenbasis $\{|\psi_0\rangle, |\psi_1\rangle, |\psi_2\rangle\}$, where $|\psi_2\rangle = |2\rangle$, the rates are modified and the reverse processes are induced:

- Pumping $|\psi_0\rangle \rightarrow |\psi_2\rangle$ at the rate $\Gamma = \cos^2\theta\,\widetilde{\Gamma}$.
- Relaxation $|\psi_2\rangle \rightarrow |\psi_1\rangle$ at the rate $\gamma_{21} = \cos^2\theta\,\widetilde{\gamma}_{21}$.
- Relaxation $|\psi_2\rangle \rightarrow |\psi_0\rangle$ at the rate $\gamma_{20} = \sin^2\theta\,\widetilde{\gamma}_{21}$.
- Pumping $|\psi_1\rangle \rightarrow |\psi_2\rangle$ at the rate $\gamma_{12} = \sin^2\theta\,\widetilde{\Gamma}$.

The total Lindblad operator is then $\mathrm{L} = \mathrm{L}_C + \mathrm{L}_\Gamma + \mathrm{L}_{\gamma_{21}} + \mathrm{L}_{\gamma_{20}} + \mathrm{L}_{\gamma_{12}}$, where

$$\mathrm{L}_{\gamma_{ij}} = \frac{\gamma_{ij}}{2}(2\sigma_{ji}\rho\sigma_{ij} - \sigma_i\rho - \rho\sigma_i). \tag{4.66}$$

At the resonance, the pumping rate in the eigenbasis is reduced to $\Gamma = 4.2\,\mathrm{GHz}$ with also $\gamma_{21} = 3.3\,\mathrm{GHz}$ while the additional transitions occur at rates $\gamma_{20} = 0.29\,\mathrm{GHz}$ and $\gamma_{12} = 0.37\,\mathrm{GHz}$.

Using the method explained in Secs. 4.1.3.a and 4.1.4, the Hamiltonian (4.64) together with the Lindblad operator L give access to the qubit and level populations as well as the output spectrum. The time evolution of the photon number and the qubit populations are showed on Fig. 4.3. The time to reach the steady state is of the order of the microsecond. A population imbalance $\langle s_z\rangle = \langle\sigma_1 - \sigma_0\rangle = 12\,\%$ and a photon number $\langle n\rangle = 122.5$ is achieved. The experimentally estimated number of photons in the cavity is $N_{\mathrm{exp}} \simeq 30$ but it can be underestimated, as the resonator internal loss is not accounted for. The

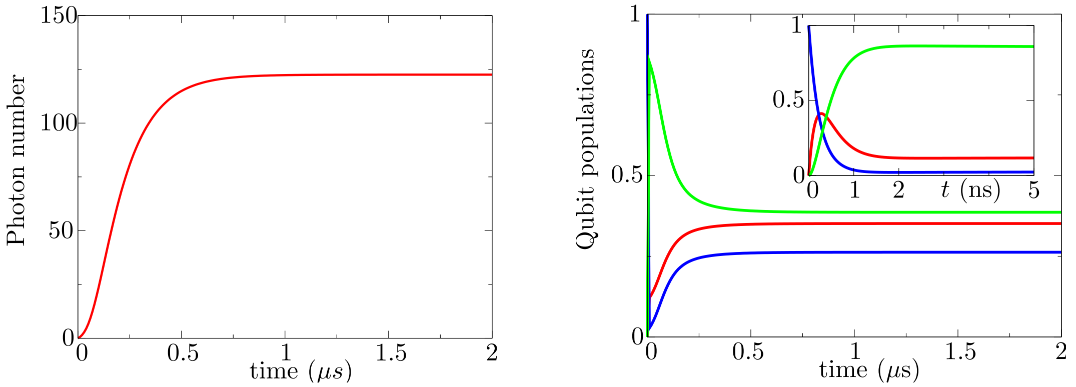

Figure 4.3: Temporal dynamics obtained for the experiment of Ref. [99]. *Left*: Time evolution of the photon number in the cavity. Time is expressed in microseconds. *Right*: Time evolution of the level populations, $\langle\sigma_0\rangle(t)$ in blue, $\langle\sigma_1\rangle(t)$ in green and $\langle\sigma_2\rangle(t)$ in red. The inset represents the qubit populations during the first nanoseconds.

stationary distribution of the photon number $\mathcal{P}(n)$ is compared to the Gaussian $\mathcal{P}_G(n)$ and Poissonian $\mathcal{P}_P(n)$ distributions

$$\mathcal{P}_G(n) = \frac{1}{\sqrt{2\pi}\sigma}\exp\left(-\frac{(n-N)^2}{2\sigma^2}\right), \tag{4.67}$$

$$\mathcal{P}_P(n) = \frac{N^n\,\mathrm{e}^{-N}}{n!}. \tag{4.68}$$

where the variance $\sigma^2$ is given by $\sigma^2 = \sum_n (n-N)^2\,\mathcal{P}(n)$. The photon number being large, the Poissonian tends to the Gaussian distribution.

### 4.2.3 Semiclassical treatment

#### 4.2.3.a Photon number

The steady state value of the photon number is obtained from a set of equations involving $\langle\sigma_z\rangle$, $\langle\sigma_1\rangle$, and $\langle\sigma_{10}a\rangle$. This set depends on the parameter $\langle\sigma_z n\rangle$, which can be factorized in the semiclassical limit. The corresponding result, similar to Eq. (4.27), is in excellent agreement with the solution from the steady state density matrix plotted in Fig. 4.4. In the limit $\kappa \ll \Gamma, \gamma_{21}$, and for $\epsilon > 0$, one finds

$$\begin{aligned} N =& \frac{\gamma_{21}}{2g^2\kappa}\,\frac{2g^2\left(\Gamma - \gamma_{12} + \frac{2\epsilon^2+E_J^2}{2\epsilon\hbar\omega_{10}}\kappa\right) - \frac{\kappa}{2}\left(\Gamma^2 + \gamma_{12}^2 + 2\frac{2\epsilon^2+E_J^2}{\epsilon^2+E_J^2}\delta^2\right)}{\Gamma + 2\gamma_{21}} \\ &+ \frac{\gamma_{12}}{4g^2}\,\frac{\frac{E_J^2}{\epsilon\hbar\omega_{10}}g^2 + \frac{E_J^2}{\epsilon^2+E_J^2}\delta^2 - \Gamma\gamma_{12}}{\gamma_{12} + 2\gamma_{20}}. \end{aligned} \tag{4.69}$$

The solution at resonance is found to be $N = 122.8$, which is in good agreement with the numerical solution (0.2 % relative difference). The steady state photon number as a function of the gate voltage is plotted in Fig. 4.4.

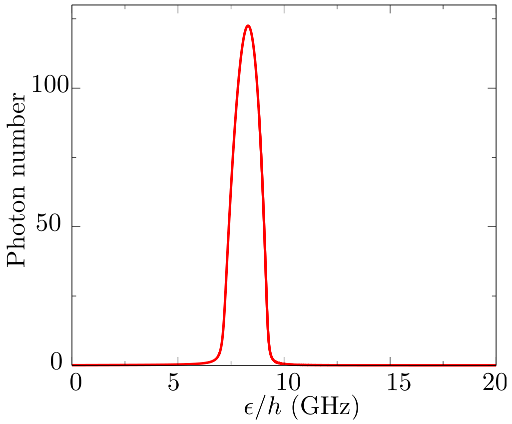

Figure 4.4: Steady state photon number obtained for the experiment of Ref. [99] as a function of the gate voltage. The photon number is maximal at the resonance.

### 4.2.3.b Output spectrum

The semiclassical result obtained for the spectrum in Sec. 4.1.4.c used the factorization $\langle\sigma_z(\tau)a^\dagger(\tau)a(0)\rangle \simeq \langle\sigma_z(0)\rangle\langle a^\dagger(\tau)a(0)\rangle$ between the qubit and the cavity. This decoupling can be improved as demonstrated in Ref. [107], where the correlator is factorized as follows

$$\begin{aligned}\langle\sigma_z(\tau)a^\dagger(\tau)a(0)\rangle &\simeq \frac{\langle\sqrt{n}\sigma_z\rangle}{\langle\sqrt{n}\rangle}\langle a^\dagger(\tau)a(0)\rangle \\ &\simeq \frac{1}{2}\left(\langle\sigma_z\rangle + \frac{\langle\sigma_z n\rangle}{\langle n\rangle}\right)\langle a^\dagger(\tau)a(0)\rangle. \end{aligned} \tag{4.70}$$

This result is obtained from the amplitude-phase representation of the operator $a$ and assuming that the correlation time of the phase fluctuations is much longer than that of the amplitude fluctuations. In the following, we use this relation to truncate correlations and then to compare the semiclassical approximation with the numerical result using the regression theorem. We note $\langle S_z\rangle = \frac{1}{2}\left(\langle\sigma_z\rangle + \langle\sigma_z n\rangle/\langle n\rangle\right)$. The improved semiclassical approximation leads to the result

$$\hat{\mathcal{S}}(\omega_0+\Delta\omega) = 2N\mathrm{Re}\left[\frac{\frac{1}{2}(\Gamma+\gamma_{12}+\kappa) + i\left(\Delta\omega - \frac{\Gamma+\gamma_{12}}{\Gamma+\gamma_{21}+\kappa}\delta\right)}{(\kappa/2+i\Delta\omega)\left((\Gamma+\gamma_{21})/2+i(\Delta\omega-\delta)\right) - g^2\langle S_z\rangle}\right]. \tag{4.71}$$

This output spectrum is well approximated with the Lorentzian

$$\hat{\mathcal{S}}(\omega_0+\Delta\omega) = \frac{2Nk_d}{(\Delta\omega-\delta\omega_0)^2+k_d^2}, \tag{4.72}$$

where

$$k_d = \frac{\kappa}{2} - 2g^2\frac{\Gamma+\gamma_{21}}{(\Gamma+\gamma_{21})^2+4\delta^2}\langle S_z\rangle, \qquad \delta\omega_0 = 4g^2\frac{\delta}{(\Gamma+\gamma_{21})^2+4\delta^2}\langle S_z\rangle. \tag{4.73}$$

The parameter $\langle S_z\rangle$ can be determined from the numerical result for the photon number.

Figure 4.5 shows the output spectrum as a function of $\epsilon$ and the probing frequency $\omega$. This simulation is compared to the experimental result. We find a maximum of

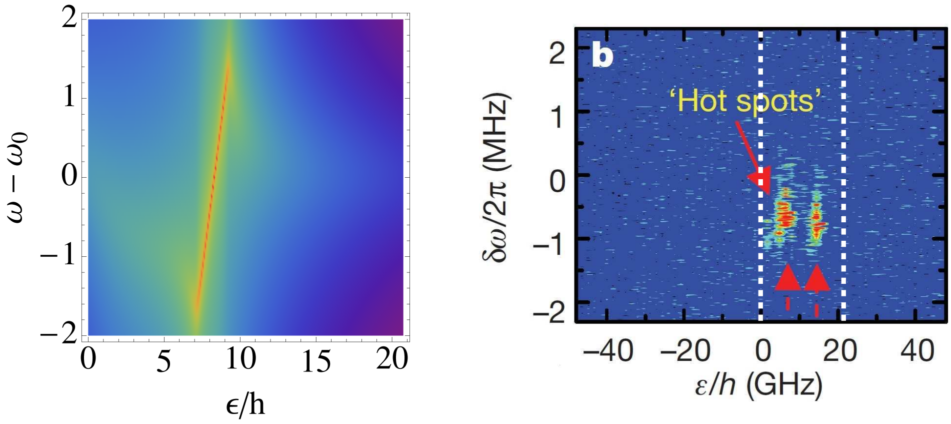

Figure 4.5: *Left*: Density plot of the spectrum from our fully-quantum model as a function of the probing frequency $(\omega - \omega_0)/2\pi$ and the gate voltage related to $\epsilon$. *Right*: measurement of the spectrum in the experiment of Ref. [99].

the spectrum close to the resonance at $\epsilon = 8.3\,\mathrm{GHz}$. The second "hot spot" at $\epsilon = 19\,\mathrm{GHz}$ is not observed in our simulation. In Fig. 4.6 the maximum value of the output spectrum is plotted as a function of $\epsilon$, for both the numerical result from the quantum regression theorem and the semiclassical result Eq. (4.71). This comparison reveals that the semiclassical treatment is not correct in the region close to the resonance. The two maxima of the semiclassical spectra, obtained first in Ref. [107], are thus artifacts of the approximation and cannot explain the second hot spot. The presence of two-photon resonance seems to be a good explanation for this second peak. A deeper analysis of two-photon processes need to be carried out. On Fig. 4.7, we see that the linewidth of the theoretical spectra is much more narrow than the experimental ones, found to be larger than 500 kHz. This is mainly due to charge fluctuations in the Cooper pair box.

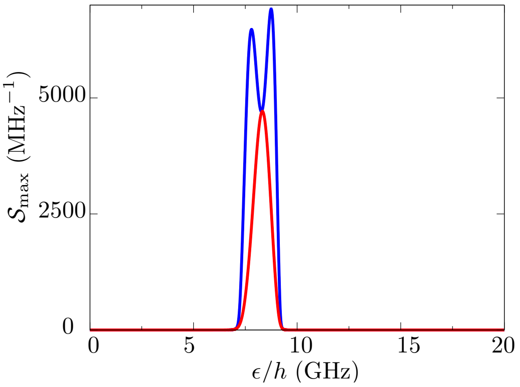

Figure 4.6: Maximum value of the spectrum as a function of $\epsilon$. The quantum solution is plotted in red and the semiclassical one in blue.

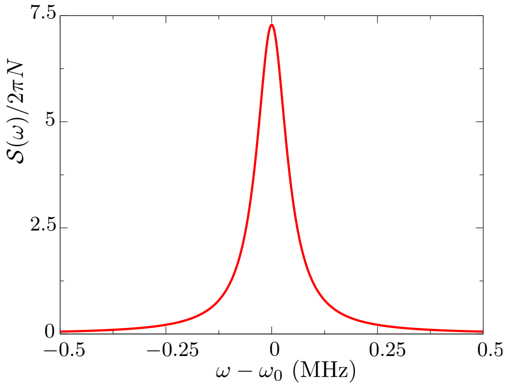

Figure 4.7: Spectrum at the resonance. The linewidth is found to be about 90 kHz.

### 4.2.4 Injection locking

#### 4.2.4.a Pumping on the cavity

We investigate the behavior of the system when it is driven by an external field $V_0 \cos((\omega_0 + \varpi)t)$. The radiation is coupled to the cavity operators through the Hamiltonian $\mathcal{H}_2 = V_0 \cos((\omega_0 + \varpi)t)(a^\dagger - a)$. In the RWA and the interaction picture, this Hamiltonian reduces to

$$\tilde{\mathcal{H}}_2 = i\hbar v_0 \left( \mathrm{e}^{-i\varpi t}\, a^\dagger - \mathrm{e}^{i\varpi t}\, a \right), \tag{4.74}$$

where $v_0 = V_0/2\hbar$ and $\varpi$ is the detuning from the cavity frequency $\omega_0$. This pumping on the cavity allows to measure the coherence property of the field in the cavity. Indeed, if the cavity field is coherent, the injection locking effect occurs and the cavity field oscillates at the same frequency as the driving field.

The presence of the driving field modifies the temporal dynamics of the density matrix. The additional elements can be implemented in the numerical calculation of the density matrix. We are then able to get the time evolution and the steady state value of any observable as well as the spectrum. This results are plotted in Figs. 4.8, 4.9, and 4.10. However, to understand the effect of the pumping on the cavity, we develop in the following a semiclassical treatment based on a rough factorization between the qubit and the cavity.

#### 4.2.4.b Photon number

The pumping on the cavity changes the time evolution of the density matrix by the term

$$\begin{aligned}\langle i, n| \frac{1}{i\hbar} \left[ \tilde{\mathcal{H}}_2, \tilde{\rho}(t) \right] |j, m\rangle =& v_0 \left( \sqrt{n} \langle i, n-1|\tilde{\rho}|j, m\rangle\, \mathrm{e}^{i\varpi t} - \sqrt{n+1} \langle i, n+1|\tilde{\rho}|j, m\rangle\, \mathrm{e}^{-i\varpi t} \right) \\ & - \sqrt{m+1} \langle i, n|\tilde{\rho}|j, m+1\rangle\, \mathrm{e}^{-i\varpi t} + \sqrt{m} \langle i, n|\tilde{\rho}|j, m-1\rangle\, \mathrm{e}^{i\varpi t} \Big) .\end{aligned} \tag{4.75}$$

This additional term affects all the elements of the density matrix, which is no longer block diagonal.

Starting from the qubit in the ground state and no photon in the cavity, the qubit is pumped at a rate $\Gamma$ and the cavity is pumped at a frequency $\omega_0 + \varpi$ once the stationary state is reached at time $t_{\mathrm{SS}}$. We have verified that the results are the same if the pumping starts from the beginning and do not depend on the initially occupied qubit level. The parameters are the same as before, except for the damping rate. To reduce the computation time we multiply $\kappa$ by ten: $\tilde{\kappa} = 10\kappa$. This change reduces the photon number but does not change the qualitative behavior. The time evolution of the photon number and the qubit populations are plotted in Fig. 4.8 at the resonance $\omega_{10} = \omega_0 = \varpi$. The pumping is switched on $0.2\,\mu$s after the beginning of the experiment with a strength $v_0 = \tilde{\kappa}$.

Analytical results can be obtained in the semiclassical approach. The dynamical equations read

$$\partial_t\langle N\rangle(t) = -\kappa\langle N\rangle(t) + g\mathcal{C}_{1r}(t) + v_0\mathcal{C}_{2r}(t), \tag{4.76}$$
$$\partial_t\langle\sigma_0\rangle(t) = -\Gamma\langle\sigma_0\rangle(t) + \mathcal{C}_{1r}b(t), \tag{4.77}$$
$$\partial_t\langle\sigma_1\rangle(t) = \gamma_{21}\langle\sigma_2\rangle(t) - \mathcal{C}_{1r}b(t), \tag{4.78}$$
$$\partial_t\langle\sigma_2\rangle(t) = -\gamma_{21}\langle\sigma_2\rangle(t) + \Gamma\langle\sigma_0\rangle(t), \tag{4.79}$$
$$\partial_t\mathcal{C}_{1r}(t) = -(\kappa+\Gamma)\mathcal{C}_{1r}(t)/2 + 2g\langle\sigma_1\rangle(t) + 2g(\langle\sigma_1\rangle(t) - \langle\sigma_0\rangle(t))\langle N\rangle(t) + v_0\mathcal{C}_{3r}(t), \tag{4.80}$$

and

$$\dot{\mathcal{C}}_{2r}(t) = -\frac{\kappa}{2}\mathcal{C}_{2r}(t) + g\mathcal{C}_{3r}(t) + i\varpi\mathcal{C}_{2i}(t) + v_0, \tag{4.81}$$
$$\dot{\mathcal{C}}_{3r}(t) = -\frac{\Gamma}{2}\mathcal{C}_{3r}(t) + g(\langle\sigma_1(t)\rangle - \langle\sigma_0(t)\rangle)\mathcal{C}_{2r}(t) + i\varpi\mathcal{C}_{3i}(t), \tag{4.82}$$
$$\dot{\mathcal{C}}_{2i}(t) = -\frac{\kappa}{2}\mathcal{C}_{2i}(t) + g\mathcal{C}_{3i}(t) + i\varpi\mathcal{C}_{2r}(t), \tag{4.83}$$
$$\dot{\mathcal{C}}_{3i}(t) = -\frac{\Gamma}{2}\mathcal{C}_{3i}(t) + g(\langle\sigma_1(t)\rangle - \langle\sigma_0(t)\rangle)\mathcal{C}_{2i}(t) + i\varpi\mathcal{C}_{3r}(t), \tag{4.84}$$

where we define

$$\mathcal{C}_{2r}(t) = \langle e^{i\varpi t}\,\tilde{a}(t) + e^{-i\varpi t}\,\tilde{a}^\dagger(t)\rangle, \qquad \mathcal{C}_{2i}(t) = \langle e^{i\varpi t}\,\tilde{a}(t) - e^{-i\varpi t}\,\tilde{a}^\dagger(t)\rangle, \tag{4.85}$$
$$\mathcal{C}_{3r}(t) = \langle e^{i\varpi t}\,\tilde{\sigma}_{01}(t) + e^{-i\varpi t}\,\tilde{\sigma}_{10}(t)\rangle, \quad \mathcal{C}_{3i}(t) = \langle e^{i\varpi t}\,\tilde{\sigma}_{01}(t) - e^{-i\varpi t}\,\tilde{\sigma}_{10}(t)\rangle. \tag{4.86}$$

The model can be simplified to calculate the photon number in the cavity in presence of pumping. We consider that the effect of the qubit is to maintain a constant photon number in the cavity $N_0 \simeq 122.5$ and treat the pumping as if the cavity were isolated. The total number of photons is then $N_0+N_P$ where $N_P$ is the number of photons created due to the pumping. The solution of this simplified problem reads

$$N_P(t) = N_0\,e^{-\kappa t} + v_0\,\mathrm{Re}\left[a^\dagger(0)\frac{e^{-(\kappa/2+i\varpi)t}}{\kappa/2 - i\varpi}\right] + \frac{v_0^2}{\varpi^2 + (\kappa/2)^2}, \tag{4.87}$$

which steady state solution is $N_P = \frac{v_0^2}{\varpi^2+(\kappa/2)^2}$, a Lorentzian of width $\kappa$. Finally, the total photon number reads

$$N = N_0 + \frac{v_0^2}{\varpi^2 + (\kappa/2)^2}. \tag{4.88}$$

The first effect of the additional pumping on the cavity is to increase the photon number in the cavity. This tendency to amplify the lasing effect is more apparent on the spectrum.

### 4.2.4.c Spectral function

To understand the effect of the driving field on the spectral function we evaluate $\mathcal{S}(t,t') = \langle a^\dagger(t)a(t')\rangle$ is the semiclassical limit. We define the center of mass and the difference of the times $t$, $t'$ as follows: $t_m = (t+t')/2$ and $\tau = t - t'$. We focus on

$$\widetilde{\mathcal{S}}(t_m,\tau) = e^{-i\omega_0(t-t')}\mathcal{S}(t,t') = e^{-i\omega_0\tau}\langle\tilde{a}^\dagger(t_m+\tau/2)\rangle\langle\tilde{a}(t_m-\tau/2)\rangle. \tag{4.89}$$

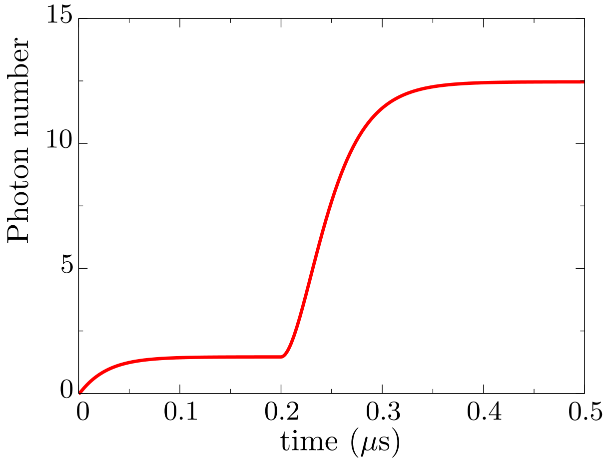

Figure 4.8: Time evolution of the photon number in the presence of a driving field on the cavity, obtained from the time evolution of the density matrix for the experiment of Ref. [99]. The driving is switched on after 200 ns with an amplitude $v_0 = \tilde{\kappa}$.

Then, in the RWA, $\widetilde{\mathcal{S}}$ satisfies the differential equation

$$\left(\frac{1}{4}\frac{\partial^2}{\partial t_m^2} - \frac{\partial^2}{\partial \tau^2}\right)\widetilde{\mathcal{S}}(t_m,\tau) = -\left(\frac{\kappa}{2}\right)^2\widetilde{\mathcal{S}}(t_m,\tau) - \frac{\kappa}{2}\frac{\partial}{\partial t_m}\widetilde{\mathcal{S}}(t_m,\tau) + v_0^2 \mathrm{e}^{i\varpi\tau} + g^2\widetilde{F}(t_m,\tau), \tag{4.90}$$

where $F(t,t')$ is the spectral function of the qubit

$$F(t,t') = \langle\sigma_{10}(t)\sigma_{01}(t')\rangle, \qquad \widetilde{F}(t_m,\tau) = \langle\tilde{\sigma}_{10}(t_m+\tau/2)\tilde{\sigma}_{01}(t_m-\tau/2)\rangle. \tag{4.91}$$

At first order in the coupling constant $g$, $\widetilde{F}(t_m,\tau)$ satisfies the differential equation

$$\left(\frac{1}{4}\frac{\partial^2}{\partial t_m^2} - \frac{\partial^2}{\partial \tau^2}\right)\widetilde{F}(t_m,\tau) = -\left(\frac{\Gamma}{2}\right)^2\widetilde{F}(t_m,\tau) - \frac{\Gamma}{2}\frac{\partial}{\partial t_m}\widetilde{F}(t_m,\tau). \tag{4.92}$$

Without pumping, the spectral function depends only on the time difference $\tau$. If $v_0 \neq 0$, we see with Eqs. (4.90) and (4.92) that in the RWA the perturbation depends only on $\tau$. Therefore we can neglect the $t_m$ dependence. This is also motivated by the fact that we are interested in the steady state solution $t_m$ large, where derivatives with respect to $t_m$ vanish. Defining $\bar{\mathcal{S}}(\tau) = \widetilde{\mathcal{S}}(\tau, t_m \gg 1)$ and $\bar{F}(\tau) = \widetilde{F}(\tau, t_m \gg 1)$, we get the coupled differential equations

$$\bar{\mathcal{S}}''(\tau) - \left(\frac{\kappa}{2}\right)^2\bar{\mathcal{S}}(\tau) = -g^2\bar{F}(\tau) - v_0^2\mathrm{e}^{i\varpi\tau}, \tag{4.93}$$

$$\bar{F}''(\tau) - \left(\frac{\Gamma}{2}\right)^2\bar{F}(\tau) = 0, \tag{4.94}$$

the solution of which is

$$\bar{\mathcal{S}}(\tau) = \left(\langle N\rangle(t_{\mathrm{SS}}) - \frac{v_0^2}{\varpi^2+(\kappa/2)^2} + \frac{4g^2\langle\sigma_1\rangle(t_{\mathrm{SS}})}{\Gamma^2-\kappa^2}\right)\mathrm{e}^{-\kappa|\tau|/2} + \frac{v_0^2}{\varpi^2+\kappa^2}\mathrm{e}^{i\varpi\tau} - \frac{4g^2\langle\sigma_1\rangle(t_{\mathrm{SS}})}{\Gamma^2-\kappa^2}\mathrm{e}^{-\Gamma|\tau|/2}. \tag{4.95}$$

The Fourier transform finally reads

$$\tilde{\mathcal{S}}(\omega_0+\omega) = \left(\langle N\rangle(t_{\mathrm{SS}}) - \frac{v_0^2}{\varpi^2+(\kappa/2)^2} + \frac{4g^2\langle\sigma_1\rangle(t_{\mathrm{SS}})}{\Gamma^2-\kappa^2}\right)\frac{\kappa}{\omega^2+(\kappa/2)^2}$$
$$+\,2\pi\frac{v_0^2}{\varpi^2+(\kappa/2)^2}\delta(\omega-\varpi) - \frac{4g^2\langle\sigma_1\rangle(t_{\mathrm{SS}})}{\Gamma^2-\kappa^2}\frac{\Gamma}{\omega^2+(\Gamma/2)^2}. \qquad (4.96)$$

The integral is equal to the photon number in the steady state: $\frac{1}{2\pi}\int_{\mathbb{R}} \mathrm{d}\omega\mathcal{S}(\omega_0+\omega) = \langle N\rangle(t_{\mathrm{SS}})$.
Let us consider the case of very low coupling, setting $g$ to zero:

$$\mathcal{S}(\omega_0+\omega) \simeq N_0\frac{\kappa}{\omega^2+(\kappa/2)^2} + 2\pi N_P\delta(\omega-\varpi). \qquad (4.97)$$

- If $v_0 = 0$, the spectral function is a Lorentzian centered around $\omega_0$.
- If $v_0 \neq 0$, the Lorentzian is reduced and a Dirac peak appears at the driving frequency. This transformation conserves the area.

The Dirac peak becomes a Lorentzian if the sinusoidal pumping has a small exponential decay. The experimental linewidth is equal to 100 kHz.

On Fig. 4.9 we plot the output spectrum resulting from our quantum treatment as a function of the pumping strength $v_0$. As $v_0$ increases from zero, the spectrum becomes more and more peaked around the driving frequency. The experimental measurement of the spectral function shows a sharp reduction of the width. This is due to the presence of charge noise which widens a lot the Lorentzian in the absence of driving. Fig. 4.10 represents the spectrum for a weak driving $v_0 = \tilde{\kappa}/10$ and another one for a strong driving $v_0 = \tilde{\kappa}/2$ to point out the shrinking of the Lorentzian. This is the signature of phase locking, as observed in experiment [99].

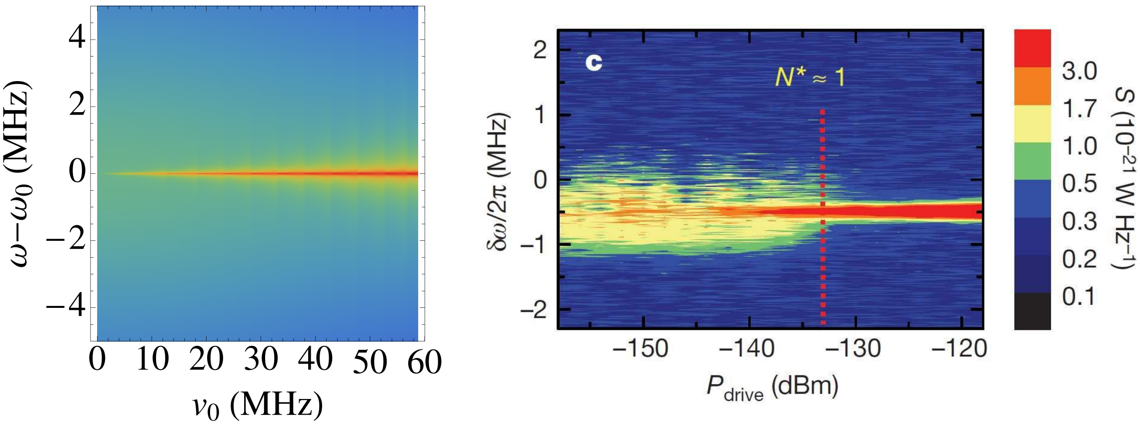

Figure 4.9: Output spectrum in the presence of a driving field on the cavity as a function of the driving strength $v_0$. Our numerical simulation, on the left with $\tilde{\kappa}$, is compared to the result of Ref. [99], on the right.

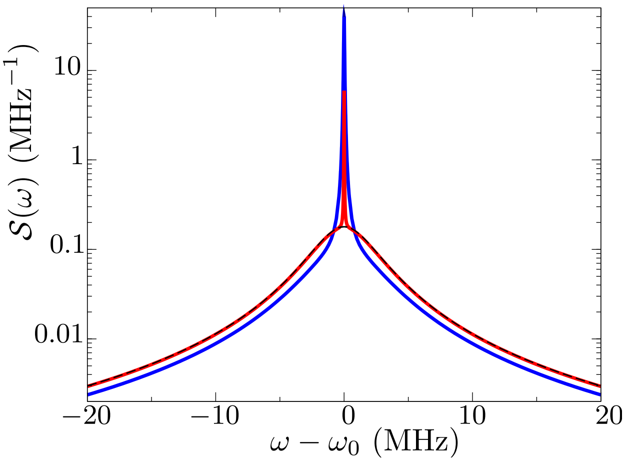

Figure 4.10: Spectra (logarithmic scale) in the presence of a driving field on the cavity obtained from the steady-state density matrix for a driving strength $v_0 = \tilde{\kappa}/10$ in red and $v_0 = \tilde{\kappa}/2$ in blue. The dashed line represents the spectrum without driving. The presence of the driving field induces phase locking which reduces the width of the spectrum.

## 4.3 Circuit QED: transmon coupled to two cavities

The recent developments in the field of circuit quantum electrodynamics (circuit QED) are based on the transmon (transmission-line shunted plasma oscillation qubit), a Cooper pair box with a large Josephson energy compared to the charging energy [110–113]. The most interesting characteristic of the transmon is to be almost insensitive to charge fluctuations in the island, conferring it long coherence times. In this section we study the lasing effect of a transmon coupled to two cavities. The transmon is pumped coherently with a microwave and the first cavity has a high quality factor. The second cavity is coupled to the transition $|2\rangle \to |1\rangle$ and has a low quality factor. This cavity contains a very small photon number compare to unity and, according to the Purcell effect, induces an effective relaxation rate $\gamma_{21}$. With this configuration the relaxation rate is controlled by the parameters of the cavity. The goal of this project is to find a configuration that optimize the lasing effect.

### 4.3.1 Circuit theory

We consider the voltage-biased circuit shown in Fig. 4.11 composed of a qubit and two cavities. The qubit is a transmon. It contains a large capacitor $C_0$ with a large charge $Q_0$ such that the ratio $Q_0/C_0 \equiv V_0$ is fixed. This constitutes the voltage bias. The transmon is modeled with a Josephson junction (flux-tunable Josephson energy $E_J$, critical current $I_J = 2eE_J/\hbar$) in parallel with a capacitance $C_B$. This junction is surrounded in parallel by two $L$-$C$ circuits ($L_1$-$C_1$ and $L_2$-$C_2$) with coupling capacitances $C_{g_1}$ and $C_{g_2}$, respectively. The two $L$-$C$ circuits play the role of the resonant cavities. These three elements are linked to the voltage bias through the gate capacitance $C_g$. According to Devoret's circuit theory [114], we choose a ground node (bottom) and four active nodes with phases $\varphi_0$, $\varphi_1$, $\varphi_2$ and $\varphi_B$. Phases are expressed in terms of the reduced flux quantum $\phi_0 = \hbar/2e$. These nodes are connected by the spanning tree (in red on the figure), which we choose to contain the capacitances. Notations for positive orientation are drawn on the circuit. Applying first Faraday's law for magnetic flux conservation and

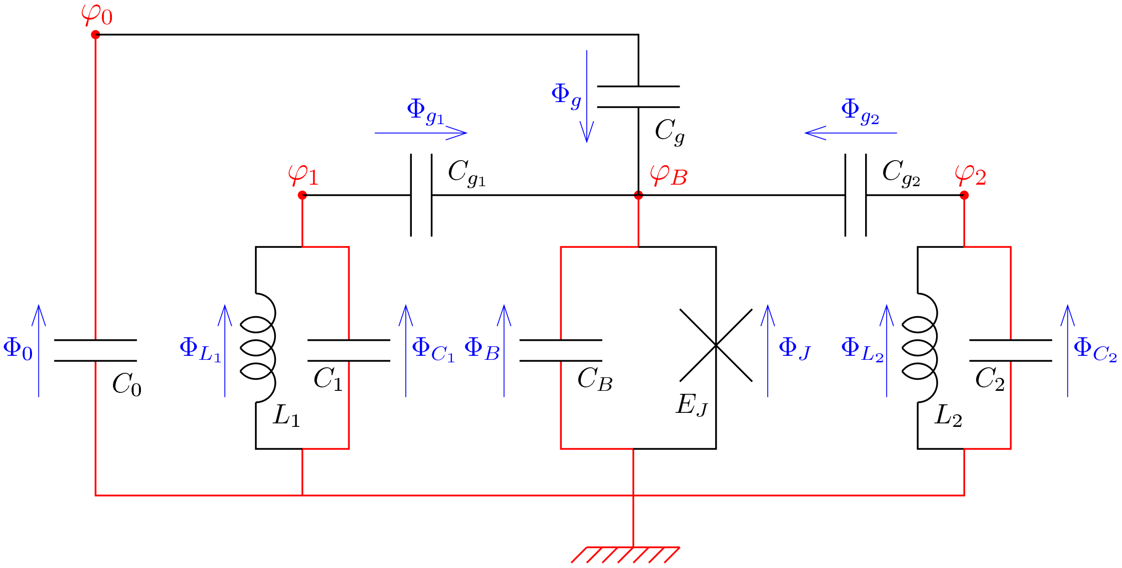

Figure 4.11: Circuit of a transmon coupled to two cavities

then Kirchhoff's law for current conservation we get two sets of equations, respectively

$$\begin{cases} \phi_0\varphi_0 = \Phi_0 \\ \phi_0\varphi_1 = \Phi_{L_1} = \Phi_{C_1} \\ \phi_0\varphi_2 = \Phi_{L_2} = \Phi_{C_2} \\ \phi_0\varphi_B = \Phi_B = \Phi_J \\ \Phi_B = \Phi_{C_1} + \Phi_{g_1} = \Phi_{C_2} + \Phi_{g_2} = \Phi_0 + \Phi_g \end{cases} , \tag{4.98}$$

and,

$$\begin{cases} C_0\ddot{\Phi}_0 = C_g\ddot{\Phi}_g \\ C_{g_1}\ddot{\Phi}_{g_1} = C_1\ddot{\Phi}_{C_1} + \Phi_{L_1}/L_1 \\ C_{g_2}\ddot{\Phi}_{g_2} = C_2\ddot{\Phi}_{C_2} + \Phi_{L_2}/L_2 \\ C_g\ddot{\Phi}_g + C_{g_1}\ddot{\Phi}_{g_1} + C_{g_2}\ddot{\Phi}_{g_2} + C_B\ddot{\Phi}_B + I_J\sin\Phi_J = 0 \end{cases} . \tag{4.99}$$

This leads to four dynamical equations for the four variables $\varphi_0$, $\varphi_1$, $\varphi_2$ and $\varphi_B$

$$\begin{aligned} \tilde{C}_0\ddot{\varphi}_0 - C_g\ddot{\varphi}_B &= 0, \\ \tilde{C}_1\ddot{\varphi}_1 - C_{g_1}\ddot{\varphi}_B &= -\varphi_1/L_1, \\ \tilde{C}_2\ddot{\varphi}_2 - C_{g_2}\ddot{\varphi}_B &= -\varphi_2/L_2, \\ \tilde{C}_B\ddot{\varphi}_B - C_g\ddot{\varphi}_0 - C_{g_1}\ddot{\varphi}_1 - C_{g_2}\ddot{\varphi}_2 &= -\phi_0^{-1}I_J\sin\varphi_B. \end{aligned} \tag{4.100}$$

where we define $\tilde{C}_0 = C_0 + C_g$, $\tilde{C}_1 = C_1 + C_{g_1}$, $\tilde{C}_2 = C_2 + C_{g_2}$ and, $\tilde{C}_B = C_B + C_g + C_{g_1} + C_{g_2}$.

This set of equations corresponds to the equations of motion $\dfrac{\partial\mathcal{L}}{\varphi_i} = \dfrac{\mathrm{d}}{\mathrm{d}t}\left(\dfrac{\partial\mathcal{L}}{\partial\dot{\varphi}_i}\right)$ of the Lagrangian

$$\begin{aligned} \phi_0^{-2}\mathcal{L} = \frac{1}{2}\tilde{C}_0\dot{\varphi}_0^2 + \frac{1}{2}\tilde{C}_1\dot{\varphi}_1^2 + \frac{1}{2}\tilde{C}_2\dot{\varphi}_2^2 + \frac{1}{2}\tilde{C}_B\dot{\varphi}_B^2 - C_g\dot{\varphi}_0\dot{\varphi}_B - C_{g_1}\dot{\varphi}_1\dot{\varphi}_B - C_{g_2}\dot{\varphi}_2\dot{\varphi}_B \\ - \left(\frac{\varphi_1^2}{2L_1} + \frac{\varphi_2^2}{2L_2} - \phi_0^{-2}E_J\cos\varphi_B\right). \end{aligned} \tag{4.101}$$

It is then possible to find the conjugate charges $Q_0$, $Q_1$, $Q_2$ and $Q_B$ using the relation $Q_i = \phi_0^{-1}\frac{\partial\mathcal{L}}{\partial\dot{\varphi}_i}$: $\phi_0 Q_0 = \tilde{C}_0\dot{\varphi}_0 - C_g\dot{\varphi}_B$, $\phi_0 Q_1 = \tilde{C}_1\dot{\varphi}_1 - C_{g_1}\dot{\varphi}_B$, $\phi_0 Q_2 = \tilde{C}_2\dot{\varphi}_2 - C_{g_2}\dot{\varphi}_B$ and, $\phi_0 Q_B = \tilde{C}_B\dot{\varphi}_B - C_g\dot{\varphi}_0 - C_{g_1}\dot{\varphi}_1 - C_{g_2}\dot{\varphi}_2$.

Taking the limit $C_0 \to \infty$ and $Q_0 \to \infty$ with $Q_0/C_0 \to V_0$, we get

$$\phi_0\dot{\varphi}_0 = V_0, \tag{4.102}$$

$$\phi_0\dot{\varphi}_1 = \frac{C_{g_1}}{\tilde{C}_1}\frac{1}{\tilde{C}_B - \frac{C_{g_1}^2}{\tilde{C}_1} - \frac{C_{g_2}^2}{\tilde{C}_2}}\left(Q_B + C_gV_0 + \frac{C_{g_2}}{\tilde{C}_2}Q_2 + \frac{\tilde{C}_B - \frac{C_{g_2}^2}{\tilde{C}_2}}{C_{g_1}}Q_1\right), \tag{4.103}$$

$$\phi_0\dot{\varphi}_2 = \frac{C_{g_2}}{\tilde{C}_2}\frac{1}{\tilde{C}_B - \frac{C_{g_1}^2}{\tilde{C}_1} - \frac{C_{g_2}^2}{\tilde{C}_2}}\left(Q_B + C_gV_0 + \frac{C_{g_1}}{\tilde{C}_1}Q_1 + \frac{\tilde{C}_B - \frac{C_{g_1}^2}{\tilde{C}_1}}{C_{g_2}}Q_2\right), \tag{4.104}$$

$$\phi_0\dot{\varphi}_B = \frac{1}{\tilde{C}_B - \frac{C_{g_1}^2}{\tilde{C}_1} - \frac{C_{g_2}^2}{\tilde{C}_2}}\left(Q_B + C_gV_0 + \frac{C_{g_1}}{\tilde{C}_1}Q_1 + \frac{C_{g_2}}{\tilde{C}_2}Q_2\right). \tag{4.105}$$

The resulting Hamiltonian $\mathcal{H} = \phi_0\dot{\varphi}_0 Q_0 + \phi_0\dot{\varphi}_1 Q_1 + \phi_0\dot{\varphi}_2 Q_2 + \phi_0\dot{\varphi}_B Q_B - \mathcal{L}$ can be written in terms of the Hamiltonian of the qubit $\mathcal{H}_{\mathrm{QB}}$, the Hamiltonian $\mathcal{H}_{\mathrm{C}_\alpha}$ of the cavity $\alpha = 1, 2$, the coupling Hamiltonian between the qubit and the cavities $\mathcal{H}_{\mathrm{QB-C}_\alpha}$ and the coupling Hamiltonian between the two cavities $\mathcal{H}_{\mathrm{C}_1-\mathrm{C}_2}$ as follows

$$\mathcal{H} = \mathcal{H}_{\mathrm{QB}} + \mathcal{H}_{\mathrm{C}_1} + \mathcal{H}_{\mathrm{C}_2} + \mathcal{H}_{\mathrm{QB-C}_1} + \mathcal{H}_{\mathrm{QB-C}_2} + \mathcal{H}_{\mathrm{C}_1-\mathrm{C}_2}, \tag{4.106}$$

$$\mathcal{H}_{\mathrm{QB}} = \frac{(Q_B + C_g V_0)^2}{2\bar{C}_B} - E_J \cos\varphi_B, \tag{4.107}$$

$$\mathcal{H}_{\mathrm{C}_\alpha} = \frac{Q_\alpha^2}{2\bar{C}_\alpha} + \frac{\varphi_\alpha^2}{2L_\alpha}, \tag{4.108}$$

$$\mathcal{H}_{\mathrm{QB-C}_\alpha} = \frac{(Q_B + C_g V_0)\, Q_\alpha}{C_{Q\alpha}}, \tag{4.109}$$

$$\mathcal{H}_{\mathrm{C}_1-\mathrm{C}_2} = \frac{Q_1 Q_2}{C_{12}}, \tag{4.110}$$

where $\bar{C}_B = \tilde{C}_B - C_{g_1}^2/\tilde{C}_1 - C_{g_2}^2/\tilde{C}_2$, $\bar{C}_\alpha^{-1} = \tilde{C}_\alpha^{-1} + C_{g_\alpha}^2/(\tilde{C}_\alpha^2(\tilde{C}_B - C_{g_1}^2/\tilde{C}_1 - C_{g_2}^2/\tilde{C}_2))$, $C_{Q\alpha} = C_{g_\alpha}/(\tilde{C}_\alpha(\tilde{C}_B - C_{g_1}^2/\tilde{C}_1 - C_{g_2}^2/\tilde{C}_2))$ and, $C_{12} = C_{g_1}C_{g_2}/(\tilde{C}_1\tilde{C}_2(\tilde{C}_B - C_{g_1}^2/\tilde{C}_1 - C_{g_2}^2/\tilde{C}_2))$.

### 4.3.2 Quantization

We turn now to the second quantization form of the Hamiltonian (4.106) of the circuit.

#### 4.3.2.a Transmon

The Hamiltonian of the qubit is the Cooper pair box Hamiltonian

$$\mathcal{H}_{\mathrm{QB}} = 4E_C(N + n_g)^2 - E_J \cos\varphi_B, \tag{4.111}$$

where we define the reduced charge $N = Q_B/2e$, the charge offset $n_g = C_g V_0/2e$ and the charging energy $E_C = e^2/2\bar{C}_B$. To reduce the charge noise, the qubit is tuned in the transmon configuration, that is to say in the regime $E_J \gg E_C$ [110–112]. The charge dispersion reducing exponentially in $E_J/E_C$, while the anharmonicity decreases algebraically, it is possible to decrease the charge noise sensitivity while sacrifying a small amount of anharmonicity. In practice, the qubit can become insensitive to charge. Due to these interesting properties, the transmon qubit is currently used as the main building block in circuit QED [113].

The energy spectrum can be obtained exactly in terms of Mathieu's functions. Indeed, the stationary Schrödinger equation corresponding to the qubit Hamiltonian $\mathcal{H}_{\mathrm{QB}}$

$$\Big[4E_C\,(-i\partial_\varphi - n_g)^2 - E_J \cos\varphi\Big]\,\psi(\varphi) = \varepsilon\psi(\varphi), \tag{4.112}$$

can be solved exactly in terms of Mathieu's characteristic value

$$\varepsilon_k(n_g) = E_C\, a_{2(n_g+k)}(-1/4\lambda^2), \tag{4.113}$$

where $\lambda = E_C/\hbar\omega_p$.

In the limit $E_J \gg E_C$, the energy levels and the eigenfunctions can be well approximated with a first order perturbation theory in $\lambda$. In this limit, the phase is well defined at a minimum of the potential energy. The potential term can then be Taylor expanded, up to fourth order, around $\varphi_B = 0$. The transmon behaves like a perturbed harmonic

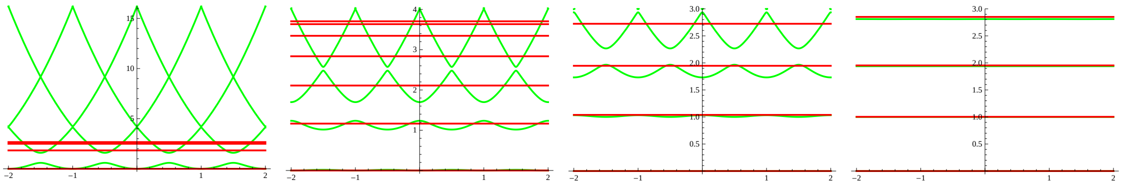

Figure 4.12: Exact spectrum $\varepsilon(n_g)$ (green) compared to the first order perturbation theory result (red) in units of the transition energy $\varepsilon_1(0.5) - \varepsilon_0(0.5)$. From left to right, $E_J/E_C = 1,\ 5,\ 10,\ 50$.

oscillator in a quartic potential with a plasma frequency $\omega_p = \sqrt{8E_C E_J}/\hbar$. Defining the bosonic canonical annihilation operator $b = \sqrt{\lambda}\left(\varphi_B + i\sqrt{2}N\right)$, we get

$$\mathcal{H}_{\mathrm{QB}} = \hbar\omega_p\left(b^\dagger b + 1/2\right) - \frac{E_C}{12}\left(b + b^\dagger\right)^4. \tag{4.114}$$

Using a first order perturbation theory in $\lambda$ we find the energy levels

$$\varepsilon_n = \hbar\omega_p(n + 1/2) - \frac{E_C}{2}(n^2 + n + 1/2). \tag{4.115}$$

The parameter $\lambda$ corresponds to the anharmonicity of the qubit:

$$\varepsilon_n - \varepsilon_{n-1} = \hbar\omega_p(1 - n\lambda/2). \tag{4.116}$$

The comparison between the first order result Eq. (4.115) and the exact one Eq. (4.113) is plotted in Fig. 4.12. When the Josephson energy is much larger than the charging energy the spectrum of the lowest levels is $n_g$-independent, rendering the transmon insensitive to charge fluctuations.

Next we express the charge $Q_B$ on the basis of the the eigenstates of the qubit $|\psi_n\rangle$ (corresponding to the level $\varepsilon_n$)

$$\begin{aligned}|\psi_n\rangle = |n\rangle + \frac{\lambda}{24}\Big((2n+3)\sqrt{(n+1)(n+2)}\,|n+2\rangle - (2n-1)\sqrt{n(n-1)}\,|n-2\rangle \\ + \frac{1}{4}\sqrt{(n+1)(n+2)(n+3)(n+4)}\,|n+4\rangle - \frac{1}{4}\sqrt{n(n-1)(n-2)(n-3)}\,|n-4\rangle\Big),\end{aligned} \tag{4.117}$$

where $|n\rangle$ are the eigenstates of the unperturbed harmonic oscillator. In the momentum representation, the eigenvectors read

$$\begin{aligned}\langle\psi_n|N\rangle =& \frac{i^n}{\sqrt{2^n n!}}\left(\frac{4\lambda}{\pi}\right)^{\frac{1}{4}} \mathrm{e}^{-2\lambda N^2}\Big(\mathrm{H}_n(2\sqrt{\lambda}N) \\ &- \frac{\lambda}{48}(2n+3)\,\mathrm{H}_{n+2}(2\sqrt{\lambda}\,N) + \frac{\lambda}{12}n(n-1)(2n-1)\,\mathrm{H}_{n-2}(2\sqrt{\lambda}\,N) \\ &+ \frac{\lambda}{384}\,\mathrm{H}_{n+4}(2\sqrt{\lambda}\,N) - \frac{\lambda}{24}n(n-1)(n-2)(n-3)\,\mathrm{H}_{n-4}(2\sqrt{\lambda}\,N)\Big).\end{aligned} \tag{4.118}$$

The charge can then be expressed in terms of the raising and lowering operators of the qubit eigenstates

$$\sigma_{ij} = |\psi_i\rangle\langle\psi_j|, \tag{4.119}$$

as follows

$$N = \sum_{i,j=0}^{\infty} \eta_{ij}\, \sigma_{ij}, \qquad \eta_{ij} = \int_{-\infty}^{+\infty} \mathrm{d}N\, N\, \langle \psi_i | N \rangle\, \langle N | \psi_j \rangle. \tag{4.120}$$

Now we focus only on the first three levels. As a result, only $\eta_{01} = -i(1-\lambda/4)/\sqrt{8\lambda} = -\eta_{10}$ and $\eta_{12} = -i(1-\lambda/4)/2\sqrt{\lambda} = -\eta_{21}$ are taken into account:

$$\frac{Q_B}{2e} = -\frac{i}{\sqrt{8\lambda}} \left[(1-\lambda/4)(\sigma_{01}-\sigma_{10}) + \sqrt{2}\,(1-\lambda/2)(\sigma_{12}-\sigma_{21})\right]. \tag{4.121}$$

At lowest order $\eta_{12} = \sqrt{2}\,\eta_{01}$.

### 4.3.2.b Cavities

Introducing the two energies $E_{C\alpha} = e^2/2\bar{C}_\alpha$ and $E_{L\alpha} = \phi_0^2/2L_\alpha$, the Hamiltonian of the cavities reads

$$\mathcal{H}_{\mathrm{C}_\alpha} = 4E_{C\alpha}\left(\frac{Q_\alpha}{2e}\right)^2 + E_{L\alpha}\varphi_\alpha^2. \tag{4.122}$$

Defining the characteristic frequency $\omega_\alpha = 1/\sqrt{L_\alpha \bar{C}_\alpha} = 4\sqrt{E_{C\alpha}E_{L\alpha}}/\hbar$, and using the creation and annihilation operators $a_\alpha$ and $a_\alpha^\dagger$ of the cavities

$$\varphi_\alpha = 2i\sqrt{\frac{E_{C\alpha}}{\hbar\omega_\alpha}}(a_\alpha^\dagger - a_\alpha), \qquad Q_\alpha = -2e\sqrt{\frac{E_{L\alpha}}{\hbar\omega_\alpha}}(a_\alpha^\dagger + a_\alpha), \qquad \left[a_\alpha, a_\alpha^\dagger\right] = 1, \tag{4.123}$$

the Hamiltonian reads

$$\mathcal{H}_{\mathrm{C}_\alpha} = \hbar\omega_\alpha\left(a_\alpha^\dagger a_\alpha + \frac{1}{2}\right). \tag{4.124}$$

### 4.3.2.c Coupling terms

The coupling Hamiltonian between the qubit and the cavity is proportional to $Q_B Q_\alpha$, which gives rise to couplings between operators $\sigma_{ij}$ and $a_\alpha^{(\dagger)}$. In the RWA, we keep only couplings between a qubit lowering operator and a cavity creation operator or a qubit raising operator with a cavity annihilation operator. This leads to four coupling energies

$$\mathcal{H}_{\mathrm{QB-C}_\alpha} = i\hbar g_{1\alpha}(\sigma_{01}b_\alpha^\dagger - \sigma_{10}b_\alpha) + i\hbar g_{2\alpha}(\sigma_{12}b_\alpha^\dagger - \sigma_{21}b_\alpha), \tag{4.125}$$

where

$$\hbar g_{1\alpha} = \sqrt{2}\,\frac{1-\lambda/4}{\sqrt{\lambda}}\,\frac{e^2}{C_{Q\alpha}}\sqrt{\frac{E_{L\alpha}}{\hbar\omega_\alpha}}, \tag{4.126}$$

$$\hbar g_{2\alpha} = 2\,\frac{1-\lambda/2}{\sqrt{\lambda}}\,\frac{e^2}{C_{Q\alpha}}\sqrt{\frac{E_{L\alpha}}{\hbar\omega_\alpha}}. \tag{4.127}$$

If the qubit is sufficiently anharmonic ($\lambda$ not too small) and if the cavity $\alpha$ is in resonance with the transition $|\alpha\rangle - |\alpha-1\rangle$, the detuning will reduce the effective couplings $g_{12}$ and $g_{21}$.

The coupling Hamiltonian between the cavities reads

$$\mathcal{H}_{\mathrm{C}_1-\mathrm{C}_2} = \hbar g_{1-2}(a_1^\dagger + a_1)(a_2^\dagger + a_2), \qquad \hbar g_{1-2} = \frac{4e^2}{C_{12}}\sqrt{\frac{E_{L1}}{\hbar\omega_1}\frac{E_{L2}}{\hbar\omega_2}}. \tag{4.128}$$

This coupling term being small, it will not be taken into account in the following.

### 4.3.2.d Pumping

The qubit is pumped coherently from the state $|0\rangle$ to the state $|2\rangle$ with a microwave of amplitude $V$ and frequency $\Omega$ in resonance with the transition $|0\rangle - |2\rangle$

$$\mathcal{H}_P = V\sin(\Omega t)(\sigma_{02} + \sigma_{20}). \tag{4.129}$$

In the RWA, this Hamiltonian is reduced to

$$\mathcal{H}_P = i\hbar E(\sigma_{02}\,\mathrm{e}^{i\Omega t} - \sigma_{20}\,\mathrm{e}^{-i\Omega t}), \tag{4.130}$$

where $E = -V/2\hbar$.

### 4.3.2.e Lindbladian

The Hamiltonian $\mathcal{H}$ of the system can be separated in two parts, first the Hamiltonian of the isolated qubit and the isolated cavities $\mathcal{H}_0$ and second the coupling Hamiltonian and the coherent pumping Hamiltonian $\mathcal{H}_1$,

$$\mathcal{H}_0 = \sum_{j=0}^{2}\varepsilon_j\sigma_j + \sum_{\alpha=1}^{2}\hbar\omega_\alpha a_\alpha^\dagger a_\alpha, \tag{4.131}$$

$$\mathcal{H}_1 = \sum_{j=1}^{2}\sum_{\alpha=1}^{2} i\hbar g_{j\alpha}(\sigma_{j-1,j}a_\alpha^\dagger - \sigma_{j,j-1}a_\alpha) + i\hbar E(\sigma_{02}\,\mathrm{e}^{i\Omega t} - \sigma_{20}\,\mathrm{e}^{-i\Omega t}). \tag{4.132}$$

In the interaction picture relative to $\mathcal{H}_0$, the Hamiltonian $\tilde{\mathcal{H}}_1$ reads

$$\tilde{\mathcal{H}}_1 = \sum_{j=1}^{2}\sum_{\alpha=1}^{2} i\hbar g_{j\alpha}\left(\sigma_{j-1,j}a_\alpha^\dagger\,\mathrm{e}^{-i\Delta_{j\alpha}} - \sigma_{j,j-1}a_\alpha\,\mathrm{e}^{i\Delta_{j\alpha}}\right) + i\hbar E(\sigma_{02}\,\mathrm{e}^{-i\Delta_P} - \sigma_{20}\,\mathrm{e}^{i\Delta_P}), \tag{4.133}$$

where we define the detunings between the qubit levels and the cavity modes

$$\forall(j,\alpha)\in\{1,2\}^2 \qquad \Delta_{j\alpha} = \omega_{j,j-1} - \omega_\alpha. \tag{4.134}$$

as well as between the qubit transition $|0\rangle - |2\rangle$ and the pumping $\Delta_P = \omega_{20} - \Omega$ (the latter will be set to zero in the following).

The dynamics of the system is also affected by the incoherent processes of the qubit level relaxation and the losses in the cavity. We take into account the non-radiative relaxation $\gamma_{10}$ from the level $|1\rangle$ to the level $|0\rangle$, and the damping $\kappa_\alpha$ in the cavities. The corresponding Lindbladian reads

$$\mathrm{L}\rho = \sum_{\alpha=1}^{2}\frac{\kappa_\alpha}{2}\left(2a_\alpha\rho a_\alpha^\dagger - a_\alpha^\dagger a_\alpha\rho - \rho a_\alpha^\dagger a_\alpha\right) + \frac{\gamma_{10}}{2}\left(2\sigma_{01}\rho\sigma_{10} - \sigma_1\rho - \rho\sigma_1\right). \tag{4.135}$$

The second cavity will be eliminated in the next subsection.

### 4.3.3 The Purcell effect

The second cavity has a low quality factor and plays the role of controllable relaxation rate $\gamma_{21}^{\text{eff}}$ for the transition $|2\rangle - |1\rangle$ (and also a relaxation rate $\gamma_{10}^{\text{eff}}$ for the detuned transition $|1\rangle - |0\rangle$). The photon number in this cavity remains small compared to unity. It is possible to express the effective relaxation rate in terms of the frequency $\omega_2$ of the cavity and its damping rate $\kappa_2$ within the approach of Ref. [115].

We consider first the situation where the transition $|2\rangle - |1\rangle$ is coupled resonantly to the second cavity in the absence of pumping. The photon number $N_2$ being small, we take into account the states $|2, n_1, 0\rangle$ and $|1, n_1, 1\rangle$. For integers $(k, l) \in \{0, 1\}^2$, we note $\varrho_{kl}(t) = \text{Tr}_{C_1}\{\langle 2 - k, n_1, k|\tilde{\rho}(t)|2 - l, n_1, l\rangle\}$. The evolution equation for the matrix elements $\mathcal{R}(t) = \begin{pmatrix} \varrho_{00}(t) \\ \varrho_{10}(t) + \varrho_{01}(t) \\ \varrho_{11}(t) \end{pmatrix}$ is then

$$\dot{\mathcal{R}}(t) = \begin{pmatrix} 0 & -g_{22} & 0 \\ 2g_{22} & -\kappa_2/2 & -2g_{22} \\ 0 & g_{22} & -\kappa_2 \end{pmatrix} \cdot \mathcal{R}(t). \tag{4.136}$$

If $\kappa_2 > 4g_{22}$, the eigenvalues of this system are real and negative. The effective relaxation time corresponds to the minimum of their absolute value, namely

$$\gamma_{21}^{\text{eff}} = \frac{\kappa_2}{2} - \frac{1}{2}\sqrt{\kappa_2^2 - 16g_{22}^2} \simeq \frac{4g_{22}^2}{\kappa_2^2} \qquad \text{if } k_2 \gg g_{22}. \tag{4.137}$$

The result $\gamma_{21}^{\text{eff}} \simeq 4g_{22}^2/\kappa_2^2$ constitutes the Purcell effect: a cavity of low quality coupled to a two-level system is equivalent to a relaxation rate for the two-level transition.

The transition $|1\rangle - |0\rangle$ is also coupled to the cavity $C_2$ through the coupling energy $\hbar g_{12}$ and the detuning $\Delta_{12}$. The cavity $C_2$ induce also a non-radiative relaxation for this transition. To calculate this relaxation rate $\gamma_{10}^{\text{eff}}$, we proceed as before with the states $|1, n_1, 0\rangle$ and $|0, n_1, 1\rangle$ and the matrix elements $\varrho_{kl}(t) = \text{Tr}_{C_1}\{\langle 1 - k, n_1, k|\tilde{\rho}(t)|1 - l, n_1, l\rangle\}$ ($(k, l) \in \{0, 1\}^2$). The matrix elements involved in the dynamics are $\mathcal{R}(t) = \begin{pmatrix} \varrho_{00}(t) \\ \varrho_{10}(t)\,\mathrm{e}^{i\Delta_{12}t} + \varrho_{01}(t)\,\mathrm{e}^{-i\Delta_{12}t} \\ i\left(\varrho_{10}(t)\,\mathrm{e}^{i\Delta_{12}t} - \varrho_{01}(t)\,\mathrm{e}^{-i\Delta_{12}t}\right) \\ \varrho_{11}(t) \end{pmatrix}$ and the system becomes

$$\dot{\mathcal{R}}(t) = \begin{pmatrix} 0 & -g_{12} & 0 & 0 \\ 2g_{12} & -\frac{\kappa_2}{2} & \Delta_{12} & -2g_{12} \\ 0 & -\Delta_{12} & -\frac{\kappa_2}{2} - \Delta_{12} & 0 \\ 0 & g_{12} & 0 & -\kappa_2 \end{pmatrix} \cdot \mathcal{R}(t). \tag{4.138}$$

The effective rate then reads

$$\gamma_{10}^{\text{eff}} \simeq \frac{g_{12}^2\kappa_2}{\Delta_{12}^2 + (\kappa_2/2)^2}. \tag{4.139}$$

The second cavity can now be replaced by the effective relaxation rates $\gamma_{21}^{\text{eff}}$ and $\gamma_{10}^{\text{eff}}$.

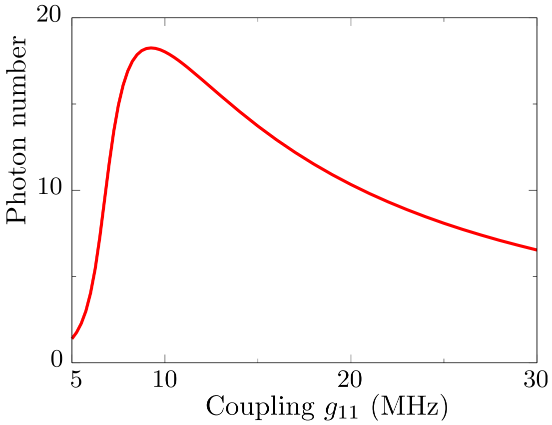

Figure 4.13: Photon number as a function of the coupling $g_{11}$. The maximum is found around $g_{11} = 10\,\mathrm{MHz}$.

## 4.3.4 Effective system

### 4.3.4.a Experimental parameters

The effective system resulting from removing the second cavity is a coherently-pumped three-level system $\{|\psi_0\rangle, |\psi_1\rangle, |\psi_2\rangle\}$ with a coupling between a high quality cavity and the transitions $|\psi_1\rangle \rightarrow |\psi_0\rangle$ and $|\psi_2\rangle \rightarrow |\psi_1\rangle$ (coupling $g_{11}$ and $g_{21}$) and with spontaneous relaxations (rates $\gamma_{21}^{\mathrm{eff}}$ and $\gamma_{10}^{\mathrm{eff}}$).

Experimentally speaking, the typical transition energies of the transmon are $\varepsilon_1 - \varepsilon_0 = h \times 7\,\mathrm{GHz}$ and $\varepsilon_2 - \varepsilon_1 = h \times 6.5\,\mathrm{GHz}$ with quality factors equal to $Q_1 = 60000$ for the high quality cavity (damping rate $\kappa_1 = 0.73\,\mathrm{MHz}$) and $Q_2 = 100$ for the second cavity. The coupling between the transmon and the second cavity is of the order of $g_{22} = 10\,\mathrm{MHz}$ and the transmon can be pumped with an amplitude $E/2\pi = 50\,\mathrm{MHz}$. These parameters give rise to the relaxation rate $\gamma_{21}^{\mathrm{eff}} = 43\,\mathrm{MHz}$ and a negligible rate $\gamma_{10}^{\mathrm{eff}}$. The maximum photon number is then found at $g_{11} \simeq 10\,\mathrm{MHz}$ from Fig. 4.13.

### 4.3.4.b Temporal dynamics

When the three-level system is “coherently closed”, that is to say when all transitions can occur with a coherent pumping or a coherent coupling with the cavity, every elements of the density matrix are perturbed. In opposition with the case of an incoherently pumped qubit, the density matrix is not block diagonal. It is then not possible to find a small closed set of matrix elements that generates the dynamics and the output spectrum. Numerical calculations are thus slower in this configuration. The temporal evolution of the photon number is shown in Fig. 4.14 for $g_{11} = 10\,\mathrm{MHz}$.

### 4.3.4.c Toy model

To evaluate the photon numbers and qubit populations with a simple model we consider an incoherent pumping $\Gamma = E/2\pi$. The resulting dynamical equation for the matrix elements $\langle i, n_1, n_2|\rho(t)|j, m_1, m_2\rangle$ can be simplified by taking into account only elements with zero or one photon imbalance between the bra and the ket. After tracing, the

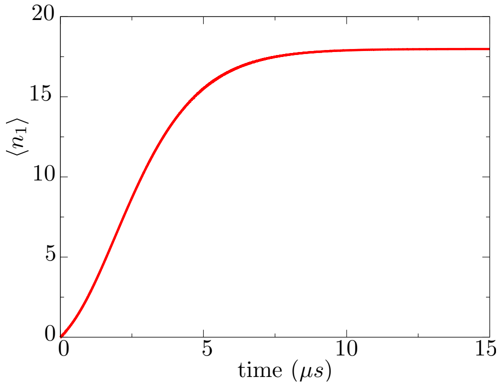

Figure 4.14: Time evolution of the photon number in the lasing cavity.

following equations for the qubit populations and photon numbers are found

$$\partial_t\langle\sigma_0\rangle = -\Gamma\langle\sigma_0\rangle + G_{11}(\langle n_1\rangle+1)\langle\sigma_1\rangle - G_{11}\langle n_1\rangle\langle\sigma_0\rangle + \gamma_{10}\langle\sigma_1\rangle, \tag{4.140}$$

$$\begin{aligned}\partial_t\langle\sigma_1\rangle =& \gamma_{21}^{\text{eff}}(\langle n_2\rangle+1)\langle\sigma_2\rangle - \gamma_{21}^{\text{eff}}\langle n_2\rangle\langle\sigma_1\rangle \\ & - G_{11}(\langle n_1\rangle+1)\langle\sigma_1\rangle + G_{11}\langle n_1\rangle\langle\sigma_0\rangle + G_{21}(\langle n_1\rangle+1)\langle\sigma_2\rangle - \gamma_{10}\langle\sigma_1\rangle,\end{aligned} \tag{4.141}$$

$$\partial_t\langle\sigma_2\rangle = \Gamma\langle\sigma_0\rangle - \gamma_{21}^{\text{eff}}(\langle n_2\rangle+1)\langle\sigma_2\rangle + \gamma_{21}^{\text{eff}}\langle n_2\rangle\langle\sigma_1\rangle - G_{21}(\langle n_1\rangle+1)\langle\sigma_2\rangle, \tag{4.142}$$

$$\partial_t\langle n_1\rangle = -\kappa_1\langle n_1\rangle + G_{11}(\langle n_1\rangle+1)\langle\sigma_1\rangle - G_{11}\langle n_1\rangle\langle\sigma_0\rangle + G_{21}(\langle n_1\rangle+1)\langle\sigma_2\rangle, \tag{4.143}$$

$$\partial_t\langle n_2\rangle = -\kappa_2\langle n_2\rangle + \gamma_{21}^{\text{eff}}(\langle n_2\rangle+1)\langle\sigma_2\rangle - \gamma_{21}^{\text{eff}}\langle n_2\rangle\langle\sigma_1\rangle, \tag{4.144}$$

where the parameters $G_{11}$ and $G_{21}$ are equal to

$$G_{11} = \frac{4g_{11}^2(\Gamma+\gamma_{10})}{(\Gamma+\gamma_{10})^2+4\Delta_{11}^2}, \qquad G_{21} = \frac{4g_{11}^2(\gamma_{21}^{\text{eff}}+\gamma_{10})}{(\gamma_{21}^{\text{eff}}+\gamma_{10})^2+4\Delta_{21}^2}. \tag{4.145}$$

This nonlinear set of differential equations can be solved numerically. The solution for the parameters of the previous subsection leads to $G_{11} = 304\,\text{MHz}$ and $G_{21} = 0.277\,\text{MHz}$. The temporal evolution of the photon number in each cavity are plotted in Fig. 4.15.

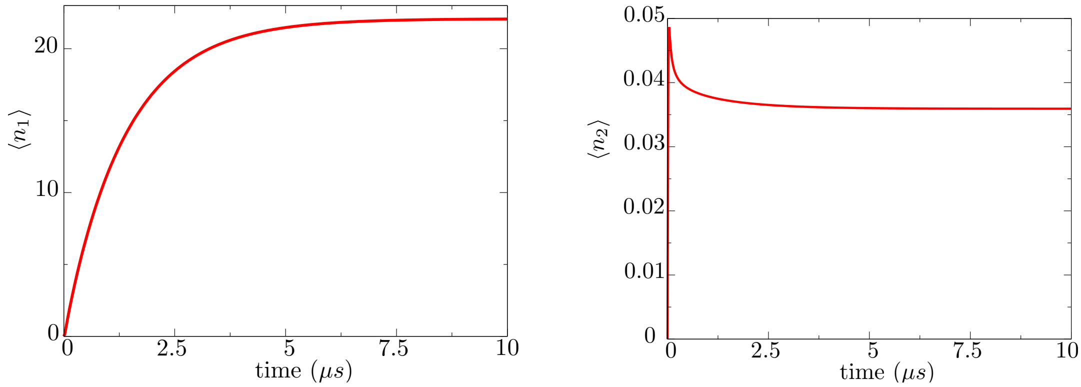

Figure 4.15: Temporal evolution of the photon number $\langle n_1\rangle$ in the cavity $C_1$ (*left*) and the photon number $\langle n_2\rangle$ cavity $C_2$ (*right*).

The steady state photon number in the cavity $C_1$ is equal to $\langle n_1\rangle = 22$, in good agreement with the solution from the density matrix. The photon number in the cavity $C_2$ is equal to $\langle n_2\rangle = 0.036$ much less than unity.

## Conclusion and perspectives

The Lindblad master equations and the quantum regression theorem are powerful tools to calculate quantum mechanically the time-evolution of the photon number and the output spectrum of the cavity. The comparison with the experimental results of Ref. [99] gives access to the typical time-scales of the system. The fully quantum treatment for a three level artificial atom, based on the density matrix of the whole system, enables us to understand the validity of the quasiclassical approximations, which do not take into account all the correlations between the qubit and the cavity. The analysis of two-photon process will help us to conclude on the nature of the double hot spots observed experimentally.

The study of the transmon coupled to two cavities ends up with a set of optimal parameters to observe the lasing effect. The Quantronics group of CEA Saclay will use them to set up a new experiment. We will carry on collaborating to analyse the experimental results.

# Effet laser avec un atome Josephson

## Résumé du chapitre

LORSQU'un qutrit est couplé à une cavité résonnante, il se produit un phénomène d'émission amplifiée et stimulée de photons, c'est-à-dire un effet laser. La fréquence étant de l'ordre du gigahertz, on parle de maser. Le qutrit se comporte comme un atome artificiel à trois niveaux, ce qui rend la description formellement analogue aux expériences d'optique quantique et a donné naissance au domaine de l'électrodynamique quantique des circuits. Nous avons considéré deux systèmes : l'un constitue la première observation de l'effet laser pour un qubit de charge, réalisé au laboratoire Riken de Tokyo, et est basé sur le cycle de quasiparticule Josephson. Le second tire partie des propriétés du transmon, lequel est utilisé comme qutrit et est couplé à deux cavités : une de facteur de qualité élevé qui lase et l'autre avec un temps de vie court qui permet de contrôler le taux de relaxation spontanée par l'effet Purcell. Ce circuit sera réalisé dans le groupe Quantronics du CEA Saclay. Nous utilisons l'équation maîtresse de Lindblad pour obtenir l'évolution de la matrice densité du système. Cette approche quantique donne accès à l'évolution temporelle des populations du qutrit et de la cavité ainsi que des corrélations entre les deux sous-systèmes. À l'aide du théorème de régression quantique nous dérivons aussi le spectre du champ laser généré. Ces résultats numériques sont aussi utilisés pour vérifier la validité des expressions analytiques obtenues dans l'approximation semi-classique.

Chapter 5

# The Josephson effect in a one-dimensional bosonic gas

**Contents**

## Introduction

This chapter is devoted to the study of a bosonic Josephson junction in a quasi-one-dimensional (quasi-1D) ring trap [116, 117]. This is one of the direction of the current experiments with ultracold atomic gases. To introduce the system, in a first part we present the experimental techniques to trap, cool down and probe Bose gases with laser beams and electromagnetic fields. We then focus more specifically on the quasi-1D geometry, and review the experimental advances. In the second part of the chapter, we present the theoretical approaches to deal with 1D bosons, namely the Luttinger liquid formalism for low energy properties and the exact Bose-Fermi mapping for the Tonks-Girardeau limit of infinitely repulsive contact interaction. In the last part of the chapter we concentrate on a 1D ring trap potential. The final aim is to study a Bose Josephson junction realized by superimposing a localized barrier on the ring. To this purpose, we study the equilibrium properties of the ring with the barrier and in particular the one- and two-body correlation functions and the momentum distribution. As the tunnel among the two sides of the barrier will be introduced as a perturbation, we consider first the case of an infinite barrier. We find a reduction in the effective Josephson coupling energy due to quantum fluctuations which depends on the length of the ring and on the interaction strength.

## 5.1 Trapping, cooling and probing atoms

With the rapid progress in producing Bose Einstein condensates in the last decade, it is possible to employ ultra-cold atoms in a large variety of setups (Bose Josephson junctions, boson-fermion mixtures, atoms in lattices, rotating condensates, effect of disorder…). However, in all experiments, the first step is to trap and cool atoms. Extremely clean alkali atoms may be produced by a chemical reaction at high temperature in an oven. Starting from a thermal gas ($\sim 800\,\mathrm{K}$, $700\,\mathrm{m.s}^{-1}$), alkali atoms are usually pre-cooled to $\sim 10\,\mu\mathrm{K}$ ($10\,\mathrm{cm.s}^{-1}$) with a laser, trapped by magnetic fields, and cooled down to $\sim 10-100\,\mathrm{nK}$ ($5\,\mathrm{mm.s}^{-1}$) with evaporative cooling. Probes are then necessary to observe the Bose gas and measure its properties. In this section we briefly present these experimental techniques in the case of a vapor of alkali atoms in three dimensions. A more detailed treatment can be found in Refs. [33, 34]. The application to one-dimensional quantum gases will be discussed in Sec. 5.3.

### 5.1.1 Influence of laser light on an atom

#### 5.1.1.a Radiation pressure

Let us consider two different electronic levels in an atom, namely $|1\rangle$ with energy $E_1$ and $|2\rangle$ with energy $E_2 > E_1$. The atom of mass $M$ is moving with the speed $\vec{v}$ in the reference frame of the laboratory. If the electron is initially in the excited state $|2\rangle$, it relaxes to the level $|1\rangle$ and emits a photon of frequency $h\nu_e$ and momentum $\vec{k}_e$. The lifetime of the excited state is $1-100\,\mathrm{ns}$ and the photon is emitted in a random direction. The energy and momentum conservation leads to [118]

$$h\nu_e = \hbar\omega_0 - E_{\mathrm{rec}} + \hbar\vec{k}_e \cdot \vec{v}, \tag{5.1}$$

with $\hbar\omega_0 = E_2 - E_1$ and where

$$E_{\mathrm{rec}} = \frac{\hbar^2 k_e^2}{2M}, \tag{5.2}$$

is the recoil energy due to the emission of the photon. The term $\hbar\vec{k}_e \cdot \vec{v}$ has its origin in the Doppler effect. Indeed, if one looks at the moving atom, the frequency of the emitted photon is higher when the atom comes in one's direction than when it moves away.
Symmetrically, if the electron is initially in the ground state $|1\rangle$, it can absorb a photon of frequency $h\nu_a$ and momentum $\vec{k}_a$, and jump to the level $|2\rangle$. To be absorbed, the photon frequency needs to satisfy

$$h\nu_a = \hbar\omega_0 + E_{\mathrm{rec}} + \hbar\vec{k}_a \cdot \vec{v}. \tag{5.3}$$

Now we irradiate the atom with a laser beam at the frequency $\nu_a$ above. The atom will absorb a photon $\vec{k}_a$, relax from the excited state and emit a photon $\vec{k}_e$, then absorb another photon $\vec{k}_a$, emit a photon $\vec{k}'_e$ and so on…The atom performs the cycle of absorption-emission at a high frequency, basically at $\tau^{-1} \sim 100\,\mathrm{MHz}$. Because photons are generated by a laser, they all have the same momentum $\vec{k}_a$. In particular, they all have the same direction whereas the emitted photons have the same probability to have the momentum $\vec{k}_e$ and the opposite one $-\vec{k}_e$. During a time $t$, $t/\tau$ cycles occur and the atoms gain the momentum $t\tau^{-1}\hbar\vec{k}$, equivalent to the so-called radiation pressure

$$P_{\mathrm{rad}} = \frac{h\nu}{\tau c}. \tag{5.4}$$

In the case of Sodium atoms, this pressure is equivalent to an acceleration equal to $10^6\,\mathrm{m.s}^{-2}$, which is $10^5$ times the gravitational acceleration on Earth.

The radiation force is therefore very strong and can be used to slow down atoms. If a laser beam is placed in front of the exit of the oven in which the alkali vapor is produced, the radiation pressure is in the direction opposite to the one of the atoms. While the atoms are slowed down, the frequency $\nu_a$ rises and the frequency of the laser needs to be increased (another method is presented in Sec. 5.1.2.e). With this technique, a thermal vapor of Sodium atoms at the temperature of $900\,\mathrm{K}$ ($1\,\mathrm{km.s}^{-1}$) can be "stopped" (actually slowed down to $\sim 30 \ll 10^3\,\mathrm{m.s}^{-1}$, *i.e.* $1\,\mathrm{K}$) in $1\,\mathrm{ms}$ on a distance of $50\,\mathrm{cm}$. At these low velocities, atoms are slow enough to be trapped in a magnetic field.

### 5.1.1.b Dipole force

In addition to the radiation pressure due to absorption-emission cycles, there is a dipole force originating from the Stark effect. Indeed, the coupling between the electric field and the electron-nucleus dipole of the atom induces shifts in the energy levels. In the dipole approximation and with a second order perturbation theory one can show that a spatially varying electric field gives rise to a force on an atom

$$\vec{F}_{\mathrm{dip}} = \frac{1}{2}\alpha(\omega)\,\vec{\nabla}\langle \vec{E}^2(\vec{r},t)\rangle, \tag{5.5}$$

where $\alpha$ is the polarizability of the atom and the time average is taken because the frequency $\omega$ of the laser is much higher than the inverse typical time of the atomic motion. The force is parallel to the gradient of luminous intensity. In a classical approach, the polarizability turns out to be

$$\alpha(\omega) = \frac{e^2}{m_e(\omega_0^2 - \omega^2)}. \tag{5.6}$$

Consequently, there are two different behaviors

- If $\omega > \omega_0$ (blue detuning) the atom is repelled from high luminous intensity regions.
- If $\omega < \omega_0$ (red detuning) the atom is attracted in high luminous intensity regions.

### 5.1.1.c Optical traps

By focusing a laser beam it is possible to create a radiation field whose intensity has a maximum in space. If the frequency of the light is detuned to the red, the dipole force pushes all atoms at this point. This constitutes the optical trap. Compared to the magnetic traps described in the following section, optical traps have the advantage not to depend on the magnetic state of the atom. Optical traps are also used when a constant magnetic field is needed, because in this situation the magnetic field cannot trap the atoms. It is particularly important in the context of Feshbach resonances [119]. These resonances have become an important tool in investigations of the basic atomic physics of cold atoms, and, because they allow to tune the scattering length by adjusting an external parameter such as the magnetic field [120].

### 5.1.2 Influence of magnetic fields on an atom

#### 5.1.2.a Zeeman effect

Alkali atoms have a simple electronic configuration, characterized by closed shells except for the outermost, occupied by a single electron. The coupling between the spin of this electron and the one of the nucleus gives rise to the hyperfine structure of the atom. When a magnetic field is applied, it couples to the angular momentum of the atom and breaks the degeneracy of the hyperfine levels. This lift of degeneracy under the influence of a magnetic field is the Zeeman effect. At first approximation, the levels depend linearly on the magnetic field $B$

$$E_i = E_i^0 - \mu_i B, \tag{5.7}$$

where $\mu_i$ is the magnetic moment of the state. The magnetic field thus induces a potential energy $-\mu_i B$ where $\mu_i$ can be positive or negative depending on the state. If the magnetic field in inhomogeneous, the atoms are spatially trapped in a minimum of $B(\vec{r})$ for states with $\mu_i < 0$. Because in a region devoid of charges and currents, the strength of a quasistatic electric or magnetic field can have local minima but not local maxima [121], the states with a positive magnetic moment cannot be trapped by a magnetic field. Moreover, an atom moving in a spatially-dependent magnetic field experience a time-dependent magnetic field that can induce transitions between Zeeman levels (called Majorana transitions). If a transition from a state with $\mu_i < 0$ to a state with $\mu_j > 0$ occurs, for instance in the case of a spin-flip, the atom is lost. However, the frequency of the Majorana transitions being of order $\mu_B B$ ($\mu_B$ is the Bohr magneton), the trap losses are appreciable in the vicinity of a zero-field point and hence, a node in the field produces a hole in the trap. A magnetic trap is thus obtained with a magnetic field having a non-zero minimum.

#### 5.1.2.b Magnetic traps

Most of the magnetic traps used in experiments are based on the quadrupole trap, where the magnetic field increases linearly in all directions from a zero minimum. It can be produced by a pair of opposed Helmholtz coils with identical current circulating in the opposite direction. To plug the hole at the center, one can apply a laser field in the region of the node in the magnetic field [30]. Indeed, as remarked in the previous section, the radiation force repels atoms from regions of high electric field at frequencies above resonance. A blue-detuned laser beam passing through the quadrupole trap centre thus prevent atoms from approaching the hole.

An alternative way to plug the hole is to superimpose on the quadrupole field a rotating, spatially-uniform, magnetic field. This is the time-averaged orbiting potential (TOP) trap [29]. The effect of the oscillating bias field is to move the instantaneous position of the node in the magnetic field. If the frequency of the bias field is larger than that of the atomic motions, an atom moves in an effective potential given by the time average of the instantaneous potential. The important result is that the time-averaged magnetic field is converted from a linear dependence with zero minimum to a quadratic dependence with a shifted minimum, and consequently there is no longer a hole in the trap.

An inhomogeneous magnetic field with a minimum at a non-zero value may be generated by a configuration based on two Helmholtz coils with additional currents carried by conductors parallel to the symmetry axis. This trap is commonly referred to as the

Ioffe-Pritchard trap [122, 123] and has the shape of a “magnetic bottle”. A convenient feature of this trap is that in the bars it is possible to make field configurations with different degrees of curvature in the axial and radial directions.

### 5.1.2.c Magneto-optical trap

In the magneto-optical trap (MOT), trapping is done with a combination of laser beams and a spatially-varying magnetic field. The basic physical effect is that, because atomic energy levels depend on the magnetic field, the radiation pressure depends on the position. With six correctly polarized lasers beam (two counter-propagating beams along each axis), the radiative force on an atom escaping from the center of the trap is always towards the origin, where the total radiation pressure vanishes. This schematic model is however too simple to describe correctly MOTs. Indeed, because of the existence of several hyperfine states in alkali atoms, off-resonant transitions occur. It is then necessary to perform an optical repumping to populate the levels in resonance with the laser field.

Once trapped in the MOT, atoms can be cooled down using the laser cooling technique based on the Doppler process (described in Sec. 5.1.3.a) or employing the evaporative cooling technique (described in Sec. 5.1.3.b and implemented in Ref. [124] in the so-called dark-spot MOT configuration).

### 5.1.2.d Piercing magnetic traps

Once atoms are trapped, one may want to extract some of them in a controlled way. For example, in evaporative cooling the hottest atoms are chased away (Sec. 5.1.3.b), in interference measurements atoms are released from two different parts of the trap (Sec. 5.1.4.b) and a coherent beam of particle is extracted in an atom laser [125]. We have seen in Sec. 5.1.2.b that only states with a positive magnetic momentum can be trapped in a magnetic field. A way to release atoms is thus to change the sign of their magnetic momentum, for instance with a Majorana transition which produces a spin flip. Due to the Zeeman effect and to the inhomogeneous magnetic field in the trap, these transitions depend on the position of the atoms. Let us consider a place where we want to pierce the trap. This position corresponds to a value of the magnetic field $B_0$. Taking into account the Zeeman effect, one can calculate the energy spectrum of the atom at $B_0$ and find a transition that changes the sign of the magnetic moment. Then, if a radio frequency radiation is sent on the cloud in resonance with this transition, all atoms subjected to the magnetic field $B_0$ will escape from the trap. With this technique, the position of the hole is determined by the radiation frequency.

### 5.1.2.e Zeeman slower

In Sec. 5.1.1.a we showed that it is possible to slow down an atomic cloud with a laser beam. Since the Doppler shift of the atomic frequency changes when the atoms are slowing down, it is necessary to adjust the laser frequency to keep it in resonance. Alternatively, it is possible to use the Zeeman energy shift to compensate the variation of the Doppler shift so that the atomic frequency does not change. The external magnetic field is generated from a Zeeman slower, a solenoid with a varying coil thickness. Once the specific geometry of the Zeeman slower is designed it is possible to slow down atoms without changing the laser beam frequency.

### 5.1.3 Techniques to cool down atoms

#### 5.1.3.a Laser cooling

The laser cooling technique uses the radiation pressure combined with the Doppler effect to reduce the atoms speed and hence their temperature. Let us consider a gas of trapped alkali atoms. We shine the cloud with two laser beams having the same frequency $\omega$ and the same intensity with opposite directions (we denote them by left and right). The lasers are tuned to be red-detuned, *i.e.* $\omega \lesssim \omega_0$. Suppose now that an atom start moving to the right. In its reference frame, due to the Doppler effect, the photons coming from the right have a frequency higher than $\omega$ (approaching resonance) and the ones coming from the left have a frequency lower than $\omega$ (moving away from resonance). The atom thus absorbs more photons from the right than from the left and the mean momentum transferred to the atom after many absorption-emission cycles points to the left. As a consequence, the atom is slowed down. The situation is the same in the opposite direction and also the same in all the directions if we use six lasers instead of two. The radiation pressure of the laser beams thus acts as a strong frictional (or viscous) force $\vec{f} \propto -\vec{v}$ which prevents atoms from moving, like a spoon in a honey pot. The atom gas sticky with photons is referred to as optical molasses. With laser cooling it is possible to cool atoms down to $100\,\mu$K.

To reach lower temperatures more subtle techniques can be used, such as the Sisyphus cooling [126] or the sub-recoil cooling [127]. The evaporative cooling remains the more commonly used in experiments, and can cool down atoms below the nanoKelvin.

#### 5.1.3.b Evaporative cooling

The temperature reached by laser cooling are impressively low, but they are not low enough to produce Bose Einstein condensation in gases at densities that are realizable experimentally. In the experiments performed to date, Bose Einstein condensation of alkali gases is achieved by using evaporative cooling after laser cooling. The basic physical effect in evaporative cooling is that, if particles escaping from a system have an energy higher than the average energy of the particle in the system, the remaining particles thermalize to a lower energy through two-body collisions, and hence are cooled [128]. This technique appropriates the natural reaction to blow on the soup to cool it down. Evaporative cooling starts by piercing a hole in a magnetic trap away from the centre, at an energy $E_{\text{evap}}$. Experimentally, one can make a hole in a magnetic trap by applying a radio-frequency radiation that changes the sign of the magnetic momentum, thereby expelling the atom from the trap, as described in Sec. 5.1.2.d. To go out of the trap, atoms need to have a kinetic energy higher than $E_{\text{evap}}$ to reach the hole. After many scattering events, most of the atoms with a temperature $T > E_{\text{evap}}/k_B$ are out. As atoms are lost from the trap and cooling proceeds, the frequency is steadily adjusted to allow loss of atoms with lower and lower energy [129]. With the evaporative cooling technique it is possible to cool atoms below 500 pK [130].

### 5.1.4 Probes for cold atoms

Cold gases of alkali atoms are dilute, neutral and metastable. With these peculiarities, usual techniques of low temperature physics cannot be used and new methods have to be developed to probe these systems. Here we present some of the techniques commonly

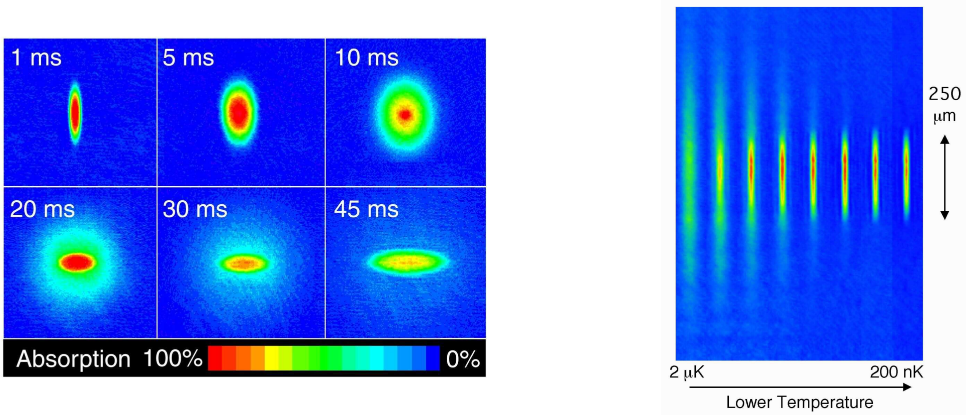

Figure 5.1: *Left panel*: Time-of-flight expansion of a Bose condensate. Absorption images were taken after a variable delay time from the release. The earliest images show the pencil-like shape of the initial cloud. When the cloud has expanded to many times its original size, such time-of-flight images represent the velocity distribution of the released cloud, from Ref. [132]. *Right panel*: Direct observation of the formation of a Bose-Einstein condensate using dispersive light scattering (phase contrast images). The intensity of the scattered light is a measure of the density of atoms (integrated along the line-of-sight), from Ref. [131].

used in experiments.

#### 5.1.4.a Laser light absorption, time-of-flight technique and in-situ imaging

A first possibility to measure the density profile is absorption imaging. The cold gas is shone with a laser beam in resonance with an atomic transition. The higher the density, the more the photons are absorbed. The examination of the absorption profile thus gives direct information on the density distribution of the atomic cloud. More precisely, one obtains the integrated density over the direction of the beam light. The major disadvantage of this technique is that it is destructive.

If the Bose gas is released from the trap before imaging, the cloud freely expands and after a sufficiently long time the density profile becomes proportional to the momentum distribution of the cloud before the expansion [37]. This exact correspondence between velocity and coordinate-space distributions is true for an ideal gas, which is a good approximation for experimental clouds after expansion. The expansion also improves the spatial resolution of the measurement. Experimental density profile results are presented on Figs. 1.10 and 5.1.

A second imaging technique is the in situ imaging. It exploits the fact that the refractive index of the gas depends on its density, and hence the optical path length is changed by the medium. These changes in optical path can be converted into intensity variations if an off-resonance light beam passes through the cloud and then interferes with a reference beam [131]. This method is almost non-destructive and can be used to observe the time evolution of a cloud (see Fig. 5.1).

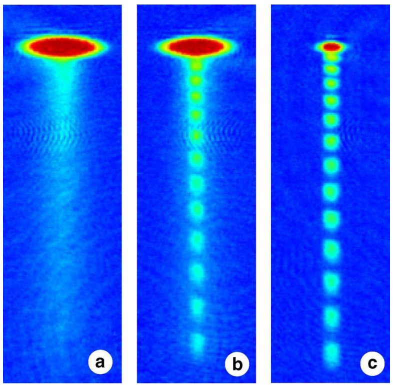

Figure 5.2: Interference pattern of matter-wave beams emitted from two spatially separated regions of a trapped Bose gas, from Ref. [133]. For a temperature well below $T_c$, the spatially uniform phase of the condensate results in a high-contrast interference pattern *(c)*. When the temperature is increased to just below $T_c$, the contrast of the interference pattern is reduced *(b)*, and it vanishes completely for temperatures above $T_c$ *(a)*.

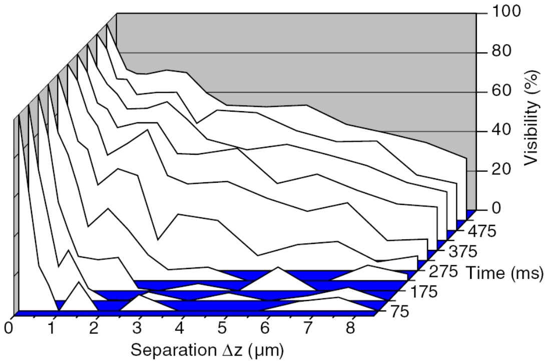

Figure 5.3: Shown is the visibility of a matter wave interference pattern originating from two regions separated by $\Delta z$ inside a trapped cloud. By shock cooling the gas is prepared in a highly nonequilibrium state and then relaxes towards thermal equilibrium. Initially the correlations are short ranged and thermal-like. The onset of Bose-Einstein condensation is marked by the appearance of long-range order, from Ref. [134].

### 5.1.4.b Interference methods

The phase coherence of a cold gas can be measured with an interference experiment. The cloud is initially trapped with a magnetic field and two holes are performed in the trap. The two holes are created with two radiofrequency radiations, as described in Sec. 5.1.2.d. Once released, the two matter waves originating from two different locations in the atom trap interfere with each other. The resulting interference pattern can be measured with a single atom counter. The visibility being proportional to the one-body density matrix, it gives a direct access to the phase-phase correlations of the cloud and its temporal evolution uncovers the formation of long-range order [133, 134] (see Figs. 5.2 and 5.3).

### 5.1.4.c Scattering methods

The inelastic scattering method gives access to the dynamic structure factor, which characterizes the dynamic behavior of quantum many-body systems. The dynamic structure factor is the Fourier transform of the density-density correlation function (see Sec. 5.4.6). In a two-photon Bragg scattering experiment, the atomic cloud is exposed to two detuned laser beams. Atoms can undergo a stimulated light scattering event by absorbing a photon from one of the beams and emitting a photon into the other. After exposure to these laser beam, the response of the system can be measure using a time-of-flight experiment by determining the net momentum transferred to the gas [37]. This method was used *e.g.* in the experiments of Refs. [135, 136].

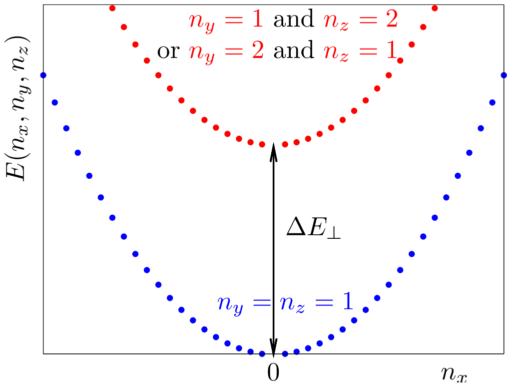

Figure 5.4: Dispersion relation of a free particle in the longitudinal direction of an elongated confining potential with $L_{//} = 10\, L_\perp$. Transverse motion is frozen in the transverse ground state $n_y = n_z = 1$ if the temperature is smaller than $\Delta E_\perp$.

## 5.2 Quantum systems in one-dimension

### 5.2.1 Confinement to 1D

The real world being three-dimensional, to obtain a one-dimensional system one needs to freeze two spatial degrees of freedom. In the case of quantum particles, this is achieved with confining potentials. Let us take the simple example of a free particle confined to a parallelepipedic box (lengths $L_x$, $L_y$ and $L_z$). Due to the boundary conditions, the energy levels are quantized and characterized by three quantum numbers $n_x$, $n_y$ and $n_z$:

$$E_{n_x,n_y,n_z} = \frac{\hbar^2\pi^2}{2M}\left[\frac{n_x^2}{L_x^2} + \frac{n_y^2}{L_y^2} + \frac{n_z^2}{L_z^2}\right], \tag{5.8}$$

where $M$ is the mass of the particle and $n_i$ is a non-zero integer. Suppose now that the box is elongated in the $x$ direction ($L_x = L_{//} \gg L_y = L_z = L_\perp$). Starting from the ground state energy $E_{1,1,1}$, the particle needs to gain the energy $\Delta E_\perp = \dfrac{3\pi^2\hbar^2}{2ML_\perp^2}$ to reach the first transverse excited state and the energy $\Delta E_{//} = \dfrac{3\pi^2\hbar^2}{2ML_{//}^2}$ to gain the first longitudinal excited state. The confining potential of this elongated box yields $\Delta E_\perp \gg \Delta E_{//}$. It is then straightforward to see that if the maximal available energy for the particle (*e.g.* from thermal agitation) is less than $\Delta E_\perp$, the transverse degrees of freedom are frozen in the transverse ground state and the particle is constraint to a one-dimensional motion in the longitudinal direction, as depicted in Fig. 5.4. In the case of a Bose gas, one-dimensionality is achieved if the temperature and the chemical potential are smaller than $\Delta E_\perp$. In experiments, Bose gases are usually confined to the minima of a 2D optical lattice [137–139]. In condensed-matter systems, one-dimensionality is obtained *e.g.* in quantum wires [140] and carbon nanotubes [141].

The possibility to create one-dimensional quantum systems offers the possibility to explore a novel physics [142]. Indeed, in a one-dimensional system, any individual motion is converted into a collective one because a moving particle cannot spare its neighbors. This peculiarity enhances the effect of interactions between particles and also strengthens

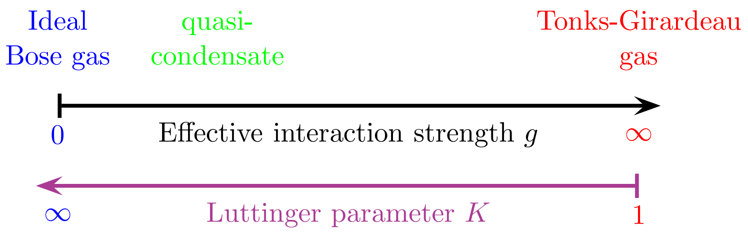

Figure 5.5: A Bose gas behaves as a quasi-condensate in the case of nearly free bosons (small interaction strength $g$) and as a Tonks-Girardeau gas in the case of impenetrable bosons (infinite hard-core repulsion). The low energy physics between these two limiting cases can be described within the Luttinger liquid formalism where the compressibility of the fluid $K$ goes from $K = 1$ for the Tonks gas to $K = \infty$ for the ideal Bose gas.

the role of quantum fluctuations. As a consequence, from the limit of free bosons to that of impenetrable bosons, there exists a rich variety of interesting behaviors.

### 5.2.2 Interaction strength: from quasi-condensates to Tonks-Girardeau gases

As we have seen in Sec. 1.4, two-body collisions in a dilute Bose gas are modeled with a hard-core pseudopotential $V_{\text{int}}(\vec{r}) = g_{3\text{D}}\,\delta(\vec{r})$ where $g_{3\text{D}} = 4\pi\hbar^2 a_S/m$ is the interaction strength in a three dimensional gas. The presence of a transverse external confinement changes the interaction strength between bosons. Indeed, for a harmonic confining potential with the transverse "frequency" $\omega_\perp$ the size of the ground state of the transverse Hamiltonian is $a_\perp = \sqrt{2\hbar/m\omega_\perp}$. The one-dimensional scattering length is given by [143]

$$a_{1\text{D}} = \frac{a_\perp^2}{2a_S}\left(\mathcal{C}\frac{a_S}{a_\perp} - 1\right), \tag{5.9}$$

where $\mathcal{C} \simeq 1.460\ldots$, and the effective interaction strength of the confined bosons is

$$g = g_{3\text{D}}\,\frac{1}{\pi a_\perp^2}\left(1 - \mathcal{C}\frac{a_S}{a_\perp}\right)^{-1}. \tag{5.10}$$

Let us consider the state of the system as the one-dimensional interaction strength $g$ goes from $g = 0$ for free bosons to $g = \infty$ in the case of impenetrable bosons (see Fig. 5.5). The regime of weak interactions induces phase fluctuations and the gas enters the regime of quasi-condensates [144]. The physical picture of this regime consists of many condensates with slightly different phases [145]. In the opposite limit of strong interactions, the so-called Tonks-Girardeau regime, the interaction mimics Pauli's exclusion principle and bosons behave in many senses like fermions [146]. In a quasi-1D geometry, the phase coherence properties of the gas are therefore drastically changed with respect to their 3D counterparts.

To describe one-dimensional systems there are various methods. The Tonks-Girardeau gas is integrable and can be solved exactly through a mapping onto a gas of free fermions (see Sec. 5.2.5). In the case of homogeneous systems, one can solve the 1D Bose gas with arbitrary contact interaction strength exactly with the Bethe ansatz [147]. The thermodynamic limit was solved by Elliott H. Lieb and Werner Liniger [148, 149]. The case of arbitrary interaction and external confinement can be treated only by numerical methods. Finally, if one is interested in the low-energy properties of a one-dimensional Bose gas, the Luttinger liquid approach is a powerful method to calculate correlators. In the following, we will introduce the Luttinger liquid formalism and use it to describe a Bose Josephson junction in a one-dimensional ring trap.

### 5.2.3 Luttinger-liquid description for bosonic field operators

In this section we consider a one-dimensional system of length $L$ containing $N$ particles with arbitrary boundary conditions and construct the field operators of the gas. We start with the density operator

$$\rho(x) = \sum_{j=1}^{N} \delta(x - x_j), \tag{5.11}$$

where $x_j$ is the position of the $j^{\text{th}}$ particle and introduce a “labeling” field $\Theta(x)$ which takes the value $\Theta(x_j) = j\pi$ at the position $x_j$. Using the properties of the delta function and Poisson’s formula, we get

$$\rho(x) = \frac{1}{\pi}\partial_x\Theta(x) \sum_{m=-\infty}^{+\infty} \mathrm{e}^{2mi\Theta(x)}. \tag{5.12}$$

The leading contribution $\partial_x\Theta(x)/\pi$ of $\rho(x)$ describes long wavelength fluctuations around the mean density $\rho_0 = N/L$. We introduce the long wavelength density fluctuations operator

$$\Pi(x) = \frac{1}{\pi}\partial_x\Theta(x) - \rho_0, \tag{5.13}$$

and the final form of the density operator then reads

$$\rho(x) = (\rho_0 + \Pi(x)) \sum_{m=-\infty}^{+\infty} \mathrm{e}^{2mi\Theta(x)}. \tag{5.14}$$

We can then write the single-particle creation operator $\Psi^\dagger(x)$ in terms of the density operator $\rho(x) = \Psi^\dagger(x)\Psi(x)$ and a phase operator $\phi(x)$

$$\Psi^\dagger(x) = \sqrt{\rho(x)}\,\mathrm{e}^{-i\phi(x)}. \tag{5.15}$$

Although the bosonic or fermionic nature of the particles does not enter into account in the definition of the density operator, their fundamental differences show up in the commutation rule satisfied by $\Psi(x)$. In the following we focus on the case of bosons, for which the commutation relation reads

$$\left[\Psi(x), \Psi^\dagger(x')\right] = \delta(x - x'). \tag{5.16}$$

At the level of the fields $\phi(x)$ and $\Pi(x)$, a sufficient condition to satisfy the previous rule is

$$\left[\Pi(x), \phi(x')\right] = i\delta(x - x'). \tag{5.17}$$

Next, using Fermi’s trick

$$\sqrt{\delta(\Theta(x) - n\pi)} = \mathcal{A}\,\delta(\Theta(x) - n\pi), \tag{5.18}$$

where $\mathcal{A}$ is a constant that depends on the way the high energy fluctuations are cut off, we can rewrite the square of the density operator. The bosonic creation field operators finally reads

$$\Psi^\dagger(x) = \mathcal{A}\,\sqrt{\rho_0 + \Pi(x)}\sum_{m=-\infty}^{+\infty} \mathrm{e}^{2mi\Theta(x)}\,\mathrm{e}^{-i\phi(x)}. \tag{5.19}$$

The derivation of the bosonic field operators shows that the bosonic gas can be described with two fields, namely the field $\Theta(x)$ that reflects the density fluctuations and the field $\phi(x)$ that conveys the phase fluctuations[1].

### 5.2.4 Low-energy Hamiltonian

The general Hamiltonian of bosons interacting with a hard core potential reads

$$\mathcal{H} = \frac{\hbar^2}{2m}\int_0^L \mathrm{d}x\,\nabla\Psi^\dagger(x)\nabla\Psi(x) + \frac{g}{2}\int_0^L \mathrm{d}x\,\rho^2(x). \tag{5.21}$$

We are interested in the low energy description of the system. In this perspective we will keep only the leading terms in the two parts of the general Hamiltonian (5.21) in terms of the fields $\phi(x)$ and

$$\theta(x) = \Theta(x) - \pi\rho_0 x. \tag{5.22}$$

At lowest order, $\nabla\Psi^\dagger(x)\nabla\Psi(x) \simeq \rho_0(\nabla\phi(x))^2$ and $\rho^2(x) \simeq (\rho_0 + \Pi(x))^2$. We obtain the Luttinger liquid Hamiltonian [150, 151]

$$\mathcal{H} = \frac{\hbar v_s}{2\pi}\int_0^L \mathrm{d}x\left[K\,(\nabla\phi(x))^2 + \frac{1}{K}\,(\nabla\theta(x))^2\right], \tag{5.23}$$

where $K$ is the Luttinger parameter and $v_s$ the sound velocity. The parameters $K$ and $v_S$ can be extracted from the Bethe-ansatz solution and expressed in terms of the reduced interaction strength $\varkappa = mg/\hbar^2\rho_0$ and the Fermi velocity $v_F = \hbar\pi\rho_0/m$. The asymptotic results in the weak coupling regime $\varkappa \ll 1$ are

$$K = \frac{\pi}{\sqrt{\varkappa}}\left(1 - \frac{\sqrt{\varkappa}}{2\pi}\right)^{-1/2}, \tag{5.24}$$

$$v_s = v_F\frac{\sqrt{\varkappa}}{\pi}\left(1 - \frac{\sqrt{\varkappa}}{2\pi}\right)^{1/2}, \tag{5.25}$$

and in the strong coupling regime $\varkappa \gg 1$ they read

$$K = 1 + \frac{4}{\varkappa}, \tag{5.26}$$

$$v_s = v_F\left(1 - \frac{4}{\varkappa}\right). \tag{5.27}$$

The various regimes are presented on Fig. 5.6. To obtain the Hamiltonian (5.23) we have kept only the leading contribution from the field operators. The higher order terms will not change the form of the Hamiltonian but only renormalize the coefficients $v_S$ and $K$ (see Ref. [142] for more details). The low-energy physics of the Bose gas is thus governed by a quadratic Hamiltonian with a linear excitation spectrum $\omega(k) = v_S k$ and is described with the two parameters $v_S$ and $K$ which depend on $g$ and $\rho_0$.

---

[1] When the particle obeys the fermionic statistics, the commutation rule (5.16) reads $\left[\Psi_F(x), \Psi_F^\dagger(x')\right]_+ = \delta(x - x')$, where $[\ ,\ ]_+$ is an anticommutator ($[A,B]_+ = AB + BA$). The corresponding fermionic creation operator can be expressed in terms of the fields $\Pi(x)$, $\Theta(x)$ and $\phi(x)$ as follows

$$\Psi_F^\dagger(x) = \mathcal{A}\,\sqrt{\rho_0 + \Pi(x)}\sum_{m=-\infty}^{+\infty} \mathrm{e}^{(2m+1)i\Theta(x)}\,\mathrm{e}^{-i\phi(x)}. \tag{5.20}$$

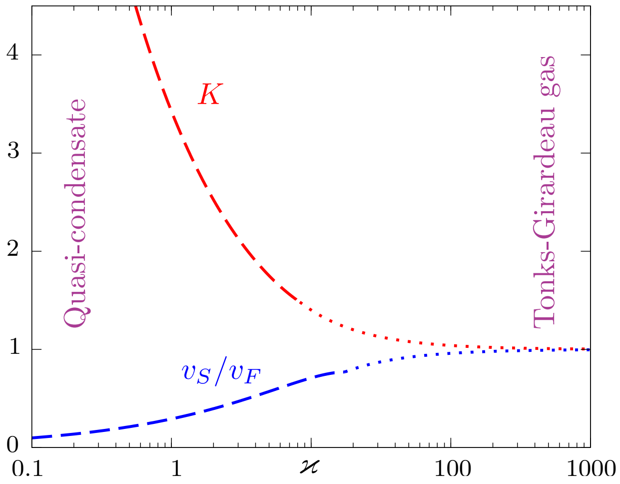

Figure 5.6: Luttinger parameter $K$ and sound velocity $v_S$ (in units of the Fermi velocity $v_F$) as a function of the dimensionless coupling strength $\varkappa = mg/\hbar^2\rho_0$. The dashed and dotted lines correspond to the asymptotic results for small and large coupling respectively. In the Tonks-Girardeau gas, the infinitely strong repulsive interaction between bosons mimics the Pauli exclusion principle and the sound velocity is close to the Fermi velocity. In the quasi-condensate limit, phase fluctuations are small and the sound velocity is strongly suppressed.

### 5.2.5 Exact description in the Tonks-Girardeau limit

In the limit of infinitely strong repulsion between the bosons, which corresponds to the value $K = 1$ for the Luttinger liquid parameter, an exact solution exists for the bosonic many-body wavefunction $\psi(x_1, ...x_N)$ (in first quantization).

The solution, due to Marvin D. Girardeau [146], is obtained by mapping the bosons onto a gas of noninteracting, spin-polarized fermions subject to the same external potential. The bosonic many-body wavefunction $\psi(x_1, ...x_N)$ is then obtained in terms of the fermionic one as

$$\psi(x_1, ...x_N) = A(x_1, ...x_N)\psi_F(x_1...x_N), \tag{5.28}$$

where the mapping function $A(x_1, ...x_N) = \Pi_{1\leq j\leq \ell \leq N}\text{sgn}(x_j - x_\ell)$ ensures the proper symmetry under exchange of two bosons. The fermionic wavefunction is given by

$$\psi_F(x_1, ...x_N) = (1/\sqrt{N!})\,\det\{\psi_j(x_k)\}_{j,k=1...N}, \tag{5.29}$$

$\psi_j(x)$ being the single particle orbitals for the given external potential. Note that $\psi_F$ vanishes every time two particles meet as required by Pauli's principle, and hence describes well the impenetrability condition $g \to \infty$ for the bosons.

As a consequence of the Bose-Fermi mapping, all the bosonic properties which do not depend on the sign of the many-body wavefunction coincide with the corresponding ones of the mapped Fermi gas. This is the case *e.g.* for the particle density profile and for the density-density correlation function. Other properties like the one-body density matrix and the momentum distribution are instead markedly different for bosons as compared to fermions. In particular, the calculation of the one-body density matrix requires in principle the calculation of a ($N$-1)-dimensional integral, which is known to simplify in some cases. Examples are the homogeneous gas with periodic boundary conditions [152] or the case of a harmonic confinement [153].

In the following, we will use the exact results for the Tonks-Girardeau gas to compare them with our results and also to fix the non universal parameters of the theory.

## 5.3 One-dimensional trapping potentials for bosons

There are two kinds of trap to confine a Bose gas to one dimension: the cigar shape potential and the ring shape potential.

### 5.3.1 Cigar-shape potential

The cigar shape potential is an elongated potential in a particular direction. This one-dimensional trap can be obtained from a three dimensional magnetic harmonic trap with a transverse trapping frequency higher than the temperature and if necessary the characteristic energy of interactions. A common way to generate these magnetic fields is to use atom chips, where electric and magnetic fields are created by microscopic wires and electrodes micro-fabricated on a carrier substrate [154]. The precision and robust alignment of the fabricated structures allow well controlled quantum manipulations of ultracold neutral atoms (see Fig 5.7).

In the limit of weak interactions, the phase fluctuations [155] as well as the density fluctuations [156] are measured using time-of-flight and in-situ absorption imaging. Finite temperature experiments are performed to study the thermodynamics [157] and the thermalization of the gas [158]. It is possible to superimpose a periodic optical lattice onto the harmonic confinement and then study the resulting dynamics for bosons in the Tonks-Girardeau regime. With this setup, one can observe the damping of dipole oscillations [159] and the transition from a superfluid to a Mott insulator [137]. A random magnetic potential can also be added to analyse the effect of disorder [160].

The one-dimensional gas can be cut into two with a radiofrequency field. Phase fluctuations are then measured with absorption imaging [161]. With this geometry, it is possible to study the relative phase fluctuations [162], the Josephson oscillations between the two systems [163], the excitation spectrum of the coupled condensates [164] and the loss of coherence between the two separated gases [165].

Cigar-shaped trapping potentials can also be obtained with optical lattices, by superimposing two orthogonal standing waves (see Fig 5.8 and Ref. [166]). In this configuration, one can obtain an array of one dimensional tubes. By varying the tunneling strength between the tubes, it is possible to study the transition between one and two dimensional systems [167].

### 5.3.2 Ring-shape potential

The possibility to study Bose-Einstein condensates confined to ring traps constitutes one of the frontiers of the experimental progress with ultracold atomic gases [138, 139]. The nontrivial topology of these traps together with the uniformity of the potential along the ring circumference makes them an ideal system for investigating persistent currents and superfluid properties of the gas. There are various techniques to generate ring shape potentials, namely with coaxial circular electromagnets [168], using the superposition of a magnetic trapping field with a standing wave [169], or with a blue-detuned laser beam

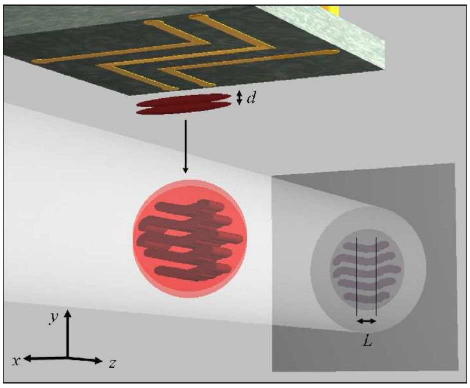

Figure 5.7: A single 1D quasi-condensate is phase coherently split into two parts separated using radiofrequency potentials on an atom chip. After the separation, the system is released from the trap and the resulting interference pattern is imaged onto a CCD camera, from Ref. [161].

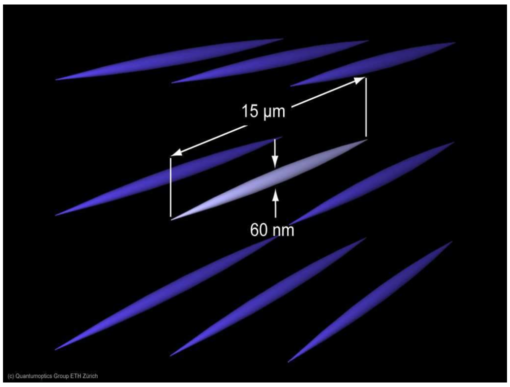

Figure 5.8: Optical lattice potentials formed by superimposing two orthogonal standing waves. Atoms are confined to an array of tightly confining 1D potential tubes, from Ref. [166]

to make a repulsive potential barrier in the middle of a harmonic magnetic trap [170]. The resulting size of the ring is of the order of the millimeter ($0.5 - 3\,\mathrm{mm}$). Atoms are cooled down to $\sim 10\,\mu\mathrm{K}$ with evaporative cooling. Measurements of the density profile and the momentum distribution are performed with the time-of-flight technique (see Figs. 5.9 and 5.10). Interference methods to measure the two points phase correlations have not been implemented on such traps yet.

## 5.4 Bosons in a quasi-one-dimensional ring trap with a localized infinite barrier

In this section we use the Luttinger-liquid approach to study the static properties of a Bose gas confined to a quasi one-dimensional ring trap which contains an infinite localized repulsive potential barrier. For the one-body density-matrix we obtain different power-law decays depending on the location of the probe points with respect to the position of the barrier. Using a regularized harmonic-fluid approach we also calculate the subleading corrections due to the density fluctuations in the thermodynamic limit. We evaluate the particle density profile as well as the density-density correlation function and show that the presence of the barrier induces Friedel oscillations of the density. This section is based on our papers [116, 117].

### 5.4.1 Mode expansion of the Luttinger fields with open boundary conditions

We consider a Bose gas confined to a quasi-one-dimensional ring trap containing a localized repulsive potential which creates a "weak link" connecting the two ends of the loop (see Fig. 5.11), a situation that may be viewed as a realization of a Bose-Josephson junction [116]. We start by considering the case of an infinitely high barrier, which corresponds to a ring with open boundary conditions. In Sec. 5.5 we will treat the case of

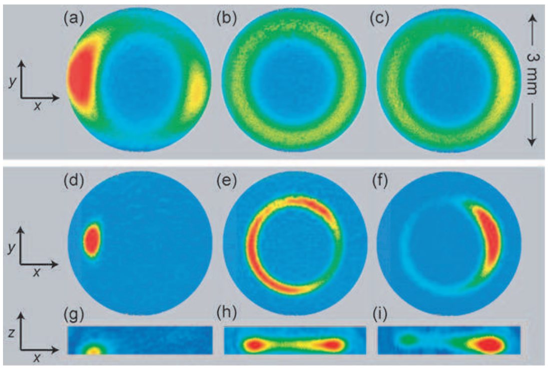

Figure 5.9: Atoms in a ring-shaped magnetic trap. Shown are top *(a)-(f)* and side *(g)-(i)* absorption images of ultracold clouds for different magnetic fields, from Ref. [168].

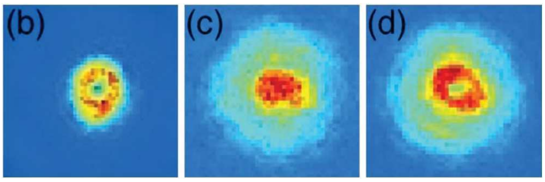

Figure 5.10: *(b)* In situ image of a BEC in the toroidal trap. *(c)* Time-of-flight image of a noncirculating BEC released from the toroidal trap. *(d)* Time-of-flight image of a circulating BEC, from Ref. [170]

a large, finite barrier by considering the tunneling among the two sides of the barrier as a perturbation.

In order to evaluate the first- and second-order correlation functions for the bosons on the ring junction, we derive here the expansion of the fields $\Pi(x) = \nabla\theta(x)/\pi$ and $\phi(x)$ in terms of the canonical bosonic annihilation and creation operators $b_k$ and $b_k^\dagger$ satisfying the commutation relations $[b_k, b_{k'}^\dagger] = \delta_{k,k'}$. Specifically, we expand the operators $\phi(x)$ and $\Pi(x)$ in Fourier modes for $x \in [0, L]$:

$$\phi(x) = \sum_{j=-\infty}^{+\infty} \left[\phi_j \, \mathrm{e}^{ik_j x} b_{k_j} + \phi_j^* \, \mathrm{e}^{-ik_j x} b_{k_j}^\dagger\right], \tag{5.30}$$

$$\Pi(x) = \sum_{j=-\infty}^{+\infty} \left[\Pi_j \, \mathrm{e}^{ik_j x} b_{k_j} + \Pi_j^* \, \mathrm{e}^{-ik_j x} b_{k_j}^\dagger\right], \tag{5.31}$$

where we have set $k_j = \frac{2\pi}{L} pj$. The constant $p$ and the complex coefficients $\phi_j$ and $\Pi_j$ are determined by imposing three constraints:

i. Commutation rule $[\Pi(x), \phi(x')] = i\,\delta(x - x')$.

ii. Reduction of the Hamiltonian to the diagonal form

$$\mathcal{H} = \sum_{k_j} \hbar\omega_{k_j} \left[b_{k_j}^\dagger b_{k_j} + \frac{1}{2}\right]. \tag{5.32}$$

iii. Boundary conditions. The open boundary conditions imply vanishing current density, *i.e.* $\nabla\phi(0) = \nabla\phi(L) = 0$, $\nabla\Pi(0) = \nabla\Pi(L) = 0$.

In order to take into account that we are using an approximate, long wavelength theory, we introduce a short distance cutoff $a \sim {\rho_0}^{-1}$ in the sum over the modes. The final result

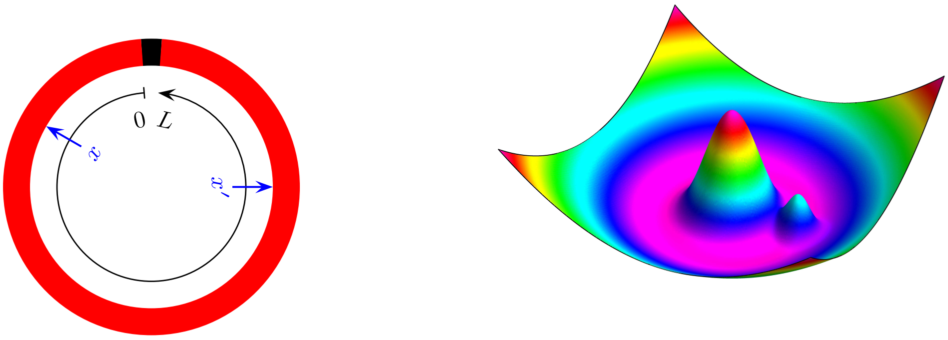

Figure 5.11: Sketch of the Bose-Josephson junction on a ring studied in this work and the corresponding trap.

reads

$$\phi(x) = \phi_0 + \frac{1}{\sqrt{K}} \sum_{j=1}^{\infty} \frac{1}{\sqrt{j}} \cos(\pi j x/L)\, \mathrm{e}^{-\frac{\pi j a}{2L}} \left[ b_{k_j} + b^{\dagger}_{k_j} \right], \tag{5.33}$$

$$\Pi(x) = \Pi_0 + i\frac{\sqrt{K}}{L} \sum_{j=1}^{\infty} \sqrt{j} \cos(\pi j x/L)\, \mathrm{e}^{-\frac{\pi j a}{2L}} \left[ b_{k_j} - b^{\dagger}_{k_j} \right], \tag{5.34}$$

the latter implying

$$\theta(x) = \pi \Pi_0 x + i\sqrt{K} \sum_{j=1}^{\infty} \frac{1}{\sqrt{j}} \sin(\pi j x/L)\, \mathrm{e}^{-\frac{\pi j a}{2L}} \left[ b_{k_j} - b^{\dagger}_{k_j} \right], \tag{5.35}$$

where $k_j = \pi j/L$ ($p = 1/2$). The zero mode $\Pi_0$ is directly related to the particle number operator through normalization: $\Pi_0 = (N - N_0)/L$ where $N_0 = \langle N \rangle = \rho_0 L$. It is conjugate to the zero-mode phase operator $\phi_0$ such that $[\Pi_0, \phi_0] = i$. Using this fact, one can explicitly check the commutation rule between $\theta(x)$ and $\phi(x')$ from the mode expansions (5.33) and (5.35); it turns out to be $[\theta(x), \phi(x')] = i\pi\, \Xi(x - x')$, where $\Xi$ is the unit step function, consistent with Eq. (5.17). Finally, inspection of the resulting diagonalized form of the Hamiltonian yields the linear dispersion relation

$$\omega_{k_j} = v_S k_j = j\pi v_S/L, \tag{5.36}$$

for the modes.

### 5.4.2 One-body density matrix for a finite ring

In this section we focus on the contribution from phase fluctuations of the one-body density matrix with the aim of analyzing the differences with respect to the case of an infinite system, as well as to the case of a ring in the absence of the barrier.

The one-body density matrix, defined as

$$\mathcal{G}(x, x') = \left\langle \Psi^{\dagger}(x)\Psi(x') \right\rangle, \tag{5.37}$$

yields a measure of the coherence along the ring. It is possible to measure the one-body density matrix and off-diagonal long range order experimentally by measuring the interference pattern of atomic matter waves coming from two holes in the trap (see *e.g.* Ref. [134] for the case of a cigar-shaped 3D Bose gas). According to Eq. (5.19) the bosonic field operator has three contributions:

i. The phase $\phi(x)$.

ii. The density fluctuation $\Pi(x)$.

iii. The higher harmonics of order $2m\theta(x)$ of the density.

The most important contribution to the one-body density matrix at large distances is the one due to the phase fluctuations which correspond to the lowest-energy modes of the bosonic fluid in the ring (see *e.g.* Refs. [142, 145]), while the two latter contributions give rise to subleading corrections which will be analyzed further in the next subsections.

To lowest order we approximate the bosonic field operator (5.19) as $\Psi(x) \simeq \mathcal{A}\sqrt{\rho_0}\, \mathrm{e}^{i\phi(x)}$; the problem then reduces to the computation of the quantum average

$$\mathcal{G}_0(x,x') = |\mathcal{A}|^2\rho_0\langle \mathrm{e}^{-i\phi(x)}\mathrm{e}^{i\phi(x')}\rangle. \tag{5.38}$$

Since the Luttinger-liquid Hamiltonian (5.23) is quadratic in the field $\phi(x)$ we immediately obtain $\mathcal{G}_0(x,x') = |\mathcal{A}|^2\rho_0 \exp\Big(-\frac{1}{2}\left\langle [\phi(x)-\phi(x')]^2\right\rangle\Big)$. The phase-phase correlation function is evaluated with the help of the mode expansion (5.33)

$$\langle\phi(x)\phi(x')\rangle = -\frac{1}{4K}\ln\!\left[(\pi/L)^4\left(a^2+d^2(x-x'|2L)\right)\left(a^2+d^2(x+x'|2L)\right)\right], \tag{5.39}$$

$d(x|L) = L|\sin(\pi x/L)|/\pi$ being the cord function. This leads to

$$\mathcal{G}_0(x,x') = \rho_0 b_{0,0}\left[\frac{\rho_0^{-2}\sqrt{[a^2+d^2(2x|2L)]\,[a^2+d^2(2x'|2L)]}}{[a^2+d^2(x-x'|2L)]\,[a^2+d^2(x+x'|2L)]}\right]^{\frac{1}{4K}}, \tag{5.40}$$

where we have introduced the nonuniversal constant $b_{0,0} = |\mathcal{A}|^2(\rho_0 a)^{\frac{1}{2K}}$. The above expression (5.40) yields the leading-order term for the one-body density matrix at large distances. By taking the limit $a \to 0$ we recover the result obtained in Ref. [171] using the methods of conformal field theory.

If the distance among $x$ and $x'$ is large compared to the cutoff length $a$, the one-body density matrix displays a power-law decay of the form $\mathcal{G}_0(x,x') \propto |x-x'|^{-\gamma}$, where the exponent $\gamma$ can be derived from the expression (5.40), and in particular depends on the location of the probed points [171]. Indeed, if the two points are away from the edges one finds $\gamma = \dfrac{1}{2K}$, which corresponds to the result obtained in the thermodynamic limit [150] whereas if they approach the edges (*i.e.* $x \lesssim a$ and $L-x' \lesssim a$) the exponent is $\gamma = \dfrac{1}{K}$, a result known in the context of quantum phase fluctuations in a 1D superconducting wire of length $L$ [172]. In the case where one point is at one edge and the other in the bulk we obtain $\gamma = \dfrac{3}{4K}$. These three different behaviors are illustrated in Fig. 5.12, where we plot the one-body density matrix $\mathcal{G}_0(x,x')$ as a function of $x'$ for various choices of the probe point $x$. In the same figure we display also the behavior for a homogeneous ring in absence of the barrier, obtained by a procedure analogous to the one outlined above,

$$\mathcal{G}_0^{\mathrm{pbc}}(x,x') = \rho_0 b_{0,0}\left[\frac{\rho_0^{-2}}{a^2+d^2(x-x'|L)}\right]^{\frac{1}{4K}}. \tag{5.41}$$

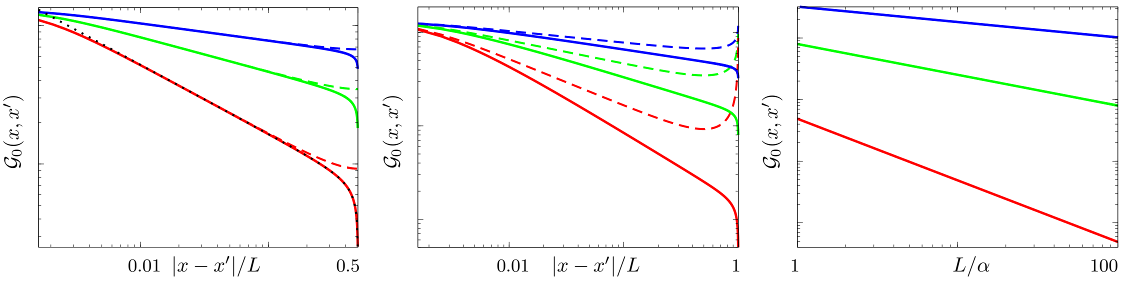

Figure 5.12: Leftmost and middle panels: one-body density matrix in logarithmic scale (arbitrary units) as a function of the coordinate $x'$ (in units of the ring circumference $L$) for various choices of the coordinate $x$ with respect to the position of the barrier, located at $x = 0$: top panel $x \simeq 0$, middle panel $x = L/2$. Rightmost panel: one-body density matrix in logarithmic scale (arbitrary units) taken at $x \simeq 0$ and $x' \simeq L$ as a function of the length $L$ of the ring (in units of the average interparticle distance $a$). In each panel we plot three values of the parameter $K$ (from bottom to top $K = 1$, $K = 2$ and $K = 4$); the solid lines correspond to the results from Eq. (5.40) and the dashed lines are the solution (5.41) for a homogeneous ring (periodic boundary conditions). The dotted line in the leftmost panel is the exact solution for a Tonks-Girardeau gas in the thermodynamic limit. The linear behavior of $\mathcal{G}_0$ in logarithmic scale corresponds to the predicted power law decays with various exponents $\gamma$ (leftmost panel, $\gamma = 1/2K$, middle panel $\gamma = 3/4K$ and rightmost panel $\gamma = 1/K$).

Note that, as the coordinate $x'$ runs along the ring, in the presence of the barrier the coherence decreases monotonically, while if the barrier is absent coherence is recovered as $x'$ approaches $L - x$.

The different power-law behaviors are in principle observable for a quasi-1D Bose gas in a ring trap geometry; it is required to have a high barrier well localized on a length scale $a$.

### 5.4.3 Regularized harmonic fluid approach in the thermodynamic limit

The contribution from the phase fluctuations to the one-body density matrix gives rise to a power-law decay which depends only on the Luttinger parameter. In this section we take into account the contribution from density fluctuations to the one-body density matrix in the thermodynamic limit, that is to say for an infinitely long ring containing an infinite number of bosons but with a finite mean density: $N \to \infty$, $L \to \infty$ and $\rho_0 = N/L$ finite.

The full calculation of the one-body density matrix for the 1D interacting Bose gas has a long history, and we start by mentioning the known results. In the Tonks-Girardeau limit where the exact many-body wavefunction is known by means of a mapping onto a gas of spinless fermions [146, 173], the problem reduces to the evaluation of a $(N-1)$-dimensional integral. This mathematical challenge has been addressed first by Andrew Lenard [174], and by several subsequent works (see *e.g.* Refs. [175–178]). The main result is the evaluation of the large-distance behavior of the one-body density matrix in the form of a series expansion (from Ref. [178]),

$$\mathcal{G}^{\mathrm{TG}}(z) = \frac{\rho_0\rho_\infty}{|z|^{1/2}}\left[1 - \frac{1}{32}\frac{1}{z^2} - \frac{1}{8}\frac{\cos(2z)}{z^2} - \frac{3}{16}\frac{\sin(2z)}{z^3} + \frac{33}{2048}\frac{1}{z^4} + \frac{93}{256}\frac{\cos(2z)}{z^4} + \dots\right], \tag{5.42}$$

where the constant $\rho_\infty$ and the coefficients have been calculated exactly. In Eq. (5.42) and in the following we express the one-body density matrix as a function of the scaled relative coordinate $z = \pi\rho_0(x - x')$.

For the case of arbitrary interaction strength, the calculation of the correlation functions remains a challenge (see *e.g.* Ref. [179]), although the model of bosons with contact repulsive interactions is integrable by the Bethe-Ansatz technique [148, 149]. The power-law decay at large distances can be inferred using a harmonic-fluid approach [150, 151, 180–183]. The resulting structure for the large-distance series of the one-body density matrix reads (from Refs. [150, 151])

$$\mathcal{G}^{\mathrm{LL}}(z) \propto \frac{\rho_0}{|z|^{1/2K}} \sum_{m=0}^{\infty} B_m \frac{\cos(2mz)}{z^{2m^2K}}, \tag{5.43}$$

where the coefficients $B_m$ are nonuniversal and cannot be obtained by the harmonic-fluid approach. By noticing that the harmonic-fluid approach is valid also in the Tonks-Girardeau regime and corresponds to the case of Luttinger parameter $K = 1$, one can directly compare the predictions of the two methods. Specifically, this comparison shows that the structure of Eq. (5.42) is richer than that of Eq. (5.43) obtained by the standard harmonic-fluid approach.

The one-body density matrix is obtained from averaging the bosonic field operator (5.19) with respect to the quadratic low-energy Hamiltonian (5.23). We will keep to full dependence of the space cutoff $a$ and take into account the presence of the long-range density fluctuations $\rho(x)$. This constitutes the generalized harmonic-fluid approach. The general expression of the one-body density matrix is then

$$\mathcal{G}(x, x') = |\mathcal{A}|^2 \sum_{(m,m')\in\mathbb{Z}^2} \langle [\rho_0 + \Pi(x)]^{1/2}\, \mathrm{e}^{i2m\Theta(x)} \mathrm{e}^{-i\phi(x)} \mathrm{e}^{i\phi(x')} \mathrm{e}^{-i2m'\Theta(x')} [\rho_0 + \Pi(x')]^{1/2} \rangle, \tag{5.44}$$

where the only nonvanishing leading terms satisfy $m = m'$ [142].

In order to display its dependence only on differences between fields, we re-write the central term as

$$\begin{aligned}\mathrm{e}^{i2m\Theta(x)} \mathrm{e}^{-i\phi(x)} \mathrm{e}^{i\phi(x')} \mathrm{e}^{-i2m\Theta(x')} = {} & \mathrm{e}^{i2m(\Theta(x)-\Theta(x'))-i(\phi(x)-\phi(x'))} \\ & \times \mathrm{e}^{m[\theta(x)+\theta(x'),\phi(x)-\phi(x')]},\end{aligned} \tag{5.45}$$

where the commutator between the $\theta$ and $\phi$ fields is computed in Eq. (5.51) below. We then perform a series expansion of the square root terms $[1 + \Pi/\rho_0]^{1/2}$ in the one-body density matrix. We define $X = \Pi(x)/\rho_0$, $Y = \Pi(x')/\rho_0$, and $Z = i2m(\theta(x) - \theta(x')) - i(\phi(x) - \phi(x'))$. Using the fact that the fields $X$, $Y$ and $Z$ are Gaussian with zero average, we obtain from Wick's theorem

$$\begin{aligned}\left\langle \sqrt{1+X}\,\mathrm{e}^{Z}\sqrt{1+Y}\right\rangle = \mathrm{e}^{\frac{1}{2}\langle Z^2\rangle}\sum_{k,l=0}^{\infty}\sum_{j=0}^{\min(k,l)} & \frac{(2k)!(2l)!}{k!l!(2k-1)(2l-1)} \\ \times\ \frac{\langle X^2\rangle^{\frac{k-j}{2}}\langle Y^2\rangle^{\frac{l-j}{2}}\langle XY\rangle^{j}}{(i\sqrt{2})^{5(k+l)-2j}j!(k-j)!(l-j)!} & \,\mathrm{H}_{k-j}\left(\frac{\langle XZ\rangle}{i\sqrt{2\langle X^2\rangle}}\right)\mathrm{H}_{l-j}\left(\frac{\langle ZY\rangle}{i\sqrt{2\langle Y^2\rangle}}\right), \end{aligned} \tag{5.46}$$

where $\mathrm{H}_n(x)$ are the Hermite polynomials. To second order in $X$ and $Y$ Eq. (5.46) reads

$$\begin{aligned}\left\langle \sqrt{1+X}\,\mathrm{e}^{Z}\sqrt{1+Y}\right\rangle \simeq \mathrm{e}^{\frac{1}{2}\langle Z^2\rangle} & \Bigg[1+\frac{1}{2}\left(\langle XZ\rangle+\langle ZY\rangle\right) \\ & -\frac{1}{8}\left(\langle X^2\rangle+\langle Y^2\rangle-2\langle XY\rangle\right)-\frac{1}{8}\left(\langle XZ\rangle-\langle ZY\rangle\right)^2\Bigg]. \end{aligned} \tag{5.47}$$

Main expression (5.46), detailed in appendix D, requires then the calculation of the various two-point correlation functions involving the three fields $X$, $Y$, and $Z$. All of them can be obtained from the following correlators in the thermodynamic limit

$$\langle\varphi(x)\varphi(x')\rangle = (\pi/L)^2\langle J_0^2\rangle xx' - \frac{1}{4K}\ln C(x-x'), \tag{5.48}$$

$$\langle\theta(x)\theta(x')\rangle = \pi^2\langle\Pi_0^2\rangle xx' - \frac{K}{4}\ln C(x-x'), \tag{5.49}$$

$$\langle\theta(x)\varphi(x')\rangle = \frac{1}{4}\ln\left[\frac{1-\mathrm{e}^{-2\pi a/L-i2\pi(x-x')/L}}{1-\mathrm{e}^{-2\pi a/L+i2\pi(x-x')/L}}\right], \tag{5.50}$$

$$\left[\theta(x),\varphi(x')\right] = i\frac{\pi}{L}(x-x') + 2\langle\theta(x)\varphi(x')\rangle, \tag{5.51}$$

where $C(x) = 1-2\cos(2\pi x/L)\,\mathrm{e}^{-2\frac{\pi a}{L}} + \mathrm{e}^{-4\frac{\pi a}{L}}$. In the thermodynamic limit, the boundary conditions do not enter into account and for convenience we have used the case of periodic boundary conditions to derive the preceding correlators. Notice that the effect of the zero-modes $\Pi_0$ and $J_0$ is absent in the thermodynamic limit, because it scales as $1/L$. We are now in a position to calculate the correlators between the fields $X$, $Y$, and $Z$ in the thermodynamic limit. Using Eqs. (5.48)–(5.50) we have

$$\exp(\langle Z^2\rangle/2) \simeq \left(\frac{\alpha^2}{z^2+\alpha^2}\right)^{\frac{1}{4K}+Km^2} \tag{5.52}$$

$$\langle XZ\rangle = \langle ZY\rangle \simeq \frac{z}{2\alpha}\frac{z+i2Km\alpha}{z^2+\alpha^2} \tag{5.53}$$

$$\langle XY\rangle \simeq \frac{K}{2}\frac{\alpha^2-z^2}{(z^2+\alpha^2)^2} \tag{5.54}$$

$$\langle X^2\rangle = \langle Y^2\rangle \simeq \frac{K}{2\alpha^2}. \tag{5.55}$$

where $\alpha = \pi\rho_0 a$. Similarly, the commutator in Eq. (5.45) is obtained from Eq. (5.51) as

$$\exp\left(m\left[\theta(x)+\theta(x'),\varphi(x)-\varphi(x')\right]\right) \simeq \left(\frac{\alpha-iz}{\alpha+iz}\right)^m \tag{5.56}$$

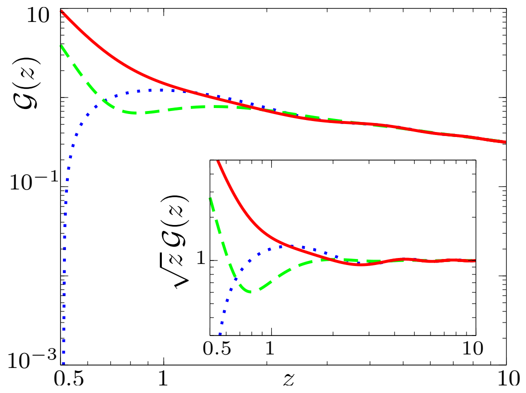

Figure 5.13: One-body density matrix in the Tonks-Girardeau limit $K = 1$ in units of $\rho_0\rho_\infty$ as a function of the scaled relative coordinate $z = \pi\rho_0(x - x')$ (dimensionless). The result of the generalized harmonic-fluid approximation Eq. (5.58) obtained without taking into account the effect of the field $\Pi(x)$ (solid line) is compared to the exact result Eq. (5.42) (dashed line) and to the usual harmonic-fluid approximation Eq. (5.43) (dotted line), with $B_0 = 1$, $B_1 = -1/2$ and $B_{m>1} = 0$. The value chosen for the cutoff parameter is $\alpha = 1/2$. The inset shows the subleading behavior $z^{1/2}\mathcal{G}(z)$ of the one-body density matrix in the same notations and units as in the main graph.

The series expansion in $\Pi/\rho_0$ is valid for small fluctuations of the field $\Pi(x)$ compared to the average density $\rho_0$, $\sqrt{\langle X^2\rangle} \lesssim 1$ *i.e.* for $\alpha \gtrsim \sqrt{K/2}$. By combining the previous equations we obtain the final result for the one-body density matrix, finding the structure:

$$\mathcal{G}(z) = \frac{\rho_0\rho_\infty}{|z|^{1/2K}}\left[1 + \sum_{n=1}^{\infty}\frac{a'_n}{z^{2n}} + \sum_{m=1}^{\infty} b_m \frac{\cos(2mz)}{z^{2m^2K}}\left(\sum_{n=0}^{\infty}\frac{b'_n}{z^{2n}}\right)\right.$$
$$\left. + \sum_{m=1}^{\infty} c_m \frac{\sin(2mz)}{z^{2m^2K+1}}\left(\sum_{n=0}^{\infty}\frac{c'_n}{z^{2n}}\right)\right], \tag{5.57}$$
$$\simeq \frac{\rho_0\rho_\infty}{|z|^{1/2K}}\left[1 + \frac{d_{0,2}}{z^2} + \frac{d_{0,4}}{z^4} + d_{1,2}\frac{\cos(2z)}{z^{2K}} + d_{1,4}\frac{\cos(2z)}{z^{2K+2}} + d_{1,3}\frac{\sin(2z)}{z^{2K+1}} + \ldots\right], \tag{5.58}$$

with $\rho_\infty = |\mathcal{A}|^2\alpha^{1/2K}d_{0,0}$. Therefore, by defining a properly regularized harmonic-fluid model the general structure of the one-body density matrix can be obtained for arbitrary values of the Luttinger parameter $K$. All the coefficients $a'_n$, $b_m$, $b'_n$, $c_m$, $c'_n$ and $d_{n,m}$ are nonuniversal and need to be calculated by a fully microscopic theory (for possible methods see *e.g.* Refs. [184, 185]). We note that Eq. (5.57)

i. generalizes Eq. (5.43).

ii. has the full structure of the exact result (5.42) in the Tonks-Girardeau limit.

As a direct consequence of the series structure (5.57) the momentum distribution will display singularities in its derivatives for $k = \pm 2m\pi\rho_0$.

A few comments are in order at this point. First, by taking the limit $a \to 0$ in Eqs. (5.48)–(5.51) we recover the results of the standard harmonic-fluid approach, *i.e.* Eq. (5.43). Moreover, the generalized harmonic-fluid method produces also the corresponding coefficients of the series, namely to the order of approximation derived in this work, we have

$$d_{0,0} \simeq 1\left[1+\frac{1}{2\alpha}-\frac{K}{8\alpha^2}+\frac{K}{16\alpha^3}\right], \qquad d_{0,2} \simeq -\frac{\alpha^2}{4K\, d_{0,0}}\left[d_{0,0}+\frac{2K}{\alpha}+\frac{K^2}{2\alpha^2}\right], \tag{5.59}$$

$$d_{0,4} \simeq \frac{(1+4K)\alpha^4}{32K^2\, d_{0,0}}\left[d_{0,0}+\frac{4K}{\alpha}+\frac{K^2}{\alpha^2}\frac{12K+1}{4K+1}-\frac{K^3}{\alpha^3}\frac{6}{4K+1}\right], \tag{5.60}$$

$$d_{1,2} \simeq -2\alpha^{2K}, \qquad d_{1,3} \simeq \frac{4\alpha^{2K+1}}{d_{0,0}}\left[d_{0,0}+\frac{K}{2\alpha}+\frac{K^2}{16\alpha^3}\right], \tag{5.61}$$

$$d_{1,4} \simeq \frac{(1+8K+4K^2)\alpha^{2K+2}}{2K\, d_{0,0}}\left[d_{0,0}+\frac{2K}{\alpha}\frac{1+4K}{1+8K+4K^2}\right.$$
$$\left.+\frac{K^2}{2\alpha^2}\frac{1}{1+8K+4K^2}+\frac{K^3}{\alpha^3}\frac{1}{1+8K+4K^2}\right]. \tag{5.62}$$

However, it should be noted that these coefficients do not necessarily coincide *e.g.* in the limit $K=1$ with the exact ones in Eq. (5.42). Our approach is still effective, as it suffers from some limitations: first of all, we have just used a single-parameter regularization which neglects the details of the spectrum of the Bose fluid. Second, our approach relies on a hydrodynamic-like expression for the field operator (5.19) which implicitly assumes that the fluctuations of the field $\Pi(x)$ are "small", which is not always the case. On the other hand, we see from our derivation that the corrections due to the $\Pi(x)$ fluctuations renormalize the coefficients of the series to all orders, giving rise to the contributions in square brackets to the $d_{ij}$ above, but do not change the series structure.

Figure 5.13 shows our results for the one-body density matrix (Eq. (5.58), solid lines) for $K=1$ and a specific choice of the cutoff parameter $\alpha=1/2$ as suggested by the analysis of other correlation functions [116]. The comparison with the exact result for the Tonks-Girardeau gas (Eq. (5.42), dashed lines) yields a reasonable agreement, the difference being due to the fact that we have used for the sake of illustration the explicit expression for the coefficients $d_{i,j}$ derived in the current work. It should be noted in particular that our generalized harmonic-fluid approach restores the correct trend at short distances as compared to the usual harmonic-fluid approach (Eq. (5.43), dotted lines).

### 5.4.4 Momentum distribution

We proceed by studying the momentum distribution $n(q)$, obtained by Fourier transformation of the one-body density matrix with respect to the relative variable,

$$n(q)=\int_0^L \mathrm{d}x \int_0^L \mathrm{d}x'\, \mathrm{e}^{-iq(x-x')}\mathcal{G}(x,x'). \tag{5.63}$$

Here we take into account the effect of the fields $\phi(x)$ and $\theta(x)$ on the one-body density matrix. Including the field $\theta$ leads to the following extension of Eq. (5.40)

$$\mathcal{G}(x,x')=\rho_0|\mathcal{A}|^2 \sum_{(m,m')\in\mathbb{Z}^2} \mathrm{e}^{i2\pi\rho_0(mx-m'x')}\,\mathrm{e}^{i2\theta_B(m-m')}\,\mathrm{e}^{[m\theta(x)+m'\theta(x'),\phi(x)-\phi(x')]/2}$$
$$\times \exp\left[-\frac{1}{2}\left\langle\left(2m\theta(x)-2m'\theta(x')-\phi(x)+\phi(x')\right)^2\right\rangle\right]. \tag{5.64}$$

The new terms of $\mathcal{G}(x,x')$ involve the correlators $\langle\theta(x)\phi(x')\rangle = [\theta(x),\phi(x')]/2$ and

$$\langle\theta(x)\theta(x')\rangle = \pi^2\langle\Pi_0^2\rangle xx' - \frac{K}{4}\ln\left[\frac{\alpha^2+d^2(x-x'|2L)}{\alpha^2+d^2(x+x'|2L)}\right]. \tag{5.65}$$

The resulting one-body density matrix reads

$$\begin{aligned}\mathcal{G}(x,x') = \rho_0 &\left[\frac{\rho_0^{-2}\sqrt{[a^2+d^2(2x|2L)]\,[a^2+d^2(2x'|2L)]}}{[a^2+d^2(x-x'|2L)]\,[a^2+d^2(x+x'|2L)]}\right]^{\frac{1}{4K}}\\ &\times\sum_{m,m'} b_{m,m'}\,\mathrm{e}^{i2\pi\rho_0(mx-m'x')}\left[\frac{\alpha^2+d^2(x+x'|2L)}{\alpha^2-d^2(x-x'|2L)}\right]^{mm'K}\\ &\times\frac{\mathrm{e}^{-i\pi\mathrm{sgn}(x-x')/2}\,\mathrm{e}^{-2\pi^2\langle\Pi_0^2\rangle(mx-m'x')^2}}{\left[\rho_0^2\left(\alpha^2+d^2(2x|2L)\right)\right]^{m^2K/2}\left[\rho_0^2\left(\alpha^2+d^2(2x'|2L)\right)\right]^{m'^2K/2}},\end{aligned} \tag{5.66}$$

with the nonuniversal coefficients $b_{m,m'} = |\mathcal{A}|^2(\rho_0 a)^{1/2+(m^2+m'^2)K}\,\mathrm{e}^{i2\theta_B(m-m')}$.

We have resorted to a numerical calculation for the evaluation of the momentum distribution taking as input the one-body density matrix obtained in Eq. (5.66). This allows us to estimate the main features of the momentum distribution at wavevectors $q$ smaller than the cutoff wavevector $q_c \sim 1/\alpha$. The behavior at large wavevectors $q \gg q_c$ needs an accurate treatment of the short-distance behavior of the many-body wavefunction [186, 187] and is beyond the regime of validity of the Luttinger-liquid method. The result for the momentum distribution is illustrated in Fig. 5.14 for two values of the boson number in the ring, and at varying interaction strength. As a general feature (see the inset of Fig. 5.14), we observe that at intermediate values of $q$ the momentum distribution displays a power-law behavior $n(q) \sim q^{1/(2K)-1}$ with the same power predicted for a homogeneous ring in the thermodynamic limit (see *e.g.* Refs. [142] and [188] for a finite-size scaling analysis). This result is readily understood as the different power laws described in Sec. 5.4.2 only occur at the edge of the integration region with a negligible weight with respect to the bulk contribution. Still, by comparing the details of the momentum distribution of the ring with the barrier with the momentum distribution of a uniform ring, (see the main panel of Fig. 5.14), we find that in the presence of the barrier the momentum distribution is decreased at small momenta. This is in agreement with the fact that the barrier reduces the coherence along the ring. The result is reminiscent of the one obtained for a 1D gas in presence of disorder [189], where the reduction of the momentum distribution at small momenta is also observed.

### 5.4.5 Friedel oscillations in the particle density profile

Extending the quantum average techniques outlined in Sec. 5.4.2 to the limit of an infinitely high barrier, it is possible to evaluate also the inhomogeneous particle-density profile and the density-density correlation functions. Interference between particles incident on and reflected by the barrier leads to the occurrence of Friedel-like oscillations in the density profile and in its correlator, which are typical of strongly correlated 1D fluids. We describe here these oscillations within the Luttinger liquid approach, for any value of the coupling strength, finding that they are more and more marked as the coupling strength increases. In the Tonks-Girardeau limit of infinite boson-boson repulsion we

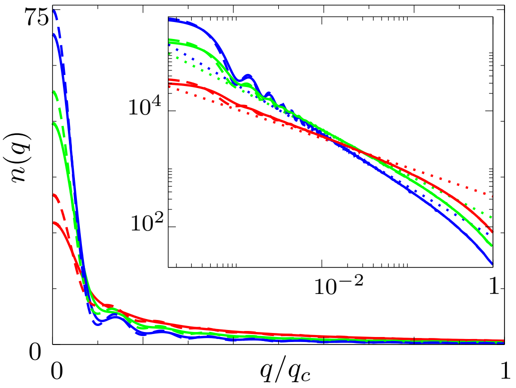

Figure 5.14: Momentum distribution $n(q)$ in units of $2\pi|\mathcal{A}|^2\alpha$ as a function of the wavevector $q$ in units of the cutoff momentum $q_c = 1/\alpha$ for $N = 10$ bosons on a ring with an infinite barrier (solid lines) and for a homogeneous ring in absence of the barrier (dashed lines) for various values of the Luttinger parameter $K$ (from top to bottom $K = 4,\ 2,\ 1$). The inset shows the same quantity (in logarithmic scale, arbitrary units, same line conventions as the main figure) evaluated for $N = 10^3$ bosons. The dotted lines indicate the predicted power law decays $q^{1/(2K)-1}$ in the thermodynamic limit.

compare the predictions of the Luttinger-liquid approach with the exact results, which enables us to fix the nonuniversal parameters of the latter.

We compute the particle-density profile by taking the quantum average $\langle\rho(x)\rangle$ of the density operator (5.69) on the ground state, namely

$$\langle\rho(x)\rangle/\rho_0 = \sum_{m=-\infty}^{+\infty} \langle(1+\Pi(x)/\rho_0)\mathrm{e}^{2mi\theta(x)}\rangle\, \mathrm{e}^{i2\pi m\rho_0 x+2im\theta_B}. \tag{5.67}$$

To evaluate the quantum averages we exploit the fact that the Hamiltonian (5.23) is quadratic in the field $\theta(x)$ (and recall that $\Pi(x) = \nabla\theta(x)/\pi$). We use the property that if $X$ and $Z$ are Gaussian variables then $\left\langle X\,\mathrm{e}^{Z}\right\rangle = \langle XZ\rangle\,\mathrm{e}^{\frac{1}{2}\langle Z^2\rangle}$. Hence, we are left with the evaluation of the $\langle\theta(x)\theta(x')\rangle$ correlation function, to be taken at equal points $x = x'$; the $\langle\Pi(x)\theta(x')\rangle$ correlation function is obtained from the previous one by taking the derivative with respect to the variable $x$. Using the mode expansion (5.35) and a procedure similar to the one outlined in Sec. 5.4.2 we obtain

$$\langle\Pi(x)\theta(x')\rangle = \pi\langle\Pi_0^2\rangle x' + \frac{K}{2\pi}\frac{d(x+x'|L)}{\alpha^2+d^2(x+x'|2L)} - \frac{K}{2\pi}\frac{d(x-x'|L)}{\alpha^2+d^2(x-x'|2L)}\mathrm{sgn}(x-x'). \tag{5.68}$$

The final expression for the density profile reads

$$\frac{\langle\rho(x)\rangle}{\rho_0} = 1 + 2\sum_{m=1}^{\infty}\left(\frac{\alpha^2}{\alpha^2+d^2(2x|2L)}\right)^{m^2K/2}\left[\cos(2m\pi\rho_0 x+2m\theta_B) - \frac{mK}{\pi\rho_0}\sin(2m\pi\rho_0 x+2m\theta_B)\frac{d(2x|L)}{\alpha^2+d^2(2x|2L)}\right]. \tag{5.69}$$

The density profile is modulated by oscillations with wavevector multiples of $2\pi\rho_0$. Notice that in the case $K = 1$, where the system can be mapped onto a noninteracting spin-polarized Fermi gas, the wavevectors of the oscillation are multiples of $2k_F$, where $k_F = \pi\rho_0$ is the Fermi wavevector, and hence correspond to the well-known Friedel oscillations [190]. For the case of generic $K$ the $m = 1$ oscillations decay with the power law $x^{-K}$ (see *e.g.* Ref. [191]).

Let us now concentrate on the case $K = 1$. In the thermodynamic limit ($L \to \infty$, $N \to \infty$, at fixed $\rho_0 = N/L$) the expression (5.69) for the density profile at short distances (to $O(1/x)$) reduces to

$$\frac{\langle\rho(x)\rangle}{\rho_0} \simeq 1 + \alpha\frac{\cos(2\pi\rho_0 x + 2\theta_B)}{x}. \tag{5.70}$$

This can be compared with the thermodynamic limit of the exact expression derived using the Bose-Fermi mapping [153, 192]

$$\frac{\langle\rho(x)\rangle}{\rho_0} \simeq 1 - \frac{\sin(2\pi\rho_0 x)}{2\pi\rho_0 x}, \tag{5.71}$$

allowing us to fix the coefficients $\alpha$ and $\theta_B$ to the values

$$\alpha = \frac{1}{2\pi\rho_0}, \tag{5.72}$$

and

$$\theta_B = \frac{\pi}{4}. \tag{5.73}$$

Note that the latter choice for $\theta_B$ is in agreement with the condition $\theta_B \neq 0, \pm\pi, \pm 2\pi \ldots$ obtained by imposing that the particle density profile should vanish at $x = 0$ and $x = L$ [171]. Once the constants $\alpha$ and $\theta_B$ are chosen, the constant $\mathcal{A}$ in Eq. (5.19) can be fixed by comparing the expression for the coefficient $b_{00}$ entering Eq. (5.40) for the one-body density matrix with the exact value $b_{00}^{\mathrm{exact}} = 2^{-1/3}\sqrt{\pi \mathrm{e}} A_G^{-6} \sim 0.521$ [152, 153] where $A_G = 1.282\ldots$ is Glaisher's constant. The result is

$$|\mathcal{A}|^2 = 2^{1/6}\pi\, \mathrm{e}^{1/2} A_G^{-6} \simeq 1.307\ldots. \tag{5.74}$$

This value has been used in plotting Fig. 5.12.

In Figure 5.15 we illustrate the density profiles for various values of $K$, obtained by the Luttinger-liquid expression (5.69) using the above choice for $\alpha$ and $\theta_B$. In absence of known results for the case of arbitrary $K$, we have adopted the same choice of parameters $\mathcal{A}$, $\alpha$ and $\theta_B$ for any value of $K$. The figure displays also the exact result for the density profile obtained from the Bose-Fermi mapping, $\rho^{\mathrm{exact}}(x) = \sum_{j=1}^{N} |\psi_j(x)|^2$. In our specific case, the orbitals are

$$\psi_j(x) = \sqrt{\frac{2}{L}}\sin(\pi j x/L), \tag{5.75}$$

with $j = 1, ..., \infty$. The comparison shows how our choice of parameters $\alpha$ and $\theta_B$ reproduces extremely well the density profile oscillations even on a finite ring. The figure also illustrates how the Friedel oscillations display maximal amplitude in the strongly interacting limit $K = 1$.

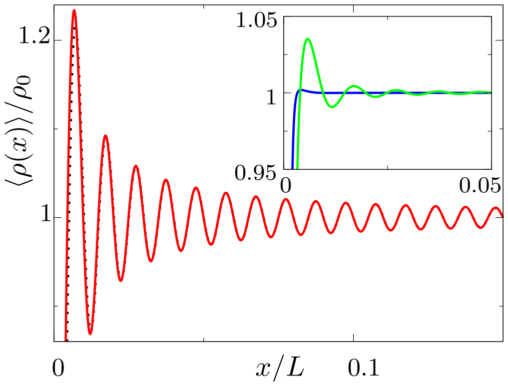

Figure 5.15: Particle density profile $\langle\rho(x)\rangle$ in units of the average particle density $\rho_0$ as a function of the spatial coordinate $x$ along the ring (in units of the ring circumference $L$) for various values of the parameter $K$. Main figure, $K = 1$ (solid line: result from the Luttinger-liquid model, dotted line, exact result from the Bose-Fermi mapping); Inset, $K = 2$ (top green line) and $K = 4$ (bottom blue line).

### 5.4.6 Density-density correlation function from Luttinger-liquid theory

We turn now to the density-density correlation function $S(x, x') = \langle\rho(x)\rho(x')\rangle - \langle\rho(x)\rangle\langle\rho(x')\rangle$. This quantity encodes the information on the structure of the fluid, *i.e.* on the correlations between density modulations at different parts of the fluid, while it vanishes for an ideal Bose gas. The Fourier transform of the density-density correlation function with respect to the relative variable is directly accessible experimentally by light-scattering methods (see *e.g.* [193] and references therein).

The density-density correlation function is obtained with the quantum average method described in Sec. 5.4.2 and 5.4.5. One has to compute

$$\langle\rho(x)\rho(x')\rangle = \sum_{m,m'=-\infty}^{+\infty} \mathrm{e}^{2i(m-m')\theta_B}\,\mathrm{e}^{i2\pi\rho_0(mx-m'x')} \\ \times \left\langle \left[{\rho_0}^2 + \rho_0(\Pi(x)+\Pi(x')) + \Pi(x)\Pi(x')\right] \mathrm{e}^{2i(m\theta(x)-m'\theta(x'))} \right\rangle . \quad (5.76)$$

The average can be performed using the general result for Gaussian variables $\left\langle XY\mathrm{e}^{Z}\right\rangle = \left(\langle XY\rangle + \langle XZ\rangle\langle YZ\rangle\right)\mathrm{e}^{\frac{1}{2}\langle Z^2\rangle}$. The novel correlator needed for the calculation in addition to Eqs. (5.65) and (5.68) is

$$\langle\Pi(x)\Pi(x')\rangle = \langle\Pi_0^2\rangle - \frac{K}{2\pi^2}\left[ \frac{d^2(x-x'|2L) - \alpha^2\cos(\pi(x-x')/L)}{(\alpha^2 + d^2(x-x'|2L))^2} \right. \\ \left. + \frac{d^2(x+x'|2L) - \alpha^2\cos(\pi(x+x')/L)}{(\alpha^2 + d^2(x+x'|2L))^2} \right] . \quad (5.77)$$

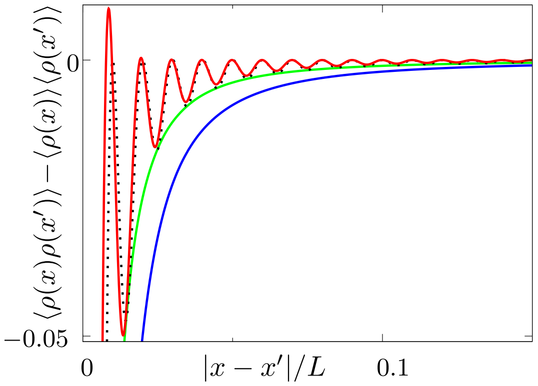

Figure 5.16: Density-density correlation function $S(x,x')$ (in units of $\rho_0^2$) from the Luttinger-liquid model as a function of the coordinate $x'$ (in units of the ring circumference $L$), with $x = L/2$ and for various values of the Luttinger parameter $K$ ($K = 1$, top red line, $K = 2$, middle green line, $K = 4$ bottom blue line). The dotted line corresponds to the exact solution obtained from the Bose-Fermi mapping in the case $K = 1$.

The final result reads

$$\begin{aligned}\langle\rho(x)\rho(x')\rangle = &\sum_{m,m'=-\infty}^{+\infty} (\rho_0\alpha)^{(m^2+m'^2)K}\,\mathrm{e}^{2i(m-m')\theta_B}\mathrm{e}^{i2\pi\rho_0(mx-m'x')}\\ &\times\Big[\rho_0^2+\langle\Pi(x)\Pi(x')\rangle+2i\rho_0\langle(\Pi(x)+\Pi(x'))(m\theta(x)-m'\theta(x'))\rangle\\ &\quad-4\langle\Pi(x)(m\theta(x)-m'\theta(x'))\rangle\langle\Pi(x')(m\theta(x)-m'\theta(x'))\rangle\Big]\\ \times&\left(\frac{\alpha^2+d^2(x+x'|2L)}{\alpha^2+d^2(x-x'|2L)}\right)^{mm'K}\left(\frac{\rho_0^{-2}}{\alpha^2+d^2(2x|2L)}\right)^{m^2K/2}\left(\frac{\rho_0^{-2}}{\alpha^2+d^2(2x'|2L)}\right)^{m'^2K/2}.\end{aligned} \tag{5.78}$$

This equation displays the general structure of the density-density correlations to all orders in $m$ and $m'$, and by considering only the first terms of the expansion $m, m' = 0, \pm 1$ we recover the known results [142, 171].

We proceed by comparing the density-density correlation function $S(x,x')$ with the exact result for $K = 1$. The latter is obtained from the Bose-Fermi mapping as [193]:

$$S^{\mathrm{exact}}(x,x') = -\left[\sum_{j=1}^{N}\psi_j{}^*(x)\psi_j(x')\right]^2, \tag{5.79}$$

where the single-particle orbitals $\psi_j(x)$ are defined in Eq. (5.75).

Figure 5.16 displays the results obtained from the Luttinger-liquid method at various values of the Luttinger parameter $K$, using the choice of parameters $\alpha$ and $\theta_B$ determined from the density profile in Sec. 5.4.5 and compares to the exact ones in the case $K = 1$. The agreement found is very good, even for the Friedel-like oscillations at wave vector $k \sim 2\pi\rho_0$; this is at the boundary of the expected regime of validity of the Luttinger-liquid theory and illustrates how a reasonable choice of the non-universal parameters in the effective model allows for surprisingly accurate predictions.

## 5.5 Bose Josephson junction in a ring trap

### 5.5.1 Josephson Hamiltonian

In this section we consider the effect of a large but finite barrier on the ring. Quantum fluctuations tend to destroy the phase coherence along the ring, while the tunneling of bosons between the ends of the loop favors a well-defined phase difference across the barrier. We will study the interplay between these competing effects in the framework of the Luttinger liquid formalism.

The barrier is realized with a localized magnetic or optical potential $V_{\rm bar}(x)$ which is non-zero only on a width $a$ around $x = 0 \equiv L$. We describe the tunneling of bosons through the barrier with the following tunnel Hamiltonian

$$\mathcal{H}_J = -\mathcal{T}\,\Psi^\dagger(L)\Psi(0) + \text{h.c.}\,, \tag{5.80}$$

where $\mathcal{T}$ is the tunneling strength that characterizes $V_{\rm bar}$. Hamiltonian (5.80) takes into account the possibility for a boson to tunnel through the barrier potential from $x = 0^+$ to $x = L^-$, and *h.c.* refers to the Hermitian conjugate corresponding to tunneling events in the opposite direction. In the hydrodynamic formulation for $\Psi^\dagger(x)$, the transfer of one boson is ensured by the operator $\exp(-i\varphi)$ where $\varphi = \phi(L) - \phi(0)$. By neglecting the density fluctuations in the field operator (5.19) we then recover the usual Josephson Hamiltonian

$$\mathcal{H}_J = -E_J \cos\varphi, \tag{5.81}$$

where $E_J = 2\rho_0\mathcal{T}$ is the Josephson energy of the junction.

### 5.5.2 Renormalization of the Josephson energy by quantum fluctuations

Quantum fluctuations of the bosons in the ring on both sides of the barrier tend to smear the phase $\varphi$ and hence suppress the tunneling strength. Indeed, from the diagonal Hamiltonian (5.32), the ring constitutes an oscillator bath for the junction with linear spectrum $\hbar\omega_{k_j} = \pi\hbar v_S j/L$; the resulting model is very similar to the one describing a superconducting Josephson junction coupled to a resistive environment [47]. The path integral renormalization group approach is presented in appendix D.2. Tunneling events thus induce excitations of the modes of the ring with energy between $\hbar\omega_0 = \pi\hbar v_S/L$ and the high energy cutoff $\hbar\omega_h = \pi\hbar v_S/a$.

When the Josephson energy is smaller than the lowest mode $\hbar\omega_0$, corresponding to small rings $L < L^* \sim \hbar v_S/E_J$, the junction can be treated as a perturbation and every mode modifies $E_J$ (see Fig. 5.17, left panel). The effective Josephson energy results from averaging $\mathcal{H}_J$, Eq. (5.81), with respect to the ground state of the unperturbed Hamiltonian (5.23): $E_J^{\rm eff} = \langle\mathcal{H}_J\rangle$ with $\langle\mathcal{H}_J\rangle/E_J = \mathcal{G}_0(L,a)/\rho_0$. Then

$$E_J^{\rm eff} = E_J\left(\frac{\pi a}{2L}\right)^{1/K} \quad \text{for } L < L^*. \tag{5.82}$$

The Josephson energy decreases with the power law $L^{-1/K}$ of the one-body density for probe points at the edges of the ring. This case includes the limit of an infinitely high barrier, where $E_J \to 0$, $L^* \to \infty$, and which is illustrated in Fig. 5.12, rightmost panel.

When $E_J$ is larger than $\hbar\omega_0$ (with $E_J < \hbar\omega_h$), only the modes with energies larger than $E_J$ contribute to the renormalization (see Fig. 5.17, right panel). Consequently,

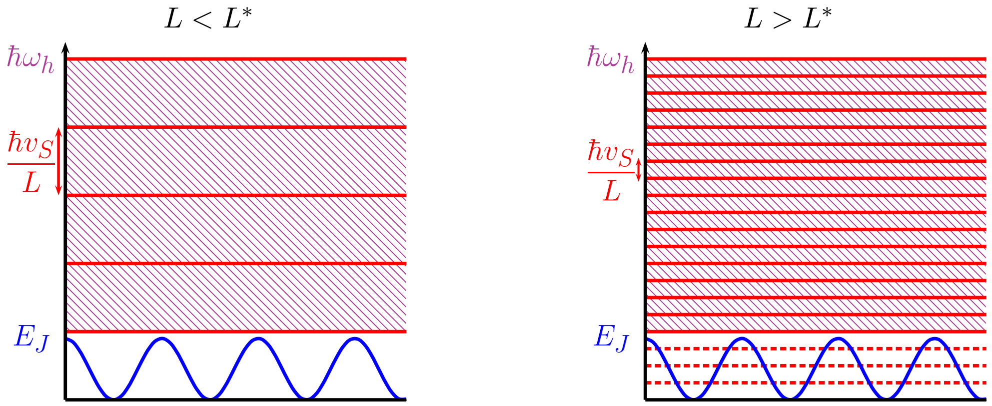

Figure 5.17: Renormalization schemes of the Josephson energy by quantum fluctuations for a small ring ($L < L^*$, left panel) and for a large ring ($L > L^*$, right panel).

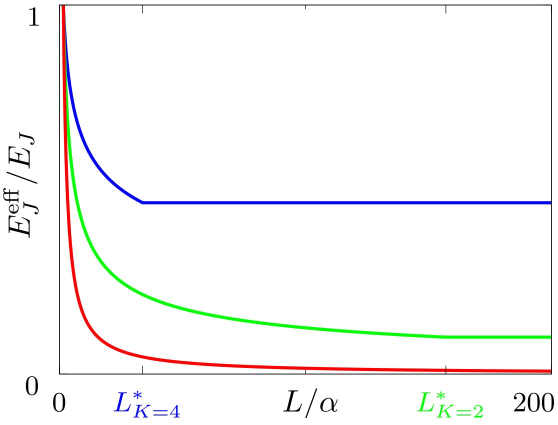

Figure 5.18: Renormalized Josephson energy as a function of the length of the ring. From top to bottom $K = 4,\ 2,\ 1$ with $\hbar\omega_h = 10\,E_J$. $E_J^{\mathrm{eff}}$ decreases as $1/L^{1/K}$ and reaches a constant value at $L = L^*$.

to obtain the effective Josephson energy we need to average over wavelengths between $a$ and the characteristic length $\ell \equiv \pi\hbar v_S/E_J^{\mathrm{eff}}$: $E_J^{\mathrm{eff}} = \langle\langle \mathcal{H}_J \rangle\rangle$ with

$$E_J^{\mathrm{eff}}/E_J = \mathcal{G}_0(L,a)/\mathcal{G}_0(\ell,a) \sim (a/\ell)^{1/K} \tag{5.83}$$

The effective Josephson energy in this case is obtained by solving the above self-consistent equation with respect to $\ell$, with the result

$$E_J^{\mathrm{eff}} = E_J \left(\frac{aE_J}{\pi\hbar v_S}\right)^{1/(K-1)} \qquad \text{for } L > L^*. \tag{5.84}$$

In this case $E_J^{\mathrm{eff}}$ is independent on the ring circumference $L$. Our results (5.82) and (5.84) are summarized in Fig. 5.18. Quantum fluctuations dramatically reduce the tunnel amplitude with respect to its bare value entering the Hamiltonian (5.80), especially in the case $K = 1$. Note however that the reduction saturates at a nonzero level for rings larger than the so-called healing length $L^*$. The continuity between the two regimes $L < L^*$ and $L > L^*$ defines the healing length of the ring $L^* = \pi a/2(\pi\hbar v_S/aE_J)^{K/(K-1)}$. As a final remark, we mention that our approach is equivalent to the renormalization group formalism [194] or the self-consistent harmonic approximation [47]. Eqs. (5.82) and (5.84) can be obtained from the flow equation Eq. (D.24), derived in appendix D.2 and also in Ref. [195].

## Conclusion and perspectives

As a main conclusion, by taking into account the effect of quantum fluctuations we find that the effective Josephson energy is reduced with respect to its bare value, in a way which depends on the length of the ring with respect to a typical healing length, a maximal reduction occurring for long rings.

The effect of the renormalization of the tunnel amplitude is expected to have strong consequences on the dynamical evolution of the ring-trapped Bose gas with a Josephson junction, especially for the study of quantum revivals resulting from a localized excitation in the density distribution.

# L'effet Josephson dans un gaz bosonique unidimensionnel

## Résumé du chapitre

L'EFFET Josephson apparaît lorsque deux objets cohérents en phase sont approchés suffisamment près l'un de l'autre pour que l'échange tunnel y soit effectif. C'est le cas pour les métaux supraconducteurs mais aussi pour les gaz quantiques. Nous étudions un gaz d'atomes ultra-froids piégé dans un potentiel circulaire comportant une barrière, créant ainsi une jonction de Bose Josephson. Bien que les premières expériences dans cette géométrie restent dans la limite bidimensionnelle, nous considérons le cas unidimensionnel. L'utilisation du formalisme du liquide de Luttinger nous permet de décrire la physique à basse énergie du système à travers les fonctions de corrélation spatiale pour une force d'interaction arbitraire. Ces propagateurs sont comparés aux résultats exacts disponibles dans le régime des très fortes interactions de Tonks Girardeau. Nous obtenons des oscillations de Friedel dues à la barrière dans le profil de densité et les corrélations densité-densité sont en bon accord avec les résultats exacts même sur des distances de l'ordre de la longueur inter-atomique moyenne. La cohérence de phase du système est donnée par la matrice densité à un corps, qui décroît selon des lois de puissance dépendant de la position des points de mesure vis-à-vis de la barrière, signature d'un quasi-ordre à longue distance. La distribution des impulsions, transformée de Fourier de la matrice densité, présente en conséquence une décroissance en loi de puissance dépendant de la force des interactions. Notre régularisation de la théorie effective génère la série complète des corrections dans la limite thermodynamique et tient compte des fluctuations de longue longueur d'onde. Enfin, nous montrons que les fluctuations quantiques dans l'anneau induisent une renormalisation de la transparence tunnel de la jonction, entraînant une réduction de l'énergie Josephson effective. Cette réduction dépend de la longueur de la boucle et de la force des interactions, l'effet étant maximal pour un gaz de Tonks Girardeau.

Chapter 6

# Conclusions and Perspectives

## Conclusions

As a conclusion, we have studied four quantum mechanical systems with the appropriate theoretical tools and, as far as possible, worked in collaboration with experimentalists to compare our results with the measurements or design new setups. Our main results in these different projects are the following

**1st chapter:** Presentation of the quantum-mechanical Josephson Hamiltonian.

**2nd chapter:** Current-voltage characteristics of an underdamped Josephson junction, from the classical to the low temperature regime; Quantum Smoluchowski equation for the quasicharge dynamics.

**3rd chapter:** Optimal line of the dc SQUID phase qubit for current noise; Escape rate in the camel-back potential.

**4th chapter:** Temporal dynamics and output spectrum from the Lindbladian of a charge qubit coupled to a cavity; Optimal parameters to observe the lasing effect for a transmon coupled to two cavities.

**5th chapter:** Power law decays, Friedel oscillations and renormalization of the Josephson energy by quantum fluctuations for a Bose Josephson junction realized with a one-dimensional ring of cold atoms closed by a localized barrier; Subleading corrections to the one-body density matrix of bosons in a homogeneous cigar shape potential in the thermodynamic limit.

Research in the field of quantum mesoscopic systems is rich and prolific, and many promising (not necessarily successful, unfortunately) ideas cross our mind. Some of these perspectives are presented in the following section.

## Perspectives

### $\alpha$ *Quantum spectral function of an underdamped Josephson junction*

The steady-state voltage is not sufficient to describe the measured signal of a Josephson junction. A useful quantity is the voltage noise, *i.e.* the two point correlation function of the voltage operator. The voltage spectral function may be of particular interest in the use of a Josephson junction as a current standard. The formalism used to calculate the current-voltage characteristics of underdamped Josephson junctions can be extended to obtain the voltage spectrum $\mathcal{S}(\omega) = \int_{-\infty}^{+\infty} \mathrm{d}\tau_0 \, \mathrm{e}^{-2i\omega\tau_0} \langle V^{s_0}(\tau_0) V^{s_{-1}}(-\tau_0)\rangle$. An Extended Nearest Neighbor Approximation is needed for analytical results. Primary results are encouraging (see Fig. 6.1). The formalism can then be applied to the case of overdamped Josephson junctions using the duality transformations.

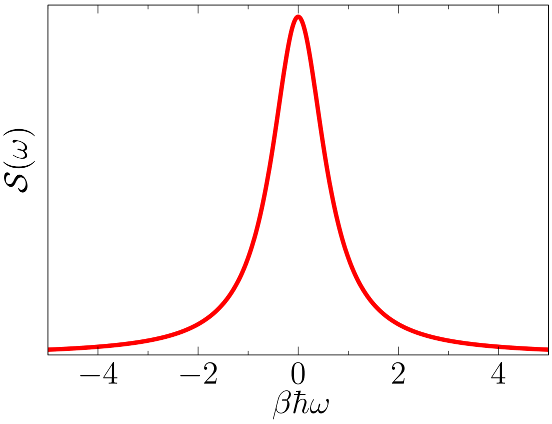

Figure 6.1: Real part of the symmetrized voltage spectrum $\mathcal{S}(\beta\hbar\omega)$ from an extended analysis of Chap. 2 with $\beta U_0 = 0.1$, $\beta\hbar\omega_c = 10$, $g = 0.1$, $I_b = V_c/R$ and $s_{-1} = -s_0$.

### $\beta$ *Possible amplification of the moments of a mesoscopic device*

All the moments of a measured quantity, *i.e.* its many-point correlation functions, are necessary to fully describe the observable. This idea was well summarized by Rolf Landauer in his famous expression “the noise is the signal” [196]. The amplitude of the third and higher moments is tiny, as a consequence it is hardly possible to measure them. They need to be amplified. We can take advantage of the nonlinear character of the Josephson junction to amplify them. The basic idea comes from the analysis of Ref. [17], where the spectral function of the voltage of an overdamped Josephson junction is found to be $\mathcal{S}_V(\omega) = \sum_k |Z_k(\omega - k\omega_J)|^2 \mathcal{S}_I(\omega - k\omega_J)$ in the classical limit. The terms $|Z_k(\omega - k\omega_J)|^2$ amplify and downconvert the current spectral function $\mathcal{S}_I(\omega)$ of a tunneling device (see Fig. 6.2). This result can be generalized to the full counting statistics to understand if it is possible to use the Josephson junction in experiments as an amplifier of the cumulants of a tunneling device [80, 197].

### $\gamma$ *Phase dynamics of a closed one-dimensional Josephson junction array*

Josephson junction arrays are used for instance to generate highly resistive environments, but their dynamics is complex and not fully understood [198, 199]. In this project, we study the dynamics of the phases in a flux biased superconducting loop interrupted by several Josephson junctions. The minimization of the Lagrangian $\mathcal{L} = \sum_{i=1}^{N} \left[C_i \dot{\varphi}_i^2/2 + E_{Ji}\cos(\varphi_i)\right] + C_{N+1}\left(\sum \dot{\varphi}_i\right)^2/2 + E_{JN+1}\cos\left(\phi - \sum \varphi_i\right)$, gives rise to

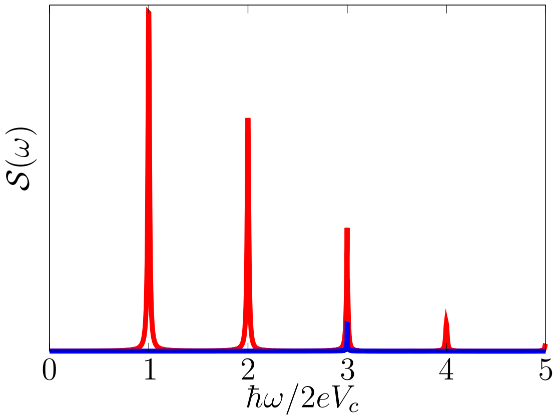

Figure 6.2: The shot noise [81] $\mathcal{S}_I(\omega)$ (blue line) of a tunneling device is amplified and downconverted in the voltage spectral function $\mathcal{S}_V(\omega)$ (red line) of a Josephson junction.

different solutions differing by the number of phase-slips along the ring (see Fig. 6.3). So as to understand the physics of this system, we analyse some of its features, including the energy spectrum, the effective action, the Zener transitions and the continuum limit. We use a group theory approach [200] to determine the energy level degeneracy. This analysis may show how this chain could be used as an inductance and how it could describe a superconducting nanowire. The study of this system has also applications in the field of cold atoms in optical lattices, it can be seen as the discrete version of the ring shape potential.

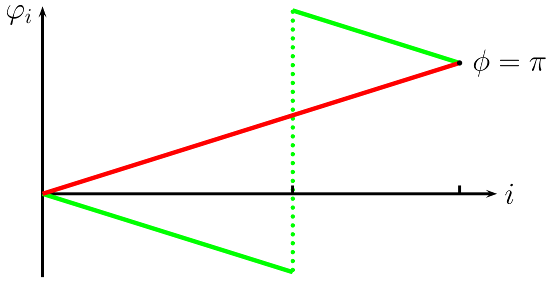

Figure 6.3: Phase distribution along the ring in the absence of phase-slip and in the presence of one phase-slip. For a flux bias equal to $\pi$, these two configurations are degenerated.

### $\delta$ *Quantum revivals of a Bose Josephson junction on a ring trap*

The analysis of Chap. 5 deals with the static properties of the Bose Josephson junction on a ring shape potential. The next step is the study of its temporal evolution. The response to a local excitation in the density, for instance a population imbalance, is an interesting project. Indeed it would explain if quantum revivals appear, as it is seen in other similar systems [201]. The answer involves the calculation of two-time correlation functions, which can be performed from our study in the stationary regime.

APPENDIX A

# Josephson junction coupled to a strongly dissipative environment

**Contents**

## Introduction

In this appendix we detail the derivation of various results for the underdamped Josephson junction studied in Chap. 2, such as the average over the bath and the $I$-$V$ characteristics.

## A.1 Wick's theorem in Keldysh formalism

To prove that $\langle \mathcal{T}_\mathcal{C}\, \mathrm{e}^{-iX} \rangle = \mathrm{e}^{-\frac{1}{2}\overline{XX}}$ with $\overline{XX} = \langle \mathcal{T}_\mathcal{C}\, XX \rangle$, we expand the exponential function in power series

$$\langle \mathcal{T}_\mathcal{C}\, \mathrm{e}^{-iX} \rangle = \sum_{n=0}^{\infty} \frac{(-i)^n}{n!} \langle \mathcal{T}_\mathcal{C}\, X^n \rangle = \sum_{n=0}^{\infty} \frac{(-1)^n}{(2n)!} \langle \mathcal{T}_\mathcal{C}\, X^{2n} \rangle. \tag{A.1}$$

The sum runs only on even exponents because the average value of an odd number of bath operators vanishes. We then prove by mathematical induction that

$$\forall n \in \mathbb{N} \qquad \langle \mathcal{T}_\mathcal{C}\, X^{2n} \rangle = \frac{(2n)!}{2^n n!} \overline{XX}^n \quad (\mathcal{P}_n) \tag{A.2}$$

- $\mathcal{P}_0$ is true.
- Let us suppose $\mathcal{P}_n$ true at the order $n$. Then, according to Wick's theorem,

$$\begin{aligned}&\langle \mathcal{T}_\mathcal{C}\, X_{2n+2}X_{2n+1}X_{2n}X_{2n-1}\dots X_2X_1\rangle\\ =&\langle \mathcal{T}_\mathcal{C}\, X_{2n+2}X_{2n+1}\rangle\langle \mathcal{T}_\mathcal{C}\, X_{2n}X_{2n-1}\dots X_2X_1\rangle\\ &+\langle \mathcal{T}_\mathcal{C}\, X_{2n+2}X_{2n}\rangle\langle \mathcal{T}_\mathcal{C}\, X_{2n+1}X_{2n-1}\dots X_2X_1\rangle\\ &+\dots\\ &+\langle \mathcal{T}_\mathcal{C}\, X_{2n+2}X_1\rangle\langle \mathcal{T}_\mathcal{C}\, X_{2n+1}X_{2n}\dots X_3X_2\rangle\\ =&(2n+1)\langle \mathcal{T}_\mathcal{C}\, X_{2n+1}X_{2n+2}\rangle\langle \mathcal{T}_\mathcal{C}\, X_1X_2\dots X_{2n}\rangle\\ =&(2n+1)\overline{XX}\,\frac{(2n)!}{2^n n!}\overline{XX}^n\\ =&\frac{(2(n+1))!}{2^{n+1}(n+1)!}\overline{XX}^{n+1}\end{aligned}\tag{A.3}$$

  Therefore $\mathcal{P}_n \Rightarrow \mathcal{P}_{n+1}$.

The proposition $\mathcal{P}_n$ is thus true on $\mathbb{N}$.

We finally obtain

$$\langle \mathcal{T}_\mathcal{C}\, \mathrm{e}^{-iX}\rangle = \sum_{n=0}^{\infty}\frac{(-1)^n}{(2n)!}\frac{(2n)!}{2^n n!}\overline{XX}^n = \sum_{n=0}^{\infty}\frac{1}{n!}\left(-\frac{\overline{XX}}{2}\right)^n = \mathrm{e}^{-\frac{1}{2}\overline{XX}},\tag{A.4}$$

Actually, this simple demonstration does not depend on the representation for the Green's functions. One only needs to define the time ordering operator properly.

## A.2 Bath spectral function

The equations of motion relative to the Hamiltonian

$$\mathcal{H} = -U_0\cos(\pi q/e-\xi) - \phi_0 I_b\phi + \sum_\alpha \frac{\hbar\omega_\alpha}{2}(p_\alpha^2 + x_\alpha^2),\tag{A.5}$$

give the following relations

$$\frac{\partial\mathcal{H}}{\partial p_\alpha} = \hbar\dot{x}_\alpha = \hbar\omega_\alpha p_\alpha,\tag{A.6}$$

$$\frac{\partial\mathcal{H}}{\partial x_\alpha} = -\hbar\dot{p}_\alpha = \hbar\omega_\alpha x_\alpha - 2e\varsigma_\alpha V,\tag{A.7}$$

which lead to the differential equation

$$\ddot{x}_\alpha + \omega_\alpha^2 x_\alpha = \varsigma_\alpha\omega_\alpha\frac{2e}{\hbar}V.\tag{A.8}$$

To express the admittance $Y$ in terms of the bath parameters, we connect the voltage $V$ to the current $I_x = 2e\sum_\alpha \varsigma_\alpha\dot{x}_\alpha$ through the relation $V = Y\, I_x$.

We define the differential operator $\mathcal{D}$ as follows

$$\mathcal{D} = \frac{d^2}{dt^2} + \omega_\alpha^2,\tag{A.9}$$

which Fourier transform reads

$$\mathrm{TF}\,\mathcal{D} = -\omega^2 + \omega_\alpha^2. \tag{A.10}$$

The Fourier transform of the retarded Green's function of the linear differential equation $\mathcal{D}g_\alpha^R(t) = \delta(t)$ is then equal to $g_\alpha^R(\omega) = \frac{-1}{(\omega+i\nu)^2-\omega_\alpha^2}$. We obtain

$$x_\alpha(t) = \frac{2e}{\hbar}\varsigma_\alpha\omega_\alpha(g_\alpha^R \otimes V)(t), \tag{A.11}$$

and then

$$I_x(t) = \frac{2\pi}{R_Q}\sum_\alpha \varsigma_\alpha^2\omega_\alpha(\dot{g}_\alpha^R \otimes V)(t). \tag{A.12}$$

The current $I_x$ is the convolution product of the voltage by the first temporal derivative of the retarded Green's function. Taking the Fourier transform gives the product of $V(\omega)$ by the admittance of the circuit

$$Y_\omega = \lim_{\nu\to 0}\frac{2\pi}{R_Q}\sum_\alpha \varsigma_\alpha^2\omega_\alpha\frac{i\omega}{(\omega+i\nu)^2-\omega_\alpha^2}, \tag{A.13}$$

the real part $\mathrm{Re}Y_\omega = 1/R$ of which reads

$$\frac{1}{R} = \frac{\pi^2}{R_Q}\sum_\alpha \varsigma_\alpha^2\omega_\alpha\delta(|\omega|-|\omega_\alpha|). \tag{A.14}$$

Eq. (A.13) constitutes the link between the environment and the circuit through the admittance.

## A.3 Bath correlation function

The Hamiltonian of the bath is

$$\mathcal{H}_{\mathrm{bath}} = \sum_\alpha \frac{\hbar\omega_\alpha}{2}(p_\alpha^2 + x_\alpha^2) = \sum_\alpha \hbar\omega_\alpha\left(a_\alpha a_\alpha^\dagger + \frac{1}{2}\right), \tag{A.15}$$

with the bath annihilation operators

$$a_\alpha = \frac{x_\alpha + ip_\alpha}{\sqrt{2}}, \tag{A.16}$$

which satisfy the commutation rule $[a_\alpha, a_\alpha^\dagger] = 1$, and have the average $\langle a_\alpha^\dagger a_\alpha\rangle = n_\alpha = 1/(\mathrm{e}^{\beta\hbar\omega_\alpha} - 1)$, the Bose-Einstein distribution. Their temporal evolution reads

$$i\hbar\frac{\partial a_\alpha(t)}{\partial t} = [a_\alpha, \mathcal{H}_\alpha] = \hbar\omega_\alpha a_\alpha(t) \quad\Rightarrow\quad a_\alpha(t) = a_\alpha(0)\mathrm{e}^{-i\omega_\alpha t}. \tag{A.17}$$

We have

$$\xi(t) = 2\pi\sum_\alpha \varsigma_\alpha x_\alpha(t) = \sqrt{2}\pi\sum_\alpha \varsigma_\alpha(a_\alpha + a_\alpha^\dagger), \tag{A.18}$$

then

$$(\xi(t)-\xi(0))\xi(0) = -2\pi^2\sum_\alpha\sum_{\alpha'}\varsigma_\alpha\varsigma_{\alpha'}\underbrace{(a_\alpha(t) + a_\alpha^\dagger(t) - a_\alpha(0) - a_\alpha^\dagger(0))(a_{\alpha'}(0) + a_{\alpha'}^\dagger(0))}_{=\chi_{\alpha,\alpha'}(t)} \tag{A.19}$$

We expand $\chi_{\alpha,\alpha'}(t)$ in products of $a_\alpha(t)$

$$\begin{aligned}
\langle\chi_{\alpha,\alpha'}(t)\rangle \;=\;& \underbrace{\langle a_\alpha(0)a_{\alpha'}(0)\rangle}_{=0}\,\mathrm{e}^{-i\omega_\alpha t} + \underbrace{\langle a_\alpha(0)a^\dagger_{\alpha'}(0)\rangle}_{=(1+n_\alpha)\delta_{\alpha,\alpha'}}\,\mathrm{e}^{-i\omega_\alpha t}\\
&+ \underbrace{\langle a^\dagger_\alpha(0)a_{\alpha'}(0)\rangle}_{=n_\alpha\delta_{\alpha,\alpha'}}\,\mathrm{e}^{i\omega_\alpha t} + \underbrace{\langle a^\dagger_\alpha(0)a^\dagger_{\alpha'}(0)\rangle}_{=0}\,\mathrm{e}^{i\omega_\alpha t}\\
&- \underbrace{\langle a_\alpha(0)a_{\alpha'}(0)\rangle}_{=0} - \underbrace{\langle a_\alpha(0)a^\dagger_{\alpha'}(0)\rangle}_{=(1+n_\alpha)\delta_{\alpha,\alpha'}} \qquad\qquad (\mathrm{A.20})\\
&- \underbrace{\langle a^\dagger_\alpha(0)a_{\alpha'}(0)\rangle}_{=n_\alpha\delta_{\alpha,\alpha'}} - \underbrace{\langle a^\dagger_\alpha(0)a^\dagger_{\alpha'}(0)\rangle}_{=0}\\
=\;& (\cos\omega_\alpha t-1)\,\coth\tfrac{\beta\hbar\omega_\alpha}{2} - i\sin\omega_\alpha t,
\end{aligned}$$

which leads to

$$J(t) = \langle(\xi(t)-\xi(0))\xi(0)\rangle = 2\pi^2\sum_\alpha \varsigma_\alpha^2((\cos\omega_\alpha t-1)\,\coth\frac{\beta\hbar\omega_\alpha}{2} - i\sin\omega_\alpha t) \qquad (\mathrm{A.21})$$

We define

$$f(\omega_\alpha) = \frac{1}{\omega_\alpha}((\cos\omega_\alpha t-1)\,\coth\frac{\beta\hbar\omega_\alpha}{2} - i\sin\omega_\alpha t), \qquad (\mathrm{A.22})$$

an even function, and calculate $f(\omega_\alpha)$ in terms of $f(\omega)$

$$f(\omega_\alpha) = \int_{-\infty}^{\infty}\mathrm{d}\omega\,\delta(\omega-\omega_\alpha)f(\omega) = \frac{1}{2}\int_{-\infty}^{\infty}\mathrm{d}\omega\,\delta(|\omega|-|\omega_\alpha|)f(\omega). \qquad (\mathrm{A.23})$$

We can introduce the expression of the admittance

$$\begin{aligned}
J(t) &= \pi^2\sum_\alpha \varsigma_\alpha^2\omega_\alpha\int_{-\infty}^{\infty}\mathrm{d}\omega\,\delta(|\omega|-\omega_\alpha)\frac{1}{\omega}((\cos\omega t-1)\,\coth\frac{\beta\hbar\omega}{2} - i\sin\omega t)\\
&= \int_{-\infty}^{\infty}\frac{\mathrm{d}\omega}{\omega}\underbrace{\pi^2\sum_\alpha \varsigma_\alpha^2\omega_\alpha\,\delta(|\omega|-|\omega_\alpha|)}_{=R_Q\mathrm{Re}Y_\omega}((\cos\omega t-1)\,\coth\frac{\beta\hbar\omega}{2} - i\sin\omega t)\\
&= R_Q\int_{-\infty}^{\infty}\frac{\mathrm{d}\omega}{\omega}\mathrm{Re}Y_\omega((\cos\omega t-1)\,\coth\frac{\beta\hbar\omega}{2} - i\sin\omega t). \qquad (\mathrm{A.24})
\end{aligned}$$

The admittance is a $R$-$L$ circuit, characterized by the cutoff frequency $\omega_c = R/L$. Its real part reads

$$\mathrm{Re}Y_\omega = \frac{1}{R}\frac{1}{1+(\omega/\omega_c)^2}, \qquad (\mathrm{A.25})$$

and we arrive at

$$J(t) = g\int_{-\infty}^{\infty}\frac{\mathrm{d}\omega}{\omega}\frac{1}{1+(\frac{\omega}{\omega_c})^2}((\cos\omega t-1)\,\coth\frac{\beta\hbar\omega}{2} - i\sin\omega t). \qquad (\mathrm{A.26})$$

This integral can be calculated using the residue theorem. The integrand can be rewritten

$$(\cos\omega t-1)\,\coth\frac{\beta\hbar\omega}{2} - i\sin\omega t = \underbrace{\frac{\mathrm{e}^{-i\omega t}-1}{1-\mathrm{e}^{-\beta\hbar\omega}}}_{=u(\omega)} + \underbrace{\frac{1-\mathrm{e}^{i\omega t}}{1-\mathrm{e}^{\beta\hbar\omega}}}_{=v(\omega)}\,. \qquad (\mathrm{A.27})$$

Using $v(-\omega) = -u(\omega)$, we get

$$J(t) = 2g \int_{-\infty}^{\infty} \mathrm{d}\omega \, \underbrace{\frac{1}{\omega} \frac{{\omega_c}^2}{\omega^2 + {\omega_c}^2} \frac{\mathrm{e}^{-i\omega t} - 1}{1 - \mathrm{e}^{-\beta\hbar\omega}}}_{=f(\omega)} . \tag{A.28}$$

The function $f(\omega)$ has three kinds of pole

- Pole $\omega = 0$ : $\quad \mathrm{Res}(0) = \lim\limits_{\omega \to 0} \omega f(\omega) = -\frac{it}{\beta\hbar}.$
- Poles $\omega = \pm i\omega_c$ : $\quad \mathrm{Res}(\pm i\omega_c) = \frac{1}{2} \frac{1 - \mathrm{e}^{\pm\omega_c t}}{1 - \mathrm{e}^{\mp i\beta\hbar\omega_c}}.$
- Poles $\omega = i\omega_k$ : $\quad \mathrm{Res}(i\omega_k) = \frac{i}{2\pi k} \frac{{\omega_c}^2}{{\omega_c}^2 - {\omega_k}^2} (1 - \mathrm{e}^{\omega_k t}).$

Depending on the sign of $t$, $J(t)$ satisfies

$$J(t) = \begin{cases} -\, i2\pi \, 2g \left( \frac{1}{2}\mathrm{Res}(0) + \mathrm{Res}(-i\omega_c) + \sum\limits_{k=1}^{\infty} \mathrm{Res}(i\omega_{-k}) \right) & \text{if } t > 0 \\ +\, i2\pi \, 2g \left( \frac{1}{2}\mathrm{Res}(0) + \mathrm{Res}(+i\omega_c) + \sum\limits_{k=1}^{\infty} \mathrm{Res}(i\omega_{+k}) \right) & \text{if } t < 0 \end{cases}$$

$$= 2g \left( -\frac{\pi|t|}{\beta\hbar} - i\pi \left( \underbrace{\frac{1 - \mathrm{e}^{-\omega_c t}}{1 - \mathrm{e}^{+i\beta\hbar\omega_c}} \Xi(t) - \frac{1 - \mathrm{e}^{+\omega_c t}}{1 - \mathrm{e}^{-i\beta\hbar\omega_c}} \Xi(-t)}_{=\frac{1}{2}j(t)} \right) - \sum_{k=1}^{\infty} \frac{1}{k} \frac{1 - \mathrm{e}^{-\omega_k|t|}}{1 - \left(\frac{\omega_k}{\omega_c}\right)^2} \right), \tag{A.29}$$

where $\Xi(t)$ is the unit step function. We use the relation

$$\frac{1}{1 - \mathrm{e}^{\pm i\beta\hbar\omega_c}} = \frac{1}{2} \left( 1 \pm i \, \cot \frac{\beta\hbar\omega_c}{2} \right), \tag{A.30}$$

to obtain the expression of the function $j(t)$

$$j(t) = \mathrm{sgn}(t) \left( 1 - \mathrm{e}^{-\omega_c|t|} \right) + i \, \cot \frac{\beta\hbar\omega_c}{2} \left( 1 - \mathrm{e}^{-\omega_c|t|} \right). \tag{A.31}$$

Finally

$$J(t) = -2g \left( \frac{\pi|t|}{\beta\hbar} - \frac{\pi}{2} \left( 1 - \mathrm{e}^{-\omega_c|t|} \right) \cot \frac{\beta\hbar\omega_c}{2} \right. \\ \left. + \sum_{k=1}^{\infty} \frac{1}{k} \frac{1 - \mathrm{e}^{-\omega_k|t|}}{1 - (\frac{\omega_k}{\omega_c})^2} + i\frac{\pi}{2} \left( 1 - \mathrm{e}^{-\omega_c|t|} \right) \mathrm{sgn}(t) \right). \tag{A.32}$$

The time independent terms can be rewritten in terms of the *cotangent* and *digamma* (noted $\Psi$)functions

$$J(t) = -2g \left( \lambda + \frac{\pi|t|}{\beta\hbar} + \frac{\pi}{2} \, \mathrm{e}^{-\omega_c|t|} \, \cot \frac{\beta\hbar\omega_c}{2} - \sum_{k=1}^{\infty} \frac{1}{k} \frac{\mathrm{e}^{-\omega_k|t|}}{1 - (\frac{\omega_k}{\omega_c})^2} + i\frac{\pi}{2} \left( 1 - \mathrm{e}^{-\omega_c|t|} \right) \mathrm{sgn}(t) \right), \tag{A.33}$$

where we note

$$\lambda = -\frac{\pi}{2}\cot\frac{\beta\hbar\omega_c}{2} + \sum_{k=1}^{\infty}\frac{1}{k}\frac{1}{1-(\frac{\omega_k}{\omega_c})^2}. \tag{A.34}$$

Use the power series of the $\cot(z)$ and $\Psi(z)$ [202] we reformulate $\lambda$

$$\lambda = \gamma + \frac{\pi}{\beta\hbar\omega_c} + \Psi\left(\frac{\beta\hbar\omega_c}{2\pi}\right). \tag{A.35}$$

## A.4 Continued fraction representation of the steady state voltage

The steady state voltage reads

$$\frac{V}{V_c} = \frac{1}{2}\sum_{n=0}^{\infty}\sum_{\{f\}}\prod_{k=1}^{2n+1} a(f_k), \tag{A.36}$$

with $V_c = \pi U_0/e$ and

$$a(f_k) = \frac{U_0}{i\hbar}\int_0^{\infty}\mathrm{d}\tau\,\sin(f_k\,A(\tau))\mathrm{e}^{i\frac{\pi}{e}If_k\tau - {f_k}^2 M(\tau)}, \tag{A.37}$$

where we note

$$J(\tau) = -i\,\mathrm{sgn}(\tau)A(\tau) - M(\tau) \tag{A.38}$$

$$A(\tau) = \pi\, g\left(1-\mathrm{e}^{-\omega_c|t|}\right) \tag{A.39}$$

$$M(\tau) = 2g\left(\frac{\pi|t|}{\beta\hbar} - \frac{\pi}{2}\left(1-\mathrm{e}^{-\omega_c|t|}\right)\cot\frac{\beta\hbar\omega_c}{2} + \sum_{n=1}^{\infty}\frac{1-\mathrm{e}^{-\omega_n|t|}}{n\left(1-(\frac{\omega_n}{\omega_c})^2\right)}\right). \tag{A.40}$$

and $a(n) \equiv a_n$. This formulation involves the integers $f_k$ which have interesting properties

$$\begin{cases} a(f_k=0)=0 \;\Rightarrow\; \forall k\in[1,2n+1]\; f_k\neq 0 \\ f_0 = f_{2n+2} = 0 \\ |f_{k+1}-f_k| = 1 \end{cases} \Longrightarrow \begin{cases} \forall k\in[1,2n+1]\; f_k>0, \\ \quad\text{or} \\ \forall k\in[1,2n+1]\; f_k<0. \end{cases} \tag{A.41}$$

Moreover, $a(-f_k) = a^*(f_k)$. Then

$$\frac{V}{V_c} = \frac{1}{2}\sum_{n=0}^{\infty}\sum_{\{f>0\}}\prod_{k=1}^{2n+1} a(f_k) + \frac{1}{2}\sum_{n=0}^{\infty}\sum_{\{f<0\}}\prod_{k=1}^{2n+1} a(f_k) = \mathrm{Re}\left(\sum_{n=0}^{\infty}\sum_{\{f>0\}}\prod_{k=1}^{2n+1} a(f_k)\right). \tag{A.42}$$

We define $G_n^r$ and $G^r$ as follows

$$\forall r\in\mathbb{N}^* \quad G_n^r = \sum_{\substack{\{f\geqslant r\}\\ f_1=f_{2n+1}=r}}\prod_{k=1}^{2n+1} a(f_k)$$

$$G^r = \sum_{n=0}^{\infty} G_n^r = \sum_{n=0}^{\infty}\sum_{\substack{\{f\geqslant r\}\\ f_1=f_{2n+1}=r}}\prod_{k=1}^{2n+1} a(f_k). \tag{A.43}$$

The voltage $V$ can then be expressed in terms of $G^1$

$$V/V_c = \operatorname{Re} G^1. \tag{A.44}$$

To calculate $G^1$, the idea is to subdivide the graph $G_n^r$ in subgraphs $G_n^{r+1}$. To proceed, it is convenient to define some ensembles

$$E_n^r = \left\{F = (f_1, \dots, f_{2n+1}) \in \mathbb{N}^{2n+1} \mid f_k \geqslant r \quad f_1 = f_{2n+1} = r \quad |f_{k+1} - f_k| = 1\right\}, \tag{A.45}$$

$$\begin{aligned} \forall F \in E_n^r \qquad A &= \{k \in [1, 2n+1] \mid f_k = r\}, && \text{(A.46)} \\ q &= \operatorname{Card} A - 1, \qquad q \in [1, n], && \text{(A.47)} \\ R_j &= j^{\text{th}} \text{ element of A} \qquad (R_1 = 1, \quad R_{q+1} = 2n+1). && \text{(A.48)} \end{aligned}$$

The integer $q$ represents the number of subgraphs $G_n^{r+1}$ contained in the graph $G_n^r$ and $R_j$ are the points which delimit two successive subgraphs $G_n^{r+1}$. We then define

$$E_n^r(q) = \left\{F = (r, F_1, r, \dots, r, F_q, r) \mid F_k \in E_{m_k}^{r+1} \quad \sum_{k=1}^{q} m_k = n - q\right\}, \tag{A.49}$$

$$\tilde{E}_n^r(q) = \left\{F = (F_1, \dots, F_q) \mid F_k \in E_{m_k}^{r+1} \quad \sum_{k=1}^{q} m_k = n - q\right\}. \tag{A.50}$$

One obtains $E_n^r = \bigcup_{q=1}^{n} E_n^r(q)$. We can then perform first the calculation of $G_n^r$

$$\begin{aligned} G_n^r &= \sum_{F \in E_n^r} \prod_{k=1}^{2n+1} a(f_k) \\ &= \sum_{q=1}^{n} \sum_{F \in E_n^r(q)} a(r)^{q+1} \prod_{\substack{k=1 \\ f_k \neq r}}^{2n+1} a(f_k) \\ &= \sum_{q=1}^{n} a(r)^{q+1} \sum_{F \in \tilde{E}_n^r(q)} \prod_{k=1}^{q} \prod_{l=R_k+1}^{R_{k+1}-1} a(f_l) \\ &= \sum_{q=1}^{n} a(r)^{q+1} \sum_{\substack{m_1 \dots\ m_q = 0 \\ \sum_{i=1}^{q} m_i = n-q}}^{n-1} \sum_{F \in E_{m_1}^{r+1}} \cdots \sum_{F \in E_{m_q}^{r+1}} \prod_{k=1}^{q} \prod_{l=R_k+1}^{R_{k+1}-1} a(f_l) \\ &= \sum_{q=1}^{n} a(r)^{q+1} \sum_{\substack{\{m\} \\ \sum_{i=1}^{q} m_i = n-q}} \prod_{k=1}^{q} \underbrace{\sum_{F \in E_{m_k}^{r+1}} \prod_{l=R_k+1}^{R_{k+1}-1} a(f_l)}_{= G_{m_k}^{r+1}} \\ &= \sum_{q=1}^{n} a(r)^{q+1} \sum_{m_1 \dots m_q} G_{m_1}^{r+1} \dots G_{m_q}^{r+1} \delta_{m_1 + \dots + m_q, n-q}, \end{aligned} \tag{A.51}$$

and second $G^r$

$$\begin{aligned} G^r = \sum_{n=0}^{\infty} G_n^r =& a(r) + a(r) \sum_{q=1}^{\infty} \sum_{n=q}^{\infty} \sum_{\{m\}} \prod_{k=1}^{q} \left(a(r)\, G_{m_k}^{r+1}\right) \delta_{m_1+\cdots+m_q,n-q} \\ =& a(r) \left( 1 + \sum_{q=1}^{\infty} \prod_{k=1}^{q} \sum_{m_k} a(r)\, G_{m_k}^{r+1} \right) \\ =& a(r) \left( 1 + \sum_{q=1}^{\infty} \left(a(r)\, G^{r+1}\right)^q \right) \\ =& \frac{a(r)}{1 - a(r)\, G^{r+1}}. \end{aligned} \tag{A.52}$$

This result can then be applied to the case $r = 1$

$$G^1 = \frac{a(1)}{1 - \frac{a(1)\, a(2)}{1 - \frac{a(2)\, a(3)}{1 - \frac{a(3)\, a(4)}{1 - \frac{a(4)\, a(5)}{1 - \frac{a(5)\, a(6)}{1 - \dots}}}}}}. \tag{A.53}$$

This finally yields the continued fraction formulation of the voltage

$$\frac{V}{V_c} = \mathrm{Re} \frac{a(1)}{1 + \frac{b_1}{1 + \frac{b_2}{1 + \dots}}}, \tag{A.54}$$

where $b_n = -a(n)\, a(n+1)$.

## A.5 Classical limit

In the classical limit $\lambda = 0$, and the coefficients $a_n$ become

$$a_n = \frac{U_0}{i\hbar} \sin(n\pi g)\, \mathrm{e}^{-2\pi n^2 \lambda} \int_0^{\infty} \mathrm{d}t\, \mathrm{e}^{i\frac{\pi}{e} I_b t n - 2 g n^2 \frac{\pi}{\beta\hbar} |t|}, \tag{A.55}$$

*i.e.*

$$a_n = \frac{z}{in + \eta} \frac{\sin(n\pi g)}{n\pi g} \mathrm{e}^{-2gn^2\lambda}, \tag{A.56}$$

with $z = \beta U_0$, and $\eta = \frac{\beta\hbar}{2eg} I_b$. In the low-$g$ limit, we have $a_n = \dfrac{1}{2} \dfrac{z}{in + \eta}$. The coefficients $G^n$ satisfy $G^n = \dfrac{a_n}{1 + a_n G^{n+1}}$. We write $G^n$ in the form $G^n = d_n \dfrac{D_n}{D_{n-1}}$. From what precedes, we deduce,

$$\frac{1}{d_n} D_{n-1} + d_{n+1} D_{n+1} = \frac{1}{a_n} D_n = i \frac{2}{z} (n - i\eta) D_n. \tag{A.57}$$

We choose $d_n = -i$, which induces

$$D_{n-1} - D_{n+1} = \frac{2}{z} (n - i\eta) D_n. \tag{A.58}$$

This equation is the characteristic relation of modified Bessel functions $\mathrm{I}_n(z)$

$$D_n = \mathrm{I}_{n-i\eta}(z), \tag{A.59}$$

and thus

$$G^n = -i\frac{\mathrm{I}_{n-i\eta}(z)}{\mathrm{I}_{n-1-i\eta}(z)}. \tag{A.60}$$

Then we have

$$\frac{V}{V_c} = \mathrm{Im}\left(\frac{\mathrm{I}_{1-i\eta}(z)}{\mathrm{I}_{-i\eta}(z)}\right). \tag{A.61}$$

We use the following property of Bessel functions $(\mathrm{I}_\lambda(z))^* = \mathrm{I}_{\lambda^*}(z)$, implying $|\mathrm{I}_\lambda(z)|^2 = \mathrm{I}_\lambda(z)\,\mathrm{I}_{\lambda^*}(z)$. Then

$$\mathrm{Im}\left(\frac{\mathrm{I}_{1-i\eta}(z)}{\mathrm{I}_{-i\eta}(z)}\right) = \frac{\mathrm{I}_{1-i\eta}(z)\mathrm{I}_{i\eta}(z) - \mathrm{I}_{-1+i\eta}(z)\mathrm{I}_{-i\eta}(z)}{2i|\mathrm{I}_{i\eta}(z)|^2} + \frac{\eta}{2} \tag{A.62}$$

We can use the Wronskian of Bessel functions [202] to obtain

$$\mathrm{I}_{1-i\eta}(z)\mathrm{I}_{i\eta}(z) - \mathrm{I}_{-1+i\eta}(z)\mathrm{I}_{-i\eta}(z) = -\frac{2i}{\pi z}\sinh(\pi\eta), \tag{A.63}$$

and hence

$$\frac{V}{V_c} = \frac{\eta}{z}\left(1 - \frac{\sinh\pi\eta}{\pi\eta}\frac{1}{|\mathrm{I}_{i\eta}(z)|^2}\right). \tag{A.64}$$

Finally, the voltage in the classical regime reads

$$V = RI_b - \frac{k_BT}{e}\frac{\sinh\pi\eta}{|\mathrm{I}_{i\eta}(z)|^2}. \tag{A.65}$$

## A.6 Limit of very low temperatures

We consider first the low temperatures limit $\beta\hbar\omega_c \to \infty$ where the functions $A$ and $M$ can be approximated with

$$A(t) = \pi g, \tag{A.66}$$

$$\lambda = \gamma + \ln\left(\frac{\beta\hbar\omega_c}{2\pi}\right), \tag{A.67}$$

$$M(t) = 2g\left(\gamma + \ln\left(\frac{\beta\hbar\omega_c}{\pi}\mathrm{sh}(\pi t/\beta\hbar)\right)\right). \tag{A.68}$$

The coefficients $a_n$ become

$$a_n = -i\frac{\beta U_0}{2\pi}\,\mathrm{e}^{-2g\gamma n^2}\left(\frac{\beta\hbar\omega_c}{2\pi}\right)^{-2gn^2}\frac{\sin(n\pi g)\sin(n\pi g(n+i\eta))}{\sin(2n^2\pi g)}\frac{|\Gamma(ng(n+i\eta))|^2}{\Gamma(2n^2g)} \tag{A.69}$$

To first order in $(\beta\hbar\omega_c)^{-1}$, we obtain the expression of the voltage at very low temperatures

$$\frac{V}{V_c} = \frac{1}{2}\frac{U_0}{\hbar\omega_c}\,\mathrm{e}^{-2g\gamma}\left(\frac{\beta\hbar\omega_c}{2\pi}\right)^{1-2g}\sinh(\pi g\eta)\frac{|\Gamma(g(1+i\eta))|^2}{\Gamma(2g)}. \tag{A.70}$$

Second, in the zero-temperature limit, we rewrite the time-independent terms of the autocorrelation function $J(t)$

$$J(t) = -2g\left(\lambda + \frac{\pi|t|}{\beta\hbar} + \frac{\pi}{2}\,\mathrm{e}^{-\omega_c|t|}\,\cot\frac{\beta\hbar\omega_c}{2} - \sum_{k=1}^{\infty}\frac{1}{k}\frac{\mathrm{e}^{-\omega_k|t|}}{1-(\frac{\omega_k}{\omega_c})^2} + i\frac{\pi}{2}\left(1-\mathrm{e}^{-\omega_c|t|}\right)\,\mathrm{sgn}(t)\right), \tag{A.71}$$

where

$$\lambda = \gamma + \frac{\pi}{\beta\hbar\omega_c} + \Psi\left(\frac{\beta\hbar\omega_c}{2\pi}\right). \tag{A.72}$$

The zero-temperature limit corresponds to $\beta \to \infty$. We use the asymptotic expression of the digamma function for large arguments [202]

$$\Psi(z) \overset{z\to\infty}{\sim} \ln z - \frac{1}{2z}, \tag{A.73}$$

to obtain

$$\lambda \overset{\beta\to\infty}{\sim} \gamma + \ln\frac{\beta\hbar\omega_c}{2\pi}, \tag{A.74}$$

and then to

$$J(t) \overset{\beta\to\infty}{\sim} -2g\left(\gamma + \ln\omega_c|t| + \frac{\pi}{2}\,\mathrm{e}^{-\omega_c|t|}\,\cot\frac{\beta\hbar\omega_c}{2} + i\frac{\pi}{2}\left(1-\mathrm{e}^{-\omega_c|t|}\right)\,\mathrm{sgn}(t)\right), \tag{A.75}$$

which can be approximated for long times compared to $\omega_c^{-1}$ by

$$J(t) \overset{T\to 0}{\sim} -2g\left(\gamma + \ln\omega_c|t| + i\frac{\pi}{2}\,\mathrm{sgn}(t)\right). \tag{A.76}$$

We use the expression for the voltage reduced to the first coefficient $a_1$

$$V = \frac{\pi U_0}{e}\mathrm{Re}\frac{U_0}{i\hbar}\int_0^{\infty}\sin(A(t))\,\mathrm{e}^{i\frac{\pi}{e}I_b t - M(t)}. \tag{A.77}$$

This equation can be rewritten in the form

$$V = \frac{\pi^2 U_0^2}{2e}\frac{1}{h}\int_{-\infty}^{\infty}\mathrm{d}t\,\mathrm{e}^{-i\,\mathrm{sgn}(t)\,A(t) - M(t) + \frac{i}{\hbar}\frac{hI}{2e}t}, \tag{A.78}$$

which is precisely the dual expression of the current calculated within the $P(E)$ theory in the overdamped regime. Indeed, let us place in the case dual to the system studied in details in Ref. [48]. The function $P(E)$ is the probability for the system to exchange the energy $E$ with the environment. In the regime $E_J \ll E_C$ and $R \ll R_Q$, the energy exchange $E$ corresponds to the tunneling of one Cooper pair. In the underdamped limit, the energy $E$ can be interpreted as the the energy exchanged for a phase slip event in the washboard potential: $\varphi$, initially well defined around the minimum $2\pi n$, is transferred to the minimum $2\pi(n+1)$.

$$P(E) = \frac{1}{h}\int_{-\infty}^{+\infty}\mathrm{d}t\,\exp\left(J(t) + \frac{i}{\hbar}Et\right). \tag{A.79}$$

Moreover, the normalization relation for $P(E)$ is $\int_{-\infty}^{+\infty}\mathrm{d}E\,P(E) = 1$. It is possible to express the law $V(I)$ as follows

$$V = \frac{\pi^2 U_0^2}{2e}\left(P(\Phi_0 I_b) - P(-\Phi_0 I_b)\right). \tag{A.80}$$

For negative values of the energy $E$, $P(E)$ is the probability that the system receives the energy $|E|$ from the environment. At zero temperature, the environment cannot give energy to the system and the $I$-$V$ characteristic takes the form

$$V = \frac{\pi^2 U_0^2}{2e} P(\Phi_0 I_b). \tag{A.81}$$

The $P(E)$ law has two interesting properties that can be exploited to plot the $I$-$V$ characteristics

- Power law for small values of the current:

$$V = \frac{\pi^2 U_0^2}{h} \frac{1}{\Gamma(2g)} \frac{1}{I_b} \left( \frac{\pi^2 g}{\mathrm{e}^\gamma} \frac{\hbar I_b}{e E_L} \right)^{2g}. \tag{A.82}$$

- Recurrence relation:

$$V(I_b) = \frac{2g}{I_b} \int_0^{I_b} \mathrm{d}I \frac{1}{1 + \left( \frac{\pi g h}{2 e E_L} (I_b - I) \right)^2} V(I). \tag{A.83}$$

To plot the $I$-$V$ characteristic, we start with very low bias currents and use the asymptotic expansion (A.82). These points are then used as initial conditions for the recurrence relation (A.83) to obtain the full $I$-$V$ characteristic.

## Appendix B

# The instantons formalism

**Contents**

## Introduction

We use the instantons technique of Ref. [94] to calculate the escape rate from the metastable state of a general quartic potential.

## B.1 Tunneling rate through a potential barrier

### B.1.1 Path integral formulation

We consider a particle of mass $M$ moving in a one-dimensional potential $\mathcal{U}(x)$ with momentum $p = M\frac{\mathrm{d}x}{\mathrm{d}t}$ according to the Hamiltonian:

$$\mathcal{H} = \frac{p^2}{2M} + \mathcal{U}(x). \tag{B.1}$$

The probability amplitude for the particle to go from a point $x_i$ at time $t_i$ to the point $x_f$ at time $t_f$ corresponds to the propagator

$$K(x_i, t_i; x_f, t_f) = \langle x_f | \, \mathrm{e}^{-\frac{i}{\hbar}\mathcal{H}(t_f - t_i)} \, | x_i \rangle \,, \tag{B.2}$$

where $|x_{i,f}\rangle$ are position eigenstates.

In order to obtain this probability amplitude, we can sum the contributions of all possible trajectories from $x_i$ to $x_f$. The phase of the contribution from a given path is the action $S$ in the unit of the quantum action $\hbar$ [95]

$$S = \int_{t_i}^{t_f} \mathrm{d}t \left[ \frac{M}{2} \left( \frac{\mathrm{d}x}{\mathrm{d}t} \right)^2 - \mathcal{U}(x) \right]. \tag{B.3}$$

We cut the interval $[t_i, t_f]$ into $N \gg 1$ infinitesimal domains of length $\delta t$. The propagator is then the product of propagators on these smaller domains

$$\begin{aligned} K(x_i,t_i;x_f,t_f) &= \langle x_f|\mathrm{e}^{-\frac{i}{\hbar}\mathcal{H}(t_f-t_i)}|x_i\rangle \\ &= \int \mathrm{d}x_1 \ldots \mathrm{d}x_{N-1} K(x_i,t_i;x_1,t_i+\delta t)\ldots K(x_{N-1},t_f-\delta t;x_f,t_f), \end{aligned} \tag{B.4}$$

For each infinitesimal time $\delta t$, at first order,

$$\mathrm{e}^{-\frac{i}{\hbar}\delta t\mathcal{H}} = \mathrm{e}^{-\frac{i}{\hbar}\delta t\mathcal{T}(p)}\mathrm{e}^{-\frac{i}{\hbar}\delta t\mathcal{U}(x)}\mathrm{e}^{-\frac{\delta t^2}{\hbar^2}[\mathcal{T},\mathcal{U}]} \simeq \mathrm{e}^{-\frac{i}{\hbar}\delta t\mathcal{T}(p)}\mathrm{e}^{-\frac{i}{\hbar}\delta t\mathcal{U}(x)}. \tag{B.5}$$

At infinitesimally short times, physics becomes classical. Then,

$$\begin{aligned} K(x_{j+1},t;x_j,t+\delta t) &= \int \mathrm{d}x \langle x_{j+1}|\mathrm{e}^{-\frac{i}{\hbar}\delta t\mathcal{U}(x)}|x\rangle\langle x|\mathrm{e}^{-\frac{i}{\hbar}\delta t\mathcal{T}(p)}|x_j\rangle \\ &= \mathrm{e}^{-\frac{i}{\hbar}\delta t\mathcal{U}(x_{j+1})}\int \frac{dp_{j+1}}{2\pi\hbar}\langle x_{j+1}|p_{j+1}\rangle \mathrm{e}^{-\frac{i}{\hbar}\delta t\mathcal{T}(p_{j+1})}\langle p_{j+1}|x_j\rangle \\ &= \mathrm{e}^{-\frac{i}{\hbar}\delta t\mathcal{U}(x_{j+1})}\int \frac{dp_{j+1}}{2\pi\hbar}\mathrm{e}^{-\frac{i}{\hbar}\delta t\mathcal{T}(p_{j+1})}\mathrm{e}^{\frac{i}{\hbar}p_{j+1}(x_{j+1}-x_j)} \\ &= \mathrm{e}^{-\frac{i}{\hbar}\delta t\mathcal{U}(x_{j+1})}\int \frac{\mathrm{d}p_{j+1}}{2\pi\hbar}\,\mathrm{e}^{-\frac{i}{\hbar}\delta t p_{j+1}^2/2M+\frac{i}{\hbar}\delta t\dot{x}_{j+1}p_{j+1}} \\ &= \sqrt{\frac{M}{i2\pi\hbar\delta t}}\,\mathrm{e}^{\frac{i}{\hbar}\tau(\mathcal{T}(\dot{x}_{j+1})-\mathcal{U}(x_{j+1}))}. \end{aligned} \tag{B.6}$$

This leads to the total propagator

$$\begin{aligned} K(x_i,t_i;x_f,t_f) &= \left(\frac{M}{i2\pi\hbar\delta t}\right)^{N/2}\int \mathrm{d}x_1\ldots\mathrm{d}x_{N-1}\,\mathrm{e}^{\frac{i}{\hbar}\delta t\sum_{n=1}^{N}(\mathcal{T}(\dot{x})-\mathcal{U}(x))} \\ &= \left(\frac{M}{i2\pi\hbar\delta t}\right)^{N/2}\int \mathrm{d}x_1\ldots\mathrm{d}x_{N-1}\,\mathrm{e}^{\frac{i}{\hbar}\int_0^T \mathrm{d}t'(\mathcal{T}(\dot{x})-\mathcal{U}(x))}. \end{aligned} \tag{B.7}$$

The path integral formulation of the propagator is then

$$K(x_i,t_i;x_f,t_f) = \mathcal{N}\int_{x(t_i)=x_i}^{x(t_f)=x_f}\mathcal{D}x\,\mathrm{e}^{\frac{i}{\hbar}S}, \tag{B.8}$$

where $\mathcal{N}$ is a normalization factor and $\mathcal{D}x$ denotes the integration over all functions $x(t)$ obeying the boundary conditions $x(t_i) = x_i$ and $x(t_f) = x_f$.

If $\bar{x}$ is any function satisfying the boundary conditions, then a general function $x$ can be written as

$$x(t) = \bar{x}(t) + y(\tau), \qquad y(\tau) = \sum_n c_n x_n(t), \tag{B.9}$$

were $\{x_n\}$ is a complete set of orthonormal functions vanishing at the boundaries:

$$\int_{-\frac{T}{2}}^{\frac{T}{2}} \mathrm{d}\tau x_n(\tau)x_m(\tau) = \delta_{n,m}, \tag{B.10}$$

$$x_n\left(\pm\frac{T}{2}\right) = 0. \tag{B.11}$$

We define the measure $\mathcal{D}x$ by

$$\mathcal{D}x = \prod_n \frac{1}{\sqrt{2\pi\hbar}}\mathrm{d}c_n. \tag{B.12}$$

### B.1.2 Escape rate

Let us consider the temporal behavior of a wave-function with energy $E = E_R - iE_I$ which is given by $\Psi(x,t) = \phi(x)\,\mathrm{e}^{-iEt\hbar} = \phi(x)\,\mathrm{e}^{-iE_Rt\hbar}\,\mathrm{e}^{-E_It\hbar}$. The norm of the state

$$\int \mathrm{d}x\,|\Psi(x,t)|^2 = \mathrm{e}^{-2E_It/\hbar} \tag{B.13}$$

decays exponentially with a decay rate $\Gamma = 2E_I/\hbar$, *i.e.*

$$\Gamma = -\frac{2}{\hbar}\,\mathrm{Im}\,E. \tag{B.14}$$

The lifetime of the state is $\Gamma^{-1}$.

### B.1.3 Euclidean action in terms of functional determinants

We focus on potentials containing an unstable quantum state like the one sketched on Fig. B.1. The classical version of this system possesses a stable equilibrium state in which the particle is at rest at $x = 0$. However, quantum corrections render this state unstable: it is a false ground state. Let's perform a Wick rotation: time $t$ is replace by the imaginary time $\tau = it$. Then the action $S$ becomes the Euclidean action $\mathcal{S}$

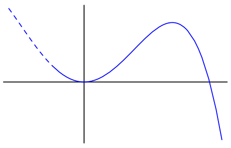

Figure B.1: Potential containing an unstable state at $x = 0$.

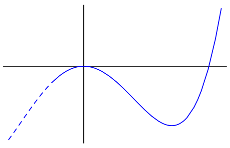

Figure B.2: Inverted potential.

$$\mathcal{S} = \int_{-\frac{T}{2}}^{\frac{T}{2}} \mathrm{d}\tau \left[\frac{M}{2}\dot{x}^2 + \mathcal{U}(x)\right], \tag{B.15}$$

where $\dot{} = \frac{\mathrm{d}}{\mathrm{d}\tau}$ and we define $it_i = -T/2$, $it_f = T/2$. We see that the effect of the Wick rotation on the action is to invert the potential.

In other words, in the part of space between $x = 0$ and $x = \sigma$, the momentum of the particle is imaginary: $p^2 = -2M\mathcal{U} < 0$. But if we choose the time variable $t$ as an imaginary variable $\tau = it$, then the motion is possible in the sense of classical dynamics in the inverted potential $-\mathcal{U}(q)$ (see Fig. B.2).

Using the method of the previous section, the Euclidean version of Feynman's sum over histories reads

$$\langle x_f|\,\mathrm{e}^{-\frac{1}{\hbar}\mathcal{H}T}\,|x_i\rangle = \mathcal{N}\int_{x_i}^{x_f} \mathcal{D}x\,\mathrm{e}^{-\mathcal{S}/\hbar}. \tag{B.16}$$

On the one hand, the left-hand side of Eq. (B.16) can be expanded on a complete set of energy eigenstates $\{|n\rangle\}$:

$$\langle x_f|\,\mathrm{e}^{-\frac{1}{\hbar}\mathcal{H}T}\,|x_i\rangle = \sum_n \mathrm{e}^{-\frac{1}{\hbar}E_nT}\langle x_f|n\rangle\langle n|x_i\rangle. \tag{B.17}$$

Thus, the leading term in this expression for large $T$ tells us the energy and wave-function of the lowest-lying energy eigenstates. This shows the interest of the Wick rotation to study the "ground state" properties.

On the other hand, the left-hand side of Eq. (B.16) can be evaluated in the semiclassical limit. In this case, the functional integral is dominated by the stationary point $\bar{x}$ of $\mathcal{S}$. If $\mathcal{S} = \int_{-T/2}^{T/2} \mathrm{d}\tau \mathcal{L}(\dot{x}, x, \tau)$, then its functional derivative with respect to $x(\tau)$ is

$$\frac{\delta \mathcal{S}}{\delta x(\tau)} = -\frac{\mathrm{d}}{\mathrm{d}\tau}\left(\frac{\partial \mathcal{L}}{\partial \dot{x}}\right) + \frac{\partial \mathcal{L}}{\partial x}. \tag{B.18}$$

Thus, $\bar{x}$ satisfies

$$\left.\frac{\delta \mathcal{S}}{\delta x}\right|_{\bar{x}} = -M\ddot{\bar{x}} + \mathcal{U}'(\bar{x}) = 0, \tag{B.19}$$

which is the equation of motion of a particle of mass $M$ moving in the potential $-\mathcal{U}(x)$. The corresponding energy is

$$E_0 = \frac{1}{2}\left(\frac{\mathrm{d}\bar{x}}{\mathrm{d}\tau}\right)^2 - \mathcal{U}(\bar{x}). \tag{B.20}$$

Let us $\{x_n\}$ be the eigenfunctions of the second variational derivative of $\mathcal{S}$ at $\bar{x}$, $\frac{\delta^2 \mathcal{S}}{\delta x^2} = -M\frac{\mathrm{d}^2}{\mathrm{d}\tau^2} + \mathcal{U}''(\bar{x})$,

$$-M\ddot{x}_n + \mathcal{U}''(\bar{x})x_n = \lambda_n x_n. \tag{B.21}$$

Then, in the small-$\hbar$ limit, we calculate the integral with the method of steepest descent where the integral is evaluated around the stationary point $\bar{x}$

$$\begin{aligned}\mathcal{S} \simeq& \int_{-\frac{T}{2}}^{\frac{T}{2}} \mathrm{d}\tau \left[\frac{M}{2}\dot{\bar{x}}^2 + \mathcal{U}(\bar{x})\right] + \int_{-\frac{T}{2}}^{\frac{T}{2}} \mathrm{d}\tau \left[\frac{M}{2}\dot{y}^2 + \frac{1}{2}\mathcal{U}(\bar{x})y^2\right] \\ =&\mathcal{S}_0 + \frac{1}{2}\int_{-\frac{T}{2}}^{\frac{T}{2}} \mathrm{d}\tau y \left[-M\frac{\mathrm{d}^2}{\mathrm{d}\tau^2} + \mathcal{U}(\bar{x})\right] y \\ =&\mathcal{S}_0 + \frac{1}{2}\sum_n \lambda_n c_n^2,\end{aligned} \tag{B.22}$$

where linear terms in $y$ in the Taylor expansion gives vanishing integrals and $\mathcal{S}_0$ is the action related to the path $\bar{x}$

$$\mathcal{S}_0 = \int_{-\frac{T}{2}}^{\frac{T}{2}} \mathrm{d}\tau \left[\frac{M}{2}\dot{\bar{x}}^2 + \mathcal{U}(\bar{x})\right]. \tag{B.23}$$

The functional integral becomes a product of Gaussian integrals

$$\begin{aligned}\int_{x_i}^{x_f} \mathcal{D}x\, \mathrm{e}^{-\frac{1}{\hbar}\mathcal{S}} &= \mathrm{e}^{-\frac{1}{\hbar}\mathcal{S}_0} \prod_n \frac{1}{\sqrt{2\pi\hbar}} \underbrace{\int_{\mathbb{R}} \mathrm{d}c_n\, \mathrm{e}^{-\frac{1}{2\hbar}\lambda_n c_n^2}}_{=\sqrt{\frac{2\pi\hbar}{\lambda_n}}} \\ &= \mathrm{e}^{-\frac{1}{\hbar}\mathcal{S}_0} \prod_n \frac{1}{\sqrt{\lambda_n}},\end{aligned} \tag{B.24}$$

and we find

$$\langle x_f|\, \mathrm{e}^{-\frac{1}{\hbar}\mathcal{H}T}\, |x_i\rangle = \mathcal{N}\, \mathrm{e}^{-\frac{1}{\hbar}\mathcal{S}_0} \left(\det\left[-M\partial_t^2 + \mathcal{U}''(\bar{x})\right]\right)^{-\frac{1}{2}}, \tag{B.25}$$

because the determinant of the product of all eigenvalues.

### B.1.4 Calculation of functional determinants: the Gelfand-Yaglom formula

In this subsection we present the Gelfand-Yaglom formula, used to calculate the functional determinants with the wavefunctions. We start from the eigenvalue equation of a particle of mass $M$ in the potential $W$

$$\left[-M\frac{\mathrm{d}^2}{\mathrm{d}\tau^2}+W\right]\psi=\lambda\psi. \tag{B.26}$$

Let us define $\psi_\lambda(\tau)$ as a solution of this equation with the boundary conditions

$$\psi_\lambda(-T/2)=0, \qquad \partial_t\psi_\lambda(-T/2)=1. \tag{B.27}$$

The operator $-M\frac{\mathrm{d}^2}{\mathrm{d}\tau^2}+W$, acting on the space of functions vanishing at $\pm\frac{T}{2}$, has an eigenvalue $\lambda_n$ if and only if

$$\psi_{\lambda_n}(T/2)=0. \tag{B.28}$$

We define the determinant as the product of all eigenvalues

$$\det\left[-M\partial_t^2+W\right]\equiv\prod_n\lambda_n. \tag{B.29}$$

Now let $\psi_\lambda^{(1)}$ and $\psi_\lambda^{(2)}$ be the wavefunctions solution of Eq. (B.26) for the potentials $W^{(1)}$ and $W^{(2)}$ respectively. Then [94]

$$\frac{\det\left[-M\partial_t^2+W^{(1)}-\lambda\right]}{\det\left[-M\partial_t^2+W^{(2)}-\lambda\right]}=\frac{\psi_\lambda^{(1)}(T/2)}{\psi_\lambda^{(2)}(T/2)}. \tag{B.30}$$

This result reveals that the ratio of two determinants of the same particle with the same energy in two different potentials is equal to the ration of the corresponding wavefunctions. In practice, it is sufficient to know the asymptotic expression of the wavefunctions for long times.

### B.1.5 Determination of the prefactor $\mathcal{N}$

#### 2.1.5.a Free particle

We calculate the propagator in the case of a free particle ($\mathcal{U}=0$) and in real time $t$:

$$\mathcal{H}=\mathcal{T}(p)=\frac{p^2}{2M}. \tag{B.31}$$

Then, from calculation (B.7),

$$\begin{aligned}K_{\mathrm{fp}}(x_i,t_i;x_f,t_f)=&\left[\prod_{n=2}^{N-1}\sqrt{\frac{M}{2i\pi\hbar\delta t}}\int\mathrm{d}x_n\mathrm{e}^{i\frac{M}{2\hbar\delta t}(x_{n+1}-x_n)^2}\right]\\&\times\sqrt{\frac{m}{2i\pi\hbar\delta t}}^2\int\mathrm{d}x_1\mathrm{e}^{i\frac{M}{2\hbar\delta t}\left((x_2-x_1)^2+(x_1-x_0)^2\right)}.\end{aligned} \tag{B.32}$$

Using the initial identity

$$\sqrt{\frac{M}{2i\pi\hbar\delta t}}^{2}\int \mathrm{d}x_1 \mathrm{e}^{i\frac{M}{2\hbar\delta t}\left((x_2-x_1)^2+(x_1-x_0)^2\right)} = \sqrt{\frac{M}{2i\pi\hbar(2\delta t)}}\mathrm{e}^{i\frac{M}{2\hbar(2\delta t)}(x_2-x_0)^2}, \tag{B.33}$$

and the recursive property

$$\begin{aligned}\sqrt{\frac{M}{2i\pi\hbar\delta t}}\int \mathrm{d}x_n \mathrm{e}^{i\frac{M}{2\hbar\delta t}(x_{n+1}-x_n)^2} \times \sqrt{\frac{M}{2i\pi\hbar(n\delta t}})\, \mathrm{e}^{i\frac{M}{2\hbar(n\delta t)}(x_n-x_0)^2} \\ = \sqrt{\frac{M}{2i\pi\hbar((n+1)\delta t}})\, \mathrm{e}^{i\frac{M}{2\hbar((n+1)\delta t)}(x_{n+1}-x_0)^2},\end{aligned} \tag{B.34}$$

we finally obtain

$$K_{\mathrm{fp}}(x_i,t_i;x_f,t_f) = \sqrt{\frac{M}{2i\pi\hbar(t_f-t_i)}}\,\mathrm{e}^{i\frac{M(x-x')^2}{2\hbar(t_f-t_i)}}. \tag{B.35}$$

The propagator in this simple case permits to calculate directly the prefactor.

### 2.1.5.b Particle in a smooth potential

We consider now a particle of mass $M$ moving in a smooth potential $\mathcal{U}(x)$. A path starting at $x(t_i)=x_i$ and ending at $x(t_f)=x_f$ can be decomposed as follows:

$$x(t) = \bar{x} + y\left(\frac{t-t_i}{t_f-t_i}+\frac{1}{2}\right) + \sum_{k=1}^{\infty} a_k \sin(k\pi(t-t_i)/(t_f-t_i)) = \bar{x} + \delta x(t), \tag{B.36}$$

where

$$\bar{x} = \frac{x_i+x_f}{2}, \quad y = x_i - x_f. \tag{B.37}$$

We expand the smooth potential at the second order in $\delta x$ :

$$\mathcal{U}(x(t)) = \bar{\mathcal{U}} + \bar{\mathcal{U}}'\delta x(t) + \frac{M}{2}\Omega^2\delta x(t)^2, \tag{B.38}$$

where we note

$$\bar{\mathcal{U}} = \mathcal{U}(\bar{x}), \quad \bar{\mathcal{U}}' = \partial_x\mathcal{U}(\bar{x}), \quad \Omega = \sqrt{\partial_x^2\mathcal{U}(\bar{x})/M}. \tag{B.39}$$

Using the relations

$$\cot z = \frac{1}{z} + 2z\sum_{k=1}^{\infty}\frac{1}{z^2-k^2\pi^2}, \qquad \sum_{k=1}^{\infty}\frac{1}{k^2\pi^2} = \frac{1}{6}, \tag{B.40}$$

$$\frac{1}{\sin z} = \frac{1}{z} + 2z\sum_{k=1}^{\infty}\frac{(-1)^k}{z^2-k^2\pi^2}, \qquad \sum_{k=1}^{\infty}\frac{(-1)^k}{k^2\pi^2} = -\frac{1}{12}, \tag{B.41}$$

one finds

$$\begin{aligned}\mathcal{S} =& \frac{My^2}{2T} - \bar{\mathcal{U}}T - \frac{M\Omega^2 y^2 T}{24}\\ &+ \frac{M}{4T}\sum_{k=1}^{\infty}(k^2\pi^2 - \Omega^2T^2)\left(a_k - \frac{T^2}{M}\frac{2\bar{\mathcal{U}}'(1-(-1)^k) + M\Omega^2 y(1+(-1)^k)}{k\pi(k^2\pi^2-\Omega^2T^2)}\right)^2\\ &+ \frac{M\Omega}{2}\left(\left(\frac{y^2}{2} + \frac{2\bar{\mathcal{U}}'^2}{M^2\Omega^4}\right)\cot\Omega T + \left(\frac{y^2}{2} - \frac{2\bar{\mathcal{U}}'^2}{M^2\Omega^4}\right)\frac{1}{\sin\Omega T}\right)\\ &- \frac{My^2}{2T}\left(1 - \frac{\Omega^2T^2}{12}\right) + \frac{\bar{\mathcal{U}}'^2 T}{2M\Omega^2}. \end{aligned} \tag{B.42}$$

The propagator reads

$$\begin{aligned} K(x_i,t_i;x_f,t_f) =& \int_{x(t_i)=x_i}^{x(t_f)=x_f} \mathcal{D}x\, \mathrm{e}^{\frac{i}{\hbar}\mathcal{S}}\\ =&C\,\mathrm{e}^{\frac{i}{\hbar}\frac{My^2}{2T} - \frac{i}{\hbar}\bar{\mathcal{U}}T - \frac{i}{\hbar}\frac{M\Omega^2 T}{24}}\\ &\times \mathrm{e}^{\frac{i}{\hbar}\frac{M\Omega}{2}\left(\left(\frac{y^2}{2}+\frac{2\bar{\mathcal{U}}'^2}{M^2\Omega^4}\right)\cot\Omega T + \left(\frac{y^2}{2}-\frac{2\bar{\mathcal{U}}'^2}{M^2\Omega^4}\right)\frac{1}{\sin\Omega T}\right) - \frac{i}{\hbar}\frac{My^2}{2T}\left(1-\frac{\Omega^2T^2}{12}\right) + \frac{i}{\hbar}\frac{\bar{\mathcal{U}}'^2 T}{2M\Omega^2}}\\ &\times \prod_{k=1}^{\infty}\int_{-\infty}^{\infty}\mathrm{d}a_k\, \mathrm{e}^{\frac{i}{\hbar}\frac{M}{4T}(k^2\pi^2-\Omega^2T^2)\left(a_k - \frac{T^2}{M}\frac{2\bar{\mathcal{U}}'(1-(-1)^k)+M\Omega^2 y(1+(-1)^k)}{k\pi(k^2\pi^2-\Omega^2T^2)}\right)^2}\\ =&C\prod_{k=1}^{\infty}\sqrt{\frac{i4\pi\hbar T}{M(k^2\pi^2-\Omega^2T^2)}}\,\mathrm{e}^{-\frac{i}{\hbar}T\left(\bar{\mathcal{U}} - \frac{\bar{\mathcal{U}}'^2}{2M\Omega^2}\right) + \frac{i}{\hbar}\frac{M\Omega}{2\sin\omega T}\left(\left(\frac{y^2}{2}+\frac{2\bar{\mathcal{U}}'^2}{M^2\Omega^4}\right)\cos\Omega T + \left(\frac{y^2}{2}-\frac{2\bar{\mathcal{U}}'^2}{M^2\Omega^4}\right)\right)}. \end{aligned} \tag{B.43}$$

The propagator of a free particle ($\mathcal{U}$=0) being (Eq. (B.35))

$$K_{\mathrm{fp}}(x_i,t_i;x_f,t_f) = \sqrt{\frac{M}{i2\pi\hbar T}}\,\mathrm{e}^{\frac{i}{\hbar}\frac{My^2}{2T}}, \tag{B.44}$$

and using

$$\prod_{k=1}^{\infty}\frac{k^2\pi^2}{k^2\pi^2-\Omega^2T^2} = \frac{\Omega T}{\sin\Omega T}, \tag{B.45}$$

we obtain

$$\begin{aligned} K(x_i,t_i;x_f,t_f) =& \sqrt{\frac{M\Omega}{i2\pi\hbar\sin\Omega T}}\\ \times&\exp\left[-\frac{i}{\hbar}T\left(\bar{\mathcal{U}} - \frac{\bar{\mathcal{U}}'^2}{2M\Omega^2}\right) + \frac{i}{\hbar}\frac{M\Omega}{2\sin\omega T}\left(\left(\frac{y^2}{2}+\frac{2\bar{\mathcal{U}}'^2}{M^2\Omega^4}\right)\cos\Omega T + \left(\frac{y^2}{2}-\frac{2\bar{\mathcal{U}}'^2}{M^2\Omega^4}\right)\right)\right]. \end{aligned} \tag{B.46}$$

The propagator for a smooth potential can then be applied to the case of a harmonic oscillator.

### 2.1.5.c Harmonic oscillator

We focus on the case $x_i = x_f = 0$. As a simple example, we can consider the case $\sigma \to \infty$. We define the bottom well pulsation $\omega_0$ by $M\omega_0^2 = \mathcal{U}''(0)$. It is obvious that the only solution obeying the boundary condition is $\bar{x} = 0$. For this solution $\mathcal{S}_0 = 0$.

If we define the prefactor $\mathcal{N}$ by $\det\big[-M\partial_t^2 + W\big] = \frac{2\pi\hbar}{M}\mathcal{N}^2\psi_0(T/2)$, where $\psi_0$ is the eigenfunction of Sec. B.1.4, then

$$\mathcal{N}\left(\det\big[-M\partial_t^2 + W\big]\right)^{-\frac{1}{2}} = \left(\frac{2\pi\hbar}{M}\psi_0(T/2)\right)^{-\frac{1}{2}}. \tag{B.47}$$

If $W = M\omega_0^2$, the eigenfunction of Eq. (B.21) is

$$\psi_0(t) = \frac{1}{\omega_0}\sinh\omega_0(t + T/2), \qquad \psi_0(T/2) \overset{T\to\infty}{\sim} \frac{\mathrm{e}^{\omega_0 T}}{2\omega_0}. \tag{B.48}$$

Therefore

$$\mathcal{N}\left(\det\big[-M\partial_t^2 + M\omega_0^2\big]\right)^{-\frac{1}{2}} = \sqrt{\frac{M\omega_0}{\pi\hbar}}\mathrm{e}^{-\omega_0 T/2}, \tag{B.49}$$

which gives the correct semiclassical shift in the ground-state energy $E_0 = \frac{1}{2}\hbar\omega_0$.

Actually, this definition of $\mathcal{N}$ is equivalent to the definition of $\mathcal{D}x$ from Feynman path integrals. Indeed, if we apply the general result (B.46) to a harmonic oscillator in imaginary time, we find

$$\langle 0|\,\mathrm{e}^{-\frac{i}{\hbar}\mathcal{H}T}\,|0\rangle = \sqrt{\frac{M\omega_0}{2\pi\hbar\sinh\omega_0 T}} \overset{T\to\infty}{\sim} \sqrt{\frac{M\omega_0}{\pi\hbar}}\mathrm{e}^{-\omega_0 T/2}, \tag{B.50}$$

with $\langle 0|\,\mathrm{e}^{-\frac{i}{\hbar}\mathcal{H}T}\,|0\rangle = \mathcal{N}\left(\det\big[-M\partial_t^2 + M\omega_0^2\big]\right)^{-\frac{1}{2}}$.

Finally,

$$\langle 0|\,\mathrm{e}^{-\frac{1}{\hbar}\mathcal{H}T}\,|0\rangle = \sqrt{\frac{M\omega_0}{\pi\hbar}}\,\mathrm{e}^{-\omega_0 T/2 - \mathcal{S}_0/\hbar}\left(\frac{\det\big[-M\partial_t^2 + \mathcal{U}''(\bar{x})\big]}{\det\big[-M\partial_t^2 + M\omega_0^2\big]}\right)^{-\frac{1}{2}} \tag{B.51}$$

We will see in the following that it is easier to calculate the ratio of such determinants.

### B.1.6 Multibounce configurations

Now we consider the case $\sigma$ finite (see Fig. B.1). There are nontrivial solutions of Eq. (B.19): the particle can begin on the top of the hill, bounce off the potential wall on the right at $x = \sigma$, and return to the top of the hill. For $T \to \infty$, we call this form “the bounce”. The bounce has an energy $E_0 = 0$, thus $\frac{\mathrm{d}\bar{x}}{\mathrm{d}\tau} = \sqrt{\frac{2}{M}\mathcal{U}(\bar{x})}$. The bounce action reads

$$\mathcal{S}_0 = M\int_{-\infty}^{+\infty}\mathrm{d}\tau\left(\frac{\mathrm{d}\bar{x}}{\mathrm{d}\tau}\right)^2 = 2M\int_0^\sigma \mathrm{d}\bar{x}\frac{\mathrm{d}\bar{x}}{\mathrm{d}\tau} = 2\int_0^\sigma \mathrm{d}x\sqrt{2M\mathcal{U}(x)}. \tag{B.52}$$

We define “the center of the bounce” the time when $\dot{\bar{x}} = 0$ or equivalently $\bar{x} = \sigma$. For large $T$, a bounce centered anywhere in the interval of integration is an approximated stationary point of the functional integrand. So also are $n$ separated bounces, with centers at $t_1, \ldots, t_n$ where $T/2 > t_1 > \cdots > t_n > -T/2$. We propose to evaluate the functional integral by summing over all these configurations.

1. The action for $n$ bounces is $n\mathcal{S}_0$.
2. We obtain $\sqrt{\frac{M\omega_0}{\pi\hbar}}\mathrm{e}^{-\omega_0 T/2}\mathcal{K}^n$ where $\mathcal{K}$ is determined by demanding that this expression gives the right answer for one bounce.

3. We must integrate over the location of the centers:

$$\int_{-\frac{T}{2}}^{+\frac{T}{2}} \mathrm{d}t_1 \int_{-\frac{T}{2}}^{t_1} \mathrm{d}t_2 \dots \int_{-\frac{T}{2}}^{t_{n-1}} \mathrm{d}t_n = \frac{T^n}{n!}. \tag{B.53}$$

We can perform the summation:

$$\langle 0|\, \mathrm{e}^{-\frac{1}{\hbar}\mathcal{H}T}\, |0\rangle = \sum_{n=0}^{\infty} \sqrt{\frac{M\omega_0}{\pi\hbar}} \mathrm{e}^{-\omega_0 T/2} \mathcal{K}^n \mathrm{e}^{-n\mathcal{S}_0/\hbar} \frac{T^n}{n!} = \sqrt{\frac{M\omega_0}{\pi\hbar}} \mathrm{e}^{-\omega_0 T/2 + \mathcal{K}\,\mathrm{e}^{-\mathcal{S}_0/\hbar} T}. \tag{B.54}$$

Thus the inclusion of the multibounce configuration has modified the ground-state energy:

$$E_0 = \frac{1}{2}\hbar\omega_0 - \hbar\mathcal{K}\,\mathrm{e}^{-\mathcal{S}_0/\hbar}. \tag{B.55}$$

Hence, from Eq. (B.14),the decay probability per unit time of the unstable state is given by

$$\Gamma = 2\,\mathrm{e}^{-\mathcal{S}_0/\hbar} \mathrm{Im}\,\mathcal{K}. \tag{B.56}$$

From Eq. (B.51) and Eq. (B.54) with $n = 1$ it yields

$$\mathcal{K} = \frac{1}{T}\left(\frac{\det\left[-M\partial_t^2 + \mathcal{U}''(\bar{x})\right]}{\det\left[-M\partial_t^2 + M\omega_0^2\right]}\right)^{-\frac{1}{2}}, \tag{B.57}$$

when there is no vanishing eigenvalues. But we will see that it is not the case in our situation.

### B.1.7 Multibounce configurations with a double escape path

We perform the calculations of the previous section in the case where the potential has two escape paths as represented on Fig. B.3. In this configuration, there are two types

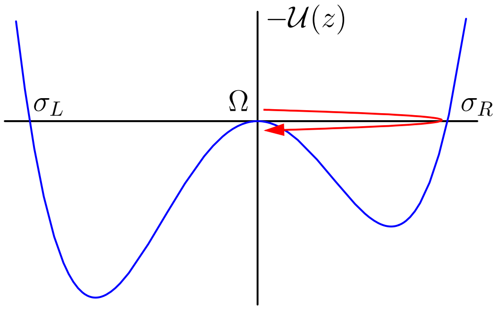

Figure B.3: Inverted potential with double escape path.

of bounce: the $\left|\begin{array}{c}\text{right bounce}\\ \text{left bounce}\end{array}\right|$ where the particle starts at the top of the hill, bounces off the potential $\left|\begin{array}{c}\text{on the right at } x{=}\sigma_R\\ \text{on the left at } x{=}\sigma_L\end{array}\right|$ and returns on the top of the hill. The bounce actions read

$$\mathcal{S}_0^R = 2\int_0^{\sigma_R} \mathrm{d}x \sqrt{2M\mathcal{U}(x)} \qquad \text{and} \qquad \mathcal{S}_0^L = 2\int_0^{\sigma_L} \mathrm{d}x \sqrt{2M\mathcal{U}(x)}. \tag{B.58}$$

The multibounce configurations consist of $n$ right bounces and $m$ left bounces. The corresponding action writes $n\mathcal{S}_0^R + m\mathcal{S}_0^L$. The resulting element of the propagator is $\sqrt{\frac{M\omega_0}{\pi\hbar}}\,\mathrm{e}^{-\omega_0 T/2}\mathcal{K}_R^n\mathcal{K}_L^m$, where

$$\mathcal{K}_{R,L} = \frac{1}{T}\left(\frac{\det\left[-M\partial_t^2 + \mathcal{U}''(\bar{x}_{R,L})\right]}{\det\left[-M\partial_t^2 + M\omega_0^2\right]}\right)^{-\frac{1}{2}}. \tag{B.59}$$

Now we sum over all possible positions of the bounce centers in two steps.

1. We enumerate the number of configurations of $n$ right bounces and $m$ left bounces:

$$\sum_{k_1=1}^{n+1}\sum_{k_2=1}^{k_1}\cdots\sum_{k_{m-1}=1}^{k_{m-2}} k_{m-1} = \binom{n+m}{m} = \frac{(n+m)!}{n!m!}. \tag{B.60}$$

2. For a given order between right and left bounces, we integrate over the location of the centers:

$$\int_{-\frac{T}{2}}^{+\frac{T}{2}}\mathrm{d}t_1\int_{-\frac{T}{2}}^{t_1}\mathrm{d}t_2\ldots\int_{-\frac{T}{2}}^{t_{n+m-1}}\mathrm{d}t_{n+m} = \frac{T^{n+m}}{(n+m)!}. \tag{B.61}$$

Then we sum over the number of right and left bounces:

$$\begin{aligned}\langle 0|\,\mathrm{e}^{-\frac{1}{\hbar}\mathcal{H}T}\,|0\rangle &= \sum_{n=0}^{\infty}\sum_{m=0}^{\infty}\sqrt{\frac{M\omega_0}{\pi\hbar}}\,\mathrm{e}^{-\omega_0 T/2}\mathcal{K}_R^n\mathcal{K}_L^m\,\mathrm{e}^{-(n\mathcal{S}_0^R+m\mathcal{S}_0^L)/\hbar}\frac{T^{n+m}}{(n+m)!}\\ &= \sqrt{\frac{M\omega_0}{\pi\hbar}}\,\exp\Big(-\omega_0 T/2 + \mathcal{K}_R\,\mathrm{e}^{-\mathcal{S}_0^R/\hbar}T + \mathcal{K}_L\,\mathrm{e}^{-\mathcal{S}_0^L/\hbar}T\Big).\end{aligned} \tag{B.62}$$

The ground-state energy of the double-multibounce configuration then reads

$$E_0 = \frac{1}{2}\hbar\omega_0 - \hbar\mathcal{K}_R\,\mathrm{e}^{-\mathcal{S}_0^R/\hbar} - \hbar\mathcal{K}_L\,\mathrm{e}^{-\mathcal{S}_0^L/\hbar}. \tag{B.63}$$

This leads to the total decay rate

$$\Gamma = \Gamma_R + \Gamma_L, \qquad \Gamma_{R,L} = 2\,\mathrm{e}^{-\mathcal{S}_0^{R,L}/\hbar}\mathrm{Im}\,\mathcal{K}_{R,L}. \tag{B.64}$$

As a conclusion, in the limit of a dilute gas of instantons, the total escape rate is simply the sum of the tunneling rates in each barrier. In the following subsections we treat on of the two escape paths for simplicity.

### B.1.8 Propagator of one bounce

To determine $\mathcal{K}$, we study Eq. (B.21) for one bounce $\bar{x}$. Using

$$\dot{\bar{x}} = \sqrt{\frac{2}{M}\mathcal{U}(\bar{x})}, \qquad \ddot{\bar{x}} = \frac{1}{M}\mathcal{U}'(\bar{x}), \qquad \dddot{\bar{x}} = \frac{1}{M}\mathcal{U}''(\bar{x})\dot{\bar{x}}, \tag{B.65}$$

we find that $x_1 \propto \dot{\bar{x}}$ is an eigenvector of Eq. (B.21) with a vanishing eigenvalue. Using the definition of $\mathcal{S}_0$ and the normalization condition, we obtain

$$x_1 = \sqrt{\frac{M}{\mathcal{S}_0}}\dot{\bar{x}}. \tag{B.66}$$

The corresponding integration over $c_1$ in the determinant gives rise to a disaster. However, noting that $\mathrm{d}x = \sqrt{\mathcal{S}_0/M}x_1\mathrm{d}\tau$ and $x_1 = \frac{\mathrm{d}x}{\mathrm{d}c_1}$, we have $(2\pi\hbar)^{-1/2}\mathrm{d}c_1 = \sqrt{\mathcal{S}_0/2M\pi\hbar}\,\mathrm{d}\tau$. The integration over $c_1$ corresponds actually to the integration over $t_1$, which has already been done in Eq. (B.53). Therefore, in evaluating the determinant, we should not include the zero eigenvalue, but we should include in $\mathcal{K}$ a factor of $\sqrt{\mathcal{S}_0/2M\pi\hbar}T$.

We note that $\bar{x}$ has a maximum at the center of the bounce. Thus $x_1$ has a node. Consequently, it does not correspond to the lowest eigenvalue. In other words, there is a negative eigenvalue, $\lambda_0$. The resulting determinant, and hence $\mathcal{K}$, is imaginary. It guarantees a finite lifetime or equivalently a non-zero escape rate. This eigenvalue thus characterizes the possibility for the particle to tunnel.

The eigenvalue $\lambda_0$ being negative, the integration over $c_0$, $(2\pi\hbar)^{-\frac{1}{2}}\int \mathrm{d}c_0 \exp\left[-\frac{\lambda_0}{2\hbar}c_0^2\right]$, has to be performed separately. In the semiclassical limit (the high-$\frac{1}{\hbar}$ limit) we can use the steepest-descent method. It consists of evaluating the integral on a modified contour which goes across a saddle point from the two neighboring valleys[1]. Here, the saddle point is located in $c_0 = 0$ and the direction of the two valleys is $\varphi = \pm\pi/2$. When $c_0$ reaches the saddle point, the contour then goes to $+i\infty$. The integration is thus performed on one half of the Gaussian peak:

$$(2\pi\hbar)^{-\frac{1}{2}}\int_{\mathbb{R}} \mathrm{d}c_0 \exp\left[-\frac{\lambda_0}{2\hbar}c_0^2\right] = \frac{1}{2}i\frac{1}{\sqrt{|\lambda_0|}} = \frac{1}{2}\frac{1}{\sqrt{\lambda_0}}. \tag{B.67}$$

Therefore, the determinant has to be divided by two:

$$\mathrm{Im}\left(\mathcal{N}\int_0^0 \mathcal{D}x\,\mathrm{e}^{-\frac{1}{\hbar}\mathcal{S}}\right)_{1\text{ bounce}} = \frac{1}{2}\mathcal{N}\,\mathrm{e}^{-\mathcal{S}_0/\hbar}\sqrt{\frac{\mathcal{S}_0}{2M\pi\hbar}}T|\mathrm{det}'\left[-M\partial_\tau^2 + \mathcal{U}''(\bar{x})\right]|^{-\frac{1}{2}}, \tag{B.68}$$

where $\det'$ indicates that the zero eigenvalue is to be omitted. Actually, this is the result (B.25) with a primed determinant and multiplied by the factor $\frac{1}{2} \times \sqrt{\mathcal{S}_0/2M\pi\hbar}T$.

The presence of the coefficient $\frac{1}{2}$ can be interpreted in two different ways.

The first one is to consider that, to escape, the particle needs to go beyond the point $x = \sigma$. Only one half of all the possible paths satisfies this condition.

From the second point of view we note that, due to $c_0$, the path $x$ acquires an imaginary part $c_0 = ic_{0,I}$. Focusing on the distance $|x| = \sqrt{(\mathrm{Re}(x))^2 + {c_{0,I}}^2}$, we see that all possibilities are taken into account if $c_{0,I}$ travels on $\mathbb{R}^+$ or $\mathbb{R}^-$. Consequently, the integration is performed only on one half of the Gaussian peak.

Comparing this to the definition of $\mathcal{K}$ (Eq. (B.54) with the term $n = 1$), we find

$$\mathrm{Im}\mathcal{K} = \frac{1}{2}\sqrt{\frac{\mathcal{S}_0}{2M\pi\hbar}}\left|\frac{\mathrm{det}'\left[-M\partial_\tau^2 + \mathcal{U}''(\bar{x})\right]}{\mathrm{det}\left[-M\partial_\tau^2 + M\omega_0^2\right]}\right|^{-\frac{1}{2}}. \tag{B.69}$$

Hence, the tunneling rate is given by

$$\Gamma = \sqrt{\frac{\mathcal{S}_0}{2M\pi\hbar}}\,\mathrm{e}^{-\mathcal{S}_0/\hbar}\left|\frac{\mathrm{det}'\left[-M\partial_\tau^2 + \mathcal{U}''(\bar{x})\right]}{\mathrm{det}\left[-M\partial_\tau^2 + M\omega_0^2\right]}\right|^{-\frac{1}{2}}. \tag{B.70}$$

---

[1] To calculate the integral $I = \int_C \mathrm{d}z\,\mathrm{e}^{\alpha f(z)}$, where $\alpha$ is positive and large, it is possible to use the saddle-point method. The approximate result reads $I = \sqrt{\frac{2\pi}{\alpha\rho}}\,\mathrm{e}^{\alpha f(z_0)}\,\mathrm{e}^{i\varphi}$, where $z_0$ is the position of the saddle-point (supposed to be unique) of the function $f(z)$, $f''(z_0) = \rho\,\mathrm{e}^{i\theta}$ and $\varphi = -\theta/2 \pm \pi/2$ is the direction of the valley.

### B.1.9 Explicit expression using the bounce orbit

So as to calculate the ratio of the two determinants, we use the result of section B.1.4. We note $W^{(1)} = \mathcal{U}''(\bar{x})$ and $W^{(2)} = M\omega_0^2$. We already know the solution $\psi_0^{(2)}(T/2) \overset{T\to\infty}{\sim} \frac{\mathrm{e}^{\omega_0 T}}{2\omega_0}$.

We define the constant $\alpha$ through the relation $x_1(\tau) \overset{\tau\to\infty}{\sim} \alpha\,\mathrm{e}^{-\omega_0\tau}$ or equivalently with $\bar{x}(\tau) \overset{\tau\to\infty}{\sim} \alpha\sqrt{\mathcal{S}_0/M}/\omega_0\,\mathrm{e}^{-\omega_0\tau}$. To construct the solution $\psi_0^{(2)}(\tau)$ we need another independent solution, $y_1(\tau)$

$$y_1(\tau) \propto x_1(\tau) \int^{\tau} \mathrm{d}\tau' \frac{1}{x_1(\tau')^2} \overset{T\to\pm\infty}{\sim} \pm\alpha\,\mathrm{e}^{-\omega_0\tau}. \tag{B.71}$$

Then,

$$\psi_0^{(2)}(\tau) = \frac{1}{2\omega_0}\left(\mathrm{e}^{\omega_0 T/2} x_1(\tau) + \mathrm{e}^{-\omega_0 T/2} y_1(\tau)\right), \tag{B.72}$$

and $\psi_0^{(2)}(T/2) = {\omega_0}^{-1}$. To find the lowest eigenvalue, we must find $\psi_\lambda(\tau)$ for small $\lambda$. At first order in $\lambda$, this can be obtained with the formula

$$\psi_\lambda(\tau) = \psi_0^{(2)}(\tau) - \frac{\lambda}{2M\omega_0\alpha^2}\int_{-\frac{T}{2}}^{\tau} \mathrm{d}\tau' \left[y_1(\tau)x_1(\tau') - x_1(\tau)y_1(\tau')\right]\psi_0^{(2)}(\tau'), \tag{B.73}$$

which becomes, for large $T$,

$$\psi_\lambda(T/2) = \frac{1}{2\omega_0}\left(1 - \frac{\lambda}{4M\omega_0\alpha^2}\,\mathrm{e}^{\omega_0 T}\right). \tag{B.74}$$

Then the condition $\psi_{\lambda_0}(T/2) = 0$ gives

$$\lambda_0 = 4M\omega_0\alpha^2\,\mathrm{e}^{-\omega_0 T}, \tag{B.75}$$

which tends to zero for large time $T$. This yields,

$$\frac{\det'\left[-M\partial_\tau^2 + \mathcal{U}''(\bar{x})\right]}{\det\left[-M\partial_\tau^2 + M\omega_0^2)\right]} = \frac{1}{2M\omega_0\alpha^2}. \tag{B.76}$$

Finally, if we define $C_0 = \sqrt{2/\omega_0}\alpha$, *i.e.*

$$\bar{x}(\tau) \overset{\tau\to\pm\infty}{\longrightarrow} C_0\sqrt{\frac{\mathcal{S}_0}{2M\omega_0}}\,\mathrm{e}^{-\omega_0|\tau|}, \tag{B.77}$$

the escape rate reads

$$\Gamma = \omega_0 C_0\sqrt{\frac{\mathcal{S}_0}{2\pi\hbar}}\,\mathrm{e}^{-\mathcal{S}_0/\hbar}. \tag{B.78}$$

The coefficient $C_0$ is a real number depending on the shape of the potential between $x = 0$ and $x = \sigma$. It can be determined from the asymptotic behavior of $\bar{x}$:

$$\bar{x} \overset{\tau\to\pm\infty}{\sim} \sigma\gamma\mathrm{e}^{-\omega_0\tau} \qquad \Longrightarrow \qquad \tau \overset{\tau\to\pm\infty}{\sim} -\frac{1}{\omega_0}\ln\bar{x} + \frac{\ln(\sigma\gamma)}{\omega_0}, \tag{B.79}$$

$$|\dot{\bar{x}}| = \sqrt{\frac{2}{M}\mathcal{U}(\bar{x})} \qquad \Longrightarrow \qquad |\tau| = \int_{\bar{x}}^{\sigma}\mathrm{d}x\left[\sqrt{\frac{M}{2\mathcal{U}(x)}} - \frac{1}{\omega_0 x}\right] - \frac{1}{\omega_0}\ln\Big(\frac{\bar{x}}{\sigma}\Big). \tag{B.80}$$

We get

$$\gamma = \mathrm{e}^{\mathcal{I}}, \qquad \mathcal{I} = \int_0^\sigma \mathrm{d}x \left[\sqrt{\frac{M\omega_0^2}{2\mathcal{U}(x)}} - \frac{1}{x}\right]. \tag{B.81}$$

As a conclusion, the tunneling rate of a particle of mass $M$ from an unstable state at $x = 0$ to the exit point at $x = \sigma$ through the barrier potential $\mathcal{U}(x)$ with the bottom-well frequency $\omega_0$ reads

$$\Gamma = \mathcal{A}\,\mathrm{e}^{-\mathcal{B}/\hbar} \tag{B.82}$$

$$\mathcal{A} = \omega_0\sqrt{\frac{M\omega_0}{\pi\hbar}}\,\sigma\,\mathrm{e}^{\mathcal{I}} \tag{B.83}$$

$$\mathcal{B} = 2\int_0^\sigma \mathrm{d}x\sqrt{2M\mathcal{U}(x)} \tag{B.84}$$

$$\mathcal{I} = \int_0^\sigma \mathrm{d}x \left[\sqrt{\frac{M\omega_0^2}{2\mathcal{U}(x)}} - \frac{1}{x}\right] \tag{B.85}$$

This general result can be applied to the case of a quartic potential, as we will see in Sec. B.2.

### B.1.10 Decay rate of metastable excited states

We consider the escape rate of the $n^{\mathrm{th}}$ excited state with energy $E_n$. Noting $\xi_n = \frac{2E_n}{\hbar\omega_0}$, from Ref. [203] we have

$$\Gamma_n = \mathcal{A}_n\,\mathrm{e}^{-\mathcal{B}_0/\hbar}, \qquad \mathcal{A}_n = \frac{T_0}{T_n}\frac{\left(\frac{\sqrt{2\pi}}{T_0}\right)^{1-\xi_n}}{\left(\frac{\xi_n-1}{2}\right)!}\,\mathcal{A}_0{}^{\xi_n}, \tag{B.86}$$

where $T_n$ is the period of oscillation in the well of the $n^{\mathrm{th}}$ state.

- In the case of an harmonic potential we have $\xi_n = 2n+1$ and $T_n = \frac{2\pi}{\omega_0}$. This leads to
$$\Gamma_n = \mathcal{A}_n\,\mathrm{e}^{-\mathcal{B}_0/\hbar}, \qquad \mathcal{A}_n = \frac{1}{n!}\left(\frac{2\pi}{\omega_0{}^2}\right)^n \mathcal{A}_0{}^{2n+1}. \tag{B.87}$$
- In the case of an anharmonic potential with level spacing depending on the anharmonicity $\Lambda$ according to $E_n - E_{n-1} = \hbar\omega_0(1-n\Lambda)$ we have $\xi_n = 2n+1-n(n+1)\Lambda$ and, at zeroth order, $T_n = \frac{2\pi}{\omega_0}$. This leads to

$$\mathcal{A}_n = \frac{1}{(n-n(n+1)\Lambda/2)!}\left(\frac{2\pi}{\omega_0{}^2}\right)^{n-n(n+1)\frac{\Lambda}{2}} \mathcal{A}_0{}^{2n+1-n(n+1)\Lambda}. \tag{B.88}$$

## B.2 Application to a polynomial potential

### B.2.1 General quartic potential

We consider a particle of mass $M$ tunneling through the potential

$$\mathcal{U}_b(x) = \frac{1}{2}M\omega_0^2x^2\left(1 - bx - ax^2\right), \tag{B.89}$$

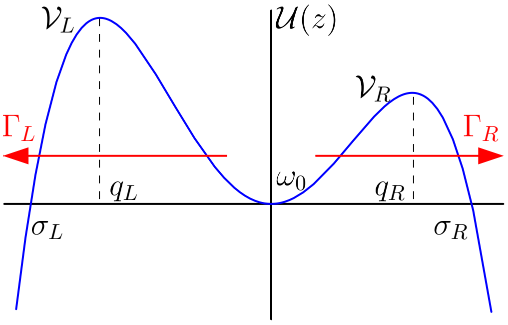

Figure B.4: The total tunneling rate is the sum of the tunneling rate in each barrier.

where $a > 0$ (see Fig. B.4). This potential has a minimum at $x = 0$, two barriers $\mathcal{V}_R$ and $\mathcal{V}_L$ located respectively at $x = q_R > 0$ and $q_L < 0$ and two exit points at $x = \sigma_R < 0$ and $\sigma_L < 0$. The total tunneling rate of a particle in the ground state of the minimum is the sum of the tunneling rate through the right and the left barrier: $\Gamma = \Gamma_R + \Gamma_L$. We define

$$\sigma_b = \sqrt{\frac{b^2}{4a^2} + \frac{1}{a}} - \frac{b}{2a}, \tag{B.90}$$

$$q_b = \sqrt{\frac{9b^2}{64a^2} + \frac{1}{2a}} - \frac{3b}{8a}, \tag{B.91}$$

$$\mathcal{V}_b = \mathcal{U}_b(q_b), \tag{B.92}$$

and

$$\Gamma_b = \mathcal{A}_b \, \mathrm{e}^{-\mathcal{B}_b/\hbar}, \tag{B.93}$$

$$\mathcal{A}_b = \omega_0 \sqrt{\frac{M\omega_0}{\pi\hbar}} \, \sigma_b \, \mathrm{e}^{\mathcal{I}_b}, \tag{B.94}$$

$$\mathcal{B}_b = 2 \int_0^{\sigma_b} \mathrm{d}x \sqrt{2M\mathcal{U}_b(x)}, \tag{B.95}$$

$$\mathcal{I}_b = \int_0^{\sigma_b} \mathrm{d}x \left[ \sqrt{\frac{M\omega_0^2}{2\mathcal{U}_b(x)}} - \frac{1}{x} \right], \tag{B.96}$$

such that $\sigma_R = \sigma_b$, $\sigma_L = -\sigma_{-b}$, $q_R = q_b$, $q_L = -q_{-b}$, $\mathcal{V}_b = \mathcal{V}_R$, $\mathcal{V}_{-b} = \mathcal{V}_L$, $\Gamma_R = \Gamma_b$, $\Gamma_L = \Gamma_{-b}$ and $\Gamma = \Gamma_b + \Gamma_{-b}$.

We note $R(x) = 1 - bx - ax^2$ and use the results

$$\int^x \mathrm{d}x \, xR(x) = -\frac{\sqrt{R(x)^3}}{3a} - b\frac{b + 2ax}{8a^2}\sqrt{R(x)} - b\frac{b^2 + 4a}{16a^2\sqrt{a}} \arcsin\left(\frac{b + 2ax}{\sqrt{b^2 + 4a}}\right), \tag{B.97}$$

$$\int^x \mathrm{d}x \left[\frac{1}{xR(x)} - \frac{1}{x}\right] = -\ln\Big(2 - bx + 2\sqrt{R(x)}\Big), \tag{B.98}$$

together with $R(0)=1$ and $R(\sigma_b)=0$ to find

$$\mathcal{I}_b = -\ln\left(\frac{2-b\sigma_b}{4}\right), \tag{B.99}$$

$$\mathcal{A}_b = 4\omega_0\sqrt{\frac{M\omega_0}{\pi\hbar}}\frac{\sigma_b}{2-b\sigma_b}, \tag{B.100}$$

$$\mathcal{B}_b = \frac{2M\omega_0}{a}\left(\frac{1}{3}+\frac{b^2}{8a}-b\frac{b^2+4a}{16a^{3/2}}\arccos\left(\frac{b}{\sqrt{b^2+4a}}\right)\right). \tag{B.101}$$

The total escape rate from the potential Eq. (B.89) is finally

$$\Gamma = \Gamma_b + \Gamma_{-b}, \tag{B.102}$$

with the tunneling rate for each barrier

$$\Gamma_b = 4\omega_0\sqrt{\frac{M\omega_0}{\pi\hbar}}\frac{\sigma_b}{2-b\sigma_b}\exp\left(-\frac{2M\omega_0}{a\hbar}\left[\frac{1}{3}+\frac{b^2}{8a}-b\frac{b^2+4a}{16a^{3/2}}\arccos\left(\frac{b}{\sqrt{b^2+4a}}\right)\right]\right). \tag{B.103}$$

Parameters $a$ and $b$ can be expressed in terms of the barrier height $\mathcal{V}_b$ and its position $q_b$:

$$a = \frac{1}{q_b^2}\left(\frac{6\mathcal{V}_b}{M\omega_0^2q_b^2}-1\right), \tag{B.104}$$

$$b = \frac{2}{q_b}\left(1-\frac{4\mathcal{V}_b}{M\omega_0^2q_b^2}\right). \tag{B.105}$$

The general result for the escape rate can be applied to the symmetric camel back potential and the cubic potential.

### B.2.2 Symmetric camel-back potential

In the limit $b\to 0$, from Eq. (B.103), the tunneling rate reads

$$\Gamma = \Gamma_R + \Gamma_L, \qquad \Gamma_{R,L} = 8\frac{\omega_0}{2\pi}\sqrt{\frac{2\pi\mathcal{V}_{R,L}}{\hbar\omega_0}}\,\mathrm{e}^{-\frac{16}{3}\frac{\mathcal{V}_{R,L}}{\hbar\omega_0}}. \tag{B.106}$$

Actually, in the case $b=0$ it is possible to determine the bounce orbit from Eq. (B.19). Indeed, when $b=0$ we have $\sigma=a^{-1/2}$, $\mathcal{V}=M\omega_0^2\sigma^2/8$ and the potential becomes $\mathcal{U}(x)=\frac{4\mathcal{V}}{\sigma^4}x^2(\sigma^2-x^2)$. The bounce orbit $\bar{x}$ satisfies the differential equation

$$\ddot{\bar{x}} = \omega_0^2\bar{x}\left(1-2\frac{\bar{x}^2}{\sigma^2}\right), \tag{B.107}$$

which solution is proportional to the Jacobi elliptic function $\mathrm{dn}(\omega_0\tau,1)=\cosh(\omega_0\tau)^{-1}$ (see Fig. 3.7):

$$\bar{x}(\tau) = \frac{\sigma}{\cosh(\omega_0\tau)}. \tag{B.108}$$

The asymptotic behavior $\bar{x}(\tau)\overset{\tau\to\pm\infty}{\sim}2\sigma\,\mathrm{e}^{-\omega_0|\tau|}$ gives the correct prefactor $C_0=\sqrt{12}$. If the potential is symmetric, the tunneling rate reads

$$\Gamma = 16\frac{\omega_0}{2\pi}\sqrt{\frac{2\pi\mathcal{V}}{\hbar\omega_0}}\exp\left[-\frac{16}{3}\frac{\mathcal{V}}{\hbar\omega_0}\right]. \tag{B.109}$$

### B.2.3 Cubic potential

In the limit $a \to 0$, depending on the sign of $b$, one of the barrier disappears: its position is shifted to $\pm\infty$ and its height becomes infinite. Therefore, only one direction of escape is allowed.

Indeed,

$$\sigma_b = \frac{1}{|b|} + \frac{|b|}{2a}\left(1 - \mathrm{sgn}(b)\right), \tag{B.110}$$

$$q_b = \frac{4}{3|b|} + \frac{3|b|}{8a}\left(1 - \mathrm{sgn}(b)\right). \tag{B.111}$$

Moreover, using the Taylor series

$$\arccos\left(\frac{1}{\sqrt{1+\epsilon}}\right) \simeq \sqrt{\epsilon}\left(1 - \frac{x}{3} + \frac{x^2}{5}\right), \tag{B.112}$$

coefficients $\mathcal{A}_b$ and $\mathcal{B}_b$ become

$$\mathcal{A}_b \simeq \sqrt{\frac{M\omega_0}{\pi\hbar}}\frac{4\omega_0}{|b|}, \tag{B.113}$$

$$\mathcal{B}_b \simeq \frac{8M\omega_0}{15b^2}\mathrm{sgn}(b) + \left(\frac{1}{3a} + \frac{b^2}{8a^2}\right)\left(1 - \mathrm{sgn}(b)\right). \tag{B.114}$$

Therefore

$$\text{If } b > 0 \qquad \left\{ \begin{array}{rcl} \sigma_R & = & \frac{1}{|b|} \\ q_R & = & \frac{4}{3|b|} \\ \sigma_L, q_L & \to & +\infty \end{array} \qquad \begin{array}{rcl} \mathcal{A}_R & = & \sqrt{\frac{M\omega_0}{\pi\hbar}}\frac{4\omega_0}{|b|} \\ \mathcal{B}_R & = & \frac{8M\omega_0}{15b^2} \\ \Gamma_L & \to & 0 \end{array} \right. \tag{B.115}$$

$$\text{If } b < 0 \qquad \left\{ \begin{array}{rcl} \sigma_L & = & \frac{1}{|b|} \\ q_L & = & \frac{4}{3|b|} \\ \sigma_R, q_R & \to & -\infty \end{array} \qquad \begin{array}{rcl} \mathcal{A}_L & = & \sqrt{\frac{M\omega_0}{\pi\hbar}}\frac{4\omega_0}{|b|} \\ \mathcal{B}_L & = & \frac{8M\omega_0}{15b^2} \\ \Gamma_R & \to & 0 \end{array} \right. \tag{B.116}$$

Finally, let us note $\mathcal{V}$ the barrier height. Then

$$\Gamma = 12\frac{\omega_0}{2\pi}\sqrt{\frac{6\pi\mathcal{V}}{\hbar\omega_0}}\,\exp\left[-\frac{36}{5}\frac{\mathcal{V}}{\hbar\omega_0}\right]. \tag{B.117}$$

This result is well-know in MQT studies.

### B.2.4 Effect of the periodicity of the camel-back potential on the tunneling rate

#### 2.2.4.a Periodic configuration

We consider the case of the symmetric and periodic camel-back potential and build a simple model to understand its dynamics. Each period is composed of two different wells (see Fig. B.5):

- A small well with a quartic shape corresponding to the well between the two humps of the camel. It is characterized by the bottom well frequency $\omega_0$, the total escape rate $2\Gamma_{\text{out}}$ and the total entrance rate $2\Gamma_{\text{in}}$.

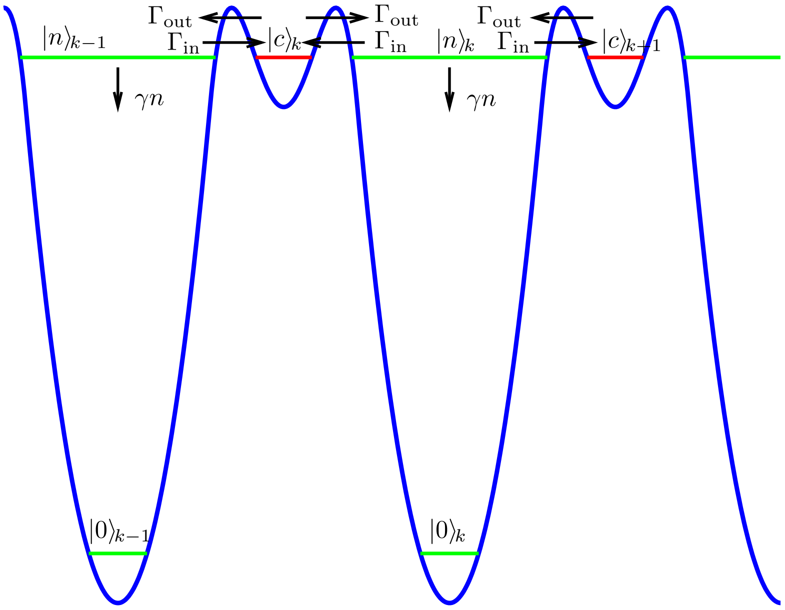

Figure B.5: Scheme of the symmetric periodic camel-back potential with the corresponding levels and rates.

- A large well supposed here to be quadratic which corresponds to the well of the neck or the tail of the camel. This harmonic potential, characterized by the bottom well frequency $\omega_p$, contains a lot of states. We assume that one of these states, the $n^{\text{th}}$ state $|n\rangle$, is in resonance with the state in the quartic well $|c\rangle$ $\left(n = \frac{E_{|c\rangle} - \frac{1}{2}\hbar\omega_p}{\hbar\omega_p}\right)$. Due to dissipation, this state has a finite lifetime. Indeed, if we note $\gamma$ the relaxation rate of a state $|m\rangle$ to the state $|m-1\rangle$ of the harmonic oscillator, one can show that the lifetime of the state $|n\rangle$ is $(n\gamma)^{-1}$. This state will finally relax to the lowest energy level $|0\rangle$.

From the preceding sections, we know the escape rate $\Gamma_{\text{out}}$. Then we can evaluate roughly the entrance rate $\Gamma_{\text{in}}$. Let us call $\mathcal{T}$ the transparency of the quartic barrier ($\mathcal{T}$ do not depend on the tunneling direction). The escape rate from the quartic well, with the bottom well frequency $\omega_0$, is equal to the transparency of the barrier times the attempting rate: $\Gamma_{\text{out}} = \omega_0\mathcal{T}$. Similarly, $\Gamma_{\text{in}} = \omega_p\mathcal{T}$. This gives $\Gamma_{\text{in}} = \frac{\omega_p}{\omega_0}\Gamma_{\text{out}}$.

We consider that this relaxation rate $\gamma$ is huge compared to $\Gamma_{\text{out}}$. Therefore we look at the effect of double tunneling only, which is equivalent to the first order correction in $1/\gamma$ of the escape rate.

Let us focus now on the $k^{\text{th}}$ period starting with a quartic well and look at the evolution of the population of the different states:

- The population of the state $|c\rangle_k$
  - decreases with the rate $2\Gamma_{\text{out}}$ due to the escape towards the state $|n\rangle_k$ or $|n\rangle_{k-1}$,
  - increases with the rate $2\Gamma_{\text{in}}$ due to the entrance from the state $|n\rangle_k$ or $|n\rangle_{k-1}$.
- The population of the state $|n\rangle_k$
  - decreases with the rate $n\gamma$ due to the relaxation towards the state $|0\rangle_k$,

- decreases with the rate $2\Gamma_{\rm in}$ due to the escape towards the state $|c\rangle_k$ or $|c\rangle_{k+1}$,
- increases with the rate $2\Gamma_{\rm out}$ due to the entrance from the state $|c\rangle_k$ or $|c\rangle_{k+1}$.

We start at $t=0$ with the particle in one of the quartic well. We want to determine the escape rate of the particle taking into account that it can jump to another quartic well via the states $|n\rangle_k$. If the lifetime $n\gamma$ of the state $|n\rangle$ was zero ($\gamma \to \infty$), this rate would be simply $2\Gamma_{\rm out}$. We call $P_{c,k}(t)$, $P_{n,k}(t)$ and $P_{0,k}(t)$ the probability of the particle to be in the state $|c\rangle_k$, $|n\rangle_k$ and $|0\rangle_k$, respectively. The preceding discussion can be traduced into the following set of differential equations:

$$\dot{P}_{c,k}(t) = -2\Gamma_{\rm out}P_{c,k}(t) + \Gamma_{\rm in}P_{n,k}(t) + \Gamma_{\rm in}P_{n,k-1}(t), \tag{B.118}$$

$$\dot{P}_{n,k}(t) = -n\gamma P_{n,k}(t) - 2\Gamma_{\rm in}P_{n,k}(t) + \Gamma_{\rm out}P_{c,k}(t) + \Gamma_{\rm out}P_{c,k+1}(t), \tag{B.119}$$

$$\dot{P}_{0,k}(t) = n\gamma P_{n,k}(t). \tag{B.120}$$

Because of the periodicity, we are interested in the probability for the particle to be in one of the states $|c\rangle$ or $|n\rangle$. Defining $P_c(t) = \sum_k P_{c,k}(t)$, $P_n(t) = \sum_k P_{n,k}(t)$, and summing all the differential equations we get

$$\partial_t \begin{pmatrix} P_c(t) \\ P_n(t) \end{pmatrix} = \mathrm{M} \begin{pmatrix} P_c(t) \\ P_n(t) \end{pmatrix}, \qquad \mathrm{M} = \begin{pmatrix} -2\Gamma_{\rm out} & 2\Gamma_{\rm in} \\ 2\Gamma_{\rm out} & -n\gamma - 2\Gamma_{\rm in} \end{pmatrix}. \tag{B.121}$$

The eigenvalues of the matrix M give rise to the escape rates. One of them is dominated by the rate $n\gamma \gg \Gamma_{\rm out}$ and, consequently, won't participate. At first order in $1/\gamma$, the other one reads

$$\tilde{\Gamma} = 2\Gamma_{\rm out} - \frac{4\Gamma_{\rm out}\Gamma_{\rm in}}{n\gamma}. \tag{B.122}$$

Due to the non-zero lifetime of the state $|n\rangle$, the escape probability $2\Gamma_{\rm out}$ is reduced by $4\,\Gamma_{\rm out}\,\frac{1}{n\gamma}\,\Gamma_{\rm in}$. This result corresponds to the four possibilities of double tunneling: the particle escapes with rate $\Gamma_{\rm out}$, stays at the state $|n\rangle$ with lifetime $1/n\gamma$ and enters with rate $\Gamma_{\rm in}$.

Explicitly,

$$\tilde{\Gamma} = 16\omega_0\sqrt{\frac{\mathcal{V}}{2\pi\hbar\omega_0}}\,\mathrm{e}^{-\frac{16}{3}\frac{\mathcal{V}}{\omega_0}} - 16^2\frac{\omega_0\omega_p}{n\gamma}\frac{\mathcal{V}}{2\pi\hbar\omega_0}\,\mathrm{e}^{-\frac{32}{3}\frac{\mathcal{V}}{\omega_0}}. \tag{B.123}$$

Due to retrapping, the escape rate is decreased.

### 2.2.4.b Quasi-periodic configuration

We consider the case of the quasi-periodic camel-back potential and calculate the retrapping rate. In this situation, the right and left tunneling rates are different ($\Gamma^R_{\rm out}$, $\Gamma^L_{\rm out}$, $\Gamma^R_{\rm in}$, $\Gamma^L_{\rm in}$). A state $|c\rangle_k$ is coupled in resonance to the $n^{\rm th}$ state $|n\rangle_k$ on its right and to the $m^{\rm th}$ state $|m\rangle_k$ on its left. At zero temperature, the double tunneling from the state $|c\rangle_k$ to the state $|c\rangle_{k-1}$ is forbidden. The lifetime of the state $|n\rangle$ is $(n\gamma)^{-1}$ because it is the higher level of the harmonic well. The occupation probability of a state $|m < n\rangle$ decreases exponentially with all rates $m\gamma$, $(m-1)\gamma \ldots\ n\gamma$. If $\gamma$ is large, we can keep the leading rate $m\gamma$. The system of differential equations reads

$$\dot{P}_{c,k}(t) = -(\Gamma_{\text{out}}^R + \Gamma_{\text{out}}^L)P_{c,k}(t) + \Gamma_{\text{in}}^R P_{n,k}(t) + \Gamma_{\text{in}}^L P_{m,k-1}(t), \tag{B.124}$$

$$\dot{P}_{n,k}(t) = -(n\gamma + \Gamma_{\text{in}}^R)P_{n,k}(t) + \Gamma_{\text{out}}^R P_{c,k}(t), \tag{B.125}$$

$$\dot{P}_{m,k}(t) = -(m\gamma + \Gamma_{\text{in}}^L)P_{m,k}(t) + \Gamma_{\text{out}}^L P_{c,k+1}(t) + n\gamma P_{n,k}(t), \tag{B.126}$$

$$\dot{P}_{0,k}(t) = m\gamma P_{m,k}(t). \tag{B.127}$$

To get the escape rate from one of the states $|c\rangle$, we sum up all the differential equations to get

$$\partial_t \begin{pmatrix} P_c(t) \\ P_n(t) \\ P_m(t) \end{pmatrix} = \mathrm{M} \begin{pmatrix} P_c(t) \\ P_n(t) \\ P_m(t) \end{pmatrix}, \qquad \mathrm{M} = \begin{pmatrix} -\Gamma_{\text{out}}^R - \Gamma_{\text{out}}^L & \Gamma_{\text{in}}^R & \Gamma_{\text{in}}^L \\ \Gamma_{\text{out}}^R & -n\gamma - \Gamma_{\text{in}}^R & 0 \\ \Gamma_{\text{out}}^L & n\gamma & -m\gamma - \Gamma_{\text{in}}^L \end{pmatrix}. \tag{B.128}$$

At first order in $1/\gamma$, the effective rate reads

$$\tilde{\Gamma} = \Gamma_{\text{out}}^R + \Gamma_{\text{out}}^L - \left( \frac{\Gamma_{\text{out}}^R \Gamma_{\text{in}}^R}{n\gamma} + \frac{\Gamma_{\text{out}}^L \Gamma_{\text{in}}^L}{m\gamma} + \frac{\Gamma_{\text{out}}^R \Gamma_{\text{in}}^L}{m\gamma} \right). \tag{B.129}$$

The correcting rate corresponds to the three possibilities of double tunneling.

Appendix C

# Quantum dynamics of the Josephson atom

## Contents

## Introduction

In this appendix we detail the calculations used in Chap. 4. We derive first the Lindblad equation of the reduced density matrix for a free field that leads to Eq. (4.14). Then we give the general result for the evolution equation of the density matrix elements. Finally we detail how we construct the semiclassical dynamical equations.

## C.1 Lindblad master equation for a free field

### C.1.1 General free field

We consider the interaction of a free field (*e.g.* photons spontaneously emitted from the relaxation of the qubit or the light mode in the cavity) with a heatbath at the temperature $T$ [100, 101]. The Hamiltonian $\mathcal{H}$ of the system is composed of

- The Hamiltonian of the free field $\mathcal{H}_F = \hbar\omega c^\dagger c$. The operator $c$ corresponds to $\sigma_{ij}$ in the case of a qubit transition $|j\rangle - |i\rangle$ with $\omega = (\varepsilon_j - \varepsilon_i)/\hbar$ or to $a_\alpha$ in the case of the mode of the cavity $\alpha$ with $\omega = \omega_\alpha$.

- The Hamiltonian of the bath is composed of an infinite number of harmonic oscillators $\mathcal{H}_B = \sum_l \hbar\omega_l b_l^\dagger b_l$ where the operators $b_l$ and $b_l^\dagger$ are the annihilation and the creation operator, respectively, in the mode $l$ of the bath.

- The coupling Hamiltonian $\mathcal{H}_{F-B} = i\hbar \sum_l g_l(c + c^\dagger)(b_l - b_l^\dagger)$ where $g_l$ is the coupling strength between the free field and the mode $l$ of the bath. To simplify the calculations we define the operator $C_1 = c$, $C_2 = c^\dagger$ and $B_1 = B_2 = i\sum_l g_l(b_l - b_l^\dagger)$.

The density matrix of the total system obeys the equation

$$\frac{\mathrm{d}\rho_{\mathrm{tot}}}{\mathrm{d}t} = \frac{1}{i\hbar}\left[\mathcal{H}, \rho_{\mathrm{tot}}\right]. \tag{C.1}$$

It is convenient to proceed in the interaction picture with respect to the Hamiltonian $\mathcal{H}_0 = \mathcal{H}_F + \mathcal{H}_B$: $\tilde{\mathcal{O}}(t) = \exp[i\mathcal{H}_0 t/\hbar]\,\mathcal{O}\exp[-i\mathcal{H}_0 t/\hbar]$ for an operator $\mathcal{O}$ in the Schrödinger picture. The interaction Hamiltonian has the form $\tilde{\mathcal{H}}_{F-B}(t) = \hbar\sum_k \tilde{C}_k(t)\tilde{B}_k(t)$ with

$$\tilde{C}_{1,2}(t) = C_k\,\mathrm{e}^{\mp i\Delta\omega t}. \tag{C.2}$$

In the interaction picture, the evolution equation for the density matrix reads

$$\dot{\tilde{\rho}}_{\mathrm{tot}}(t) = \frac{1}{i\hbar}\left[\tilde{\mathcal{H}}_{F-B}(t), \tilde{\rho}_{\mathrm{tot}}(t)\right]. \tag{C.3}$$

Noting $\rho_0 = \tilde{\rho}_{\mathrm{tot}}(0)$, we get from the first derivative

$$\begin{aligned}\tilde{\rho}_{\mathrm{tot}}(t) = \rho_0 + \sum_{m=1}^{\infty} \frac{1}{(i\hbar)^m}\int_0^t \mathrm{d}\tau_1 \int_0^{\tau_1}\mathrm{d}\tau_2 \ldots \int_0^{\tau_{m-1}}\mathrm{d}\tau_m \\ \times\left[\tilde{\mathcal{H}}_{F-B}(\tau_1), \left[\tilde{\mathcal{H}}_{F-B}(\tau_2), \left[\ldots, \left[\tilde{\mathcal{H}}_{F-B}(\tau_m), \rho_0\right]\ldots\right]\right]\right].\end{aligned} \tag{C.4}$$

At second order ($m = 2$) it yields

$$\begin{aligned}\tilde{\rho}_{\mathrm{tot}}(t) = \rho_0 &+ \frac{1}{i\hbar}\int_0^t \mathrm{d}\tau\left[\tilde{\mathcal{H}}_{F-B}(\tau), \rho_0\right] \\ &- \frac{1}{\hbar^2}\int_0^t \mathrm{d}\tau_1\int_0^{\tau_1}\mathrm{d}\tau_2\Big\{\tilde{\mathcal{H}}_{F-B}(\tau_1)\tilde{\mathcal{H}}_{F-B}(\tau_2)\rho_0 - \tilde{\mathcal{H}}_{F-B}(\tau_1)\rho_0\tilde{\mathcal{H}}_{F-B}(\tau_2) \\ &\qquad -\tilde{\mathcal{H}}_{F-B}(\tau_2)\rho_0\tilde{\mathcal{H}}_{F-B}(\tau_1) + \rho_0\tilde{\mathcal{H}}_{F-B}(\tau_2)\tilde{\mathcal{H}}_{F-B}(\tau_1)\Big\}.\end{aligned} \tag{C.5}$$

We eliminate the heatbath variables by tracing over the heatbath

$$\tilde{\rho} = \mathrm{Tr}_B\tilde{\rho}_{\mathrm{tot}}. \tag{C.6}$$

To proceed, we use four approximations

i. *Born approximation.* We assume that at time $t = 0$ the total density matrix factorizes in that of the free field $\rho(0)$ and that of the heatbath $\rho_B$, which also factorizes into the density matrices of the individual baths:

$$\rho_0 = \rho(0)\rho_B. \tag{C.7}$$

The bath is at thermal equilibrium at the temperature $T$,

$$\rho_B = Z^{-1}\exp(-\beta\mathcal{H}_B), \tag{C.8}$$

$$Z = \mathrm{Tr}_B\exp(-\beta\mathcal{H}_B), \tag{C.9}$$

where $\beta = 1/k_BT$. The first order term being linear in the bath operators, its average vanishes. Concerning the second order term, we find

$$\begin{aligned}\tilde{\rho}(t) = \rho(0) - \int_0^t \mathrm{d}\tau_1 \int_0^{\tau_2} \mathrm{d}\tau_2 \sum_{k_1,k_2} \Big[ & \tilde{C}_{k_1}(\tau_1)\tilde{C}_{k_2}(\tau_2)\rho(0)\mathrm{Tr}_B\Big(\tilde{B}_{k_1}(\tau_1)\tilde{B}_{k_2}(\tau_2)\rho_B\Big) \\ & - \tilde{C}_{k_1}(\tau_1)\rho(0)\tilde{C}_{k_2}(\tau_2)\mathrm{Tr}_B\Big(\tilde{B}_{k_1}(\tau_1)\rho_B\tilde{B}_{k_2}(\tau_2)\Big) \\ & - \tilde{C}_{k_1}(\tau_2)\rho(0)\tilde{C}_{k_2}(\tau_1)\mathrm{Tr}_B\Big(\tilde{B}_{k_1}(\tau_2)\rho_B\tilde{B}_{k_2}(\tau_1)\Big) \\ & + \rho(0)\tilde{C}_{k_1}(\tau_2)\tilde{C}_{k_2}(\tau_1)\mathrm{Tr}_B\Big(\rho_B\tilde{B}_{k_1}(\tau_2)\tilde{B}_{k_2}(\tau_1)\Big)\Big].\end{aligned} \tag{C.10}$$

We define

$$K_{k_1,k_2}(\tau_1,\tau_2) = \mathrm{Tr}_B\left[\tilde{B}_{k_1}(\tau_1)\tilde{B}_{k_2}(\tau_2)\rho_B\right] = K_{k_1,k_2}(\tau_1-\tau_2), \tag{C.11}$$

for a stationary interaction. Let us focus, for example, on the first of the four terms. With the time transformation $\tau = \tau_2 - \tau_1$ we get

$$\begin{aligned}&\int_0^t \mathrm{d}\tau_1 \int_0^{\tau_2} \mathrm{d}\tau_2 \tilde{C}_{k_1}(\tau_1)\tilde{C}_{k_2}(\tau_2)\rho(0)\mathrm{Tr}_B\Big(\tilde{B}_{k_1}(\tau_1)\tilde{B}_{k_2}(\tau_2)\rho_B\Big) \\ &\qquad = C_{k_1}C_{k_2}\rho(0)\int_0^t \mathrm{d}\tau_1\, \mathrm{e}^{i(\Delta\omega_{k_1}+\Delta\omega_{k_2})\tau_1}\int_0^{\tau_1}\mathrm{d}\tau\, \mathrm{e}^{-i\Delta\omega_{k_2}\tau}K_{k_1,k_2}(\tau).\end{aligned} \tag{C.12}$$

We now make three further essential assumptions

ii. *Markov approximation.* We assume that the heatbath has a short memory so that $K_{k_1,k_2}(\tau)$ is only nonvanishing for $\tau < \tau_0$. In the following we consider times $t$ which are large compared to the correlation time $\tau_0$. Then we may replace the upper limit $\tau_1$ by $\infty$.

iii. We assume that the interaction with the heatbath is so small that during the time $t$ the density matrix has changed very little. This allows us to make the replacement

$$\frac{\tilde{\rho}(t)-\tilde{\rho}(0)}{t} = \frac{\mathrm{d}\tilde{\rho}(t)}{\mathrm{d}t}. \tag{C.13}$$

iv. We consider only terms satisfying the condition $\Delta\omega_{k_1} + \Delta\omega_{k_2} = 0$ because otherwise the temporal integration in Eq. (C.12) vanishes. Consequently the integral becomes $\int_0^t \mathrm{d}\tau_1\, \mathrm{e}^{i(\Delta\omega_{k_1}+\Delta\omega_{k_2})\tau_1} = t$.

Using the cyclic property of traces, we obtain

$$\frac{\mathrm{d}\tilde{\rho}(t)}{\mathrm{d}t} = \sum_{k_1,k_2} \Big[ -C_{k_1}C_{k_2}\rho(0)\int_0^\infty \mathrm{d}\tau\, \mathrm{e}^{-i\Delta\omega_{k_2}\tau}\mathrm{Tr}_B\Big(\tilde{B}_{k_1}(\tau)\tilde{B}_{k_2}(0)\rho_B\Big) \tag{C.14}$$

$$+ C_{k_1}\rho(0)C_{k_2}\int_0^\infty \mathrm{d}\tau\, \mathrm{e}^{-i\Delta\omega_{k_2}\tau}\mathrm{Tr}_B\Big(\tilde{B}_{k_2}(0)\tilde{B}_{k_1}(\tau)\rho_B\Big) \tag{C.15}$$

$$+ C_{k_1}\rho(0)C_{k_2}\int_0^\infty \mathrm{d}\tau\, \mathrm{e}^{-i\Delta\omega_{k_1}\tau}\mathrm{Tr}_B\Big(\tilde{B}_{k_2}(\tau)\tilde{B}_{k_1}(0)\rho_B\Big) \tag{C.16}$$

$$-\rho(0)C_{k_1}C_{k_2}\int_0^\infty \mathrm{d}\tau\, \mathrm{e}^{-i\Delta\omega_{k_1}\tau}\mathrm{Tr}_B\Big(\tilde{B}_{k_1}(0)\tilde{B}_{k_2}(\tau)\rho_B\Big)\Big]. \tag{C.17}$$

If we note $k = k_1$ and $k' = k_2$ in Eqs. (C.14) and (C.17) and vice versa in Eqs. (C.15) and (C.16) we obtain

$$\frac{\mathrm{d}\tilde{\rho}(t)}{\mathrm{d}t} = \sum_{k,k'} \left( \left[C_{k'}\tilde{\rho}(t), C_k\right] A_{k,k'} + \left[C_{k'}, \tilde{\rho}(t)C_k\right] A'_{k,k'} \right), \tag{C.18}$$

where $A$ and $A'$ are defined by

$$A_{k,k'} = \int_0^\infty \mathrm{d}\tau\, \mathrm{e}^{-i\Delta\omega_{k'}\tau}\mathrm{Tr}_B\Big(\tilde{B}_k(\tau)\tilde{B}_{k'}(0)\rho_B\Big), \tag{C.19}$$

$$A'_{k,k'} = \int_0^\infty \mathrm{d}\tau\, \mathrm{e}^{-i\Delta\omega_{k}\tau}\mathrm{Tr}_B\Big(\tilde{B}_k(0)\tilde{B}_{k'}(\tau)\rho_B\Big). \tag{C.20}$$

Under the assumption that $B_k^\dagger = B_{k'}$, which is needed to ensure that the coupling Hamiltonian is Hermitian, we have

$$A'_{k,k'} = A^*_{k,k'}. \tag{C.21}$$

Then we evaluate the trace over the heatbath in the energy representation of the heatbath alone. We denote the energy of the state $n$ by $\hbar\Omega_n$. Using $\langle n|\rho_B|m\rangle = \mathrm{e}^{-\beta\hbar\Omega_n}\delta_{n,m}$ and $\langle n|\tilde{B}_k(\tau)|m\rangle = \mathrm{e}^{i(\Omega_n-\Omega_m)\tau}\langle n|B_k|m\rangle$, this yields

$$A_{k,k'} = Z^{-1}\int_0^\infty \mathrm{d}\tau\, \mathrm{e}^{-i\Delta\omega_{k'}\tau}\sum_{n,m}\langle n|B_k|m\rangle\langle m|B_k^\dagger|n\rangle\, \mathrm{e}^{i(\Omega_n-\Omega_m)\tau-\beta\hbar\Omega_n} \tag{C.22}$$

$$= Z^{-1}\sum_{n,m}|\langle n|B_k|m\rangle|^2\, \mathrm{e}^{-\beta\hbar\Omega_n}\left(\pi\delta(\Omega_n-\Omega_m-\Delta\omega_{k'}) + i\mathrm{P}\frac{1}{\Omega_n-\Omega_m-\Delta\omega_{k'}}\right), \tag{C.23}$$

where P is the principal value operator and

$$A_{k',k} = Z^{-1}\sum_{n,m}|\langle n|B_k|m\rangle|^2\, \mathrm{e}^{-\beta\hbar\Omega_m}\left(\pi\delta(\Omega_n-\Omega_m+\Delta\omega_{k}) + i\mathrm{P}\frac{1}{\Omega_m-\Omega_n-\Delta\omega_{k}}\right). \tag{C.24}$$

From these equations we get the detailed balance relation (see Ref. [204])

$$\mathrm{Re}\, A_{k,k'} = \mathrm{Re}\, A_{k',k}\, \mathrm{e}^{\beta\hbar\Delta\omega_{k'}}. \tag{C.25}$$

Finally, we may transform $\tilde{\rho}$ (interaction representation) into $\rho$ (Schrödinger representation). We obtain

$$\frac{\mathrm{d}\rho(t)}{\mathrm{d}t} = \frac{1}{i\hbar}\left[\mathcal{H}_F, \rho\right] + \sum_{k,k'} \left( \left[\bar{C}_{k'}\rho, \bar{C}_k\right] A_{k,k'} + \left[\bar{C}_{k'}, \rho\bar{C}_k\right] A^*_{k,k'} \right), \tag{C.26}$$

where

$$\bar{C}_k = \mathrm{e}^{-i\mathcal{H}_F\tau/\hbar} C_k \, \mathrm{e}^{i\mathcal{H}_F\tau/\hbar} = C_k \, \mathrm{e}^{\pm i\Delta\omega t}. \tag{C.27}$$

The time evolution of $\rho$ is now explicitly determined by two different terms: the commutator between $\mathcal{H}_F$ and $\rho$ describes the coherent evolution of the system whereas the other terms under the sum describe the incoherent processes.

### C.1.2 Application to qubit transitions

In the case of a qubit transition, the Hamiltonian of the field is $\mathcal{H}_F = \sum_i \varepsilon_i \sigma_{ii}$. This implies that $C_1 = \sigma_{ij}$, $C_2 = \sigma_{ji}$ and also $\Delta\omega_1 = -(\varepsilon_j - \varepsilon_i)/\hbar = -\Delta\omega_2$. Eq. (C.26) leads to

$$\frac{\mathrm{d}\rho(t)}{\mathrm{d}t} = -i\sum_j \frac{\varepsilon_j}{\hbar}\left[\sigma_{jj}, \rho\right] + \sum_{i,j}\left( \left[\sigma_{ji}\rho, \sigma_{ij}\right] A_{ij,ji} + \left[\sigma_{ji}, \rho\sigma_{ij}\right] A^*_{ij,ji} \right). \tag{C.28}$$

To understand the physical meaning of the coefficients $A$, we derive the evolution equation for the average of the operator $\sigma_{kl}$:

$$\begin{aligned} \frac{\mathrm{d}\langle\sigma_{kl}\rangle}{\mathrm{d}t} =& -i\sum_j \frac{\varepsilon_j}{\hbar}\left(\langle\sigma_{kl}\sigma_{jj}\rangle - \langle\sigma_{jj}\sigma_{kl}\rangle\right) \\ &+ \sum_{i,j} A_{ij,ji}\left(\langle\sigma_{ij}\sigma_{kl}\sigma_{ji}\rangle - \langle\sigma_{kl}\sigma_{ij}\sigma_{ji}\rangle\right) \\ &+ \sum_{i,j} A^*_{ij,ji}\left(\langle\sigma_{ij}\sigma_{kl}\sigma_{ji}\rangle - \langle\sigma_{ij}\sigma_{ji}\sigma_{kl}\rangle\right). \end{aligned} \tag{C.29}$$

This expression can be simplified

$$\frac{\mathrm{d}\langle\sigma_{kl}\rangle}{\mathrm{d}t} = \langle\sigma_{kl}\rangle\left(i\omega_{kl} + i\Delta\omega_{kl} - \phi_{kl}\right) \qquad \text{if } k \neq l, \tag{C.30}$$

$$\frac{\mathrm{d}\langle\sigma_{kk}\rangle}{\mathrm{d}t} = \sum_j \left(\langle\sigma_{jj}\rangle\gamma_{jk} - \langle\sigma_{kk}\rangle\gamma_{kj}\right), \tag{C.31}$$

where

$$\gamma_{jk} = A_{jk,kj} + A^*_{jk,kj}, \tag{C.32}$$

$$\phi_{kl} = \sum_i \mathrm{Re}\left(A_{ki,ik} + A^*_{li,il}\right) = \frac{1}{2}\sum_i \left(\gamma_{ki} + \gamma_{li}\right), \tag{C.33}$$

$$\Delta\omega_{kl} = \sum_i \mathrm{Im}\left(A_{ki,ik} + A^*_{li,il}\right). \tag{C.34}$$

The parameter $\gamma_{ij}$ is straightforwardly identified with the transition rate between the state $|i\rangle$ and the state $|j\rangle$, while $\phi_{ij}$ is the phase halfwidth. From now on we consider the coefficient $A$ to be real and equal to the transition rate $A_{ij,ji} = \gamma_{ij}/2$.

The Lindbladian equation in the interaction picture is thus

$$\dot{\tilde{\rho}}(t) = \sum_{ij} \mathrm{L}_{\gamma_{ij}} \tilde{\rho}(t), \tag{C.35}$$

where $\mathrm{L}_{\gamma_{ij}}$ is the Lindblad operator associated to the transition $|i\rangle \to |j\rangle$ with the rate $\gamma_{ij}$

$$\mathrm{L}_{\gamma_{ij}}\rho = \frac{\gamma_{ij}}{2}\left(2\sigma_{ji}\rho\sigma_{ij} - \sigma_{ii}\rho - \rho\sigma_{ii}\right). \tag{C.36}$$

There are two kinds of transition

- $i > j$ *Spontaneous emission*: The photon generated by the transition from $|i\rangle$ to $|j\rangle$ is lost in the environment with a rate $\gamma_{ij}$ and is not kept by the cavity. In a three-level qubit there are three types of spontaneous emissions

$$\mathrm{L}_{\gamma_{21}}\rho = \frac{\gamma_{21}}{2}\left(2\sigma_{12}\rho\sigma_{21} - \sigma_{22}\rho - \rho\sigma_{22}\right), \tag{C.37}$$

$$\mathrm{L}_{\gamma_{10}}\rho = \frac{\gamma_{10}}{2}\left(2\sigma_{01}\rho\sigma_{10} - \sigma_{11}\rho - \rho\sigma_{11}\right), \tag{C.38}$$

$$\mathrm{L}_{\gamma_{20}}\rho = \frac{\gamma_{20}}{2}\left(2\sigma_{02}\rho\sigma_{20} - \sigma_{22}\rho - \rho\sigma_{22}\right). \tag{C.39}$$

- $i < j$ *Incoherent pumping*: The qubit is incoherently pumped from the state $|i\rangle$ to the state $|j\rangle$ with the pumping rate $\gamma_{ij}$. In practice the pumping occurs from the state $|0\rangle$ to the state $|2\rangle$ at a rate $\Gamma \equiv \gamma_{02}$ to ensure the population imbalance. The corresponding Lindblad operator $\mathrm{L}_P = \mathrm{L}_{\gamma_{02}}$ reads

$$\mathrm{L}_P\rho = \frac{\Gamma}{2}\left(2\sigma_{20}\rho\sigma_{02} - \sigma_{00}\rho - \rho\sigma_{00}\right). \tag{C.40}$$

### C.1.3 Application to a cavity mode

In the case of the coupling between a transition in the qubit and the bath, $\mathcal{H}_F = \hbar\omega a_\alpha^\dagger a_\alpha$. We make the following identifications $C_1 = a_\alpha,\ C_2 = a_\alpha^\dagger$ and $\Delta\omega_1 = -\omega_\alpha,\ \Delta\omega_2 = \omega_\alpha$. Eq. (C.18) then takes the form

$$\frac{\mathrm{d}\tilde{\rho}(t)}{\mathrm{d}t} = \left[a_\alpha\tilde{\rho}(t), a_\alpha^\dagger\right] A_{21} + \left[a_\alpha^\dagger\tilde{\rho}(t), a_\alpha\right] A_{12} + \left[a_\alpha, \tilde{\rho}(t)a_\alpha^\dagger\right] A_{21}^* + \left[a_\alpha^\dagger, \tilde{\rho}(t)a_\alpha\right] A_{12}^*. \tag{C.41}$$

Since the imaginary parts of $A$ give rise to mere frequency shift which can be absorbed into the frequency of the actual oscillator we keep only the real part and put

$$A_{21} = \xi, \qquad A_{12} = \delta = \xi\,\mathrm{e}^{-\beta\hbar\omega}. \tag{C.42}$$

In the Schrödinger representation we have

$$\begin{aligned}\frac{\mathrm{d}\rho(t)}{\mathrm{d}t} =& -i\omega\left[a_\alpha^\dagger a_\alpha, \rho\right] + \xi\left(\left[a_\alpha\rho, a_\alpha^\dagger\right] + \left[a_\alpha, \rho a_\alpha^\dagger\right]\right) + \delta\left(\left[a_\alpha^\dagger\rho, a_\alpha\right] + \left[a_\alpha^\dagger, \rho a_\alpha\right]\right)\\ =& -i\omega\left(a_\alpha^\dagger a_\alpha\rho - \rho a_\alpha^\dagger a_\alpha\right)\\ &+ \xi\left(2a_\alpha\rho a_\alpha^\dagger - a_\alpha^\dagger a_\alpha\rho - \rho a_\alpha^\dagger a_\alpha\right) + \delta\left(2a_\alpha^\dagger\rho a_\alpha - a_\alpha a_\alpha^\dagger\rho - \rho a_\alpha a_\alpha^\dagger\right).\end{aligned} \tag{C.43}$$

To get some insight into the meaning of the constants $\delta$ and $\xi$, we derive an equation for the average value $\langle a_\alpha^\dagger a_\alpha\rangle$: $\partial_t\langle a_\alpha^\dagger a_\alpha\rangle = \mathrm{Tr}\Big\{\dot{\rho} a_\alpha^\dagger a_\alpha\Big\}$. We obtain

$$\frac{\mathrm{d}\langle a_\alpha^\dagger a_\alpha\rangle}{\mathrm{d}t} = 2\delta - 2(\xi-\delta)\langle a_\alpha^\dagger a_\alpha\rangle, \tag{C.44}$$

this allows us to identify $2(\xi-\delta)$ with the decay rate $\kappa_\alpha$. Finally, noting $n_\alpha^{\mathrm{th}}$ the Bose-Einstein distribution, we obtain $2\delta = \kappa_\alpha n_\alpha^{\mathrm{th}}$ and $2\xi = \kappa_\alpha(1+n_\alpha^{\mathrm{th}})$. As a consequence

$$\begin{aligned}\frac{\mathrm{d}\rho(t)}{\mathrm{d}t} &= -i\omega\left(a_\alpha^\dagger a_\alpha\rho - \rho a_\alpha^\dagger a_\alpha\right)\\ &+ \frac{\kappa_\alpha}{2}(1+n_\alpha^{\mathrm{th}})\left(2a_\alpha\rho a_\alpha^\dagger - a_\alpha^\dagger a_\alpha\rho - \rho a_\alpha^\dagger a_\alpha\right) + \frac{\kappa_\alpha}{2}n_\alpha^{\mathrm{th}}\left(2a_\alpha^\dagger\rho a_\alpha - a_\alpha a_\alpha^\dagger\rho - \rho a_\alpha a_\alpha^\dagger\right).\end{aligned} \tag{C.45}$$

In the interaction picture and at very low temperature ($k_B T \ll \hbar\omega \implies n_\alpha^{\mathrm{th}} = 0$) the Lindblad equation reads

$$\frac{\mathrm{d}\tilde{\rho}(t)}{\mathrm{d}t} = \sum_\alpha \mathrm{L}_{C_\alpha}\tilde{\rho}(t), \tag{C.46}$$

with the Lindblad operator of the cavities

$$\mathrm{L}_{C_\alpha}\rho = \frac{\kappa_\alpha}{2}\left(2a_\alpha\rho a_\alpha^\dagger - a_\alpha^\dagger a_\alpha\rho - \rho a_\alpha^\dagger a_\alpha\right). \tag{C.47}$$

This general result can be applied to the calculation of the steady state density matrix and the output spectrum.

## C.2 Incoherently pumped qubit coupled to one cavity

### C.2.1 Temporal evolution and steady state of the density matrix

We study the population dynamics of a three-level qubit coupled to one cavity using the density matrix time-evolution. We consider the case of an incoherent pumping (rate $\Gamma$) with the presence of non-radiative relaxations $|i\rangle \to |j\rangle$ (rate $\gamma_{ij}$). We take also into account the presence of a detuning $\delta = \omega_{10} - \omega_0$ between the lasing transition and the cavity mode. The temporal derivative of a general matrix element reads

$$\begin{aligned}\langle i,n|\dot{\tilde{\rho}}(t)|j,m\rangle &= \kappa\sqrt{n+1}\sqrt{m+1}\langle i,n+1|\tilde{\rho}(t)|j,m+1\rangle - \frac{\kappa}{2}(n+m)\langle i,n|\tilde{\rho}(t)|j,m\rangle\\ &+ \Gamma\langle 0,n|\tilde{\rho}(t)|0,m\rangle\,\delta_{i,j,2} - \frac{\Gamma}{2}\langle i,n|\tilde{\rho}(t)|j,m\rangle\,(\delta_{i,0}+\delta_{j,0})\\ &+ \sum_{k,l}\gamma_{kl}\left[\langle k,n|\tilde{\rho}(t)|k,m\rangle\,\delta_{i,j,l} - \frac{1}{2}\langle i,n|\tilde{\rho}(t)|j,m\rangle\,(\delta_{i,k}+\delta_{j,k})\right]\\ &+ g\sqrt{n}\langle 1,n-1|\tilde{\rho}(t)|j,m\rangle\,\mathrm{e}^{-i\delta t}\,\delta_{i,0} + g\sqrt{m}\langle i,n|\tilde{\rho}(t)|1,m-1\rangle\,\mathrm{e}^{i\delta t}\,\delta_{j,0}\\ &- g\sqrt{n+1}\langle 0,n+1|\tilde{\rho}(t)|j,m\rangle\,\mathrm{e}^{i\delta t}\,\delta_{i,1} - g\sqrt{m+1}\langle i,n|\tilde{\rho}(t)|0,m+1\rangle\,\mathrm{e}^{-i\delta t}\,\delta_{j,1}.\end{aligned} \tag{C.48}$$

We restrict the cavity states to $|0\rangle \to |M\rangle$. To determine the diagonal elements $\langle i,n|\tilde{\rho}(t)|i,n\rangle$ we need six auxiliary matrix elements. We build the column matrix $B(t) = \big(b_i(t)\big)_{i\in\{1,\dots,M\}}$

with

$$b_{n>0}(t)=\begin{pmatrix}\langle 0,n|\tilde{\rho}(t)|0,n\rangle\\ \langle 1,n|\tilde{\rho}(t)|1,n\rangle\\ \langle 2,n|\tilde{\rho}(t)|2,n\rangle\\ \mathrm{Re}\big\{\langle 0,n|\tilde{\rho}(t)|1,n-1\rangle\,\mathrm{e}^{i\delta t}\big\}\\ \mathrm{Im}\big\{\langle 0,n|\tilde{\rho}(t)|1,n-1\rangle\,\mathrm{e}^{i\delta t}\big\}\end{pmatrix},\quad b_0(t)=\begin{pmatrix}\langle 0,0|\tilde{\rho}(t)|0,0\rangle\\ \langle 1,0|\tilde{\rho}(t)|1,0\rangle\\ \langle 2,0|\tilde{\rho}(t)|2,0\rangle\end{pmatrix}. \tag{C.49}$$

The time-derivative $\dot{B}(t)$ is linked to $B(t)$ through the matrix $\mathcal{M}$

$$\dot{B}(t)=\mathcal{M}\cdot B(t), \tag{C.50}$$

with

$$\mathcal{M}=\begin{pmatrix}\mathcal{M}_0^C & \mathcal{M}_0^R & & & \\ \mathcal{M}_1^L & \mathcal{M}_1^C & \mathcal{M}_1^R & & \\ & \ddots & \ddots & \ddots & \\ & & \mathcal{M}_{M-1}^L & \mathcal{M}_{M-1}^C & \mathcal{M}_{M-1}^R\\ & & & \mathcal{M}_M^L & \mathcal{M}_M^C\end{pmatrix}. \tag{C.51}$$

The submatrices of $\mathcal{M}$ are equal to

$$\begin{aligned}\mathcal{M}_n^C = & -\operatorname{diag}\{\kappa n+\Gamma+\gamma_{01}, \kappa n+\gamma_{10}+\gamma_{12}, \kappa n+\gamma_{21}+\gamma_{20},\\ & \qquad \kappa(n-1/2)+(\Gamma+\gamma_{10})/2, \kappa(n-1/2)+(\Gamma+\gamma_{10})/2,\\ & +\begin{pmatrix}0 & \gamma_{10} & \gamma_{20} & 2g\sqrt{n} & 0\\ \gamma_{01} & 0 & \gamma_{21} & 0 & 0\\ \Gamma & \gamma_{12} & 0 & 0 & 0\\ -g\sqrt{n} & 0 & 0 & 0 & -\delta\\ 0 & 0 & 0 & \delta & 0\end{pmatrix},\end{aligned} \tag{C.52}$$

where diag$\{\dots\}$ represents the element of a diagonal matrix,

$$\mathcal{M}_n^L=\begin{pmatrix}0 & 0 & 0 & 0 & 0\\ 0 & 0 & 0 & 0 & 0\\ 0 & 0 & 0 & 0 & 0\\ 0 & g\sqrt{n} & 0 & 0 & 0\\ 0 & 0 & 0 & 0 & 0\end{pmatrix}, \tag{C.53}$$

and

$$\mathcal{M}_n^R=\begin{pmatrix}\kappa(n+1) & 0 & 0 & 0 & 0\\ 0 & \kappa(n+1) & 0 & -2g\sqrt{n+1} & 0\\ 0 & 0 & \kappa(n+1) & 0 & 0\\ 0 & 0 & 0 & \kappa\sqrt{n(n+1)} & 0\\ 0 & 0 & 0 & 0 & \kappa\sqrt{n(n+1)}\end{pmatrix}. \tag{C.54}$$

The top left hand side $\mathcal{M}_0^C$, $\mathcal{M}_0^R$ and $\mathcal{M}_1^L$ have to be adapted in accordance with the elements of $b_0(t)$. The time evolution is then obtained using a Runge Kutta method to integrate the system from the initial condition corresponding to the qubit in the ground state and an empty cavity.

To find the steady state, we set the time derivatives to zero and solve the system using the property of the trace of the density matrix

$$\sum_{i=0}^{2}\sum_{n=0}^{M}\langle i,n|\tilde{\rho}(t)|i,n\rangle = 1. \tag{C.55}$$

To include the closure condition in the system we express the element $\langle 0,0|\tilde{\rho}(t)|0,0\rangle$ in terms of the other diagonal elements. As a consequence,

$$b_0(t) = \begin{pmatrix}\langle 1,0|\tilde{\rho}(t)|1,0\rangle \\ \langle 2,0|\tilde{\rho}(t)|2,0\rangle\end{pmatrix}, \quad \text{and} \quad \mathcal{M} = \begin{pmatrix} \mathcal{M}_0^C & \mathcal{M}_0^R & \mathcal{M}^{RR} & \cdots & \mathcal{M}^{RR} \\ \mathcal{M}_1^L & \mathcal{M}_1^C & \mathcal{M}_1^R & & \\ & \ddots & \ddots & \ddots & \\ & & \mathcal{M}_{M-1}^L & \mathcal{M}_{M-1}^C & \mathcal{M}_{M-1}^R \\ & & & \mathcal{M}_M^L & \mathcal{M}_M^C \end{pmatrix}, \tag{C.56}$$

where the submatrices corresponding to $n=0$ are modified as follows

$$\mathcal{M}_0^C = \begin{pmatrix}\gamma_{01}+\gamma_{10}+\gamma_{12} & \gamma_{01}-\gamma_{21} \\ \Gamma-\gamma_{12} & \Gamma+\gamma_{21}+\gamma_{20}\end{pmatrix}, \quad \mathcal{M}_1^L = \begin{pmatrix}0 & 0 \\ 0 & 0 \\ 0 & 0 \\ g & 0 \\ 0 & 0\end{pmatrix}, \tag{C.57}$$

$$\mathcal{M}_0^R = \begin{pmatrix}\gamma_{01} & \gamma_{01}-\kappa & \gamma_{01} & 2g & 0 \\ \Gamma & \Gamma & \Gamma-\kappa & 0 & 0\end{pmatrix}, \tag{C.58}$$

with the new submatrix

$$\mathcal{M}^{RR} = \begin{pmatrix}\gamma_{01} & \gamma_{01} & \gamma_{01} & 0 & 0 \\ \Gamma & \Gamma & \Gamma & 0 & 0\end{pmatrix}. \tag{C.59}$$

The solution is then simply

$$B(t_{SS}) = \mathcal{M}^{-1}\cdot\begin{pmatrix}\gamma_{01} \\ \Gamma \\ 0 \\ \vdots \\ 0\end{pmatrix}, \tag{C.60}$$

and,

$$\langle 0,0|\tilde{\rho}({}_{SS})|0,0\rangle = \frac{1}{\Gamma+\gamma_{01}}\left(\gamma_{10}\langle 1,0|\tilde{\rho}(t_{SS})|1,0\rangle + \gamma_{20}\langle 2,0|\tilde{\rho}(t_{SS})|2,0\rangle + \kappa\langle 0,1|\tilde{\rho}(t_{SS})|0,1\rangle\right). \tag{C.61}$$

In this specific configuration of incoherent pumping a small number of matrix elements is non-zero.

### C.2.2 Output spectrum

The output spectrum $\mathcal{S}(\omega) = 2\,\mathrm{Re}\int_0^\infty \mathrm{d}\tau\,\mathrm{e}^{i\omega\tau}\langle a_H^\dagger(0)a_H(\tau)\rangle$, where $\tau = t - t_{SS}$, is equal to

$$\mathcal{S}(\omega) = 2\mathrm{Re}\sum_{i=0}^{2}\sum_{n=0}^{\infty}\sqrt{n+1}\langle i,n+1|\widehat{A}(\omega-\omega_0)|i,n\rangle, \tag{C.62}$$

where

$$\dot{A}_I(\tau) = \mathcal{L}(\tau)[A_I(\tau)]\,, \tag{C.63}$$

$$A_I(0) = \rho_I(0)a_I^\dagger(0). \tag{C.64}$$

From Eq. C.48, six auxiliary matrix elements are necessary to find $\langle i, n+1|A_I(\tau)|i, n\rangle$, contained in the matrix $B(t) = \big(b_0(t), \ldots, b_n(t), \ldots, b_M(t)\big)^{\mathrm{t}}$ where

$$b_n(\tau) = \begin{pmatrix} \langle 0, n+1|A_I(\tau)|0, n\rangle \\ \langle 1, n+1|A_I(\tau)|1, n\rangle \\ \langle 2, n+1|A_I(\tau)|2, n\rangle \\ \langle 0, n+2|A_I(\tau)\,\mathrm{e}^{i\delta\tau}|1, n\rangle \\ \langle 1, n|A_I(\tau)\,\mathrm{e}^{-i\delta\tau}|0, n\rangle \end{pmatrix},\ b_{M-1}(\tau) = \begin{pmatrix} \langle 0, M|A_I(\tau)|0, M-1\rangle \\ \langle 1, M|A_I(\tau)|1, M-1\rangle \\ \langle 2, M|A_I(\tau)|2, M-1\rangle \\ \langle 1, M-1|A_I(\tau)\,\mathrm{e}^{-i\delta\tau}|0, M-1\rangle \end{pmatrix}. \tag{C.65}$$

Then, the derivatives $\langle i, n{+}1|A_I(\tau)|i, n\rangle$ are linked linearly to $\langle i, n{+}1|A_I(\tau)|i, n\rangle$ through the matrix $\mathcal{W}$: $\dot{B}(\tau) = \mathcal{W}\cdot B(\tau)$ with

$$\mathcal{W} = \begin{pmatrix} C_0 & D_0^R & & & \\ D_1^L & C_1 & D_1^R & & \\ & \ddots & \ddots & \ddots & \\ & & D_{M-2}^L & C_{M-2} & D_{M-2}^R \\ & & & D_{M-1}^L & C_{M-1} \end{pmatrix}, \tag{C.66}$$

where the submatrices read

$$\begin{aligned} \mathcal{W}_n^C = &-\mathrm{diag}\{\kappa(n+1/2)+\Gamma+\gamma_{01}, \kappa(n+1/2)+\gamma_{10}+\gamma_{12}, \kappa(n+1/2)+\gamma_{21}+\gamma_{20}, \\ &\qquad \kappa(n+1)+(\Gamma+\gamma_{10})/2-i\delta, \kappa n+(\Gamma+\gamma_{10})/2+i\delta\} \\ &+\begin{pmatrix} 0 & \gamma_{10} & \gamma_{20} & 0 & g\sqrt{n+1} \\ \gamma_{01} & \gamma_{12} & \gamma_{21} & -g\sqrt{n+2} & 0 \\ \Gamma & 0 & 0 & 0 & 0 \\ 0 & g\sqrt{n+2} & 0 & 0 & 0 \\ -g\sqrt{n+1} & 0 & 0 & 0 & 0 \end{pmatrix}, \end{aligned} \tag{C.67}$$

and

$$\mathcal{W}_n^L = \begin{pmatrix} 0 & 0 & 0 & g\sqrt{n} & 0 \\ 0 & 0 & 0 & 0 & 0 \\ 0 & 0 & 0 & 0 & 0 \\ 0 & 0 & 0 & 0 & 0 \\ 0 & g\sqrt{n} & 0 & 0 & 0 \end{pmatrix}, \tag{C.68}$$

and with

$$\begin{aligned} \mathcal{W}_n^R = &\mathrm{diag}\Big\{\kappa\sqrt{(n+1)(n+2)}, \kappa\sqrt{(n+1)(n+2)}, \kappa\sqrt{(n+1)(n+2)}, \\ &\qquad \kappa\sqrt{(n+1)(n+3)}, \kappa(n+1)\Big\} \\ &+\begin{pmatrix} 0 & 0 & 0 & 0 & 0 \\ 0 & 0 & 0 & 0 & -g\sqrt{n+1} \\ 0 & 0 & 0 & 0 & 0 \\ -g\sqrt{n+1} & 0 & 0 & 0 & 0 \\ 0 & 0 & 0 & 0 & 0 \end{pmatrix}. \end{aligned} \tag{C.69}$$

The matrices $\mathcal{W}^C_{M-1}$, $\mathcal{W}^L_{M-1}$ and $\mathcal{W}^R_{M-2}$ have to be resized in accordance with $b_{M-1}(\tau)$. The temporal spectral function reads

$$\mathcal{S}(\tau) = \mathrm{e}^{-i\omega_0\tau} \sum_{n=0}^{M-1} \sum_{j=0}^{2} \sqrt{n+1}\, B_{5n+j}(\tau). \tag{C.70}$$

Next, noting $\widehat{B}(\omega) = \mathrm{TL}\{B(\tau)\}(\omega)$, and using the property $\mathrm{TL}\{f'(\tau)\}(\omega) = -i\omega \mathrm{TL}\{f(\tau)\}(\omega) - f(0)$, we get

$$i\omega\widehat{A}(\omega) + \mathcal{L}\Big[\widehat{A}(\omega)\Big] = -A_I(0), \tag{C.71}$$

or equivalently

$$\widehat{B}(\omega) = -\left(\mathcal{W} + i\omega\mathbb{I}\right)^{-1} \cdot B(0), \tag{C.72}$$

where the elements of $B(0)$ read

$$b_n(0) = \sqrt{n+1} \begin{pmatrix} \langle 0, n+1|\tilde{\rho}(t_{SS})|0, n+1\rangle \\ \langle 1, n+1|\tilde{\rho}(t_{SS})|1, n+1\rangle \\ \langle 2, n+1|\tilde{\rho}(t_{SS})|2, n+1\rangle \\ \langle 0, n+2|\tilde{\rho}(t_{SS})\,\mathrm{e}^{i\delta t_{SS}}|1, n+1\rangle \\ \langle 1, n|\tilde{\rho}(t_{SS})\,\mathrm{e}^{-i\delta t_{SS}}|0, n+1\rangle \end{pmatrix}. \tag{C.73}$$

These matrix elements can be obtained directly by the procedure of the previous section. Finally, the relation

$$\mathcal{S}(\omega_0 + \Delta\omega) = 2\,\mathrm{Re} \sum_{n=0}^{M-1} \sum_{j=0}^{2} \sqrt{n+1}\, \widehat{B}_{5n+i}(\Delta\omega), \tag{C.74}$$

leads directly to the spectrum.

The case of a coherent pumping can be easily obtained with the same method. In this case, 9 elements are needed in $b_n$.

## C.3 Semiclassical model

We consider the general case of two cavities and try to find a simplified description to calculate the photon number $n_\alpha = a^\dagger_\alpha a_\alpha$ in each cavity. We note $\Delta_{i,\alpha}$ the frequency difference between the transition $|i+1\rangle - |i\rangle$ and the cavity modes $\omega_\alpha$. To proceed, we consider the dynamical equation of $n_\alpha$

$$\frac{\mathrm{d}\langle n_\alpha\rangle}{\mathrm{d}t} = \frac{1}{i\hbar}\left\langle \left[n_\alpha, \tilde{\mathcal{H}}_1\right]\right\rangle + \mathrm{Tr}\{n_\alpha \mathrm{L}\tilde{\rho}\} \tag{C.75}$$

$$= -\kappa_\alpha\langle n_\alpha\rangle + g_{1\alpha}\left\langle \sigma_{01}a^\dagger_\alpha\,\mathrm{e}^{i\Delta_{1\alpha}t} + \sigma_{10}a_\alpha\,\mathrm{e}^{-i\Delta_{1\alpha}t}\right\rangle + g_{2\alpha}\left\langle \sigma_{12}a^\dagger_\alpha\,\mathrm{e}^{i\Delta_{2\alpha}t} + \sigma_{21}a_\alpha\,\mathrm{e}^{-i\Delta_{2\alpha}t}\right\rangle. \tag{C.76}$$

The differential equations for the photon numbers give rise to auxiliary correlators. Their derivative can be obtained with

$$\begin{aligned}\frac{\mathrm{d}\langle\sigma_{j-1,j}a_\alpha^\dagger\rangle}{\mathrm{d}t} =& -\frac{1}{2}\left[\kappa_\alpha+\Gamma\,\delta_{j,1}+\sum_{k>l}\gamma_{kl}(\delta_{k,j}+\delta_{k,j-1})\right]\langle\sigma_{j-1,j}a_\alpha^\dagger\rangle\\ &+E\left[\langle\sigma_{21}a_\alpha^\dagger\rangle\,\delta_{j,1}-\langle\sigma_{10}a_\alpha^\dagger\rangle\,\delta_{j,2}\right]\\ &+\sum_{\beta=1}^{2}\Big[\left(g_{2\beta}\,\mathrm{e}^{i\Delta_{2,\beta}t}\,\delta_{j,1}-g_{1\beta}\,\mathrm{e}^{i\Delta_{1,\beta}t}\,\delta_{j,2}\right)\langle\sigma_{02}a_\alpha^\dagger a_\beta^\dagger\rangle\\ &\qquad+g_{j\beta}\,\mathrm{e}^{-i\Delta_{j,\beta}t}\left(\langle(\sigma_{jj}-\sigma_{j-1,j-1})a_\alpha^\dagger a_\beta\rangle+\langle\sigma_{jj}\rangle\,\delta_{\alpha,\beta}\right)\Big]\,. \end{aligned}\tag{C.77}$$

Among the new auxiliary fields, some are of the same kind

$$\begin{aligned}\frac{\mathrm{d}\langle\sigma_{j,j-1}a_\alpha^\dagger\rangle}{\mathrm{d}t} =& -\frac{1}{2}\left[\kappa_\alpha+\Gamma\,\delta_{j,1}+\sum_{k>l}\gamma_{kl}(\delta_{k,j}+\delta_{k,j-1})\right]\langle\sigma_{j,j-1}a_\alpha^\dagger\rangle\\ &+E\left[\langle\sigma_{12}a_\alpha^\dagger\rangle\,\delta_{j,1}-\langle\sigma_{01}a_\alpha^\dagger\rangle\,\delta_{j,2}\right]\\ &+\sum_{\beta=1}^{2}\Big[g_{j\beta}\,\mathrm{e}^{i\Delta_{j,\beta}t}\,\langle(\sigma_{jj}-\sigma_{j-1,j-1})a_\alpha^\dagger a_\beta^\dagger\rangle\\ &\qquad+\left(g_{2\beta}\,\mathrm{e}^{-i\Delta_{2,\beta}t}\,\delta_{j,1}-g_{1\beta}\,\mathrm{e}^{-i\Delta_{1,\beta}t}\,\delta_{j,2}\right)\langle\sigma_{20}a_\alpha^\dagger a_\beta\rangle\\ &\qquad+g_{2\beta}\,\mathrm{e}^{-i\Delta_{2,\beta}t}\langle\sigma_{20}\rangle\,\delta_{j,1}\delta_{\alpha,\beta}\Big]\,. \end{aligned}\tag{C.78}$$

The time-evolution of the qubit operators is needed

$$\begin{aligned}\frac{\mathrm{d}\langle\sigma_{k,l}\rangle}{\mathrm{d}t} =& -\frac{1}{2}\left[\Gamma(\delta_{k,0}+\delta_{l,0})+\sum_{i>j}\gamma_{ij}(\delta_{i,k}+\delta_{i,l})\right]\langle\sigma_{k,l}\rangle+\Gamma\langle\sigma_{00}\rangle\,\delta_{k,l,2}+\sum_{i>j}\gamma_{ij}\langle\sigma_{ii}\rangle\,\delta_{k,l,j}\\ &+E\left[\langle\sigma_{k2}\rangle\,\delta_{l,0}-\langle\sigma_{0l}\rangle\,\delta_{k,2}-\langle\sigma_{k0}\rangle\,\delta_{l,2}+\langle\sigma_{2l}\rangle\,\delta_{k,0}\right]\\ &+\sum_{\alpha=1}^{2}\Big[g_{l+1,\alpha}\langle\sigma_{k,l+1}a_\alpha^\dagger\rangle\,\mathrm{e}^{i\Delta_{l+1,\alpha}t}-g_{k,\alpha}\langle\sigma_{k-1,l}a_\alpha^\dagger\rangle\,\mathrm{e}^{i\Delta_{k,\alpha}t}\\ &\qquad+g_{k+1,\alpha}\langle\sigma_{k+1,l}a_\alpha\rangle\,\mathrm{e}^{-i\Delta_{k+1,\alpha}t}-g_{l,\alpha}\langle\sigma_{k,l-1}a_\alpha\rangle\,\mathrm{e}^{-i\Delta_{l,\alpha}t}\Big]\,. \end{aligned}\tag{C.79}$$

Correlators with three operators are also generated

$$\begin{aligned}\frac{\mathrm{d}\langle\sigma_{kl}a_\alpha^\dagger a_\beta^{(\dagger)}\rangle}{\mathrm{d}t} =& -\frac{1}{2}\left[\kappa_\alpha+\kappa_\beta+\Gamma\left(\delta_{k,0}+\delta_{l,0}\right)+\gamma_{21}\left(\delta_{k,2}+\delta_{l,2}\right)\right]\langle\sigma_{kl}a_\alpha^\dagger a_\beta^{(\dagger)}\rangle \\ &+\Gamma\langle\sigma_{00}a_\alpha^\dagger a_\beta^{(\dagger)}\rangle\,\delta_{k,l,2}+\gamma_{21}\langle\sigma_{22}a_\alpha^\dagger a_\beta^{(\dagger)}\rangle\,\delta_{k,l,0} \\ &+E\left[\langle\sigma_{k2}a_\alpha^\dagger a_\beta^{(\dagger)}\rangle\,\delta_{l,0}-\langle\sigma_{0l}a_\alpha^\dagger a_\beta^{(\dagger)}\rangle\,\delta_{k,2}-\langle\sigma_{k0}a_\alpha^\dagger a_\beta^{(\dagger)}\rangle\,\delta_{l,2}+\langle\sigma_{2l}a_\alpha^\dagger a_\beta^{(\dagger)}\rangle\,\delta_{k,0}\right] \\ &+\sum_{\gamma=1}^{2}\Big[g_{l+1,\gamma}\langle\sigma_{k,l+1}a_\alpha^\dagger a_\beta^{(\dagger)}a_\gamma^\dagger\rangle\,\mathrm{e}^{i\Delta_{l+1,\gamma}t}-g_{k,\gamma}\langle\sigma_{k-1,l}a_\gamma^\dagger a_\alpha^\dagger a_\beta^{(\dagger)}\rangle\,\mathrm{e}^{i\Delta_{k,\gamma}t} \\ &\qquad -g_{l,\gamma}\langle\sigma_{k,l-1}a_\alpha^\dagger a_\beta^{(\dagger)}a_\gamma\rangle\,\mathrm{e}^{-i\Delta_{l,\gamma}t}+g_{k+1,\gamma}\langle\sigma_{k+1,l}a_\gamma a_\alpha^\dagger a_\beta^{(\dagger)}\rangle\,\mathrm{e}^{-i\Delta_{k+1,\gamma}t}\Big]\,.\end{aligned} \tag{C.80}$$

Up to now the calculations are exact but every time we calculate the time evolution of an auxiliary correlator, correlators with one more cavity operator are generated by the coupling Hamiltonian. The expectation value of these operators corresponds to the coherence between states more and more far from the diagonal terms. In the following, we will consider only off-diagonal terms with differing by maximum two cavity states in each cavity: $\langle i,n_1,n_2|\rho|j,n_1\pm2,n_2\rangle$, $\langle i,n_1,n_2|\rho|j,n_1,n_2\pm2\rangle$, and $\langle i,n_1,n_2|\rho|j,n_1\pm1,n_2\pm1\rangle$. Consequently terms such as $\langle\sigma_{kl}a_\alpha^\dagger a_\alpha^\dagger a_\beta^\dagger\rangle$ and $\langle\sigma_{kl}a_\alpha^\dagger a_\alpha^\dagger a_{\beta\neq\alpha}\rangle$ will be ignores and set to zero. The others terms will be factorized to express them in terms of known correlators

$$\langle\sigma_{kl}a_\alpha^\dagger a_\alpha a_\beta^{(\dagger)}\rangle \simeq\langle n_\alpha\rangle\langle\sigma_{kl}a_\beta^{(\dagger)}\rangle, \tag{C.81}$$

and,

$$\langle\sigma_{kl}a_\alpha^\dagger a_\beta a_{\beta\neq\alpha}\rangle \simeq\langle a_\alpha^\dagger a_\beta\rangle\langle\sigma_{kl}a_\beta\rangle. \tag{C.82}$$

The last derivative necessary to complete the set of equations is

$$\begin{aligned}\frac{\mathrm{d}\langle a_1^\dagger a_2\rangle}{\mathrm{d}t} =& -\left[\kappa_1+\kappa_2\right]\langle a_1^\dagger a_2\rangle \\ &+\sum_{j=1}^{2}\left[g_{j,1}\langle\sigma_{j,j-1}a_2\rangle\,\mathrm{e}^{-i\Delta_{j,1}t}+g_{j,2}\langle\sigma_{j-1,j}a_1^\dagger\rangle\,\mathrm{e}^{i\Delta_{j,2}t}\right].\end{aligned} \tag{C.83}$$

This semiclassical model can be improved to take into account more multi-transition processes.

Appendix D

# Quantum fluctuations of a Bose gas in a ring trap

**Contents**

## Introduction

We detail the derivation of two main results presented in Chap. 5. First, we show our method to take into account the long range density fluctuations in the one-body density matrix. Second, we treat the renormalization of the Josephson energy with a functional integral approach.

## D.1 Effect of the field Π on the one-body density matrix

In the expression of the bosonic field operator Eq. (5.19), the field $\Pi(x)$ is present. In the Luttinger liquid literature however, this field is not usually taken into account in the calculation of the one-body density matrix. In this section we propose a method to include the effect of the long range density fluctuations in $\mathcal{G}(x,x')$. We note $\bar{\theta}(x) = \langle\Theta(x)\rangle$, $\theta(x) = \Theta(x) - \bar{\theta}(x)$, $\bar{\phi}(x) = \langle\phi(x)\rangle$, and $\varphi(x) = \phi(x) - \bar{\phi}(x)$. We also define $X = \Pi(x)/\rho_0$, $Y = \Pi(x')/\rho_0$, and $Z = 2im\theta(x) - 2im'\theta(x') - i\varphi(x) + i\varphi(x')$. In these notations, it follows

$$\mathcal{G}(x,x') = \rho_0 \sum_{m,m'} D_{m,m'}(x,x') \left\langle \sqrt{1+X}\mathrm{e}^{Z}\sqrt{1+Y} \right\rangle, \tag{D.1}$$

where $D_{m,m'}(x,x') = |\mathcal{A}|^2 \mathrm{e}^{2im\bar{\theta}(x)-2im'\bar{\theta}(x')-i\bar{\phi}(x)+i\bar{\phi}(x')}\,\mathrm{e}^{[m\theta(x)+m'\theta(x'),\varphi(x)-\varphi(x')]}$. Supposing that the density fluctuations $\Pi(x)$ are much smaller than the average density $\rho_0$, we expand the square root in power series of $\Pi(x)/\rho_0$. This expansion generates correlators of the type $\langle X^k \mathrm{e}^Z Y^l \rangle$, where $k$ and $l$ are two integers. This average can be performed using the generating function

$$\Phi(\chi_1, \chi_2) = \left\langle \mathrm{e}^{\chi_1 X}\, \mathrm{e}^Z\, \mathrm{e}^{\chi_2 Y} \right\rangle , \tag{D.2}$$

which gives

$$\frac{\partial^k}{\partial \chi_1^k} \frac{\partial^l}{\partial \chi_2^l} \Phi(\chi_1 = 0, \chi_2 = 0) = \left\langle X^k \mathrm{e}^Z Y^l \right\rangle . \tag{D.3}$$

The generating function can be reformulated as follows

$$\Phi(\chi_1, \chi_2) = \exp\left[\frac{1}{2}\langle X^2\rangle {\chi_1}^2 + \frac{1}{2}\langle Y^2\rangle {\chi_2}^2 + \chi_1\langle XZ\rangle + \chi_2\langle ZY\rangle + \chi_1\chi_2\langle XY\rangle + \frac{1}{2}\langle Z^2\rangle\right] . \tag{D.4}$$

The derivatives of $\Phi$ can then be expressed in terms of Hermite polynomials $\mathrm{H}_n(x)$

$$\begin{aligned} \frac{\partial^k}{\partial \chi_1^k} \frac{\partial^l}{\partial \chi_2^l} \Phi(\chi_1, \chi_2) = \Phi(\chi_1, \chi_2) &\left(i\sqrt{\frac{\langle X^2\rangle}{2}}\right)^k \left(i\sqrt{\frac{\langle Y^2\rangle}{2}}\right)^l \\ \times &\sum_{j=0}^{\mathrm{Min}(k,l)} \frac{k!l!}{(k-j)!(l-j)!j!} \left(\frac{-2\langle XY\rangle}{\sqrt{\langle X^2\rangle\langle Y^2\rangle}}\right)^j \\ \times \mathrm{H}_{k-j}\left(\frac{\langle X^2\rangle\chi_1 + \langle XY\rangle\chi_2 + \langle XZ\rangle}{i\sqrt{2\langle X^2\rangle}}\right) &\mathrm{H}_{l-j}\left(\frac{\langle XY\rangle\chi_1 + \langle Y^2\rangle\chi_2 + \langle ZY\rangle}{i\sqrt{2\langle X^2\rangle}}\right) . \end{aligned} \tag{D.5}$$

The noise being Gaussian, the expression of $\Psi(0,0) = \langle \mathrm{e}^Z\rangle$ is derived with Wick's theorem, which leads to $\langle \mathrm{e}^Z\rangle = \mathrm{e}^{\langle Z^2\rangle/2}$. From the series expansion of the square root function, $\forall\, x \in ]-1,1[ \quad \sqrt{1+x} = \sum_{n=0}^{\infty} \frac{(-1)^{n+1}(2n)!}{n!^2(2n-1)2^{2n}} x^n$, it is then straightforward to obtain Eq. (5.46).

## D.2 Renormalization of the Josephson energy

We study the effect of quantum fluctuations on the Josephson junction with a different viewpoint from the one presented in Sec. 5.5. Here we make use of the path integral method to obtain the flow equation of the renormalization (see, *e.g.*, Ref. [195]).

### D.2.1 Effective action

Instead of using the Hamiltonian to describe the Luttinger liquid, we adopt the Euclidean action alternative. This description involve the time dependence of the fluctuations of the various fields. We concentrate on the symmetric phase difference across the barrier, which defines the new field

$$\widetilde{\varphi}(x,t) = \phi(L-x,t) - \phi(x,t). \tag{D.6}$$

The total action $\mathcal{S}$ is composed of the Luttinger liquid action

$$\mathcal{S}_0 = \frac{\hbar K v_S}{8\pi} \int_0^{\beta\hbar} \mathrm{d}t \int_0^L \mathrm{d}x \left[(\partial_x \widetilde{\varphi}(x,t))^2 + \frac{1}{v_S^2}\left(\partial_t \widetilde{\varphi}(x,t)\right)^2\right] \tag{D.7}$$

and the tunneling part $-E_J \int_0^{\beta\hbar} \mathrm{d}t \cos\widetilde{\varphi}(0,t)$. The goal is to find an effective action in terms of the phase difference at the barrier $\varphi(t) = \widetilde{\varphi}(0,t)$ by averaging out all the fluctuations in the ring. It is more convenient to switch to the double Fourier transform

$$\widetilde{\varphi}(x,t) = \frac{1}{\hbar\beta} \sum_{\omega_\nu} \left( \frac{1}{2}\widetilde{\varphi}_0(\omega_\nu) + \sum_{n>0} \widetilde{\varphi}_n(\omega_\nu) \cos(2\pi n x/L) \right) \mathrm{e}^{i\omega_\nu t}, \tag{D.8}$$

where $\omega_\nu = 2\pi\nu/\beta\hbar$ are the Matsubara frequencies. In terms of $\widetilde{\varphi}_n(\omega_\nu)$, the action reads

$$\mathcal{S}_0 = \frac{\pi v_S K}{4L\beta} \sum_{\omega_\nu} \left[ \frac{1}{2} \left( \frac{L\omega_\nu}{2\pi v_S} \right)^2 \widetilde{\varphi}_0(\omega_\nu)\widetilde{\varphi}_0(-\omega_\nu) + \sum_{n>0} \left( n^2 + \frac{L^2\omega_\nu^2}{4\pi^2 v_S^2} \right) \widetilde{\varphi}_n(\omega_\nu)\widetilde{\varphi}_n(-\omega_\nu) \right]. \tag{D.9}$$

The definition of the phase difference at the barrier $\varphi(t)$ becomes

$$\frac{1}{2}\widetilde{\varphi}_0(\omega) + \sum_{n>0} \widetilde{\varphi}_n(\omega) = \varphi(\omega). \tag{D.10}$$

We now turn to the calculation of the effective action $\mathcal{S}_0^{\mathrm{eff}}$. We use the path integral formulation to integrate out the fluctuations $\widetilde{\varphi}_n(\omega_\nu)$. To express the resulting effective action in terms of the field $\varphi(\omega)$ we introduce Lagrange multipliers $\gamma_{\omega_\nu}$

$$\mathrm{e}^{-\mathcal{S}_0^{\mathrm{eff}}} = \left\{ \lim_{\nu\to\infty} \prod_{\omega_\nu} \prod_n \int \mathcal{D}\widetilde{\varphi}_n(\omega_\nu) \right\} \mathrm{e}^{-\mathcal{S}_0} \times \left\{ \lim_{\nu\to\infty} \prod_{\omega_\nu} \int \mathcal{D}\gamma_{\omega_\nu} \right\} \mathrm{e}^{i\sum_{\omega_\nu} \gamma_{\omega_\nu} \left[ \sum_n \widetilde{\varphi}_n(\omega_\nu) - \varphi(\omega_\nu) \right]}. \tag{D.11}$$

The result for the Gaussian integral is $\int \mathcal{D}x \, \mathrm{e}^{-xMx+xJ} = \frac{\pi^{n/2}}{\sqrt{|\det M|}} \mathrm{e}^{\frac{1}{4}JM^{-1}J}$. In our case $M^{-1} = M$ and $|\mathrm{det} M| = 1$. We get

$$\mathrm{e}^{-\mathcal{S}_0^{\mathrm{eff}}} \propto \exp\left[ -\frac{\pi v_S K}{4L\beta} \sum_{\omega_\nu} \left( \frac{1}{2} \frac{1}{(L\omega_\nu/2\pi v_S)^2} + \sum_{n>0} \frac{1}{n^2 + (L\omega_\nu/2\pi v_S)^2} \right)^{-1} \varphi(\omega_\nu)\varphi(-\omega_\nu) \right]. \tag{D.12}$$

Upon performing the sums, one gets

$$\mathcal{S}_0^{\mathrm{eff}} = \frac{\hbar}{2} \frac{K}{2\pi} \int_{-\infty}^{+\infty} \frac{\mathrm{d}\omega}{2\pi} \frac{\omega |\varphi(\omega)|^2}{\coth(L\omega/2v_S)}. \tag{D.13}$$

In the limit of a large ring $L\omega/v_S \gg 1$, we finally have

$$\mathcal{S}_0^{\mathrm{eff}} = \frac{\hbar}{2} \int_{-\infty}^{+\infty} \frac{\mathrm{d}\omega}{2\pi} \sigma(\omega) |\varphi(\omega)|^2, \qquad \text{where } \sigma(\omega) = \frac{K}{2\pi}|\omega|. \tag{D.14}$$

The effective action will be used to find the two-point correlation function of the field $\varphi$.

### D.2.2 Coarse-graining

Now we average the action $\mathcal{S}_0^{\mathrm{eff}}$ over the fast modes of the field $\varphi$. We introduce a running cut-off energy $\lambda \ll \Lambda$, $\Lambda$ being the initial cut-off energy of the system. In the case of the ring, the high energy cutoff is $\Lambda = \pi\hbar v_S/a$. We then divide the field into slow and fast modes relative to $\lambda$

$$\varphi(\omega) = \underbrace{\varphi_{\mathrm{s}}(\omega)}_{\neq 0 \text{ for } \hbar\omega<\lambda} + \underbrace{\varphi_{\mathrm{f}}(\omega)}_{\neq 0 \text{ for } \hbar\omega>\lambda} . \tag{D.15}$$

Then, averaging the tunneling action over $\varphi_{\mathrm{f}}(\omega)$ yields

$$\left\langle E_J \int_0^{\hbar\beta} \mathrm{d}t \cos(\varphi_{\mathrm{s}}(t) + \varphi_{\mathrm{f}}(t)) \right\rangle = E_J \left\langle \cos\varphi_{\mathrm{f}}(t) \right\rangle \int_0^{\hbar\beta} \mathrm{d}t \cos\varphi_{\mathrm{s}}(t). \tag{D.16}$$

The average of the cosine is

$$\langle \cos\varphi_{\mathrm{f}}(t) \rangle = \mathrm{e}^{-\frac{1}{2}\langle \varphi_{\mathrm{f}}^2(t) \rangle} = \mathrm{e}^{-\frac{1}{2}G(0)}, \tag{D.17}$$

where $G(t)$ is the two-point correlation function [195]

$$G(t) = \langle \varphi_{\mathrm{f}}(t)\varphi_{\mathrm{f}}(0) \rangle = \int_{-\Lambda}^{\Lambda} \frac{\mathrm{d}\omega}{2\pi} \sigma^{-1}(\omega)\, \mathrm{e}^{i\omega t} W\left(\left|\frac{\omega}{\lambda}\right|\right) = \frac{2}{K} \int_0^{\Lambda} \frac{\mathrm{d}\omega}{2\pi} \frac{\cos(\omega t)}{\omega} W(\omega/\lambda), \tag{D.18}$$

where $W(x)$ is a function which separates the slow from the fast modes. For instance, we can use $W(x) = \frac{x^\eta}{1+x^\eta}$, $\frac{x^\eta}{\sqrt{1+x^{2\eta}}}$, $\Xi(x)\ldots$ and, in the case $\Lambda \gg \lambda$, we get

$$G(0) = \frac{2}{K} \ln(\Lambda/\lambda). \tag{D.19}$$

Consequently

$$\langle \cos\varphi_{\mathrm{f}}(t) \rangle = \left(\frac{\lambda}{\Lambda}\right)^{1/K} . \tag{D.20}$$

This is the power-law decay that we obtained with a direct use of the one-body density matrix in Sec. 5.5. Finally the total effective action reads,

$$\mathcal{S}^{\mathrm{eff}} = \frac{\hbar}{2} \frac{K}{2\pi} \int_{-\infty}^{+\infty} \frac{\mathrm{d}\omega}{2\pi} |\omega| |\varphi_{\mathrm{s}}(\omega)|^2 - E_J(\Lambda) \left(\frac{\lambda}{\Lambda}\right)^{1/K} \int_0^{\hbar\beta} \mathrm{d}t \cos\varphi_{\mathrm{s}}(t). \tag{D.21}$$

This effective action gives rise to the renormalization group flow equation of the Josephson energy.

### D.2.3 Flow equation

If we match the two tunneling actions

$$E_J(\Lambda) \left(\frac{\lambda}{\Lambda}\right)^{1/K} \int_0^{\hbar\beta} \mathrm{d}t \cos\varphi_{\mathrm{s}}(t) = E_J(\lambda) \int_0^{\hbar\beta} \mathrm{d}t \cos\varphi(t), \tag{D.22}$$

where $E_J(\lambda)$ is the renormalized Josephson energy. We find the relation

$$E_J(\lambda) = \left(\frac{\lambda}{\Lambda}\right)^{1/K} E_J(\Lambda). \tag{D.23}$$

This renormalization group approach leads to the flow equation of the system [195]

$$\frac{\partial \bar{E}_J}{\partial \ell} = \left(1 - \frac{1}{K}\right) \bar{E}_J(\lambda), \tag{D.24}$$

where $\bar{E}_J(\lambda) = E_J(\lambda)/\lambda$ is the reduced Josephson energy and $\mathrm{d}\ell = -\mathrm{d}\mu/\mu$. This flow equation can be integrated and, depending on the length of the ring compared to the healing length $L^*$, the renormalization reaches two different fixed points, as explained in Sec. 5.5.

# Appendix E

# Publications

Contents

A Letters Journal Exploring the Frontiers of Physics

August 2008

EPL, **83** (2008) 47012
doi: 10.1209/0295-5075/83/47012

www.epljournal.org

# Quantum charge diffusion in underdamped Josephson junctions and superconducting nanowires

A. Zazunov, N. Didier and F. W. J. Hekking

*Université Joseph Fourier, Laboratoire de Physique et de Modélisation des Milieux Condensés, CNRS*
*BP 166, 38042 Grenoble, France, EU*

received 11 March 2008; accepted in final form 8 July 2008

PACS 74.78.Na – Mesoscopic and nanoscale systems
PACS 74.50.+r – Tunneling phenomena; point contacts, weak links, Josephson effects
PACS 73.23.Hk – Coulomb blockade; single-electron tunneling

**Abstract** – The effect of quantum fluctuations on the current-voltage characteristics of Josephson junctions and superconducting nanowires is studied in the underdamped limit. Quantum fluctuations induce transitions between a Coulomb blockade and a supercurrent branch, and can significantly modify the shape of current-voltage characteristics in the case of a highly resistive environment. Owing to the phase-charge duality, our results can be directly extended to the opposite overdamped limit.

**Introduction.** – A small-capacitance Josephson junction is a quantum system with rich dynamics. The two conjugate variables are the superconducting phase difference $\phi$ across the junction and the charge $Q$ on its electrodes. Correspondingly, at low temperatures the behavior of the junction is determined by the competition between the Josephson energy $E_J$ and the charging energy $E_C = (2e)^2/2C$, where $C$ is the junction capacitance [1]. If $E_J \gg E_C$, $\phi$ is well defined and a phase-coherent Cooper-pair current can flow through the junction in the absence of an external voltage $V$. In the opposite limit $E_J \ll E_C$ an insulating state with a well-defined charge $Q$ on the electrodes is possible. At the same time, the dynamics of $\phi$ and $Q$ is crucially influenced by dissipation caused by the electromagnetic environment surrounding the junction. Because of the mutual interplay of quantum mechanics, nonlinearity and dissipation, the consistent theoretical description of Josephson junctions still remains far from being complete.

The dc current-voltage ($I$-$V$ ) characteristics of a Josephson junction embedded in a circuit of resistance $R$ have been well studied in the so-called overdamped [1] case corresponding to small values of $R/R_Q$ ($R_Q = h/4e^2$ is the resistance quantum) and the ratio $E_J/E_C$ [2–8]. For small $R < R_Q$, the supercurrent peak at zero voltage acquires a finite width. With increasing $R$, quantum fluctuations of the phase become more important and the supercurrent peak gradually moves to higher voltages. This corresponds to the transition (driven by the environment) from superconducting behavior found for small $R$ to a complete Coulomb blockade when $R > R_Q$. Meanwhile, the opposite underdamped regime, which has been extremely difficult to achieve experimentally, has attracted less attention. However, recently experiments were performed [9,10] on junctions with $E_J/E_C > 1$, embedded in a tunable, highly resistive environment, $R \gg R_Q$, enabling the study of the same junction in different environments. In particular, a voltage peak near zero current followed by a back-bending to lower voltages at higher currents was observed. This is the so-called Bloch nose [11] which, in accordance with a duality property [4,12–14], resembles the $I$-$V$ characteristic of an overdamped junction but with the role of voltage and current interchanged. A quantitative comparison between theory and experiment has been made in the classical limit where thermal fluctuations dominate [10,15].

In this letter we study for the first time the influence of quantum fluctuations on the $I$-$V$ characteristics of an underdamped Josephson junction. We show that the quantum-mechanical nature of the electromagnetic environment can strongly modify the crossover from Coulomb blockade to superconducting behavior. Without fluctuations the $I$-$V$ characteristic contains a sharp cusp that connects two distinct branches: a zero-current finite-voltage branch corresponding to Coulomb blockade and a supercurrent branch corresponding to Bloch oscillations of the voltage. Thermal fluctuations induce transitions between these branches thereby smearing the cusp. This

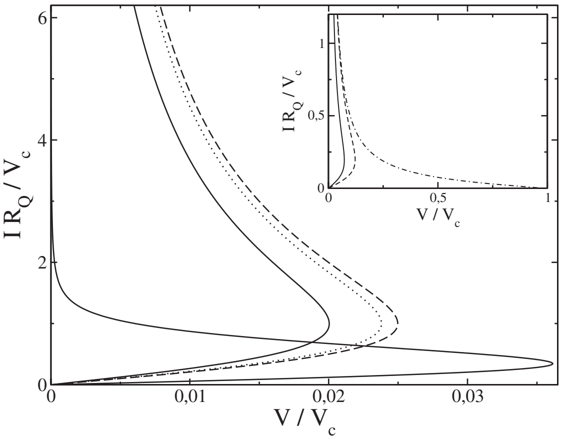

Fig. 1: *I*-*V* characteristics for $g=0.1$ and $\beta U_0=0.1$. The dashed line corresponds to the classical expression (28) while the dotted line gives the quasiclassical solution from (29) for $\beta\hbar\omega_c=1$. Solid lines depict the result from (17) with $\beta\hbar\omega_c=10$ for the rounded *I*-*V* characteristic and $\beta\hbar\omega_c=0.1$ for the sharp one. Inset: (from right to left) the classical limit without fluctuations (6), the result (28), and the solution from (17) for $g=0.1$, $\beta U_0=0.5$, and $\beta\hbar\omega_c=50$.

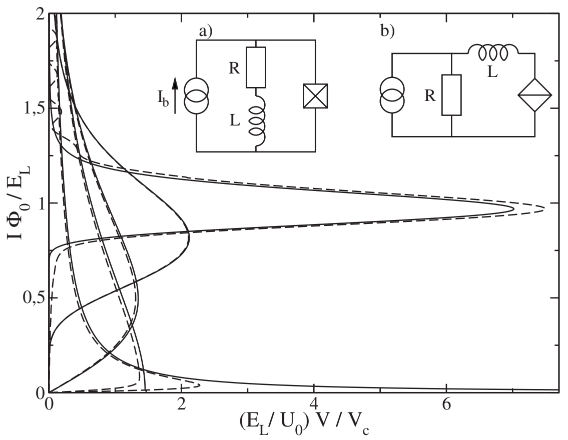

Fig. 2: *I*-*V* characteristics at $T=0$ for $\hbar\omega_c=100\,U_0$. From top to bottom, solid lines represent (34) with $g=100$, 5, 1, 0.5 and 0.1. Dashed lines are the corresponding curves for the solution from (17) with $\beta U_0=0.5$ and $\beta\hbar\omega_c=50$. While decreasing $R$ the Bloch nose is shifted to the finite current $I=\Phi_0/2L$, where the tunneling of a flux quantum requires an energy exchange with the bath. Insets: equivalent circuits of current-biased Josephson junction (a) and nanowire-based QPS (b) with the diamond symbol representing the phase-slip process.

thermal smearing can be described using a Fokker-Planck approach [15]. Quantum effects show up at temperatures comparable with the characteristic cutoff frequency $\omega_c$ of the environmental modes. As we will detail below, at intermediate temperatures $k_BT\lesssim\hbar\omega_c$, a quasiclassical regime exists. In this regime small quantum corrections to the thermal smearing are found, described by the so-called quantum Smoluchowski equation. In the limit of low temperatures $k_BT\ll\hbar\omega_c$, quantum fluctuations not only smear the cusp but also shift its position. Specifically, with increasing dissipation strength the voltage peak shifts to nonzero current: quantum fluctuations induce tunneling events of flux quanta that disrupt the Bloch oscillations.

Due to the duality symmetry, our results can be directly mapped to the case of an overdamped junction, where we have found that the role of quantum fluctuations has not been adequately studied, for instance, in the quantum Smoluchowski regime (see eq. (29) and discussion below). Finally, we demonstrate that all our results also apply to the case of the recently proposed quantum phase-slip junctions which are realized in superconducting nanowires [16].

**Model.** – We start our analysis by considering a current-biased Josephson junction (see inset a) of fig. 2). The junction is shunted by a resistance $R$ and biased by an external dc current $I_b$. As long as quasiparticle excitations are neglected, the system is described by the following Hamiltonian:

$$H=\frac{(Q-Q_x)^2}{2C}-E_J\cos\phi-\frac{\hbar}{2e}I_b\,\phi+H_{\text{bath}},\qquad(1)$$

where the operators $Q$ and $\phi$ obey the commutation relation $[\phi,Q]=2ei$. The fluctuating charge $Q_x$ is associated with the current $I_x=\dot{Q}_x$ flowing through the shunting resistor. The latter is modeled by a bath of harmonic oscillators with frequencies $\{\omega_\alpha\}$, which is described by $H_{\text{bath}}=\sum_\alpha\hbar\omega_\alpha\left(p_\alpha^2+x_\alpha^2\right)/2$. In this model, $Q_x$ is represented by a weighted sum of oscillator coordinates $\{x_\alpha\}$, $Q_x=2e\sum_\alpha\lambda_\alpha x_\alpha$, while the influence of the bath on the junction dynamics is entirely determined by the weighted spectral function, $K(\omega)=(\pi/2)\sum_\alpha\lambda_\alpha^2\delta(|\omega|-\omega_\alpha)$. As follows from the equations of motion generated by $H$, the choice $K(\omega)=R_Q\text{Re}Y(\omega)/2\pi\omega$ with $Y(0)=1/R$ reproduces the linear response (Ohm's law) of current $I_x$ to the voltage drop $V=(\hbar/2e)\dot{\phi}$ on the resistor, $I_x(\omega)=Y(\omega)V(\omega)$ (for Fourier transforms). In the case of interest here, $E_J\gg E_C$, it is advantageous to switch to the Bloch-band description of the Josephson junction [11]. Assuming that the junction dynamics is confined to the lowest energy band $\epsilon_0(q)=-U_0\cos(\pi q/e)$, we arrive at the tight-binding (TB) model of our system with the Hamiltonian:

$$H_{\text{TB}}=-U_0\cos(\pi q/e-\chi)-(\hbar/2e)I_b\phi+H_{\text{bath}},\qquad(2)$$

where $q$ is the operator corresponding to the quasicharge and $U_0=4\sqrt{2/\pi}E_C(2E_J/E_C)^{3/4}\exp(-4\sqrt{2E_J/E_C})$ is the Bloch bandwidth. The reduced fluctuating charge

$$\chi=2\pi\sum_\alpha\lambda_\alpha x_\alpha\qquad(3)$$

gives rise to the bath correlation function $J(\tau)=\langle(\chi(\tau)-\chi(0))\chi(0)\rangle$, or explicitly,

$$J(\tau)=2R_Q\int_{-\infty}^{+\infty}\mathrm{d}\omega\,\frac{\mathrm{Re}Y(\omega)}{\omega}\,\frac{\mathrm{e}^{-\mathrm{i}\omega\tau}-1}{1-\mathrm{e}^{-\beta\hbar\omega}},\tag{4}$$

where $\beta=1/k_BT$ is the inverse temperature.

Hamiltonian (2) describes the quasicharge dynamics in the lowest Bloch band under the influence of the current $I=I_b-I_x$. The group velocity associated with the quasicharge, $\mathrm{d}\epsilon_0/\mathrm{d}q=(\pi U_0/e)\sin(\pi q/e)$, corresponds to the voltage across the junction. Hence for a resistive environment Ohm's law yields $I_x=(V_c/R)\sin(\pi q/e)$, where $V_c=\pi U_0/e$ is the maximal (critical) voltage the junction can sustain. Classically, the problem is equivalent to the equation of motion [11],

$$\dot{q}=I_b-(V_c/R)\sin(\pi q/e),\tag{5}$$

describing overdamped quasicharge diffusion with damping rate $\pi V_c/eR$. A stationary solution $\dot{q}=0$ exists if $I_b<V_c/R$: all the current flows through the resistor, while the junction stays in a zero-current Coulomb blockade state with a voltage drop $V=RI_b$. If $I_b>V_c/R$, $\dot{q}\neq 0$ and a dynamical state exists at finite current with Bloch oscillations of the voltage. From eq. (5) one finds the frequency of the oscillations to be $f_B=I/2e$; by direct integration of eq. (5) over one period one obtains the dc voltage [11]

$$V=RI_b-\sqrt{(RI_b)^2-V_c^2}.\tag{6}$$

The resulting $I$-$V$ characteristic corresponds to the aforementioned Bloch nose and is depicted in fig. 1, inset.

We now turn to the effect of fluctuations and introduce a cutoff of the bath spectrum at frequency $\omega_c$, chosen to be smaller than the gap $\omega_g=\sqrt{2E_JE_C}/\hbar$ between the lowest Bloch bands but higher than the Bloch bandwidth. Furthermore, the competition between the cutoff energy and the temperature determines the nature, rather classical or quantum, of the environment. Indeed, starting from a classical thermal bath when $k_BT\sim\hbar\omega_c$, quantum fluctuations appear in the quasiclassical region $k_BT\lesssim\hbar\omega_c$ and become dominant at low temperatures $k_BT\ll\hbar\omega_c$. Assuming that the effective impedance seen by the junction is given by a resistance $R$ in series with an inductance $L$, we can set $Y(\omega)=1/(R-i\omega L)$, leading to $\omega_c=R/L$. Then, from evaluating the integral (4) one obtains

$$J(\tau)=-\mathrm{i}\,\mathrm{sign}(\tau)\;A(\tau)-M(\tau),\tag{7}$$

with

$$A(\tau)=\pi g(1-\mathrm{e}^{-\omega_c|\tau|}),\tag{8}$$

$$M(\tau)=2g\left[\frac{\pi|\tau|}{\beta\hbar}-\frac{\pi}{2}\cot\left(\frac{\beta\hbar\omega_c}{2}\right)\left\{1-\mathrm{e}^{-\omega_c|\tau|}\right\}+\sum_{k=1}^{+\infty}\frac{1-\mathrm{e}^{-\nu_k|\tau|}}{k\,(1-\nu_k^2/\omega_c^2)}\right],\tag{9}$$

where $g=R_Q/R$ is the dimensionless conductance, and $\nu_k=2\pi k/\hbar\beta$ is a Matsubara frequency.

Before proceeding, we want to comment on the magnitude of the effective inductance $L$ which has been associated with the cutoff $\omega_c$. The restriction $\omega_c<\omega_g$ imposes a lower boundary on the values of $L$ to be consistent with our assumption of single-band charge dynamics:

$$L>\frac{2\pi g^{-1}}{\sqrt{2E_C/E_J}}\,L_J,\tag{10}$$

where $L_J=(\Phi_0/2\pi)^2/E_J$ is the Josephson inductance and $\Phi_0=h/2e$ is the flux quantum. For relatively large $g>1$, the condition (10) can be satisfied even for an autonomous Josephson junction, where $L\sim L_J$ corresponds to the Bloch inductance [17]. In the opposite limit of small $g\ll 1$, an experimental realization of this model would be the use of an environment composed of Josephson junction SQUID arrays, whose effective inductance can be tuned to relatively large values by magnetic flux [18]. Another option includes the use of a quantum phase-slip junction where there is no limitation on $\omega_c$, as discussed at the end of the paper.

**Current-voltage characteristics.** – To determine the $I$-$V$ characteristics, we calculate the average of the operator for the voltage across the junction

$$V(t)=V_c\,\langle\mathcal{U}_C(t,0)\,\sin\theta(t)\rangle,\tag{11}$$

where $\theta=(\pi/e)\,q-\chi$. The time evolution operator (in the interaction picture),

$$\mathcal{U}_C(t,0)=T_C\exp\left\{(\mathrm{i}U_0/\hbar)\int_0^t\mathrm{d}\tau\sum_{s=\pm}s\cos\theta^s(\tau)\right\},\tag{12}$$

is defined along the Keldysh contour with the Keldysh index $s=+/-$ refering to the forward/backward branch of the contour, and $T_C$ denotes the Keldysh time-ordering. Expanding $\mathcal{U}_C$ in $U_0$, averaging over the bath and performing summation over the Keldysh indices yield

$$V(t)=(V_c/2\mathrm{i})\sum_{n=0}^{+\infty}(-1)^n\,(U_0/\hbar)^{2n+1}\times\int_0^t\mathrm{d}\tau_1\ldots\int_0^{\tau_{2n}}\mathrm{d}\tau_{2n+1}\sum_{\{f_k\}}\left(\prod_{k=1}^{2n+1}\sin G_k\right)\mathrm{e}^{\Gamma_n},\tag{13}$$

where for given $n$ the discrete variables $f_k$ satisfy

$$|f_{k+1}-f_k|=1\tag{14}$$

with the constraint $f_0=f_{2n+2}=0$ [5,19], and

$$G_k=A_{k,k-1}f_k+\sum_{k'=1}^{k-1}\delta A_{kk'}f_{k-k'},\tag{15}$$

$$\Gamma_n = -\mathrm{i}(\pi/e) I_b \sum_{k=1}^{2n+1} (\tau_k - \tau_{k-1})\, f_k - \sum_{k=1}^{2n+1} M_{k,k-1} f_k^2 + \sum_{k=2}^{2n+1} \sum_{k'=1}^{k-1} \delta M_{kk'} f_k f_{k'}. \qquad (16)$$

Here $\delta M_{kk'} = M_{kk'} + M_{k-1,k'-1} - M_{k-1,k'} - M_{k,k'-1}$, $\delta A_{kk'} = A_{k,k-k'-1} - A_{k,k-k'}$, with the shorthand notation $A_{kk'} = A(\tau_k - \tau_{k'})$, and similar for $M_{kk'}$. The above equations are in a form suitable to apply the "nearest-neighbor approximation" (NNA), where one assumes that $\delta M_{kk'} \approx 0$ and $\delta A_{kk'} \approx 0$ [5] on the relevant time scale $\tau > 1/\omega_c$. Then, in the limit $t \to \infty$, the expression (13) can be evaluated exactly, and one obtains for the dc voltage $V$ across the junction:

$$V = V_c \,\mathrm{Im}\,(W_1/W_0)\,, \qquad (17)$$

where $W_n$ obey the following recurrent relation ($n \geqslant 1$ ):

$$\mathrm{i}a_n\,(W_{n-1} - W_{n+1}) = W_n, \qquad (18)$$

$$a_n = \frac{U_0}{\mathrm{i}\hbar} \int_0^{+\infty} \mathrm{d}\tau\, \sin\,(nA(\tau))\; \mathrm{e}^{\mathrm{i}(\pi/e) I_b n\tau - n^2 M(\tau)}. \qquad (19)$$

Equations (17)–(19) constitute the central result of this letter. The quantities $W_n$ should be identified with the Fourier transform of the quasicharge distribution function $W(q)$ in the steady state,

$$W(q) = \sum_{n=-\infty}^{+\infty} \mathrm{e}^{-\mathrm{i}n\pi q/e}\; W_n, \qquad (20)$$

with the property $W_{-n} = W_n^*$. This becomes obvious by noticing that eq. (17) can be viewed as a result of averaging the voltage operator with the quasicharge distribution $W(q)$,

$$V/V_c = W_0^{-1} \int_{-e}^{+e} \mathrm{d}q\; W(q) \sin\,(\pi q/e)\,. \qquad (21)$$

**Quasiclassical limit.** – To shed light on the range of applicability of the NNA for our system, we first study the quasiclassical limit where the typical time scale of the quasicharge dynamics, determined by the damping rate $gU_0/\hbar$ and the frequency of Bloch oscillations $f_B$ (see eq. (5)), is slow. Indeed, if

$$gU_0/\hbar, \quad f_B \ll 1/\hbar\beta, \quad \omega_c, \qquad (22)$$

one can neglect the terms $\mathcal{O}(\mathrm{e}^{-\nu_k \tau},\ \mathrm{e}^{-\omega_c \tau})$ in eqs. (8) and (9). We thus approximate ($\Theta(\tau)$ is the unit step function)

$$A(\tau) = \pi g\, \Theta(|\tau| - 1/\omega_c), \qquad (23)$$

and

$$M(\tau) = (g\nu_1 |\tau| + \lambda)\, \Theta(|\tau| - 1/\omega_c), \qquad (24)$$

with

$$\lambda = 2g \left[\gamma + \frac{\pi}{\beta\hbar\omega_c} + \psi\!\left(\frac{\beta\hbar\omega_c}{2\pi}\right)\right], \qquad (25)$$

where $\gamma = 0.577\dots$ is the Euler constant and $\psi(x)$ is the digamma function. Introducing the short-time cutoff for the approximated $A(\tau)$ and $M(\tau)$ is the simplest way to provide that they vanish at $\tau = 0$ (see the exact expressions (8) and (9)), which is necessary for the consistency of the applied NNA. Assuming also $g \ll 1$, one obtains for $a_n$ entering the recurrent relation (18),

$$a_n = \frac{z}{2\mathrm{i}} \frac{\mathrm{e}^{-\Lambda n^2}}{n - \mathrm{i}\eta}, \qquad (26)$$

where $z = \beta U_0$, $\eta = (e/\pi)\beta R I_b$, and [20]

$$\Lambda = 2g \left[\gamma + \frac{2\pi}{\beta\hbar\omega_c} + \psi\!\left(\frac{\beta\hbar\omega_c}{2\pi}\right)\right]. \qquad (27)$$

Inspection of the terms dropped in the NNA reveals that in the range (22), where $A(\tau)$ and $M(\tau)$ can be simplified by their asymptotic expressions, the NNA becomes exact in the quasiclassical region where $\lambda$ is small. Note that for small $g$, the NNA can be applicable even at low temperature.

**Quantum Smoluchowski equation.** – The crossover between the classical and quantum limit is controlled by the parameter $\lambda$ which is related to quantum corrections to the position dispersion of a fictitious Brownian particle in the harmonic potential [21]. The classical limit corresponds to $\beta\hbar\omega_c \sim 1$ and $g \ll 1$, or equivalently $\lambda,\ \Lambda \to 0$. The recurrences (18) can then be solved analytically in terms of the modified Bessel functions, $W_n = I_{n-\mathrm{i}\eta}(z)$, resulting in the $I$-$V$ characteristics obtained in ref. [15]:

$$V = RI_b - \frac{\sinh\,(\pi\eta)}{e\beta\, |I_{\mathrm{i}\eta}(z)|^2}. \qquad (28)$$

Now expanding $a_n$ in eq. (26) to the first order in $\Lambda$ to include quantum corrections, one can derive from eq. (18) a differential equation for the quasicharge distribution $W(q)$,

$$\partial_q \left[\hat{\mathcal{L}}(q, \partial_q) - \Lambda\, (e/\pi)^4\, U'''(q)\, \partial_q^2\right] W(q) = 0, \qquad (29)$$

where $U(q) = -U_0 \cos(\pi q/e) - RI_b q$ is a washboard potential in the charge variable, $U'(q) \equiv \partial_q U$. The corresponding Smoluchowski differential operator,

$$\hat{\mathcal{L}}(q, \partial_q) = U'_{\mathrm{eff}}(q) + \beta^{-1} D(q)\, \partial_q, \qquad (30)$$

is renormalized by quantum fluctuations through both the effective potential

$$U_{\mathrm{eff}}(q) = U(q) + \Lambda (e/\pi)^2\; U''(q) \qquad (31)$$

and the $q$-dependent diffusion coefficient

$$D(q) = 1 + 2\beta\Lambda (e/\pi)^2\; U''(q). \qquad (32)$$

Equation (29) is the so-called Quantum Smoluchowski Equation (QSE) [20,21] and constitutes the other main result of this letter. Equation (29) describes the leading quantum corrections to the charge dynamics which originate from the quantum nature of the bath. According to eq. (27), the influence of quantum fluctuations becomes more substantial with increasing parameter $\beta\hbar\omega_c$. The $I$-$V$ characteristics, parametrically dependent on the bias $I_b$ and calculated for different $\beta\hbar\omega_c$, are shown in fig. 1. For $\beta\hbar\omega_c \gg 1$, quantum fluctuations reduce the blockade voltage and facilitate a crossover to the Bloch oscillations. Interestingly, for small $\beta\hbar\omega_c < 1$, the influence of thermal fluctuations becomes suppressed by the inertia effect of the "heavy" Brownian particle with an effective mass scaled as $\omega_c^{-1}$. For a wide range of $I_b$, the junction is locked in the insulating state because of the lack of energy exchange with the environment, which results in a sharp crossover to the Bloch oscillations. In other words, reducing the cutoff energy below the temperature is equivalent to decoupling the junction from the environment (see fig. 1).

We note in passing that the structure of the QSE obtained here from the series expansion (17) is different from the one derived in ref. [21] for a Brownian particle in a slightly anharmonic potential and later applied to an overdamped junction [20]. Therefore we cannot exploit the duality property (see below) to treat the Smoluchowski range for underdamped junctions using the results of ref. [20]. Another approximation consists of evaluating expression (13) using the asymptotes for long times (23) and (24) [12]. Such an approach leads to coefficients $a_n = \beta U_0\, \mathrm{e}^{-\lambda/2} \exp(-2\pi g n^2/\beta\hbar\omega_c)/2\mathrm{i}(n-\mathrm{i}\eta)$, which tend towards the result (26) in the quasiclassical region. As a consequence, a QSE equivalent to the solution (29) is also recovered.

**Low temperatures.** – We proceed by studying eqs. (17)–(19) in the low-temperature limit, beyond the quasiclassical region (22). At very low temperature, $\beta\hbar\omega_c \gg 1$, the $I$-$V$ characteristics are entirely determined by the first coefficient $a_1$, eq. (19), consistent with the fact that the NNA is exact to the lowest order in $U_0^2$. Closed-form analytical expressions can be obtained in several cases. For instance, at finite temperatures and for small values of $g$, the $I$-$V$ characteristic can be written as

$$V/V_c = u\,\frac{|\Gamma(g+\mathrm{i}\hbar\beta I_b/2e)|^2}{\Gamma(2g)}\sinh(\pi\hbar\beta I_b/2e), \qquad (33)$$

where $u = (\beta U_0/4\pi)\,(\beta\hbar\omega_c\,\mathrm{e}^{\gamma}/2\pi)^{-2g}$ and $\Gamma(x)$ is the Gamma-function. The resulting linear resistance $R$ varies as a power law with temperature, $R \propto T^{2(g-1)}$, in agreement with the asymptotic analysis of ref. [4]. At zero-temperature one recovers

$$V/V_c = (\pi U_0/2)\,P(hI_b/2e), \qquad (34)$$

where $P(E) = 1/h\int \mathrm{d}t\,\exp\left[J(t) + iEt/\hbar\right]$, dual to the well-known result for the $I$-$V$ characteristic for incoherent Cooper pair tunneling in an overdamped junction [2]. In fig. 2, we plot $I$-$V$ characteristics for different $g$, both at zero and at finite temperatures. As $g$ increases, the voltage peak shifts to finite values of the supercurrent. This behavior can be interpreted in terms of incoherent tunneling of the phase [22]. Indeed, for small values of $g$, few environmental modes are available. Consequently, only elastic tunneling is allowed and a flat Bloch nose is recovered. When $g$ is large, the equivalent circuit consists of a loop containing the junction closed by the inductance $L$. A phase-slip event occurs when the energy to be released $\Phi_0 I_b$ corresponds to the energy $\Phi_0^2/2L$ to add one flux quantum $\Phi_0$ in the loop, *i.e.*, when $I_b = \Phi_0/2L$. At this finite current, phase tunneling disrupts the Bloch oscillations and gives rise to a voltage peak.

**Overdamped Josephson junctions.** – A similar analysis within the Keldysh formalism can be achieved in the case of a voltage-biased overdamped Josephson junction in series with a resistance $R$. This circuit is conventionally described by the Hamiltonian $H = (Q+Q_x)^2/2C - E_J\cos\phi - V_b Q_x + H_{\mathrm{bath}}$, where $Q_x$ is a fluctuating charge on the junction capacitor and $V_b$ is the bias voltage. Using an analysis of the equations of motion similar to the one preceding eq. (2) and performing canonical transformations, one can show that the model description of the junction is equivalently given by the weak-binding (WB) Hamiltonian

$$H_{\mathrm{WB}} = -E_J\cos(\phi - \chi/2\pi) + V_b Q + H_{\mathrm{bath}}, \qquad (35)$$

with $\chi$ the bath variable defined as before, eq. (3). In this representation, the junction capacitance $C$ is encoded in terms of the bath parameters, $C^{-1} = (R_Q/2\pi)\sum_\alpha \lambda_\alpha^2\omega_\alpha$, while the weighted spectral function of the bath is given by $K_{\mathrm{WB}}(\omega) = 2\pi\mathrm{Re}Z(\omega)/R_Q\,\omega$, with $Z^{-1}(\omega) = 1/R - \mathrm{i}\omega C$. The operator for the current flowing through the junction is given by $I = I_c\sin(\phi - \chi/2\pi)$, where $I_c = 2eE_J/\hbar$ is the critical current. The Hamiltonians $H_{\mathrm{TB}}$ and $H_{\mathrm{WB}}$ are related by the following transformation:

$$\begin{gathered}(\pi q/e,\ \phi) \leftrightarrow (\phi,\ -\pi Q/e)\,,\\ U_0 \leftrightarrow E_J, \quad I_b \leftrightarrow V_b/R_Q, \quad \chi \leftrightarrow \chi/2\pi.\end{gathered} \qquad (36)$$

Consequently, the series expansions for $V/V_c$ in the TB model and for $I/I_c$ in the WB model are dual: we can transpose our results obtained for the quasicharge dynamics in an underdamped junction onto the dual case of the phase dynamics in an overdamped junction. A unified approach is thus provided, as well as new results such as the series expansion for $I/I_c$ (see footnote [1]) and the quantum Smoluchowski equation.

**Superconducting nanowires.** – We conclude by considering quantum phase-slip (QPS) dynamics in superconducting nanowires. Based on a duality argument,

---

[1] The WB expansion for $I/I_c$, which is dual to (13), is similar but not identical to the one obtained in ref. [7] using a different kind of approximation (not the NNA).

ref. [16] suggests the following model Hamiltonian to describe QPS events:

$$H_{\mathrm{QPS}}(\phi, Q) = E_L\,(\phi/2\pi)^2 - E_S \cos\left(\pi Q/e\right), \qquad (37)$$

where $E_S$ is an energy associated with the phase-slip process which changes the phase difference $\phi$ over the nanowire by $2\pi$, and $E_L = \Phi_0^2/2L$ is an inductive energy of the wire with a kinetic inductance $L$. Correspondingly, the Hamiltonian of a current-biased QPS junction (see inset b) of fig. 2) can be written as

$$H = H_{\mathrm{QPS}}(\phi + \phi_x, Q) + (\hbar/2e) I_b \phi_x + H_{\mathrm{bath}}, \qquad (38)$$

where a fluctuating phase across the junction $\phi_x$ is related to the voltage drop $V_R = R(\dot{Q} - I_b)$ on the resistor, $\dot{\phi}_x = (2e/\hbar)V_R$. It is straightforward to see that the Hamiltonian (38) is exactly dual to the Hamiltonian of a voltage-biased Josephson junction, and can correspondingly be mapped onto the Hamiltonian (2) with $U_0$ replaced by $E_S$, while the inductance $L$ of nanowire is encoded in terms of the bath parameters, $L^{-1} = (2\pi/R_Q)\sum_\alpha \lambda_\alpha^2 \omega_\alpha$. With this device, the frequency $\omega_c = R/L$ results from the physical resistance and inductance of the wire, providing a natural cutoff of the bath. Our previous analysis for an underdamped Josephson junction, and thus the *I*-*V* characteristics, can be directly applied to a superconducting nanowire (not being restricted by the TB limit). A typical case of nanowire inductance $L \sim 1\,\mathrm{nH}$ corresponds to $\omega_c/2\pi \sim g^{-1} \times 1\,\mathrm{THz}$. Assuming $E_S/h \gtrsim 10\,\mathrm{GHz}$ [16] and $T \sim 1\,\mathrm{K}$, as follows from eq. (21), we estimate that the QSE range for nanowires is relevant for $g \lesssim 0.1$. Note from the parameters used in fig. 1 that the quantum fluctuations in QPS junctions should be substantial.

**Summary. –** To summarize, we have studied the influence of quantum fluctuations on the *I*-*V* characteristics of an underdamped Josephson junction. We have applied a unifying approach based on the Keldysh formalism that enables us to obtain quantitative results for a wide range of parameters. Using the NNA approximation, we show the significant role of quantum fluctuations revealed both in the quasiclassical Smoluchowski regime and in the low-temperature quantum regime. In the Smoluchowski regime, compared to the case of thermal fluctuations, quantum fluctuations mainly lead to a renormalization of the parameters describing the quasicharge dynamics of the junction [12]. The NNA becomes exact in the case of incoherent phase-slip events at low temperatures. In this limit, phase tunneling disrupts the Bloch oscillations, leading to a voltage peak at finite current. The quantum effects are sensitive to both the dissipation strength and cutoff frequency, and could be observed in experiments as in refs. [9,10] with a tunable environment. Besides Josephson junctions, our results are also relevant for superconducting nanowires modeled as quantum phase-slip junctions at low temperature.

* * *

We thank B. Douçot, H. Grabert, W. Guichard, L. B. Ioffe, P. Schuck and U. Weiss for useful discussions. Financial support from Institut universitaire de France and IST-3-015708-IP EuroSQIP is gratefully acknowledged.

REFERENCES

[1] Tinkham M., *Introduction to Superconductivity* (McGraw-Hill, New-York) 1996.

[2] Ingold G.-L. and Nazarov Yu. V., *Single Charge Tunneling*, edited by Grabert H. and Devoret M. H. *NATO ASI Ser. B*, Vol. **294** (Plenum, New York) 1991.

[3] Ivanchenko Yu. M. and Zil'berman L. A., *Sov. Phys. JETP*, **28** (1969) 1272.

[4] Schön G. and Zaikin A., *Phys. Rep.*, **198** (1990) 237.

[5] Zwerger W., *Phys. Rev. B*, **35** (1987) 4737.

[6] Ingold G.-L., Grabert H. and Eberhardt U., *Phys. Rev. B*, **50** (1994) 395.

[7] Grabert H., Ingold G.-L. and Paul B., *Europhys. Lett.*, **44** (1998) 360.

[8] Ingold G.-L. and Grabert H., *Phys. Rev. Lett.*, **83** (1999) 3721.

[9] Watanabe M. and Haviland D. B., *Phys. Rev. Lett.*, **86** (2001) 5120; *Phys. Rev. B*, **67** (2003) 094505.

[10] Corlevi S., Guichard W., Hekking F. W. J. and Haviland D. B., *Phys. Rev. Lett.*, **97** (2006) 096802.

[11] Averin D. V., Zorin A. B. and Likharev K. K., *Sov. Phys. JETP*, **61** (1985) 407; Likharev K. K. and Zorin A. B., *J. Low Temp. Phys.*, **59** (1985) 347.

[12] Weiss U., *Quantum Dissipative Systems* (World Scientific, Singapore) 1999.

[13] Schmid A., *Phys. Rev. Lett.*, **51** (1983) 1506.

[14] Guinea F., Hakim V. and Muramatsu A., *Phys. Rev. Lett.*, **54** (1985) 263.

[15] Beloborodov I. S., Hekking F. W. J. and Pistolesi F., *New Directions in Mesoscopic Physics* (*Towards Nanoscience*), edited by Fazio R., Gantmakher V. F. and Imry Y. (Kluwer Academic Publisher, Dordrecht) 2002.

[16] Mooij J. E. and Nazarov Yu. V., *Nat. Phys.*, **2** (2006) 169.

[17] Zorin A. B., *Phys. Rev. Lett.*, **96** (2006) 167001.

[18] Ågren P., Andersson K. and Haviland D. B., *J. Low Temp. Phys.*, **124** (2001) 291.

[19] Lenard A., *J. Math. Phys.*, **2** (1961) 682.

[20] Ankerhold J., *Europhys. Lett.*, **67** (2004) 280; Ankerhold J., Grabert H. and Pechukas P., *Chaos*, **15** (2005) 026106.

[21] Ankerhold J., Pechukas P. and Grabert H., *Phys. Rev. Lett.*, **87** (2001) 086802.

[22] Averin D. V., Nazarov Yu. V. and Odintsov A. A., *Physica B*, **165** & **166** (1990) 945.

PRL **102,** 097004 (2009) PHYSICAL REVIEW LETTERS week ending 6 MARCH 2009

# Quantum Dynamics in a Camelback Potential of a dc SQUID

E. Hoskinson,[1] F. Lecocq,[1] N. Didier,[2] A. Fay,[1] F. W. J. Hekking,[2] W. Guichard,[1] and O. Buisson[1]

[1]*Institut Néel, C.N.R.S.–Université Joseph Fourier, BP 166, 38042 Grenoble-cedex 9, France*

[2]*LPMMC, C.N.R.S.–Université Joseph Fourier, BP 166, 38042 Grenoble-cedex 9, France*

R. Dolata, B. Mackrodt, and A. B. Zorin

*Physikalisch-Technische Bundesanstalt, Bundesallee 100, 38116 Braunschweig, Germany*

(Received 13 October 2008; published 6 March 2009)

We investigate a quadratic-quartic anharmonic oscillator formed by a potential well between two potential barriers. We realize this novel potential with a dc SQUID at near-zero current bias and flux bias near half a flux quantum. Escape out of the central well can occur via tunneling through either of the two barriers. We find good agreement with a generalized double-path macroscopic quantum tunneling theory. We also demonstrate an "optimal line" in current and flux bias along which the oscillator, which can be operated as a phase qubit, is insensitive to decoherence due to low-frequency current fluctuations.

DOI: 10.1103/PhysRevLett.102.097004 PACS numbers: 85.25.Cp, 03.67.Lx, 85.25.Dq

Superconducting devices, based on the nonlinearity of the Josephson junction (JJ), exhibit a wide variety quantum phenomena. During the last decade, inspired by macroscopic quantum tunneling (MQT) studies [1], quantum dynamics of the current biased JJ, dc SQUID and the rf SQUID phase qubit have been extensively studied [2–6]. In each of these devices, dynamics are analogous to those of a quantum particle in a quadratic-cubic potential. The flux qubit [7], realized by three or four JJs in a loop, is described by a double well potential.

We study a new potential shape called hereafter a "camelback" double barrier potential, shown in Fig. 1(c). This potential is obtained using the dc SQUID circuit shown in Fig. 1(a) in a new way. Characteristics including depth and relative barrier height are controlled by the SQUID current bias $I_b$ and flux bias $\Phi_{\rm ext}$. There is an "optimal line" in the plane ($I_b$, $\Phi_{\rm ext}$) along which the barrier heights are equal and anharmonicity is quartic. We investigate the dynamics of the quantum system formed from the two lowest energy levels of the central well.

A dc SQUID circuit has 2 degrees of freedom corresponding to the phase differences $\phi_1$ and $\phi_2$ across its two JJs. Dynamics are analogous to those of a particle of mass $m = 2C(\Phi_0/2\pi)^2$ in the 2D potential [8,9]

$$U(x, y) = U_0[-\cos x \cos y - sx + b(y - y_b)^2 - \alpha \sin x \sin y - \eta s y]. \qquad (1)$$

Here $x = (\phi_1 + \phi_2)/2$, $y = (\phi_1 - \phi_2)/2$, $U_0 = I_c\Phi_0/2\pi$, $b = \Phi_0/\pi L I_c$, $\alpha = (I_{c2} - I_{c1})/I_c$, $\eta = (L_2 - L_1)/L$, $I_c = I_{c1} + I_{c2}$, $I_{c1}$, and $I_{c2}$ are the critical currents of the two junctions, $L_1$ and $L_2$ are the geometric inductances of the arms of the SQUID loop, $L = L_1 + L_2$, $C$ is the capacitance of each junction, and $\Phi_0 = h/2e$ is the quantum of flux. The external control parameters enter through $y_b = \pi\Phi_{\rm ext}/\Phi_0$ and $s = I_b/I_c$. For our sample, $I_c = 11.22\ \mu$A, $C = 250.3$ fF, $b = 3.05$, $\eta = 0.72$, and $\alpha = 0.0072$.

Stable, stationary states correspond to minima of $U(x, y)$. There can exist one or more minima families corresponding to distinct fluxoid states $[n\Phi_0]$. For each, when $s$ exceeds a flux dependent critical value $s_c[n\Phi_0](y_b)$, the related minima disappear. For small $b$, the parabolic term in $U(x, y)$ is shallow, and there can be many fluxoid states. For $b \gg 1/\pi$, as in our case, the parabolic term is steep and there is only one stable fluxoid state except in a small region around $\Phi_{\rm ext}/\Phi_0 \approx 0.5$ (mod 1) where there are two states with opposite circulating currents. Hereafter we focus on this region.

In general, dynamics is described by 2D motion in the potential. In our device, motion is well approximated as 1D along the minimum energy path which connects minima and saddle points [black line in Fig. 1(b)]. A large curvature in the orthogonal direction confines the system to this path. For example, at the $[0\Phi_0]$ minima in Fig. 1(b), the oscillation frequency along the path is $\omega_{px} \equiv \sqrt{(\partial^2 U/\partial x^2)/m} = 2\pi \times 15.4$ GHz, whereas $\omega_{py} = 2\pi \times 104$ GHz. We parametrize the path with the phase length $z$. $U(z)$ in Fig. 1(c) depicts the camelback potential shape we are investigating. In a typical experiment, the system is initialized in the central well ($[0\Phi_0]$ state). The system can escape via tunneling through the barriers in either of the two physically distinct directions to the $[-1\Phi_0]$ state.

In the symmetric case, the potential near the central minimum will be harmonic with a quartic perturbation. More generally, the Hamiltonian for small oscillations in $U(z)$ is $\hat{H} = \hbar\omega_p(\hat{P}^2 + \hat{Z}^2)/2 - \sigma\hbar\omega_p\hat{Z}^3 - \delta\hbar\omega_p\hat{Z}^4$. Here $\omega_p$ is the zero amplitude oscillation frequency in the direction of minimum curvature, and $\hat{Z} = z\sqrt{m\omega_p/\hbar}$ and $\hat{P} = p/\sqrt{\hbar\omega_p m}$ are the reduced position and corresponding momentum operators. Treating the anharmonic

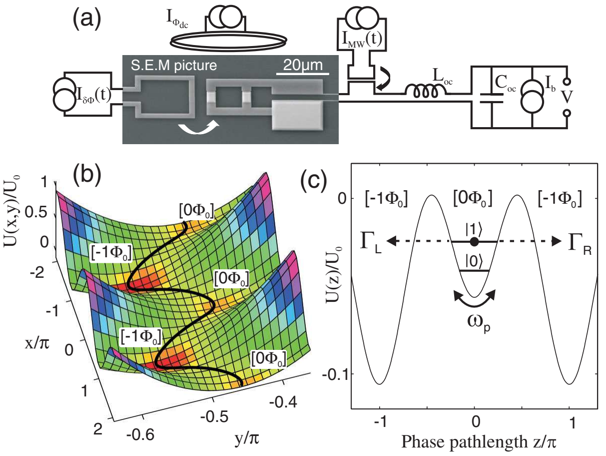

FIG. 1 (color online). Experimental setup. (a) Circuit layout. The two small white squares in the central loop are the SQUID JJs. Connected on the right are current bias and voltage leads. These are heavily filtered at various stages of the cryostat, including the on-chip low-pass filter formed by $L_{oc} = 10$ nH and $C_{oc} = 200$ pF [14]. Fast flux pulses $\delta\Phi$ inductively couple via the on-chip loop to the left of the SQUID. Microwave excitation is applied via an on-chip loop which couples inductively to the current bias leads [15]. An off-chip coil provides a dc flux bias $\Phi_{dc}$. The total externally applied flux is $\Phi_{ext} = \Phi_{dc} + \delta\Phi$. The SQUID chip is enclosed in a copper box thermally anchored to the mixing chamber of a dilution refrigerator with a 30 mK base temperature. The cryostat is surrounded by superconducting Pb, $\mu$ metal, and soft iron shielding. (b) Full 2D potential for $b = 3.05$, $\eta = 0.72$, $\alpha = 0$, $\Phi_{ext} = -0.508\Phi_0$, $I_b = 0$, showing the families of minima associated with the $[0\Phi_0]$ and $[-1\Phi_0]$ fluxoid states. The black line follows the minimum energy path. Note the difference in the $x$ and $y$ scales. (c) Potential along the minimum energy path, parametrized by the path length.

terms as perturbations, to second order the transition energy between levels $n-1$ and $n$ is $h\nu_{n-1,n} = \hbar\omega_p(1 - n\Lambda)$, where the anharmonicity is $\Lambda = \frac{15}{2}\sigma^2 + 3\delta$.

We have calculated the escape probability for the camelback potential with a double escape path in the quantum limit using the instanton formalism [10]. For a duration $\Delta t$, it reads $P_{esc}(I_b, \Phi_{ext}) = 1 - e^{-(\Gamma_R+\Gamma_L)\Delta t}$, where $\Gamma_{R,L} = A_{R,L}\omega_p\sqrt{N_{R,L}}\exp[-B_{R,L}N_{R,L}]$. Here $R$ and $L$ refer to the right and left barriers. $N_{R,L} = \Delta U_{R,L}/\hbar\omega_p$ are the normalized barrier heights. The general expressions for $A_{R,L}$, and $B_{R,L}$ depend on the potential shape. In the symmetric case where $\sigma(I_b, \Phi_{ext}) = 0$, the potential is quadratic quartic, $A_{R,L} = 2^{5/2}\pi^{-1/2}$, and $B_{R,L} = 16/3$. Far from this symmetric line the potential is quadratic cubic, the escape rate through one barrier is dominant (e.g., $\Gamma_L = 0$), and we retrieve the standard MQT situation ($\delta = 0$): $A_R = 6^{3/2}\pi^{-1/2}$ and $B_R = 36/5$ [1].

A schematic of our experimental setup is shown in Fig. 1(a). Our sample was fabricated at Physikalisch-Technische Bundesanstalt using a Nb/AlO$_x$/Nb trilayer process with SiO$_2$ dielectric [11]. The two 5 $\mu$m$^2$ junctions are embedded in a $10 \times 10$ $\mu$m$^2$ square loop.

Figure 2(a) shows the escape lines, $I_{50\%}$ versus $\Phi_{ext}$. These data were obtained with a standard technique in which $I_b$ pulses of varying amplitude are applied and a dc voltage detected across the SQUID when it switches to its voltage state. With this scheme there is no direct indication of multiply stable flux states. In Fig. 2(b) we use a novel technique to measure the overlapping escape lines of

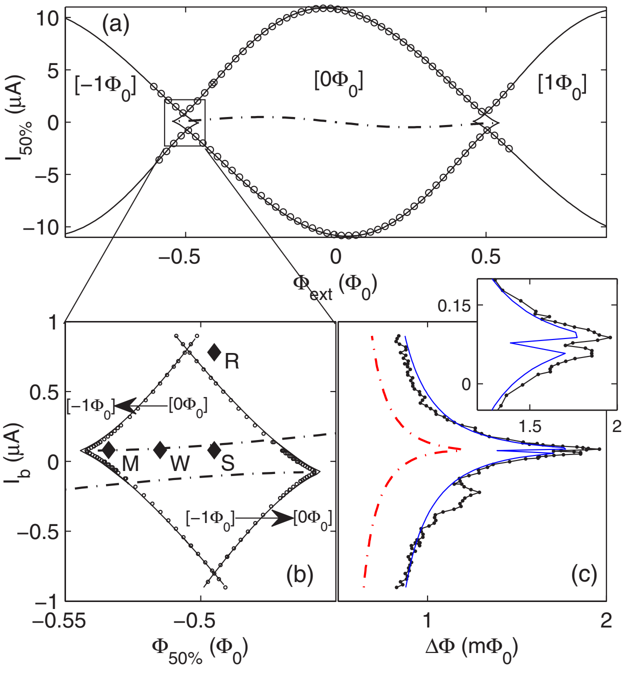

FIG. 2 (color online). Ground-state escape. (a) Escape lines of three fluxoid states as measured by $I_{50\%}$, the amplitude of a 60 $\mu$s $I_b$ pulse that yields $P_{esc} = 50\%$ to the voltage state of the SQUID. Data (symbols), and standard MQT theory fit (solid lines). Here $\delta\Phi = 0$, $\Phi_{ext} = \Phi_{dc}$. The calculated optimal line $I_b^{op}(\Phi_{ext})$ for the $[0\Phi_0]$ state is indicated by the dash-dotted line. (b) Overlapping escape lines in the region $\Phi_{ext} \simeq -\Phi_0/2$. Data (symbols), and generalized MQT theory fit (solid lines), as measured by $\Phi_{50\%}$, where $\Phi_{\chi\%}$ is the total applied flux $\Phi_{ext} = \Phi_{dc} + \delta\Phi$ that yields $P_{esc} = \chi\%$ from the $[-1\Phi_0]$ to the $[0\Phi_0]$ state (right cusp) or vice versa (left cusp). $\delta\Phi$ is the amplitude of a 100 ns flux pulse. The cusps occur at a nonzero current bias $I_b^{cusp} \simeq \pm\alpha I_c = \pm 81$ nA due to the critical current asymmetry $\alpha$. The horizontal separation of the cusps scales precisely with $1/b$. The upper (lower) dash-dotted line indicates the calculated $I_b^{op}(\Phi_{ext})$ for the $[0\Phi_0]$ ($[-1\Phi_0]$) state. The points $S$, $W$, $M$, and $R$ indicate the starting, working, quantum measurement, and readout points for a typical camelback phase qubit experiment. (c) Width $\Delta\Phi = |\Phi_{80\%} - \Phi_{20\%}|$ of the $[0\Phi_0] \rightarrow [-1\Phi_0]$ ground-state escape, measurements (points + lines), and generalized MQT theory with (solid line) and without (dash-dotted line) 9 nA rms low-frequency current noise. The location of the dip near the maximum $\Delta\Phi$ (see inset) corresponds to the point where symmetry leads to a reduction in sensitivity to noise.

the $[0\Phi_0]$ and $[-1\Phi_0]$ flux states close to $\Phi_{\rm ext}/\Phi_0 = -0.5$. For $|I_b|$ less than about 0.5 $\mu$A, these two interior escape lines represent transitions between the two flux states, rather than transitions to the voltage state.

We illustrate our escape measurement method by describing a sequence used to measure $P_{\rm esc}$ at a point, noted $M$, near the left cusp of Fig. 2(b). The sequence starts at point $S$, with current bias $I_b$ and $\Phi_{\rm ext} = \Phi_{\rm dc}$. Here the system is initialized in the $[0\Phi_0]$ fluxoid state, if necessary with an adiabatic pulse on the fast flux line. A flux pulse $\delta\Phi$ is then applied via the fast line for a fixed nanosecond-scale duration, bringing the total externally applied flux $\Phi_{\rm ext} = \Phi_{\rm dc} + \delta\Phi$ to point $M$ close to the critical line. This has the effect of reducing the heights $\Delta U_{R,L}$ of the two potential barriers, greatly enhancing $P_{\rm esc}$, and the system may escape to the $[-1\Phi_0]$ fluxoid state. $\Phi_{\rm ext}$ drops back to $\Phi_{\rm dc}$ (point $S$), where both fluxoid states are stable. The fluxoid state is then read out via a slow ($\sim$10 $\mu$s) $I_b$ pulse which brings the system to point $R$ outside the critical line of fluxoid state $[-1\Phi_0]$ but well within that of $[0\Phi_0]$. If the system is in state $[-1\Phi_0]$, the SQUID will switch, producing a voltage which is detected [12]. If it is in state $[0\Phi_0]$, it will not switch. We achieve a one-shot discrimination between flux states of 100%. The process is completed by bringing $I_b$ to zero for 100 $\mu$s where retrapping occurs and heat generated by a switching event dissipates. Multiple repetitions, at a rate of 5 kHz, yield $P_{\rm esc}$ at point $M$. By varying points $S$, $M$, $R$, and the initial fluxoid state, we are able to measure $P_{\rm esc}$ for each of the two fluxoid states at any $(I_b, \Phi_{\rm ext})$ point in this region. For $|I_b| > 0.5$ $\mu$A, the system escapes directly to the voltage state at point $M$, rendering point $R$ unnecessary.

As shown by the fit in Fig. 2(b), our generalized MQT theory is accurately able to reproduce the data. Of the parameters that go into this theory, $b$ and $\alpha$ are treated as free parameters in this fit, $I_c$, $\eta$, and the $\Phi_{\rm dc}$ calibration are determined by the fit in Fig. 2(a), the fast flux pulse calibration is determined by matching $P_{\rm esc}(\Phi_{\rm ext})$ curves obtained with different values of $\Phi_{\rm dc}$, and $C$ is determined by a fit to spectroscopic data.

Along the escape line of a given fluxoid state, for $I_b$ above or below the value $I_b^{\rm cusp}$, the potential [Fig. 1(c)] is tilted to the right or to the left, and escape occurs preferentially in that direction. At $I_b^{\rm cusp}$, the camelback potential is symmetric around the minimum ($\sigma = 0$), the two potential barrier heights are equal, and escape occurs with equal probability in either direction. The cusps in Fig. 2(b) correspond therefore to a double-path escape.

The width of the escape process contains additional information about the dependence of the potential on the bias parameters, and on fluctuations in the bias parameters [13]. In Fig. 2(c), we plot the width as a function of $I_b$. This plot peaks around $I_b^{\rm cusp}$, except that at this point there is a sharp dip (see inset). This behavior is explained by double-path MQT if we include low-frequency current fluctuations. In this circuit thermal fluctuations are expected in $I_b$, which we estimate to be on the order of 10 nA rms by the equipartition theorem $\frac{1}{2}kT = \frac{1}{2}L_{\rm oc}I_{\rm RMS}^2$, where $k$ is Boltzmann's constant, $T \simeq 40$ mK is the circuit temperature, and $L_{\rm oc} = 10$ nH is the series isolating inductance. Because of this noise, $P_{\rm esc}(I_b, \Phi_{\rm ext})$ is convolved with the probability distribution of $I_b$, which we assume to be Gaussian with standard deviation $I_{\rm RMS}$. As shown in Fig. 2(c), $I_{\rm RMS} = 9$ nA is accurately able to explain both the increase in the overall width, and the presence of a distinctive dip at $I_b^{\rm cusp}$, a result of symmetry in escape direction. The presence of the dip and our ability to reproduce it with MQT theory is a striking confirmation of double-path escape and low-frequency $I_b$ fluctuations in our sample.

In Fig. 3 we investigate the operation of a phase qubit composed of the $|0\rangle$ and $|1\rangle$ levels of the anharmonic central well of the camelback potential. We use the same procedure as for the ground-state escape measurements, except $\delta\Phi$ is split into two steps. The first takes the system from point $S$ to $W$, where the qubit is manipulated by microwave (MW) pulses applied to the fast current line. The system is then taken to point $M$ for 5 ns, which projects the qubit state onto the flux state of the SQUID. This is possible because $P_{\rm esc}$ depends exponentially on the excitation level of the qubit. The flux coordinate of $M$ is tuned such that escape will occur with high probability if the qubit is excited, and low probability if it is not. This measurement step thus projects the quantum states $|0\rangle$ and $|1\rangle$ of the qubit onto the classical fluxoid states

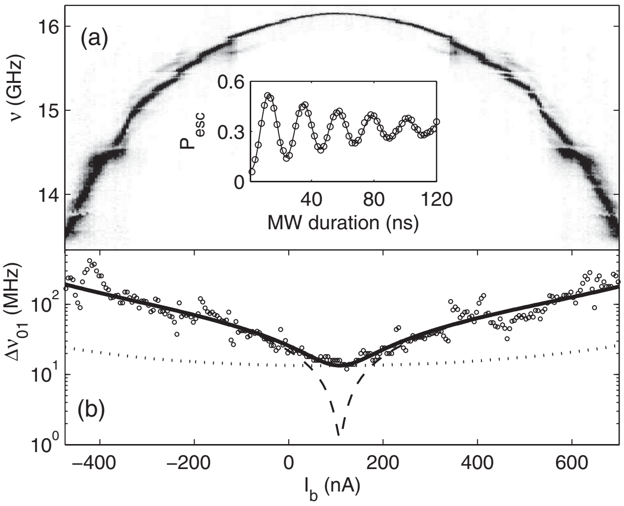

FIG. 3. Camelback phase qubit dynamics. (a) Spectroscopy $P_{\rm esc}(I_b, \nu)$ at $\Phi_{\rm ext} = -0.503\Phi_0$ in the $[0\Phi_0]$ fluxoid state. Dark and bright gray scale correspond to high and small $P_{\rm esc}$. $P_{\rm esc}$ is enhanced when $\nu$ matches $\nu_{01}$. Inset: Rabi oscillations on the optimal line. (b) Width of the $\nu_{01}$ resonance on a semilog scale. The dashed line is the predicted contribution due to 9 nA rms low-frequency current noise. The dotted line is for $40\mu\Phi_0$ rms low-frequency flux noise. The sum of these two contributions, the solid line, accurately reproduces the data (symbols).

$[0\Phi_0]$ and $[-1\Phi_0]$ of the SQUID, which are stable at point $S$. Readout of the fluxoid state at point $R$ reveals the projected qubit state. Repetition yields $P_{\rm esc}$, giving the probability of finding the qubit in its excited state, with a contrast of about 50%.

$P_{\rm esc}$ was measured as a function of $I_b$ and the frequency $\nu$ of a single 800 ns duration MW pulse applied to the qubit. Because the duration is much longer that the relaxation time $T_1 \simeq 100$ ns, the qubit reaches a steady state. $P_{\rm esc}$ is enhanced when $\nu$ matches the qubit transition frequency $\nu_{01}$ [Fig. 3(a)]. The maximum in $\nu_{01}$ occurs at $I_b^{\rm op}(\Phi_{\rm ext})$, which corresponds to the camelback potential symmetric point. Apparent in this spectroscopic image are avoided level crossings with what are likely microscopic two-level fluctuators, as first observed in Ref. [3]. We observe on average 20 crossings per GHz. In Fig. 3(b), the spectroscopic width $\Delta\nu_{01}$ of the $\nu_{01}$ transition, obtained from Fig. 3(a), is plotted as a function of $I_b$. A sharp minimum is observed at $I_b = 108$ nA, corresponding to the flat maximum in $\nu_{01}$.

We can accurately model $\Delta\nu_{01}(I_b)$ with a combination of low-frequency current and flux fluctuations. Because $\nu_{01}$ depends on the bias parameters, fluctuations cause $\nu_{01}$ to vary from repetition to repetition, smearing out the observed resonance. Assuming a Gaussian fluctuation distribution, the predicted variance in $\nu_{01}$ is $(\Delta\nu_I/2)^2 = (\partial_{I_b}\nu)^2 I_{\rm RMS}^2 + (\partial_{I_b}^2\nu)^2 I_{\rm RMS}^4/2$, for current fluctuations alone, and $(\Delta\nu_\Phi/2)^2 = (\partial_{\Phi_{\rm ext}}\nu)^2\Phi_{\rm RMS}^2$ for flux fluctuations alone. Here $\partial_x\nu \equiv \partial\nu_{01}/\partial x$. $\Delta\nu_I$ has been expanded to second order in $I_{\rm RMS}$ since $\partial_{I_b}\nu$ is zero at the optimal line. In Fig. 3(b), the predicted $\Delta\nu_I$ is plotted as a dashed line for $I_{\rm RMS} = 9$ nA, precisely the same value used in Fig. 2(c). The dotted line plots $\Delta\nu_\Phi$ for $\Phi_{\rm RMS} = 40\mu\Phi_0$. The solid line is the combined prediction $\Delta\nu = \sqrt{\Delta\nu_I^2 + \Delta\nu_\Phi^2}$. The dashed line is obscured behind the solid line except in a small region around the optimal current. This plot vividly demonstrates the idea of the optimal line: the effects of current bias fluctuations, which accurately account for the spectral width away from the optimal line, are rendered negligible on the optimal line. The residual width, about 15 MHz, can be explained by a flux noise of $40\mu\Phi_0$ rms.

Since the decoherence time $T_2$ scales inversely with $\Delta\nu_{01}$, $I_b^{\rm op}(\Phi_{\rm ext})$ is optimal for qubit operations. We measured Rabi oscillations on this line by varying the duration of a resonant MW excitation pulse, as shown in the inset to Fig. 3(a). We find a typical Rabi decay time of $T_{\rm Rabi} = 67$ ns for this sample. The anharmonicity is large enough and the applied power small enough that excitation beyond the first excited state is negligible, as we have verified by the linearity of Rabi frequency versus power. The system is confined to its lowest two levels and can therefore be considered a qubit.

In conclusion, we have studied the quantum dynamics of a novel quadratic-quartic camelback potential. Ground-state escape exhibits critical line cusps and a dip in the escape width versus bias current. We explain these two effects with a generalized double-path MQT escape theory. Because of symmetry, quantum dynamics are insensitive in first order to current fluctuations along an optimal line $I_b^{\rm op}(\Phi_{\rm ext})$. Along this line, the dc SQUID can be used as a phase qubit whose main decoherence source is residual flux noise. Future optimization and exploitation of the unique properties of this system will aid in the understanding of decoherence mechanisms in quantum circuits and has the potential to yield a competitive phase qubit.

This work was supported by two ACI programs, by the EuroSQIP and INTAS (Ref. No. 05-1000008-7923) projects.

[1] *Quantum Tunneling in Condensed Media*, edited by Yu. Kagan and A. J. Leggett, Modern Problems in Condensed Matter Sciences Vol. 34 (North-Holland, Amsterdam, 1992).
[2] J. M. Martinis *et al.*, Phys. Rev. Lett. **89**, 117901 (2002).
[3] K. B. Cooper *et al.*, Phys. Rev. Lett. **93**, 180401 (2004).
[4] J. Claudon *et al.*, Phys. Rev. Lett. **93**, 187003 (2004).
[5] J. Lisenfeld *et al.*, Phys. Rev. Lett. **99**, 170504 (2007).
[6] S. K. Dutta *et al.*, Phys. Rev. B **78**, 104510 (2008).
[7] I. Chiorescu *et al.*, Science **299**, 1869 (2003).
[8] C. D. Tesche and J. Clarke, J. Low Temp. Phys. **29**, 301 (1977).
[9] V. Lefevre-Seguin *et al.*, Phys. Rev. B **46**, 5507 (1992).
[10] C. G. Callan and S. Coleman, Phys. Rev. D **16**, 1762 (1977).
[11] R. Dolata *et al.*, J. Appl. Phys. **97**, 054501 (2005).
[12] The flux coordinate of point $R$, equal to $\Phi_{\rm dc}$, must be chosen to be close to the intersection of the $[-1\Phi_0]$ and $[0\Phi_0]$ critical lines, where the $[0\Phi_0]$ well is relatively shallow. This ensures that SQUID voltage switching can be achieved, as opposed to retrapping in the $[0\Phi_0]$ well.
[13] J. Claudon *et al.*, Phys. Rev. B **76**, 024508 (2007).
[14] A. Fay, Ph.D. thesis, Université Joseph Fourier, 2008.
[15] The MW excitation must be in *current*, rather than flux, because for the symmetric camelback potential, small amplitude oscillations occur mainly in the $x$ direction, and therefore are excited via the $-sx$ term in $U(x, y)$.

Quantum Inf Process (2009) 8:155–182
DOI 10.1007/s11128-009-0094-0

# Quantum dynamics of superconducting nano-circuits: phase qubit, charge qubit and rhombi chains

**O. Buisson · W. Guichard · F. W. J. Hekking ·
L. Lévy · B. Pannetier · R. Dolata · A. B. Zorin ·
N. Didier · A. Fay · E. Hoskinson · F. Lecocq ·
Z. H. Peng · I. M. Pop**

**Abstract** We have studied different quantum dynamics of superconducting nano-circuits with Josephson junctions. A dc SQUID, when it is strongly decoupled from the environment, demonstrates two-level and multilevel dynamics. We have realized a two qubits coupled circuit based on a dc SQUID in parallel with an asymmetric Cooper pair transistor (ACPT). The ACPT behaves as a charge qubit. Its asymmetry produces a strong tunable coupling with the dc SQUID which is used to realize entangled states between the two qubits and new read-out of the charge qubit based on adiabatic quantum transfer. We have measured the current–phase relations of different rhombi chains in the presence or absence of quantum fluctuations which confirm theoretical predictions.

**Keywords** Superconducting qubit device · Josephson quantum nano-circuits

**PACS** 03.67.Lx · 73.23.-b · 74.81.Fa · 85.25.Cp

---

O. Buisson (✉) · W. Guichard · L. Lévy · B. Pannetier · A. Fay ·
E. Hoskinson · F. Lecocq · Z. H. Peng · I. M. Pop
Institut Néel, C.N.R.S. and Université Joseph Fourier, BP 166,
38042 Grenoble Cedex 9, France
e-mail: olivier.buisson@grenoble.cnrs.fr

F. W. J. Hekking · N. Didier
LPMMC, C.N.R.S. and Université Joseph Fourier, BP 166,
38042 Grenoble Cedex 9, France

R. Dolata · A. B. Zorin
Physikalisch-Technische Bundesanstalt, Bundesallee 100,
38116 Braunschweig, Germany

## 1 Introduction

This review paper summarizes the results of a series of experiments on Josephson junction-based superconducting nanocircuits performed in Grenoble during the past six years. Our first experiments have mainly focused on the dynamics of a current-biased dc SQUID, in the limit where it behaves as a quantum mechanical anharmonic oscillator. We will discuss the quantum measurement procedure we have developed [2,3,7], and present results for the dynamics of the SQUID in the presence of coherent microwave (μw) field [6]. The number of quantum states involved in the dynamics depends on the μw amplitude and we will discuss the transition from quantum two-level behavior (phase qubit) at low amplitudes to classical multi-level behavior at larger amplitude [9]. We will also present results for a more complicated circuit in which a charge qubit is coupled to a phase qubit [15]. The charge qubit is realized by an asymmetric Cooper pair transistor (ACTP) which ensures a new optimal point where the coupling is very strong. The phase qubit is obtained by a SQUID in its two-level limit. We demonstrate tunability of the coupling over a large frequency range. Whenever appropriate, we will comment on various sources of decoherence [8,20].

Our more recent work [31] deals with Josephson junction (JJ) chains that are made out of rhombi with each rhombus containing four Josephson junctions. The rhombi are threaded by a magnetic flux. Arrays possessing this distinct topology have been discussed in the context of fault-tolerant quantum computation as they can produce quantum states that are relatively insensitive to local noise. Here we will focus on the ground-state properties of rhombi chains, presenting measurements of the current–phase relation at various flux frustrations. Our experimental findings concerning the periodicity and the amplitude of the current–phase relation reveal various features that are characteristic for the complex ground state of rhombi chains, in agreement with theoretical predictions.

This paper is organized as follows. In Sect. 2, we will discuss the results of the dc SQUID operating as a multilevel system and as a phase qubit. In Sect. 3, we will present the asymmetric Cooper pair transistor and will concentrate on the properties of a new optimal point. In Sect. 4, we will discuss the coupling between the ACPT and the dc SQUID. In Sect. 5, recent results on rhombi chains will be described. Section 6 will describe briefly the set-up used for the quantum experiments.

## 2 DC SQUID as a driven quantum anharmonic oscillator

The current-biased dc SQUID is a basic quantum circuit, the dynamics of which can be described in terms of the quantum anharmonic oscillator driven by an external monochromatic force. In the past years we have studied some properties of its quantum dynamics which reveals very rich and complex physics. These efforts were motivated by the need to be able to control and manipulate the quantum states either in its two-level limit as a phase qubit or in its multilevel limit. In the same period, a variety of phase qubits were realized using a single current-biased Josephson junction [40], rf-SQUID [34], large inductance rf-SQUID [27] and dc SQUID [13]. Below we will discuss different quantum properties of a dc SQUID: the two-dimensional effect of

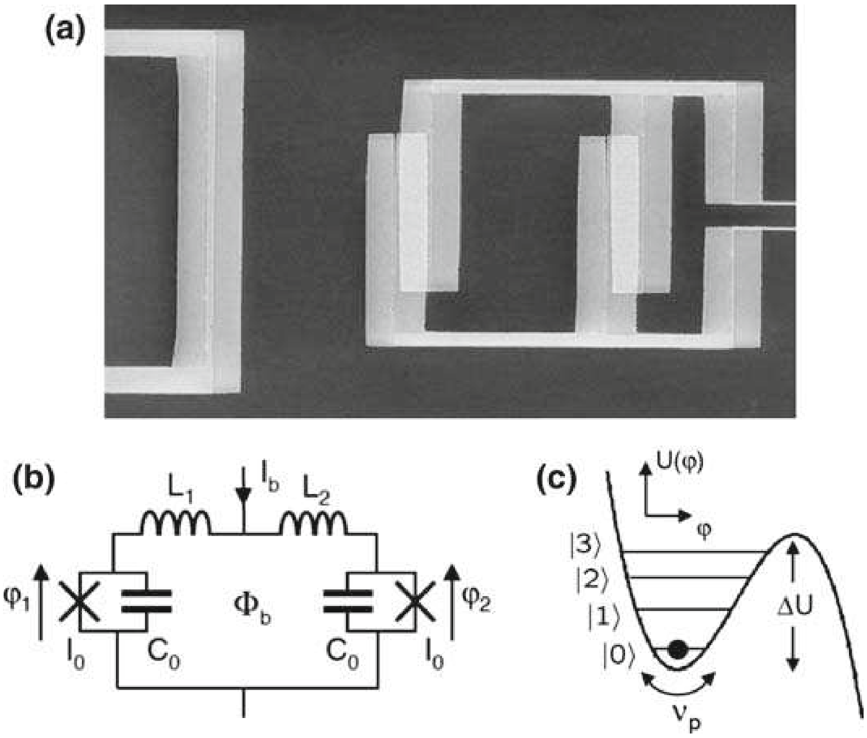

**Fig. 1** **a** SEM image of an aluminum dc SQUID with the μw control line at the left. **b** Electrical schematic of the dc SQUID. **c** The quantum states under study are oscillator states within the potential well

MQT escape [2], the quantum measurement procedure and its performance [3,7] and also the coherent oscillations in a multilevel system [6]. We will consider the decoherence processes in this quantum circuit [8] and mention recent results obtained at zero bias current where the half-flux-quantum biased SQUID behaves as a phase qubit [20].

## 2.1 Device and model

The dc SQUID (Fig. 1a) consists of two nominally identical Josephson junctions (JJ), each with a critical current $I_0$ and a capacitance $C_0$. The junctions are embedded in a superconducting loop of total inductance $L_s$ which is unequally distributed among the two arms. The inductance asymmetry is characterized by the parameter $\eta = (L_1 - L_2)/L_s$, where $L_1$ and $L_2$ are the inductance of the first and second arm, respectively. In our circuit, the Josephson energy $E_J = (\Phi_0/2\pi)I_0$ is more than three orders of magnitude larger than the Cooper pair Coulomb energy $E_c = (2e)^2/2C_0$ ($\Phi_0 = h/2e$ is the superconducting flux quantum). In this limit, the two superconducting phase differences $\varphi_1$ and $\varphi_2$ across the two Josephson junctions are the natural variables to describe the dynamics of the system.

The corresponding two-dimensional phase dynamics can be treated as that of a fictitious particle of mass $m = 2C_0(\Phi_0/2\pi)^2$ moving in a two-dimensional potential [24,36]

$$U(x, y) = 2E_J \left[ -\left(\frac{I_b}{2I_0}\right)(x + \eta y) - \cos x \cos y + b\left(y - \pi\frac{\Phi_b}{\Phi_0}\right)^2 \right], \qquad (1)$$

where $x = \frac{1}{2}(\varphi_1 + \varphi_2)$ and $y = \frac{1}{2}(\varphi_1 - \varphi_2)$. The shape of the potential, which contains valleys and mountains, is experimentally controlled through the bias current $I_b$ and the bias flux $\Phi_b$ threading the superconducting loop. Here, the inductance coupling parameter $b = \Phi_0/(2\pi L_s I_0)$ is of order unity. With the values of $I_b$ and $\Phi_b$ used in our experiments, the potential surface displays only one type of local minimum. They are separated from each other by saddle points, where the particle can escape [24]. Along the escape direction, which makes an angle $\theta$ with the $x$-axis, the potential is cubic and is completely characterized by the frequency $\nu_p$ at the bottom of the well and barrier height $\Delta U$ (Fig. 1c). These two quantities depend on the magnetic flux and vanish at the SQUID's critical current $I_c(\Phi_b)$. When small oscillations are considered, we assume complete separation of the variables along the escape direction and the transverse one by neglecting the coupling terms between these two directions. In this approximation, the phase dynamics of the SQUID along the escape direction is similar to that of a current-biased single Josephson junction. The parameters $\Delta U$ and $\nu_p$ are renormalized, thereby taking into account the two-dimensional nature of the potential.

For bias currents $I_b < I_c$, the particle is trapped in a local minimum and its quantum dynamics is described by the Hamiltonian

$$\hat{H}_0 = \frac{1}{2} h\nu_p \left[ \hat{P}^2 + \hat{X}^2 \right] - \sigma h\nu_p \hat{X}^3. \tag{2}$$

Here, $\hat{X} = (2\pi\sqrt{m\nu_p/h})\hat{\phi}$ represents the reduced phase operator, associated with the phase $\hat{\phi} = \cos\theta\hat{x} + \sin\theta\hat{y}$ along the escape direction. $\hat{P}$ is the reduced momentum conjugate to $\hat{X}$. The relative magnitude $\sigma$ of the cubic term compared to the harmonic term is related to the barrier height $\Delta U = h\nu_p/54\sigma^2$. For $I_b$ below $I_c$, several low-lying quantum states are found near the local minimum. These states, describing the oscillatory motion within the anharmonic potential, are denoted $|n\rangle$ for the $n$th level, with $n = 0, 1, 2, \ldots$ The corresponding energies $E_n$ were calculated in Refs. [22,23]. The transition frequency associated with the transition $n \to k$ is denoted $\nu_{nk}$ in the following.

A microwave flux pulse characterized by its frequency $\nu$ and amplitude $\Phi_{\mu w}$ can be used to manipulate the quantum state of the system. It induces a time-dependent perturbation term $-\hbar\Omega_1\sqrt{2}\cos(2\pi\nu t)\hat{X}$ in the Hamiltonian, which couples neighboring levels. In this expression, $\Omega_1$ is proportional to $\Phi_{\mu w}$ and corresponds to the frequency of the Rabi oscillation between $|0\rangle$ and $|1\rangle$ for an excitation tuned to $\nu_{01}$.

Since energy levels are trapped in a finite-height potential barrier, the states are metastable. Escape out of the potential well is possible both by tunneling and by thermal activation. For temperatures well below $T^* = h\nu_p/(2\pi k_B)$, the so-called cross-over temperature, the thermal process can be neglected [2,25]. On the timescale of the experiment, only the three highest energy levels, closest to the top of the barrier, undergo a significant tunneling effect. The lower energy levels are stable.

## 2.2 MQT in a dc SQUID

When $I_b$ is slightly lower than the critical current of the SQUID, we have measured the escape probability of the SQUID from the superconducting state to the resistive

**Fig. 2** Escape probability versus bias current at different temperatures for a SQUID at zero flux bias

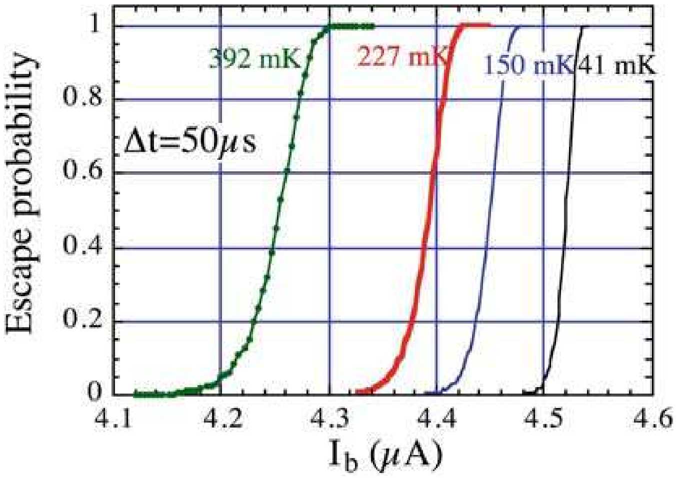

**Fig. 3** Measured critical current and width of the probability distribution versus flux at 40 mK (*dots*). *Solid lines* correspond to the fit using the 2D MQT prediction, *dashed line* to the usual 1D MQT model

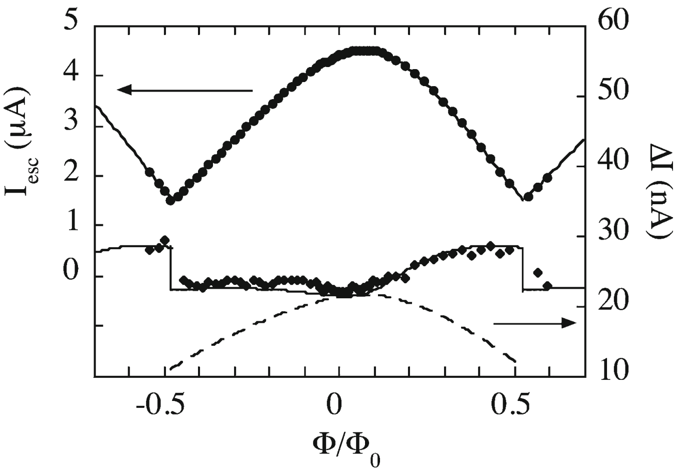

state as function of the current bias (Fig. 2), the magnetic flux and the temperature. This escape to the resistive state is described by the escape of the fictitious particle in the two-dimensional potential discussed above. At high temperature (above 90 mK), the thermal activated regime is observed. At low temperature, the escape current and the width of the probability distribution are temperature independent but they do vary with flux (Fig. 3). As seen from this figure, the experimental results do not fit the usual one-dimensional (1D) Macroscopic Quantum Tunneling (MQT) law but are perfectly accounted by using the two-dimensional (2D) model of Sect. 2.1.

## 2.3 Quantum measurement procedure

Our procedure to perform quantum experiments consists of the repetition of an elementary sequence, which is decomposed into four successive steps. First, the bias current $I_b$ through the SQUID is switched on at a fixed magnetic flux $\Phi_b$. The working point $(I_b, \Phi_b)$ defines the geometry of the potential well. The $I_b$ rise time is short enough to induce an adiabatic modification of the potential, leaving the circuit in its initial state $|0\rangle$. Then a microwave flux pulse is applied to manipulate the quantum state of the system. At the end of the μw pulse, a dc flux pulse of amplitude $\Phi_m$ is applied which brings the system to the measuring point $(I_b, \Phi_b + \Phi_m)$. This flux pulse adiabatically

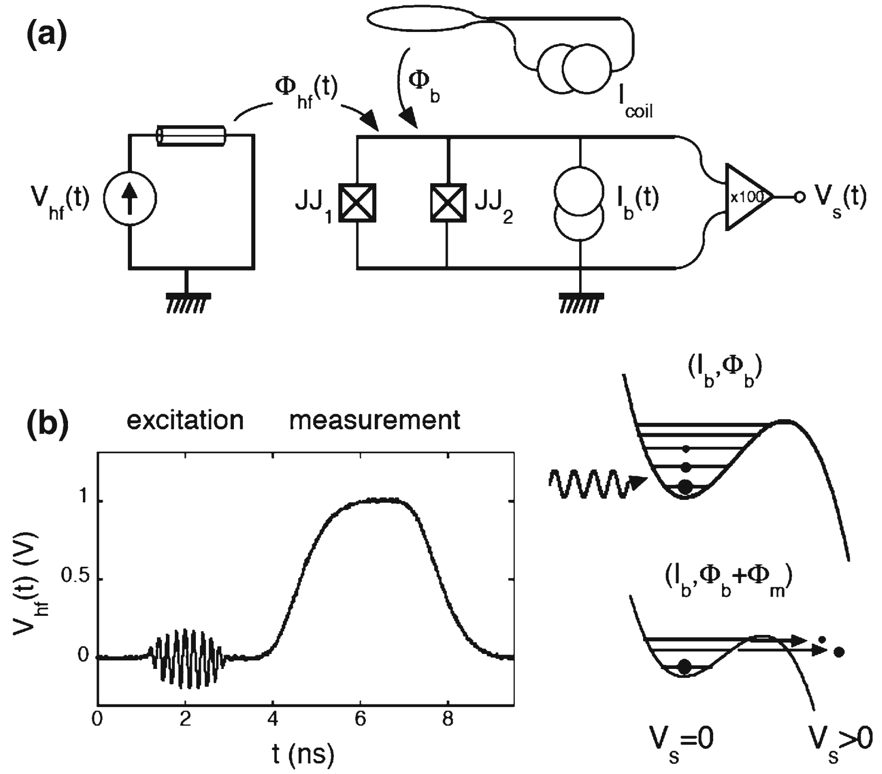

**Fig. 4** **a** Schematic of the electrical circuit. In our experiments, $I_b$ is first switched on through the SQUID at fixed magnetic flux $\Phi_b$, defining the shape of the potential well. A high frequency flux signal is then applied to the superconducting loop with a microwave antenna. **b** A digital sampling oscilloscope record of the signal is presented. It is composed of a microwave pulse which induces transitions between adjacent energy levels, followed by a measuring dc pulse which adiabatically reduces the barrier height and induces a selective tunneling escape of excited states. This escape is detected by a voltage $V_s$ across the circuit, amplified at room temperature. At the end of the sequence, $I_b$ is switched off and the circuit is reset to the superconducting ground state

reduces the barrier height and allows tunneling escape of the localized states to a finite voltage state during a time $\Delta t$ of the order of a few nanoseconds (Fig. 4). With precise adjustment of $\Phi_m$ it is theoretically possible to induce a selective escape of excited states. Because the SQUID is hysteretic, the zero and finite voltage states are stable and the result of the measurement can be read out by monitoring the voltage $V_s$ across the dc SQUID. Escape out of the well corresponds to the detection of a voltage which is twice the superconducting gap of the circuit material. The current bias $I_b$ must be switched off to reset the circuit in the ground state. This elementary sequence is repeated to extract with sufficient accuracy the occupancies of the excited states.

We have measured the escape probability of the ground state which is governed by standard MQT theory, with a small correction due to residual noise in the bias current (Fig. 5). In the two-level limit, where the SQUID constitutes a phase qubit, a contrast of 0.54 has been measured. It indicates a significant loss in contrast compared to the MQT prediction. This loss is attributed to spurious depolarization (loss of excited state occupancy) during the rise of the adiabatic flux measurement pulse. We have developed a simple phenomenological model [7] which introduces a relaxation time during the rise of the measurement pulse. This model explains both the measured contrast in the two level limit (Fig. 5) as well as the escape probability in the multilevel limit (Fig. 6).

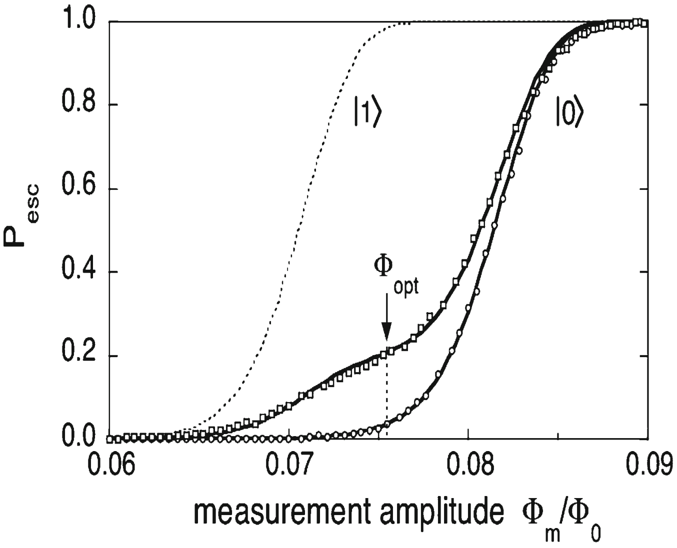

**Fig. 5** Probability of escape of the ground state $|0\rangle$ fitted by MQT theory assuming the presence of low frequency current noise (*continuous line*). Detection of level $|1\rangle$ partially populated with a $a_{\mu w} = 16.4\,\text{MHz}$ amplitude microwave pulse (*square symbol*). The *solid line* is a fit assuming a level $|1\rangle$ occupation probability of $p_1 = 18\%$. The experimental detection probability of the ground state (*circle*), and the calculated detection probability of $|1\rangle$ (*dashed line*) are also plotted

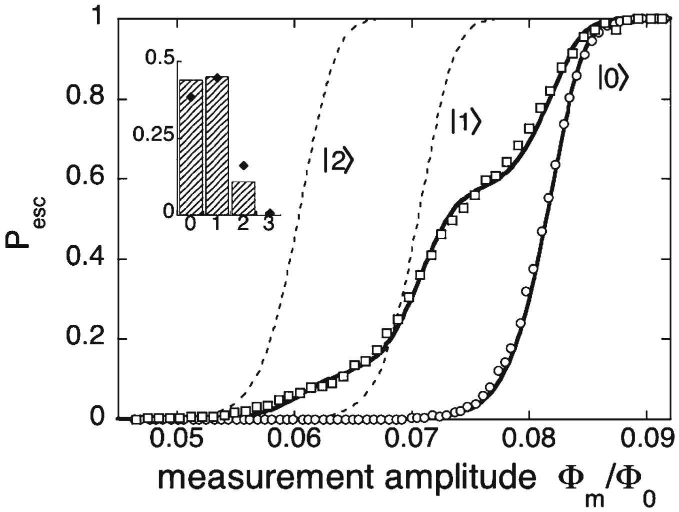

**Fig. 6** Detection of multilevel excited states populated by a Rabi pulse with duration $t_{\mu w} = 3.8\,\text{ns}$. The *solid line* is a theoretical adjustment of experimental data (*square*). For comparison, the experimental detection probability of $|0\rangle$ is plotted (*circle*). The calculated detection efficiencies of pure states $|0\rangle$ to $|2\rangle$ are also plotted as *dashed lines*. Inset: The *dashed bars* are the experimental populations extracted from the fit. The *diamonds* correspond to the calculated population distribution assuming relaxation during the flux ramping

## 2.4 Coherent oscillations in a multilevel quantum system

The transient nonlinear dynamics of the SQUID is probed using a fast µw flux pulse followed by a measuring dc pulse. The µw excitation is tuned to the resonance frequency obtained from low power spectroscopy and the µw pulse duration is increased from 2 to 80 ns. The measurement delay, as well as the other measurement pulse settings, remain unchanged. During the transient regime, Rabi-like oscillations (RLO) are observed, as shown in Fig. 7a. From a fit of the first oscillations to a damped sine function, the RLO frequency $\nu_R$ and the damping characteristic time $T_{2,Rabi}$ are extracted. The dependence of $\nu_R$ on the µw amplitude is plotted in Fig. 8.

The interpretation of the experimental data relies on a full quantum treatment taking into account multilevel processes. Since moderate decoherence has a minor impact on the Rabi-like frequency, we have developed a purely Hamiltonian theory [5,6]

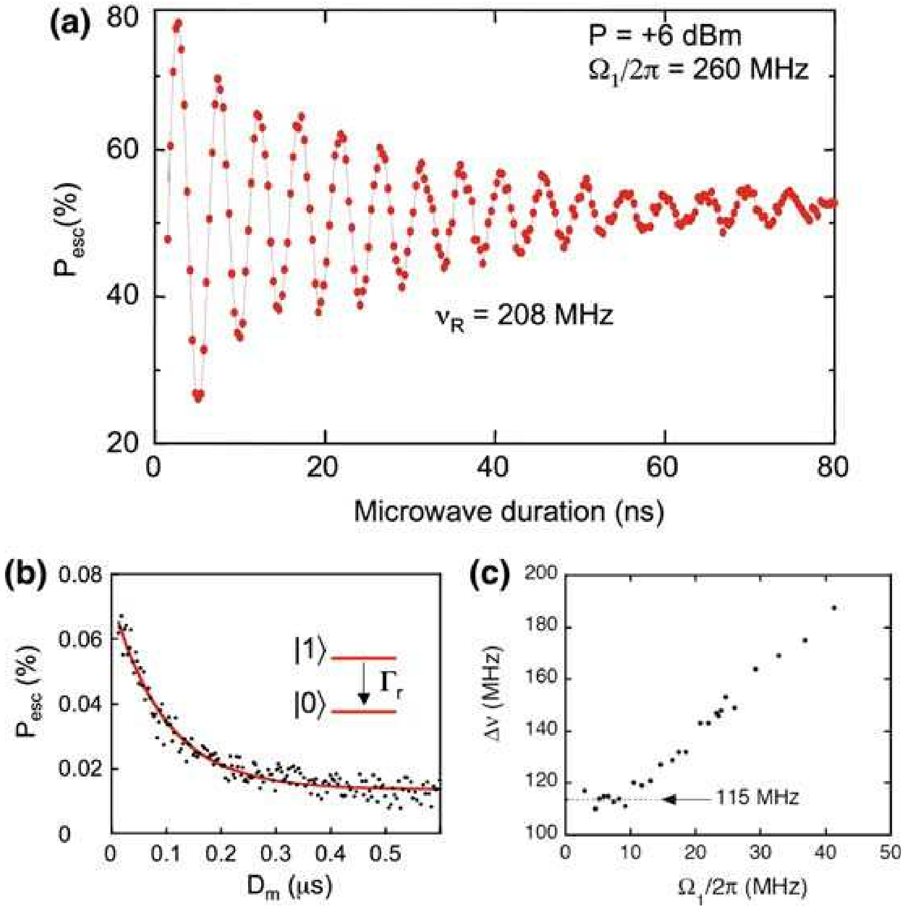

**Fig. 7** **a** Rabi-like oscillation observed in the transient regime for high power µw driving ($V_{\mu w} = 631$ mV). The oscillation frequency and the damping time $T_{2,Rabi}$ are extracted from a fit to an exponentially damped sine function. **b** Energy relaxation as a function of the measurement delay $T_m$, fitted to an exponential law with the damping time $T_1$. **c** Width of the resonance peak versus $\Omega_1$. The 115 MHz finite width will be strongly reduced by working at zero current bias (see next section)

**Fig. 8** Rabi like oscillation frequency versus microwave amplitude $\Omega_1$ (experimental data: points). *Dashed line* shows the linear dependence expected for a two-level system. *Continuous line* is the quantum prediction taking into account the multilevel process, *dotted line* the classical model [17]. The *vertical dotted line* indicates the anharmonicity strength: $\nu_{01} - \nu_{12}$

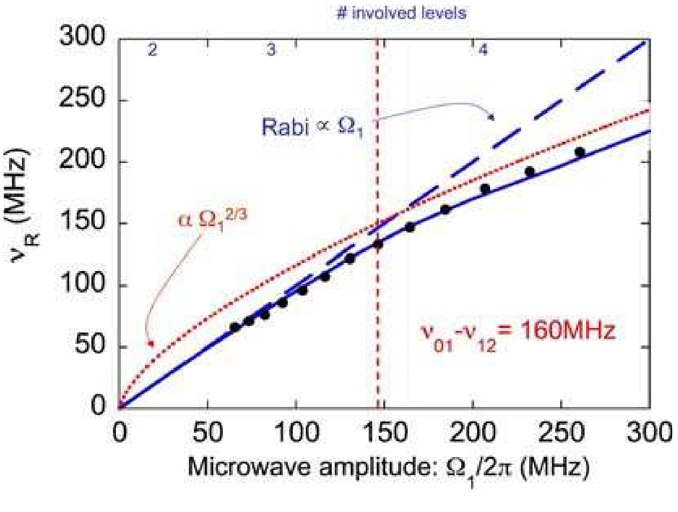

(see also Ref. [35]). The particle is assumed to be initially in the ground state. At $t = 0$, the µw flux is instantaneously switched on, and the particle's quantum state $|\Psi(t)\rangle$ evolves into a superposition of the eigenstates $|n\rangle$ according to the Schrödinger equation with the Hamiltonian:

$$\hat{H}(t) = \hat{H}_0 + \sqrt{2}\hbar\Omega_1 \cos(2\pi\nu t)\hat{X}. \tag{3}$$

The expression Eq. 3 contains all the characteristic frequencies of the problem: (i) the bottom well frequency $\nu_p$, (ii) the detuning $\delta = \nu_{01} - \nu_{12}$ linked to the potential anharmonicity and (iii) $\Omega_1$, the Rabi frequency in the two-level limit for a microwave excitation frequency $\nu = \nu_{01}$.

To solve this time-dependent problem, we introduce a new picture in which the evolution of the particle's state $|\Psi_{RO}(t)\rangle$ is driven by the Hamiltonian $\hat{H}_{RO}(t)$. This new picture is related to the Schrödinger one by:

$$\langle n|\Psi_{RO}(t)\rangle = e^{i2\pi n\nu t}\langle n|\Psi(t)\rangle. \tag{4}$$

In the two-level limit, this transformation corresponds to the introduction of the well-known rotating frame at frequency $\nu$. To proceed, we apply the rotating wave approximation (RWA) to simplify the Hamiltonian $\hat{H}_{RO}(t)$. Considering a potential well with $N$ trapped energy levels, the resulting Hamiltonian $\hat{H}_{RO,RWA}$ can be expressed in the $\{|n\rangle\}$ basis as follows:

$$\hat{H}_{RO,RWA} = h \begin{pmatrix} 0 & \frac{\nu_1}{2} & 0 & 0 \\ \frac{\nu_1}{2} & \Delta_1(\nu) & \ddots & 0 \\ 0 & \ddots & \ddots & \sqrt{N-1}\frac{\nu_1}{2} \\ 0 & 0 & \sqrt{N-1}\frac{\nu_1}{2} & \Delta_{N-1}(\nu) \end{pmatrix}. \tag{5}$$

Here, $\Delta_n(\nu) = \nu_{0n} - n\nu$ and the ground state energy $E_0$ has been set equal to 0. Starting from the initial state $|0\rangle$ which is the ground state in the absence of μw, the time evolution of this quantum state can be deduced using the eigenstates $|e_{nRO}\rangle$ of $\hat{H}_{RO,RWA}$. This model predicts coherent oscillations of the populations of the levels. Moreover the frequency versus μw amplitude dependence predicted by this quantum theory fits very well the experimental data (Fig. 8). Note that our experimental data cover the cross-over from two-level to multilevel dynamics. Indeed, when the μw amplitude is small compared to the anharmonicity ($\Omega_1 \ll \delta$), the dynamics only concerns the first two levels and one retrieves the familiar result $\nu_R = \Omega_1/2\pi$. This is nearly the case for the first measured point, which corresponds to $\Omega_1/2\pi = 65$ MHz and presents an occupation of level $|2\rangle$ below 10%. When $\Omega_1/2\pi \sim \delta$, the coupling between neighboring levels starts to distort the energy spectrum of the lowest energy levels of $\hat{H}_{RO,RWA}$. In this regime, the $\nu_R$ dependence on $\Omega_1$ starts to deviate from a linear behavior, indicating the onset of two-photon processes [13,35]. When $\Omega_1/2\pi > \delta$, an increasing number of levels is involved. As an example, the experimental oscillations presented in Fig. 7a involve four states. At larger μw amplitude, a large number of levels is involved. The multilevel dynamics is characterized by a clear saturation of the $\nu_R(t)$ dependence, compared to the low power linear behavior (Ref. [6]).

## 2.5 Decoherence processes

We describe here the experiments performed in the two-level limit involving the lowest energy states $|0\rangle$ and $|1\rangle$. In Fig. 7b we show the measured characteristic time for energy relaxation ($T_1 \approx 100\,\text{ns}$). We performed low power microwave spectroscopy for different bias current and flux. The dephasing times are extracted from the widths of the measured resonant peaks at low µw amplitude (Fig. 7c). The main source of decoherence of the current-biased dc SQUID are the thermal current fluctuations of the environment. Because of the large magnitude of the current noise $\left\langle \delta I_{noise}^2 \right\rangle^{1/2} = 6\,\text{nA}$, the dephasing time during the Rabi oscillations was short ($T_{2,Rabi} = 25\,\text{ns}$) and the spectroscopy width large (about 115 MHz). Recently this limitation was overcome by inducing the quantum dynamics at zero current bias. In this particular working point the SQUID is insensitive to current noise in first order. Some preliminary results are presented in the next section.

## 2.6 Two-level dynamics

To be able to perform quantum experiments at zero current bias where escape to voltage state is impossible, a new experimental procedure was implemented. In a small region close to half a flux quantum, two stable fluxoid states $[-1\Phi_0]$ and $[0\Phi_0]$ coexist.

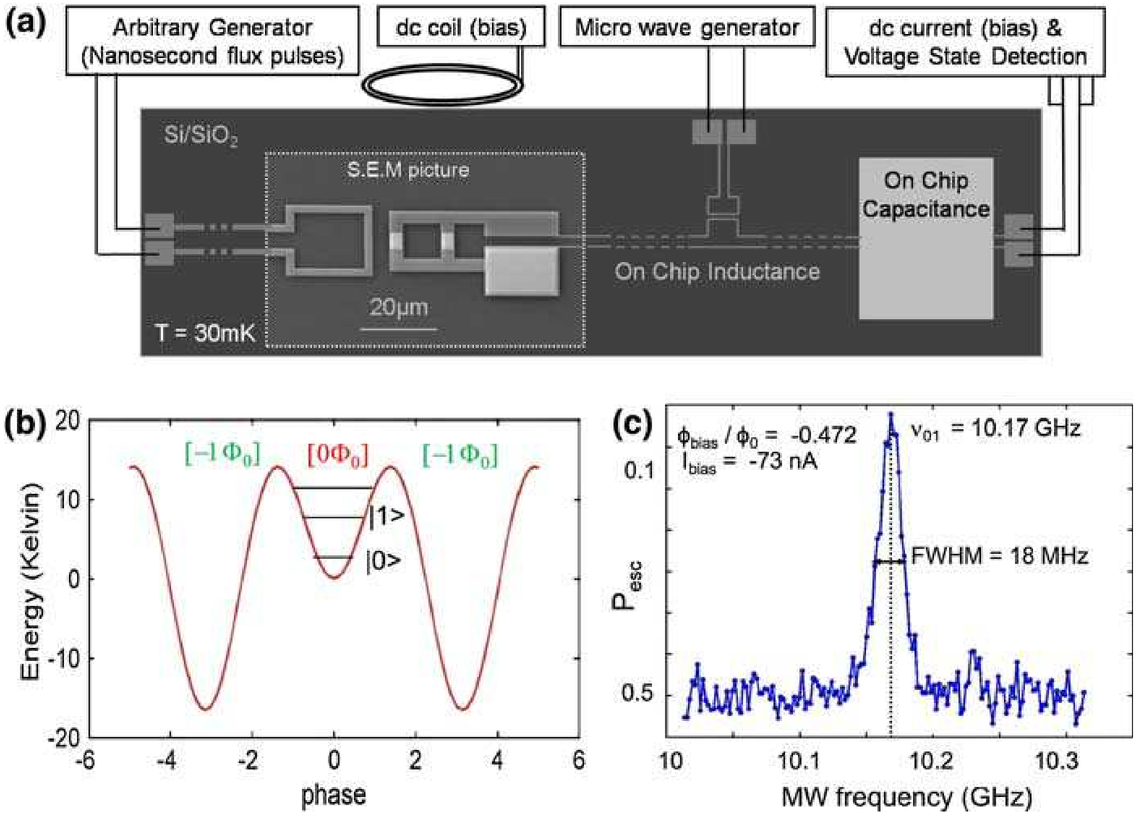

**Fig. 9** **a** Schematic circuit to study a Nb dc SQUID at the particular working point: zero-current bias and half a flux quantum bias. **b** New potential shape called "camel back potential". The phase qubit with states $|0\rangle$ and $|1\rangle$ is realized in the shallow central potential related to the flux quanta $[0\Phi_0]$. **c** Typical spectroscopy of the phase qubit along the optimal line

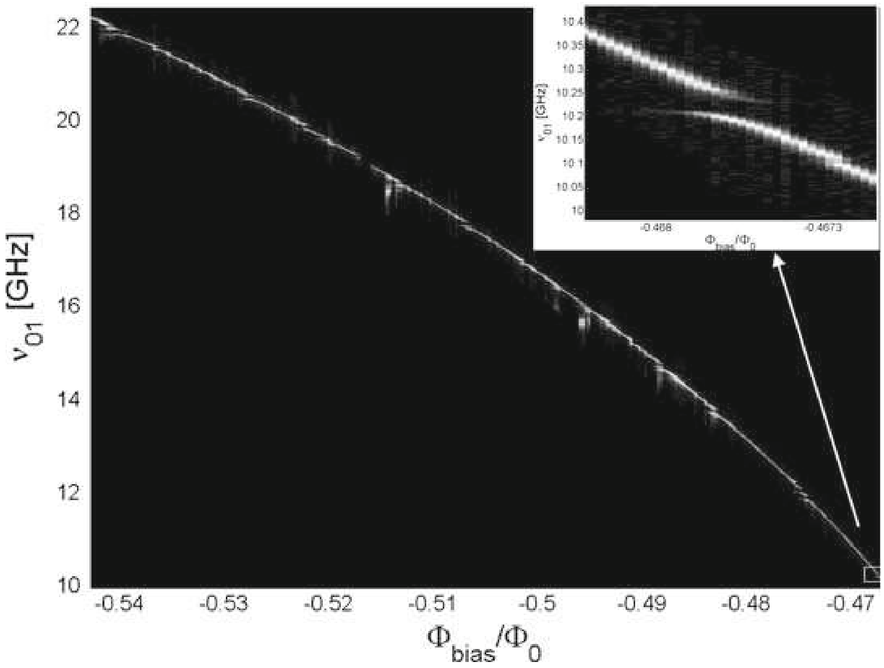

**Fig. 10** Probablity of escape versus $\Phi_b$ and μw frequency along the optimal line of the dc SQUID phase qubit. *Dark and bright regions* correspond to small and high $P_{esc}$. The density of fluctuators inside the circuit observed in this figure is about 50 MHz$^{-1}$. Inset: anticrossing of levels due coupling of the phase qubit and microscopic fluctuators

Along the escape direction, the potential presents two different wells related to the two different fluxoid state as indicated in Fig. 9b. In the central well related to the $[0\Phi_0]$ fluxoid states, the anharmonicity is quartic and the two low-lying oscillator states are used to realize a phase qubit. Our quantum measurement procedure is based on escape to the $[-1\Phi_0]$ fluxoid state. The sample used for this study was fabricated using a Nb/AlO$_x$/Nb trilayer process with SiO$_2$ insulating layer [11]. Along the zero-current bias line, the dephasing time is improved, as was demonstrated by spectroscopy measurements (Fig. 10), yielding a linewidth of about 15 MHz. Rabi and Ramsey oscillations were observed giving respectively $T_{2,Rabi} = 67$ ns and $T_{2,Ramsey} = 18$ ns. This finite dephasing time is explained by a rms 40μ$\Phi_0$ low frequency flux noise and by coupling with microscopic two-level fluctuators (as observed in Fig. 10 and also in Ref. [34]). The relaxation time $T_1$ is on the order of 100 ns.

## 3 Asymmetric Cooper pair transistor

A symmetric Cooper pair transistor in parallel with a classical switching Josephson junction [10,38] was extensively studied as a two-level system in the last years. Here we consider an asymmetric Cooper pair transistor (ACPT). This device (Fig. 11a), which is analyzed as a charge qubit [29], presents a new optimal point compared to the quantronium [10,38]. Its asymmetry also produces a strong coupling with a dc SQUID which will be used to realize entangled state and new read out based on adiabatic quantum transfer.

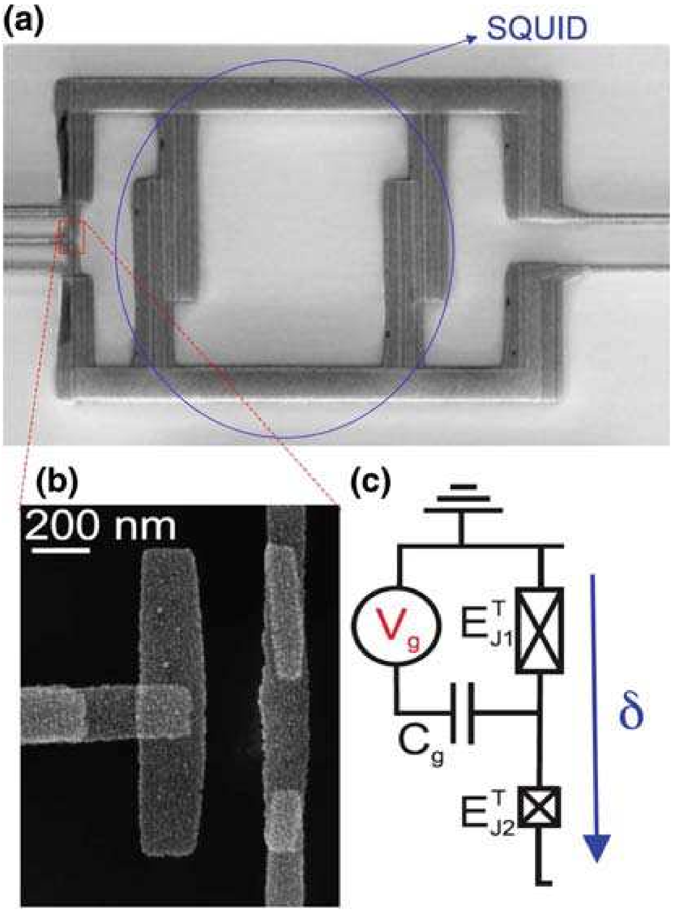

**Fig. 11** **a** SEM image of the coupled circuit. Central part: the SQUID; on the left: the transistor with gate-voltage. **b** SEM image of the ACPT circuit with the gate. The asymmetry is obtained using a different surface size of the two Josephson junctions. **c** Electric schematic of the ACPT which can be controlled by the gate voltage or the phase difference $\delta(I_b, \Phi_b)$

## 3.1 The device

The ACPT consists of a superconducting island connected by two Josephson junctions of different area (0.02 and 0.05 $\mu m^2$) to the superconducting electrodes (see Fig. 11b). The ACPT is connected in parallel to a dc SQUID. The dynamics related to the coupling between the transistor and the SQUID will be discussed in the next section. In the present section we will consider the ACPT alone. We will neglect the coupling between the ACPT and the SQUID which is valid when the two quantum circuits are far from the resonance condition.

## 3.2 Theory

In the charge representation, the Hamiltonian of the ACPT is given as a function of the control parameters $n_g \equiv C_g V_g / 2e$ (the gate-induced charge) and $\delta$ (the phase drop over the transistor) by:

$$\begin{aligned}\hat{H}_{ACPT} &= E_C^T (\hat{n} - n_g)^2 - \frac{\rho_j(\delta)}{2} \\ &\times \left[ \sum_n e^{-i(\delta/2+\chi)} |n\rangle\langle n+1| + \sum_n e^{i(\delta/2+\chi)} |n+1\rangle\langle n| \right] \qquad (6)\end{aligned}$$

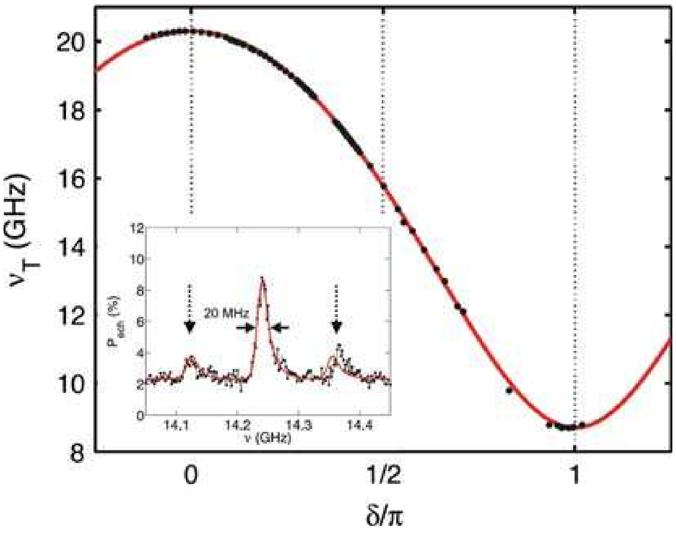

**Fig. 12** The measured ACPT energy (points) versus $\delta$ at $n_g = 0.5$ fitted by the ACPT Hamiltonian using four different charge states (*line*). In the inset, probability of escape versus μw frequency at $n_g$, $\delta$)=(1/2,0.47$\pi$) fitted by a model taking into account flux and charge noise with Gaussian distribution (*line*). The *dashed arrows* indicate the two sattelite peaks produced by the 115 MHz resonant environment mode

where $E_C^T = (2e)^2/2C_T$ is the transistor charging energy, $E_J^T \equiv E_{J2}^T + E_{J1}^T$ the total Josephson energy and $\mu \equiv (E_{J2}^T - E_{J1}^T)/E_J^T$ the Josephson energy asymmetry. Furthermore, $\tan\chi = \mu \tan(\delta/2)$ and $\rho_j(\delta)^2 = {E_J^T}^2(\cos^2(\delta/2) + \mu^2 \sin^2(\delta/2))$.

At $n_g = 0.5$, the degeneracy of the charge states $|0_{2e}\rangle$ and $|1_{2e}\rangle$ is lifted by the Josephson coupling. Then, the ACPT can be described as a two-level system (a charge qubit) characterized by the states $|-\rangle$ and $|+\rangle$ with an energy level splitting close to $\rho_j(\delta)$. In this two-level description, the Hamiltonian can be written in terms of the Pauli matrices,

$$\widehat{H}_{ACPT} = \frac{h\nu_T}{2}\hat{\sigma}_z^T, \tag{7}$$

where the energy $h\nu_T$ is defined as the energy difference between the states $|-\rangle$ and $|+\rangle$.

## 3.3 Energy spectrum

The excited level of the ACPT is detected using an adiabatic quantum transfer between the ACPT and the SQUID. This new read-out will be discussed in Sect. 4.4. The spectroscopy measurements are performed by a flux or a gate-voltage microwave pulse just followed by the quantum measurement nanosecond flux pulse. The energy spectrum versus the phase difference across the transistor is plotted in Fig. 12 at $n_g = 1/2$. The qubit resonant frequency $\nu_T$ versus $\delta$ can be fitted within 1% error by considering that the $|+\rangle$ and $|-\rangle$ states are superpositions of the four charge states ($|-1_{2e}\rangle$, $|0_{2e}\rangle$, $|1_{2e}\rangle$ and $|2_{2e}\rangle$). The ACPT has two optimal working points for qubit manipulations: one at ($n_g$, $\delta$)=(1/2,0) [10,38] and an additional one at ($n_g$, $\delta$)=(1/2,$\pi$) due to the transistor asymmetry.

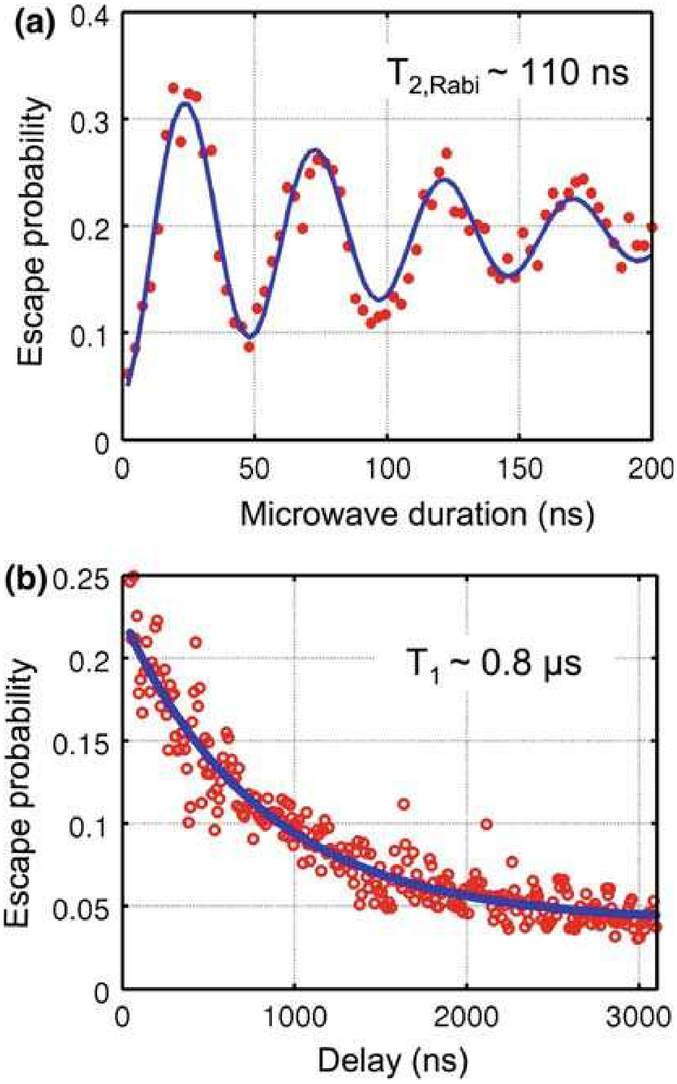

**Fig. 13** **a** Escape probability versus µw pulse duration for −3 dB m room temperature µw power. **b** Escape probability versus delay time between µw and measurement pulses, fitted by an exponential decay (*continuous line*) giving $T_1 = 810\,\mathrm{ns}$

### 3.4 Decoherence times

In the inset of Fig. 12, we show a typical resonance peak. The width of the resonance peak far from the optimal points is around 20 MHz but on the both sides small resonant peaks emerge. They are separated by 115 MHz from the central peak. Such spectroscopy features can be explained by thermal current noise related to a resonant environment mode observed at 115 MHz [8,14]. At the new optimal points $\delta = \pi$, the two satellite peaks disappear and the width of the central peak remains about 20 MHz. The finite width at this second optimal point can be explained by second order effects associated with charge noise. Indeed the second order charge noise sensitivity in this ACPT is large $(\partial^2\nu_T/\partial^2 n_g) = 329\,\mathrm{GHz/h}$. This sensitivity can be strongly reduced by increasing the $E_J^T/E_C^T$ ratio.

Figure 13a presents Rabi oscillations in the ACPT at the new optimal point $(n_g, \delta)$= $(1/2,\pi)$. The Rabi frequency follows a linear dependance on the µw amplitude as expected for a two-level quantum system. The observed relaxation time is rather long: about 800 ns (Fig. 13b).

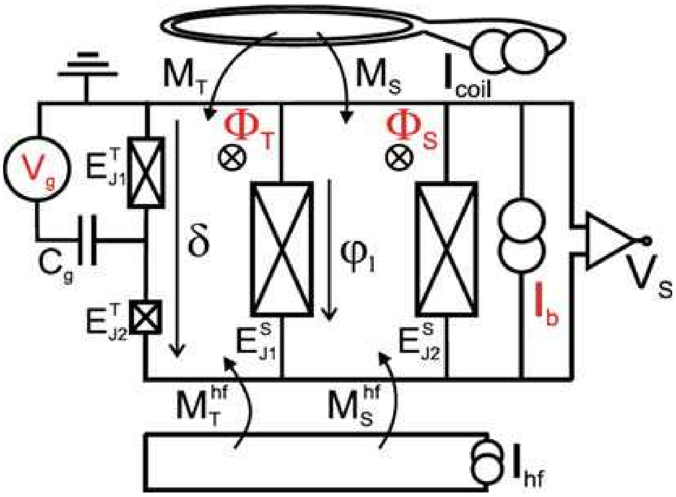

**Fig. 14** Electrical schematic of the coupled circuit. The working point is controlled by the dc gate-voltage $V_g$, the bias current $I_b$ and the fluxes $\Phi_T$ and $\Phi_S$. The current $I_{coil}$ and $I_{hf}$ produce a flux through the loops containing the SQUID and transistor via the mutual inductances $M_S$, $M_T$ and $M_S^{hf}$, $M_T^{hf}$. The high-frequency (hf) line is also used to produce µw and nanosecond flux pulses for the escape measurement of the SQUID

## 4 Coupled circuit

In this section we will study a quantum circuit coupling the charge qubit (ACPT) and the phase qubit (current-biased dc SQUID) whose schematic electrical circuit is shown in Fig. 14. This experimental work was motivated by a previous theoretical study considering a two-level system coupled to a quantum resonator [3,4,18]. This coupled circuit can be also presented as an alternative device of a qubit coupled to a cavity resonator [39]. In our device, the dc SQUID plays the role of an anharmonic microcavity which is highly tunable.

These new results present, to the best of our knowledge for the first time, the coupling between two different kinds of qubits and clearly show the entangled states between these two circuits. Moreover the coupling strength is tunable over a large scale, between 60 and 1200 MHz which can be compared to results obtained between two flux qubits [19,30]. In the following the two charge qubit states are denoted $|+\rangle$ and $|-\rangle$ and the two phase qubit states $|0\rangle$ and $|1\rangle$. The working points are controlled by the gate-voltage, the bias current and the dc flux. The qubits are excited either by µw gate-voltage or flux.

### 4.1 Hamiltonian of the coupled circuit

Here we will focus on the low-energy properties of the coupled circuit in the case when both qubits are close to resonance. It then suffices to consider the lowest two excited levels of the SQUID and the ACPT. When the coupling effect can be neglected, they are described by the respective two-level Hamiltonians $H_S = h\nu_S\sigma_S^z$ and $H_T = h\nu_T\sigma_T^z$ where $\sigma$ denotes a Pauli matrix. When determining the theoretical coupling Hamiltonian, we consider that the ACPT states $|-\rangle$ and $|+\rangle$ are superpositions of two charge states only; moreover we neglect anharmonicity effects of the SQUID potential on the frequency $\nu_S$. We then obtain the following Jaynes–Cummings type Hamiltonian for the coupling at $n_g = 1/2$:

$$H_{coupling} = \frac{1}{2} hg \left( \sigma_S^+ \sigma_T^- + \sigma_S^- \sigma_T^+ \right), \tag{8}$$

where the coupling strength $g = \left( E_{c,c}/2 - E_{c,j} \cos(\delta/2 - \chi) \right) / h$ and $\sigma_{S/T}^{+/-}$ creates or annihilates an excitation in the SQUID or the ACPT. The strength $g$ is due to a simultaneous capacitive coupling $E_{c,c} = (1 - \lambda)\sqrt{E_C^S / h\nu_p h\nu_p}$ and a $\delta$-dependent Josephson coupling $E_{c,j} = (1 - \mu)\sqrt{E_C^S / h\nu_p E_j^T} / 2$. Here $E_C^S = e^2 / C^S$ is the charging energy of the SQUID and $\lambda = (C_1^T - C_2^T)/(C_1^T + C_2^T)$ the transistor capacitance asymmetry.

## 4.2 Coupling strength

When the two qubits are in resonance, $\nu_T = \nu_S$, the states $|0, +\rangle$ and $|1, -\rangle$ are degenerate in the absence of coupling. In Fig. 15, the energy spectrum of the two qubits is plotted versus bias flux. Far from the resonance condition the value can be well estimated assuming two uncoupled qubits. In the vicinity of the resonance condition, an anti-level crossing occurs modifying the resonance frequency of each qubit. Anti-level crossing is clearly observed with a splitting which depends on the working points. When the resonance condition is satisfied, the quantum states are maximally entangled

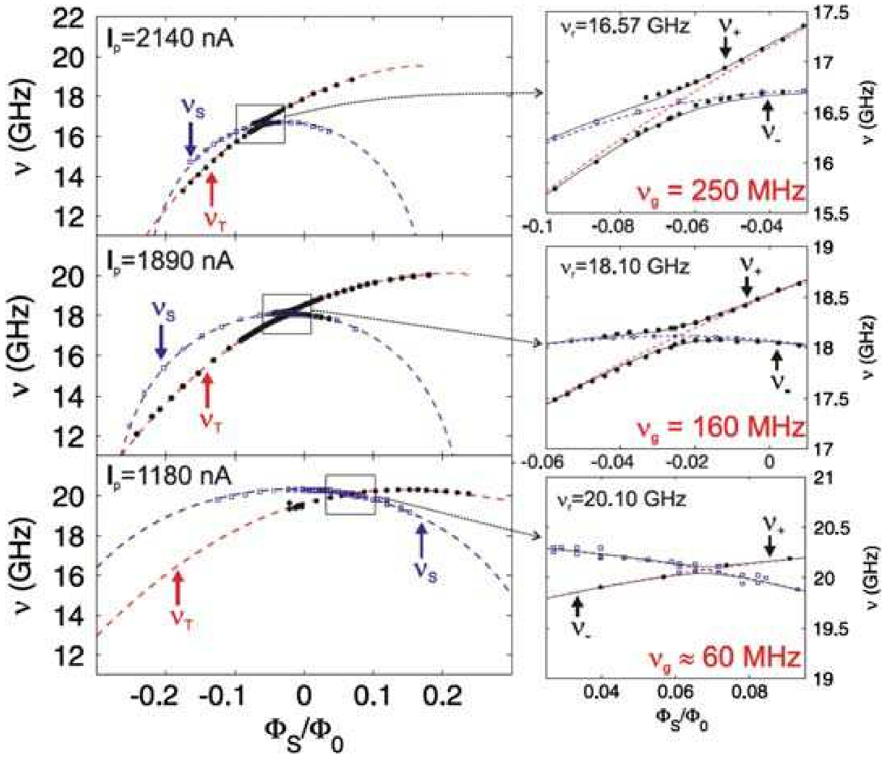

**Fig. 15** Spectroscopy of the coupled circuit versus flux for three different bias currents at $n_g = 1/2$ (*filled points*) and $n_g = 1$ (*empty points*). The *dashed lines* correspond to $\nu_T$ and $\nu_S$ obtained by the uncoupled theory. The *continuous line* is the fit taking into account a coupling strength

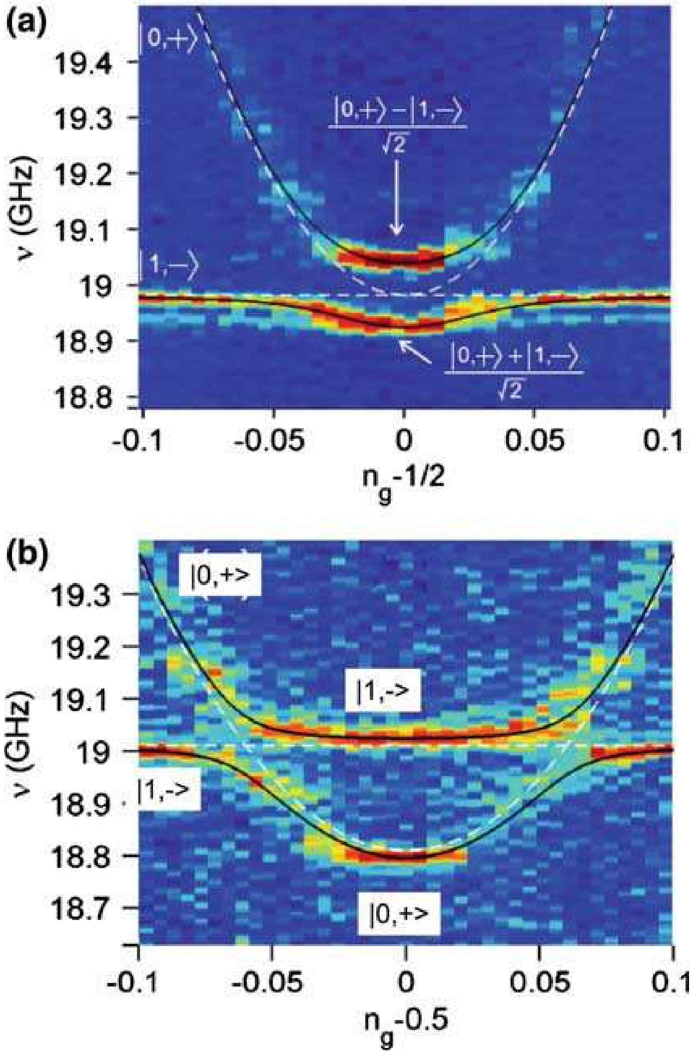

**Fig. 16** **a** $P_{esc}$ versus $n_g$ and μw frequency at the working point $I_b = 1647\,\text{nA}$, $\Phi_S = 0.03\ \Phi_0$ and $\delta = 0.26\pi$. **b** $P_{esc}$ versus $n_g$ and μw frequency at the working point $I_b = 1647\,\text{nA}$, $\Phi_S = 0.02\ \Phi_0$ and $\delta = 0.28\pi$. *Dark color* corresponds to small. *Dashed and continuous lines* correspond to uncoupled and coupled cases, respectively

$(|0,+\rangle \pm |1,-\rangle)/\sqrt{2}$. We also observed anti-crossing phenomena when we measured the escape probability versus $n_g$. At $n_g = 1/2$ we observe either the resonant regime (Fig. 16a) or the dispersive regime (Fig. 16b).

## 4.3 Tunable coupling

The qubit-qubit coupling strength is measured at $n_g = 1/2$ for working points where the resonance condition $\nu_T = \nu_S$ is satisfied. The frequency splitting is plotted versus the resonant frequency in Fig. 17. The coupling is minimal at $\nu_T = 20.3\,\text{GHz}$ and strongly increases with decreasing resonant frequency up to a maximum value of 1.2 GHz. Note that when the resonance frequency changes from 20.3 down to 8.8 GHz the absolute value of the phase over the ACPT changes from $\delta = 0$ to $|\delta| = \pi$. We find therefore nearly zero coupling at $\delta = 0$ and a very strong coupling of 1.2 GHz at $|\delta| = \pi$.

By taking the asymmetry parameters deduced from the ACPT energy spectrum fit ($\mu = \lambda = 41.9\%$) the coupling strength can be very well fitted without any free

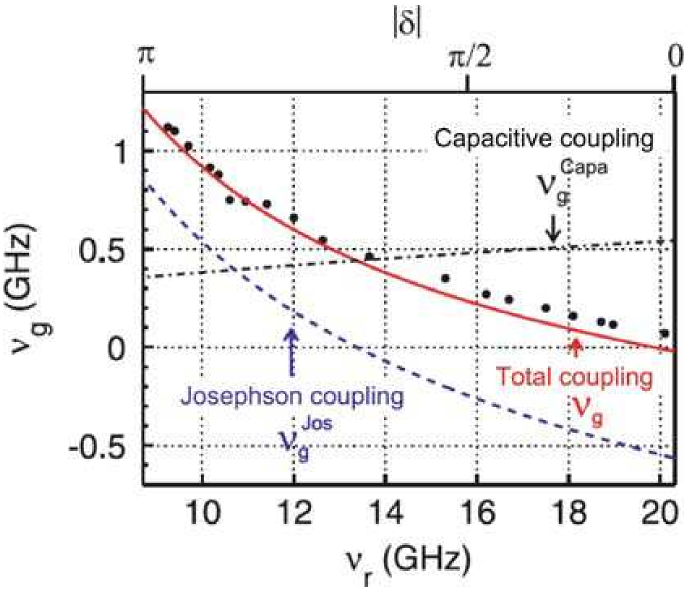

**Fig. 17** Experimental coupling strength versus frequency at the resonance condition between the two qubits for $n_g = 1/2$ (*points*). The two *dashed lines* correspond to the theoretical coupling strength due to capacitive and Josephson coupling; the *continuous line* is the total coupling without free parameters

parameters as can be seen in Fig. 17. The capacitance and the Josephson coupling are also plotted showing a very weak $\delta$-dependence on the capacitance coupling and a strong one on the Josephson coupling.

We stress that the coupling strength at $n_g = 1/2$ depends only on the $\delta$ parameter. If we replace one of the transistor junctions by a pure capacitance ($E^T_{J,2} = 0$) we obtain $E_{c,j} = 0$ and we retrieve the capacitive coupling calculated for a Cooper pair box coupled to a quantum resonator [4] or a SQUID [18]. For a *symmetric* transistor ($\lambda = \mu = 0$) the charge and the Josephson coupling compensate each other, giving zero coupling for any value of the parameter $\delta$. It is the asymmetry of the transistor which enables nonzero coupling at the optimum point of the charge qubit. In particular, for the case that $\lambda = \mu$—which is realized for a transistor containing two junctions having the same plasma frequency—the total coupling vanishes at $\delta = 0$ but becomes non zero at the second optimum point at $\delta = \pi$. This enables to manipulate the ACPT at zero coupling, and exchange information with the SQUID at nonzero coupling, both at minimum decoherence.

## 4.4 Adiabatic quantum transfer

The coupling at the resonance between the charge qubit and the SQUID can explain the quantum measurement process on the ACPT. Indeed the energy levels of the ACPT can be determined by escape probability measurements on the SQUID via a new read-out based on adiabatic quantum transfer. We apply a μw signal of 1 μs on the gate line at fixed frequency when the ACPT and the SQUID are off resonance. If the applied μw frequency matches the ACPT frequency the $|+\rangle$ level is populated. For the measurement a nanosecond flux pulse with a rise time of 2 ns drives the two systems adiabatically across the resonance where the coupling is about 1 GHz. The initial state $|+, 0\rangle$ is thereby transferred into the state $|-, 1\rangle$ [3]. Afterwards an

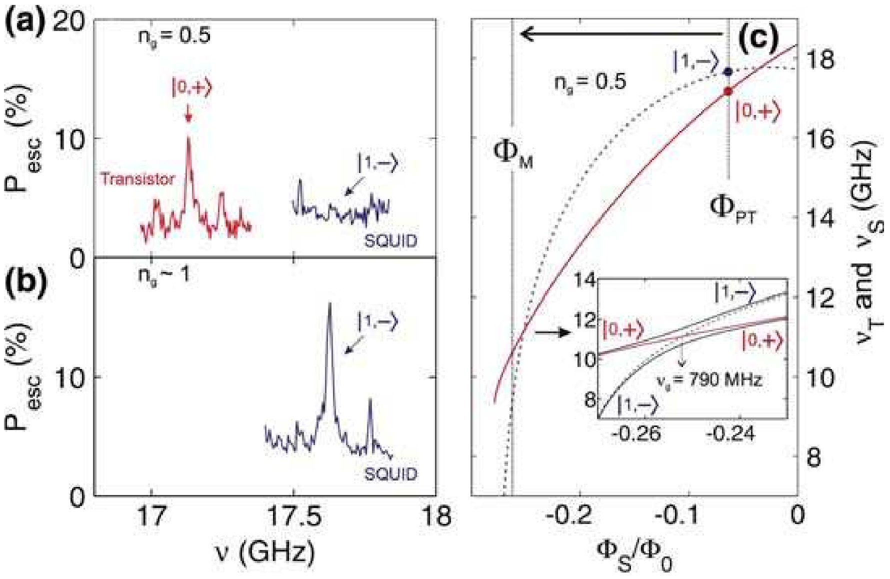

**Fig. 18** Quantum measurements at ($I_b = 1957\,\mathrm{nA}$, $\Phi_b = -0.064\Phi_0$). **a** Escape probability versus frequency at n$_g$=1/2 shows resonance peak of the transistor and no peak for the SQUID. **b** Escape probability versus frequency at n$_g \approx 1$ shows resonance peak of the SQUID. These measurements were obtained with a large negative flux nanosecond pulse $\Phi_{pulse} = -0.265\Phi_0$ indicated by the *long arrow* in (**c**). **c** Energy level evolution during the flux pulse at n$_g$=1/2. The two *vertical dotted lines* indicate the flux value at the working point $\Phi_{PT}$ and at the escape point $\Phi_M$. The inset shows details of the crossing point. The *crossing dashed and continuous lines* correspond to the uncoupled energy levels of the SQUID and ACPT and the *anti-crossing lines* correspond to the energy when coupling is taken into account

escape measurement is performed on the SQUID, revealing its quantum state (inset of Fig. 18c).

## 5 Josephson junction chains

In this section, we will summarize measurements performed on phase-biased Josephson junction chains composed of elementary cells consisting of one rhombus (for details see [31]). Each rhombus contains four Josephson junctions, and can be threaded by a magnetic flux. Such chains have been studied theoretically in the context of fault-tolerant quantum computation [12,16,21,32,33,37]. Indeed, their distinct topology gives rise to specific symmetries leading to the appearance of quantum states that are protected against local perturbations.

We will focus on the ground-state properties of rhombi chains in the classical and quantum regime. The ground-state energy $E_0(\gamma)$ of the chain, as a function of the bias phase $\gamma$, can be determined by the measurement of the chain's current–phase relation $I(\gamma)$: the supercurrent is given by the derivative of $E_0(\gamma)$ as a function of $\gamma$.

The magnetic flux threading the rhombus loop leads to the occurrence of interference phenomena specific for the rhombus geometry. At full flux frustration, for instance, destructive interference is predicted to lead to a suppression of the $2e$ supercurrent in favor of the appearance of a $4e$ supercurrent, carried by correlated Cooper pairs [32].

Below we will present measurements of the current–phase relation at various flux frustrations, focussing on the periodicity and the amplitude of the supercurrent oscillations. Close to full flux frustration, the period changes from $2\pi$ to $\pi$. The oscillation amplitude decreases when the charging energy of the junctions is increased, due to quantum fluctuations.

## 5.1 Measurement set-up

In order to measure the current–phase relation of a rhombi chain, we implemented an escape measurement using a large JJ which is connected in parallel to the chain (Fig. 19). The critical current of this JJ ($I_{cL} \approx 1-2\,\mu$A) is much larger than that of the chain ($I_c \approx 1-100\,$nA). Therefore, near the switching event of the whole device the phase difference over the large JJ is close to $\pi/2$ independent of the magnetic flux $\Phi_c$ within the large loop containing the chain and the JJ. As a consequence the flux $\Phi_c$ controls directly the phase-difference $\gamma$ over the chain and the measurement of the $\gamma$

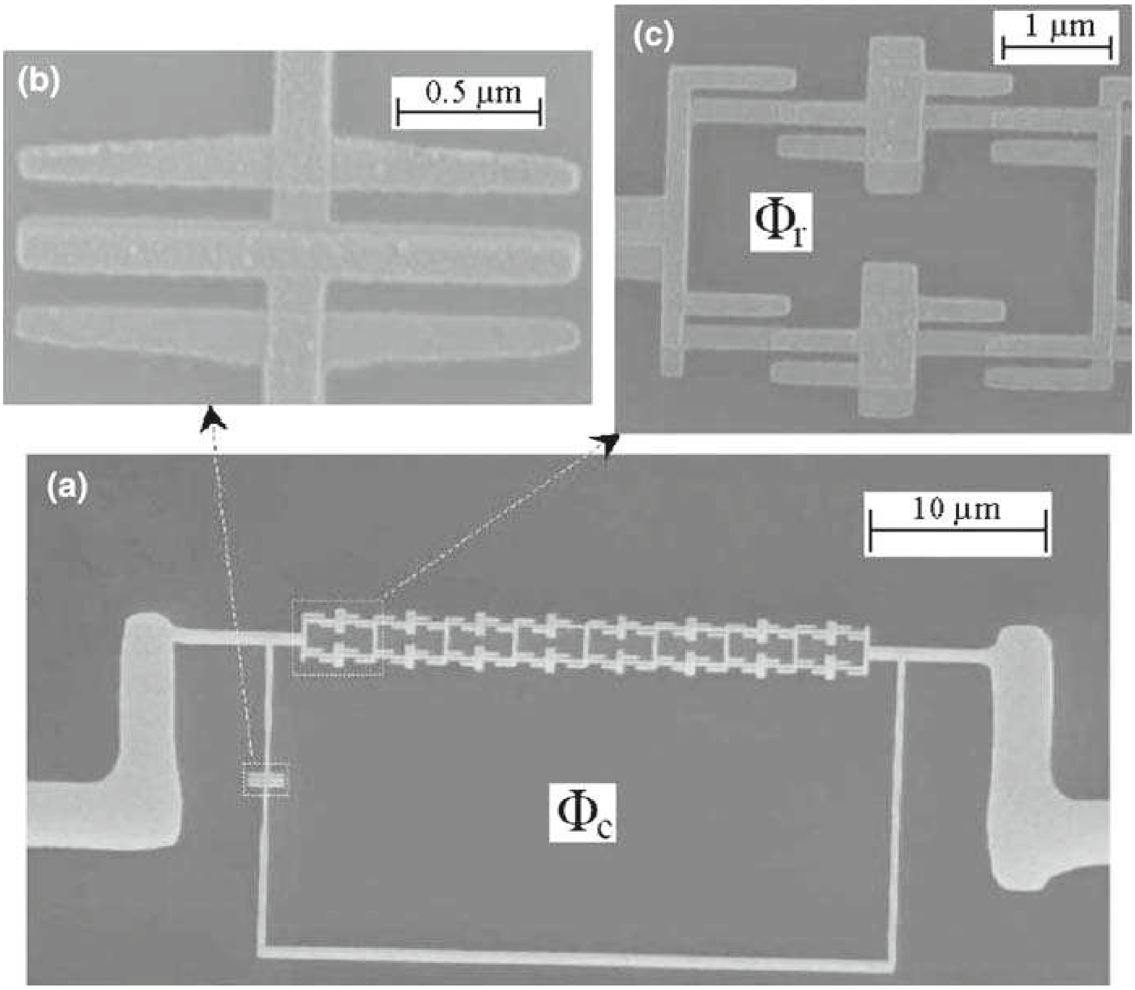

**Fig. 19** **a** SEM image of a rhombi chain ($N = 8$, sample C) in the closed superconducting circuit. The shunt junction is visible on the left *vertical line*; **b** an enlarged image of this JJ. **c** An enlarged image of one rhombi is also presented. For small magnetic field variations, the flux inside the rhombi practically remains constant, while the total phase on the array varies

dependence of the switching current of the shunted rhombi chain yields the current–phase relation of the rhombi chain. The flux frustration $f$ of the chain is controlled by the flux $\Phi_R$ through the small loop formed by each rhombus. The area of the large loop is about hundred times larger than the one of a single rhombus, which enables us to tune the frustration $f$ of the rhombus independently of the phase-difference $\gamma$ over the chain.

## 5.2 Classical chains

We first discuss the ground-state properties of a chain with $E_J/E_c \approx 20$ (sample A) when quantum fluctuations can be neglected. Such chains are called hereafter classical chains. The measured current–phase relation is plotted in Fig. 20a and b for two different frustration parameters $f = 0$ and $f = 0.5$. In both cases they follow a sawtooth dependence as expected, since in the classical regime $E_0(\gamma)$ is a series of shifted parabolas as a function of $\gamma$ (see Fig. 21a, d). Interestingly, the period of the supercurrent oscillations as a function of the phase difference changes abruptly from $2\pi$ to $\pi$ as the rhombi are tuned to the vicinity of full frustration. This double periodicity can be explained by the existence of two different persistent current configuration states (circulating clockwise and counterclockwise) in each rhombus for frustration close to 1/2. For convenience we associate a pseudospin up (down) to each rhombus carrying a clockwise (counterclockwise) circular supercurrent.

Away from full flux frustration, these two spin states have very different energy. The configuration yielding the lowest energy of the chain therefore corresponds to a fully spin polarized spin chain, regardless of the phase difference $\gamma$ (see

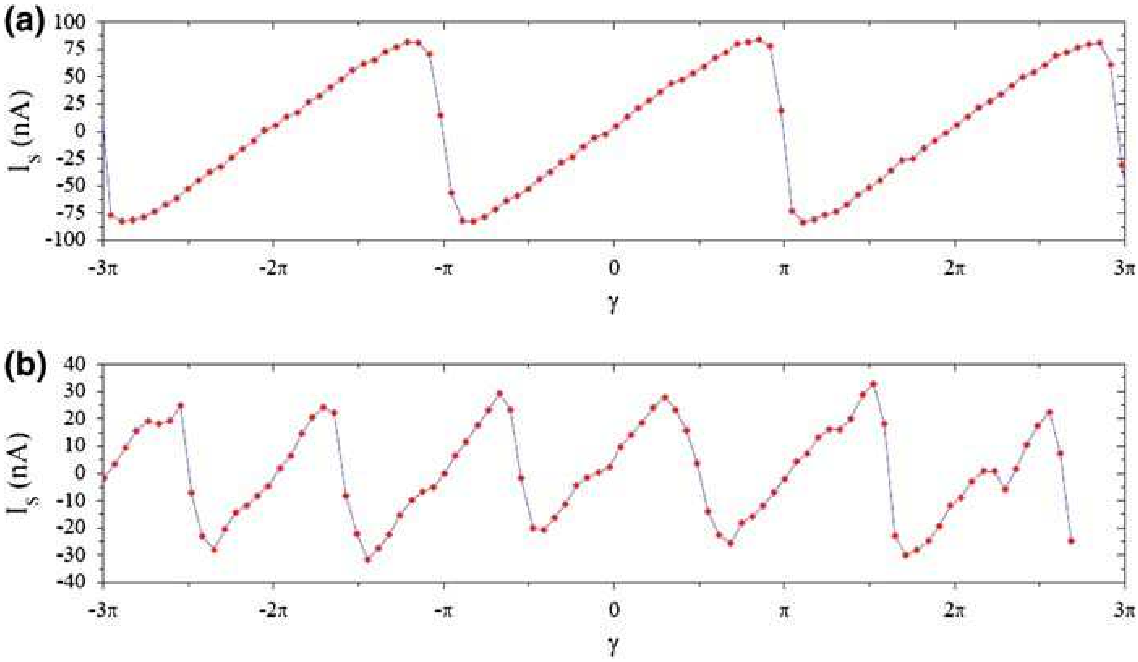

**Fig. 20** Sample A: classical chain. Measured current–phase relation deduced from the switching current versus external magnetic field at $T = 26\,\text{mK}$. **a** Dependence near rhombus frustration $f = 0$. **b** Dependence near full rhombi frustration $f = 0.5$

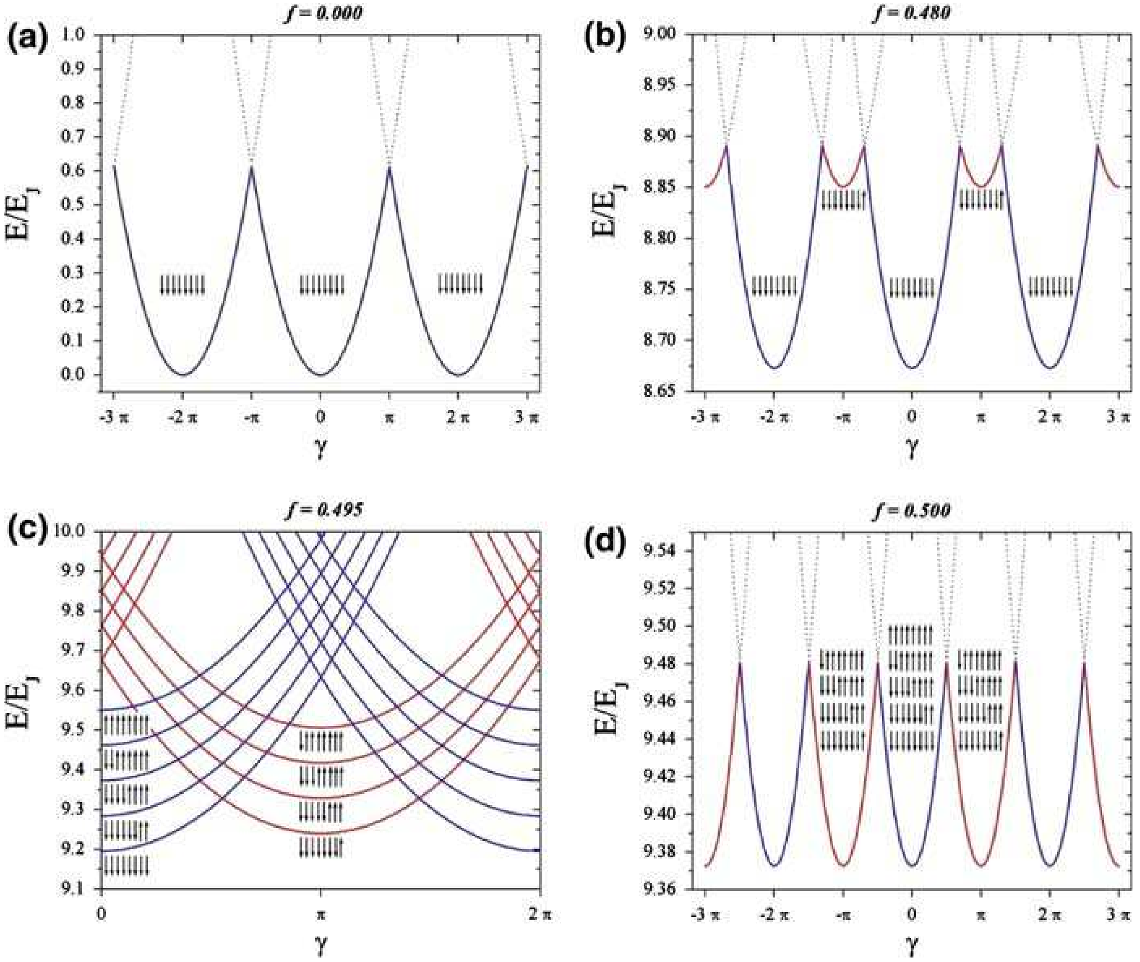

**Fig. 21** Identification of the lowest energy states of a classical rhombi chain as a function of the phase $\gamma$ for different frustrations (here the number of rhombi is N = 8). The supercurrent flowing through the chain is given by the derivative of the energy as a function of $\gamma$ and consists of a series of unequal sawtooth in the vicinity of $f = 0.5$. The *up and down arrows* indicate the spin states of the eight rhombi. Near full frustration ($f = 0.5$) note the change in the parity for the number of switched rhombi between successive minima

Fig. 21a). In fact, for $f = 0$, each rhombus of the chain behaves as a single junction, characterized by an effective Josephson and charging energy $E_{J,eff}$, $E_{C,eff}$. The rhombi chain then behaves as a linear array of effective Josephson junctions. In the classical limit $E_{J,eff} \gg E_{C,eff}$, the current–phase relation is a $2\pi$-periodic sawtooth, with amplitude $E_{J,eff}/N$, $N$ being the number of rhombi in the chain.

However, upon approaching full frustration $f = 0.5$, the two spin states for a single rhombus become more and more degenerate. For the whole chain this means that for a phase difference near $\pi$, the system can lower its energy by flipping the spin of one of the rhombi. This leads to an additional feature in the energy-phase dependence of the chain that in turn gives rise to the appearance of an additional sawtooth branch on the level of the current–phase relation (see Fig. 21b). Very close to $f = 1/2$ (Fig. 21c), for odd values of $\gamma/\pi$, the chain states with an odd number of rhombi in the state $|\uparrow\rangle$ (so-called odd states) correspond to a minimum of energy. At full frustration $f = 0.5$ all chain states with an even and odd number of flipped rhombi become,

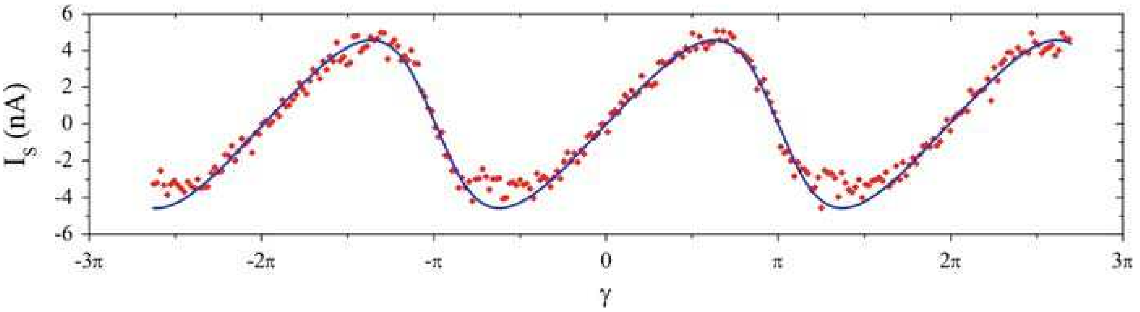

**Fig. 22** Sample C: quantum chain. The experimental plot (*dots*) of the switching current versus external magnetic field in the zero frustration region for sample C at $T = 280\,\text{mK}$. The *line* represents the theoretical fit which gives an effective value for the Josephson energy $E_J^* = 0.5E_J$

respectively, degenerate (Fig. 21d). The high degeneracy of these chain states will be essential for the construction of a topologically protected qubit. At full frustration the energy as a function of the bias phase $\gamma$ becomes $\pi$ periodic and so does the resulting current–phase relation. In terms of the supercurrent this implies a suppression of the $2e$ supercurrent in favor of the appearance of a $4e$ supercurrent, carried by correlated Cooper pairs.

### 5.3 Quantum chains

Here we present results obtained in a chain with $E_J/E_C \approx 2$ (sample C) close to zero frustration. The current–phase relation measured at zero frustration is plotted in Fig. 22 and shows again a $2\pi$ periodicity. The main feature here is the smearing of the sawtooth dependence to a smooth sinusoidal one. The abrupt jumps observed at (2n+1)$\pi$ phase value in the classical chains are now strongly softened. This measured current–phase relation can be explained by the presence of quantum fluctuations, that grow with decreasing ratio $E_J/E_c$ and increasing number of JJ rhombi. Quantum fluctuations lift the degeneracy at the crossing points of the parabola in the classical energy spectrum (see Fig. 21a). They produce therefore phase slip events on individual rhombi that smear the sawtooth function obtained in the classical regime. Moreover, quantum fluctuations decrease the amplitude of the maximum supercurrent flowing through the chain. The measured current–phase relation could be fitted by a tight binding model initially proposed by Matveev et al. [28] for single junction chains and extended to rhombi chains in Ref. [31].

## 6 Experimental setup

The three different aluminum circuits which are presented in this review were realized using e-beam lithography and shadow evaporation of aluminium on an oxidized silicon chip. SEM pictures of the different circuits are presented in Figs. 1, 11 and 19.

The experimental set-up is schematically illustrated in Fig. 23 for the coupled circuit. But a similar set-up was used for the SQUID experiments or the JJ chains measurements.

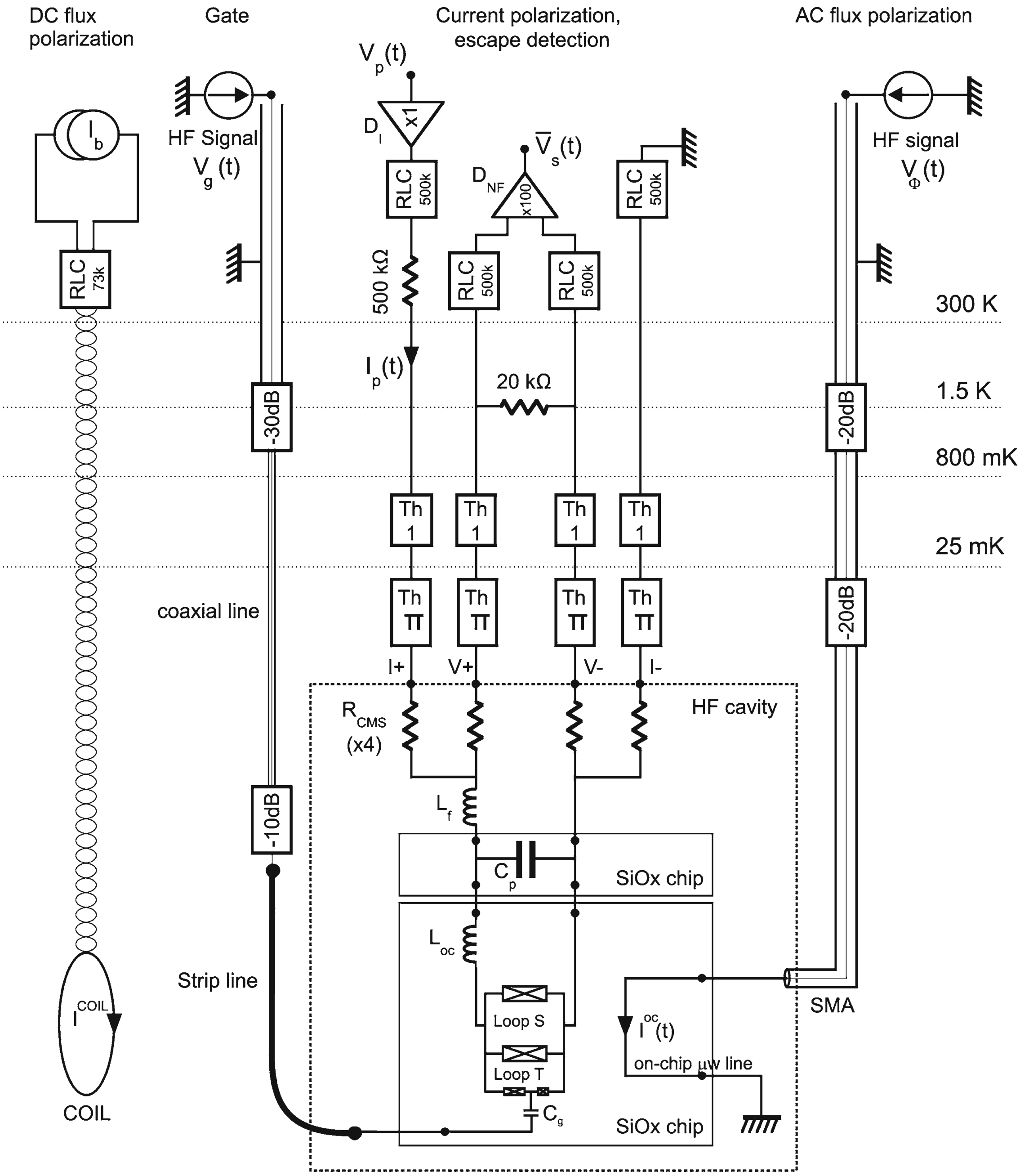

**Fig. 23** Schematics of the experimental setup with temperatures indicated on the right. RLC stands for a second order low-pass rlc filter, Th-1 is a 1 m lossy thermocoax and Th-$\pi$ is composed of two cascaded $\pi$ filters and two meters of lossy thermocoax. x dB is a 50 Ω attenuator

To avoid spurious microwave resonances, the chip is mounted in a shielded copper cavity whose cut-off frequency is above 20 GHz. The four probe dc lines are designed to decouple the circuit from the external room temperature classical electrical apparatus. It consists of cascaded filters. The first and most important filter includes a 9-nH on-chip inductance, $L_{oc}$, introduced by long on-chip superconducting thin wires, and a thin film 150 pF parallel capacitor, $C_p$. As illustrated in Fig. 23, additional filters based on thermocoax [41] and $\pi$-filters are used at the different stages of the dilution fridge. Bias flux is applied with a copper coil cooled down to 30 mK. External low frequency flux fluctuations are screened with soft iron and mu-metal at room temperature and a superconducting lead shield at 1.5 K. The room temperature high frequency flux and gate voltage signals are guided by two different 50 Ω coax lines and attenuated twice by 20 dB at 1.5 K and 30 mK, before reaching the circuit. The high frequency flux line for the SQUID and the coupled circuit are terminated by an on-chip short circuit. The high frequency gate voltage for the ACPT circuit is terminated by an on-chip gate capacitance. The antenna which produces the µw flux signal is located 10 µm from the SQUID, leading to a 1.5 pH mutual inductance coupling. The µw line is terminated by an inductance estimated to be 2 nH which introduces an additional 6 dB attenuation at 10 GHz. Special care was taken to minimize the coupling between the high frequency antenna and the bonding wire loops in the direct electrical environment of the SQUID.

The high frequency signal used in our experiments results from the combination of a microwave excitation pulse and a measurement dc pulse (Fig. 4b). The µw pulse is generated by mixing continuous microwaves with a shaping dc pulse. We define the risetime as the duration to reach 95% of the peak amplitude starting from 5%. The duration is defined as the time interval where the pulse amplitude is at least 95% of the maximal amplitude. With this convention, the shaping pulse has a 0.8 ns risetime and a duration tuneable from 1 ns to several milliseconds. The measurement pulse has a 1.6 ns risetime and a minimum duration of 1.6 ns. Both microwave shaping and measurement pulse are produced by two outputs of one dc pulse generator, allowing precise control of timing. In Fig. 4b, a digital sampling oscilloscope record of the signal is presented. As a demonstration of signal generation performance, the duration of the microwave and measurement pulse have been reduced to the minimum: the whole sequence is then finished in less than 7 ns. Except the specific measurements, the delay between microwave and measurement is kept as short as 1 ns to minimize depolarization due to population relaxation.

To limit heating in the SQUID voltage state, a specific electronic circuit cuts the bias current to zero as soon as a finite voltage across the SQUID is detected. The voltage readout time, about 10 µs, is determined by the bandwidth of the strongly filtered voltage lines. With a wait of 1 ms after each voltage measurement to allow the sample to cool back down to base temperature, the overall repetition rate is about 1 kHz. The experiment sequence is repeated up to 5,000 times such that the statistical noise on $P_e$ has a theoretical standard deviation lower than $4 \times 10^{-3}$. More details on the experiments can be found in the different thesis realised in Grenoble [1,5,14].

## 7 Conclusion

We have studied the quantum dynamics of a dc SQUID in different situations. We have demonstrated that it behaves as a phase qubit when the working point is chosen on an optimal line, insensitive to current fluctuations. At these points Rabi and Ramsey oscillations have been observed in the two-level limit. The measured $T_{2,Rabi} = 67$ ns and $T_{2,Ramsey} = 18$ ns can be significantly improved by reducing the $40\mu\Phi_0$ rms flux noise and the density of micro-resonators observed in our sample. At large µw amplitude the circuit develops very rich and complex dynamics in the transient regime just after application of the μw field. A cross-over from two-level to multilevel behavior has been observed.

We have fabricated an asymmetric Cooper pair transistor that behaves as a charge qubit. It has the advantage to contain two optimal points: one similar to the "quantronium optimal point [10,38]" at ($n_g$, $\delta$)=(1/2,0) and a new one at ($n_g$, $\delta$)=(1/2,$\pi$). At this working point the decoherence times were $T_1 = 800$ ns, $T_{2,Rabi} = 110$ ns and $T_{2,spectroscopy} \approx 20$ ns. The decoherence time can be strongly improved by increasing slightly the $E_J/E_C$ ratio.

We have shown for the first time a strong coupling between two different kinds of superconducting qubits: a charge and a phase qubit. The coupling strength is tunable and varies in our experiment from 60 MHz up to 1.1 GHz. The strong coupling close to the escape line of the dc SQUID produces a new read-out based on adiabatic quantum transfer. We have analyzed theoretically the quantum dynamics of the coupled circuit. This analysis is able to explain the tunable coupling strength by a combination of a capacitive and a Josephson coupling between the two qubits. In the future, it might be possible to manipulate independently the two qubits when they are out of resonance (single qubit operation). By changing the working point, the two qubits can be put in resonance with a strong coupling in order to realize two-qubit operations. All these manipulations can be performed by keeping the charge qubit in its optimal point.

We have analyzed the ground-state of a rhombi chain by measuring its current-phase relation. We confirmed for the first time the tight binding model proposed intially by Matveev et al. [28] for the ground state of a JJ chain in the presence of quantum fluctuations. In the future we would like to do spectroscopy measurements on rhombi chains and give experimental evidence for the macroscopic quantum state established over the chain.

**Acknowledgements** The authors are grateful to Nanofab-CNRS for sample fabrication. We thank the electronics and cryogenics service of Institut Néel for their permanent helps. This work would not have been possible without the excellent work of F. Balestro, J. Claudon and J. Pekola. We thank B. Douçot, F. Faure, M. Feigel'man, L. B. Ioffe, I. Protopopov, A. Ratchov and A. Zazunov for fruitfull discussions. This work was supported by two ACI programs, by the EuroSQIP project, by INTAS Ref. Nr 05-1000008-7923, by European STREP MIDAS and by the Institut de Physique de la Matière Condensée.

## References

1. Balestro, F.: Dynamique quantique d'un SQUID-DC. PhD Thesis, Universite Joseph Fourier, Grenoble, France (2003)
2. Balestro, F., Claudon, J., Pekola, J., Buisson, O.: Evidence of two-dimensional macroscopic quantum tunneling of a current-biased dc SQUID. Phys. Rev. Lett. **91**, 158301 (2003)
3. Buisson, O., Balestro, F., Pekola, J.P., Hekking, F.W.J.: One shot quantum measurement using a hysteretic dc SQUID. Phys. Rev. Lett. **90**, 238304 (2003)
4. Buisson O., Hekking, F.W.J.: Entangled states in a Josephson charge qubit coupled to a superconducting resonator. In: Averin, D., Ruggiero, B., Silvestrini, P. (eds.) Macroscopic Quantum Coherence and Computing, p. 137. Kluwer Academic, New York (2001)
5. Claudon, J.: Ocillations cohérentes dans un circuit quantique supraconducteur: le SQUID dc. Ph.D. Thesis, Université Joseph Fourier, Grenoble, France (2005)
6. Claudon, J., Balestro, F., Hekking, F.W.J., Buisson, O.: Coherent oscillations in a superconducting multilevel quantum system. Phys. Rev. Lett. **93**, 187003 (2004)

7. Claudon, J., Fay, A., Hoskinson, E., Buisson, O.: Nanosecond quantum state detection in a current-biased dc SQUID. Phys. Rev. B **76**, 024508 (2007)
8. Claudon, J., Fay, A., Lévy, L.P., Buisson, O.: Decoherence processes in a current biased dc SQUID. Phys. Rev. B **73**, 180502(R) (2006)
9. Claudon, J., Zazunov, A., Hekking, F.W.J., Buisson, O.: Rabi-like oscillations of an anharmonic oscillator: classical versus quantum interpretation. Phys. Rev. B **78**, 184503 (2008)
10. Collin, E., Ithier, G., Aassime, A., Joyez, P., Vion, D., Urbina, C., Esteve, D.: Manipulating the quantum state of an electrical circuit. Phys. Rev. Lett. **93**, 157005 (2004)
11. Dolata, R., Scherer, H., Zorin, A.B., Niemeyer, J.: Single-charge devices with ultrasmall Nb/AlOx/Nb trilayer Josephson junctions. J. Appl. Phys. **97**, 054501 (2005)
12. Douçot, B., Vidal, J.: Pairing of Cooper pairs in a fully frustrated Josephson-junction chain. Phys. Rev. Lett. **88**, 227005 (2002)
13. Dutta, S.K., Strauch, F.W., Lewis, R.M., Mitra, K., Paik, H., Palomaki, T.A., Tiesinga, E., Anderson, J.R., Dragt, A.J., Lobb, C.J., Wellstood, F.C.: Multilevel effects in the Rabi oscillations of a Josephson phase qubit. Phys. Rev. B **78**, 104510 (2008)
14. Fay, A.: Couplage variable entre un qubit de charge et un qubit de phase. PhD Thesis, Universite Joseph Fourier, Grenoble, France (2008)
15. Fay, A., Hoskinson, E., Lecocq, F., Levy, L.P., Hekking, F.W.J., Guichard, W., Buisson, O.: Strong tunable coupling between a superconducting charge and phase qubit. Phys. Rev. Lett. **100**, 187003 (2008)
16. Gladchenko, S., Olaya, D., Dupont-Ferrier, E., Doucot, B., Ioffe, L.B., Gershenson, M.E.: Superconducting nanocircuits for topologically protected qubits. Nature Phys. **5**(1) (2008)
17. Gronbech-Jensen, N., Cirillo, M.: Rabi-type oscillations in a classical Josephson junction. Phys. Rev. Lett. **95**, 067001 (2005)
18. Hekking, F.W.J., et al. In: Martin, T., Montambaux, G. (eds.) Electronic Correlations: From Meso- to Nano-physics, p. 515. J. Tran Thanh Van. EDP Sciences, Les Ulis (2001)
19. Hime, T. et al.: Solid-state qubits with current-controlled coupling. Science **314**, 1427 (2006)
20. Hoskinson, E., Lecocq, F., Didier, N., Fay, A., Hekking, F.W.J., Guichard, W., Dolata, R., Mackrodt, B., Zorin, A.B., Buisson, O.: Quantum dynamics of a camel back potential of a dc SQUID. arXiv:0810.2372v1. Phys. Rev. Lett. (to be published)
21. Ioffe, L.B., Feigelõman, M.V.: Possible realization of an ideal quantum computer in Josephson junction array. Phys. Rev. B **66**, 224503 (2002)
22. Ivlev, B.I., Ovchinnikov, Yu.N.: Effect of level quantization on the lifetime of metastable states. Sov. Phys. JETP **64**, 185 (1986)
23. Larkin, A.I. , Ovchinnikov, Y.N.: Effect of level quantization on the lifetime of metastable states. Sov. Phys. JETP **64**, 185 (1986)
24. Lefevre-Seguin, V., Turlot, E., Urbina, C., Esteve, D., Devoret, M.H.: Thermal activation of a hysteretic dc superconducting quantum interference device from its zero-voltage states. Phys. Rev. B **46**, 5507 (1992)
25. Lisenfeld, J., Lukashenko, A., Ansmann, M., Martinis, J.M., Ustinov, A.V.: Temperature dependence of coherent oscillations in Josephson phase qubits. Phys. Rev. Lett. **99**, 170504 (2007)
26. Marchese, J.E., Cirillo, M., Gronbech-Jensen, N.: Classical analysis of phase-locking transients and Rabi-type oscillations in microwave-driven Josephson junctions. Phys. Rev. B **73**, 174507 (2006)
27. Martinis, J.M., Nam, S., Aumentado, J., Urbina, C.: Rabi oscillations in a large Josephson junction qubit. Phys. Rev. Lett. **89**, 117901 (2002)
28. Matveev, K.A., Larkin, A.I., Glazman, L.I.: Persistent current in superconducting nanorings. Phys. Rev. Lett. **89**, 096802 (2002)
29. Nakamura, Y., Pashkin, Yu.A., Tsai, J.S.: Coherent control of macroscopic quantum states in a single-Cooper-pair box. Nature **398**, 786 (1999)
30. Niskanen, A.O., et al.: Quantum coherent tunable coupling of superconducting qubits. Science **316**, 723 (2007)
31. Pop, I.M., Hasselbach, K., Buisson, O., Guichard, W., Pannetier, B., Protopopov, I.: Measurement of the current-phase relation in Josephson junction rhombi chains. Phys. Rev. B **78**, 104504 (2008)
32. Protopopov, I., Feigel'man, M.: Anomalous periodicity of supercurrent in long frustrated Josephson-junction rhombi chains. Phys. Rev. B **70**, 184519 (2004)
33. Protopopov, I., Feigel'man, M.: Coherent transport in Josephson-junction rhombi chain with quenched disorder. Phys. Rev. B **74**, 064516 (2006)

34. Simmonds, R.W., Lang, K.M., Hite, D.A., Nam, S., Pappas, D.P., Martinis, J.M.: Decoherence in Josephson phase qubits from junction resonators. Phys. Rev. Lett. **93**, 077003 (2004)
35. Strauch, F.W., Dutta, S.K., Paik, H., Palomaki, T.A., Mitra, K., Cooper, B.K., Lewis, R.M., Anderson, J.R., Dragt, A.J., Lobb, C.J., Wellstood, F.C.: Strong-field effects in the Rabi oscillations of the superconducting phase qubit. IEEE Trans. Appl. Supercond. **17**, 105 (2007)
36. Tesche, C.D., Clarke, J.J.: dc SQUID : noise and optimization. Low Temp. Phys. **29**, 301 (1977)
37. Vidal, J., Mosseri, R., Douçot, B.: Aharonov-Bohm cages in two-dimensional structures. Phys. Rev. Lett. **81**, 5888 (1998)
38. Vion, D.D., Aassime, A., Joyez, A., Pothier, H., Urbina, C., Esteve, D., Devoret, M.H.: Manipulating the quantum state of an electrical circuit. Science **296**, 886 (2002)
39. Wallraff, A., Ithier, D.I., Blais, A., Frunzio, L., Huang, R.-S., Majer, J., Kumar, S., Girvin, S.M., Schoelkopf, R.J.: Strong coupling of a single photon to a superconduting qubit using circuit quantum electrodynamics. Nature **431**, 161 (2004)
40. Yu, Y., Han, S., Chu, X., Chu, S., Wang, Z.: Coherent temporal oscillations of macroscopic quantum states in a Josephson junction. Science **296**, 889 (2002)
41. Zorin, A.B.: The thermocoax cable as the microwave frequency filter for single electron circuits. Rev. Sci. Instrum. **66**, 4296 (1995)

PHYSICAL REVIEW A **79**, 063633 (2009)

# Quantum fluctuations of a Bose-Josephson junction in a quasi-one-dimensional ring trap

N. Didier,* A. Minguzzi,† and F. W. J. Hekking‡
*Laboratoire de Physique et de Modélisation des Milieux Condensés, Université Joseph Fourier and CNRS,*
*BP 166, 38042 Grenoble, France*

(Received 27 March 2009; published 30 June 2009)

Using a Luttinger-liquid approach we study the quantum fluctuations of a Bose-Josephson junction, consisting of a Bose gas confined to a quasi-one-dimensional ring trap which contains a localized repulsive potential barrier. For an infinite barrier we study the one-particle and two-particle static correlation functions. For the one-body density-matrix we obtain different power-law decays depending on the location of the probe points with respect to the position of the barrier. This quasi-long-range order can be experimentally probed in principle using an interference measurement. The corresponding momentum distribution at small momenta is also shown to be affected by the presence of the barrier and to display the universal power-law behavior expected for an interacting one-dimensional fluid. We also evaluate the particle-density profile, and by comparing with the exact results in the Tonks-Girardeau limit we fix the nonuniversal parameters of the Luttinger-liquid theory. Once the parameters are determined from one-body properties, we evaluate the density-density correlation function, finding a remarkable agreement between the Luttinger-liquid predictions and the exact result in the Tonks-Girardeau limit, even at the length scale of the Friedel-like oscillations which characterize the behavior of the density-density correlation function at intermediate distance. Finally, for a large but finite barrier we use the one-body correlation function to estimate the effect of quantum fluctuations on the renormalization of the barrier height, finding a reduction in the effective Josephson coupling energy, which depends on the length of the ring and on the interaction strength.

DOI: 10.1103/PhysRevA.79.063633 PACS number(s): 03.75.Lm, 67.85.−d, 05.30.Jp

## I. INTRODUCTION

The possibility to study Bose-Einstein condensates confined to ring traps constitutes one of the frontiers of the experimental progress with ultracold atomic gases [1]. The nontrivial topology of these traps together with the uniformity of the potential along the ring circumference makes them an ideal system for investigating persistent currents and superfluid properties of the gas.

While current experimental setups display relatively weak transverse (i.e., radial) confinements, we analyze in this work the case where the transverse confinement is so strong that only longitudinal (i.e., tangential) quasi-one-dimensional (quasi-1D) motion is allowed along the ring. In a quasi-1D geometry, the phase coherence properties of the gas are drastically changed with respect to their three-dimensional (3D) counterparts. Phase fluctuations destroy true long-range order, and by increasing the interaction strength the gas changes from a quasicondensate, i.e., a condensate with fluctuating phase [2,3] to a Tonks-Girardeau gas [4], where repulsions are so strong that they mimic the effect of Pauli pressure in a Fermi gas and the condensate is strongly depleted. Here we consider such a one-dimensional ring trap containing a localized repulsive potential which creates a "weak link" connecting the two ends of the loop (see Fig. 1), a situation that may be viewed as a realization of a Bose-Josephson junction. Bose-Josephson junctions have been already experimentally realized using double-well geometry and arrays [5]. In the configuration considered here, quantum fluctuations tend to destroy the phase coherence along the ring, while the tunneling of bosons between the ends of the loop favors a well-defined phase difference across the barrier. We will study the interplay between these competing effects.

We start by investigating how the presence of the barrier affects the quantum fluctuations and hence the coherence properties of a Bose-Josephson junction in a quasi-1D ring at arbitrary values of the interaction strength. In the absence of the barrier, these properties have been extensively studied, employing a variety of techniques, from low-energy Luttinger-liquid approaches and conformal field theory [6,7], to exact methods in the Tonks-Girardeau regime [8,9]. In the presence of an infinitely high barrier, using the Luttinger-liquid approach for a finite ring, we evaluate here the first-order correlation function, which describes the decay of phase coherence along the ring, and recover a previous result from conformal field theory [6]. We then compare the results for the one-body density matrix and for the particle-density profile along the ring with the corresponding exact results in the Tonks-Girardeau limit of impenetrable bosons obtained through a Bose-Fermi mapping method [4]. This enables us to determine the numerical values of the nonuniversal parameters of the Luttinger-liquid theory. Knowing these parameters we estimate two-particle properties such as the density-density correlation function. Finally, we turn to the case of a large but finite barrier, treating the tunneling across the barrier as a perturbation. We use the results for the first-order correlation function in the infinite-barrier limit to estimate the effect of the quantum fluctuations on the effective height of the barrier, i.e., on the Josephson coupling energy. As a result, we predict how the renormalization of the Jo-

---

*nicolas.didier@grenoble.cnrs.fr
†anna.minguzzi@grenoble.cnrs.fr
‡frank.hekking@grenoble.cnrs.fr

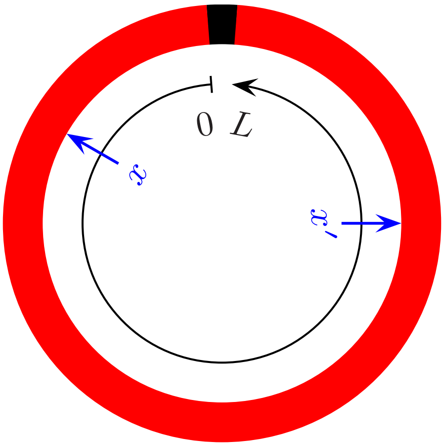

FIG. 1. (Color online) Sketch of the Bose-Josephson junction on a ring trap studied in this work.

sephson energy depends on the ring length and on the interaction strength.

## II. LUTTINGER-LIQUID DESCRIPTION FOR A RING WITH A LOCALIZED BARRIER

We consider $N$ bosons confined to a uniform, quasi-1D ring-shaped trap of circumference $L$ to which a localized repulsive potential $V_{\mathrm{barr}}(x)$, located at $x=0\equiv L$, has been superimposed. The bosons interact with each other through a repulsive contact potential $v(x-x')=g\delta(x-x')$. The corresponding Hamiltonian in terms of the bosonic field operators $\Psi(x)$, $\Psi^\dagger(x)$ reads

$$\mathcal{H}=\int \mathrm{d}x\Psi^\dagger(x)\left(-\frac{\hbar^2}{2m}\nabla^2+V_{\mathrm{barr}}(x)\right)\Psi(x) + \frac{g}{2}\int \mathrm{d}x\Psi^\dagger(x)\Psi^\dagger(x)\Psi(x)\Psi(x). \tag{1}$$

The presence on the ring of the (very large) barrier potential will be taken into account below by imposing open boundary conditions at $x=0\equiv L$ (see Sec. II B) and by adding a tunnel term (see Sec. VI).

### A. Low-energy theory

In order to evaluate the equilibrium correlation functions at large and intermediate distances we adopt the Luttinger-liquid approach, i.e., we approximate the system Hamiltonian (1) by the following effective low-energy Hamiltonian in terms of the fields $\theta(x)$ and $\phi(x)$ which describe the density and phase fluctuations on the ring [10],

$$\mathcal{H}_{LL}=\frac{\hbar v_s}{2\pi}\int_0^L \mathrm{d}x\left\{K[\nabla\phi(x)]^2+\frac{1}{K}[\nabla\theta(x)]^2\right\}. \tag{2}$$

The parameters $K$ and $v_s$ are related to the microscopic interaction parameter of the original Hamiltonian (1) [6], the phase field $\phi(x)$ is related to the velocity of the fluid $v(x)=\hbar\nabla\phi(x)/m$ and the field $\theta(x)$ defines the fluctuations in the density profile $\rho(x)$ according to

$$\rho(x)=[\rho_0+\Pi(x)]\sum_{m=-\infty}^{+\infty} e^{2mi\theta(x)+i2\pi m\rho_0 x+2im\theta_B}, \tag{3}$$

where $\rho_0=N/L$ is the average density of the fluid, $\Pi(x)=\nabla\theta(x)/\pi$ and $\theta_B$ is a constant fixing the position of the first particle with respect to the origin of the $x$ axis. The fields $\Pi$ and $\phi$ satisfy the commutation relation [6,10],

$$[\Pi(x),\phi(x')]=i\delta(x-x'). \tag{4}$$

Note that this approach includes not only the lowest-order hydrodynamic expression for the density fluctuation at long wavelength: the higher order terms in the sum (3) enable the description of the discrete nature of the particles up to distances $\alpha\sim 1/\rho_0$. Our approach does not allow however to probe shorter distance scales because of the assumption of linear phonon-dispersion modes in the effective Hamiltonian (2). The bosonic field operator is obtained from the hydrodynamic expression $\Psi^\dagger(x)=\sqrt{\rho(x)}e^{-i\phi(x)}$ and reads

$$\Psi^\dagger(x)=\mathcal{A}\sqrt{\rho_0+\Pi(x)}\times\sum_{m=-\infty}^{+\infty} e^{2mi\theta(x)+2im\pi\rho_0 x+2im\theta_B}e^{-i\phi(x)}, \tag{5}$$

where $\mathcal{A}$ is a nonuniversal constant, the value of which depends on the way the Luttinger-liquid approach is regularized in the short-wavelength limit. This issue will be discussed in Sec. V A below, where the value of the constants $\mathcal{A}$ and $\theta_B$ will be fixed. The field operators $\Psi$ and $\Psi^\dagger$ as defined through Eq. (5) satisfy the standard bosonic commutation relations as a consequence of the commutation relation (4) among the field operators $\Pi$ and $\phi$.

### B. Mode expansion of the Luttinger fields $\theta$ and $\phi$ with open boundary conditions

We start by considering the case of an infinitely high barrier, which corresponds to a ring with open boundary conditions. In Sec. VI we will treat the case of a large, finite barrier by considering the tunneling among the two sides of the barrier as a perturbation.

In order to evaluate the first- and second-order correlation functions for the bosons on the ring junction, we derive here the expansion of the fields $\Pi(x)=\nabla\theta(x)/\pi$ and $\phi(x)$ in terms of the canonical bosonic annihilation and creation operators $b_k$ and $b_k^\dagger$ satisfying the commutation relations $[b_k,b_{k'}^\dagger]=\delta_{k,k'}$. Specifically, we expand the operators $\phi(x)$ and $\Pi(x)$ in Fourier modes for $x\in[0,L]$,

$$\phi(x)=\sum_{j=-\infty}^{+\infty}[\phi_{1,j}b_{k_j}+\phi_{2,j}b_{k_j}^\dagger]e^{ik_jx}, \tag{6}$$

$$\Pi(x)=\sum_{j=-\infty}^{+\infty}[\Pi_{1,j}b_{k_j}+\Pi_{2,j}b_{k_j}^\dagger]e^{ik_jx}, \tag{7}$$

where we have set $k_j=\frac{2\pi}{L}pj$. The constant $p$ and the complex coefficients $\phi_{1,j}$, $\phi_{2,j}$, $\Pi_{1,j}$, and $\Pi_{2,j}$ are determined by imposing three constraints: (i) the commutations rules

$[\Pi(x),\phi(x')]=i\delta(x-x')$; (ii) the open boundary conditions, which imply vanishing current density, i.e., $\nabla\phi(0)=\nabla\phi(L)=0$, $\nabla\Pi(0)=\nabla\Pi(L)=0$; (iii) reduction in the Hamiltonian to the diagonal form $\mathcal{H}=\Sigma_{k_j}\hbar\omega_{k_j}[b_{k_j}^\dagger b_{k_j}+\frac{1}{2}]$. In order to take into account that we are using an approximate, long-wavelength theory, we introduce a short-distance cutoff $\alpha \sim \rho_0^{-1}$ in the sum over the modes. The final result reads

$$\phi(x) = \phi_0 + \frac{1}{\sqrt{K}}\sum_{j=1}^{\infty}\frac{1}{\sqrt{j}}\cos(\pi jx/L)e^{-\pi j\alpha/2L}[b_{k_j}+b_{k_j}^\dagger], \quad (8)$$

$$\Pi(x) = \Pi_0 + i\frac{\sqrt{K}}{L}\sum_{j=1}^{\infty}\sqrt{j}\,\cos(\pi jx/L)e^{-\pi j\alpha/2L}[b_{k_j}-b_{k_j}^\dagger], \quad (9)$$

the latter implying

$$\theta(x) = \pi\Pi_0 x + i\sqrt{K}\sum_{j=1}^{\infty}\frac{1}{\sqrt{j}}\sin(\pi jx/L)e^{-\pi j\alpha/2L}[b_{k_j}-b_{k_j}^\dagger], \quad (10)$$

where $k_j=\pi j/L$ $(p=1/2)$. The zero mode $\Pi_0$ is directly related to the particle number operator through normalization: $\Pi_0=(N-N_0)/L$ where $N_0=\langle N\rangle=\rho_0 L$. It is conjugate to the zero-mode phase operator $\phi_0$ such that $[\Pi_0,\phi_0]=i$. Using this fact, one can explicitly check the commutation rule between $\theta(x)$ and $\phi(x')$ from the mode expansions (8) and (10); it turns out to be $[\theta(x),\phi(x')]=i\pi u(x-x')$, where $u$ is the unit step function, consistent with Eq. (4). Finally, inspection of the diagonalized form of the Hamiltonian yields the linear dispersion relation $\omega_{k_j}=v_s k_j$ for the modes.

## III. EXACT DESCRIPTION IN THE TONKS-GIRARDEAU LIMIT $K=1$

In the limit of infinitely strong repulsion between the bosons, which corresponds to the value $K=1$ for the Luttinger-liquid parameter, an exact solution exists for the bosonic many-body wave function $\Phi(x_1,\ldots,x_N)$ (in first quantization). We shall use it throughout this paper in order to test the results of the Luttinger-liquid theory in the limit $K=1$, thereby fixing the values of its nonuniversal parameters.

The solution, due to Girardeau [4], is obtained by mapping the bosons onto a gas of noninteracting, spin-polarized fermions subject to the same external potential. The bosonic many-body wave function $\Phi(x_1,\ldots,x_N)$ is then obtained in terms of the fermionic one as

$$\Phi(x_1,\ldots,x_N) = A(x_1,\ldots,x_N)\Phi_F(x_1,\ldots,x_N), \quad (11)$$

where the mapping function $A(x_1,\ldots,x_N)=\Pi_{1\le j\le \ell\le N}\,\mathrm{sgn}(x_j-x_\ell)$ ensures the proper symmetry under exchange of two bosons. The fermionic wave function is given by $\Phi_F(x_1,\ldots,x_N)=(1/\sqrt{N!})\det[\psi_j(x_k)]_{j,k=1\ldots N}$, $\psi_j(x)$ being the single-particle orbitals for the given external potential. Note that $\Phi_F$ vanishes every time two particles meet as required by Pauli's principle, and hence describes well the impenetrability condition $g\to\infty$ for the bosons. In our specific case, the orbitals for a ring of circumference $L$ in the presence of an infinitely high barrier at $x=0\equiv L$ are

$$\psi_j(x) = \sqrt{(2/L)}\sin(\pi jx/L), \quad (12)$$

with $j=1,\ldots,\infty$. This expression is consistent with the open boundary conditions discussed in Sec. II B.

As a consequence of the Bose-Fermi mapping, all the bosonic properties which do not depend on the sign of the many-body wave function coincide with the corresponding ones of the mapped Fermi gas. This is the case, e.g., for the particle-density profile and for the density-density correlation function. Other properties such as the one-body density matrix and the momentum distribution are instead markedly different for bosons as compared to fermions. In particular, the calculation of the one-body density matrix requires in principle the calculation of a (N-1)-dimensional integral, which is known to simplify in some cases. Examples are the homogeneous gas with periodic boundary conditions [8] or the case of a harmonic confinement [9].

## IV. ONE-BODY DENSITY MATRIX AND MOMENTUM DISTRIBUTION IN THE INFINITE-BARRIER LIMIT

In this section we focus on the one-body density matrix and on the momentum distribution for the case of a bosonic ring of circumference $L$ with an infinite barrier, with the aim of analyzing the differences with respect to the case of an infinite system, as well as to the case of a ring in the absence of the barrier.

### A. Contribution from phase fluctuations to the one-body density matrix

The one-body density matrix, defined as $\mathcal{G}(x,x')=\langle\Psi^\dagger(x)\Psi(x')\rangle$ yields a measure of the coherence along the ring. It is possible to measure the one-body density matrix and off-diagonal long-range order experimentally by measuring the interference pattern of atomic matter waves coming from two holes in the trap (see e.g., [11] for the case of a cigar-shaped 3D Bose gas). According to Eq. (5) the bosonic field operator has three contributions: (i) the phase $\phi(x)$ (ii) the density fluctuation $\Pi(x)$, and (iii) the higher harmonics of order $2m\theta(x)$ of the density. The most important contribution to the one-body density matrix at large distances is the one due to the phase fluctuations which correspond to the lowest-energy modes of the bosonic fluid in the ring (see, e.g., [2,7]), while the two latter contributions give rise to subleading corrections which we do not analyze further here.

To lowest order we approximate the bosonic field operator (5) as $\Psi(x)\simeq\mathcal{A}\sqrt{\rho_0}e^{i\phi(x)}$; the problem then reduces to the computation of the quantum average $\mathcal{G}_0(x,x')=|\mathcal{A}|^2\rho_0\langle e^{-i\phi(x)}e^{i\phi(x')}\rangle$. Since the Luttinger-liquid Hamiltonian (2) is quadratic in the field $\phi(x)$ we immediately obtain $\mathcal{G}_0(x,x')=|\mathcal{A}|^2\rho_0\exp(-\frac{1}{2}\langle[\phi(x)-\phi(x')]^2\rangle)$. The phase-phase correlation function is evaluated with the help of the mode expansion (8); using the fact that the ground-state average over the bosonic modes is $\langle(b_k+b_k^\dagger)(b_l+b_l^\dagger)\rangle=\delta_{kl}$ and

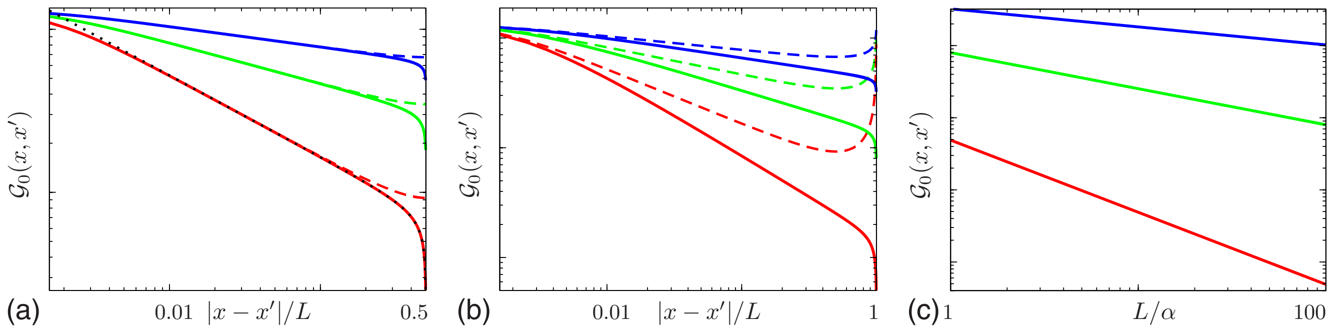

FIG. 2. (Color online) (a) and (b): one-body density matrix in logarithmic scale (arbitrary units) as a function of the coordinate $x'$ (in units of the ring circumference $L$) for various choices of the coordinate $x$ with respect to the position of the barrier; $x \simeq 0$ in (a) and $x = L/2$ in (b). (c) One-body density matrix in logarithmic scale (arbitrary units) taken at $x \simeq 0$ and $x' \simeq L$ as a function of the length $L$ of the ring (in units of the cutoff length $\alpha$). In each panel we plot three values of the parameter $K$ (from bottom to top $K=1$, $K=2$, and $K=4$); the solid lines correspond to the results from Eq. (14) and the dashed lines are the solution (15) for a homogeneous ring (periodic boundary conditions). The dotted line in (a) is the exact solution for a Tonks-Girardeau gas in the thermodynamic limit. The linear behavior of $\mathcal{G}_0$ in logarithmic scale corresponds to the predicted power law decays with various exponents $\gamma$; (a) $\gamma=1/2K$, (b) $\gamma=3/4K$, and (c) $\gamma=1/K$.

the property $\Sigma_{j=1}^{\infty}\frac{1}{j}e^{-\alpha j}\cos(\gamma j) = -\frac{1}{2}\ln[1-2\cos\gamma e^{-\alpha}+e^{-2\alpha}]$ one readily obtains

$$\langle\phi(x)\phi(x')\rangle = -\frac{1}{4K}\ln\{(\pi/L)^4[\alpha^2+d^2(x-x'|2L)]\times[\alpha^2 + d^2(x+x'|2L)]\}, \tag{13}$$

$d(x|L)=L|\sin(\pi x/L)|/\pi$ being the cord function. This leads to

$$\mathcal{G}_0(x,x') = \rho_0 b_{0,0} \times \left[\frac{\rho_0^{-2}\sqrt{[\alpha^2+d^2(2x|2L)][\alpha^2+d^2(2x'|2L)]}}{[\alpha^2+d^2(x-x'|2L)][\alpha^2+d^2(x+x'|2L)]}\right]^{1/4K}, \tag{14}$$

where we have introduced the nonuniversal constant $b_{0,0} = |\mathcal{A}|^2(\rho_0\alpha)^{1/2K}$. The above expression [Eq. (14)] yields the leading-order term for the one-body density matrix at large distances. By taking the limit $\alpha \to 0$ we recover the result obtained in [6] using the methods of conformal field theory.

If the distance among $x$ and $x'$ is large compared to the cutoff length $\alpha$, the one-body density matrix displays a power-law decay of the form $\mathcal{G}_0(x,x') \propto |x-x'|^{-\gamma}$, where the exponent $\gamma$ can be derived from the expression (14), and in particular depends on the location of the probed points [6]. Indeed, if the two points are away from the edges one finds $\gamma=\frac{1}{2K}$, which corresponds to the result obtained in the thermodynamic limit [10] whereas if they approach the edges (i.e., $x \lesssim \alpha$ and $L-x' \lesssim \alpha$) the exponent is $\gamma=\frac{1}{K}$, a result known in the context of quantum phase fluctuations in a 1D superconducting wire of length $L$ [12]. In the case where one point is at one edge and the other in the bulk we obtain $\gamma = \frac{3}{4K}$. These three different behaviors are illustrated in Fig. 2, where we plot the one-body density matrix $\mathcal{G}_0(x,x')$ as a function of $x'$ for various choices of the probe point $x$. In the same figure we display also the behavior for a homogeneous ring in absence of the barrier, obtained by a procedure analogous to the one outlined above,

$$\mathcal{G}_0^{\mathrm{hom}}(x,x') = \rho_0 b_{0,0}\left[\frac{\rho_0^{-2}}{\alpha^2+d^2(x-x'|L)}\right]^{1/4K}. \tag{15}$$

Note that, as the coordinate $x'$ runs along the ring, in the presence of the barrier the coherence decreases monotonically, while if the barrier is absent coherence is recovered as $x'$ approaches $L-x$.

The different power-law behaviors are in principle observable for a quasi-1D Bose gas in a ring trap geometry; it is required to have a high barrier well localized on a length scale $\alpha$.

### B. Momentum distribution

We proceed by studying the momentum distribution $n(q)$, obtained by Fourier transformation of the one-body density matrix with respect to the relative variable,

$$n(q) = \int_0^L \mathrm{d}x \int_0^L \mathrm{d}x' e^{-iq(x-x')}\mathcal{G}(x,x'). \tag{16}$$

We have resorted to a numerical calculation for the evaluation of the momentum distribution taking as input the one-body density matrix obtained in Eq. (14). This allows to estimate the main features of the momentum distribution at wave vectors $q$ smaller than the cutoff wave vector $q_c \sim 1/\alpha$. The behavior at large wave vectors $q \gg q_c$ needs an accurate treatment of the short-distance behavior of the many-body wave function [13,14] and is beyond the regime of validity of the Luttinger-liquid method. The result for the momentum distribution is illustrated in Fig. 3 for two values of the boson number in the ring, and at varying interaction strength. As a general feature (see the inset of Fig. 3), we observe that at intermediate values of $q$ the momentum distribution displays a power-law behavior $n(q) \sim q^{1/(2K)-1}$ with the same power predicted for a homogeneous ring in the thermodynamic limit (see, e.g., [7,15] for a finite-size scaling analysis). This result is readily understood as the different power laws described in Sec. IV A only occur at the edge of the integration region with a negligible weight with respect

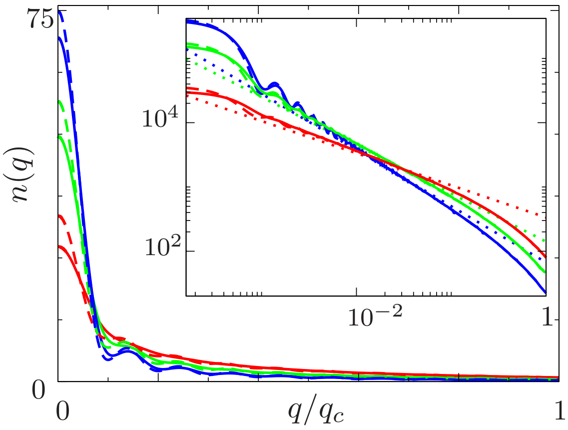

FIG. 3. (Color online) Momentum distribution $n(q)$ in units of $2\pi|\mathcal{A}|^2\alpha$ as a function of the wave vector $q$ in units of the cutoff momentum $q_c=1/\alpha$ for $N=10$ bosons on a ring with an infinite barrier (solid lines) and for a homogeneous ring in absence of the barrier (dashed lines) for various values of the Luttinger parameter $K$ (from top to bottom $K=4,2,1$). The inset shows the same quantity (in logarithmic scale, arbitrary units, same line conventions as the main figure) evaluated for $N=10^3$ bosons. The dotted lines indicate the predicted power law decays $q^{1/(2K)-1}$ in the thermodynamic limit.

to the bulk contribution. Still, by comparing the details of the momentum distribution of the ring with the barrier with the momentum distribution of a uniform ring, (see the main panel of Fig. 3), we find that in the presence of the barrier the momentum distribution is decreased at small momenta. This is in agreement with the fact that the barrier reduces the coherence along the ring. The result is reminiscent of the one obtained for a 1D gas in presence of disorder [16], where the reduction in the momentum distribution at small momenta is also observed.

## V. PARTICLE-DENSITY PROFILE AND DENSITY-DENSITY CORRELATION FUNCTION IN THE INFINITE-BARRIER LIMIT

Extending the quantum average techniques outlined in Sec. IV to the limit of an infinitely high barrier it is possible to evaluate also the inhomogeneous particle-density profile and the density-density correlation functions. Interference between particles incident on and reflected by the barrier leads to the occurrence of Friedel-like oscillations in the density profile and in its correlator, which are typical of strongly correlated 1D fluids. We describe here these oscillations within the Luttinger-liquid approach, for any value of the coupling strength, finding that they are more and more marked as the coupling strength increases. In the Tonks-Girardeau limit of infinite boson-boson repulsion we compare the predictions of the Luttinger-liquid approach with the exact results, which enables us to fix the nonuniversal parameters of the latter.

### A. Friedel oscillations in the particle-density profile

We compute the particle-density profile by taking the quantum average $\langle\rho(x)\rangle$ of the density operator (3) on the ground state, namely,

$$\langle\rho(x)\rangle/\rho_0 = \sum_{m=-\infty}^{+\infty} \langle(1+\Pi(x)/\rho_0)e^{2mi\theta(x)}\rangle e^{i2\pi m\rho_0 x+2im\theta_B}. \tag{17}$$

To evaluate the quantum averages we exploit the fact that the Hamiltonian (2) is quadratic in the field $\theta(x)$ [and recall that $\Pi(x)=\nabla\theta(x)/\pi$]. We use the property that if $X$ and $Z$ are Gaussian variables then $\langle Xe^{Z}\rangle=\langle XZ\rangle e^{1/2\langle Z^2\rangle}$. Hence, we are left with the evaluation of the $\langle\theta(x)\theta(x')\rangle$ correlation function, to be taken at equal points $x=x'$; the $\langle\Pi(x)\theta(x')\rangle$ correlation function is obtained from the previous one by taking the derivative with respect to the variable $x$. Using the mode expansion (10) and a procedure similar to the one outlined in Sec. IV we obtain

$$\langle\theta(x)\theta(x')\rangle = \pi^2\langle\Pi_0^2\rangle xx' - \frac{K}{4}\ln\left[\frac{\alpha^2+d^2(x-x'|2L)}{\alpha^2+d^2(x+x'|2L)}\right], \tag{18}$$

and

$$\langle\Pi(x)\theta(x')\rangle = \pi\langle\Pi_0^2\rangle x' + \frac{K}{2\pi}\frac{d(x+x'|L)}{\alpha^2+d^2(x+x'|2L)} - \frac{K}{2\pi}\frac{d(x-x'|L)}{\alpha^2+d^2(x-x'|2L)}\mathrm{sgn}(x-x'). \tag{19}$$

The final expression for the density profile reads

$$\frac{\langle\rho(x)\rangle}{\rho_0} = 1 + 2\sum_{m=1}^{\infty}\left(\frac{\alpha^2}{\alpha^2+d^2(2x|2L)}\right)^{m^2K/2} \times\left[\cos(2m\pi\rho_0 x+2m\theta_B) - \frac{mK}{\pi\rho_0}\sin(2m\pi\rho_0 x + 2m\theta_B)\frac{d(2x|L)}{\alpha^2+d^2(2x|2L)}\right]. \tag{20}$$

The density profile is modulated by oscillations with wave-vector multiples of $2\pi\rho_0$. Notice that in the case $K=1$, where the system can be mapped onto a noninteracting spin-polarized Fermi gas, the wave vectors of the oscillation are multiples of $2k_F$, where $k_F=\pi\rho_0$ is the Fermi wave vector, and hence correspond to the well-known Friedel oscillations [17]. For the case of generic $K$ the $m=1$ oscillations decay with the power law $x^{-K}$ (see, e.g., [18]).

Let us now concentrate on the case $K=1$. In the thermodynamic limit ($L\to\infty$, $N\to\infty$, at fixed $\rho_0=N/L$) the expression (20) for the density profile at short distances [to $O(1/x)$] reduces to

$$\frac{\langle\rho(x)\rangle}{\rho_0} \simeq 1 + \frac{\alpha\cos(2\pi\rho_0 x+2\theta_B)}{x}. \tag{21}$$

This can be compared with the thermodynamic limit of the exact expression derived using the Bose-Fermi mapping [9,19]

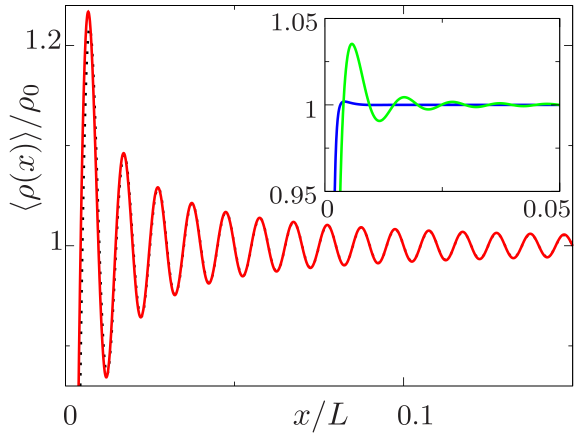

FIG. 4. (Color online) Particle-density profile $\langle\rho(x)\rangle$ in units of the average particle density $\rho_0$ as a function of the spatial coordinate $x$ along the ring (in units of the ring circumference $L$) for various values of the parameter $K$. Main figure, $K=1$ (solid line: result from the Luttinger-liquid model, dotted line, exact result from the Bose-Fermi mapping); inset, $K=2$ (top line) and $K=4$ (bottom line).

$$\frac{\langle\rho(x)\rangle}{\rho_0} \simeq 1 - \frac{\sin(2\pi\rho_0 x)}{2\pi\rho_0 x}, \tag{22}$$

allowing us to fix the coefficients $\alpha$ and $\theta_B$ to the values $\alpha = 1/(2\pi\rho_0)$ and $\theta_B = \pi/4$. Note that the latter choice for $\theta_B$ is in agreement with the condition $\theta_B \neq 0, \pm\pi, \pm 2\pi, \ldots$ obtained by imposing that the particle-density profile should vanish at $x=0$ and $x=L$ [6]. Once the constants $\alpha$ and $\theta_B$ are chosen, the constant $\mathcal{A}$ in Eq. (5) can be fixed by comparing the expression for the coefficient $b_{00}$ entering Eq. (14) for the one-body density matrix with the exact value $b_{00}^{\text{exact}} = 2^{-1/3}\sqrt{\pi e}A_G^{-6} \sim 0.521$ [8,9] where $A_G = 1.282\ldots$ is Glaisher's constant. The result is $|\mathcal{A}|^2 = 2^{1/6}\pi e^{1/2} A_G^{-6} \sim 1.307$. This value has been used in plotting Fig. 2.

In Fig. 4 we illustrate the density profiles for various values of $K$, obtained by the Luttinger-liquid expression (20) using the above choice for $\alpha$ and $\theta_B$ [20]. The figure displays also the exact result for the density profile obtained from the Bose-Fermi mapping, $\rho^{\text{exact}}(x) = \sum_{j=1}^{N} |\psi_j(x)|^2$, where the single-particle orbitals $\psi_j(x)$ are defined in Eq. (12). The comparison shows how our choice of parameters $\alpha$ and $\theta_B$ reproduces extremely well the density profile oscillations even on a finite ring. The figure also illustrates how the Friedel oscillations display maximal amplitude in the strongly interacting limit $K=1$.

### B. Density-density correlation function from Luttinger-liquid theory

We turn now to the density-density correlation function $S(x,x') = \langle\rho(x)\rho(x')\rangle - \langle\rho(x)\rangle\langle\rho(x')\rangle$. This quantity encodes the information on the structure of the fluid, i.e., on the correlations between density modulations at different parts of the fluid, while it vanishes for an ideal Bose gas. The Fourier transform of the density-density correlation function with respect to the relative variable is directly accessible experimentally by light-scattering methods (see e.g., [21] and references therein).

The density-density correlation function is obtained with the quantum average method described in Secs. IV and V. One has to compute

$$\begin{aligned}\langle\rho(x)\rho(x')\rangle = {} & \sum_{m,m'=-\infty}^{+\infty} e^{2i(m-m')\theta_B} e^{i2\pi\rho_0(mx-m'x')} \\ & \times \langle\{\rho_0^2 + \rho_0[\Pi(x)+\Pi(x')] + \Pi(x)\Pi(x')\} \\ & \times e^{2i[m\theta(x)-m'\theta(x')]}\rangle. \end{aligned}\tag{23}$$

The average can be performed using the general result for Gaussian variables $\langle XYe^Z\rangle = (\langle XY\rangle + \langle XZ\rangle\langle YZ\rangle)e^{1/2\langle Z^2\rangle}$. The novel correlator needed for the calculation in addition to Eqs. (18) and (19) is

$$\begin{aligned}\langle\Pi(x)\Pi(x')\rangle = {} & -\frac{K}{2\pi^2}\left\{\frac{d^2(x-x'|2L) - \alpha^2\cos[\pi(x-x')/L]}{[\alpha^2 + d^2(x-x'|2L)]^2}\right. \\ & \left. + \frac{d^2(x+x'|2L) - \alpha^2\cos[\pi(x+x')/L]}{[\alpha^2 + d^2(x+x'|2L)]^2}\right\} \\ & + \langle\Pi_0^2\rangle. \end{aligned}\tag{24}$$

The final result reads

$$\begin{aligned}\langle\rho(x)\rho(x')\rangle = {} & \sum_{m,m'=-\infty}^{+\infty} (\rho_0\alpha)^{(m^2+m'^2)K} e^{2i(m-m')\theta_B} e^{i2\pi\rho_0(mx-m'x')} \\ & \times \{\rho_0^2 + \langle\Pi(x)\Pi(x')\rangle + 2i\rho_0\langle[\Pi(x)+\Pi(x')] \\ & \times [m\theta(x) - m'\theta(x')]\rangle - 4\langle\Pi(x)[m\theta(x) \\ & - m'\theta(x')]\rangle\langle\Pi(x')[m\theta(x) - m'\theta(x')]\rangle\} \\ & \times \left[\frac{\alpha^2 + d^2(x+x'|2L)}{\alpha^2 + d^2(x-x'|2L)}\right]^{mm'K} \\ & \times \left[\frac{\rho_0^{-2}}{\alpha^2 + d^2(2x|2L)}\right]^{m^2K/2} \\ & \times \left[\frac{\rho_0^{-2}}{\alpha^2 + d^2(2x'|2L)}\right]^{m'^2K/2}. \end{aligned}\tag{25}$$

This equation displays the general structure of the density-density correlations to all orders in $m$ and $m'$, and by considering only the first terms of the expansion $m,m' = 0, \pm 1$ we recover the known results [6,7].

We proceed by comparing the density-density correlation function $S(x,x')$ with the exact result for $K=1$. The latter is obtained from the Bose-Fermi mapping as [21]

$$S^{\text{exact}}(x,x') = -\left[\sum_{j=1}^{N} \psi_j^*(x)\psi_j(x')\right]^2, \tag{26}$$

where the single-particle orbitals $\psi_j(x)$ are defined in Eq. (12).

Figure 5 displays the results obtained from the Luttinger-liquid method at various values of the Luttinger parameter $K$, using the choice of parameters $\alpha$ and $\theta_B$ determined from the density profile in Sec. V A and compares to the exact ones in

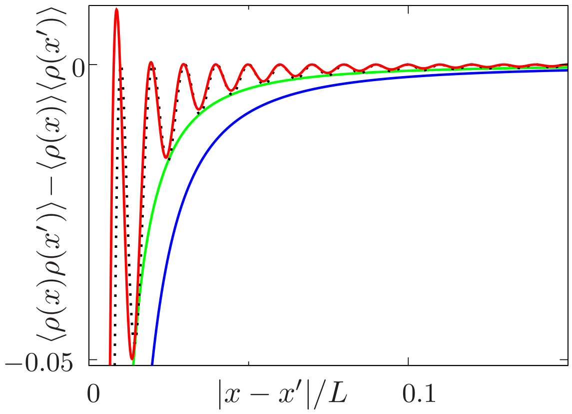

FIG. 5. (Color online) Density-density correlation function $S(x,x')$ (in units of $\rho_0^2$) from the Luttinger-liquid model as a function of the coordinate $x'$ (in units of the ring circumference $L$), with $x{=}L/2$ and for various values of the Luttinger parameter $K$ ($K{=}1$, top red line, $K{=}2$, middle green line, $K{=}4$ bottom blue line). The dotted line corresponds to the exact solution obtained from the Bose-Fermi mapping in the case $K{=}1$.

the case $K{=}1$. The agreement found is very good, even for the Friedel-like oscillations at wave vector $k\sim 2\pi\rho_0$; this is at the boundary of the expected regime of validity of the Luttinger-liquid theory and illustrates how a reasonable choice of the nonuniversal parameters in the effective model allows for surprisingly accurate predictions.

## VI. RENORMALIZATION OF THE JOSEPHSON ENERGY BY QUANTUM FLUCTUATIONS

In this section we consider the effect of a finite barrier on the ring located at $x{=}0\equiv L$ and characterized by the tunneling strength $\mathcal{T}$. The barrier potential yields the following tunneling term in the Hamiltonian (1):

$$\mathcal{H}_J = -\mathcal{T}\Psi^\dagger(L)\Psi(0) + \text{H.c.} \tag{27}$$

The above equation takes into account the possibility for a boson to tunnel through the barrier potential, and H.c. refers to the Hermitian conjugate corresponding to tunneling events in the opposite direction. In the hydrodynamic formulation for $\Psi^\dagger(x)$, the transfer of one boson is ensured by the operator $\exp(-i\varphi)$ where $\varphi{=}\phi(L)-\phi(0)$. By neglecting the density fluctuations in the field operator (5) we then recover the usual Josephson Hamiltonian

$$\mathcal{H}_J = -E_J\cos\varphi, \tag{28}$$

where $E_J{=}2\rho_0\mathcal{T}$ is the Josephson energy of the junction.

Quantum fluctuations of the bosons in the ring on both sides of the barrier tend to smear the phase $\varphi$ and hence suppress the tunneling strength. Indeed, from the diagonal Hamiltonian of Sec. II B, the ring constitutes an oscillator bath for the junction with linear spectrum $\hbar\omega_{k_j}{=}\pi\hbar v_S j/L$; the resulting model is very similar to the one describing a superconducting Josephson junction coupled to a resistive environment [22]. Tunneling events thus induce excitations of the modes of the ring with energy between $\hbar\omega_0$ $=\pi\hbar v_S/L$ and the high energy cutoff $\hbar\omega_h{=}\pi\hbar v_S/\alpha$.

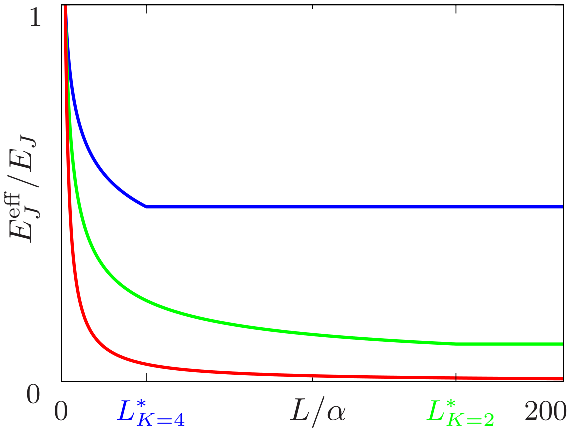

FIG. 6. (Color online) Renormalized Josephson energy as a function of the length of the ring. From top to bottom $K{=}4,2,1$ with $\hbar\omega_h{=}10E_J$. $E_J^{\rm eff}$ decreases as $1/L^{1/K}$ and reaches a constant value at $L{=}L^*$.

When the Josephson energy is smaller than the lowest mode $\hbar\omega_0$, corresponding to small rings $L<L^*\sim\hbar v_S/E_J$, the junction can be treated as a perturbation and every mode modifies $E_J$. The effective Josephson energy results from averaging $\mathcal{H}_J$, Eq. (28), with respect to the ground state of the unperturbed Hamiltonian (2): $E_J^{\rm eff}{=}\langle\mathcal{H}_J\rangle$ with $\langle\mathcal{H}_J\rangle/E_J$ $=\mathcal{G}_0(L,\alpha)/\rho_0$. Then

$$E_J^{\rm eff} = E_J\left(\frac{\pi\alpha}{2L}\right)^{1/K} \quad \text{for } L<L^*. \tag{29}$$

The Josephson energy decreases with the power law $L^{-1/K}$ of the one-body density for probe points at the edges of the ring. This case includes the limit of an infinitely high barrier, where $E_J\to 0$, $L^*\to\infty$, and which is illustrated in Fig. 2, bottom panel.

When $E_J$ is larger than $\hbar\omega_0$ (with $E_J<\hbar\omega_h$), only the modes with energies larger than $E_J$ contribute to the renormalization. Consequently, to obtain the effective Josephson energy we need to average over wavelengths between $\alpha$ and the characteristic length $\ell\equiv\pi\hbar v_S/E_J^{\rm eff}$: $E_J^{\rm eff}{=}\langle\langle\mathcal{H}_J\rangle\rangle$ with

$$E_J^{\rm eff}/E_J = \mathcal{G}_0(L,\alpha)/\mathcal{G}_0(\ell,\alpha)\sim(\alpha/\ell)^{1/K}. \tag{30}$$

The effective Josephson energy in this case is obtained by solving the above self-consistent equation with respect to $\ell$, with the result

$$E_J^{\rm eff} = E_J\left(\frac{\alpha E_J}{\pi\hbar v_S}\right)^{1/(K-1)} \quad \text{for } L>L^*. \tag{31}$$

In this case $E_J^{\rm eff}$ is independent of the ring circumference $L$. Our results (29) and (31) are summarized in Fig. 6. As a main conclusion, we find that quantum fluctuations dramatically reduce the tunnel amplitude with respect to its bare value entering the Hamiltonian (27), especially in the case $K{=}1$. Note however that the reduction saturates at a nonzero level for rings larger than the so-called healing length $L^*$. The continuity between the two regimes $L<L^*$ and $L>L^*$

defines the healing length of the ring $L^* = \pi\alpha/2(\pi\hbar v_S/\alpha E_J)^{K/(K-1)}$.

As a final remark, we would like to mention that our approach is equivalent to the renormalization-group formalism [23] or the self-consistent harmonic approximation [22].

## VII. SUMMARY AND CONCLUDING REMARKS

In summary, in this paper we have studied the equilibrium properties of a quasi-1D interacting Bose gas confined in a ring trap with a localized barrier. In the limit of infinite barrier we have studied the coherence, density profiles and density-density correlations of the gas using a Luttinger-liquid approach and the quantum average method. Our results recover and extend those previously known by the use of conformal field theory methods. As physical consequences of our analysis, we find that the one-body density matrix, when probed at various points with respect to the barrier position, is expected to display universal power-law behaviors with different exponents which depend only on the Luttinger parameter $K$. We also find that our method permits to describe accurately the Friedel oscillations (due to the presence of the barrier) occurring in the particle-density profile and in the density-density correlation function. Once the nonuniversal parameters entering the effective model are fixed by comparing the density profile to the exact one in the Tonks-Girardeau case $K=1$, we find that the Luttinger-liquid model well agrees with the exact result for the density-density correlation function at a length scale which is at the boundary of the validity of the Luttinger-liquid model.

The analysis performed in the limit of infinite barrier is then use to study perturbatively the presence of a large, finite barrier. By taking into account the effect of quantum fluctuations we find that the effective Josephson energy (i.e., the tunnel amplitude across the barrier) is reduced with respect to its bare value, in a way which depends on the length of the ring with respect to a typical healing length, a maximal reduction occurring for long rings. The effect of the renormalization of the tunnel amplitude is expected to have strong consequences on the dynamical evolution of the ring-trapped Bose gas with a Josephson junction.

## ACKNOWLEDGMENTS

We acknowledge stimulating discussions with R. Citro, L.I. Glazman, J. Schmiedmayer. We thank IUF, CNRS, and the MIDAS-STREP project for financial support.

[1] S. Gupta, K. W. Murch, K. L. Moore, T. P. Purdy, and D. M. Stamper-Kurn, Phys. Rev. Lett. **95**, 143201 (2005); O. Morizot, Y. Colombe, V. Lorent, H. Perrin, and B. M. Garraway, Phys. Rev. A **74**, 023617 (2006); C. Ryu, M. F. Andersen, P. Clade, V. Natarajan, K. Helmerson, and W. D. Phillips, Phys. Rev. Lett. **99**, 260401 (2007).

[2] V. N. Popov, Theor. Math. Phys. **11**, 478 (1972); V. N. Popov, *Functional Integrals in Quantum Field Theory and Statistical Physics* (Reidel, Dordrecht, 1983), Chap. 6.

[3] D. S. Petrov, G. V. Shlyapnikov, and J. T. M. Walraven, Phys. Rev. Lett. **85**, 3745 (2000).

[4] M. Girardeau, J. Math. Phys. **1**, 516 (1960); M. D. Girardeau, Phys. Rev. **139**, B500 (1965).

[5] F. Cataliotti S. Burger, C. Fort, P. Maddaloni, F. Minardi, A. Trombettoni, A. Smerzi, and M. Inguscio, Science **293**, 843 (2001); M. Albiez, R. Gati, J. Foelling, S. Hunsmann, M. Cristiani, and M. K. Oberthaler, Phys. Rev. Lett. **95**, 010402 (2005); Y. Shin, G. B. Jo, M. Saba, T. A. Pasquini, W. Ketterle, and D. E. Pritchard, *ibid.* **95**, 170402 (2005); S. Levy, E. Lahoud, I. Shomroni, and J. Steinhauer, Nature (London) **449**, 579 (2007); J. Sebby-Strabley, B. L. Brown, M. Anderlini, P. J. Lee, W. D. Phillips, J. V. Porto, and P. R. Johnson, Phys. Rev. Lett. **98**, 200405 (2007); G.-B. Jo, Y. Shin, S. Will, T. A. Pasquini, M. Saba, W. Ketterle, D. E. Pritchard, M. Vengalattore, and M. Prentiss, *ibid.* **98**, 030407 (2007); S. Foelling, S. Trotzky, P. Cheinet, M. Feld, R. Saers, A. Widera, T. Müller, and I. Bloch, Nature (London) **448**, 1029 (2007); J. Esteve *et al.*, *ibid.* **455**, 1216 (2008).

[6] M. A. Cazalilla, J. Phys. B **37**, S1 (2004).

[7] T. Giamarchi, *Quantum Physics in One Dimension* (Oxford University Press, New York, 2003).

[8] A. Lenard, Pacific J. Math. **42**, 137 (1972).

[9] P. J. Forrester, N. E. Frankel, T. M. Garoni, and N. S. Witte, Phys. Rev. A **67**, 043607 (2003).

[10] F. D. M. Haldane, Phys. Rev. Lett. **47**, 1840 (1981); J. Phys. C **14**, 2585 (1981).

[11] S. Ritter, A. Ottl, T. Donner, T. Bourdel, M. Kohl, and T. Esslinger, Phys. Rev. Lett. **98**, 090402 (2007).

[12] F. W. J. Hekking and L. I. Glazman, Phys. Rev. B **55**, 6551 (1997).

[13] A. Minguzzi, P. Vignolo, and M. P. Tosi, Phys. Lett. A **294**, 222 (2002).

[14] M. Olshanii and V. Dunjko, Phys. Rev. Lett. **91**, 090401 (2003); New J. Phys. **5**, 98 (2003).

[15] M. A. Cazalilla, Europhys. Lett. **59**, 793 (2002).

[16] A. De Martino, M. Thorwart, R. Egger, and R. Graham, Phys. Rev. Lett. **94**, 060402 (2005).

[17] J. Friedel, Nuovo Cimento, Suppl. **7**, 287 (1958).

[18] R. Egger and H. Grabert, in *Quantum Transport in Semiconductor Submicron Structures*, edited by B. Kramer, NATO Advanced Studies Institute, Series E: Applied Science (Kluwer, Dordrecht, 1996).

[19] M. D. Girardeau and A. Minguzzi, Phys. Rev. A **79**, 033610 (2009).

[20] In absence of known results for the case of arbitrary $K$, we have adopted the same choice of parameters $\mathcal{A}$, $\alpha$, and $\theta_B$ for any value of $K$.

[21] P. Vignolo, A. Minguzzi, and M. P. Tosi, Phys. Rev. A **64**, 023421 (2001).

[22] G. Schön and A. D. Zaikin, Phys. Rep. **198**, 237 (1990).

[23] C. L. Kane and M. P. A. Fisher, Phys. Rev. Lett. **68**, 1220 (1992).

PHYSICAL REVIEW A **80**, 033608 (2009)

# Complete series for the off-diagonal correlations of a one-dimensional interacting Bose gas

N. Didier,[*] A. Minguzzi,[†] and F. W. J. Hekking[‡]
*Laboratoire de Physique et de Modélisation des Milieux Condensés, Université Joseph Fourier and CNRS, BP 166, 38042 Grenoble, France*

(Received 4 May 2009; published 11 September 2009)

We use a regularized harmonic-fluid approach, based on the effective low-energy Luttinger-liquid Hamiltonian, for a one-dimensional Bose gas with repulsive contact interactions to compute the complete series corresponding to the large-distance off-diagonal behavior of the one-body density matrix for any value of the Luttinger parameter $K$. We compare our results with the exact ones known in the Tonks-Girardeau limit of infinitely large interactions (corresponding to $K=1$), and different from the usual harmonic-fluid approach, we recover the full structure of the series. The structure is conserved for arbitrary values of the interaction strength with power laws fixed by the universal parameter $K$ and a sequence of subleading corrections.

DOI: 10.1103/PhysRevA.80.033608 PACS number(s): 03.75.Hh, 05.30.Jp, 67.85.−d, 02.30.Ik

## I. INTRODUCTION

Quasi-one-dimensional (1D) quantum fluids display unique properties due to the major role played by quantum fluctuations in reduced dimensionality (see, e.g., [1]). For example, in an interacting 1D Bose fluid quantum fluctuations destroy the off-diagonal long-range order of the one-body density matrix (or first-order coherence function), defined as $\rho_1(x_1,x_2)=\langle\Psi^\dagger(x_1)\Psi(x_2)\rangle$, where $\Psi(x)$ is the bosonic field annihilation operator at position $x$. In contrast to its three-dimensional (3D) counterpart, where the one-body density matrix at large distances tends to a constant which corresponds to the fraction of Bose-condensed atoms [2], in 1D the one-body density matrix at zero temperature decays as a power law [3,4], the coefficient of the power law being fixed by the interaction strength: the decay is faster as the interaction strength increases from the quasicondensate regime with a fluctuating phase [5] to the Tonks-Girardeau regime [6] of impenetrable bosons.

The one-body density matrix is not only a fundamental quantity as it measures the macroscopic coherence properties of a quantum fluid with bosonic statistics but also because it is directly related (by Fourier transformation) to the momentum distribution of the fluid. While the momentum distribution for a Bose fluid is typically narrow and peaked around wave vector $k=0$, its specific form, its broadening due to interactions, and its possible singularities give a wealth of information about the nature of the correlated fluid under study.

Quasi-one-dimensional Bose fluids find an experimental realization in experiments with ultracold atomic gases confined to the minima of a two-dimensional (2D) optical lattice [7]. For those systems, the momentum distribution is one of the most common observables and the one-body density matrix has been measured as well [8] although not yet in the quasi-1D geometry.

From a theoretical point of view, the calculation of the one-body density matrix for the 1D interacting Bose gas has a long history. In the Tonks-Girardeau limit where the exact many-body wave function is known by means of a mapping onto a gas of spinless fermions [6], the problem reduces to the evaluation of a $(N-1)$-dimensional integral. This mathematical challenge was addressed first by Lenard [9] and by several subsequent works (see, e.g., [10–13]). The main result is the evaluation of the large-distance behavior of the one-body density matrix in the form of a series expansion (from [13]),

$$\rho_1^{\mathrm{TG}}(z)=\frac{\rho_0\rho_\infty}{|z|^{1/2}}\left[1-\frac{1}{32}\frac{1}{z^2}-\frac{1}{8}\frac{\cos(2z)}{z^2}-\frac{3}{16}\frac{\sin(2z)}{z^3}+\frac{33}{2048}\frac{1}{z^4}+\frac{93}{256}\frac{\cos(2z)}{z^4}+\cdots\right], \tag{1}$$

where the constant $\rho_\infty$ and the coefficients have been calculated exactly. In Eq. (1) and in the following we express the one-body density matrix as a function of the scaled relative coordinate $z=\pi\rho_0(x_1-x_2)$, where $\rho_0$ is the average particle density.

For the case of arbitrary interaction strength, the calculation of the correlation functions remains a challenge (see, e.g., [14]) although the model of bosons with contact repulsive interactions is integrable by the Bethe-ansatz technique [15]. The power-law decay at large distances can be inferred using a harmonic-fluid approach [3,4,16–18]. The latter is based on an effective low-energy Hamiltonian describing the long-wavelength collective excitations of the fluid having a linear excitation spectrum $\omega(k)=v_sk$. The resulting structure for the large-distance series of the one-body density matrix reads (from [4]) as

$$\rho_1^{\mathrm{LL}}(z)\sim\frac{\rho_0}{|z|^{1/2K}}\sum_{m=0}^{\infty}B_m\frac{\cos(2mz)}{z^{2m^2K}}, \tag{2}$$

where $K=\hbar\pi\rho_0/Mv_s$ is the universal Luttinger-liquid parameter and the coefficients $B_m$ are nonuniversal and cannot be obtained by the harmonic-fluid approach. By noticing that the harmonic-fluid approach is valid also in the Tonks-Girardeau regime and corresponds to the case of Luttinger parameter $K=1$, one can directly compare the predictions of the two methods. Specifically, this comparison shows that the

---

[*] nicolas.didier@grenoble.cnrs.fr

[†] anna.minguzzi@grenoble.cnrs.fr

[‡] frank.hekking@grenoble.cnrs.fr

structure of Eq. (1) is richer than that of Eq. (2) obtained by the standard harmonic-fluid approach.

The central result of this work is that by defining a properly regularized harmonic-fluid model (to be detailed below) the following general structure of the one-body density matrix can be obtained *for arbitrary values of the Luttinger parameter K*:

$$\rho_1(z) \sim \frac{\rho_0}{|z|^{1/2K}}\left[1+\sum_{n=1}^{\infty}\frac{a_n'}{z^{2n}}+\sum_{m=1}^{\infty} b_m\frac{\cos(2mz)}{z^{2m^2K}}\left(\sum_{n=0}^{\infty}\frac{b_n'}{z^{2n}}\right)\right.$$
$$\left.+\sum_{m=1}^{\infty} c_m\frac{\sin(2mz)}{z^{2m^2K+1}}\left(\sum_{n=0}^{\infty}\frac{c_n'}{z^{2n}}\right)\right], \tag{3}$$

where all the coefficients $a_n'$, $b_m$, $b_n'$, $c_m$, and $c_n'$ are nonuniversal and need to be calculated by a fully microscopic theory (for possible methods see, e.g., [19,20]). We note that Eq. (3) (i) generalizes Eq. (2) and (ii) has the full structure of the exact result (1) in the Tonks-Girardeau limit. As a direct consequence of the series structure [Eq. (3)] the momentum distribution will display singularities in its derivatives for $k = \pm 2m\pi\rho_0$.

## II. REGULARIZED HARMONIC-FLUID APPROACH FOR BOSONS

We proceed by outlining the method used. We describe the Bose gas with contact interactions (Lieb-Liniger model [15]) by a harmonic-fluid Hamiltonian expressed in terms of the fields $\theta(x)$ and $\phi(x)$ which describe the density and phase fluctuations of the fluid [4]:

$$\mathcal{H}_{LL}=\frac{\hbar v_s}{2\pi}\int_0^L dx\left\{K[\nabla\phi(x)]^2+\frac{1}{K}[\nabla\theta(x)]^2\right\}. \tag{4}$$

The parameters $K$ and $v_s$ entering Eq. (4) above are related to the microscopic interaction parameters [21], the phase field $\phi(x)$ is related to the velocity of the fluid $v(x)=\hbar\nabla\phi(x)/M$, and the field $\theta(x)$ defines the fluctuations in the density profile. We have adopted here an effective low-energy description, which assumes that the collective excitations in the fluid are noninteracting and phononlike. The description breaks down at a length scale $a$ of the order of the typical interparticle distance $\rho_0^{-1}$ as it neglects the broadening and curvature of the Bose gas spectrum at finite momentum [15,22]. Within the harmonic-fluid approximation, the bosonic field operator is expressed as $\Psi^\dagger(x)=\sqrt{\rho(x)}e^{-i\phi(x)}$. Specifically, its expression in terms of the fields $\theta(x)$ and $\phi(x)$ reads as [4,21]

$$\Psi^\dagger(x)=\mathcal{A}[\rho_0+\Pi(x)]^{1/2}\sum_{m=-\infty}^{+\infty}e^{2mi\Theta(x)}e^{-i\phi(x)}, \tag{5}$$

where $\mathcal{A}$ is a nonuniversal constant, $\Pi(x)=\nabla\theta(x)/\pi$, and for compactness of notation we have introduced the field $\Theta(x)=\theta_B+\pi\rho_0 x+\theta(x)$, where $\theta_B$ is chosen in order to ensure that the average of $\theta(x)$ vanish.

In order to calculate the one-body density matrix, we expand the fields $\theta(x)$ and $\phi(x)$ in terms of the normal modes (bosonic) operators $b_j$, $b_j^\dagger$ which diagonalize Hamiltonian (4) such that $\mathcal{H}_{LL}=\Sigma_j\hbar\omega_j b_j^\dagger b_j$, with $\omega_j=v_s k_j$. As we are interested in the thermodynamic limit, we have chosen for simplicity the periodic boundary conditions for a Bose gas in a uniform box of length $L$, where $k_j=2\pi j/L$. In this case the mode expansion reads as

$$\phi(x)=\sqrt{\frac{\pi}{2KL}}\sum_{j\neq0}\frac{\operatorname{sgn}(k_j)e^{-a|k_j|/2}}{\sqrt{|k_j|}}(e^{ik_jx}b_j+e^{-ik_jx}b_j^\dagger)+\phi_0$$
$$+\frac{\pi x}{L}J, \tag{6}$$

$$\Theta(x)=\sqrt{\frac{\pi K}{2L}}\sum_{j\neq0}\frac{e^{-a|k_j|/2}}{\sqrt{|k_j|}}(e^{ik_jx}b_j+e^{-ik_jx}b_j^\dagger)+\theta_0+\frac{\pi x}{L}N, \tag{7}$$

with $N$ and $J$ being the particle number and angular momentum operators, and $\phi_0,\theta_0$ being their conjugate fields in the phase-number representation [4]. The zero-mode fields $\phi_0$ and $\theta_0$ do not enter the calculation of the one-body density matrix as it turns out to depend only on the differences $\theta(x_1)-\theta(x_2)$ and $\phi(x_1)-\phi(x_2)$. In expressions (6) and (7) above we have introduced the short-distance cutoff $a\sim\rho_0^{-1}$, thus regularizing the effective theory. The one-body density matrix $\rho_1(x_1,x_2)=\langle\Psi^\dagger(x_1)\Psi(x_2)\rangle$ is obtained in the regularized harmonic-fluid approach from Eq. (5) as

$$\rho_1(x_1,x_2)=|\mathcal{A}|^2\sum_{(m,m')\in\mathbb{Z}^2}\langle[\rho_0+\Pi(x_1)]^{1/2}e^{i2m\Theta(x_1)}e^{-i\phi(x_1)}$$
$$\times e^{i\phi(x_2)}e^{-i2m'\Theta(x_2)}[\rho_0+\Pi(x_2)]^{1/2}\rangle, \tag{8}$$

where the only nonvanishing leading terms satisfy $m=m'$ [1].

We detail now the calculation of the quantum average appearing in Eq. (8). In order to display its dependence only on differences between fields, we rewrite the central term as

$$e^{i2m\Theta(x_1)}e^{-i\phi(x_1)}e^{i\phi(x_2)}e^{-i2m\Theta(x_2)}=e^{i2m[\Theta(x_1)-\Theta(x_2)]-i[\phi(x_1)-\phi(x_2)]}$$
$$\times e^{m[\theta(x_1)+\theta(x_2),\varphi(x_1)-\varphi(x_2)]}, \tag{9}$$

where $\varphi(x)=\phi(x)-\pi x\langle J\rangle/L$ and the commutator between the $\theta$ and $\phi$ fields is computed in Eq. (15) below.[1] We then perform a series expansion of the square-root terms $[1+\Pi/\rho_0]^{1/2}$ in the one-body density matrix. We define $X=\Pi(x_1)/\rho_0$, $Y=\Pi(x_2)/\rho_0$, and $Z=i2m[\theta(x_1)-\theta(x_2)]-i[\varphi(x_1)-\varphi(x_2)]$. Using the fact that the fields $X$, $Y$, and $Z$ are Gaussian with zero average, we obtain from Wick's theorem

---

[1] In the following we will not consider the case of a macroscopic vorticity in the system, i.e., we assume $\langle J\rangle \ll N$.

$$\langle\sqrt{1+X}e^{Z}\sqrt{1+Y}\rangle = e^{\langle Z^2\rangle/2}\sum_{k,l=0}^{\infty}\sum_{j=0}^{\min(k,l)}\frac{(2k)!\,(2l)!}{k!\,l!\,(2k-1)(2l-1)} \times \frac{\langle X^2\rangle^{(k-j)/2}\langle Y^2\rangle^{(l-j)/2}\langle XY\rangle^{j}}{(i\sqrt{2})^{5(k+l)-2j}j!\,(k-j)!\,(l-j)!} \times H_{k-j}\left(\frac{\langle XZ\rangle}{i\sqrt{2\langle X^2\rangle}}\right)H_{l-j}\left(\frac{\langle ZY\rangle}{i\sqrt{2\langle Y^2\rangle}}\right), \quad (10)$$

where $H_n(x)$ are the Hermite polynomials. To second order in $X$ and $Y$ Eq. (10) reads

$$\langle\sqrt{1+X}e^{Z}\sqrt{1+Y}\rangle \simeq e^{\langle Z^2\rangle/2}\left[1+\frac{1}{2}(\langle XZ\rangle+\langle ZY\rangle)-\frac{1}{8}(\langle X^2\rangle + \langle Y^2\rangle - 2\langle XY\rangle)-\frac{1}{8}(\langle XZ\rangle-\langle ZY\rangle)^2\right]. \quad (11)$$

Main expression (10) requires then the calculation of the various two-point correlation functions involving the three fields $X$, $Y$, and $Z$. All of them can be obtained from

$$\langle\varphi(x_1)\varphi(x_2)\rangle = \frac{\pi^2}{L^2}\langle J_0^2\rangle x_1x_2 - \frac{1}{4K}\ln C(x_1-x_2), \quad (12)$$

$$\langle\theta(x_1)\theta(x_2)\rangle = \pi^2\langle\Pi_0^2\rangle x_1x_2 - \frac{K}{4}\ln C(x_1-x_2), \quad (13)$$

$$\langle\theta(x_1)\varphi(x_2)\rangle = \frac{1}{4}\ln\left[\frac{1-e^{-2\pi a/L-i2\pi(x_1-x_2)/L}}{1-e^{-2\pi a/L+i2\pi(x_1-x_2)/L}}\right], \quad (14)$$

$$[\theta(x_1),\varphi(x_2)] = i\frac{\pi}{L}(x_1-x_2)+2\langle\theta(x_1)\varphi(x_2)\rangle, \quad (15)$$

where $C(x)=1-2\cos(2\pi x/L)e^{-2\pi a/L}+e^{-4\pi a/L}$, $\Pi_0=(N-\langle N\rangle)/L$, and $J_0=J-\langle J\rangle$. We are now in a position to calculate the correlators between the fields $X$, $Y$, and $Z$ in the thermodynamic limit ($L\to\infty$, $N\to\infty$ at fixed $N/L=\rho_0$). Using Eqs. (12)–(14) we have

$$\exp(\langle Z^2\rangle/2) \simeq \left(\frac{\alpha^2}{z^2+\alpha^2}\right)^{1/4K+Km^2}, \quad (16)$$

$$\langle XZ\rangle = \langle ZY\rangle \simeq \frac{z}{2\alpha}\frac{z+i2Km\alpha}{z^2+\alpha^2}, \quad (17)$$

$$\langle XY\rangle \simeq \frac{K}{2}\frac{\alpha^2-z^2}{(z^2+\alpha^2)^2}, \quad (18)$$

$$\langle X^2\rangle = \langle Y^2\rangle \simeq \frac{K}{2\alpha^2}, \quad (19)$$

where $\alpha=\pi\rho_0 a$. Similarly, the commutator in Eq. (9) is obtained from Eq. (15) as

$$e^{m[\theta(x_1)+\theta(x_2),\varphi(x_1)-\varphi(x_2)]} \simeq \left(\frac{\alpha-iz}{\alpha+iz}\right)^{m}. \quad (20)$$

Notice that the effect of the zero modes $\Pi_0$ and $J_0$ is absent in the thermodynamic limit because it scales as $1/L$. The series expansion in $\Pi/\rho_0$ is valid for small fluctuations of the field $\Pi(x)$ compared to the average density $\rho_0$, $\sqrt{\langle X^2\rangle}\lesssim 1$, i.e., for $\alpha\gtrsim\sqrt{K/2}$. By combining the previous equations we obtain the final result for the one-body density matrix in rescaled units, finding the structure displayed in Eq. (3):

$$\rho_1(z) = \frac{\rho_0\rho_\infty}{|z|^{1/2K}}\left[1+\frac{c_{0,2}}{z^2}+\frac{c_{0,4}}{z^4}+c_{1,2}\frac{\cos(2z)}{z^{2K}}+c_{1,4}\frac{\cos(2z)}{z^{2K+2}} + c_{1,3}\frac{\sin(2z)}{z^{2K+1}}+\cdots\right], \quad (21)$$

with $\rho_\infty=|\mathcal{A}|^2\alpha^{1/2K}c_{0,0}$.

A few comments are in order at this point. First, by taking the limit $a\to 0$ in Eqs. (12)–(15) we recover the results of the standard harmonic-fluid approach, i.e., Eq. (2). Moreover, the regularized harmonic-fluid method produces also the corresponding coefficients of the series, namely, to the order of approximation derived in this work, we have $c_{0,0}\simeq 1\{1+(1/2\alpha)-(K/8\alpha^2)+(K/16\alpha^3)\}$; $c_{0,2}\simeq-(\alpha^2/4K)\times\{c_{0,0}+(2K/\alpha)+(K^2/2\alpha^2)\}/c_{0,0}$; $c_{0,4}\simeq[(1+4K)\alpha^4/32K^2]\times\{c_{0,0}+(4K/\alpha)+[(K^2/\alpha^2)(12K+1)/(4K+1)]-(K^3/\alpha^3)6/(4K+1)\}/c_{0,0}$; $c_{1,2}\simeq-2\alpha^{2K}$; $c_{1,3}\simeq 4\alpha^{2K+1}\{c_{0,0}+(K/2\alpha)+(K^2/16\alpha^3)\}/c_{0,0}$; $c_{1,4}\simeq[(1+8K+4K^2)\alpha^{2K+2}/2K]\{c_{0,0}+[(2K/\alpha)(1+4K)+(K^2/2\alpha^2)+(K^3/\alpha^3)]/(1+8K+4K^2)\}/c_{0,0}$. However, it should be noted that these coefficients do not necessarily coincide, e.g., in the limit $K=1$ with the exact ones in Eq. (1). Our approach is still effective as it suffers from some limitations: first of all, we have just used a single-parameter regularization which neglects the details of the spectrum of the Bose fluid. Second, our approach relies on a hydrodynamiclike expression for the field operator [Eq. (5)] which implicitly assumes that the fluctuations of the field $\Pi(x)$ are "small," which is not always the case. On the other hand, we see from our derivation that the corrections due to the $\Pi(x)$ fluctuations renormalize the coefficients of the series to all orders, giving rise to the contributions in curly brackets to the $c_{ij}$ above but do not change the series structure.

Figure 1 shows our results for the one-body density matrix [Eq. (21), solid lines] for $K=1$ and a specific choice of the cut-off parameter $\alpha=1/2$ as suggested by the analysis of other correlation functions [23]. The comparison with the exact result for the Tonks-Girardeau gas [Eq. (1), dashed lines] yields a reasonable agreement, the difference being due to the fact that we have used for the sake of illustration the explicit expression for the coefficients $c_{i,j}$ derived in the current work. It should be noted in particular that our regularized harmonic-fluid approach restores the correct trend at short distances as compared to the usual harmonic-fluid approach [Eq. (2), dotted lines].

## III. APPLICATION TO FERMIONS

It is possible to apply the above approach to the case of a 1D spinless Fermi gas with odd-wave interparticle interac-

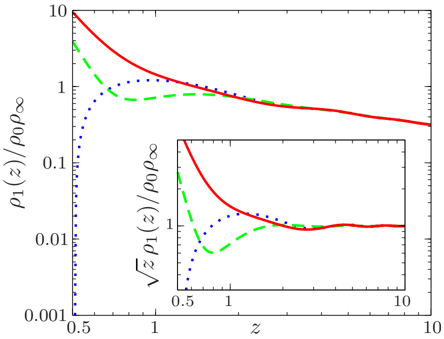

FIG. 1. (Color online) One-body density matrix in the Tonks-Girardeau limit $K=1$ in units of $\rho_0\rho_\infty$ as a function of the scaled relative coordinate $z=\pi\rho_0(x_1-x_2)$ (dimensionless). The result of the regularized harmonic-fluid approximation [Eq. (21)] obtained without taking into account the effect of the field $\Pi(x)$ (solid line) is compared to the exact result [Eq. (1)] (dashed line) and to the usual harmonic-fluid approximation [Eq. (2)] (dotted line), with $B_0=1$, $B_1=-1/2$, and $B_{m>1}=0$. The value chosen for the cutoff parameter is $\alpha=1/2$. The inset shows the subleading behavior $z^{1/2}\rho_1(z)$ of the one-body density matrix in the same notations and units as in the main graph.

tion [24], i.e., the 1D analog of $p$-wave interactions. For any value of the coupling strength the (attractive) Fermi gas can be mapped onto a (repulsive) Bose gas described by the Lieb-Liniger model with dimensionless coupling strength given by $\gamma_B=-1/\gamma_F$ [24,25], the spectrum of collective excitations being the same for the two models. Hence, it is possible to describe the interacting Fermi gas by the Luttinger-liquid Hamiltonian (4) as well, except for the so-called Fermi-Tonks-Girardeau limit $\gamma_F=-\infty$ mapped onto the noninteracting Bose gas limit where the collective excitation spectrum is quadratic. This allows us to estimate the fermionic one-body density matrix with a method similar to the one described above for the bosons, the fermionic nature of the particles being taken into account by a Jordan-Wigner transformation [4] on the bosonic field operator (5). In particular, we generalize the series expansion known from the usual harmonic-fluid approach, which in rescaled units reads (from [4]) as

$$\rho_{1F}^{\mathrm{LL}}(z) \sim \frac{\rho_0}{|z|^{1/2K}} \sum_{m=0}^{\infty} C_m \frac{\sin[(2m+1)z]}{z^{2(m+1/2)^2K}} \tag{22}$$

to the following series structure:

$$\rho_{1F}(z) \sim \frac{\rho_0}{|z|^{1/2K}} \left[ \sum_{m=0}^{\infty} d_m \frac{\sin[(2m+1)z]}{z^{2(m+1/2)^2K}} \left( \sum_{n=0}^{\infty} \frac{d_n'}{z^{2n}} \right) + \sum_{m=0}^{\infty} e_m \frac{\cos[(2m+1)z]}{z^{2(m+1/2)^2K+1}} \left( \sum_{n=0}^{\infty} \frac{e_n'}{z^{2n}} \right) \right]. \tag{23}$$

The coefficients in Eq. (23) are nonuniversal and need a separate treatment. The limit $K=1$ is an exception though. It corresponds to the case of noninteracting fermions where the exact result for the one-body density matrix $\rho_{1F}^{(0)}(x_1,x_2) = \Sigma_{|k|<k_F}\psi_k^*(x_1)\psi_k(x_2)$, with $\psi_k(x)$ being the single-particle orbitals, in the thermodynamic limit and in rescaled units reads

$$\rho_{1F}^{(0)}(z) = \pi\rho_0 \frac{\sin(z)}{z}. \tag{24}$$

Hence, it turns out that for noninteracting fermions all the coefficients of series expression (23) vanish except the leading one.

## IV. CONCLUSION

In conclusion, we have used a regularized harmonic-fluid approximation to evaluate the large-distance behavior of the one-body density matrix both for one-dimensional interacting bosons and fermions at arbitrary values of the interaction strength—the latter expressed in terms of the Luttinger parameter $K$. In the case of bosons in the Tonks-Girardeau limit $K=1$ we recover the full structure of the series expansion known for the exact result. In the case of noninteracting fermions, the exact result shows that the series has only one nonvanishing term. In perspective, it could be interesting to estimate the coefficients of the series expansion at arbitrary interaction strength.

Our results could be especially relevant for the experiments on ultracold atomic gases in the case of a strongly correlated Bose gas ($K\simeq 1$) or a Bose gas with dipolar interactions ($K<1$) [26], where the subleading corrections of the series become more important. It would be also interesting to take into account the effects of finite size and inhomogeneity of the confinement to compare with experimental observables such as the momentum distribution.

## ACKNOWLEDGMENTS

We acknowledge discussions with D. M. Gangardt, L. I. Glazman, R. Santachiara, and M. B. Zvonarev. We thank IUF, CNRS, and the MIDAS-STREP project for financial support.

---

[1] T. Giamarchi, *Quantum Physics in One Dimension* (Oxford University Press, New York, 2003).
[2] O. Penrose and L. Onsager, Phys. Rev. **104**, 576 (1956).
[3] A. Luther and I. Peschel, Phys. Rev. B **9**, 2911 (1974).
[4] F. D. M. Haldane, Phys. Rev. Lett. **47**, 1840 (1981); J. Phys. C **14**, 2585 (1981).
[5] V. N. Popov, Theor. Math. Phys. **11**, 478 (1972); *Functional Integrals in Quantum Field Theory and Statistical Physics* (Reidel, Dordrecht, 1983), Chap. 6.
[6] M. Girardeau, J. Math. Phys. **1**, 516 (1960); Phys. Rev. **139**, B500 (1965).
[7] B. Paredes, A. Widera, V. Murg, O. Mandel, S. Fölling, I.

Cirac, G. V. Shlyapnikov, T. W. Hänsch, and I. Bloch, Nature (London) **429**, 277 (2004); T. Kinoshita, T. R. Wenger, and D. S. Weiss, Science **305**, 1125 (2004).
[8] S. Ritter, A. Öttl, T. Donner, T. Bourdel, M. Köhl, and T. Esslinger, Phys. Rev. Lett. **98**, 090402 (2007).
[9] A. Lenard, J. Math. Phys. **5**, 930 (1964).
[10] H. G. Vaidya and C. A. Tracy, J. Math. Phys. **20**, 2291 (1979).
[11] M. Jimbo, T. Miwa, Y. Mori, and M. Sato, Physica (Utrecht) **1D**, 80 (1980).
[12] N. M. Bogoliubov, A. G. Izergin, and N. A. Kitanine, Nucl. Phys. B **516**, 501 (1998).
[13] D. M. Gangardt, J. Phys. A **37**, 9335 (2004).
[14] V. E. Korepin, N. M. Bogoliubov, and A. G. Izergin, *Quantum Inverse Scattering Method and Correlation Functions* (Cambridge University Press, Cambridge, 1993).
[15] E. H. Lieb and W. Liniger, Phys. Rev. **130**, 1605 (1963).
[16] S. Tomonaga, Prog. Theor. Phys. **5**, 544 (1950).
[17] D. C. Mattis and E. H. Lieb, J. Math. Phys. **6**, 304 (1965).
[18] K. B. Efetov and A. I. Larkin, Sov. Phys. JETP **42**, 390 (1975).
[19] L. Amico and V. Korepin, Ann. Phys. **314**, 496 (2004).
[20] J.-S. Caux, P. Calabrese, and N. Slavnov, J. Stat. Mech. (2007) 01008.
[21] M. A. Cazalilla, J. Phys. B **37**, S1 (2004).
[22] M. Khodas, M. Pustilnik, A. Kamenev, and L. I. Glazman, Phys. Rev. Lett. **99**, 110405 (2007); A. Imambekov and L. I. Glazman, *ibid.* **100**, 206805 (2008).
[23] N. Didier, A. Minguzzi, and F. W. J. Hekking, Phys. Rev. A **79**, 063633 (2009).
[24] T. Cheon and T. Shigehara, Phys. Lett. A **243**, 111 (1998); Phys. Rev. Lett. **82**, 2536 (1999).
[25] B. E. Granger and D. Blume, Phys. Rev. Lett. **92**, 133202 (2004).
[26] R. Citro, E. Orignac, S. De Palo, and M. L. Chiofalo, Phys. Rev. A **75**, 051602(R) (2007).

# Bibliography

[1] O. Buisson, W. Guichard, F.W.J. Hekking, L. Lévy, B. Pannetier, R. Dolata, A.B. Zorin, N. Didier, A. Fay, E. Hoskinson, F. Lecocq, Z.H. Peng, and I.M. Pop, *Quantum dynamics of superconducting nano-circuits: phase qubit, charge qubit and rhombi chains*, Quantum Inf. Process. **8**, 155 (2009).

[2] W. H. Zurek, *Decoherence and the Transition from Quantum to Classical*, Phys. Today **44** (10), 36 (1991).

[3] Richard P. Feynman. *The Feynman Lectures on Physics.* Addison-Wesley, 1964. Vol. 3: *Quantum Mechanics*, Chap. 21: *The Schrödinger equation in a classical context: a seminar on superconductivity.*

[4] Richard P. Feynman. *Statistical mechanics.* W.A. Benjamin, inc., 1972. Chap. 10: *Superconductivity.*

[5] B. D. Josephson, *Possible new effects in superconductive tunnelling*, Physics Letters **1**, 251 (1962).

[6] B. D. Josephson, *Supercurrents through barriers*, Advances in Physics **14**, 419 (1965).

[7] S. Shapiro, *Josephson Currents in Superconducting Tunneling: The Effect of Microwaves and Other Observations*, Phys. Rev. Lett. **11**, 80 (1963).

[8] H. Frolich, *Isotop Effect in Superconductivity*, Proc. Roy. Soc. (London) **A63**, 778 (1950).

[9] J. Bardeen, *Zero-Point Vibrations and Superconductivity*, Phys. Rev. **79**, 167 (1950).

[10] L. N. Cooper, *Bound electron pairs in a degenerate Fermi gas*, Phys. Rev. **104**, 1189 (1956).

[11] J. Bardeen, L. N. Cooper, and J. R. Schrieffer, *Microscopic Theory of Superconductivity*, Phys. Rev. **106**, 162 (1957).

[12] J. Bardeen, L. N. Cooper, and J. R. Schrieffer, *Theory of Superconductivity*, Phys. Rev. **108**, 1175 (1957).

[13] P. G. De Gennes. *Superconductivity of Metals and Alloys.* W.A. Benjamin, inc., 1966.

[14] P. H. Smith, S. Shapiro, J. L. Miles, and J. Nicols, *Superconducting Characteristics of Superimposed Metal Films*, Phys. Rev. Lett. **6**, 686 (1961).

[15] P. W. Anderson and J. M. Rowell, *Probable Observation of the Josephson Superconducting Tunneling Effect*, Phys. Rev. Lett. **10**, 230 (1963).

[16] Michael Tinkham. *Introduction to Superconductivity.* Physics & Astronomy Series. McGraw-Hill, second edition, 1996.

[17] Konstantin K. Likharev. *Dynamics of Josephson Junctions and Circuits.* Gordon and Breach Publishers, 1986.

[18] Y. M. Ivanchenko and L. A. Zilberman, *The Josephson Effect on Small Size Tunnel Contacts*, Soviet Physics JETP **28**, 1272 (1969).

[19] A. Steinbach, P. Joyez, A. Cottet, D. Esteve, M. H. Devoret, M. E. Huber, and J. M. Martinis, *Direct Measurement of the Josephson Supercurrent in an Ultrasmall Josephson Junction*, Phys. Rev. Lett. **87**, 137003 (2001).

[20] J. Flowers, *The Route to Atomic and Quantum Standards*, Science **306**, 1324 (2004).

[21] A. J. Leggett, *Cooper pairing in spin-polarized Fermi systems*, J. Phys. (Paris) **41**, 7 (1980).

[22] P. Nozières and S. Schmitt-Rink, *Bose Condensation in an Attractive Fermion Gas: From Weak to Strong Coupling Superconductivity*, J. Low Temp. Phys. **59**, 195 (1985).

[23] C. A. Regal, M. Greiner, and D. S. Jin, *Observation of Resonance Condensation of Fermionic Atom Pairs*, Phys. Rev. Lett. **92**, 040403 (2004).

[24] R. Loudon. *The Quantum Theory of Light.* Oxford Science Publications, third edition, 2000.

[25] G. J. Milburn, J. Corney, E. M. Wright, and D. F. Walls, *Quantum dynamics of an atomic Bose-Einstein condensate in a double-well potential*, Phys. Rev. A **55**, 4318 (1997).

[26] S. Raghavan, A. Smerzi, S. Fantoni, and S. R. Shenoy, *Coherent oscillations between two weakly coupled Bose-Einstein Condensates: Josephson effects, $\pi$-oscillations, and macroscopic quantum self trapping*, Phys. Rev. A **59**, 620 (1999).

[27] S. N. Bose, *Plancks Gesetz und Lichtquantenhypothese*, Z. Phys. **26**, 178 (1925).

[28] A. Einstein, *Quantentheorie des einatomigen idealen Gases*, Sitzber. Kgl. Preuss. Akad. Wiss. pages 3–14 (1925).

[29] M. H. Anderson, J. R. Ensher, M. R. Matthews, C. E. Wieman, and E. A. Cornell, *Observation of Bose-Einstein Condensation in a Dilute Atomic Vapor*, Science **269**, 198 (1995).

[30] K. B. Davis, M.-O. Mewes, M. R. Andrews, N. J. van Druten, D. S. Durfee, D. M. Kurn, and W. Ketterle, *Bose-Einstein Condensation in a Gas of Sodium Atoms*, Phys. Rev. Lett. **75**, 3969 (1995).

[31] C. C. Bradley, C. A. Sackett, J. J. Tollett, and R. G. Hulet, *Evidence of Bose-Einstein Condensation in an Atomic Gas with Attractive Interactions*, Phys. Rev. Lett. **75**, 1687 (1995), erratum: Phys. Rev. Lett. **79**, 1170 (1997).

[32] M. R. Andrews, C. G. Townsend, H.-J. Miesner, D. S. Durfee, D. M. Kurn, and W. Ketterle, *Observation of interference between two Bose condensates*, Science **275**, 637 (1997).

[33] C. Cohen-Tannoudji. *Cours de physique atomique et moléculaire.* Leçons du Collège de France, 1973-2004. http://www.phys.ens.fr/cours/college-de-france/.

[34] C. J. Pethick and H. Smith. *Bose-Einstein condensation in atomic gases.* Cambridge University Press, 2002.

[35] F. Shimizu, K. Shimizu, and H. Takuma, *Double-slit interference with ultracold metastable neon atoms*, Phys. Rev. A **46**, R17 (1992).

[36] O. Penrose and L. Onsager, *Bose-Einstein Condensation and Liquid Helium*, Phys. Rev. A **104**, 576 (1956).

[37] L. P. Pitaevskii and S. Stringari. *Bose-Einstein Condensation.* Oxford University Press, 2003.

[38] E. P. Gross, *Structure of a quantized vortex in boson systems*, Il Nuovo cimento **20**, 454 (1961).

[39] L. P. Pitaevskii, *Vortex Lines in an Imperfect Bose Gas*, Soviet Phys. JETP **13**, 451 (1961).

[40] M. Albiez, R. Gati, J. Fölling, S. Hunsmann, M. Cristiani, and M. K. Oberthaler, *Direct Observation of Tunneling and Nonlinear Self-Trapping in a single Bosonic Josephson Junction*, Phys. Rev. Lett. **95**, 010402 (2005).

[41] J. Ruostekoski and D. F. Walls, *Bose-Einstein condensate in a double-well potential as an open quantum system*, Phys. Rev. A **58**, R50 (1998).

[42] I. Zapata, F. Sols, and A. J. Leggett, *Josephson effect between trapped Bose-Einstein condensates*, Phys. Rev. A **57**, R28 (1998).

[43] S. Levy, E. Lahoud, I. Shomroni, and J. Steinhauer, *The a.c. and d.c. Josephson effects in a Bose–Einstein condensate*, Nature **449**, 579 (2007).

[44] F. S. Cataliotti, S. Burger, C. Fort, P. Maddaloni, F. Minardi, A. Trombettoni, A. Smerzi, and M. Inguscio, *Josephson Junction Arrays with Bose-Einstein Condensates*, Science **293**, 843 (2001).

[45] J. Sebby-Strabley, B. L. Brown, M. Anderlini, P. J. Lee, W. D. Phillips, and J. V. Porto, *Preparing and Probing Atomic Number States with an Atom Interferometer*, Phys. Rev. Lett. **98**, 200405 (2007).

[46] G. Ferrini, A. Minguzzi, and F. W. J. Hekking, *Number squeezing, quantum fluctuations, and oscillations in mesoscopic Bose Josephson junctions*, Phys. Rev. A **78**, 023606 (2008).

[47] Gerd Schön and A. D. Zaikin, *Quantum Coherent Effects, Phase Transitions, and the Dissipative Dynamics of Ultra Small Tunnel Junctions*, Physics Report **198**, 237 (1990).

[48] Gert-Ludwig Ingold and Yu V. Nazarov. Charge Tunneling Rates in Ultrasmall Junctions. In Hermann Grabert and Michel H. Devoret, editors, *Single Charge Tunneling*, volume 294 of *NATO ASI Series B: Physics.* Plenum Press, 1992.

[49] W. Zwerger, *Quantum effects in the current-voltage characteristic of a small Josephson junction*, Phys. Rev. B **35**, 4737 (1987).

[50] G.-L. Ingold, H. Grabert, and U. Eberhardt, *Cooper-pair current through ultrasmall Josephson junctions*, Phys. Rev. B **50**, 395 (1994).

[51] H. Grabert, G.-L. Ingold, and B. Paul, *Phase diffusion and charging effects in Josephson junctions*, Europhys. Lett. **44**, 360 (1998).

[52] Gert-Ludwig Ingold and Hermann Grabert, *Effect of Zero Point Phase Fluctuations on Josephson Tunneling*, Physical Review Letters **83**, 3721 (1999).

[53] M. Watanabe and D. B. Haviland, *Coulomb Blockade and Coherent Single-Cooper-Pair Tunneling in Single Josephson Junctions*, Phys. Rev. Lett. **86**, 5120 (2001).

[54] M. Watanabe and D. B. Haviland, *Quantum effects in small-capacitance single Josephson junctions*, Phys. Rev. B **67**, 094505 (2003).

[55] S. Corlevi, W. Guichard, F. W. J. Hekking, and D. B. Haviland, *Phase-charge duality of a Josephson junction in a fluctuating electromagnetic environment*, Phys. Rev. Lett. **97**, 096802 (2006).

[56] D. V. Averin, 1. B. Zorin, and K. K. Likharev, *Bloch oscillations in small-size Josephson-junctions*, Sov. Phys. JETP **61**, 407 (1985).

[57] K. K. Likharev and A. B. Zorin, *Theory of the Bloch-Wave Oscillations in Small Josephson Junctions*, Journal of Low Temperature Physics **59**, 347 (1985).

[58] Albert Schmidt, *Diffusion and Localization in a Dissipative Quantum System*, Physical Review Letters **51**, 1506 (1983).

[59] F. Guinea, V. Hakim, and A. Muramatsu, *Diffusion and Localization of a Particle in a Periodic Potential Coupled to a Dissipative Environment*, Phys. Rev. Lett. **54**, 263 (1985).

[60] Ulrich Weiss. *Quantum Dissipative Systems*, volume 13 of *Modern Condensed Matter Physics*. World Scientific, third edition, 2008.

[61] I. S. Beloborodov, F. W. J. Hekking, and F. Pistolesi. Influence of Thermal Fluctuations on an Underdamped Josephson Tunnel Jonction. In R. Fazio, V. F. Gantmakher, and Y. Imry, editors, *New directions in Mesoscopic Physics (Towards Nanoscience)*, Dordrecht, 2002. Kluwer Academic Publisher. cond-mat/0304102.

[62] A. Zazunov, N. Didier, and F.W.J. Hekking, *Quantum charge diffusion in underdamped Josephson junctions and superconducting nanowires*, Europhys. Lett. **83**, 47012 (2008).

[63] A. O. Caldeira and A. J. Leggett, *Quantum Tunnelling in a Dissipative System*, Ann. Phys. **149**, 374 (1983).

[64] A. B. Zorin, *Bloch Inductance in Small-Capacitance Josephson Junctions*, Phys. Rev. Lett. **96**, 167001 (2006).

[65] P. Ågren, K. Andersson, and D. B. Haviland, *Kinetic inductance and Coulomb blockade in one dimensional Josephson junction arrays*, J. Low Temp. Phys. **124**, 291 (2001).

[66] A. A. Abrikosov, L. P. Gorkov, and I. E. Dzyaloshinski. *Methods of Quantum Field Theory in Statistical Physics*. Dover Publications, 1975.

[67] Alexander L. Fetter and John Dirk Walecka. *Quantum theory of many-particle systems*. McGraw-Hill, 1971.

[68] L. V. Keldysh, *Diagram technique for nonequilibrium processes*, Sov. Phys. JETP **20**, 1018 (1965).

[69] J. Rammer and H. Smith, *Quantum field-theoretical methods in transport-theory of metals*, Rev. Mod. Phys. **58**, 323 (1986).

[70] A. Lenard, *Exact Statistical Mechanics of a One-Dimensional System with Coulomb Forces*, J. Math. Phys. **2**, 682 (1961).

[71] L. S. Kuzmin and D. B. Haviland, *Observation of the Bloch oscillations in an ultrasmall Josephson junction*, Phys. Rev. Lett. **67**, 2890 (1991).

[72] J. Ankerhold, *Overdamped quantum phase diffusion and charging effects in Josephson junctions*, Europhys. Lett. **67**, 280 (2004).

[73] J. Ankerhold, H. Grabert, and P. Pechukas, *Quantum Brownian motion with large friction*, Chaos **15**, 026106 (2005).

[74] J. Ankerhold, P. Pechukas, and H. Grabert, *Strong friction limit in quantum mechanics: the quantum Smoluchowski equation*, Phys. Rev. Lett. **87**, 086802 (2001).

[75] M. Smoluchowski, *Zur kinetischen Theorie der Brownschen Molekularbewegung und der Suspensionen*, Ann. d. Phys. **21**, 756 (1906).

[76] D. V. Averin, Yu. V. Nazarov, and A. A. Odintsov, *Incoherent tunneling of the Cooper pairs and magnetic-flux quanta in ultrasmall Josephson-junctions*, Physica B **165** & **166**, 945 (1990).

[77] J. E. Mooij and Yu V. Nazarov, *Quantum Phase Slip Junctions*, Condensed Matter (2005), cond-mat/0511535.

[78] W. Guichard and F. W. J. Hekking, *Phase-charge duality in Josephson junction circuits: Role of inertia and effect of microwave irradiation*, to be published (2009).

[79] R. L. Kautz, *Noise, chaos, and the Josephson voltage standard*, Rep. Prog. Phys. **59**, 935 (1996).

[80] Yu. V. Nazarov and M. Kindermann, *Full counting statistics of a general quantum mechanical variable*, Eur. Phys. J. B **35**, 413 (2003).

[81] Ya. M. Blanter and M. Büttiker, *Shot noise in mesoscopic conductors*, Phys. Rep. **336**, 1 (2000).

[82] J.T. Peltonen, A.V. Timofeev, M. Meschke, T.T. Heikkilä, and J.P. Pekola, *Detecting non-Gaussian current fluctuations using a Josephson threshold detector*, Physica E **40**, 111 (2007).

[83] E. Lhotel, O. Coupiac, F. Lefloch, H. Courtois, and M. Sanquer, *Divergence at Low Bias and Down-Mixing of the Current Noise in a Diffusive Superconductor–Normal-Metal–Superconductor Junction*, Phys. Rev. Lett. **99**, 117002 (2007).

[84] E. Hoskinson, F. Lecocq, N. Didier, A. Fay, F.W.J. Hekking, W. Guichard, O. Buisson, R. Dolata, B. Mackrodt, and A.B. Zorin, *Quantum Dynamics in a Camelback Potential of a dc SQUID*, Phys. Rev. Lett. **102**, 097004 (2009).

[85] L. D. Landau and L. M. Lifshitz. *Quantum Mechanics.* Butterworth-Heinemann, third edition, 1981.

[86] J. Claudon, F. Balestro, F. W. J. Hekking, and O. Buisson, *Coherent Oscillations in a Superconducting Multilevel Quantum System*, Phys. Rev. Lett. **93**, 187003 (2004).

[87] K. B. Cooper, M. S. R. McDermott, R. W. Simmonds, S. Oh, D. A. Hite, D. P. Pappas, and J. M. Martinis, *Observation of Quantum Oscillations between a Josephson Phase Qubit and a Microscopic Resonator Using Fast Readout*, Phys. Rev. Lett. **93**, 180401 (2004).

[88] J. Lisenfeld, A. Lukashenko, M. Ansmann, J. M. Martinis, and A. V. Ustinov, *Temperature Dependence of Coherent Oscillations in Josephson Phase Qubits*, Phys. Rev. Lett. **99**, 170504 (2007).

[89] S. K. Dutta, F. W. Strauch, R. M. Lewis, K. Mitra, H. Paik, T. A. Palomaki, E. Tiesinga, J. R. Anderson, A. J. Dragt, C. J. Lobb, and F. C. Wellstood, *Multilevel effects in the Rabi oscillations of a Josephson phase qubit*, Phys. Rev. B **78**, 104510 (2008).

[90] Yu. Kagan and A. J. Leggett. Quantum tunnelling in condensed media. In *Modern Problems in Condensed Matter Science.* North Holland, 1992.

[91] M. Razavy. *Quantum Theory of Tunneling.* World Scientific Publishing, 2002.

[92] S. Takagi. *Macroscopic Quantum Tunneling.* Cambridge University Press, 2005.

[93] C. G. Callan and S. Coleman, *Fate of the false vacuum. II. First quantum corrections*, Phys. Rev. D **16**, 1762 (1977).

[94] S. Coleman. The uses of instantons. In *The Whys of Subnuclear Physics*, 1977.

[95] R. P. Feynman and A. R. Hibbs. *Quantum mechanics and path integrals.* McGraw-Hill, 1965.

[96] H. Jirari, F. W. J. Hekking, and O. Buisson, *Optimal control of superconducting N-level quantum systems*, Europhys. Lett. **87**, 28004 (2009).

[97] J. Claudon, A. Fay, E. Hoskinson, and O. Buisson, *Nanosecond quantum state detection in a current-biased dc SQUID*, Phys. Rev. B **76**, 024508 (2007).

[98] V. Lefevre-Seguin, E. Turlot, C. Urbina, D. Esteve, and M. H. Devoret, *Thermal activation of a hysteretic dc superconducting quantum interference device from its different zero-voltage states*, Phys. Rev. B **46**, 5507 (1992).

[99] O. Astafiev, K. Inomata, A. O. Niskanen, T. Yamamoto, Yu. A. Pashkin, Y. Nakamura, and J. S. Tsai, *Single artificial-atom lasing*, Nature **449**, 588 (2007).

[100] H. Haken. *Light, vol. 1: Waves, photons, atoms.* North-Holland physics publishing, 1981.

[101] H. Haken. *Light, vol. 2: Laser light dynamics.* North-Holland physics publishing, 1985.

[102] U. Gnutzmann, *Quantum mechanical calculation of multiple-time-correlation functions and its application to the laser theory*, Z. Physik **225**, 416 (1969).

[103] L. Onsager, *Reciprocal relations in irreversible processes*, Phys. Rev. **37**, 405 (1931).

[104] M. Lax, *Formal Theory of Quantum Fluctuations from a Driven State*, Phys. Rev. **129**, 2342 (1963).

[105] M. O. Scully and M. S. Zubairy. *Quantum optics.* Cambridge University press, sixth edition, 2008.

[106] H. J. Carmichael. *Statistical Methods in Quantum Optics*, volume 1, Master Equations and Fokker-Planck Equations. Springer, 1999.

[107] S. André, V. Brosco, A. Shnirman, and G. Schön, *Phase diffusion and locking in single-qubit lasers*, Phys. Rev. B **79**, 053848 (2009).

[108] T. A. Fulton, P. L. Gammel, D. J. Bishop, L. N. Dunkleberger, and G. J. Dolan, *Observation of combined Josephson and charging effects in small tunnel junction circuits*, Phys. Rev. Lett. **63**, 1307 (1989).

[109] D. V. Averin and V. Ya Aleshkin, *Resonance tunneling of Cooper pairs in a system of two small Josephson junctions*, JETP Lett. **50**, 367 (1989).

[110] J. Koch, T. M. Yu, J. Gambetta, A. A. Houck, D. I. Schuster, J. Majer, A. Blais, M. H. Devoret, S. M. Girvin, and R. J. Schoelkopf, *Charge insensitive qubit design derived from the Cooper pair box*, Phys. Rev. A **76**, 042319 (2007).

[111] J. A. Schreier, A. A. Houck, J. Koch, D. I. Schuster, B. R. Johnson, J. M. Chow, J. M. Gambetta, J. Majer, L. Frunzio, M. H. Devoret, S. M. Girvin, and R. J. Schoelkopf, *Suppressing charge noise decoherence in superconducting charge qubits*, Phys. Rev. B **77**, 180502(R) (2008).

[112] A. A. Houck, J. Koch, M. H. Devoret, S. M. Girvin, and R. J. Schoelkopf, *Life after charge noise: recent results with transmon qubits*, Quantum Inf. Process. **8**, 105 (2009).

[113] A. Wallraff, D. I. Schuster, A. Blais, L. Frunzio, R.-S. Huang, J. Majer, S. Kumar, S. M. Girvin, and R. J. Schoelkopf, *Strong coupling of a single photon to a superconducting qubit using circuit quantum electrodynamics*, Nature **431**, 162 (2004).

[114] M. H. Devoret. Quantum fluctuations in electrical circuits. Elsevier, Amsterdam, 1997.

[115] S. Haroche and J.-M. Raimond. *Exploring the Quantum.* Oxford university press, 2006.

[116] N. Didier, A. Minguzzi, and F.W.J. Hekking, *Quantum fluctuations of a Bose-Josephson junction in a quasi-one-dimensional ring trap*, Phys. Rev. A **79**, 063633 (2009).

[117] N. Didier, A. Minguzzi, and F.W.J. Hekking, *Complete series for the off-diagonal correlations of a one-dimensional interacting Bose gas*, Phys. Rev. A **80**, 033608 (2009).

[118] C. Cohen-Tannoudji, J. Dupont-Roc, and G. Grynberg. *Processus d'interaction entre photons et atomes.* EDP Sciences - CNRS Éditions, 2001.

[119] H. Feshbach, *A Unified Theory of Nuclear Reactions. II*, Ann. Phys. **19**, 287 (1962).

[120] S. Inouye, M. R. Andrews, J. Stenger, H.-J. Miesner, D. M. Stamper-Kurn, and W. Ketterle, *Observation of Feshbach resonances in a Bose-Einstein condensate*, Nature **392**, 151 (1998).

[121] W. H. Wing, *On neutral particle trapping in quasistatic electromagnetic fields*, Prog. Quant. Electr. **8**, 181 (1984).

[122] Yu. V. Gott, M. S. Ioffe, and V. G. Tel'kovskii, *Some new results on confinement in magnetic traps*, Nucl. Fusion Suppl. **3**, 1045 (1962).

[123] D. E. Pritchard, *Cooling Neutral Atoms in a Magnetic Trap for Precision Spectroscopy*, Phys. Rev. Lett. **51**, 1336 (1983).

[124] W. Ketterle, K. B. Davis, M. A. Joffe, A. Martin, and D. E. Pritchard, *High densities of cold atoms in a dark spontaneous-force optical trap*, Phys. Rev. Lett. **70**, 2253 (1993).

[125] M.-O. Mewes, M. R. Andrews, D. M. Kurn, D. S. Durfee, C. G. Townsend, and W. Ketterle, *Output Coupler for Bose-Einstein Condensed Atoms*, Phys. Rev. Lett. **78**, 582 (1997).

[126] J. Dalibard and C. Cohen-Tannoudji, *Laser cooling below the Doppler limit by polarization gradients: simple theoretical models*, J. Opt. Soc. Am. B **6**, 2023 (1989).

[127] A. Aspect, E. Arimondo, R. Kaiser, N. Vansteenkiste, and C. Cohen-Tannoudji, *Laser Cooling below the One-Photon Recoil Energy by Velocity-Selective Coherent Population Trapping*, Phys. Rev. Lett. **61**, 826 (1988).

[128] H. F. Hess, *Evaporative cooling of magnetically trapped and compressed spin-polarized hydrogen*, Phys. Rev. B **34**, 3476 (1986).

[129] W. Ketterle and N. J. Van Druten, *Evaporative cooling of trapped atoms*, Adv. At. Mol. Opt. Phys. **37**, 181 (1996).

[130] A. E. Leanhardt, T. A. Pasquini, M. Saba, A. Schirotzek, Y. Shin, D. Kielpinski, D. E. Pritchard, and W. Ketterle, *Cooling Bose-Einstein Condensates Below 500 Picokelvin*, Science **301**, 1513 (2003).

[131] M. R. Andrews, M.-O. Mewes, N. J. van Druten, D. S. Durfee, D. M. Kurn, and W. Ketterle, *Direct, Nondestructive Observation of a Bose Condensate*, Science **273**, 84 (1996).

[132] M.-O. Mewes, M.R. Andrews, N.J. van Druten, D.M. Kurn, D.S. Durfee, and W. Ketterle, *Bose-Einstein condensation in a tightly confining dc magnetic trap*, Phys. Rev. Lett. **77**, 416 (1996).

[133] I. Bloch, T. W. Hänsch, and T. Esslinger, *Measurement of the spatial coherence of a trapped Bose gas at the phase transition*, Nature **403**, 166 (2000).

[134] S. Ritter, A. Öttl, T. Donner, T. Bourdel, M. Köhl, and T. Esslinger, *Observing the Formation of Long-Range Order during Bose-Einstein Condensation*, Phys. Rev. Lett. **98**, 090402 (2007).

[135] J. Stenger, S. Inouye, A. P. Chikkatur, D. M. Stamper-Kurn, D. E. Pritchard, and W. Ketterle, *Bragg Spectroscopy of a Bose-Einstein Condensate*, Phys. Rev. Lett. **82**, 4569 (1999).

[136] D. M. Stamper-Kurn, A. P. Chikkatur, A. Görlitz, S. Inouye, S. Gupta, D. E. Pritchard, and W. Ketterle, *Excitation of Phonons in a Bose-Einstein Condensate by Light Scattering*, Phys. Rev. Lett. **83**, 2876 (1999).

[137] T. Stöferle, H. Moritz, C. Schori, M. Köhl, and T. Esslinger, *Transition from a Strongly Interacting 1D Superfluid to a Mott Insulator*, Phys. Rev. Lett. **92**, 130403 (2004).

[138] T. Kinoshita, T.R. Wenger, and D.S. Weiss, *Observation of a One-Dimensional Tonks-Girardeau Gas*, Science **305**, 1125 (2004).

[139] B. Paredes, A. Widera, V. Murg, O. Mandel, S. Fölling, I. Cirac, G. V. Shlyapnikov, T. W. Hänsch, and Immanuel Bloch, *Tonks–Girardeau gas of ultracold atoms in an optical lattice*, Nature **429**, 277 (2004).

[140] M. P. A. Fisher and L. I. Glazman. Transport in a one-dimensional luttinger liquid. In L. L. Sohn, L. P. Kowenhoven, and G. Schön, editors, *Mesoscopic Electron Transport.* Kluwer, Dordrecht, 1996.

[141] R. Saito, G. Dresselhaus, and M. S. Dresselhaus. *Physical Properties of Carbon Nanotubes.* World scientific, 1998.

[142] T. Giamarchi. *Quantum Physics in One Dimension.* Oxford University Press, 2003.

[143] M. Olshanii, *Atomic Scattering in the Presence of an External Confinement and a Gas of Impenetrable Bosons*, Phys. Rev. Lett. **81**, 938 (1998).

[144] D.S. Petrov, G.V. Shlyapnikov, and J.T.M. Walraven, *Regimes of Quantum Degeneracy in Trapped 1D Gases*, Phys. Rev. Lett. **85**, 3745 (2000).

[145] V.N. Popov. *Functional integrals in Quantum Field Theory and Statistical Physics.* Reidel, Dordrecht, 1983.

[146] M. Girardeau, *Relationship between Systems of Impenetrable Bosons and Fermions in One Dimension*, J. Math. Phys. **1**, 516 (1960).

[147] H. Bethe, *Zur Theorie der Metalle. I. Eigenwerte und Eigenfunktionen der linearen Atomkette*, Z. Phys. A **71**, 205 (1931).

[148] E.H. Lieb and W. Liniger, *Exact Analysis of an Interacting Bose Gas. I. The General Solution and the Ground State*, Phys. Rev. **130**, 1605 (1963).

[149] E.H. Lieb and W. Liniger, *Exact Analysis of an Interacting Bose Gas. II. The Excitation Spectrum*, Phys. Rev. **130**, 1616 (1963).

[150] F.D.M. Haldane, *Effective Harmonic-Fluid Approach to Low-Energy Properties of One-Dimensional Quantum Fluids*, Phys. Rev. Lett. **47**, 1840 (1981).

[151] F.D.M. Haldane, *'Luttinger liquid theory' of one-dimensional quantum fluids. I. Properties of the Luttinger model and their extension to the general 1D interacting spinless Fermi gas*, J. Phys. C **14**, 2585 (1981).

[152] A. Lenard, *Some Remarks on Large Toeplitz Matrices*, Pacific J. Math. **42**, 137 (1972).

[153] P.J. Forrester, N.E. Frankel, T.M. Garoni, and N.S. Witte, *Finite one-dimensional impenetrable Bose systems: Occupation numbers*, Phys. Rev. A **67**, 043607 (2003).

[154] R. Folman, P. Krüger, J. Schmiedmayer, J. Denschlag, and C. Henkel, *Microscopic atom optics: From wires to an atom chip*, Adv. At. Mol. Opt. Phys. **48**, 263 (2002).

[155] S. Dettmer, D. Hellweg, P. Ryytty, J. J. Arlt, W. Ertmer, K. Sengstock, D. S. Petrov, G.V. Shlyapnikov, H. Kreutzmann, L. Santos, and M. Lewenstein, *Observation of Phase Fluctuations in Elongated Bose-Einstein Condensates*, Phys. Rev. Lett. **87**, 160406 (2001).

[156] J. Esteve, J.-B. Trebbia, T. Schumm, A. Aspect, C. I. Westbrook, and I. Bouchoule, *Observations of Density Fluctuations in an Elongated Bose Gas: Ideal Gas and Quasicondensate Regimes*, Phys. Rev. Lett. **96**, 130403 (2006).

[157] A. H. van Amerongen, J. J. P. van Es, P. Wicke, K.V. Kheruntsyan, and N. J. van Druten, *Yang-Yang Thermodynamics on an Atom Chip*, Phys. Rev. Lett. **100**, 090402 (2008).

[158] I.E. Mazets, T. Schumm, and J. Schmiedmayer, *Breakdown of integrability in a quasi-one-dimensional ultracold bosonic gas*, Phys. Rev. Lett. **100**, 210403 (2008).

[159] C. D. Fertig, K. M. O'Hara, J. H. Huckans, S. L. Rolston, W. D. Phillips, and J.V. Porto, *Strongly Inhibited Transport of a Degenerate 1D Bose Gas in a Lattice*, Phys. Rev. Lett. **94**, 120403 (2005).

[160] D.-W. Wang, M. D. Lukin, and E. Demler, *Disordered Bose-Einstein Condensates in Quasi-One-Dimensional Magnetic Microtraps*, Phys. Rev. Lett. **92**, 076802 (2004).

[161] S. Hofferberth, I. Lesanovsky, B. Fischer, T. Schumm, and J. Schmiedmayer, *Non-equilibrium coherence dynamics in one-dimensional Bose gases*, Nature **449**, 324 (2007).

[162] N. K. Whitlock and I. Bouchoule, *Relative phase fluctuations of two coupled one-dimensional condensates*, Phys. Rev. A **68**, 053609 (2003).

[163] I. Bouchoule, *Modulational instabilities in Josephson oscillations of elongated coupled condensates*, Eur. Phys. J. D **35**, 147 (2005).

[164] V. Gritsev, A. Polkovnikov, and E. Demler, *Linear response theory for a pair of coupled one-dimensional condensates of interacting atoms*, Phys. Rev. B **75**, 174511 (2007).

[165] I.E. Mazets and J. Schmiedmayer, *Dephasing in two decoupled one-dimensional Bose-Einstein condensates and the subexponential decay of the interwell coherence*, Eur. Phys. J. B **68**, 335–339 (2009).

[166] I. Bloch, *Ultracold quantum gases in optical lattices*, Nat. Phys. **1**, 23 (2005).

[167] C. Kollath, Julia S. Meyer, and T. Giamarchi, *Dipolar bosons in a planar array of one-dimensional tubes*, Phys. Rev. Lett. **100**, 130403 (2008).

[168] S. Gupta, K. W. Murch, K. L. Moore, T. P. Purdy, and D. M. Stamper-Kurn, *Bose-Einstein Condensation in a Circular Waveguide*, Phys. Rev. Lett. **95**, 143201 (2005).

[169] O. Morizot, Y. Colombe, V. Lorent, H. Perrin, and B. M. Garraway, *Ring trap for ultracold atoms*, Phys. Rev. A **74**, 023617 (2006).

[170] C. Ryu, M. F. Andersen, P. Cladé, Vasant Natarajan, K. Helmerson, and W. D. Phillips, *Observation of Persistent Flow of a Bose-Einstein Condensate in a Toroidal Trap*, Phys. Rev. Lett. **99**, 260401 (2007).

[171] M.A. Cazalilla, *Bosonizing one-dimensional cold atomic gases*, J. Phys. B **37**, S1 (2004).

[172] F.W.J. Hekking and L.I. Glazman, *Quantum fluctuations in the equilibrium state of a thin superconducting loop*, Phys. Rev. B **55**, 6551 (1997).

[173] M. Girardeau, *Permutation Symmetry of Many-Particle Wave Functions*, Phys. Rev. **139**, B500 (1965).

[174] A. Lenard, *Momentum Distribution in the Ground State of the One-Dimensional System of Impenetrable Bosons*, J. Math. Phys. **5**, 930 (1964).

[175] H.G. Vaidya and C.A. Tracy, *One particle reduced density matrix of impenetrable bosons in one dimension at zero temperature*, J. Math. Phys. **20**, 2291 (1979).

[176] M. Jimbo, T. Miwa, Y. Mori, and M. Sato, *Density matrix of an impenetrable Bose gas and the fifth Painlevé transcendent*, Physica D **1**, 80 (1980).

[177] N.M. Bogoliubov, A.G. Izergin, and N.A. Kitanine, *Correlation functions for a strongly correlated boson system*, Nucl. Phys. B **516**, 501 (1998).

[178] D.M. Gangardt, *Universal correlations of trapped one-dimensional impenetrable bosons*, J. Phys. A **37**, 9335 (2004).

[179] V.E. Korepin, N.M. Bogoliubov, and A.G. Izergin. *Quantum inverse scattering method and correlation functions.* Cambridge Univ. Press, 1993.

[180] S. Tomonaga, *Remarks on Bloch's Method of Sound Waves applied to Many-Fermion Problems*, Prog. Theor. Phys. **5**, 544 (1950).

[181] D.C. Mattis and E.H. Lieb, *Exact Solution of a Many-Fermion System and Its Associated Boson Field*, J. Math. Phys. **6**, 304 (1965).

[182] K.B. Efetov and A.I. Larkin, *Correlation functions in one-dimensional systems with a strong interaction*, Sov. Phys. JETP **42**, 390 (1975).

[183] A. Luther and I. Peschel, *Single-particle states, Kohn anomaly, and pairing fluctuations in one dimension*, Phys. Rev. B **9**, 2911 (1974).

[184] L. Amico and V. Korepin, *Universality of the one-dimensional Bose gas with delta interaction*, Ann. Phys. **314**, 496 (2004).

[185] J.-S. Caux, P. Calabrese, and N. Slavnov, *One-particle dynamical correlations in the one-dimensional Bose gas*, J. Stat. Mech. page P01008 (2007).

[186] A. Minguzzi, P. Vignolo, and M.P. Tosi, *High-momentum tail in the Tonks gas under harmonic confinement*, Phys. Lett. A **294**, 222 (2002).

[187] M. Olshanii and V. Dunjko, *Short-Distance Correlation Properties of the Lieb-Liniger System and Momentum Distributions of Trapped One-Dimensional Atomic Gases*, Phys. Rev. Lett. **91**, 090401 (2003).

[188] M.A. Cazalilla, *Low-energy properties of a one-dimensional system of interacting bosons with boundaries*, Europhys. Lett. **59**, 793 (2002).

[189] A. De Martino, M. Thorwart, R. Egger, and R. Graham, *Exact Results for One-Dimensional Disordered Bosons with Strong Repulsion*, Phys. Rev. Lett. **94**, 060402 (2005).

[190] J. Friedel, *Metallic alloys*, Nuovo Cimento Suppl. **7**, 287 (1958).

[191] R. Egger and H. Grabert. In B. Kramer, editor, *Quantum Transport in Semiconductor Submicron Structures*, NATO-ASI Series E. Kluwer, Dordrecht, 1996.

[192] M.D. Girardeau and A. Minguzzi, *Motion of an impurity particle in an ultracold quasi-one-dimensional gas of hard-core bosons*, Phys. Rev. A **79**, 033610 (2009).

[193] P. Vignolo, A. Minguzzi, and M.P. Tosi, *Light scattering from a degenerate quasi-one-dimensional confined gas of noninteracting fermions*, Phys. Rev. A **64**, 023421 (2001).

[194] C.L. Kane and M.P.A. Fisher, *Transport in a one-channel Luttinger liquid*, Phys. Rev. Lett. **68**, 1220 (1992).

[195] M. P. A. Fisher and W. Zwerger, *Quantum Brownian motion in a periodic potential*, Phys. Rev. B **32**, 6190 (1985).

[196] R. Landauer, *Condensed-matter physics: The noise is the signal*, Nature **392**, 658 (1998).

[197] Yu V. Nazarov. *Quantum Noise in Mesoscopic Physics.* NATO Science Series II: Mathematics, Physics and Chemistry. Springer, 2003.

[198] P. A. Bobbert, R. Fazio, G. Schön, and A. D. Zaikin, *Phase transitions in dissipative Josephson chains: Monte Carlo results and response functions*, Phys. Rev. B **45**, 2294 (1992).

[199] K. A. Matveev, A. I. Larkin, and L. I. Glazman, *Persistent Current in Superconducting Nanorings*, Phys. Rev. Lett. **89**, 096802 (2002).

[200] M. Hamermesh. *Group theory.* Addison-Wesley Publishing Company, 1964.

[201] K. E. Nagaev and M. Buttiker, *Ground-state energy fluctuations of a system coupled to a bath*, Europhys. Lett. **58**, 475 (2002).

[202] Milton Abramowitz and Irene A. Stegun. *Handbook of Mathematical Functions with Formulas, Graphs, and Mathematical Tables*, volume 5 of *Applied Mathematics.* National Bureau of Standards, 1964.

[203] U. Weiss and W. Haeffner, *Complex-time path integrals beyond the stationary-phase approximation: Decay of metastable states and quantum statistical metastability*, Phys. Rev. D **27**, 2916 (1983).

[204] F. Reif. *Fundamentals of Statistical and Thermal Physics.* McGraw-Hill Book Company, Inc., 1965.

## L'EFFET JOSEPHSON DANS LES SUPRACONDUCTEURS ET LES GAZ QUANTIQUES

GRÂCE aux avancées techniques récentes, les physiciens jouent pleinement avec la beauté de la mécanique quantique. Dans ce travail de théorie sur l'effet Josephson mésoscopique, nous exploitons les collaborations avec les expérimentateurs ainsi que les échanges entre les communautés des atomes froids et de la matière condensée. Nous considérons différents systèmes basés sur la jonction Josephson, en commençant par sa description quantique dans le régime sous-amorti. En utilisant le formalisme de Keldysh, nous obtenons les caractéristiques courant-tension du régime classique à la limite de température nulle et l'équation de Smoluchowski quantique dans la limite semi-classique. Nous étudions ensuite la dynamique quantique d'un qubit de phase réalisé avec un SQUID dans une configuration inédite où l'échappement se produit à travers deux barrières quartiques. Le taux d'échappement tunnel dans ce nouveau potentiel, calculé avec la technique des instantons, nous permet de décrire les expériences. L'électrodynamique quantique des circuits prévoit qu'un effet laser apparaît lorsqu'un qubit est couplé à une cavité résonnante. Nous considérons le cas d'un qubit de charge et celui d'un transmon qui exploite l'effet Purcell. Avec le Lindbladien nous obtenons la matrice densité dont nous dérivons le spectre du champ créé. Enfin, nous étudions un gaz d'atomes froids dans un piège circulaire comportant une barrière, créant une jonction de Bose Josephson. La physique à basse énergie est décrite à travers les fonctions de corrélation avec la théorie du liquide de Luttinger. Nous montrons que les fluctuations quantiques dans l'anneau induisent une renormalisation de l'énergie Josephson.

## THE JOSEPHSON EFFECT IN SUPERCONDUCTORS AND QUANTUM GASES

WITH the recent technical breakthroughs, physicists fully play with the beauty of quantum mechanics. In this theoretical work on the mesoscopic Josephson effect, we take advantage of the collaborations with experimentalists as well as the exchanges between the cold atoms and condensed matter communities. We consider various systems based on the Josephson junction, beginning with its quantum description in the underdamped regime. Using the Keldysh formalism, we obtain the current-voltage characteristics from the classical to the zero temperature regime and the quantum Smoluchowski equation in the quasi-classical limit. We then study the quantum dynamics of a phase qubit realized with a SQUID in a novel configuration where tunneling events occur through two quartic barriers. The escape rate in this camel-back potential, calculated with the instantons technique, allows us to describe the experiments. Circuit quantum electrodynamics predicts that a lasing effect appears when a qubit is coupled to a resonant cavity. We consider the case of a charge qubit and also that of a transmon which exploits the Purcell effect. With the Lindbladian we obtain the density matrix from which we derive the spectrum of the output field. Finally, we study a gas of cold atoms in a ring shape trap comprising a barrier, thus creating a Bose Josephson junction. The low energy physics is described through the correlation functions with the Luttinger liquid theory. We show that the quantum fluctuations in the ring induce a renormalization of the Josephson energy.